



Micro-cartographie P-T-” dans les roches métamorphiques. Applications aux Alpes et à l’Himalaya

Pierre Lanari

► To cite this version:

Pierre Lanari. Micro-cartographie P-T-” dans les roches métamorphiques. Applications aux Alpes et à l’Himalaya. Sciences de la Terre. Université de Grenoble, 2012. Français. NNT : 2012GRENU033 . tel-00799283

HAL Id: tel-00799283

<https://theses.hal.science/tel-00799283>

Submitted on 20 Mar 2013

HAL is a multi-disciplinary open access archive for the deposit and dissemination of scientific research documents, whether they are published or not. The documents may come from teaching and research institutions in France or abroad, or from public or private research centers.

L’archive ouverte pluridisciplinaire **HAL**, est destinée au dépôt et à la diffusion de documents scientifiques de niveau recherche, publiés ou non, émanant des établissements d’enseignement et de recherche français ou étrangers, des laboratoires publics ou privés.

THÈSE

Pour obtenir le grade de

DOCTEUR DE L'UNIVERSITÉ DE GRENOBLE

Spécialité : **Sciences de la Terre, de l'Univers, et de l'Environnement**

Arrêté ministériel : 7 août 2006

Présentée par

Pierre LANARI

Thèse dirigée par **Olivier Vidal**

et codirigée par **Stéphane Schwartz**

préparée au sein de **l'institut des Sciences de la Terre de Grenoble (ISTerre)**
et de **l'Ecole doctorale Terre Univers Environnement (TUE)**

Micro-cartographie P-T- ϵ dans les roches métamorphiques. Applications aux Alpes et à l'Himalaya.

Thèse soutenue publiquement le **26 Octobre 2012**,
devant le jury composé de :

M. Peter van der Beek

Professeur, Université de Grenoble, Président

M. Martin Engi

Professeur, University of Bern, Rapporteur

M. Roland Oberhänsli

Professeur, University of Potsdam, Rapporteur

M. Thomas Wagner

Professeur, University of Helsinki, Examineur

M. Philippe Goncalves

Maître de conférences, Université de Besançon, Examineur

M. Olivier Vidal

Directeur de recherche, Université de Grenoble, Directeur de thèse

M. Stéphane Schwartz

Maître de conférences, Université de Grenoble, Co-Directeur de thèse



Université de Grenoble
l'Institut des Sciences de la Terre de Grenoble (ISTerre)

Thèse

présentée à
l'Université de Grenoble
pour obtenir le grade de
Docteur de l'Université de Grenoble
spécialité « Sciences de la Terre, de l'Univers et de l'Environnement »
par

Pierre Lanari

Micro-cartographie P-T- ϵ dans les roches métamorphiques. Applications aux Alpes et à l'Himalaya.

Thèse soutenue publiquement le 26 Octobre 2012 devant le jury composé de :

M. MARTIN ENGI	Professeur, Univ. Bern	(Rapporteur)
M. ROLAND OBERHÄNSLI	Professeur, Univ. Potsdam	(Rapporteur)
M. THOMAS WAGNER	Professeur, Univ. Helsinki	(Examineur)
M. PHILIPPE GONCALVES	Maître de conférences, Univ. Besançon	(Examineur)
M. PETER VAN DER BEEK	Professeur, Univ. Grenoble	(Président)
M. OLIVIER VIDAL	Directeur de recherche, Univ. Grenoble	(Directeur de thèse)
M. STÉPHANE SCHWARTZ	Maître de conférences, Univ. Grenoble	(Directeur de thèse)

- *C'est notre métier, à nous, d'étudier les pierres de cette montagne,
comme toi d'y garder tes moutons.*

- *Et l'autre montagne, là-bas de l'autre côté de la vallée ?*

- *Aussi, nous y monterons ce soir. Ça t'étonne ? Mais c'est ainsi.
Après une montagne nous en escaladons une autre,
et une autre encore : c'est notre métier !*

- *Eh bien, c'est un métier de fou ...*¹

1. Récit d'une rencontre entre deux géologues catalans et un petit berger (XIXe) d'après Cailleux (1961) - Histoire de la Géologie.

Remerciements

C'est au moment d'achever ce formidable projet que je me rend compte que ce travail de thèse n'aurait jamais pu aboutir de cette manière sans l'aide et le soutien de nombreuses personnes. Je tiens donc à les remercier chaleureusement ici.

Pour débiter, je souhaite remercier mes deux fantastiques directeurs de thèse, Olivier Vidal et Stéphane Schwartz, pour leur encadrement et leur soutien indéfectible durant de ces trois années. Grâce à vous, cette aventure a vraiment été fantastique. Merci à toi, Olivier, pour m'avoir initié aux joies et parfois aux peines de la thermodynamique que tu m'as fait découvrir avec une immense passion et toujours une grande disponibilité. Je pense avoir maintenant attrapé le virus à ton contact et j'espère être digne de porter les couleurs de la «Vidal's team». Un immense merci à toi, Stéphane, pour ta disponibilité et pour toutes les connaissances des Alpes occidentales que tu as toujours su partager avec moi.

Je tiens maintenant à exprimer mes plus profonds remerciements à mon jury de thèse pour avoir accepté de juger ce travail. Merci à mes deux rapporteurs, Martin Engi et Roland Oberhänsli, ainsi qu'aux examinateurs, Thomas Wagner, Yann Rolland, Philippe Goncalves et Peter van der Beek. J'espère que la lecture de ce manuscrit vous aura été des plus agréable.

Ce travail de thèse est le résultat de nombreuses collaborations avec des membres du laboratoire LGCA fusionné dans ISTerre en 2011. Je souhaite tout d'abord remercier Stéphane Guillot pour m'avoir accueilli à Grenoble en M1 et pour m'avoir, depuis, toujours accompagné et suivi de prêt. Un grand merci à Pierre Tricart pour ses nombreux conseils et son incroyable connaissance de la géologie des Hautes Alpes, à Éric Lewin pour la résolution de problèmes numériques et mathématiques complexes, à Anne-Marie Boullier pour ses conseils et son intérêt toujours très chaleureux à mon travail et enfin à Emilie Janots, pour sa joie de vivre et pour m'avoir toujours fait partagé ses grandes connaissances en pétrologie métamorphique. J'ai également eu la chance de collaborer avec de nombreux chercheurs d'autres laboratoires. Je remercie chaleureusement Thomas Wagner, pour m'avoir accueilli à l'ETH Zurich et m'avoir fait découvrir un autre formalisme thermodynamique ; Benoit Dubacq pour m'avoir fourni ses propres programmes Matlab qui ont été indispensables à la réalisation de ce travail ainsi que pour son assistance lors de nombreux échanges par email sur la partie thermodynamique de cette thèse ; Yann Rolland, pour son implication dans la partie radiochronologique de ce travail et pour son aide, très utile, dans certaines interprétations pétrologiques ; Céline Martin, pour son énergie et ses nombreuses idées pour utiliser l'approche cartographique dans l'étude des roches «extra-terrestres» ; Amaury Pourteau, pour m'avoir impliqué dans son travail et pour son aide à Potsdam ; Irene Cantarero, pour sa patience et sa gentillesse lors du traitement des couples chlorite-phengite de ses échantillons ; Alexandra Robert, pour son éternelle bonne humeur et sa pas-

sion de la pétrologie ; Philippe Agard et Michael Jentzer, pour leur aide en nous fournissant des données microsondes sur des échantillons passionnants et Vincent De Andrade pour avoir toujours porté un intérêt à mon travail.

Au cours de ces trois années, j'ai eu l'occasion et le plaisir d'encadrer ou de co-encadrer plusieurs étudiants de Master, et je souhaite les remercier ici pour leur implication et pour les nombreuses améliorations, en particulier des programmes, qui résultent de leurs travaux. Un grand merci donc à mes deux M1, Blandine Gardonio et Félix Bernier, pour leur passion de la recherche, même avec des échantillons «peu favorables». Merci également à Chloé Loury, Matthieu Dupuis et Benjamin Sauter pour leur entrain tout au long des nombreuses étapes pour l'estimation des conditions P-T.

Pour les côtés plus techniques de ce travail, un grand merci à Fayçal Soufi pour la préparation de nombreuses lames minces dans des lithologies difficiles, à Jean-Luc Devidal, François Bussy, Christina Günter et Frédéric Couffignal, pour leur accompagnement sur les différentes microsondes où j'ai eu la chance d'acquérir des données. Enfin, cette thèse a eu son lot de bricolages divers et de tentatives plus ou moins abouties, et pour ça je souhaite remercier pour leur aide Matthieu Corazzi et Nathaniel Findling.

Les différents membres administratifs et techniques du laboratoire, de l'école doctorale et de l'Université Joseph-Fourier qui ont toujours su me faciliter les nombreuses démarches administratives doivent être remerciés ici. En particulier, Rodolphe Pinon, notre maître informaticien, pour la résolution des problèmes informatiques inhérent à tout travail de recherche, même depuis le Japon. Merci également à Christine Bigot, France Blanc, Félicette Boero, Marie Corminier, Claudine Meugniot, Jacques Pellet, Abderrahman Salhi et Claudie Senebier. Un immense merci à notre bibliothécaire, Pascale Talour, qui a toujours su me trouver les références que je cherchais et ce dans les plus brefs délais.

Cette thèse a pu se dérouler dans les meilleures conditions grâce aux différents collègues que j'ai eu la chance de côtoyer à ISTerre. Ces trois années peuvent être résumées en un seul mot, convivialité. Un grand merci donc aux enseignants chercheur et chercheurs de l'équipe «TRB», Mathias Bernet, Thierry Dumont, Christophe Basile, Jean Braun, Etienne Jaillard, Arnaud Pêcher, Anne Replumaz, Laurence Audin, Fabienne Giraud, Pascale Huyghe Julien Carcaillet, Abir Chihaoui de l'équipe «minéralogie», Fabrice Brunet, Manu Munoz et German Montes-Hernandez et de l'équipe «géochimie» Catrine Chauvel, Nick Arndt, Carole Cordier et Alexanra Gourlan ainsi que nos deux PRAG, Jérôme Nomade et Marie Dubernet. Parmi les nombreux étudiants en thèse maintenant, je remercie chaleureusement Nicolas Riel, co-bureau et co-signataire, ami et soutien dans les moments de doute ; Morgane Ledevin et Marion Garçon, mes deux formidables acolytes depuis maintenant cinq années ; Yohann Poprawski, Charlotte Fillon et

Violaine Vignon du cru précédent, Romain Lafay, Jonathan Mercier Karim Malamoud et Adrien Boissard de celui de l'année prochaine, mais également Andy Rathbun et Thibault Candela, deux super co-bureaux. Merci également à Christophe Robin, Marc Ulrich, Romain Jolivet, Florent Gimbert, Sébastien Jourdan et Benjamin Malvoisin Mélanie Nouri, Rachel Abrahami. Je tiens également à remercier pour l'ambiance et la bonne humeur les nombreux étudiants des différentes promotions de M2R qui sont passés par le dernier étage de la maison des Géosciences... Un grand merci à Xavier Robert pour le template Latex qui m'a tant fait gagner de temps dans les dernières semaines de rédaction. Enfin une mention spéciale à tous ceux que j'aurais malencontreusement oubliés dans cette liste non exhaustive.

Je dédie ce travail à Jean-Michel Bertrand, qui nous a quitté le vendredi 18 mars 2011. Il m'a transmis sa passion pour l'étude des zones métamorphiques, en particulier dans les Alpes de Savoie qu'il arpentait depuis une cinquantaine d'années. Tout particulièrement sans lui, je n'en serai pas là.

Pour conclure cette grande tirade, je remercie mes amis et ma famille qui m'ont beaucoup soutenu tout au long de cette grande aventure et enfin Camille pour son amour, son aide et son soutien inébranlable au jour le jour.

Entre Chambéry et Grenoble, le 30 septembre 2012

Résumé

L'étude de la dynamique de la lithosphère, en particulier les processus de transports verticaux et horizontaux de matière, requiert de pouvoir reconstruire avec la plus grande précision l'évolution géodynamique des chaînes de montagne. C'est le rôle des trajets pression-température-temps-déformation (P-T-t- ϵ) qui permettent, pour un fragment de roche, de reconstruire son histoire à partir de l'étude texturale et chimique des minéraux métamorphiques à l'équilibre. En effet, les roches métamorphiques présentent des mosaïques de paléo-équilibres thermodynamiques locaux entre des minéraux de paragenèses qui cristallisent à différentes conditions de pressions et de températures. Le problème abordé dans ce mémoire est celui de la reconstruction des trajets pression-température, en combinant l'utilisation d'approches thermobarométriques directes, comme les pseudosections calculées par minimisation d'énergie, et indirectes, comme la technique du multi-équilibre avec une vision en deux dimensions grâce à une approche micro-cartographique. Cependant, l'utilisation conjointe de techniques d'imagerie chimiques et d'estimations thermobarométriques requiert un grand nombre de calculs, et donc des logiciels conviviaux à la disposition de la communauté. Dans cette thèse, nous proposons des programmes pour la cartographie et les calculs thermodynamiques, puis un nouveau modèle de solution solide pour les chlorites et, enfin, des exemples d'applications dans les Alpes et en Himalaya.

Nous avons développé un jeu de programmes écrits en MATLAB©, qui permettent (1) de traiter des images chimiques et de calculer des cartes pression-température : XMAPTOOLS, et (2) de chercher des équilibres thermodynamiques et de tracer des réactions chimiques : PT-LINES, MULTIPLOT et MEAMP. Un modèle de solution solide pour les chlorites a été proposé en ajoutant un pôle pur di-trioctahédriques. Ce modèle permet de calculer, par minimisation d'énergie, des pseudosections à basse température, ou encore de modéliser des interactions fluide-roche. Dans un deuxième temps, nous proposons d'appliquer les techniques de micro-cartographie et de thermobarométrie à des exemples naturels variés afin d'essayer d'apporter des contraintes supplémentaires pour reconstruire des modèles d'évolutions géodynamiques des chaînes de subduction-collision. Pour les Alpes, des trajets P-T- ϵ et P-T-t ont été proposés pour des unités où jusqu'ici, faute de techniques disponibles, les estimations étaient basées uniquement sur la présence de minéraux index du métamorphisme. Ces nouvelles données ont permis de mettre en évidence un fort couplage entre l'exhumation du prisme océanique et l'écaillage crustal de la plaque continentale subduite. Pour l'Himalaya, nous avons montré qu'il est possible de reconstruire un trajet pression-température continu à partir d'images chimiques en utilisant notre nouvel outil : XMAPTOOLS

Mots-clés *Thermodynamique, Micro-cartographie, Estimations P-T, Phyllosilicates, Alpes occidentales, Himalaya*

Abstract

The study of the lithosphere dynamics such as vertical and horizontal material transport processes requires the detailed reconstruction of the geodynamic evolution of the mountain belts. These geodynamic models are classically constrained using pressure-temperature-time-deformation (P-T-t- ϵ) paths unravelled from textural and chemical study of metamorphic rocks fragments. Metamorphic rocks are made by mosaic of local thermodynamic equilibria involving minerals that grew at different temporal, pressure, and temperature conditions. The topic of this thesis is the reconstruction of pressure-temperature paths by combining direct techniques such as pseudosection computed by energy minimization and inverse techniques such as multi-equilibrium, in space, i.e. two-dimensions, using a micro-mapping approach. The use of chemical images and thermodynamic modelling requires user-friendly programs freely available for the community. In this thesis, we first propose a set of programs and a new solid solution model for chlorite and also two application examples are proposed in the Alps and the Himalaya.

We propose a set of programs written in MATLAB® (1) for microprobe image processing and the computation of pressure temperature maps : XMAPTOOLS, (2) for multi-equilibrium calculations using different thermodynamic data and solid solution models : PT-LINES, MULTIPLOT and MEAMP. A new solid solution model for chlorite is presented including a di-trioctahedral chlorite end-member. This model can be used to calculate pseudosection phase diagrams and for fluid-rock interaction modelling. Thermodynamic modelling and micro-mapping techniques are used together to add new constraints to the geodynamic models of subduction-collision mountain belts. In the French Western Alps, P-T- ϵ and P-T-t paths are recovered for some metamorphic units in which the available estimates were only based on the occurrence of index minerals. These new thermobarometric and radiometric data indicate a strong coupling between the exhumation of the oceanic accretionary wedge and the continental subducting plate. In The Himalaya, we studied a new eclogite occurrence and we propose a detailed and continuous P-T path calculated using our newly created program XMAPTOOLS.

Keywords *Thermodynamics, Micro-mapping, P-T estimates, Phyllosilicates, Western Alps, Himalaya*

TABLE DES MATIÈRES

Table des matières	xiii
1 Introduction générale	1
2 Estimations P-T et thermodynamique des phyllosilicates	11
2.1 Introduction : estimations P-T et phyllosilicates	13
2.1.1 Intérêt de la reconstruction des trajets P-T	13
2.1.2 Minéraux index et faciès métamorphiques	14
2.1.3 Rappels de thermodynamique à l'équilibre	15
2.1.3.1 Equation générale de l'énergie libre de Gibbs d'une réaction	16
2.1.3.2 Stabilité des minéraux et réactions métamorphiques	17
2.1.3.3 Equilibre thermodynamique à l'échelle de la lame mince	18
2.1.4 Approches de type « thermobarométrie classique »	19
2.1.4.1 Calibration empirique	19
2.1.4.2 Exemple : thermomètre chlorite-chloritoïde	20
2.1.5 Approches non empiriques	21
2.1.5.1 L'approche directe	22
2.1.5.2 L'approche inverse	23
2.1.6 L'intérêt des phyllosilicates	23
2.2 Approche inverse et multi-équilibres	25
2.2.1 Introduction	25
2.2.1.1 Modèles disponibles	25
2.2.1.2 Stratégie	29
2.2.2 Formalisme thermodynamique	30
2.2.2.1 Base de données thermodynamiques inter-cohérentes	30
2.2.2.2 Logiciels de calcul	30

2.2.2.3	Modèles d'activités	31
2.2.2.4	Pôles purs et réactions	31
2.2.3	Article 1 : Comment on "The role of H_3O^+ in the crystal structure of illite" by F. Nieto, M. Melini, and I. Abad (published in <i>Clays and Clay Minerals</i>)	33
2.2.3.1	Introduction	33
2.2.3.2	Conclusion	38
2.2.4	Evolution of the Vallès fault from chlorite and mica equilibrium	39
2.2.4.1	Introduction	41
2.2.4.2	Results	42
2.2.4.3	Discussion	45
2.2.4.4	Conclusions	47
2.2.4.5	Acknowledgements	48
2.2.5	Etude de l'incertitude du thermomètre Chl+Qtz+ H_2O ($T < 350^\circ C$)	49
2.2.6	Limites du thermomètre Chl+Qtz+ H_2O à HT ($T > 350^\circ C$)	51
2.2.7	Logiciel 1 - PTLINES	53
2.2.7.1	Modèles Phg+Qtz+ H_2O et Chl+Qtz+ H_2O : lignes d'équilibres	55
2.2.7.2	PTlines	56
2.2.8	Logiciel 2 - MULTIPLOT	58
2.2.8.1	Mode Chl + Qtz + H_2O	59
2.2.8.2	Mode Multi	61
2.3	Approche directe et pseudosections	65
2.3.1	Introduction	65
2.3.1.1	Modèles disponibles	66
2.3.1.2	Stratégie	66
2.3.2	Formalisme thermodynamique	68
2.3.2.1	Base de données thermodynamiques inter-cohérentes	68
2.3.2.2	Logiciels de calcul	68
2.3.2.3	Modèles d'activités	69
2.3.2.4	Pôles purs et réactions	69

2.3.3	Article 2 : A thermodynamic model for di-trioctahedral chlorite from experimental and natural data in the system MgO-FeO-Al ₂ O ₃ -SiO ₂ -H ₂ O. Applications to pseudosections, geothermometry and fluid-mineral equilibria modeling (to be submitted to <i>Contributions to Mineralogie and Petrology</i>)	71
2.3.3.1	Introduction	73
2.3.3.2	New thermodynamic model for chlorite : <i>Chl(LWV)</i>	76
2.3.3.3	Model calibration	80
2.3.3.4	Results	86
2.3.3.5	A new semi-empirical geothermometer	89
2.3.3.6	Applications and discussion	91
2.3.3.7	Conclusions	98
2.3.3.8	Acknowledgments	99
2.3.3.9	Appendix : From structural formulae to composition variables	99
2.3.3.10	Appendix : Coding of the the <i>Chl(LWV)</i> model for <i>Perple_X</i>	100
2.3.3.11	Appendix : New sudoite thermodynamic standard state properties in 'hp02.ver'	101
2.3.4	Logiciel 3 - MEAMP	101
2.3.5	Discussion : formalisme de Holland et Powell, exemple des chlorites	101
2.3.5.1	Extension du modèle aux chlorites siliceuses et paramètre d'ordre	102
2.3.5.2	Relations internes et propriétés standards	111
2.4	Conclusions et Perspectives	115
3	Cartographie chimique	117
3.1	Imagerie chimique à l'échelle de la lame mince	119
3.1.1	Microsonde électronique	119
3.1.2	Cartographie WDS	122
3.1.3	Standardisation des cartes d'intensités	123
3.1.4	Avantages de la cartographie WDS	125

3.1.5	Protocole d'acquisition et recommandations	129
3.1.5.1	Image BSE, résolution et durée d'acquisition	130
3.1.5.2	Durée d'analyse	132
3.1.5.3	Analyses ponctuelles pour la standardisation	132
3.1.5.4	Discussion sur l'ordre d'acquisition	133
3.1.6	Traitement des données	134
3.2	Article 3 : XMAPTOOLS a Matlab©-based graphic user interface for microprobe X-ray images processing (submitted to Computers and Geosciences)	135
3.2.1	Introduction	137
3.2.2	Description of the program	138
3.2.2.1	Raw data treatment (Xray)	139
3.2.2.2	Calculations from quantified data (Quanti)	142
3.2.2.3	Chemical plots	146
3.2.2.4	Others functions	146
3.2.3	Tests and evaluation	148
3.2.3.1	Data acquisition	148
3.2.3.2	From X-ray intensities to map of composition	148
3.2.3.3	Precision and resolution of quantification	152
3.2.3.4	Combined P and T functions : P-T maps of Cpx	153
3.2.4	Concluding remarks	155
3.2.5	Acknowledgments	157
3.2.6	Appendix : User Notice	157
3.3	Article 4 : REE and Hf distribution among mineral phases in the CV- CK clan : a way to explain ϵ Hf heterogeneities in CHUR (submitted to Geochimica and Cosmochimica Acta)	158
3.3.1	Introduction	160
3.3.2	Meteorites samples, preparation and analytical techniques	163
3.3.2.1	Samples preparation	163
3.3.2.2	Analytical techniques	164
3.3.3	Results	167
3.3.3.1	Samples petrology	167

3.3.3.2	In situ trace-elements data	171
3.3.3.3	Whole-rock analyses	173
3.3.3.4	Mass balance calculations	173
3.3.3.5	Trace-element patterns	179
3.3.4	Discussion	183
3.3.4.1	Mineralogy abundances and evolution during metamorphism	183
3.3.4.2	Are phosphates the key to explain Lu-Hf whole-rock discrepancies ?	186
3.3.4.3	Have CK and CV chondrites a close origin ?	189
3.3.5	Summary and Conclusions	191
3.3.6	Acknowledgments	193
3.4	Conclusions et perspectives	194
4	Application aux Alpes occidentales	197
4.1	Introduction : les Alpes occidentales	199
4.1.1	Généralités sur la partie occidentale de la chaîne alpine	199
4.1.2	Bref historique des études géologiques des Alpes françaises	203
4.1.2.1	Stratigraphie et déformations alpines	203
4.1.2.2	Métamorphisme	206
4.1.2.3	Études récentes	207
4.2	Etude des unités briançonnaises	210
4.2.1	Introduction	210
4.2.1.1	Données disponibles sur le métamorphisme	210
4.2.1.2	Stratégie	210
4.2.2	Article 5 : Diachronous evolution of the alpine continental subduction wedge : Evidence from P-T estimates in the Briançonnais Zone houillère (France - Western Alps) (Published in Journal of Geodynamics).	212
4.2.2.1	Introduction	214
4.2.2.2	Geological setting	218
4.2.2.3	Sampling	223
4.2.2.4	Analytical and thermobarometric methods	225

4.2.2.5	Thermobarometric results	229
4.2.2.6	Discussion	235
4.2.2.7	Conclusion	243
4.2.2.8	Acknowledgments	244
4.2.3	Etude des micas blancs de l'écaille de Vautisse	245
4.2.4	Article 6 : P-T-t estimation of syn-kinematic strain in low-grade rocks (< 300°C) using thermodynamic modelling and $^{40}\text{Ar}/^{39}\text{Ar}$ dating techniques : example of the Plan-de-Phasy shear zone (Briançonnais Zone, Western Alps). (Submitted to Terra Nova)	248
4.2.4.1	Introduction	249
4.2.4.2	Geological setting	251
4.2.4.3	Petrological and chemical studies	253
4.2.4.4	P-T estimates	255
4.2.4.5	Ar-Ar phengite dating	256
4.2.4.6	Discussion and geodynamic implications	257
4.2.4.7	Conclusion	259
4.2.4.8	Acknowledgements	259
4.3	Premiers résultats sur l'étude du complexe des Schistes lustrés du Queyras	260
4.3.1	Introduction	260
4.3.1.1	Schistes lustrés du Queyras	260
4.3.1.2	Métamorphisme	262
4.3.1.3	Stratégie	262
4.3.2	Etude Raman de la matière carbonée	264
4.3.3	Zone MT-BS : Affleurement du Gouret	266
4.3.3.1	Etude minéralogique	267
4.3.3.2	Etude thermobarométrique	269
4.3.4	Zone HT-BS : Arkose de Roca Nera	273
4.3.4.1	Etude Minéralogique	275
4.3.4.2	Circulation fluide et recristallisation tardive	276
4.3.4.3	Etude thermobarométrique	276

4.3.5	Nouvelles données radiochronologiques	280
4.3.5.1	Affleurement du Gouret - zone MT-BS	280
4.3.5.2	Affleurement de l'Arkose de Roca Nera - zone HT-BS	282
4.4	Synthèse et perspectives	283
4.4.1	Méthodologie	283
4.4.2	Synthèse	283
4.4.3	Perspectives	286
5	Application à l'Himalaya	291
5.1	Introduction : éclogites et Himalaya	293
5.1.1	Chaîne himalayenne et éclogites	293
5.1.2	Massif de Stak	295
5.1.3	Stratégie	297
5.2	Article 7 : Deciphering high-pressure metamorphism in collisional context using microprobe-mapping methods : Application to the Stak eclogitic massif (NW Himalaya). (In press, Geology)	298
5.2.1	Introduction	300
5.2.2	Geological setting and sample description	301
5.2.3	Microprobe mapping and treatment methods	302
5.2.4	Chemical and thermobarometry results	303
5.2.5	Metamorphic and tectonic implications	306
5.2.6	Acknowledgments	308
5.2.7	Supplementary material	309
5.2.7.1	Uncertainties on P-T estimates	309
5.2.7.2	Supplementary figures	309
5.2.7.3	Supplementary tables	314
6	Conclusion générale	317
	Bibliographie	323
A	Annexes	357
A.1	Thermodynamique	359
A.1.1	Calcul de G^0 (formalisme de Berman et Brown)	359
A.1.2	Calcul de G^0 (formalisme de Holland et Powell)	360

A.1.3	Réactions internes et relations internes	362
A.2	Logiciel MEAMP	367
A.2.1	Mode « Plot »	367
A.2.2	Mode « Minim »	368
A.3	Modèle Clay	373
A.4	XMapTools - User Notice	395
A.5	Articles supplémentaires	443
A.5.1	Article 8 : Guillot et al., (in press), Lithos	444
A.5.2	Article 9 : Pourteau et al. (in revision), Journal of Metamor- phic Geology	459
A.5.3	Article 10 : Riel et al., (in press), Lithos	489

INTRODUCTION GÉNÉRALE

1

Les chaînes de montagnes sont les principaux marqueurs topographiques des limites de plaques en convergence et résultent de l'évolution dynamique de la lithosphère associée à de la déformation et à du métamorphisme ([Hamilton 1969](#), [Coney 1970](#), [Dewey 1970](#), [Coney 1972](#)). Ces zones sont donc particulièrement adaptées à l'étude de la tectonique des plaques et des processus à l'origine des transports verticaux et horizontaux de matière à l'échelle lithosphérique. Cependant, ces investigations sont possibles uniquement si l'on possède une image du trajet suivi par les roches dans la lithosphère et que l'on peut donc reconstruire un modèle d'évolution géodynamique. C'est le rôle des chemins Pression-Température-temps (P-T-t) qui permettent de reconstruire, pour un échantillon donné, son trajet durant les différents épisodes de formation de la chaîne de montagne. Pour obtenir de tels trajets, il faut étudier en détail les roches métamorphiques qui sont issues de la transformation de roches préexistantes en réponse à des changements de conditions physico-chimiques du milieu. Cependant, en raison des limites cinétiques des réactions métamorphiques, une roche ne se ré-équilibre presque jamais entièrement lors d'un seul événement métamorphique et préserve donc des mosaïques d'équilibres locaux atteints à différents temps de son histoire, soit à différents "points" du trajet Pression-Température (P-T).

Différentes méthodes thermobarométriques sont à la disposition du pétrologue pour estimer les conditions P-T enregistrées par les roches métamorphiques (e.g. [Spear 1993](#), [Vidal et al. 2006](#), [Powell 2008](#)). Ces conditions sont enregistrées par les différentes paragénèses (assemblage de minéraux en équilibre thermodynamique à certaines conditions P-T) observables au sein d'un échantillon naturel. Afin de relier les observations des échantillons naturels et les conditions P-T enregistrées par les différentes paragénèses, il est possible d'utiliser un formidable outil : la thermodynamique. L'objectif *in fine* sera de relier les conditions P-T de ces différentes paragénèses avec des événements tectoniques majeurs, comme par exemple les phases d'enfouissement ou d'exhumation durant un épisode de subduction.

Trois principales approches peuvent être utilisées pour reconstruire des conditions P-T pour une paragénèse donnée. La première approche, qui est à l'heure actuelle la plus utilisée par les pétrologues, peut être appelée « approche directe ».

En utilisant la composition de la roche totale de l'échantillon il est possible de calculer, par minimisation d'énergie, la paragénèse (association de minéraux avec la plus basse énergie de Gibbs) la plus stable pour des conditions P-T données et ensuite de comparer le résultat avec les assemblages minéralogiques observés dans l'échantillon. La seconde approche suit une philosophie inverse, qui consiste à calculer les conditions P-T d'équilibres d'une paragénèse observée en utilisant les compositions chimiques des minéraux qui la constitue. Avec ce type d'approche, les conditions P-T sont estimées en se basant sur la position P-T d'un ou plusieurs équilibres minéralogiques, calculées en utilisant des calibrations empiriques ou avec un calcul thermodynamique complet comme la technique des multi-équilibres (Berman 1991, Lieberman et Petrakakis 1991). La troisième approche vise à relier les estimations P-T et la déformation (De Andrade 2006, De Andrade et al. 2006, Vidal et al. 2006) en utilisant des cartes chimiques acquises à la microsonde qui sont transformées en cartes P-T. Cette approche « micro-cartographique » est similaire à l'approche inverse, mais elle utilise des images chimiques qui permettent de visualiser les paléo-équilibres locaux et de valider les choix de paragénèses et les relations avec la déformation et donc avec les interprétations géodynamiques.

Classiquement, les métapélites sont peu utilisées pour la caractérisation des conditions P-T et les pétrologues leur préfèrent les roches basiques. Cependant, les phyllosilicates des métapélites sont de très bons indicateurs des conditions P-T, car leur composition varie de manière significative avec ces conditions, même à basse température. Plusieurs modèles de solutions solides pour les phyllosilicates ont été développés ces dernières années (Vidal et al. 2001, Parra et al. 2002a, Vidal et al. 2005; 2006, Dubacq et al. 2010), et ont été essentiellement utilisés avec l'approche inverse du multi-équilibre (Trotet et al. 2001, Parra et al. 2002b, Ganne et al. 2003, Augier et al. 2005b, Rimmelé et al. 2006, Grosch et al. 2012), puis avec l'approche micro-cartographique (De Andrade 2006, Vidal et al. 2006, Yamato et al. 2007, Dubacq 2008, Ganne et al. 2012, Lanari et al. 2012a).

Cependant, l'utilisation conjointe des techniques de micro-cartographie chimique et des multi-équilibres est relativement limitée, en l'absence de logiciels

conviviaux à disposition de la communauté. En effet, le traitement des images chimiques brutes de la microsonde et leur transformation en cartes P-T nécessite un grand nombre de calculs. La technique des multi-équilibres nécessite de calculer la position dans un champ P-T de nombreux équilibres chimiques pour de grands jeux de compositions. De plus, les modèles pour les phyllosilicates cités précédemment ont été développés pour être utilisés principalement avec la technique du multi-équilibre et permettent de travailler dans des zones de chaînes de montagnes où aucune estimation P-T n'était disponible. C'est en particulier le cas des zones de BT, ce qui ouvre ainsi de nombreuses perspectives d'applications. D'un point de vue plus théorique, il est nécessaire de faire le lien entre les modèles développés pour des approches inverses et l'approche directe de minimisation d'énergie, afin de pouvoir améliorer la qualité des pseudosections à BT.

Le premier objectif de cette thèse a été d'apporter de nouveaux outils (i.e. logiciels) et de nouvelles méthodes (i.e. modèle de solution solide) pour l'estimation de trajets P-T et de micro-cartographies P-T dans les roches métamorphiques. Le deuxième objectif était d'appliquer les techniques de micro-cartographie et/ou de thermobarométrie à des exemples naturels variés, afin de répondre à des problématiques géologiques, comme l'évolution tectono-métamorphique des chaînes de montagnes, comme les Alpes et l'Himalaya, ou encore l'évolution des proportions de phases et de leurs concentrations dans les chondrites.

Au cours de ces trois années, mon travail a consisté à :

(1) Extraire des données thermodynamiques et des paramètres de solutions solides pour les chlorites avec la calibration d'un nouveau modèle $Chl(LWV)$ compatible avec la base thermodynamique intercohérente de [Holland et Powell \(1998\)](#) qui est utilisée dans les programmes de minimisation d'énergie comme *Perple_X* ([Connolly et Kerrick 1987](#), [Connolly 1990; 2005; 2009](#)) ou encore *GEM-Selektor* ([Kulik et al. in press](#), [Wagner et al. in press](#)). La compilation de données naturelles de la littérature effectuée pour contraindre le modèle m'a permis, dans un deuxième temps, de dériver une nouvelle calibration empirique pour calculer les

températures de cristallisations de chlorites en équilibre avec du quartz et de l'eau. Cette partie du travail a été réalisée en collaboration avec T. Wagner de l'ETH Zurich.

(2) Concevoir un logiciel de calcul thermodynamique pour l'ajustement de paramètres thermodynamiques ou de solutions solides en utilisant de large jeux de contraintes expérimentales ou de données naturelles compatibles avec le formalisme et la base de données thermodynamiques de (Holland et al. 1998) : Logiciel MEAMP.

(3) Concevoir deux logiciels pour faire des calculs de multi-équilibre en utilisant le formalisme et la base de données thermodynamiques de Berman (1988) qui permettent de traiter de grands jeux de données : PTLINES et MULTIPLOT. Ces logiciels ont été développés à partir d'une série de fonctions de thermodynamique fonctionnant sous MATLAB© initialement programmées par Benoît Dubacq, Vincent De Andrade, Éric Lewin et Olivier Vidal.

(4) Concevoir un programme convivial pour le traitement des données microsondes : XMAPTOOLS (disponible en téléchargement libre à l'adresse suivante : <http://www.xmaptools.com>). Ce programme permet de transformer les images chimiques mesurées par microsonde en cartes de concentrations, puis en microcartographies P-T en utilisant un large jeu de calibrations empiriques tirées de la littérature.

(5) Réaliser un échantillonnage de différentes zones internes des Alpes occidentales : Zone houillère ; Zone Briançonnaise ; Zone liguro-piémontaise et d'appliquer les techniques couplées de micro-cartographie et de multi-équilibre pour identifier des conditions P-T. Pour certains échantillons des datations $^{39}\text{Ar}/^{40}\text{Ar}$ sur phengites ont été réalisées en collaboration avec Yann Rolland de l'Université de Nice.

(6) Utiliser les programmes développés pour aider à résoudre des problèmes géologiques. (1) XMAPTOOLS a été utilisé pour calculer des cartes P-T pour un échantillon provenant d'un nouveau massif éclogitique découvert dans la syntaxe NW

himalayenne (travail réalisé en collaboration avec Nicolas Riel et Stéphane Guillot d'ISTerre Grenoble), et pour calculer des cartes de phases minéralogiques et déterminer les abondances modales dans des échantillons de chondrites (collaboration avec Céline Martin de l'Université Libre de Bruxelles). (2) XMAPTOOLS, PTLINES et MULTIPLOT ont été utilisés conjointement pour estimer les conditions P-T enregistrées dans des métapélites d'Anatolie (collaboration avec Amaury Pourteau de l'Université de Potsdam) de la chaîne des Longmen (collaboration avec Julia de Sigoyer et Alexandra Robert de l'ENS Paris) et à BT dans des failles de la chaîne catalane côtière (collaboration avec Irene Cantarero de l'Université de Barcelone).

La suite du présent document est organisée en quatre chapitres :

Le premier chapitre est consacré à l'estimation P-T et la thermodynamique des phyllosilicates. La première partie introductive présente différentes approches thermobarométriques « classiques » puis la thermodynamique des solutions solides et enfin pourquoi les phyllosilicates sont de bons candidats pour les estimations P-T. Dans une deuxième partie, je décrirais l'approche « inverse », en particulier la technique « Multi-équilibre ». Cette partie est constituée d'un article de [Vidal et al. \(2010\)](#) publié dans la revue *Clays and Clay Minerals*, discutant de l'incorporation de molécules de H₂O en position interfoliaire des illites et d'un exemple d'application à BT de [Cantarero et al. \(2012\)](#). La troisième partie de ce chapitre est consacrée à l'approche « directe ». Je présente un nouveau modèle de solution solide pour les chlorites, compatible avec la base de données et le formalisme de [Holland et Powell \(1998\)](#). Ce travail est présenté sous la forme d'un article de Lanari et al. à soumettre à la revue *Contribution to Mineralogy and Petrology*. Les implications thermodynamiques de ce formalisme concernant l'estimation des propriétés thermodynamiques standards des pôles purs dépendants est discutée.

Le chapitre suivant est consacré à l'imagerie chimique. La première partie introductive présente les avantages de la cartographie WDS et les conditions analytiques ainsi que la méthode de standardisation proposée par [De Andrade et al. \(2006\)](#). Dans une deuxième partie, je décris en détail le logiciel XMAPTOOLS sous la forme d'un article de Lanari et al. soumis à la revue *Computers and Geosciences*.

Cet article est composé d'une description des fonctions du logiciel et d'un exemple d'application en utilisant une éclogite Himalayenne (données de [Lanari et al. in press](#)), qui permet de discuter de la précision analytique de la méthode. La troisième et dernière partie traite de l'application des méthodes de micro-cartographie à l'étude de l'évolution minéralogique et chimique de chondrites. Les résultats de ce travail sont présentés sous la forme d'un article de Martin et al. à soumettre à la revue *Geochimica and Cosmochimica Acta*.

Le chapitre suivant est consacré à l'application des techniques de Multi-équilibres et de micro-cartographie à l'étude de l'évolution tectono-métamorphique de la chaîne alpine. La première partie introductive présente les Alpes occidentales ainsi que les travaux menés sur cette portion de la chaîne. La deuxième partie est consacrée à l'étude des unités briançonnaises. Elle est constituée de deux publications. La première de [Lanari et al. \(2012a\)](#) publié dans la revue *Journal of Geodynamics* rapporte les résultats d'une étude de l'évolution tectono-métamorphique de la Zone houillère au Nord de Briançon avec l'identification de deux trajets P-T, le premier dans les minéraux alpins et le deuxième dans les minéraux détritiques hercyniens. La deuxième publication de Lanari et al. soumise à la revue *Terra Nova* est consacrée à l'étude des conditions P-T-t enregistrées par le « Granite de Plan de Phasy », qui est une écaille de socle actuellement coincée dans le chevauchement Briançonnais frontal au Sud-Ouest de Guillestre. La troisième partie traite des premiers résultats P-T-t obtenus pour deux affleurements du complexe des Schistes lustrés du Queyras.

Le dernier chapitre est consacré à l'application des techniques de micro-cartographie à l'étude d'une éclogite Himalayenne. La première partie introductive présente brièvement la chaîne Himalayenne et le massif de Stak au Pakistan. La deuxième partie est consacrée à la reconstruction d'un chemin P-T et de cartes P-T en utilisant le logiciel XMAPTOOLS et des calibrations empiriques. Elle est constituée d'un article de [Lanari et al. \(in press\)](#) en cours de publication dans la revue *Geology*.

Enfin, en conclusion de ce mémoire, je présente une synthèse des principaux résultats et propose des perspectives de travail futur.

ESTIMATIONS P-T ET THERMODYNAMIQUE DES PHYLLOSILICATES

SOMMAIRE

2.1	INTRODUCTION : ESTIMATIONS P-T ET PHYLLOSILICATES	13
2.2	APPROCHE INVERSE ET MULTI-ÉQUILIBRES	25
2.3	APPROCHE DIRECTE ET PSEUDOSECTIONS	65
2.4	CONCLUSIONS ET PERSPECTIVES	115

CE chapitre introduit la thermodynamique des solutions solides, propose une synthèse non-exhaustive des modèles récents pour les phyllosilicates et propose un nouveau modèle de solution solide pour les chlorites.

THIS chapter introduces the thermodynamic of solid solutions, review the existing models available for the study of metapelites and proposes a new solid-solution model for chlorite.

2.1 INTRODUCTION : ESTIMATIONS P-T ET PHYLLOSILICATES

★ *La reconstruction des trajets P-T enregistrés par les roches métamorphiques est indispensable afin de proposer des modèles géodynamiques cohérents et d'étudier les processus de transport de matière à l'échelle de la lithosphère.*

★ *Deux approches thermodynamiques permettent d'estimer les conditions P-T enregistrées par une paragenèse. On distinguera les « approches directes », comme les pseudosections qui prédisent les assemblages stables pour une composition de roche donnée. Ces résultats sont comparés avec les assemblages et compositions minérales observés dans l'échantillon. Les « approches inverses » permettent de calculer les conditions de P-T d'équilibre d'une paragenèse en utilisant directement les compositions des minéraux que l'on suppose à l'équilibre thermodynamique. La technique des multi-équilibres est un exemple d'approche inverse.*

★ *Dans cette partie introductive, après un bref rappel des techniques thermobarométriques classiques, nous présenterons les deux approches, directe et inverse. Puis, nous expliquerons pourquoi les phyllosilicates sont de bons candidats pour l'estimation des conditions P-T.*

2.1.1 Intérêt de la reconstruction des trajets P-T

Les limites de plaques en convergence sont des zones privilégiées pour l'étude de la tectonique des plaques et des processus à l'origine des transports verticaux de matière à l'échelle lithosphérique. Cependant, l'étude des processus d'enfouissement et d'exhumation des roches métamorphiques requiert la reconstruction la plus précise possible de l'évolution géodynamique de la chaîne, à travers des modèles tectono-métamorphiques. La construction de tels modèles nécessite de connaître avec la plus grande précision les trajets pression température temps (P-T-t) enregistrés par les roches des différentes unités de la chaîne.

La reconstitution des trajets P-T enregistrés par les roches métamorphiques nécessite des techniques thermobarométriques afin d'estimer les conditions d'équilibres auxquelles les minéraux ont cristallisé au sein d'une paragenèse. Cet objectif nécessite notamment l'utilisation d'une base physique avec des lois de sa variation

et de son évolution à la fois dans l'espace et dans le temps. La thermodynamique, que l'on peut définir comme la science des grands systèmes en équilibre, est un outil essentiel en Sciences de la Terre pour l'estimation des conditions de cristallisation d'un ou plusieurs minéraux.

2.1.2 Minéraux index et faciès métamorphiques

L'étude des assemblages minéralogiques dans les roches métamorphiques, associée à l'étude des textures, fournissent des informations qualitatives sur les conditions P-T auxquelles les différents assemblages minéralogiques se sont formés. En effet, certains minéraux reflètent des conditions P-T particulières, comme par exemple les omphacites qui sont des clinopyroxènes de haute pression¹. Le concept de « minéral index » caractéristique de zones métamorphiques a été introduit par [Barrow \(1912\)](#) suite à une étude de cartographie détaillée du métamorphisme, enregistré par une série de roches d'origine sédimentaire et riches en aluminium, dans les Highlands écossais. Avec l'augmentation des conditions P-T, on observe fréquemment la séquence suivante (e.g. [Harvey et Tracy 1996](#)) :

- zone à chlorite (quartz, chlorite, muscovite, plagioclase)
- zone à biotite (quartz, muscovite, biotite, chlorite, plagioclase)
- zone à grenat (quartz, muscovite, biotite, garnet, plagioclase)
- zone à staurotide (quartz, muscovite, biotite, garnet, staurolite, plagioclase)
- zone à disthène (quartz, muscovite, biotite, garnet, kyanite, plagioclase)
- zone à silimanite (quartz, muscovite, biotite, garnet, sillimanite, plagioclase).

Il est tout de même important de noter que toutes les compositions de roches ne permettent pas la cristallisation de minéraux index.

Quelques années plus tard [Eskola \(1915; 1921\)](#) a défini les célèbres faciès métamorphiques (Fig. 2.1) nommés d'après la minéralogie rencontrée dans un metabasalte, soumis à différentes conditions P-T. Les faciès les plus fréquemment utilisés sont : schiste vert (basse pression - basse température, BP-BT) ; schiste bleu (haute pression - basse température, HP-BT) ; éclogite (haute pression - haute tempéra-

1. Nous reviendrons par la suite sur cet exemple lors de l'étude d'une éclogite Himalayenne

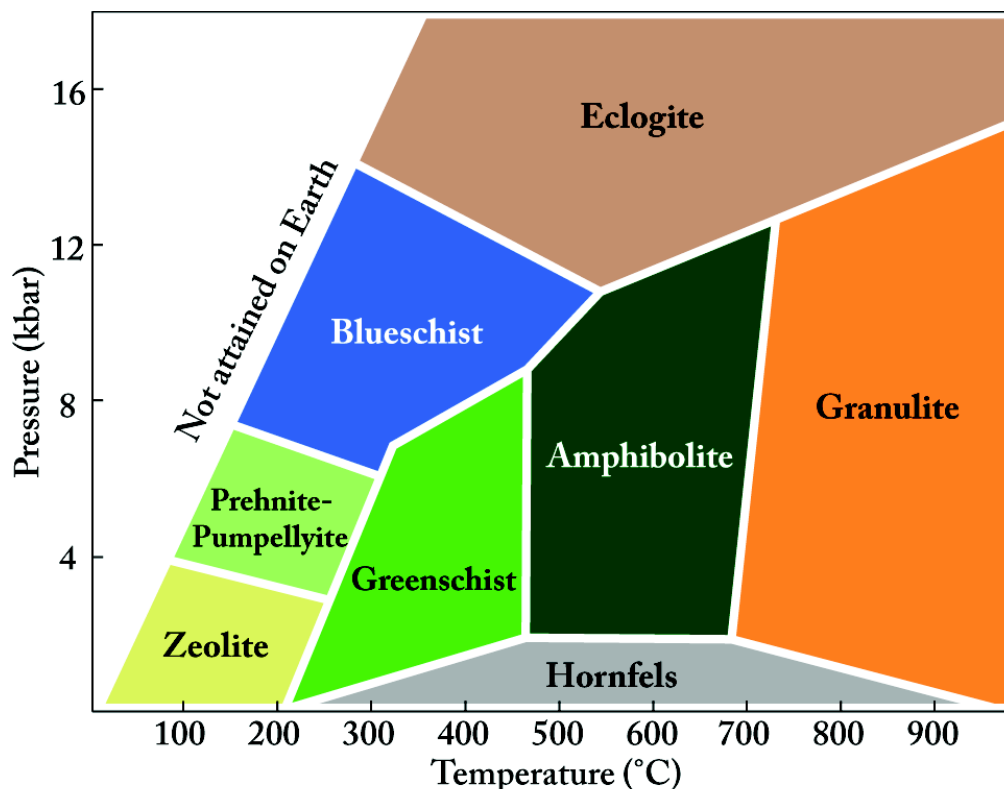


FIGURE 2.1 – Champs P-T des principales faciès métamorphiques

ture, HP-HT) ; amphibolite (basse pression - haute température, BP, HT) ; granulite (basse pression - ultra-haute température, BP-UHT).

Le problème des méthodes qualitatives décrites ci-dessus est que les minéraux diagnostiques apparaissent pour des compositions de roches et des conditions P-T particulières (e.g. MP et BT-HT pour le métamorphisme barrovien). Dans le meilleur des cas, on pourra estimer des conditions relatives de P ou T, mais pas de valeur absolue nécessaire pour l'interprétation géodynamique. Une telle détermination précise des conditions P-T de formation des minéraux passe par des approches thermodynamiques décrites dans la suite.

2.1.3 Rappels de thermodynamique à l'équilibre

La thermodynamique est *stricto sensu* l'étude de l'énergie et de ses transformations. Par exemple, une réaction chimique entre différents minéraux qui intervient dans une roche, va inévitablement impliquer des changements quantitatifs et spatiaux de l'énergie du système. En utilisant la thermodynamique pour étudier les variations d'énergie, nous allons voir comment il est possible de déterminer à quelles

conditions une réaction va se produire, ou bien de prédire quel sera l'assemblage minéralogique le plus stable pour des conditions données.

2.1.3.1 Equation générale de l'énergie libre de Gibbs d'une réaction

Pour une réaction métamorphique avec n constituants, il est possible de calculer l'énergie libre de Gibbs totale de la réaction en utilisant la loi de Hess :

$$\Delta G_{reaction} = \sum_{i=1}^n v_i \mu_i \quad (2.1)$$

avec v_i les coefficients stoechiométriques de la réaction et μ_i le potentiel chimique d'un constituant i . L'expression du potentiel chimique est divisée en une partie standard ($\mu_i^0 = G^0$) et une seconde partie qui dépend de la composition du constituant et donc de son activité dans une phase (a_i) :

$$\mu_i = \mu_i^0 + RT \ln(a_i) \quad (2.2)$$

La partie standard du potentiel chimique, ou énergie libre de Gibbs apparente, peut être calculée pour une pression et une température donnée en utilisant la relation :

$$\mu_i^0 = H^0 f_i - T S_i^0 + \int_{T_0}^T C_p dT + \int_{P_0}^P V dP - T \int_{T_0}^T \frac{C_p}{T} dT \quad (2.3)$$

avec $H^0 f$ et S^0 les valeurs d'enthalpie de formation et d'entropie standards à 1 bar et 25°C, C_p la fonction de la capacité calorifique et V celle du volume. Le calcul du potentiel chimique standard est décrit en détail dans les annexes, pour le formalisme utilisé par Berman et Brown (A.1.1) et celui utilisé par Holland et Powell (A.1.2).

La partie activité du potentiel chimique va dépendre de l'activité a_i du constituant. Pour un pôle pur, l'activité sera toujours égale à 1, ce qui annulera alors le terme en $RT \ln(a_i)$. Pour un composant d'une solution solide, l'activité sera toujours différente de 1 et dépendra, entre autres, de sa fraction molaire dans la phase. Ce terme d'activité est divisé en deux parties, l'une idéale ($a_{ideale(i)}$) et l'autre non-idéale (γ_i) :

$$RT \ln(a_i) = RT \ln(a_{ideale(i)}) + RT \ln(\gamma_i) \quad (2.4)$$

Nous allons voir que la plupart des applications en géothermobarométrie nécessitent un modèle d'activité plus ou moins complexe pour les solutions solides. Ce modèle peut être de type macroscopique ou de type microscopique. Le modèle macroscopique (ou moléculaire) est plus simple, car il suppose que les mélanges interviennent en mélanges cristallins entre les différents pôles purs. À l'inverse, un modèle microscopique (ou ionique) suppose que les mélanges de cations se font sur des sites cristallographiques bien particuliers.

2.1.3.2 Stabilité des minéraux et réactions métamorphiques

Considérons une réaction métamorphique entre deux pôles purs $A \rightleftharpoons B$, comme par exemple la réaction :



Il est possible de calculer l'énergie libre de Gibbs totale de cette réaction en fonction de P et T, en utilisant l'équation générale (2.1). On peut distinguer les trois cas suivants :

- Si $\Delta G_{\text{reaction}} > 0$, alors c'est la réaction coésite \rightarrow quartz qui se produit et la coésite se transforme en quartz. On est dans le champ de stabilité du quartz (noté 1 sur la figure 2.2)
- Si $\Delta G_{\text{reaction}} < 0$ alors la réaction quartz \rightarrow coésite se produit et le quartz se transforme en coésite. On est dans le champ de stabilité de la coésite (noté 2 sur la figure 2.2).
- Si $\Delta G_{\text{reaction}} = 0$, alors le quartz et la coésite coexistent, ils sont à l'équilibre thermodynamique (noté 3 sur la figure 2.2) et il n'y a pas de différence d'énergie libre de Gibbs entre les réactifs et les produits.

Le quartz et la coésite ne peuvent coexister que si le $\Delta G_{\text{reaction}} = 0$, qui est la condition d'équilibre thermodynamique. On peut donc ré-écrire l'équation (2.1) en la combinant avec les relations (2.2) et (2.1) pour qu'elle respecte la condition d'équilibre thermodynamique :

$$0 = \Delta H^0_f - T \Delta S^0 + \int_{T_0}^T C_p dT + \int_{P_0}^P V dP - T \int_{T_0}^T \frac{C_p}{T} dT - RT \ln(K) \quad (2.6)$$

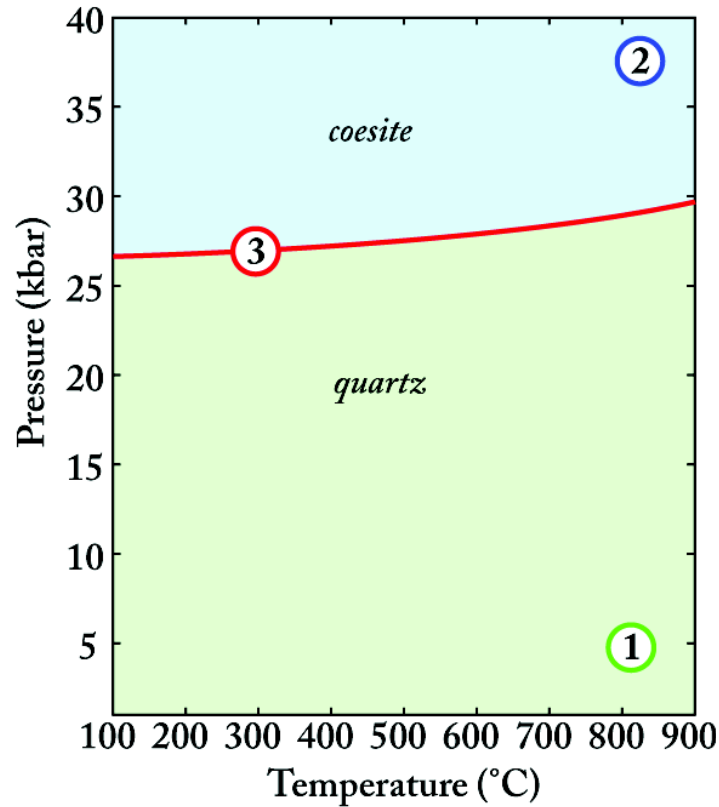


FIGURE 2.2 – Réaction "coésite = quartz" tracée dans un diagramme P-T en utilisant la base de données thermodynamiques de [Holland et Powell \(1998\)](#) et le programme MEAMP (c.f. 2.3.3). (1) quartz stable, (2) coésite stable, (3) coésite et quartz coexistent

avec K la constante d'équilibre de la réaction définie comme le produit des activités des différents constituants :

$$K = \prod_i (a_i)^{v_i} \quad (2.7)$$

2.1.3.3 Equilibre thermodynamique à l'échelle de la lame mince

L'état d'équilibre thermodynamique est atteint par un système lorsque celui-ci est à l'équilibre à la fois thermique, mécanique et chimique. Cette définition générale signifie que, pour un petit échantillon de roche, à l'échelle de la lame mince par exemple, l'équilibre ne peut être atteint que si les conditions P-T ne varient pas et que si le système est totalement isolé du milieu extérieur et donc sans échange de chaleur de travail ou de matière. Bien évidemment, ces conditions ne sont jamais réunies dans le système naturel, tout du moins, à l'échelle d'un échantillon de roche. L'équilibre thermodynamique ne peut donc être qu'approché, localement, dans l'espace et dans le temps.

Au cours de son histoire tectonique, généralement composée d'une phase d'enfouissement suivie d'une phase d'exhumation, une roche métamorphique voit sa composition minéralogique évoluer en réponse à des déséquilibres thermiques (T), mécaniques (P- ϵ) et/ou chimiques (variation des conditions redox, du pH ...). Cependant, en raison de la cinétique des réactions qui est faible, notamment à basse température, les roches ne se ré-équilibrent pas totalement lors du trajet rétrograde et peuvent conserver des minéraux et donc potentiellement des paléo-équilibres thermodynamiques locaux. Le préfixe paléo- indique dans ce cas là que ces équilibres thermodynamiques ont été atteints à un temps t . En effet, les minéraux métamorphiques que nous observons en conditions P-T de surface sont métastables, c'est-à-dire cinétiquement stables, mais en déséquilibre thermodynamique.

2.1.4 Approches de type « thermobarométrie classique »

Les approches de type « thermobarométrie classique » sont basées sur la position dans un diagramme P-T d'une réaction chimique. En négligeant les termes en ΔC_p et $\frac{\Delta C_p}{T}$ et en supposant que le changement de volume en fonction de la pression est faible et que $V(P, T) = (P - 1)V^0$, on peut simplifier la relation (2.6) :

$$\Delta H^0 f - T \Delta S^0 + (P - 1)\Delta V^0 - RT \ln(K) = 0 \quad (2.8)$$

ce qui signifie que le logarithme de la constante d'équilibre de la réaction chimique, qui peut être calculé à partir des compositions des minéraux, varie en fonction de la pression et de la température :

$$\ln(K) = \frac{\Delta H^0 f + (P - 1)\Delta V^0}{R T} - \frac{\Delta S^0}{R} = \frac{A}{T} - B \quad (2.9)$$

Comme la pente de la réaction dans un champ P-T est égale à $\frac{\Delta S^0}{\Delta V^0}$, une réaction avec un ΔV^0 faible sera fortement dépendante de la température et donc un bon thermomètre, alors qu'une réaction avec un ΔV^0 élevé, sera un bon baromètre (Fig. 2.3). Les réactions d'échange Fe-Mg par exemple sont classiquement utilisées comme thermomètres alors que la réaction *albite* \rightleftharpoons *jadeite* + *quartz* comme un baromètre.

2.1.4.1 Calibration empirique

Si les constantes A et B de l'équation (2.8) sont obtenues sans passer par un calcul thermodynamique complet de ΔH^0 , ΔS^0 et ΔV^0 , on parlera alors de calibrations

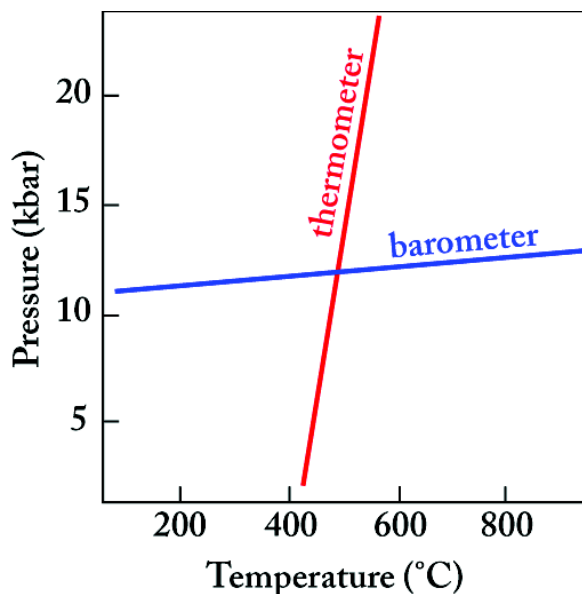


FIGURE 2.3 – Thermobarométrie « classique » et estimation P-T en utilisant pour une paragenèse donnée : un équilibre dépendant de la température (thermomètre, réaction en rouge) et un de la pression (baromètre, réaction en bleu).

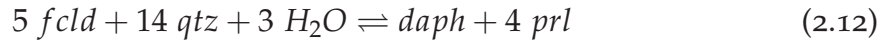
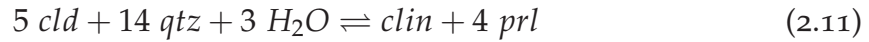
empiriques. Les calibrations empiriques ont été beaucoup utilisées notamment par les thermomètres basés sur les réactions d'échange Fe-Mg. L'avantage de ces calibrations est de ne pas nécessiter de calcul thermodynamique complexe et donc de pouvoir être appliqué à un grand nombre de données très rapidement (c.f. Chap. 3 sur la cartographie).

2.1.4.2 Exemple : thermomètre chlorite-chloritoïde

Considérons un système chimique à 5 composants indépendants : SiO_2 , Al_2O_3 , FeO , MgO , H_2O , et les 7 pôles purs suivants : clinochlore (*clin*, $\text{Mg}_5\text{Al}_2\text{Si}_3\text{O}_{10}(\text{OH})_8$) et daphnite (*daph*, $\text{Fe}_5\text{Al}_2\text{Si}_3\text{O}_{10}(\text{OH})_8$) pour la chlorite, Mg-chloritoïde (*cld*, $\text{Mg}_1\text{Al}_2\text{Si}_1\text{O}_5(\text{OH})_2$) et Fe-chloritoïde (*fcld*, $\text{Fe}_1\text{Al}_2\text{Si}_1\text{O}_5(\text{OH})_2$) pour le chloritoïde, la pyrophyllite (*prl*, $\text{Al}_2\text{Si}_4\text{O}_{10}(\text{OH})_2$), le quartz (*qtz*, SiO_2) et l'eau (H_2O). Le nombre de réactions indépendantes (IR), dépend du nombre de pôles purs (PP) ainsi que du nombre de composants indépendants du système chimique (C) et peut être calculé en utilisant la relation suivante (e.g. Spear 1993) :

$$IR = PP - C \quad (2.10)$$

Avec les pôles purs définis précédemment, on peut écrire les deux réactions indépendantes suivantes ($IR = 7 - 5 = 2$) :



qui sont les réactions entre chlorite, chloritoïde, pyrophyllite, quartz et H_2O dans le système magnésien (Eq. 2.11) et dans le système ferreux (Eq. 2.12). On peut combiner ces deux réactions pour écrire la relation dépendante suivante :



qui est la réaction d'échange Fe-Mg entre la chlorite et le chloritoïde. Un thermomètre chlorite+chloritoïde a été proposé par Vidal et al. (1999), en utilisant une calibration empirique de la dépendance entre le $\ln(K)$ de cette réaction et la température.

2.1.5 Approches non empiriques

La thermobarométrie « classique » permet de reconstruire à la fois les conditions pression et température à partir de compositions de minéraux à l'équilibre si l'on peut écrire deux réactions, l'une qui dépend de la pression et l'autre de la température. La limite de cette approche est qu'elle utilise des calibrations empiriques et qu'il existe souvent plusieurs calibrations dérivées à partir de différentes données thermodynamiques, comme par exemple pour le thermomètre grenat-clinopyroxène qui a plus de 10 calibrations (e.g. Mysen et Heier 1972, Raheim et Green 1974, Mori et Green 1978, Ellis et Green 1979, Ganguly 1979, Dahl 1980, Powell 1985, Krogh 1988, Pattison et Newton 1989, Sengupta et al. 1989, Ai 1994, Korgh Ravna 2000b) qui donnent des résultats différents. C'est ce qui entraîne Berman (1991) à faire le constat suivant : *"This situation has led many geologists to use several, many, or all different formulations, and rely on other geological evidence, inter-sample consistency, or simply geological intuition (!) to select preferred result"*.

Pour résoudre ce problème, il est nécessaire, dans un premier temps, d'utiliser une approche non-empirique avec un calcul « complet » du potentiel chimique standard μ^0 (Eq. 2.3). Ce calcul nécessite de connaître les valeurs de H^0f ,

S^0 , V^0 et des différents coefficients des fonctions C_p et V . Il faut donc utiliser une base de données thermodynamiques inter-cohérentes afin de pouvoir calculer le $\Delta G_{reaction}$ de réactions impliquant plusieurs minéraux. L'intégralité des données thermodynamiques d'une base de données est générée en une seule fois à partir d'un grand nombre de données expérimentales (expériences de calorimétrie, équilibre de phases). Les données obtenues sont inter-cohérentes et peuvent donc être utilisées les unes avec les autres. Différentes bases de données ont été proposées ces vingt dernières années (Berman 1988, Ghiorso et Sack 1995, Robie et Hemingway 1995, Gottschalk 1997, Chatterjee et al. 1998, Holland et Powell 1998; 2011), mais celles de Berman (1988) et Holland et Powell (1998) sont les plus couramment utilisées.

Deux types d'approches peuvent être utilisées pour estimer les conditions P-T à partir des observations et des mesures chimiques d'échantillon naturel : une approche directe et une approche inverse. Ces deux approches brièvement décrites ici seront plus longuement présentées et discutées dans les deux parties suivantes (Part. 2.2 et Part. 2.3).

2.1.5.1 L'approche directe

L'approche directe est la méthode actuellement la plus utilisée pour l'estimation des conditions P-T (e.g. Powell 2008). Elle est basée sur le principe de la minimisation de l'énergie libre de Gibbs du système et ne nécessite ni de faire des hypothèses sur les minéraux en équilibre ni de faire de calculs de $\Delta G_{reaction}$. Pour des conditions P-T et une composition de roche totale données, l'assemblage le plus stable est calculé en minimisant la somme des potentiels chimiques de tous les constituants possibles. L'avantage de cette approche est de pouvoir directement comparer les assemblages prédits aux assemblages observés dans la lame mince. En revanche, elle nécessite de pouvoir reproduire les compositions des minéraux mesurées avec les différents jeux de pôles purs utilisés dans les modèles de solutions solides. Dans le cas contraire, ces minéraux ne pourront pas être considérés lors du calcul de minimisation d'énergie, ou alors avec une chimie différente, et donc une stabilité différente.

2.1.5.2 L'approche inverse

L'approche inverse quant à elle, est basée sur l'utilisation d'équilibres chimiques dont la position P-T dépendent notamment de la composition des différents minéraux. À l'inverse de l'approche directe, elle nécessite de faire des hypothèses sur les assemblages minéralogiques à l'équilibre. Les conditions P-T peuvent être calculées, comme nous l'avons vu précédemment, en utilisant une calibration empirique, ou bien en utilisant un calcul thermodynamique "complet" avec la technique des multi-équilibres (Berman 1991, Lieberman et Petrakakis 1991). Cette technique est basée sur l'hypothèse que pour une paragenèse à l'équilibre thermodynamique, tous les équilibres chimiques doivent se recouper à une pression et une température (soit pour toutes les réactions $\Delta G_{reaction} = 0$ à ces conditions P et T d'équilibre).

2.1.6 L'intérêt des phyllosilicates

Les phyllosilicates, appelés également silicates lamellaires, sont des minéraux appartenant au groupe des silicates. Ils sont construits par empilement de feuillets tétraédriques (T) et octaédriques (O) occupés par différents cations. Ils sont classiquement divisés en trois groupes en fonction de l'épaisseur du feuillet : (i) les phyllosilicates T-O (une couche T, une couche O) de 7Å comme les serpentines, ou bien encore la kaolinite. (ii) les phyllosilicates T-O-T de 10Å comme les micas, le talc ou encore les argiles. (iii) les phyllosilicates T-O-T:O de 14Å. comme les chlorites. Ces minéraux sont fréquemment observés depuis des conditions diagénétiques, avec les argiles, jusqu'au métamorphisme de moyenne à haute température avec les micas et les chlorites.

Dans les pélites de bas degré de métamorphisme (i.e. $< 450^{\circ}\text{C}$), les phyllosilicates sont des minéraux ubiquistes présentant de fortes variations chimiques. Ils sont de bons candidats pour déterminer les conditions P-T en utilisant une approche de type multi-équilibres car ils présentent plusieurs substitutions qui peuvent être modélisées avec plusieurs pôles purs. Par exemple, trois principales substitutions interviennent dans la solution solide des chlorites : la substitution Fe-Mg (Fe-Mg_{-1}) et les deux substitutions couplées : « Tschermak » ($\text{Al}_{iv}\text{Al}_{vi}\text{Si}_{-1}(\text{Mg}, \text{Fe})_{-1}$) et di/trioctahédrique ($(\text{Mg}, \text{Fe}^{2+})_3\text{V}_{-1}\text{Al}_{-2}$) et le domaine

de composition des chlorites peut être par exemple modélisé en utilisant cinq pôles purs (Vidal et al. 2005; 2006). La chimie des phyllosilicates est très sensible aux conditions d'équilibre comme la pression et la température, ou encore à la fugacité de l'oxygène, au pH, ou à l'activité de l'eau.

2.2 APPROCHE INVERSE ET MULTI-ÉQUILIBRES

★ *La technique des multi-équilibres nécessite de calculer un grand nombre d'équilibres chimiques et peut être appliquée à de très grands jeux de données comme les cartographies microsondes.*

★ *De nombreux modèles de solutions solides pour les phyllosilicates ont été développés ces dernières années afin de déterminer les conditions P-T enregistrées par les métasédiments. Ces modèles permettent notamment de tester un équilibre thermodynamique entre plusieurs minéraux d'une paragenèse, comme par exemple les équilibres chlorite + phengite + quartz + H₂O. Ils permettent également de tracer des équilibres comme phengite + quartz + H₂O qui sont des outils très utiles pour la communauté des pétrographes.*

★ *Dans cette partie, nous allons présenter la technique des multi-équilibres et les modèles de solutions solides disponibles. Puis nous discuterons des limites du modèles chlorite + quartz + H₂O de Vidal et al. (2006) à HT et de l'incorporation de H₂O dans les illites. Enfin, nous proposerons deux logiciels PTLINES et MULTIPLOT permettant de calculer des conditions d'équilibres pour une paragenèse donnée.*

2.2.1 Introduction

La technique des multi-équilibres est né des travaux de Berman (1991), Lieberman et Petrakakis (1991) qui ont proposé d'utiliser la position de tous les équilibres chimiques pour une paragenèse donnée. Dans le cas "idéal" où les compositions mesurées ainsi que les données thermodynamiques sont parfaites et que tous les minéraux ont cristallisés aux mêmes conditions d'équilibre, toutes ces réactions doivent se couper en un point dans un diagramme P-T (Fig. 2.4). Cette méthode permet de vérifier l'équilibre thermodynamique à partir du moment où l'on utilise plus de deux équilibres indépendants.

2.2.1.1 Modèles disponibles

Au cours des dix dernières années, plusieurs modèles de solutions solides ont été développés afin de permettre l'utilisation des techniques de multi-équilibres pour reconstruire les trajets P-T dans les métapélites. Ce développement a notam-

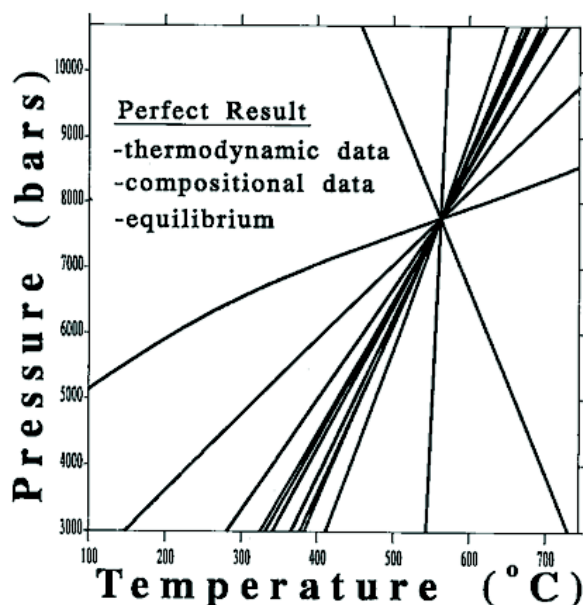


FIGURE 2.4 – Diagramme P-T qui montre un résultat idéal de multi-équilibres dans le cas de données thermodynamiques et de compositions parfaites et où les minéraux cristallisent aux mêmes conditions P-T (d'après [Berman 1991](#)).

ment été l'objet de trois thèses, avec en premier [Parra \(2001\)](#) qui a travaillé sur les équilibres chlorite-phengite et leur application en thermobarométrie. Puis la technique a été appliquée plus systématiquement par [De Andrade \(2006\)](#), en utilisant non plus des analyses ponctuelles, mais des cartographies chimiques microsondes. Enfin, [Dubacq \(2008\)](#) a travaillé sur l'application de ces techniques au domaine des basses températures avec le développement de nouveaux modèles pour les phyllosilicates alumineux. Différents modèles de solutions solides pour les phyllosilicates ont été développés, tous compatibles avec la base de données thermodynamiques de [Berman \(1988\)](#).

Modèle pour les chlorites de Vidal et al. (2001) Ce modèle de solution solide inclut les quatre pôles purs de chlorite *ames*, *clin*, *daph*, *sud* (abréviation et composition disponibles Tab. 2.1). À partir des propriétés standards des pôles purs déjà disponibles (e.g. [Berman 1988](#), [Vidal et al. 1992; 1999](#)), [Vidal et al. \(2001\)](#) ont utilisé des données expérimentales (e.g. [Staudigel et Schreyer 1977](#), [Chopin et Schreyer 1983](#), [Jenkins et Chernovsky 1986](#), [Bryndzia et Scott 1987](#), [Massonne 1989](#), [Saccoccia et Seyfried 1994](#), [Baker et Holland 1996](#)) et des données naturelles de plus de 200 analyses de chlorites avec des estimations indépendantes

Chlorite						
pôle pur	abréviation	T1(2)	T2(2)	M1(1)	M2M3(4)	M4(1)
Amesite-Mg	ames	Si,Si	Al,Al	Al	Mg,Mg,Mg,Mg	Al
Amesite-Fe	fames	Si,Si	Al,Al	Al	Fe,Fe,Fe,Fe	Al
Clinocllore	clin	Si,Si	Si,Al	Mg	Mg,Mg,Mg,Mg	Al
Daphnite	daph	Si,Si	Si,Al	Fe	Fe,Fe,Fe,Fe	Al
Sudoite	sud	Si,Si	Si,Al	Lac	Al,Al,Mg,Mg	Al

Mica						
pôle pur	abréviation	T1(2)	T2(2)	M1(1)	M2M3(2)	A(1)
Celadonite-Mg	cel	Si,Si	Si,Si	Lac	Al,Mg	K
Celadonite-Fe	fcel	Si,Si	Si,Si	Lac	Al,Fe	K
Muscovite	mus	Si,Si	Si,Al	Lac	Al,Al	K
Pyrophyllite	prl	Si,Si	Si,Si	Lac	Al,Al	Lac
Pyrophyllite-1H	prl1h	Si,Si	Si,Si	Lac	Al,Al	H ₂ O
Paragonite	para	Si,Si	Si,Al	Lac	Al,Al	Na
Margarite	marg	Si,Si	Al,Al	Lac	Al,Al	Ca
Phlogopite	phl	Si,Si	Si,Al	Mg	Mg,Mg	K
Annite	ann	Si,Si	Si,Al	Fe	Fe,Fe	K

TABLE 2.1 – Compositions et abréviations des différents pôles purs de chlorite et de mica d’après Vidal et Parra (2000), Vidal et al. (2001), Parra et al. (2002a), Vidal et al. (2005; 2006), Dubacq et al. (2010). Lac : lacune

de la température, pour contraindre les différents paramètres standards et de solutions solides. Le modèle de Vidal et al. (2001) permet de calculer la température de cristallisation d’une chlorite à l’équilibre avec du quartz et de l’eau, en utilisant à une pression donnée la température de l’équilibre chlorite + quartz ($2 \text{ clin} + 3 \text{ sud} = 4 \text{ ames} + 4 \text{ H}_2\text{O} + 7 \text{ qtz}$).

Modèle mica de Parra et al. (2002) Ce modèle de solution solide inclut les sept pôles purs de micas blancs potassiques *cel*, *fcel*, *mus*, *prl*, *para*, *phl*, *ann* (Tab. 2.1). Parra et al. (2002a) ont calibré le modèle en utilisant des contraintes expérimentales (e.g. Massonne et Schreyer 1986, Frey et al. 1988, Jiang et al. 1992, Massonne et Szpurka 1997, Giorgetti et al. 1998, Schmidt 1998) et également un jeu de données naturelles de mica dont les conditions P-T étaient connues.

Multi-équilibre chlorite mica de Vidal et Parra (2000) Dans le système $K_2O\text{-}Al_2O_3\text{-}MgO\text{-}SiO_2\text{-}H_2O$ l’utilisation conjointe des deux modèles de solutions solides de (Vidal et al. 2001) et de (Parra et al. 2002a) permet d’estimer des conditions P-T enregistrées par des paires d’analyses de chlorite et de phengite à l’équilibre avec le quartz et l’eau, en traçant les 14 équilibres (dont 3 indépendants) dans un champ P-T (Vidal et Parra 2000).

Modèle chlorite de Vidal et al. (2006) - Chl+Qtz+W Les nouvelles données expérimentales pour les chlorites ferreuses de Parra et al. (2005) ont permis à Vidal et al. (2005; 2006) d'ajouter le pôle pur *fames* (c.f. Tab. 2.1) au modèle de solution solide des chlorites de Vidal et al. (2001). Avec les cinq pôles purs *ames*, *fames*, *clin*, *daph* et *sud*, avec du quartz et de l'eau, il est possible de tracer quatre réactions dont deux sont indépendantes. Comme ces réactions ne convergent pas forcément dans le champ P-T, Vidal et al. (2006) propose d'ajouter du Fe^{3+} dans la chlorite jusqu'à convergence pour une pression donnée. Vidal et al. (2006) propose de calculer la température à partir d'une composition de chlorite en équilibre avec du quartz et de l'eau avec un taux de Fe^{3+} minimum dès que l'écart entre les deux équilibres indépendants est inférieur à 30°C.

Modèle mica de Dubacq et al., (2010) - Phg+Qtz+W Un modèle de solution solide commun à tous les phyllosilicates dioctaédriques alumineux a été proposé par Dubacq et al. (2010) pour étendre aux argiles le modèle de Parra et al. (2002a). Ce modèle unique inclut notamment les smectites, les illites et les phengites. Pour les micas blancs potassiques métamorphiques qui nous intéressent ici, ce modèle est basé sur les huit pôles purs suivants : *mus*, *para*, *cel*, *fcel*, *phl*, *ann*, *prl* et *prl1h* (Tab. 2.1). Les propriétés thermodynamiques nécessaires (propriétés standards et paramètres de Margules) ont été calibrées pour reproduire au mieux un vaste jeu d'analyses dont les conditions P-T de cristallisation étaient connues. Ce modèle est très utile pour calculer les conditions d'équilibre des phengites en équilibre avec le quartz et l'eau. Cette approche permet d'estimer facilement soit la température (pour une pression donnée), soit la pression (pour une température donnée) d'une phengite. En effet, en utilisant les réactions qui interviennent entre les différents pôles purs listés précédemment, le quartz et l'eau, on peut pour chaque analyse de phengite tracer dans un champ P-T une ligne d'équilibre le long de laquelle la phengite est à l'équilibre avec le quartz et l'eau et seul son état d'hydratation varie (c.f. Fig. 3 de Dubacq et al. 2010). Nous allons utiliser cette méthode conjointement avec le thermomètre pour les chlorites de Vidal et al. (2006) lors des exemples d'applications pour estimer les conditions de pressions et de températures enregistrées par les assemblages chlorite-mica des zones faiblement métamorphiques des Alpes

internes (Chap. 4). Ce modèle repose sur l'hypothèse que les lacunes interfoliaires des phengites peuvent être partiellement hydratées. La présence d'eau a été mesurée par [Drits et McCarty \(2007\)](#) pour les illites et par [Dubacq et al. \(2010\)](#) pour les phengites.

2.2.1.2 Stratégie

L'objectif de mon travail a été d'appliquer les techniques disponibles à des cas naturels, en utilisant des cartographies microsondes (c.f. exemples d'applications Chap. 4). Cet objectif a nécessité la création de logiciels conviviaux pour faire des calculs thermodynamiques impliquant un grand nombre de réactions et d'analyses chimiques. De plus, il est également nécessaire de fournir à la communauté ce genre de programme, indispensable à l'application des techniques développées. À partir d'un large jeu de fonctions initialement développées par B. Dubacq, V. De Andrade, E. Lewin et O. Vidal, j'ai créé deux programmes avec des interfaces graphiques utilisateurs : PTLINES et MULTIPLOT. Le premier permet de tracer des équilibres chlorite + quartz + H_2O et phengite + quartz + H_2O en fonction de la teneur en Fe^{3+} des chlorites (modèle de [Vidal et al. 2006](#)) et de la teneur en $H_2O_{interfoliaire}$ des phengites (modèle de [Dubacq et al. 2010](#)). Le second logiciel permet de calculer des équilibres chimiques pour des paragenèses plus complexes en incluant d'autres phases comme la carpholite, le chloritoïde ou encore le grenat. Ces programmes ont été largement utilisés durant ce travail pour l'estimation de conditions P-T. Nous avons traité de grands jeux de données (ponctuelles et cartographiques) sur des échantillons naturels de provenances variées (Alpes occidentales et centrales, Anatolie, Andes, Carpates, Chaîne Hercynienne, Longmen Shan, Pyrénées). Les résultats de ces études en cours n'ont pas pu tous être présentés dans ce mémoire, mais ces nombreux tests ont permis d'identifier certains problèmes dans les calibrations existantes. Après avoir présenté une application sur des chlorites et phengites de BP et BT, nous allons discuter des incertitudes sur les températures de chlorite obtenues avec la calibration de [Vidal et al. \(2006\)](#) et identifier certains problèmes pour les analyses de HT. Nous présenterons également dans un article de [Vidal et al. \(2010\)](#) publié dans la revue *Clays and Clay minerals* les arguments en

Thermodynamic data	
I.C.T.D.	Berman (1988; 1990) and updates
Equations	
G ⁰	Berman and Brown convention (Annexe A.1.1)
C _p function	Maier (1932), Haas et Fisher (1976), Berman et Brown (1985)
Lambda transitions	Helgeson et al. (1978), Berman et Brown (1985)
Disorder contrib.	Berman et Brown (1985)
Volume function	Simple volume function for solids (Berman 1988)
Activity models	
Ideal	ionic model (Guggenheim 1966, Price 1985, Mäder et al. 1994)
Non-ideal	ionic model (Margules 1895, Berman et Brown 1984)
Programs	
Multi-equilibrium	TWEEQ (Berman 1991; 2007)
Minimization	THERIAK-DOMINO (De Capitani et Brown 1987, De Capitani et Petrakakis 2010)

TABLE 2.2 – Principales références (base de données thermodynamiques, équations et logiciels) sur le formalisme de Berman (1988) utilisé pour la technique des multi-équilibres (voir texte). I.C.T.D., Internally consistent thermodynamic dataset. Un tableau similaire est proposé Tab. 2.5 dans la partie consacrée aux pseudosections - formalisme de (Holland et Powell 1998).

faveur de l’incorporation de H₂O en position interfoliaire dans les illites plutôt que des ions hydronium (H₃O⁺).

2.2.2 Formalisme thermodynamique

Le formalisme thermodynamique utilisé lors des calculs de multi-équilibres sera présenté brièvement dans cette partie. En effet, celui-ci diffère en partie du formalisme utilisé dans la partie suivante pour les calculs thermodynamiques par minimisation d’énergie en utilisant l’approche directe (Part. 2.3).

2.2.2.1 Base de données thermodynamiques inter-cohérentes

La base de données utilisée est la base de données de Berman (1988) et les nombreuses mises à jour disponibles (JUN92 de Christian de Capitani, notice de THERIAK-DOMINO, et modèles d’Olivier Vidal).

2.2.2.2 Logiciels de calcul

TWEEQU (Thermobarometry With Estimation of EQUilibration state) est un logiciel qui permet de tracer toutes les réactions pour une paragenèse et des compositions de minéraux données.

Nous signalerons également ici THERIAK-DOMINO qui est un jeu de programmes permettant de calculer et tracer des fonctions thermodynamiques, des assemblages

à l'équilibre et de calculer par minimisation d'énergie des pseudosections, notamment avec la même base de données que celle de TWEEQU.

2.2.2.3 Modèles d'activités

Un modèle ionique, basé sur la répartition des éléments sur les différents sites cristallins, est utilisé pour décrire l'activité idéale d'un composant d'une solution solide (on-site mixing model, e.g. [Spear 1993](#), [Powell et Holland 1993](#)). Cette activité idéale est calculée en utilisant la relation suivante ([Guggenheim 1966](#), [Price 1985](#), [Mäder et al. 1994](#)) :

$$a_{ideal_i} = \prod_s \prod_m \left(\frac{n_s}{r_m} X_m \right)^{r_m} \quad (2.14)$$

avec n_s est la multiplicité du site s , r_m le nombre d'atomes m sur le site s et X_m la fraction molaire de m sur le site s .

Un modèle ionique est également utilisé pour décrire l'activité non-idéale ([Berman et Brown 1984](#)). Pour des interactions symétriques, le terme d'excès microscopique d'un composant i peut être calculé en utilisant la relation suivante :

$$n_s RT \ln(\gamma_i) = \sum W_{G_{jk}} X_j X_k \left(\frac{Q_i}{X_i} - 1 \right) \quad (2.15)$$

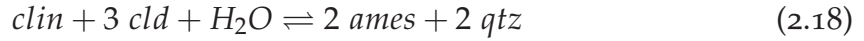
avec Q_i le nombre d'indices j, k égal à i (0 ou 1) dans chaque $W_{G_{jk}}$, les paramètres de Margules ([Margules 1895](#)) qui s'écrivent :

$$W_G = W_H - (T - T_0)W_S + (P - P_0)W_V \quad (2.16)$$

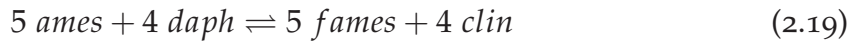
2.2.2.4 Pôles purs et réactions

La technique des multi-équilibres permet d'estimer les conditions d'équilibre en traçant toutes les réactions, dépendantes et indépendantes, qui interviennent entre les différents pôles purs, chimiquement dépendants et indépendants [Berman \(1991\)](#), [Lieberman et Petrakakis \(1991\)](#). Dans la partie 2.1.4 nous avons montré que dans un système à cinq composants chimiques indépendants et en choisissant un jeu de sept pôles purs, *clin* et *daph* pour la chlorite, *cld* et *fcd* pour le chloritoïde, *prl*, *qtz* et H_2O , on pouvait écrire deux réactions indépendantes (Eq. 2.11 et 2.12) plus une troisième dépendante qui est la réaction d'échange Fe-Mg entre la chlorite et le chloritoïde (Eq. 2.13).

Si l'on ajoute maintenant des pôles purs, on va augmenter le nombre de réactions indépendantes (cf. Eq. 2.10) et donc le nombre de contraintes, toujours pour un assemblage chlorite + chloritoïde + pyrophyllite + quartz + H_2O . Ajoutons dans un premier temps deux pôles purs supplémentaires à la solution solide des chlorites : Mg-amesite (*ames*, $Mg_4Al_4Si_2O_{10}(OH)_8$) et Fe-amesite (*fames*, $Mg_4Al_4Si_2O_{10}(OH)_8$). Cela permet de prendre en compte la substitution Tschermak. Dans ce cas, on peut calculer 33 équilibres chimiques dont 4 sont indépendants ($IR = 9 - 5 = 4$). On rajoute donc les deux réactions indépendantes chlorite + chloritoïde + quartz + H_2O suivantes :



L'ajout de ces deux pôles purs fait apparaître également une réaction interne, car elle ne fait intervenir que des pôles purs de chlorite :



Si maintenant, on étend le modèle de solution solide des chlorites vers les chlorites di/trioctaédriques, en ajoutant le pôle sudoite (*sud*, $Mg_2Al_4Si_3O_{10}(OH)_8$), on peut calculer 97 équilibres chimiques dont 5 sont indépendants ($IR = 10 - 5 = 5$). On a encore ajouté une contrainte supplémentaire qui est l'équilibre chlorite + quartz + H_2O suivant :



et ainsi de suite. Plus on ajoute des pôles purs, plus on ajoute des contraintes supplémentaires. On pourrait, par exemple ici, continuer en ajoutant un pôle Fe-sudoite (*fsud*, $Fe_2Al_4Si_3O_{10}(OH)_8$) qui ajouterai une réaction indépendante chlorite + quartz + H_2O dans le système ferreux. Cependant, la limite est fixée par les données expérimentales disponibles. À l'heure actuelle, il manque des contraintes expérimentales pour ajouter la *fsud* au modèle de solution solide des chlorites. C'est pourquoi le modèle de Vidal et al. (2006) présenté précédemment se limite aux cinq pôles purs : *ames*, *fames*, *clin*, *daph*, *sud*.

2.2.3 Article 1 : Comment on "The role of H_3O^+ in the crystal structure of illite" by F. Nieto, M. Melini, and I. Abad (published in *Clays and Clay Minerals*)

Cette partie contient un article de Vidal et al., (2010) publié dans la revue *Clays and Clay Minerals*.

Comment on "The role of H_3O^+ in the crystal structure of illite" by F. Nieto, M. Melini, and I. Abad

Olivier Vidal, Benoît Dubacq and Pierre Lanari

Clays and Clay Minerals, Vol. 58, No. 5, 717-720, 2010

Abstract - The arguments of [Nieto et al. \(2010\)](#) in favor of the incorporation of H_3O^+ rather than H_2O in interlayer positions of illite are disputable. Stoichiometric arguments suggest that the excess water in the Silver Hill illite is in the form of H_2O . Moreover, recent thermodynamic models assuming the incorporation of interlayer H_2O in illite provide reasonable estimates of temperature and water content using the AEM/TEM analyses of [Nieto et al. \(2010\)](#).

2.2.3.1 Introduction

Illite is a dioctahedral alkali-deficient mica with excess water incorporated in apparent interlayer vacancies ([Hower et Mowatt 1966](#), [Loucks 1991](#), [Drits et McCarty 2007](#), [Vidal et Dubacq 2009](#), [Dubacq et al. 2010](#), [Nieto et al. 2010](#)). These vacancies are cation-free crystallographic sites that appear due to charge-balance constraints of the pyrophyllitic substitution $K^+ + Al^{3+} = Vac + Si^{4+}$ (e.g. [Abad et al., 2006](#)). Excess water in the interlayer is generally considered to be in the form of H_2O because a significant incorporation of H_3O^+ would imply unrealistically low pH ([Hower et Mowatt 1966](#), [Loucks 1991](#), [Jiang et al. 1994](#)). However, [Nieto et al. \(2010\)](#) suggest that the excess water in illite is in the form of H_3O^+ . If this is true, a modification of the common assumptions made to calculate the structural formu-

lae of alkali-deficient mica is necessary. A revision of the recent thermodynamic models of Vidal et Dubacq (2009) and Dubacq et al. (2010) would also be necessary, as the hydrated and dehydrated interlayer vacancies in illite are modeled using dehydrated and hydrated pyrophyllite end-members.

Although Nieto et al. (2010) performed a very careful and welcome study, we think that their arguments in favor of the incorporation of H_3O^+ instead of H_2O in interlayer position are disputable. Thermogravimetric analyses (Drits et McCarty 2007, Nieto et al. 2010) or Fourier-transform infrared (FTIR) measurements (e.g. Dubacq et al. (2010)) indicate the presence of water in alkali-deficient mica, but do not allow us to distinguish H_3O^+ from H_2O . Consequently, the arguments of Nieto et al. (2010) rely mainly on the calculation of structural formulae assuming the presence of either H_2O or H_3O^+ :

(1) The amount of interlayer water ($H_2O(i) = 0.42$ a.p.f.u.) calculated from the chemical data of Silver Hill illites and the water content measured by Hower et Mowatt (1966) is higher than the available space in interlayer position ($= 0.3$ a.p.f.u.). (a.p.f.u. = atoms or molecules per formula unit).

However, the amount of water measured by Hower et Mowatt (1966) ($H_2O = 6.4\%$) is too great for the analysis selected by Nieto et al. (2010) as it leads to an oxide total >100 wt.%. Ignoring TiO_2 as in the study of Nieto et al. (2010), an oxide total of 100 wt.% is obtained for $H_2O = 5.88\%$, which corresponds to 0.305 a.p.f.u. ($H_2O(i)$ in the first column of table 2.3, Case 1) and to the number of apparent interlayer vacancies. The same reasoning can be used for the structural formulae of illite reported by Nieto et al. (2010). With the value of $H_2O = 5.88\%$ determined above, $H_2O(i) = 0.28$ a.p.f.u. for the "average" composition listed in their table 2, which is again compatible with the value of 0.3 apparent interlayer vacancies. For the AEM/TEM analyses listed in table 1 of Nieto et al. (2010), the apparent vacancies range between 0.115 and 0.463. Assuming that they are occupied by molecular water, H_2O is found to range between 5 and 6.64 wt.%, with an average value of 5.8 wt.% (Tab. 2.3). The average value is in agreement with the value estimated above from the analysis by Hower et Mowatt (1966).

	HM(66)	Imt-2/1	Imt-2/2	Imt-2/3	Imt-2/4	Imt-2/6	Imt-2/7	Imt-2/12	Imt-2/13
Case 1 : interlayer vacancies filled by H_2O									
H_3O^+ wt. %	0.00	0.00	0.00	0.00	0.00	0.00	0.00	0.00	0.00
H_2O wt. %	5.89	6.00	5.51	5.89	6.15	5.99	6.63	5.53	6.39
Si a.p.f.u.	3.66	3.44	3.41	3.38	3.43	3.44	3.63	3.34	3.45
Al_{IV}	0.34	0.56	0.59	0.62	0.57	0.56	0.37	0.66	0.55
Al_{VI}	1.38	1.48	1.48	1.51	1.58	1.65	1.51	1.57	1.51
Fe^{2+}	0.08	0.07	0.07	0.06	0.06	0.04	0.07	0.06	0.06
Fe^{3+}	0.27	0.21	0.23	0.19	0.17	0.12	0.21	0.17	0.20
Mg	0.28	0.33	0.28	0.35	0.28	0.24	0.26	0.27	0.35
K+Ca+Na	0.69	0.67	0.77	0.69	0.64	0.68	0.54	0.77	0.59
$H_2O(i)$	0.31	0.33	0.23	0.31	0.36	0.32	0.46	0.23	0.41
OC	2.00	2.09	2.06	2.11	2.09	2.05	2.05	2.07	2.12
XPrI+XPrIH	0.31	0.33	0.23	0.31	0.36	0.32	0.46	0.23	0.41
XBt	0.00	0.09	0.06	0.11	0.09	0.05	0.05	0.07	0.12
XCel	0.36	0.11	0.18	0.07	0.07	0.12	0.16	0.11	0.04
XMusc	0.34	0.46	0.53	0.51	0.48	0.51	0.32	0.59	0.42
Case 2 : interlayer vacancies filled by H_3O^+									
H_3O^+ wt. %	1.52	1.64	4.56	4.56	1.76	1.57	2.24	1.12	1.99
H_2O wt. %	1.12	1.51	6.04	6.61	6.97	6.73	7.67	6.06	7.29
Si a.p.f.u.	3.61	3.39	3.37	3.33	3.37	3.38	3.55	3.30	3.39
Al_{IV}	0.39	0.61	0.63	0.67	0.63	0.62	0.45	0.70	0.61
Al_{VI}	1.31	1.40	1.42	1.43	1.48	1.57	1.40	1.51	1.41
Fe^{2+}	0.08	0.07	0.07	0.06	0.05	0.04	0.07	0.05	0.06
Fe^{3+}	0.25	0.21	0.23	0.19	0.17	0.12	0.21	0.17	0.19
Mg	0.27	0.33	0.28	0.34	0.28	0.24	0.25	0.27	0.34
K+Ca+Na	0.67	0.66	0.76	0.68	0.63	0.67	0.53	0.76	0.58
H_3O^+	0.32	0.34	0.24	0.32	0.37	0.33	0.47	0.24	0.42
OC	1.91	2.00	1.99	2.03	1.99	1.96	1.92	2.01	2.01
XCel	0.35	0.39	0.35	0.40	0.33	0.27	0.32	0.32	0.40
XMusc	0.65	0.61	0.65	0.60	0.67	0.73	0.68	0.68	0.60

table continued next page...

(2) When assuming that the excess water corresponds to H_3O^+ and eventually adjusting the Fe^{2+}/Fe^{3+} ratio, the calculated structural formulae have an octahedral occupancy (OC) of 2 and an interlayer occupancy (IC) of 1. It follows that the Si in excess of 3 a.p.f.u. and the amount of $Mg + Fe^{2+}$ are explained by the Tschermak substitution alone. The total number of cations in the illite structural formula, calculated on the basis of 22 negative charges ($O_{10}(OH)_2$) and assuming that $(K^+ + Na^+ + H_3O^+)_{interlayer} = 1 \text{ a.p.f.u.}$, is indeed less than if H_2O is assumed to be incorporated in the interlayer position. As a result, both the Si content and the OC decrease and the extent of both di-trioctahedral and pyrophyllitic substitutions is reduced.

	Imt-2/14	Imt-2/16	Imt-2/20	Imt-2/22	Imt-2/23	Imt-2/24	Imt-2/25	Imt-2/26	Imt-2/27
Case 1 : interlayer vacancies filled by H_2O									
H_3O^+ wt.%	0.00	0.00	0.00	0.00	0.00	0.00	0.00	0.00	0.00
H_2O wt.%	5.61	5.53	5.86	6.55	5.00	6.66	5.04	5.32	5.29
Si a.p.f.u.	3.33	3.44	3.40	3.63	3.28	3.68	3.43	3.35	3.42
Al_{IV}	0.67	0.56	0.60	0.37	0.72	0.32	0.57	0.65	0.58
Al_{VI}	1.54	1.45	1.55	1.63	1.54	1.65	1.43	1.49	1.48
Fe^{2+}	0.07	0.06	0.06	0.05	0.06	0.04	0.07	0.07	0.06
Fe^{3+}	0.21	0.19	0.20	0.14	0.18	0.13	0.21	0.23	0.20
Mg	0.26	0.37	0.26	0.19	0.28	0.17	0.32	0.27	0.30
K+Ca+Na	0.75	0.77	0.70	0.57	0.88	0.55	0.87	0.81	0.82
$H_2O(i)$	0.25	0.23	0.30	0.43	0.12	0.45	0.13	0.19	0.18
OC	2.08	2.07	2.07	2.01	2.06	1.99	2.03	2.06	2.04
XPrI+XPrIH	0.25	0.23	0.30	0.43	0.12	0.45	0.13	0.19	0.18
XBt	0.08	0.07	0.07	0.01	0.06	0.00	0.03	0.06	0.04
XCel	0.08	0.21	0.10	0.20	0.16	0.23	0.30	0.16	0.24
XMusc	0.59	0.49	0.52	0.36	0.66	0.32	0.54	0.59	0.54
Case 2 : interlayer vacancies filled by H_3O^+									
H_3O^+ wt.%	1.21	1.12	1.46	2.11	0.58	2.21	0.63	0.92	0.87
H_2O wt.%	6.18	6.05	6.54	7.51	5.28	7.66	5.35	5.75	5.70
Si a.p.f.u.	3.29	3.40	3.35	3.56	3.26	3.60	3.41	3.32	3.39
Al_{IV}	0.71	0.60	0.65	0.44	0.74	0.40	0.59	0.68	0.61
$?Al_{VI}$	1.48	1.39	1.48	1.52	1.51	1.53	1.40	1.44	1.43
Fe^{2+}	0.07	0.06	0.06	0.04	0.06	0.04	0.07	0.07	0.06
Fe^{3+}	0.21	0.19	0.19	0.14	0.18	0.13	0.21	0.23	0.20
?Mg	0.26	0.37	0.26	0.19	0.28	0.17	0.32	0.27	0.30
?K+Ca+Na	0.74	0.76	0.69	0.56	0.88	0.54	0.87	0.80	0.82
H_3O^+	0.26	0.24	0.31	0.44	0.12	0.46	0.13	0.20	0.18
?OC	2.01	2.01	1.99	1.89	2.02	1.87	1.99	2.01	1.99
XCel	0.32	0.43	0.32	0.23	0.34	0.21	0.38	0.34	0.36
XMusc	0.68	0.57	0.68	0.77	0.66	0.79	0.62	0.66	0.64

TABLE 2.3 – Structural formulae and maximum amount of H_2O and H_3O^+ wt.% calculated from the AEM/TEM analyses of [Nieto et al. \(2010\)](#) and the analysis from Hower and Mowatt (1966) (HM66). In Case 1, H_2O was calculated assuming all apparent vacancies ($= 1 - Na - K$) being filled by molecular water, $(XPrI + XPrIH) = (Si - 3 - XCel)$, $XBt = (OC - 2)$, $(XCel)_{Case1} = (Fe^{2+} + Mg - 3XBt)$, $(XMusc)_{Case1} = (Al_{VI} + Fe^{3+} - 2(XPrI + XPrIH) - XCel)/2$. In Case 2, the structural formulae were recalculated on the basis of 22 negative charges, and H_3O^+ (a.p.f.u.) was estimated in order to have $(K + Na + H_3O^+) = 1$, $(XCel)_{Case2} = (Fe^{2+} + Mg)$, $(XMusc)_{Case2} = 1 - (XCel)_{Case2}$.

Unfortunately, [Nieto et al. \(2010\)](#) compared the structural formulae calculated assuming the incorporation of H_2O or H_3O^+ for the average illite composition only. The structural formulae of all the individual TEM/ AEM analyses reported by [Nieto et al. \(2010\)](#) are listed in Table 2.3. In Case 2 (incorporation of H_3O^+), they have been calculated on a 22 negative charge basis, and H_3O^+ was adjusted in order to obtain $(K^+ + Na^+ + H_3O^+)_{interlayer} = 1$. In contrast with the statement of [Nieto et al. \(2010\)](#), the OC is generally different from the ideal value of 2 a.p.f.u. (Tab. 2.3). It is often less than this value, which implies that the composition of illite cannot be explained by the Tschermak substitution alone ([Ransom et Helgeson 1993](#)). This point is further illustrated in figure. 2.5, which shows that a linear combination of the celadonite ($XCel = Mg + Fe^{2+}$) and muscovite ($XMusc = 1 - XCel$) end-members does not reproduce the Si content of the structural formulae. The

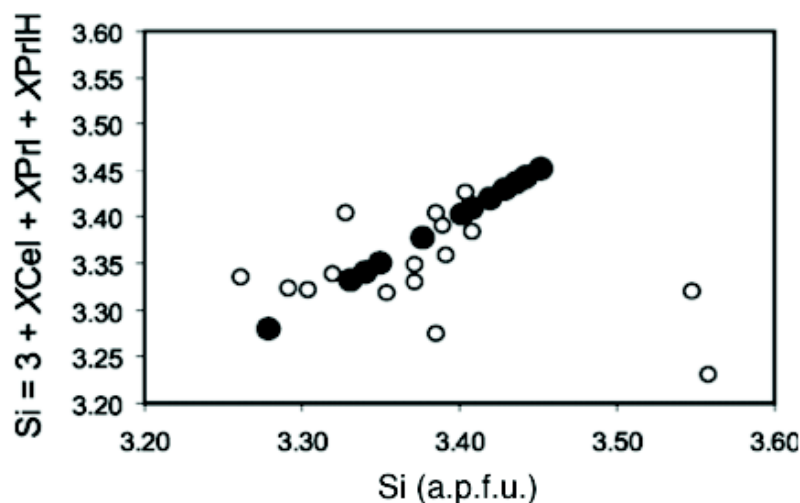


FIGURE 2.5 – *Si* content calculated from the proportion of end- members in Cases 1 (incorporation of H_2O , filled symbols) and 2 (incorporation of H_3O^+ , open symbols) vs. *Si* content of the structural formulae. In Case 2, the molar fraction of Cel and Musc are calculated from the octahedral ($Mg + Fe^{2+}$) content.

scatter of the open symbols in figure. 2.5 shows that the octahedral ($Fe^{2+} + Mg$) and tetrahedral *Si* contents cannot both be described by the Tschermak substitution alone between (K^+, H_3O^+) -celadonite and muscovite. Additional end-members are thus required. The OC obtained when assuming the incorporation of H_2O (Case 1) are also different but generally > 2 . This is easily explained by the incorporation of a trioctahedral component in illite, as observed in phengite at high temperature or smectite at lower temperature. In this case, the molar fraction of pyrophyllite ($Prl : Si_4(Al, Fe^{3+})_2O_{10}(OH)_2$), hydrated pyrophyllite ($PrlH : Si_4(Al, Fe^{3+})_2O_{10}(OH)_2.H_2O$), biotite ($Bt : (Si_3Al)(Mg, Fe^{2+})_3KO_{10}(OH)_2$), celadonite ($Cel : Si_4(Al, Fe^{3+})(Mg, Fe^{2+})KO_{10}(OH)_2$), and muscovite ($Musc : (Si_3Al)(Al, Fe^{3+})_2KO_{10}(OH)_2$) end-members proposed by Dubacq et al. (2010) are listed in table 2.3. The structural formulae are fully reproduced with these end-members, e.g. the *Si* content of the structural formulae (Fig. 2.5, filled symbols).

Because of the stoichiometric reasons listed above, the excess water in the illite grains analysed by Nieto et al. (2010) is more likely, or at least possibly, in the form of molecular water rather than H_3O^+ . The thermodynamic model of Dubacq et al. (2010) was used to estimate the amount of $H_2O(i)$ and the temperature of equilibrium among the Silver Hill illite, quartz, and water at 1 kbar (Fig. 2.6). Although

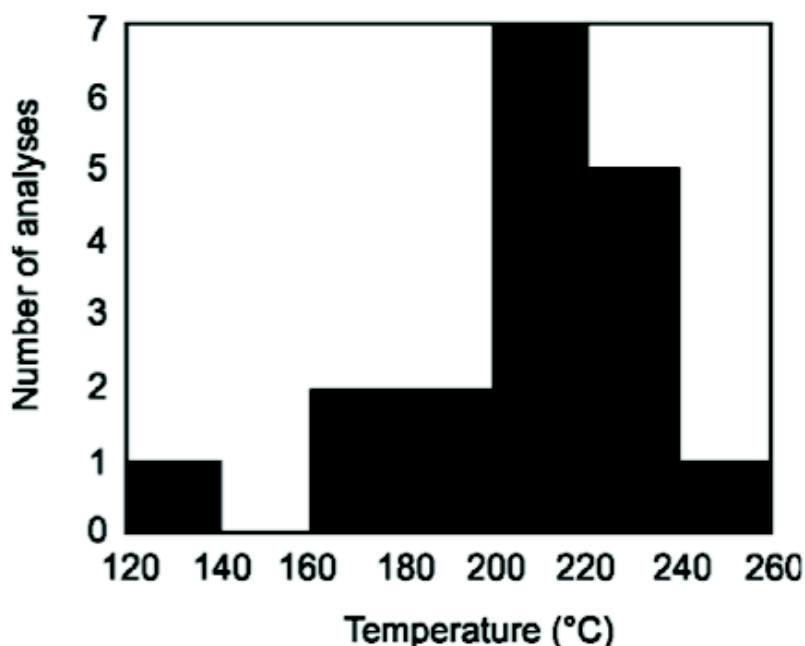


FIGURE 2.6 – Si content calculated from the proportion of end- members in Cases 1 (incorporation of H_2O , filled symbols) and 2 (incorporation of H_3O^+ , open symbols) vs. Si content of the structural formulae. In Case 2, the molar fraction of Cel and Musc are calculated from the octahedral ($Mg + Fe^{2+}$) content.

the illite compositions reported by Nieto et al. (2010) are highly variable, the calculated temperatures are quite similar and define conditions at 210°C (Fig. 2.6). Moreover, the predicted amount of interlayer water is very close in each case to the maximum value estimated from the stoichiometric criteria above. These results can be viewed as an additional and independent argument in favor of the incorporation of neutral water in the apparent vacancies of illite.

2.2.3.2 Conclusion

(1) We agree with Nieto et al. (2010) that thermobarometric estimates cannot be made without consideration of excess water in illite, i.e. using the model of Vidal et Parra (2000) or Parra et al. (2002a) derived for phengites. However, stoichiometric and thermodynamic arguments both suggest that the excess water in the Silver Hill illite is in the form of H_2O rather than H_3O^+ . An independent argument against a significant incorporation of H_3O^+ is that it would imply unrealistically low pH, as already discussed by Hower et Mowatt (1966), Loucks (1991) and Jiang et al. (1994).

(2) No evidence was found to support the assumption that octahedral occupancy in illite should exactly equal 2 or that the interlayers should sum exactly to unity.

(3) The thermobarometric model of [Dubacq et al. \(2010\)](#) gives reasonable estimates of equilibrium conditions and water content when assuming that H_2O is incorporated in the interlayer position of illite. The thermodynamic model of [Dubacq et al. \(2010\)](#) is, therefore, in good agreement with the analytical results of [Nieto et al. \(2010\)](#).

2.2.4 Evolution of the Vallès fault from chlorite and mica equilibrium

Cette partie contient un abstract étendu de Cantarero et al., (2012) publié dans un recueil de résumés à l'occasion du *VIII Congreso Geológico de España*.

Evolution of the Vallès fault from chlorite and mica equilibrium

Cantarero I., Lanari P., Vidal O., Alias G. Travé A. Bacqués V.

VIII Congreso Geológico de España

Abstract - The neoformation of mica and chlorite within the Vallès fault has allowed constrain the P-T conditions during fault evolution using chlorite-mica multi-equilibrium. Three events have been distinguished. The first one corresponds to the crystallisation of muscovite-rich *M1* and *M2* mica as the result of deuteritic alteration during the exhumation of the pluton ($T > 325^{\circ}\text{C}$). The second event is attributed to the Mesozoic rifting, which is characterised by the crystallisation of pyrophyllite-rich *M3* and *M4* mica together with chlorite at temperatures between 200 and 300°C . Finally, during the Neogene extension, another generation of chlorite is formed at temperatures below 190°C in absence of mica. During these tectonic events faults acted as conduits for hot and Si-rich fluids producing anomalous high geothermal gradients ($50^{\circ}\text{C}/\text{km}$ minimum). The estimated decrease of pressure is consistent with exhumation produced during both Alpine compression and Neogene extension.

Resumen - La neoformación de mica y clorita en la falla del Vallès ha permitido estimar las condiciones P-T durante la evolución de la falla usando el multi-equilibrio mica-clorita. Se han identificado tres episodios. El primero corresponde a la cristalización de las micas ricas en moscovita *M1* y *M2* como resultado de la alteración deutérica durante la exhumación del plutón ($T > 325^{\circ}\text{C}$). El segundo episodio se atribuye al rifting Mesozoico y se caracteriza por la cristalización de las micas ricas en pirofilita *M3* y *M4* junto con la clorita a temperaturas entre 200 y 300°C . Finalmente, durante la extensión Neógena, otra generación de clorita se formó a menos de 190°C en ausencia de mica. Durante estos eventos tectónicos las fallas actuaron como conductos de fluidos calientes y ricos en Si produciendo gradientes geotermales locales anormalmente altos ($50^{\circ}\text{C}/\text{km}$ mínimo). El descenso de

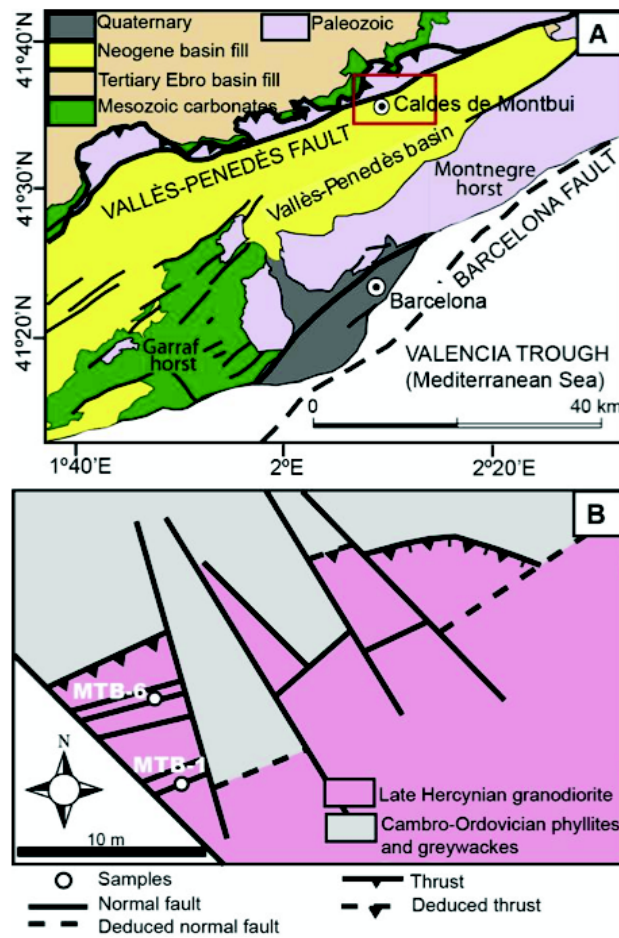


FIGURE 2.7 – A) Simplified geological map of the central part of the Catalan Coastal Ranges. B) Outcrop sketch with location of the studied samples.

presión estimado es coherente con la exhumación causada tanto por la compresión Alpina como por la extensión Neógena.

2.2.4.1 Introduction

The composition of chlorite and mica is temperature and pressure dependent, and it has been used successfully to constrain P-T conditions in low temperature pelites free of minerals index of metamorphism (e.g. Parra et al. 2002a, Vidal et al. 2005; 2006, Lanari et al. 2012a). Chlorite and mica are also common low temperature alteration products of granodiorites, as observed in the Vallès fault, which is one of the main extensional faults that constitute the Catalan Coastal Ranges. These ranges are formed by a system of horsts and grabens controlled by main NE-SW trending faults (Fig.2.7). Some of these faults are the result of the negative inversion of Paleogene thrusts, which, in turn, inverted extensional Mesozoic faults.

Although temperature conditions during their evolution are not well known, structural studies have constrained the maximum burial at which outcropping samples have been, which yields to a maximum pressure of 1 *kbar* during Mesozoic.

The T and P conditions of deformation of the Vallès fault were estimated from the composition of chlorite and phengite using chlorite-mica multi-equilibrium techniques associated with recent thermodynamic models (Vidal et al. 2006, Dubacq et al. 2010). The solid solution end-members for chlorite are clinocllore, (Fe,Mg)-amesite, daphnite and sudoite whereas for mica are (Fe, Mg)-celadonite, pyrophyllite, pyrophyllite.1H₂O, muscovite, paragonite and biotite.

Hot springs are spread along the Vallès fault, as in the vicinity of Caldes de Montbui, where this study is made. Two hydrothermal events have been described in the area, one during the Mesozoic and the other during the Neogene (Cardellach et al. 2002).

The Vallès fault separates the late Hercynian granodiorite from the late Miocene sandstones and it is segmented by NW-SE faults. The studied outcrop is located in its footwall, at 100 *m* from the Neogene main fault plain (Fig. 2.7-b). The paragenesis of the granodiorite is composed by quartz-microcline-plagioclase-biotite. Deformation along the fault produces brittle fault rocks in the granodiorite (from breccias to ultracataclasites), which show a greenish color because of chloritisation. The neoformed minerals in the fault rock are chlorite-mica-calcite-laumontite, and in a lesser extent epidote. In order to obtain P-T estimates, chlorites and micas of two samples have been studied.

2.2.4.2 Results

Chlorite occurs along fractures or as patches in the cataclasite and ultracataclasite matrix. The composition of chlorite in the studied samples evolves along a trend corresponding to a decrease of amesite and an increase of sudoite end-member proportions (Fig. 2.8).

Two kinds of mica have been identified. Coarse crystals (M1) of muscovite-rich mica (Fig. 2.8) with rims of pale color and poor cleavage at the margins (M2)

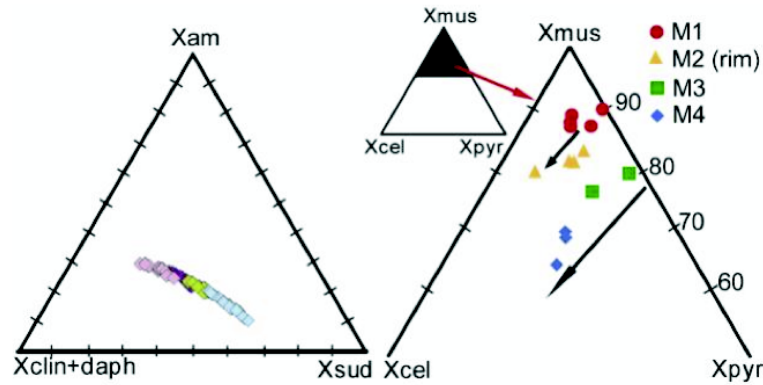


FIGURE 2.8 – End-members ternary plot of chlorites (left) and micas (right). Colors from chlorites symbol correspond to the temperature ranges shown in figure 2.10. Am : amesite ; clin : clinocllore ; daph : daphnite ; sud : sudoite ; mus : muscovite ; cel : celadonite ; pyr : pyrophyllite.

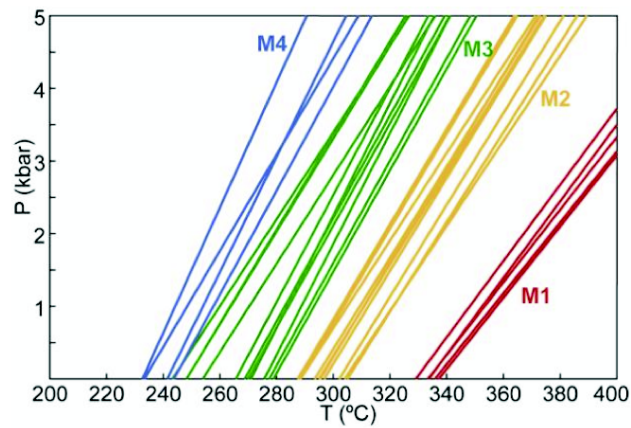


FIGURE 2.9 – diagram showing the results of mica-quartz-water thermometer for the four established groups of micas

occur in the slightly brecciated granodiorite. Another kind of flakes of smaller size pyrophyllite-rich mica (M3 and M4) is restricted to plains inside the fault rock. M4 crystallizes after M3 and both overgrowth detrital flakes of the previous mica. Both kinds show a similar trend described by an increase in celadonite proportion caused by Tschermak exchange (Fig. 2.8).

For each mica composition, a P-T line corresponding to the mica-quartz-water equilibrium has been calculated. We have used the model of Dubacq et al. (2010), which takes into account the hydration of mica with varying P-T (Fig. 2.9).

The chlorite-quartz-water equilibria are located at temperatures between 125 and 310°C at 1 kbar, maximum pressure conditions according to structural data

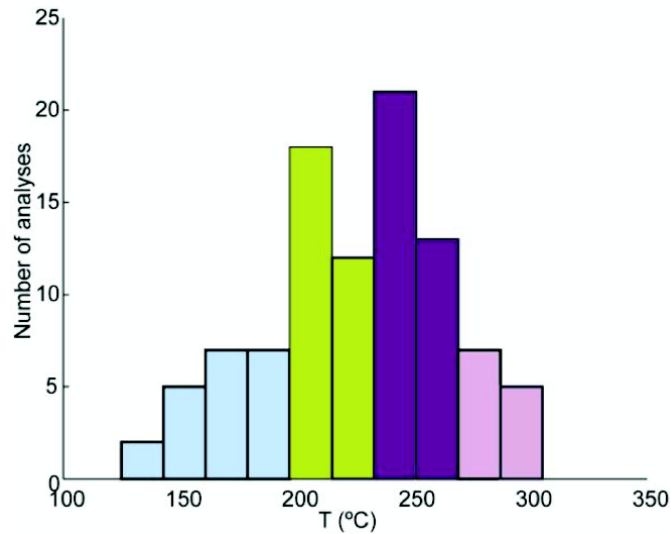


FIGURE 2.10 – Histogram of temperature of chlorite formation using the solid-solution model of Vidal *et al.* (2006).

(fig. 2.10). No relationship was evidenced between the calculated temperatures of chlorite formation and their microstructural location.

P-T conditions were estimated from chlorite-mica-quartz-water multi-equilibrium. As shown in figure 2.9, M1 and M2 mica were calculated to crystallize at higher temperature than M3 and M4 micas at a fixed pressure. The M1 and M2 mica-quartz-water P-T lines are located at higher temperature than the chlorite-quartz-water equilibria at the same pressure of 1 *kbar*.

In contrast, M3 and M4 mica-quartz-water P-T lines are located at the same range of temperature as the chlorite-quartz-water equilibria. The temperature estimated from the chlorite-mica multi-equilibrium from the fault rock ranged from 250 to 310°C ($\pm 50^\circ\text{C}$) for M3 mica and from 190 to 260°C ($\pm 50^\circ\text{C}$) for M4 mica. Calculated pressure conditions ranged from 0 to 4 ± 2 *kbar*, except for a group of M4 mica that are clearly below 1 *kbar*. Although the scatter and the uncertainty on the calculated P-T conditions is significant (fig. 2.10), the inferred PT path followed by the fault rocks in the Vallès fault describes a decrease of temperature and pressure.

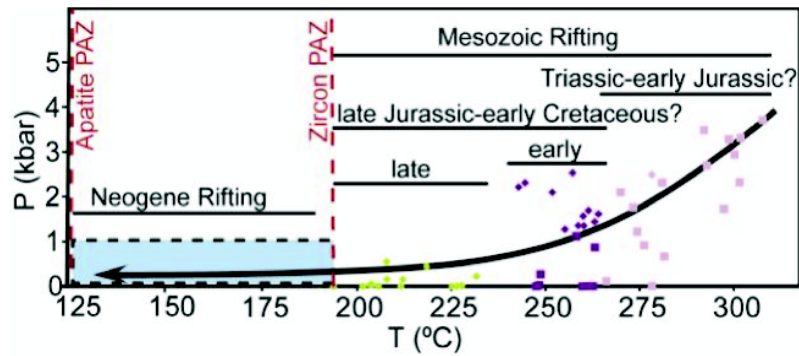


FIGURE 2.11 – PT path of fault rocks in the Vallès fault. Squares represent chlorite in equilibrium with M3 mica and diamonds represents chlorite in equilibrium with M4 mica. In red, the closure temperature of the partial annealing zone of zircon and apatite.

2.2.4.3 Discussion

According to the petrologic observations of fault and host rocks, M1 mica is a product of deuteric alteration produced by igneous fluids ($T > 325^{\circ}\text{C}$) in fractures produced during the exhumation of the granodiorite. Pluton exhumation took place during the Permian as denoted by the unconformity between the granodiorite and Triassic materials of Buntsandstein facies outcropping in the area. M1 mica is in turn partially replaced by M2 mica as a result of the reequilibration at lower temperatures ($T > 300^{\circ}\text{C}$) during the exhumation path. M1 and M2 mica have lower pyrophyllite component than M3 and M4 micas. This compositional difference can be related to the circulation through the fault of a fluid richer in Si, probably in combination with a localized increase of pressure due to tectonic stress in the fault core. After exhumation, plutons were newly buried at about 800 m because of the sedimentation of Mesozoic materials during the initial phase of rifting (Anadon et al. 1979).

Fission-track and (U-Th)/He studies with apatites and zircons in this sector of the Catalan Coastal Ranges, have shown that the isotherm of 190°C (closure temperature for zircon PAZ) was only crossed during the Mesozoic (Juez-Larré 2003). This observation constrains the neoformation of M3 and M4 mica and their related chlorite to this period (Fig. 2.11). Our work lets to describe the evolution of temperatures during the extensional tectonic event related to this time. Three stages according to several mica and chlorite associations can be described. The

first stage is characterized by *M3* mica in equilibrium with chlorite between 260 and 310°C, the second one is marked by the coexistence of *M3* and *M4* mica and chlorite between 240 and 260°C and, finally, the third one is defined by *M4* mica and chlorite between 190 and 240°C. It is likely that this P-T evolution is related to the first rifting event of Triassic-early Jurassic age and to the earlier and late stages of the late Jurassic-early Cretaceous rifting event.

Fission-track studies have also established that the isotherm of 110°C (closure temperature for apatite PAZ) was crossed at the onset of the rifting event related to the Neogene. On the other hand, temperatures between 130 and 150°C were estimated by fluid inclusion analyses in Neogene calcites in the area ([Cardellach et al. 2002](#)). Both statements points to a Neogene neoformation of the low temperature chlorites (125-190°C) that crystallize in the absence of mica. Maximum burial of the outcropping samples reached 3.6 *km* before the Paleogene compression and 2.5 *km* before the Miocene extension ([Juez-Larré 2003](#)). Thus, the estimated pressures above 1 *kbar* are not compatible with these results. This inconsistency is possibly due to errors in the P estimates caused by errors in the used thermodynamic models and the microprobe analyses. However, the estimated path (decrease of P) is consistent with tectonic evolution since during the Alpine compression granodiorite followed an initial phase of uplift and during the Neogene extension uplift and erosion continued on the footwall until the actual situation.

The regional geothermal gradient during the two periods of extensional tectonics, Mesozoic and Neogene, was 27-35°C/km and 30°C/km, respectively ([Juez-Larré 2003](#)). However, if the geothermal gradient is calculated from our T estimates and the maximum burial conditions, the obtained geothermal gradient is higher. This suggests that during these tectonic events fault acted as conduits for hot and Si- rich fluids producing anomalous high geothermal gradients (50°C/km minimum) along fractures. This fact is also supported by the resetting of fission-tracks near fault zones ([Juez-Larré 2003](#)).

2.2.4.4 Conclusions

The Vallès fault is a Neogene extensional fault that separates the Hercynian granodiorite from the Miocene sandstones, at the vicinity of Caldes de Montbui. Deformation in the granodiorite originated from breccias to ultracataclasites.

The neoformed mica and chlorite within the faults can be used to estimate the P-T conditions during fault evolution. In addition, fission-track data are a good temporal constrain for these estimates. Coarse crystals of mica rich in muscovite component (*M1*), rimmed by new formed celadonite-rich muscovite (*M2*), have been interpreted as a deuteric alteration during the late- Hercynian exhumation of the granodiorite at temperatures above 325°C. On the other hand, small flakes of mica (*M3*) richer in pyrophyllite content and with a large celadonite substitution (*M4*) crystallized together with chlorite during two episodes of the Mesozoic rifting. The first took place at temperatures between 260 and 310°C, possibly during the Triassic, and the other at temperatures that decrease from 260 to 190°C, possibly during the late Jurassic-early Cretaceous. A later generation of chlorite formed at temperatures below 190°C, in absence of mica, is related to the Neogene extension. Late Hercynian fractures in granodiorite were reactivated during Mesozoic and Neogene extension events, and acted as conduits for hydrothermal fluids. This circulation produced anomalous high geothermal gradients, as pointed by previous works based on fission-track data and mineral deposits in the Catalan Coastal Ranges and the Iberian Chain.

The P-T evolution of the late Hercynian granodiorite indicates that after the intrusion, granodiorite was exhumed during Permian and afterwards became newly buried at about 800 *m* because overburden of Mesozoic sediments. The P path from this moment is consistent with exhumation due to isostatic rebound (during extension) and uplift and erosion (during compression). During the Neogene extension, exhumation of the granodiorite described a nearly isobaric cooling path.

2.2.4.5 Acknowledgements

This work was funded by the of DGICYT Spanish Project *CGL2010-18260*, the "Grup Consolidat de Recerca Geologia Sedimentària" 2009*SGR*-1451 and the grants 2011*FI_B*2 00179 and *BE2010* supported by the Comissionat per a Universitats i Recerca del Departament d'Innovació, Universitats i Empresa de la Generalitat de Catalunya i el Fons Social Europeu.

2.2.5 Etude de l'incertitude du thermomètre $\text{Chl}+\text{Qtz}+\text{H}_2\text{O}$ ($T < 350^\circ\text{C}$)

Le thermomètre chlorite+quartz+ H_2O (appelé $\text{Chl}+\text{Qtz}+\text{H}_2\text{O}$ dans la suite) est utile car il permet d'estimer à la fois la température de la chlorite et son état d'oxydation à partir d'une seule analyse de chlorite. Cette méthode a été utilisée ces dernières années, pour différents contextes géodynamiques (Vidal et al. 2006, Dubacq 2008, Plissart et al. 2009, Saravanan et al. 2009, Tarantola et al. 2009, Verlaquet et al. 2011, Cantarero et al. 2012, Grosch et al. 2012, Lacroix et al. 2012, Lanari et al. 2012a).

La caractérisation de l'incertitude associée aux estimations P-T est extrêmement importante en thermobarométrie et de nombreuses études ont eu pour objectif d'essayer de la quantifier (voir par exemple les travaux de Hodges et McKenna 1987, Kohn 1993, Kohn et Spear 1991a;b, Vidal et Parra 2000, Worley et Powell 2000). Cette incertitude résulte de deux principales sources d'erreurs, l'une analytique, directement sur la mesure des compositions et l'autre sur les données thermodynamiques utilisées lors du calcul des conditions d'équilibre.

L'incertitude "réelle" sur les données thermodynamiques comme les entropies, les enthalpies, les coefficients C_p , les coefficients de volume, et les modèles d'activités est quasiment impossible à estimer. Dans la pratique, comme les bases de données sont inter-cohérentes, on peut observer une compensation entre les différentes incertitudes qui ne sont pas indépendantes mais souvent corrélées entre elles. On notera également que ces incertitudes sont très étroitement liées à la procédure utilisée pour l'optimisation de la base de données. Comme nous le discutons dans le "supplementary material" de l'article Lanari et al. (in press), l'incertitude sur les données thermodynamiques a toujours un effet systématique sur la position absolue d'une réaction (ici en température) et non sur sa position relative. C'est pourquoi l'incertitude absolue d'une estimation P-T est toujours, quelque soit la méthode, d'au moins $\pm 50^\circ\text{C}$ et ± 2.5 kbar.

À l'inverse de l'incertitude sur les données thermodynamiques, l'erreur analytique de la mesure, qui correspondra à une incertitude relative sur l'estimation P-T,

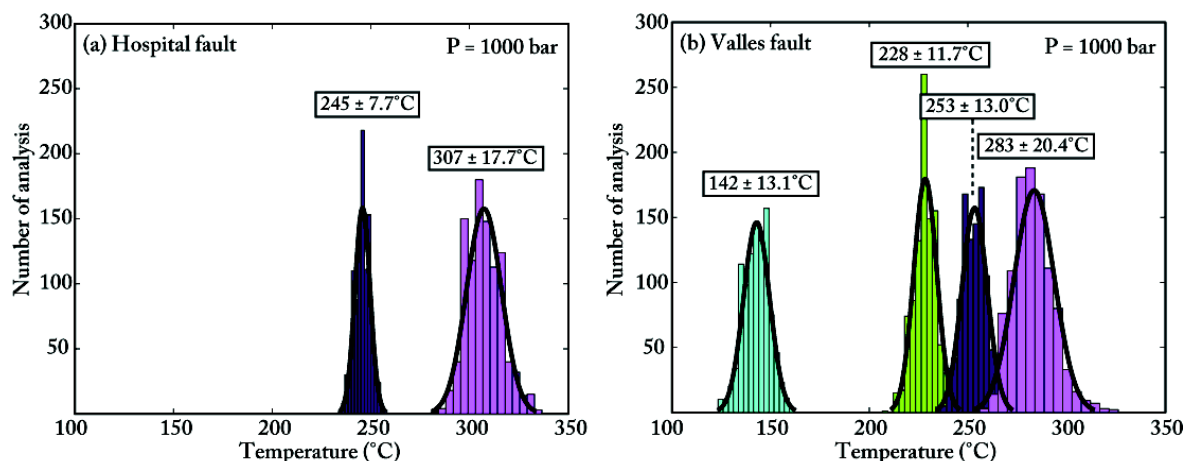


FIGURE 2.12 – Résultats de la simulation de Monte-Carlo pour l'étude de l'incertitude "analytique" liée aux estimations de températures pour les différents groupes de chlorites de [Cantarero et al. \(2012\)](#). Chaque histogramme correspond au calcul des températures pour 1000 compositions simulées de chlorites. Les compositions originales utilisées pour le tirage de Monte-Carlo (voir texte) sont disponibles Tab. 2.4

peut être assez facilement estimée. Pour cela, il faut connaître la précision de la machine utilisée pour mesurer la composition et utiliser une méthode de propagation d'incertitudes comme l'approche de Monte-Carlo ([Hodges et McKenna 1987](#), [Lieberman et Petrakakis 1991](#), [Kohn et Spear 1991b](#), [Vidal et Parra 2000](#), [Rimmelé et al. 2006](#), [De Andrade 2006](#), [Lanari et al. in press](#)).

Une caractérisation de l'incertitude "analytique" associée aux estimations de températures des chlorites calculées avec le thermomètre $\text{Chl} + \text{Qtz} + \text{H}_2\text{O}$ a été réalisée en utilisant les analyses de chlorites de [Cantarero et al. \(2012\)](#) présentées précédemment. Cette étude a porté sur la caractérisation des températures enregistrées par les chlorites de deux échantillons prélevés dans deux failles "Hospital fault" et "Valles fault", à proximité de Barcelone (Espagne). Dans les deux cas, la chlorite est visible soit en remplacement d'ancienne biotite du protolite granitique, soit en minéraux néoformés cristallisants aux joints de grains, dans une matrice fine, parfois associée à de la phengite ([Cantarero et al. 2012](#)). À partir d'analyses ponctuelles à la microsonde, différents groupes de températures ont été identifiés par [Cantarero et al. \(2012\)](#) : 2 groupes pour l'Hospital fault et 4 groupes pour la Valles fault avec des températures comprises entre 140°C et 310°C. Une analyse ponctuelle de chlorite mesurée à la microsonde a été sélectionnée

comme représentative de chaque groupe. Ces analyses sont reportées dans le tableau 2.4. À partir de chacune d'entre elle, 1000 compositions de chlorites ont été aléatoirement générées afin de reproduire une distribution de type loi normale avec une dispersion de $1\sigma = 1\%$ (en relatif) pour chaque élément mesuré (SiO_2 , Al_2O_3 , FeO , MnO , MgO , CaO , Na_2O , K_2O). Pour chaque composition générée, une formule structurale a été calculée afin de tester la validité de l'analyse. Puis les températures ont été estimées à 1 kbar pour chaque composition mesurée en utilisant la méthode $\text{Chl}+\text{Qtz}+\text{H}_2\text{O}$ et le logiciel MULTIPLOT (Part. 2.2.8). La figure 2.12 regroupe les histogrammes de températures calculées pour chaque cas pour l'Hospital fault (2.12-a) et la Valles fault (2.12-b).

L'incertitude en température résultant de l'incertitude analytique, est comprise entre $7,7^\circ\text{C}$ et $20,4^\circ\text{C}$. Elle semble augmenter légèrement avec l'augmentation de la température. Pour la Valles Fault, cette étude met en évidence que les trois groupes respectivement à $228 \pm 11,7^\circ\text{C}$, $253 \pm 13,0^\circ\text{C}$ et $283 \pm 20,4^\circ\text{C}$ correspondent bien à trois groupes de températures différentes et que cette variation n'est pas due à l'erreur analytique. Une incertitude analytique inférieure à 20°C est raisonnable pour étudier les températures des chlorites et les regrouper en différents groupes de températures.

2.2.6 Limites du thermomètre $\text{Chl}+\text{Qtz}+\text{H}_2\text{O}$ à HT ($T > 350^\circ\text{C}$)

Le même calcul d'incertitude analytique a été réalisé pour une analyse de chlorite de plus haut grade de métamorphisme (analyse Tab. 2.4) provenant de l'unité HT des Schistes lustrés (c.f. 4.3). Un jeu de 1000 compositions ont été aléatoirement générées et les températures calculées à 15 Kbar en utilisant la méthode $\text{Chl}+\text{Qtz}$ (Vidal et al. 2006). Les résultats ont été reportés sur la figure 2.13. Dans ce cas, deux groupes distincts de températures sont visibles, le premier à environ 380°C et le second plus petit autour de 460°C . L'incertitude calculée sur la température est donc beaucoup plus grande que dans le cas précédent avec une température pour cette chlorite de $392 \pm 59^\circ\text{C}$.

Cette exemple montre que si l'on calcule les températures d'une centaine d'analyses de cette chlorite en absence de toute zonation chimique, deux groupes dis-

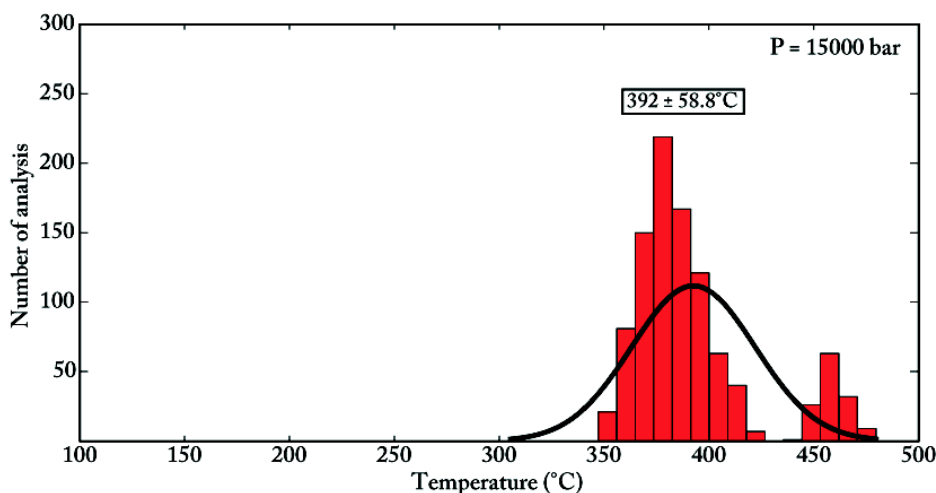


FIGURE 2.13 – Résultats de la simulation de Monte-Carlo pour l'étude de l'incertitude "analytique" liée aux estimations de températures pour le groupe de chlorites de HT ($> 300^{\circ}\text{C}$). L'histogramme en rouge correspond au calcul des températures pour 1000 compositions de chlorites simulées à partir de la composition originale (Tab. 2.4) avec une approche de Monte-Carlo (voir texte)

tincts de températures peuvent être générés en raison de l'erreur sur les analyses microsondes (Fig. 2.13). Cette distribution anormale des températures résulte de deux problèmes majeurs, (1) de calcul, car la température de la chlorite est estimée avec un taux "minimum" de Fe^{3+} et (2) de calibration, car le modèle *Chl* de Vidal et al. (2006) a été contraint en utilisant des chlorites de HP.

(1) Le calcul de la température de cristallisation d'une chlorite est effectué à une pression donnée en ajoutant du Fe^{3+} jusqu'à convergence entre les quatre équilibres $\text{chl} + \text{qtz} + \text{H}_2\text{O}$. Dès que l'écart entre les réactions est inférieur à 30°C à cette pression donnée, le programme s'arrête et donne un résultat avec une quantité minimum de Fe^{3+} . Cependant, il est possible pour les chlorites de HT de les équilibrer à plus basse température en ajoutant du Fe^{3+} (Grosch et al. 2012). Ce problème d'incertitude analytique élevé résulte directement de l'approche utilisée pour calculer la température et n'intervient donc pas pour les équilibres chlorite + phengite (c.f. De Andrade 2006).

(2) Ce problème résulte de l'utilisation, lors de la calibration du modèle, d'une majorité d'analyses de chlorites de HP ($P > 10 \text{ kbar}$ pour $T > 400^{\circ}\text{C}$). Nous avons essayé sans succès, durant ce travail, de calculer les températures de plusieurs chlo-

	Hospital Fault ⁽¹⁾		Valles Fault ⁽¹⁾			SL ⁽²⁾	
	1	2	3	4	5	6	7
SiO ₂	26.85	24.57	28.73	27.16	26.44	26.39	25.03
Al ₂ O ₃	18.36	18.46	21.77	21.56	21.46	21.93	23.95
FeO	26.87	33.15	25.84	25.54	25.85	27.21	23.35
MnO	0.62	0.65	0.55	0.59	0.52	0.46	0.25
MgO	13.53	9.33	11.13	13.39	13.65	13.20	14.05
CaO	0.07	0.05	0.56	0.10	0.10	0.15	0.11
Na ₂ O	0.00	0.00	0.06	0.00	0.02	0.00	0.03
K ₂ O	0.03	0.04	0.18	0.02	0.08	0.04	0.05
Atom site distribution (14 anhydrous-oxygen basis including Fe ³⁺)							
Si _(T1+T2)	2.80	2.71	2.87	2.77	2.71	2.71	2.62
Al _(T2)	1.19	1.29	1.11	1.23	1.28	1.29	1.38
Al _(M1)	0.19	0.29	0.11	0.23	0.28	0.29	0.38
Mg _(M1)	0.23	0.18	0.17	0.22	0.23	0.24	0.25
Fe _(M1) ²⁺	0.15	0.29	0.13	0.17	0.18	0.23	0.21
V _(M1)	0.43	0.24	0.59	0.37	0.31	0.23	0.16
Mg _(M2+M3)	1.87	1.35	1.49	1.81	1.86	1.77	1.94
Fe _(M2+M3)	1.21	2.10	1.16	1.37	1.44	1.70	1.68
Al _(M2+M3)	0.85	0.48	1.21	0.75	0.63	0.46	0.33
Al _(M4)	0.02	0.33	0.14	0.37	0.40	0.60	0.86
Fe _(M4) ³⁺	0.98	0.67	0.86	0.63	0.60	0.40	0.14
T _{Chl+Qtz} (°C)	245.8	307.3	142.9	228.4	253.4	283.6	392.6
± (°C)	7.7	17.7	13.1	11.7	12.9	20.4	58.8

TABLE 2.4 – Analyses utilisées pour l'estimation de l'incertitude "analytique" de la méthode Chl+Qtz+W

rites de BP-HT. En effet, le modèle de Vidal et al. (2006) ne permet pas d'estimer une température pour les chlorites de $T > 400^\circ\text{C}$ et $P < 5 \text{ kbar}$. De la même manière, il sera impossible d'équilibrer une chlorite avec une phengite dans cette gamme de conditions P-T. Des tentatives de corrections ont été menées en essayant d'ajouter un ou plusieurs pôles purs ferriques. Cependant, ce travail n'a pas pu être mené à son terme, car le développement d'un nouveau modèle pour les chlorites nécessiterait de considérer des couples de chlorites et phengites à l'équilibre afin de garantir une bonne compatibilité entre les deux modèles de solutions solides.

2.2.7 Logiciel 1 - PTLines

Le logiciel PTLines² qui fonctionne également sous MATLAB© a été développé en utilisant des fonctions développées par P. Lanari, B. Dubacq, V. De Andrade, E. Lewin et O. Vidal. PTLines permet de calculer des conditions d'équilibre pour des chlorites et phengites qui coexistent avec du quartz et H₂O en fonction du $X_{\text{Fe}^{3+}}$ des chlorites et du $X_{\text{H}_2\text{O},\text{interfoliaire}}$ des phengites. Nous allons tout d'abord voir comment tracer des lignes d'équilibres Chl+Qtz+W et Phg+Qtz+W. Ensuite nous présenterons rapidement le logiciel PTLines.

2. Version actuelle : PTlines 3.0 - Public (Septembre 2012)

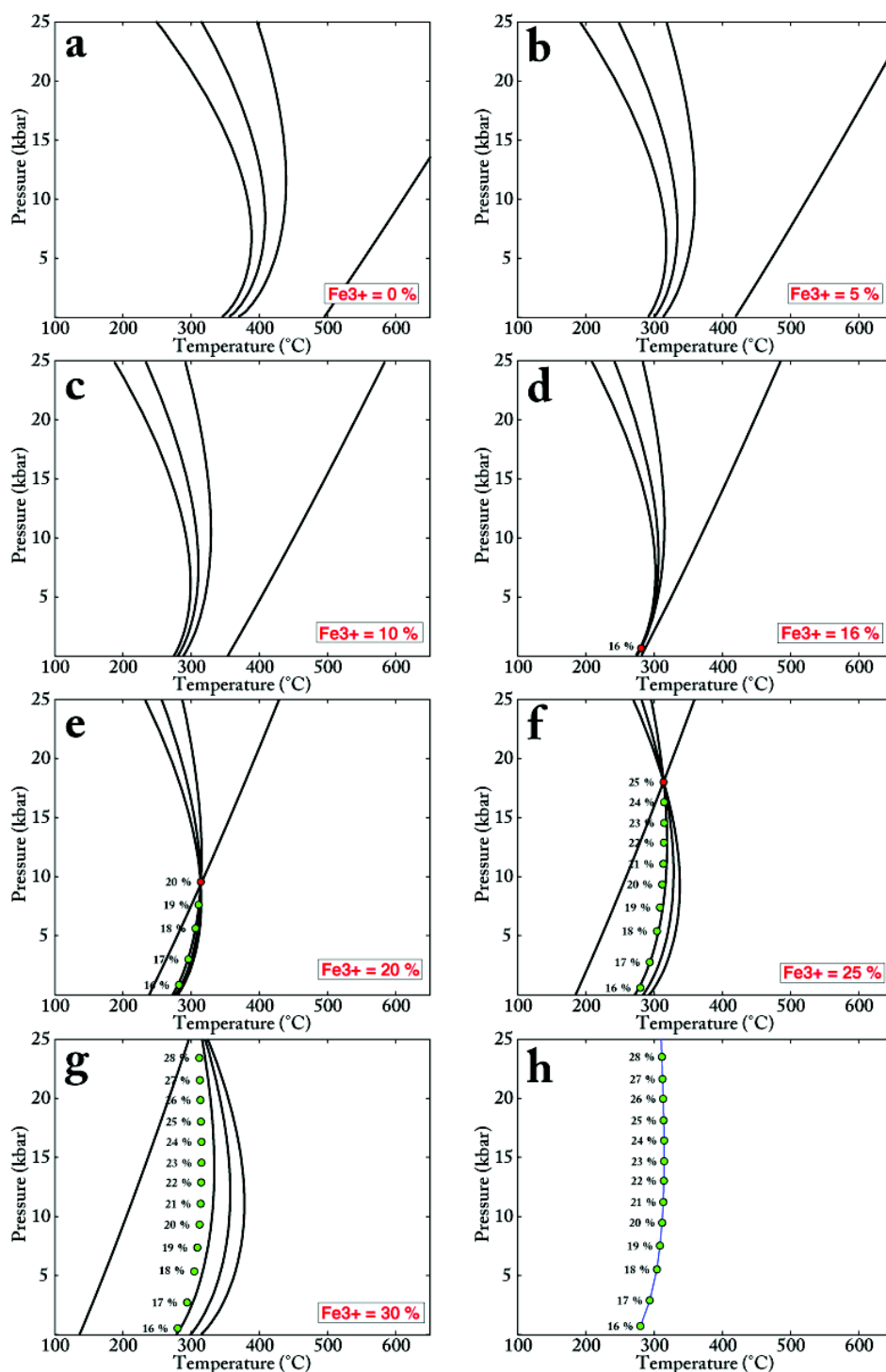
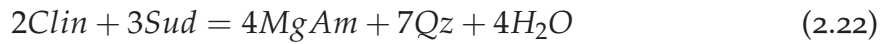


FIGURE 2.14 – Méthode de calcul d'une ligne d'équilibres $chl+qtz+H_2O$ pour une composition de chlorite en utilisant la calibration de Vidal *et al.* (2006). Les différentes figures (a, b, c, d, e, f, g, h) correspondent à différentes proportions de Fe^{3+} (en rouge sur la figure) dans la chlorite ($Fe^{3+}(\%) = \frac{Fe^{2+}}{Fe^{2+}+Fe^{3+}} \times 100$).

2.2.7.1 Modèles Phg+Qtz+H₂O et Chl+Qtz+H₂O : lignes d'équilibres

Comme nous l'avons vu précédemment, (Part. 2.2.1.1) le modèle de Dubacq et al. (2010) permet pour chaque analyse de phengite de tracer un équilibre dans un champ P-T le long de laquelle la phengite est en équilibre avec le quartz et l'eau et son état d'hydratation varie.

La même approche peut être utilisée pour les chlorites, en faisant varier la quantité de Fe^{3+} . Nous avons sélectionné une analyse de chlorite de Vidal et al. (2006) avec une température de cristallisation à 300°C. Les quatre réactions intervenant entre les cinq pôles purs de chlorite *fames*, *ames*, *clin*, *daph* et *sud*, le quartz et l'eau sont :



Les positions de ces équilibres sont calculées pour différents pourcentages de Fe^{3+} ($Fe^{3+}(\%) = \frac{Fe^{2+}}{Fe^{2+}+Fe^{3+}} \times 100$) et sont reportées sur la figure 2.14. Si l'on considère que tout le Fe de la chlorite est du Fe^{2+} , les réactions ne se croisent pas dans le champ P-T (Fig. 2.14-a). Lorsque l'on ajoute du Fe^{3+} 5% (Fig. 2.14-b) puis 10% (Fig. 2.14-c), les quatre réactions se déplacent vers les basses températures. Comme le Fe^{3+} est mis sur le site M4 des chlorites (Vidal et al. 2005), l'Al initialement en M4 va être incorporé en M2M3 qui va provoquer une augmentation apparente de la proportion de *sud* et une diminution des proportions de *clin* et de *daph*. Le rapport $XFe = \frac{Fe^{2+}}{Fe^{2+}+Mg^{2+}}$ va également changer et donc les proportions d'*ames* et *fames*. Comme la *sud* est le pôle de basse température résultant de la substitution di/trioctaédrique, les réactions vont se déplacer vers les basses températures.

Pour 16% de Fe^{3+} , les réactions se croisent en un point et la chlorite est donc à l'équilibre avec le quartz et l'eau pour des conditions P-T de 1 kbar et 290°C (Fig. 2.14-d). Si l'on augmente encore la proportion de Fe^{3+} (20%, Fig. 2.14-e, puis 25%, Fig. 2.14-f, puis 30%, Fig. 2.14-g) en enregistrant les intersections pour chaque

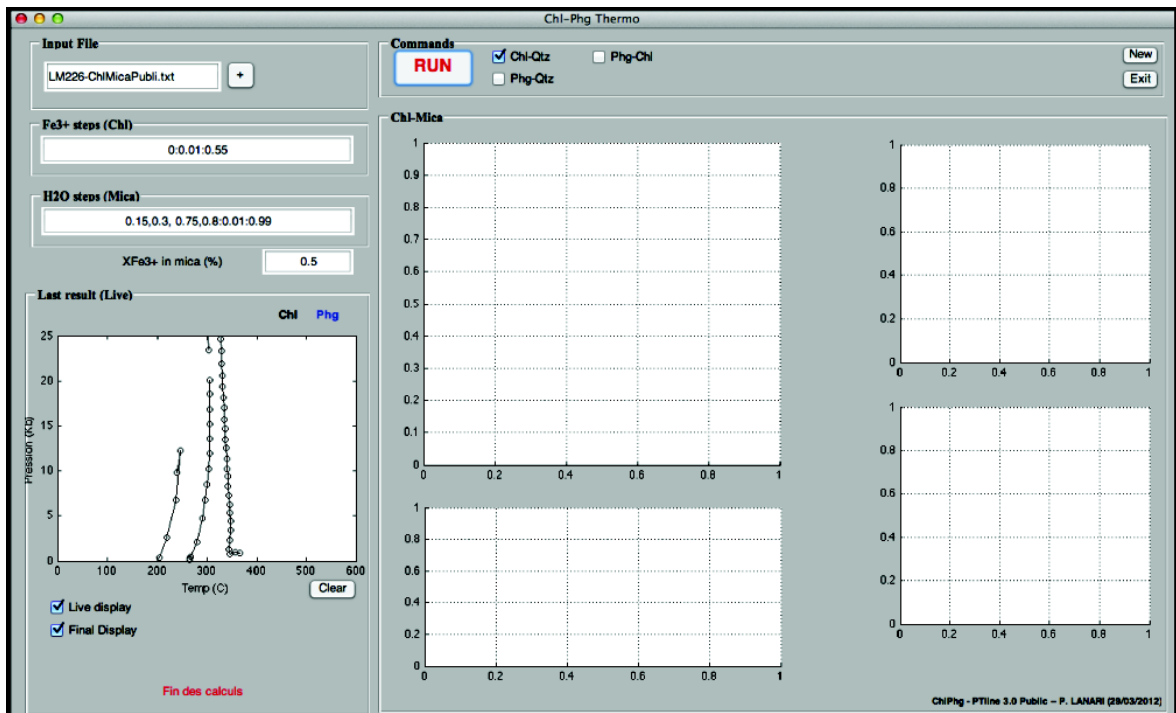


FIGURE 2.15 – PTLINES en mode "Chl+Qtz"

pourcentage de Fe^{3+} , on obtient une ligne d'équilibre le long de laquelle la chlorite est à l'équilibre avec le quartz et l'eau, et seul son état d'oxydation change (Fig. 2.14-h).

2.2.7.2 PTlines

Le logiciel PTLINES a été développé pour tracer dans un champ P-T les lignes d'équilibres $Phg+Qtz+H_2O$ et $Chl+Qtz+H_2O$ et de chercher des équilibres $Chl+Phg+Qtz+H_2O$. Ce logiciel permet de traiter un fichier contenant des analyses de phengites et de chlorites en suivant les trois étapes suivantes :

- (1) *Le mode Chl+Qtz+H₂O* (Fig. 2.15) permet de tracer les lignes d'équilibre des chlorites avec le quartz et l'eau en faisant varier le pourcentage de Fe^{3+} .
- (2) *Le mode Phg+Qtz+Qtz+H₂O* (Fig. 2.16) permet de tracer les lignes d'équilibre des phengites avec le quartz et l'eau en faisant varier le pourcentage de H_2O présent en position interfoliaire.

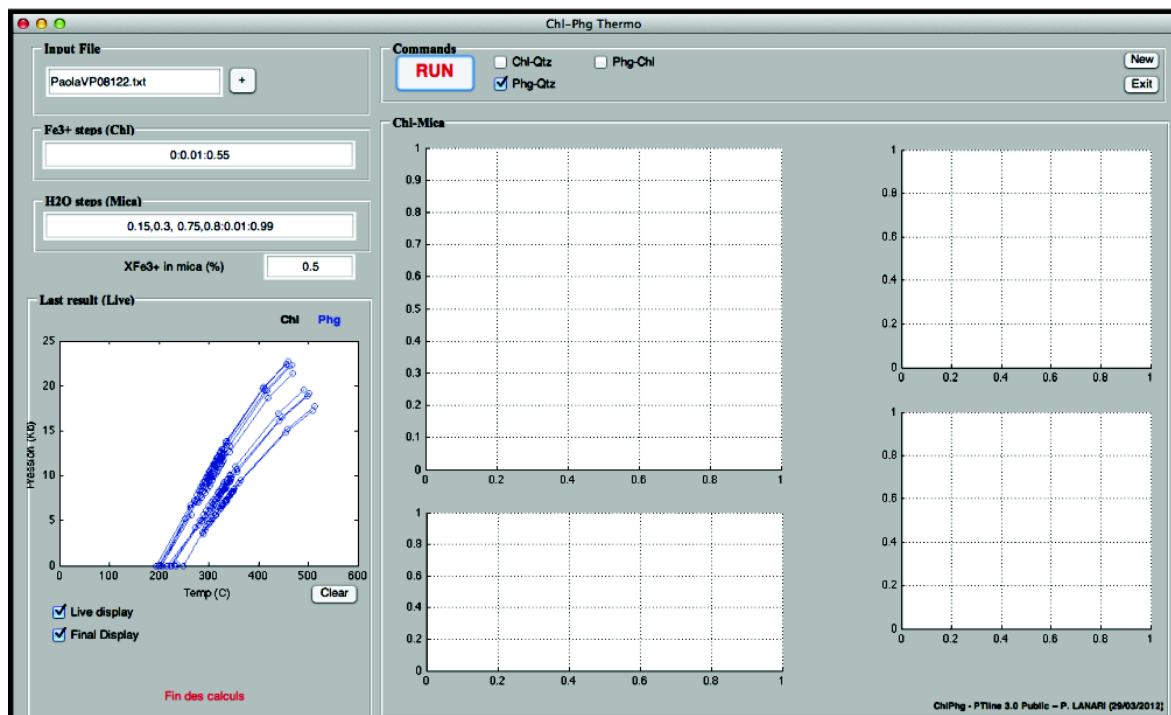


FIGURE 2.16 – PTLINES en mode "Phg+Qtz"

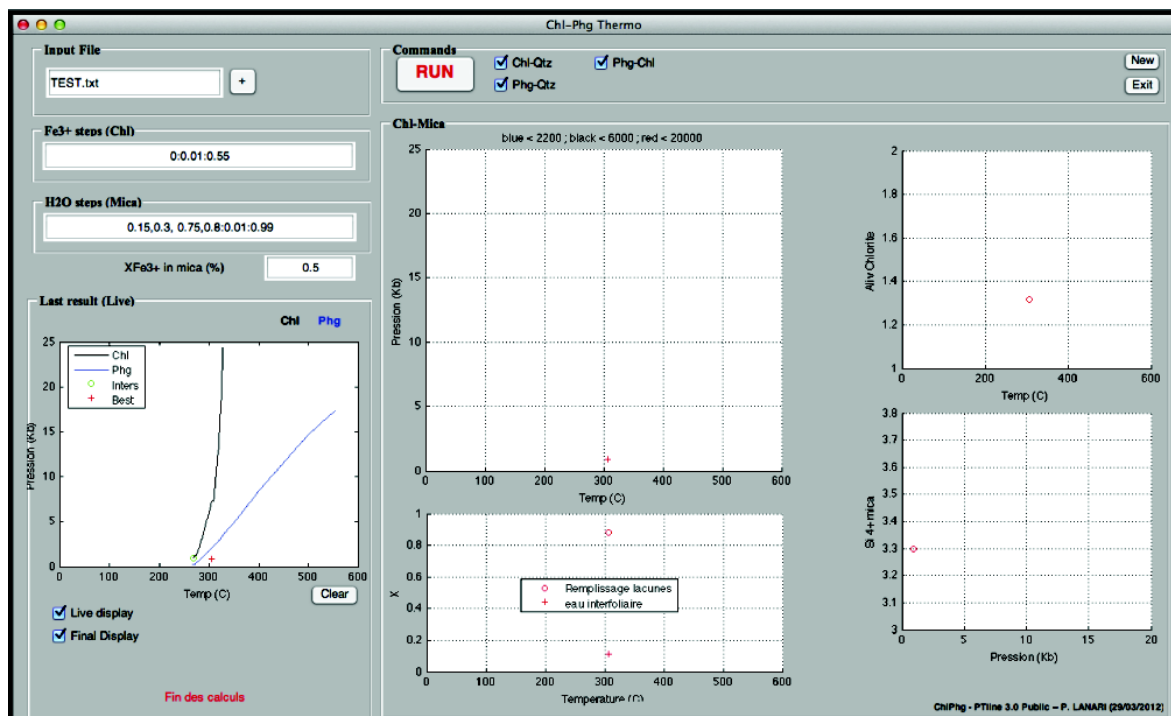
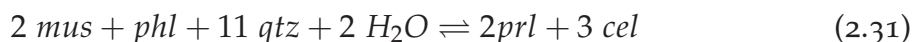
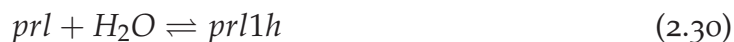
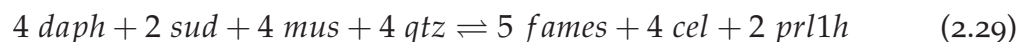
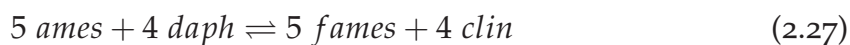
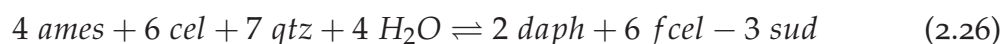
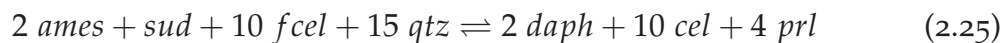


FIGURE 2.17 – PTLINES en mode "Chl+Qtz, Phg+Qtz et Chl+Phg+Qtz".

(3) Le mode $Chl+Phg+Qtz+H_2O$ (Fig. 2.17) va scanner toutes les combinaisons possibles de chlorites et micas en cherchant les intersections entre les deux lignes d'équilibres. Pour chaque intersection trouvée, si elle existe, (point vert sur le Fig. 2.17), le programme va chercher un équilibre entre la chlorite et la phengite en utilisant les sept réactions suivantes :



Les proportions initiales de Fe^{3+} pour les chlorites et H_2O pour les phengites, ainsi que la proportion de Fe^{3+} dans les phengites sont ajustées automatiquement, en commençant avec les valeurs calculées au niveau de l'intersection des lignes P-T. Le résultat (point P-T) est affiché sur la figure 2.17. Note : PTLINES ne permet pas de tracer les réactions dans un diagramme P-T, mais peut afficher dans le "Command Window" de MATLAB© les compositions dans un format compatible avec TWEEQ.

2.2.8 Logiciel 2 - MultiPlot

Le logiciel MULTIPLOT³ qui fonctionne également sous MATLAB© a été développé en collaboration par Pierre Lanari et Olivier Vidal en utilisant comme pour PTLINES, des fonctions développées par P. Lanari, B. Dubacq, V. De Andrade, E. Lewin et O. Vidal. MULTIPLOT est divisé en deux parties. (1) Un mode $Chl+Qtz+H_2O$ qui permet de calculer la température et la teneur en Fe^{3+} ($XFe^{3+} = Fe^{3+} / (Fe^{2+} + Fe^{3+})$) pour des analyses de chlorites, en utilisant la procédure de

3. Version actuelle : MultiPlot 2.1 - Public (Septembre 2012)

Vidal et al. (2005; 2006). (2) Un mode Multi qui permet de tracer des équilibres chimiques pour une paragenèse donnée. Ces deux modes seront traités séparément dans la suite.

Ce logiciel sera brièvement introduit dans ce travail, mais il ne s'agit pas de la version « finale ». C'est donc la nouvelle version (version 3), en cours d'élaboration, qui sera compatible avec XMAPTOOLS qui fera l'objet d'une publication.

2.2.8.1 Mode Chl + Qtz + H_2O

L'interface graphique du mode « Chl + Qtz + H_2O » est présentée figure 2.18. Ce mode permet de calculer les températures et XFe^{3+} à partir d'analyses chimiques de chlorites fournies dans un fichier d'entrée ("Input file", noté (a) sur la Fig. 2.18).

L'utilisateur peut choisir dans la fenêtre "Setup" (noté (b) sur la Fig. 2.18) la pression à laquelle sera calculée la température; l'écart en température entre les réactions pour considérer la chlorite à l'équilibre avec le quartz et H_2O (par défaut 30°C comme dans Vidal et al. 2006); l'activité de l'eau; les valeurs minimales et maximales de XFe^{3+} ; et la température maximale.

Les fichiers de données thermodynamiques peuvent être choisis dans la fenêtre "Thermodynamics" pour les propriétés standards et le modèle de solution solide des chlorites (noté (c) sur la Fig. 2.18).

Différents boutons (notés (d) sur la Fig. 2.18) permettent de réaliser plusieurs actions. Le bouton "clean" permet de nettoyer les figures graphiques. Le bouton "run" permet de lancer un calcul de températures. Le bouton "plot" permet de tracer les équilibres chimiques pour une composition de chlorite utilisée. Le bouton "tripplot" permet de tracer les analyses de chlorites dans un diagramme triangulaire en utilisant le module TRIPLOT3D de XMAPTOOLS. Le bouton "export" permet d'exporter les différents graphiques. Le bouton "save" permet de sauvegarder les résultats qui peuvent être par la suite chargés en utilisant le bouton "load" lors d'une nouvelle session.

Lors d'un calcul, différents résultats graphiques sont affichés. Les températures calculées sont représentées sous la forme d'un histogramme (noté (e) sur la Fig.

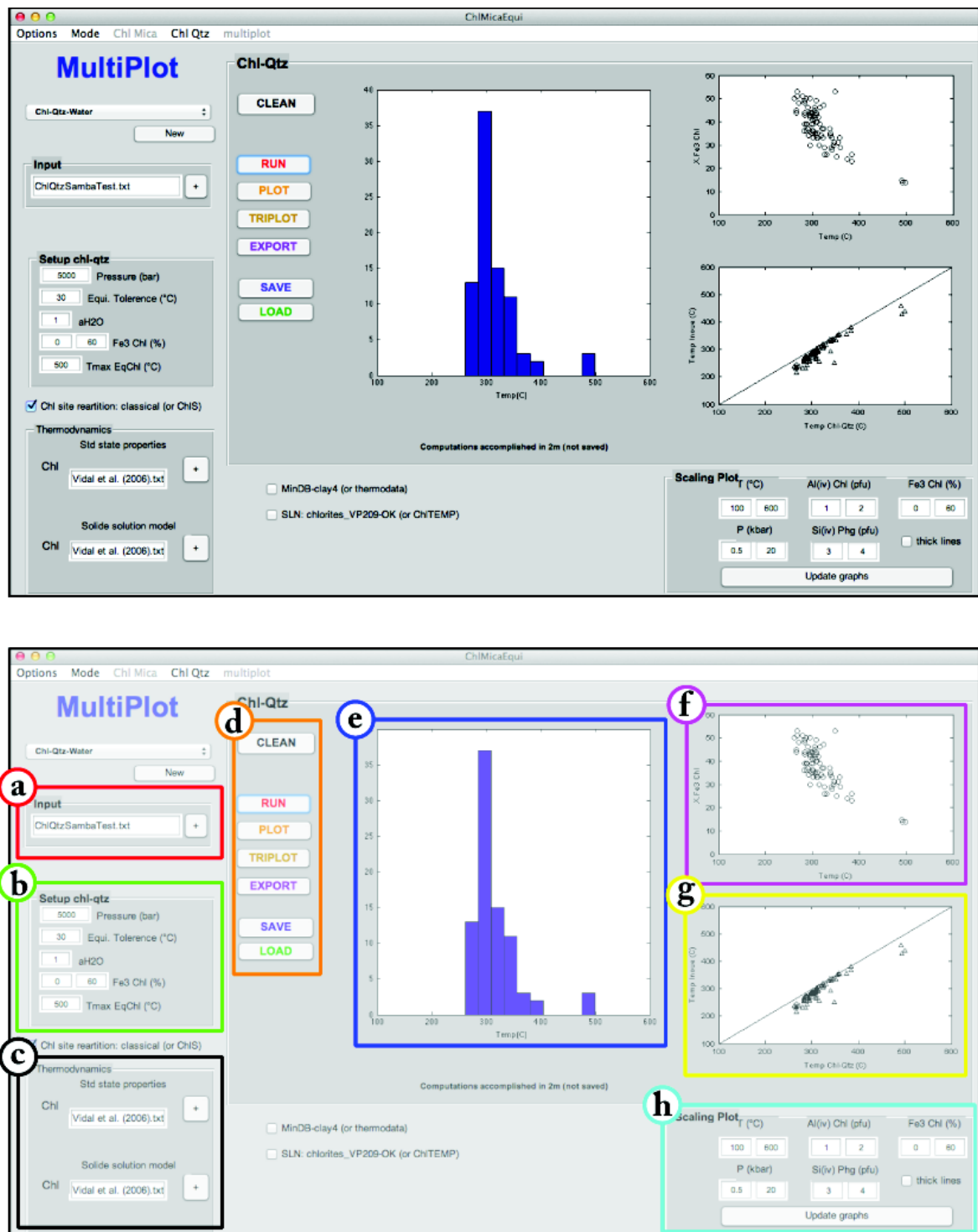


FIGURE 2.18 – PTLINES en mode Chl+Qtz+H₂O. (a) Nom du fichier d'entrée sélectionné qui contient les analyses chimiques. (b) Setup du mode Chl+Qtz+H₂O. (c) Nom des fichiers de données thermodynamiques et de modèles de solutions solides pour les chlorites. (d) Différents boutons du mode. (e) Fenêtre graphique principale avec affichage d'un histogramme des températures calculées. (f) Diagramme pourcentage de Fe³⁺ de la chlorite vs température. (g) Diagramme température estimée avec le modèle Chl+Qtz+H₂O vs température calculée avec le thermomètre de Inoue et al. (2009). (h) Options d'affichage des différentes fenêtres graphiques.

2.18), d'un diagramme XFe^{3+} vs température (noté (f) sur la Fig. 2.18) et d'un diagramme température de chl + Qtz + H_2O vs température de Inoue et al. (2009) estimée pour la quantité de XFe^{3+} modélisée (noté (g) sur la Fig. 2.18).

Les échelles des axes des différentes fenêtres graphiques peuvent être changées en utilisant les différentes options disponibles dans la fenêtre "scaling plot".

2.2.8.2 Mode Multi

Pour une paragenèse donnée avec i pôles purs et un jeu de m réactions chimiques, le programme MULTIPLOT peut chercher les conditions P-T du meilleur équilibre en minimisant la fonction suivante (détails dans De Andrade 2006) :

$$f(P, T, X_1, X_2, \dots, X_n) = \sqrt{\sum_{r=1}^m \Delta G_r^2} \quad (2.32)$$

avec X_n des variables de compositions que l'on peut ajuster comme la quantité de Fe^{3+} dans les chlorites ou les micas, ou encore la quantité de H_2O en position interfoliaire dans les phengites. Pour chaque paragenèse, MULTIPLOT sélectionne automatiquement le jeu de réactions à utiliser. Le nombre de réactions est toujours supérieur ou égal au nombre de réactions indépendantes. Pour chaque équilibre testé, le programme va fournir un résidu en joules qui est la valeur de la fonction (2.32) avec les valeurs finales de P,T et des X_n . La qualité de l'équilibre en terme de convergence des équilibres est directement reliée à la valeur de ce résidu pour une paragenèse donnée.

Le programme PTLINES en mode *Multi* permet (1) de chercher les équilibres pour une paragenèse donnée et des analyses chimiques de chlorites fournies dans un fichier d'entrée (noté (a) sur la Fig. 2.19) en utilisant l'option « Find » (Fig. 2.19) et (2) de tracer les réactions en utilisant l'option « Plot » (Fig. 2.20).

Option « Find »

L'utilisateur peut choisir dans la fenêtre "Setup Multi mode" (noté (a) sur la Fig. 2.19) le résidu maximal pour lequel l'équilibre sera retenu (et donc affiché); l'activité de l'eau; les valeurs minimales et maximales de XFe^{3+} pour les chlorites et les micas.

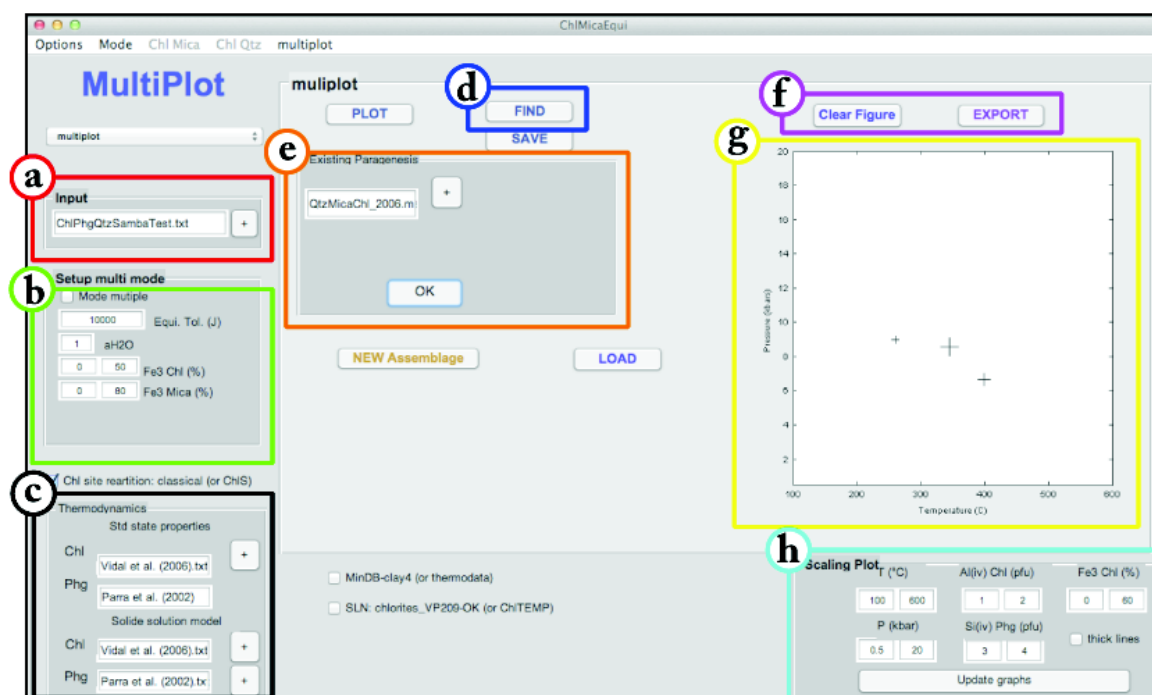
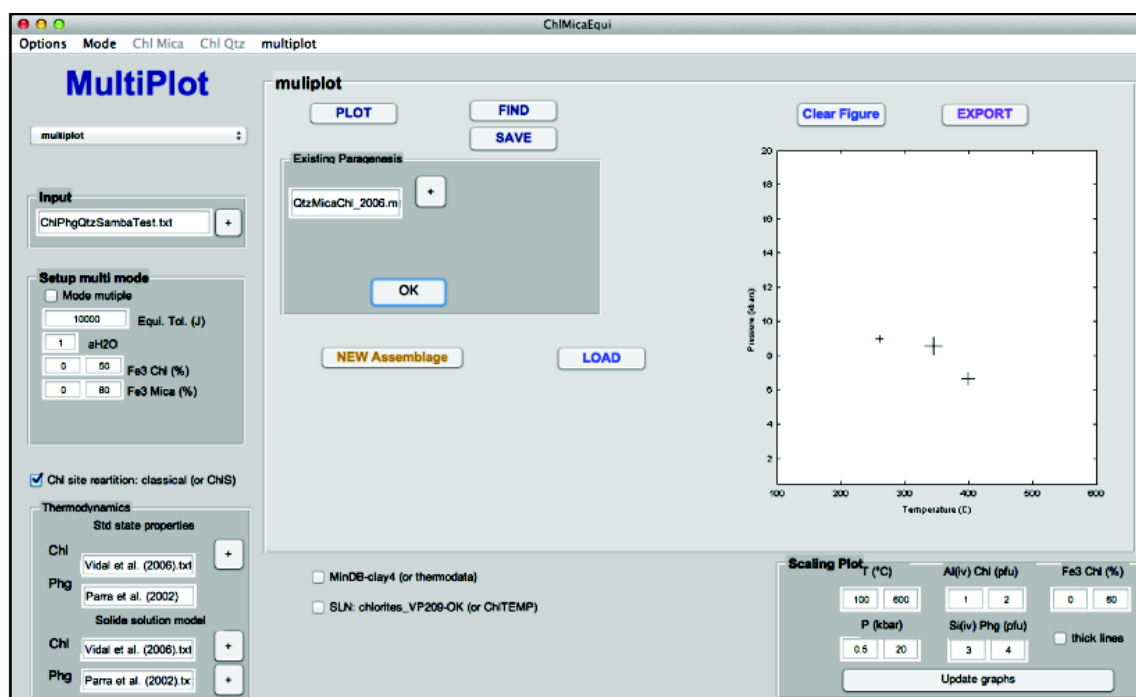


FIGURE 2.19 – PTLINES en mode Multi - « Find ». (a) Nom du fichier d'entrée sélectionné qui contient les analyses chimiques. (b) Setup du mode Multi. (c) Nom des fichiers de données thermodynamiques et de modèles de solutions solides (chlorite et phengite). (d) Outil « Find ». (e) Options de l'outil « Find », sélection de la paragenèse. (f) Boutons de gestion du graphique (g) Fenêtre graphique avec affichage des points P-T trouvés. (h) Options d'affichage de la fenêtre graphique.

Les fichiers de données thermodynamiques peuvent être choisis dans la fenêtre "Thermodynamics" pour les propriétés standards et le modèle de solution solide des chlorites et les micas (noté (c) sur la Fig. 2.19).

La fenêtre « Find » (notée (e) sur la Fig. 2.19) est activée en utilisant le bouton du même nom (notée (d) sur la Fig. 2.19). L'utilisateur peut alors choisir un fichier d'"assemblage" contenant les réactions chimiques et le jeu de pôle pur sélectionné. Ce fichier d'assemblage peut être créé en utilisant le bouton "new assemblage". Le calcul se lance quand le bouton "Ok" est cliqué. Les conditions P-T d'équilibres trouvées sont affichées dans la fenêtre graphique (notée (g) sur la Fig. 2.19). La taille de la croix est proportionnelle au résidu. À la fin des calculs, un bouton "Save" apparaît et permet de sauvegarder les résultats.

Option « Plot »

Les résultats peuvent être affichés en utilisant l'option «Plot» (notée (b) sur la Fig. 2.20) qui est activée en utilisant le bouton du même nom (notée (a) sur la Fig. 2.20). Il faut alors sélectionner un assemblage et un fichier de sauvegarde des résultats puis cliquer sur "ok" pour tracer toutes les réactions chimiques pour la paragenèse donnée.

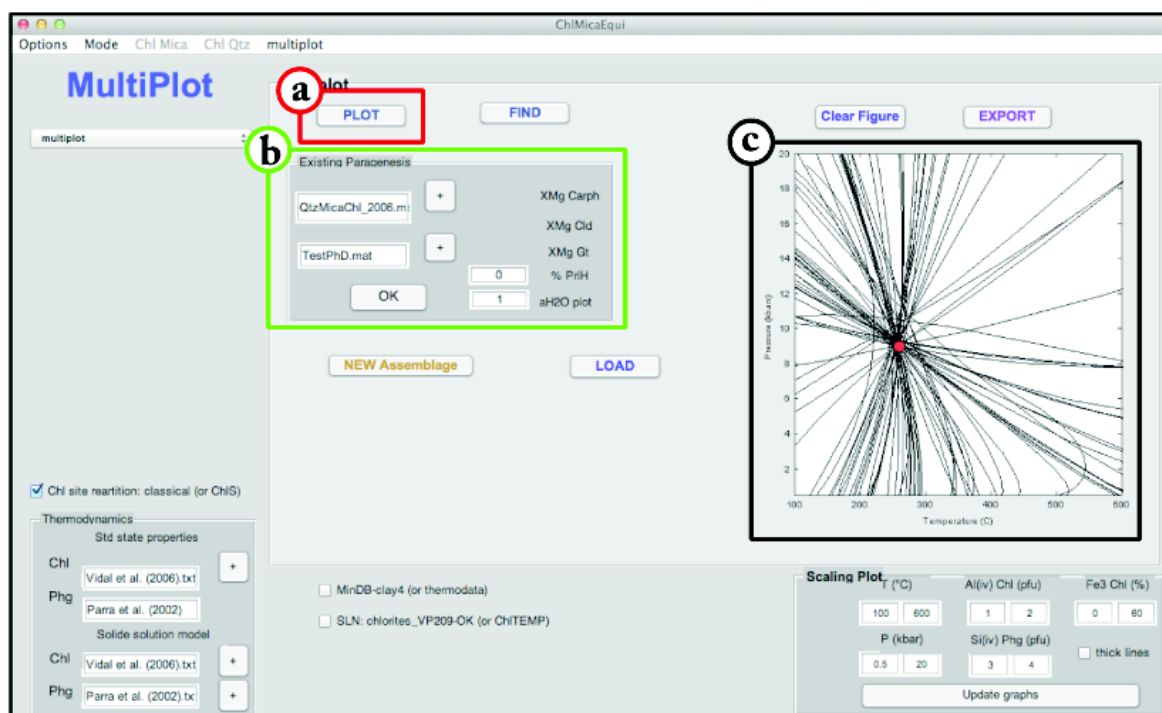
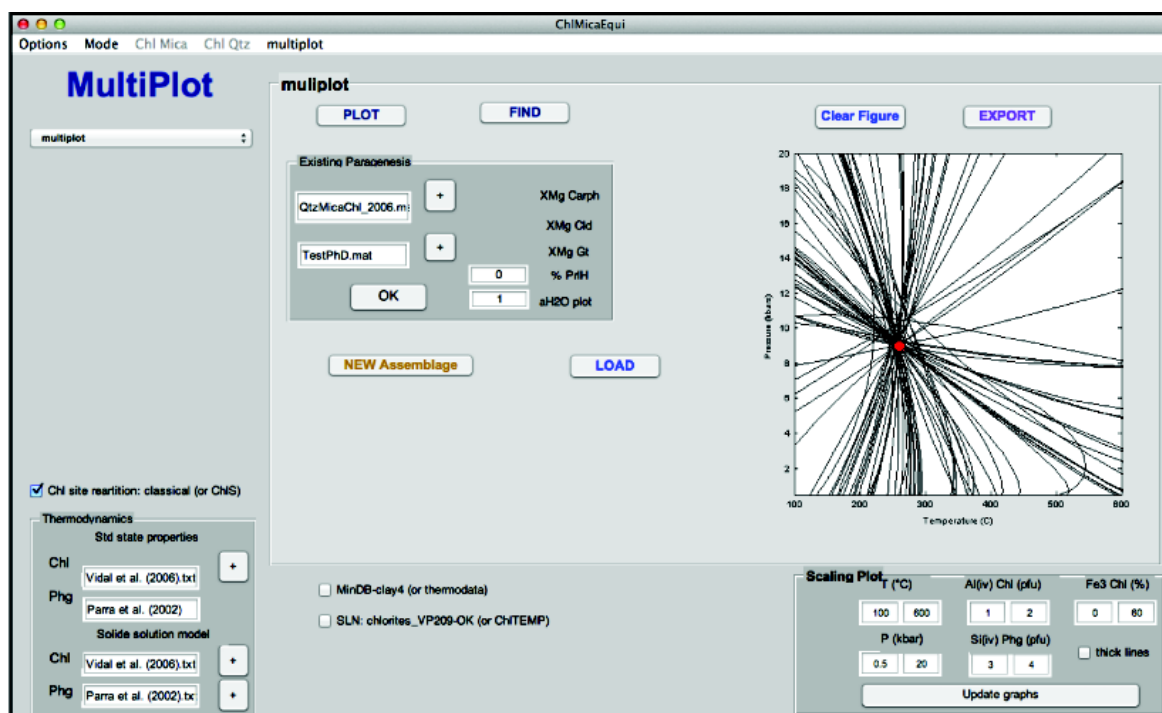


FIGURE 2.20 – PTLINES en mode Multi - « Plot ». (a) Outil « Plot ». (e) Options de l'outil « Plot », sélection de la paragenèse et du résultat à afficher. (c) Fenêtre graphique avec affichage des équilibres chimiques.

2.3 APPROCHE DIRECTE ET PSEUDOSECTIONS

★ *Les pseudosections calculées par minimisation d'énergie requièrent des modèles de solutions solides qui peuvent décrire les compositions classiquement observées dans les échantillons naturels.*

★ *Des modèles de solutions solides compatibles avec la base de données thermodynamiques de Holland et Powell, (1998) sont disponibles pour les phyllosilicates, mais ils n'incluent pas les substitutions di/trioctaédrique pour les chlorites, ni pyrophyllitique pour les phengites.*

★ *Dans cette partie, nous allons proposer un nouveau modèle de solution solide pour les chlorites en ajoutant un pôle di/trioctaédrique : la sudoite. Nous proposerons également un thermomètre semi-empirique basé sur la température de l'équilibre chlorite + quartz + H₂O. Dans un deuxième temps, nous discuterons les implications du formalisme de Holland et Powell en utilisant l'exemple des chlorites.*

2.3.1 Introduction

Comme nous l'avons vu précédemment, la technique des multi-équilibres permet de calculer les conditions d'équilibre d'une paragenèse en utilisant les compositions des minéraux et en traçant toutes les réactions qui interviennent entre les différents pôles purs. Pour les échantillons ayant enregistré plusieurs événements métamorphiques, cette méthode permet de considérer un équilibre local et donc de distinguer plusieurs phases de cristallisation distinctes (e.g. [Lanari et al. 2012a](#)). L'inconvénient de la technique des multi-équilibres est qu'une hypothèse doit être faite sur les chlorites et les phengites en équilibre.

Une autre approche consiste à calculer des diagrammes de phases qui indiquent les domaines de stabilité des différents assemblages minéralogiques en fonction de P et T. Une pseudosection est un type de diagramme de phase qui montre les champs de stabilité de différents minéraux en équilibre pour une composition de roche totale donnée. Cette approche est utilisée dans les logiciels PERPLE_X ou encore THERIAK-DOMINO afin de construire par minimisation d'énergie des pseudosections avec la base de données thermodynamiques inter-cohérentes de [Holland](#)

et Powell (1998) ou Berman (1988). L'avantage de cette approche est de calculer la paragenèse complète et la composition des phases à l'équilibre et de pouvoir comparer les résultats avec les paragenèses et compositions observées. Elle est couramment utilisée pour estimer les trajets P-T dans des échantillons présentant plusieurs paragenèses.

2.3.1.1 Modèles disponibles

La base de données thermodynamiques de Holland et Powell (1998) est la base de données actuellement la plus utilisée par la communauté. Pour les phyllosilicates, deux modèles sont utilisés pour calculer des pseudosections avec cette base de données. Il s'agit des modèles de Holland et al. (1998) pour les chlorites (avec les pôles purs : Al-free-chlorite (*afchl*), amesite (*ames*), clinochlore (*clin*) et daphnite (*daph*)), et de Coggon et Holland (2002) pour les phengites (avec les pôles purs : muscovite (*mus*), celadonite (*cel*) et ferroceldonite (*fcel*)). Ces deux modèles ont été calibrés à partir de données expérimentales pour des températures entre 500 et 800°C (e.g. Green et Hellman 1982, Hynes et Forest 1988, Massonne 1989, Baker et Holland 1996, Massonne et Szpurka 1997) et n'incluent pas les substitutions di/trioctahédrique pour les chlorites et pyrophyllitique pour les phengites qui interviennent à basse température (Agard et al. 2001b, Vidal et al. 2001).

2.3.1.2 Stratégie

L'objectif de mon travail a été de développer un nouveau modèle pour les chlorites (LWV c.f. Part. 2.3.3) compatible avec la base de données thermodynamiques inter-cohérentes de Holland et Powell (1998) afin de réaliser des applications dans la thermobarométrie ou encore dans la modélisation des interactions fluide-roche. Ce nouveau modèle est une extension de celui de Holland et al. (1998) vers le domaine des chlorites di-trioctahédriques qui sont nécessaires pour décrire les compositions des chlorites avec des températures inférieures à 450-500°C. La calibration de ce modèle a nécessité d'ajuster les propriétés standards de la sudoite pour être en accord avec les résultats expérimentaux de Vidal et al. (1992) et d'utiliser un large jeu de données naturelles pour lesquelles les conditions P-T était connues afin de contraindre les paramètres d'interactions macroscopiques du modèle. À

Thermodynamic data	
I.C.T.D.	Holland et Powell (1998) and updates
Equations	
G^0	Benson-Helgeson convention (Annexe ??)
C_p function	Holland et Powell (1998)
Landau	Holland (1989), Holland et Powell (1998)
Volume function	Holland et Powell (1998)
Activity models	
Ideal	Ionic model (Guggenheim 1966, Price 1985, Mäder et al. 1994)
Non-ideal	Molecular model (Margules 1895, Powell et Holland 1993, Holland et Powell 1996a;b; 2003)
Programs	
Pseudosection	THERMOCALC (Powell et Holland 1988; 1994, Powell et al. 1998, Powell 2008)
Pseudosection	PERPLE_X (Connolly et Kerrick 1987, Connolly 1990; 2005; 2009)
Pseudosection	THERIAK (De Capitani et Brown 1987, De Capitani et Petrakakis 2010)

TABLE 2.5 – Principales références (base de données thermodynamiques, équations et logiciels) sur le formalisme de Holland et Powell (1998) utilisées pour les pseudosections (voir texte). I.C.T.D., Internally consistent thermodynamic dataset. Un tableau similaire est proposé Tab. 2.2 dans la partie consacrée au multi-équilibres - formalisme de (Berman 1988).

des fins thermobarométriques, un thermomètre semi-empirique a été calibré à partir du modèle Chl(LWV) en considérant un modèle d'activité idéal. Trois exemples d'applications directes de ces nouvelles calibrations ont été réalisés. (1) Le modèle Chl(LWV) a été codé dans le logiciel PERPLE_X (Connolly et Kerrick 1987, Connolly 1990; 2005; 2009) afin de calculer une pseudosection d'un échantillon de HP-BT provenant de Crête (Theye et al. 1992). Les résultats sont comparés à ceux obtenus avec le modèle de Holland et al. (1998). (2) Le thermomètre semi-empirique a été utilisé pour calculer une carte de température des chlorites d'un échantillon de la zone Houillère dans les Alpes françaises afin de comparer les températures obtenues avec l'approche empirique et l'approche des multi-équilibres. (3) Le modèle a été utilisé pour modéliser les interactions fluides-roches grâce au logiciel GEM-SELEKTOR v.3 (Kulik et al. in press, Wagner et al. in press). L'intégralité de ce travail sera présenté sous la forme d'un article de Lanari et al. à soumettre à *Contributions to mineralogy and petrology*. Cet article sera suivi d'une présentation du logiciel MEAMP programmé pour minimiser des paramètres thermodynamiques et tracer des équilibres, puis d'une discussion sur le formalisme utilisé par Holland et Powell (relations d'ordre et relations internes) en prenant toujours l'exemple des chlorites.

2.3.2 Formalisme thermodynamique

Le formalisme thermodynamique utilisé lors des calculs de minimisation d'énergie sera présenté brièvement dans cette partie. En effet, celui-ci diffère en partie du formalisme utilisé précédemment avec la technique des multi-équilibres (Part. 2.2).

2.3.2.1 Base de données thermodynamiques inter-cohérentes

La base de données utilisée est la base de données de [Holland et Powell \(1998\)](#) avec les nombreuses mises à jour publiées ou non, et synthétisées dans le fichier "tcds55"⁴ du logiciel THERMOCALC.

2.3.2.2 Logiciels de calcul

Une pseudosection dans un système chimique constitué de cinq à dix éléments est quasiment impossible à calculer "à la main". C'est pourquoi plusieurs programmes de calcul ont été développés pour aider à construire ou à calculer automatiquement ces diagrammes par minimisation d'énergie.

THERMOCALC ([Powell et Holland 1988; 1994, Powell et al. 1998, Powell 2008](#)) est un programme de calcul thermodynamique qui permet de construire un grand nombre de diagrammes : comme les projections P-T, les pseudosections P-T, P-X et T-X, des diagrammes de compatibilité ou de potentiels chimiques. Il utilise un jeu d'équations non-linéaires pour calculer un équilibre thermodynamique demandé par l'utilisateur.

PERPLE_X ([Connolly et Kerrick 1987, Connolly 1990; 2005; 2009](#)) est une collection de programmes pour calculer des diagrammes de phase par minimisation d'énergie : diagrammes de composition, projections de Schreinemakers, diagrammes multi-variables, pseudosections et champs de stabilité.

THERIAK ([De Capitani et Brown 1987, De Capitani et Petrakakis 2010](#)) permet aussi de calculer par minimisation d'énergie des pseudosections à partir d'une

4. Version actuellement disponible (septembre 2012)

composition de roche totale en utilisant le formalisme et la base de données de [Holland et Powell \(1998\)](#).

2.3.2.3 Modèles d'activités

De la même manière que pour le formalisme des multi-équilibres, l'activité idéale d'un composant d'une solution solide est décrite en utilisant un modèle ionique et la relation 2.14 de mélange sur sites ([Guggenheim 1966](#), [Price 1985](#), [Spear 1993](#), [Powell et Holland 1993](#), [Mäder et al. 1994](#)).

Un modèle macroscopique est utilisé pour décrire l'activité non idéale ([Powell et Holland 1993](#), [Holland et Powell 1996a,b; 2003](#)). Pour des interactions symétriques, le terme d'excès macroscopique d'un composant i peut être calculé en utilisant la relation :

$$RT \ln(\gamma_i) = - \sum_{j=1}^{n-1} \sum_{k>j}^n q_j q_k W_{G_{jk}} \quad (2.33)$$

avec $q_j = 1 - X_j$ quand $j = i$ et $q_k = -X_k$ quand $k \neq i$ et $W_{G_{jk}}$ le paramètre d'interaction de Margules qui est simplement dépendant de la pression et de la température :

$$W_G = W_H + TW_S + PW_V \quad (2.34)$$

Pour les modèles de mélanges asymétriques, un modèle de type Van-Laar est utilisé. Nous renvoyons le lecteur au papier de [Holland et Powell \(2003\)](#).

2.3.2.4 Pôles purs et réactions

L'approche utilisée ici pour décrire la thermodynamique d'une solution solide est différente de celle utilisée précédemment. L'approche Holland et Powell fait l'hypothèse que les pôles purs dépendants d'une solution solide ont des propriétés thermodynamiques standards qui sont également dépendantes, c'est-à-dire qu'elles sont des combinaisons linéaires des propriétés standards des pôles purs indépendants. Cette hypothèse a deux avantages évidents :

- (1) Toutes les relations internes intervenant dans les minéraux qui présentent des substitutions couplées (e. g. chlorites, micas, amphiboles) sont vérifiées

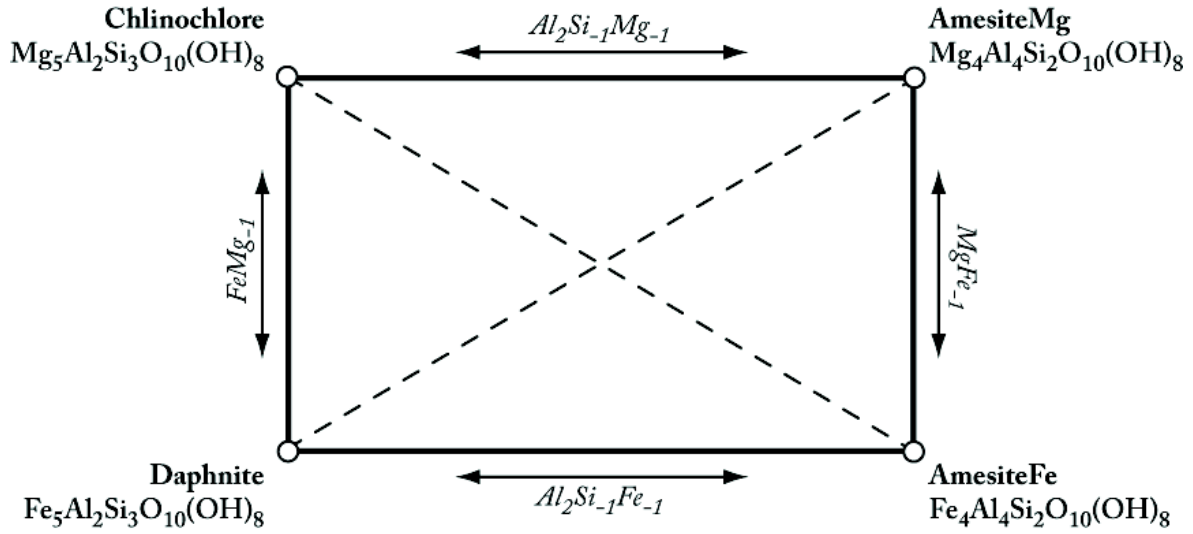
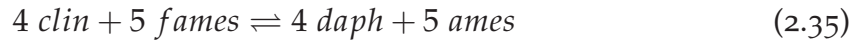


FIGURE 2.21 – Diagramme de composition des chlorites

($\Delta G_{\text{reaction}} = 0$) quelles que soient les compositions et les conditions P-T. Considérons par exemple l'équilibre interne des chlorites identifié précédemment :



qui peut être visualisé par les lignes pointillées sur la figure 2.21. Dans le modèle de Vidal et al. (2005), cette réaction interne n'est vérifiée que pour des compositions et des conditions P-T particulières :

$$\begin{aligned} \Delta \mu_{\text{reaction}} = & RT \ln \left[\frac{(X_{\text{Fe},M1})^4 (X_{\text{Mg},M2M3})^4}{(X_{\text{Fe},M2M3})^4 (X_{\text{Mg},M1})^4} \right] \\ & + 4 \mu_{\text{clin}}^0 + 5 \mu_{\text{fames}}^0 - 4 \mu_{\text{daph}}^0 - 5 \mu_{\text{ames}}^0 \\ & + 4 X_{\text{Al},M1} (W_{\text{Al-Fe}} - W_{\text{Al-Mg}}) \end{aligned} \quad (2.36)$$

Au contraire, le formalisme utilisé par Holland et Powell suppose que cette relation est indépendante de la composition :

$$\begin{aligned} \Delta \mu_{\text{reaction}} = & RT \ln \left[\frac{(X_{\text{Fe},M1})^4 (X_{\text{Mg},M2M3})^4}{(X_{\text{Fe},M2M3})^4 (X_{\text{Mg},M1})^4} \right] \\ & + 4 \mu_{\text{clin}}^0 + 5 \mu_{\text{fames}}^0 - 4 \mu_{\text{daph}}^0 - 5 \mu_{\text{ames}}^0 \\ & + 4 W_{\text{ames-daph}} - 4 W_{\text{ames-clin}} - \frac{16}{5} W_{\text{clin-daph}} \end{aligned} \quad (2.37)$$

ce qui revient, pour $\Delta \mu_{\text{reaction}} = 0$ et en supposant une équipartition Fe-Mg à écrire

la relation interne suivante :

$$\begin{aligned}\mu_{fames}^0 &= \mu_{ames}^0 + \frac{4}{5} \mu_{daph}^0 - \frac{4}{5} \mu_{clin}^0 \\ &+ \frac{4}{5} W_{ames-daph} - \frac{4}{5} W_{ames-clin} - \frac{16}{25} W_{clin-daph}\end{aligned}\quad (2.38)$$

La méthode pour dériver cette relation est explicitée dans l'annexe A.1.3. Cette relation interne implique que l'on peut estimer le μ_{fames}^0 sans utiliser les propriétés standards de *fames*. D'un autre coté, on peut re-calculer des propriétés standards de *fames* à partir des propriétés standards des autres pôles purs en utilisant les contraintes suivantes qui dérivent de la relation interne A.28 :

$$\begin{aligned}H_{fames}^0 &= H_{ames}^0 + \frac{4}{5} H_{daph}^0 - \frac{4}{5} H_{clin}^0 \\ &+ \frac{4}{5} W_{ames-daph} - \frac{4}{5} W_{ames-clin} - \frac{16}{25} W_{clin-daph}\end{aligned}\quad (2.39)$$

$$S_{fames}^0 = S_{ames}^0 + \frac{4}{5} S_{daph}^0 - \frac{4}{5} S_{clin}^0 \quad (2.40)$$

$$V_{fames}^0 = V_{ames}^0 + \frac{4}{5} V_{daph}^0 - \frac{4}{5} V_{clin}^0 \quad (2.41)$$

$$Cp_{fames} = Cp_{ames} + \frac{4}{5} Cp_{daph} - \frac{4}{5} Cp_{clin} \quad (2.42)$$

Cela sera discuté plus loin (Part. 2.3.5.2).

(2) Les relations internes permettent de simplifier les calculs, car seules les réactions indépendantes doivent être calculées, les réactions dépendantes étant toujours vérifiées.

2.3.3 Article 2 : A thermodynamic model for di-trioctahedral chlorite from experimental and natural data in the system MgO-FeO-Al₂O₃-SiO₂-H₂O. Applications to pseudosections, geothermometry and fluid-mineral equilibria modeling (to be submitted to *Contributions to Mineralogy and Petrology*)

Cette partie contient un article de Lanari et al., à soumettre à la revue *Contributions to mineralogy and petrology*.

A thermodynamic model for di-trioctahedral chlorite from experimental and natural data in the system $MgO-FeO-Al_2O_3-SiO_2-H_2O$. Applications to pseudosections, geothermometry and fluid-mineral equilibria modeling

Pierre Lanari⁵, Thomas Wagner⁶ and Olivier Vidal⁷

Submitted to Contributions to Mineralogy and Petrology

Abstract - We present a new thermodynamic activity-composition model for di-trioctahedral chlorite in the system $FeO-MgO-Al_2O_3-SiO_2-H_2O$ (FMASH) that is based on the Holland-Powell internally consistent thermodynamic data set. The model is formulated in terms of four linearly independent end-members, which are amesite, clinocllore, daphnite and sudoite. These account for the most important crystal-chemical substitutions in chlorite, the Fe-Mg, Tschermaks and vacancy substitution. The ideal part of end-member activities is modeled with a mixing-on-site formalism, and nonideality is described by a macroscopic symmetric (regular) formalism. The symmetric interaction parameters were calibrated using a set of 271 published chlorite analyses for which robust independent temperature estimates are available. In addition, adjustment of the standard state thermodynamic properties of sudoite was required to accurately reproduce experimental brackets involving sudoite. This new model was tested by calculating representative pseudosections for metasediments at low temperatures ($< 400^\circ\text{C}$), in particular sudoite and chlorite bearing metapelites from Crete. Comparison between the calculated mineral assemblages and field data shows that the new model is able to predict the coexistence of chlorite and sudoite at low metamorphic temperatures. The predicted lower limit of the chloritoid stability field is also in better agreement with petro-

5. ISTerre, University of Grenoble 1, CNRS, 1381 rue de la Piscine, 38041 Grenoble, France

6. Department of Geosciences and Geography, Division of Geology, University of Helsinki, Gustaf Hållströmin katu 2a, FI-00014 Helsinki, Finland

logical observations. For practical applications to metamorphic and hydrothermal environments, a new semi-empirical chlorite geothermometer was calibrated. This geothermometer has been applied to detrital chlorite partially recrystallized from the Zone houillère in the French Western Alps. Chlorite temperature distribution maps have been calculated from electron microprobe X-ray maps and show that the detrital chlorite grains recorded formation temperatures of 350°C-400°C and were partially recrystallized during the Alpine metamorphism at lower temperatures of 200-275°C.

2.3.3.1 Introduction

Chlorite minerals are commonly observed in a large variety of diverse geological environments including sedimentary, metamorphic and hydrothermally altered rocks (Laird 1988). This common rock-forming mineral occurs within pelitic, mafic, ultramafic and calc-silicate assemblages resulting in a large compositional variability. In addition, the chemical composition of chlorite in hydrothermal alteration zones changes systematically with proximity to fluid pathways and hydrothermal veins and can be utilized for reconstructing the fluid composition (Walshe 1986, Mountain et Williams-Jones 1995, Halter et al. 1998). Chlorite can occur as replacement of pre-existing grains such as biotite that control its chemical composition. Conversely, chlorite can directly grow as newly formed metamorphic or diagenetic grains, with the chemical composition dictated by the bulk rock composition and mineral equilibria. Thus, it is now well established that the chemical composition of chlorite does also depend on the conditions of formation such as temperature and pressure (Cathelineau et Nieva 1985, Walshe 1986, Kranidiotis et MacLean 1987, Cathelineau 1988, Hillier et Velde 1991, Jowett 1991, de Caritat et al. 1993, Zang et Fyfe 1995, Baker et Holland 1996, Holland et al. 1998, Vidal et al. 2001; 2005; 2006, Inoue et al. 2009; 2010, Lanari et al. 2012a). All these observations make chlorite a good candidate for geothermobarometric investigations. During the last thirty years, three different approaches to chlorite geothermometry were more or less successfully utilized :

(1) Several Empirical calibrations have been proposed that use the compositional variability of chlorite as a proxy for estimating the temperature of crystallization. The first chlorite geothermometers were based on the amount of tetrahedral aluminium (Al_{IV}) or on the amount of octahedral vacancies (Vac) of chlorite in hydrothermal and geothermal systems (Cathelineau et Nieva 1985, Kranidiotis et MacLean 1987, Cathelineau 1988). Hillier et Velde (1991) extended these calibrations to early diagenetic and low-grade metamorphic rocks using a set of 500 natural data. Unfortunately, chlorite minerals from low-temperature environments show compositional differences compared to those formed in higher-grade metamorphic or hydrothermal environments (de Caritat et al. 1993, and references therein). Therefore, it is not possible to calibrate an universal chlorite geothermometer based only on the Al_{IV} content that would cover the entire pressure-temperature range over which chlorite is stable. Thus, subsequent empirical calibrations were based on using both the amount of Al_{IV} and the XMg value ($XMg = Mg^{2+} / (Fe^{2+} + Mg^{2+})$) to estimate the paleotemperature (Jowett 1991, Zang et Fyfe 1995). Although these modifications resulted in considerable improvement for certain P-T conditions, they would not provide a reliable chlorite thermometer that could be applied over wide ranges in pressure and temperature.

(2) Because the empirical calibrations were not able to constrain the chlorite formation temperature over a large compositional range (de Caritat et al. 1993), thermodynamic modeling was applied to solve this problem. Semi-empirical geothermometers were calibrated using the relationship between the temperature ($1/T$) and the equilibrium constant (K) of a reaction involving chlorite end-members and typically quartz and water. The equilibrium constant is estimated using ideal mixing of cations on energetically equivalent sites (Walshe 1986, Inoue et al. 2009). The last published approach from Inoue et al. (2009) provided an useful calibration based on the composition of chlorite including an estimate for XFe^{3+} ($XFe^{3+} = Fe^{3+} / (Fe^{2+} + Fe^{3+})$) obtained from Mössbauer spectroscopy. However, this geothermometer is strongly dependent on the XFe^{3+} of chlorite that is not routinely determinable using electron microprobe analysis. This approach does also suffer from two additional problems, which are (i) the assumption of ideal

mixing in chlorite sublattices that appears to be not compatible with the models used in thermodynamic phase equilibria computation packages (see below), and (ii) the impossibility of using these calibrations in the framework of an internally consistent thermodynamic data set.

(3) Following the experiments of [Baker et Holland \(1996\)](#), mixing properties and activity-composition relationships of chlorite were thermodynamically modelled by [Holland et al. \(1998\)](#). The resulting model, which is termed *Chl(HP)* for the remainder of this contribution, was used in equilibrium phase diagram computations such as THERMOCALC ([Powell et al. 1998](#), [Powell 2008](#)), PERPLE_X ([Connolly 2005; 2009](#), [Connolly et Petrini 2002](#)) or THERIAK ([De Capitani et Petrakakis 2010](#)) in conjunction with the [Holland et Powell \(1998\)](#) internally consistent thermodynamic data set. The solid solution model of [Holland et al. \(1998\)](#) is derived for trioctahedral chlorites, and the compositional space is modeled with four linearly independent end-members : Al-free-chlorite (*afchl*), amesite (*ames*), clinocllore (*clin*) and daphnite (*daph*). Unfortunately, this model does not include the di/trioctahedral chlorites such as the sudoite (*sud*) end-member. This precludes the use of the *Chl(HP)* model at low temperature ($< 450^{\circ}\text{C}$), which is a serious limitation when considering the full temperature range of chlorite stability ([Cathelineau 1988](#), [Hillier et Velde 1991](#), [de Caritat et al. 1993](#), [Vidal et al. 2001; 2005](#)).

The chlorite solid solution models of [Vidal et al. \(2001; 2005; 2006\)](#) include a sudoite end-member, but they are not compatible with the [Holland et Powell \(1998\)](#) internally consistent thermodynamic data set. Chlorite compositions are modelled using *ames*, *clin*, *daph*, and the *sud* end-member ([Vidal et al. 2001](#)) with an extension to Fe-amesite (*fames*) in updated versions ([Vidal et al. 2005; 2006](#)). These models were successfully applied to metapelites using multi-equilibrium techniques (see e.g. [Trotet et al. 2001](#), [Parra et al. 2002b](#), [Ganne et al. 2003](#), [Augier et al. 2005b;a](#), [Vidal et al. 2006](#), [Rimmelé et al. 2006](#), [Yamato et al. 2007](#), [Ganne et al. 2012](#), [Grosch et al. 2012](#), [Lanari et al. 2012a](#)). However, these models cannot be used for phase diagram computation with the [Holland et Powell \(1998\)](#) internally consistent thermodynamic data set.

Addressing some of the limitations of the existing approaches, the purpose of

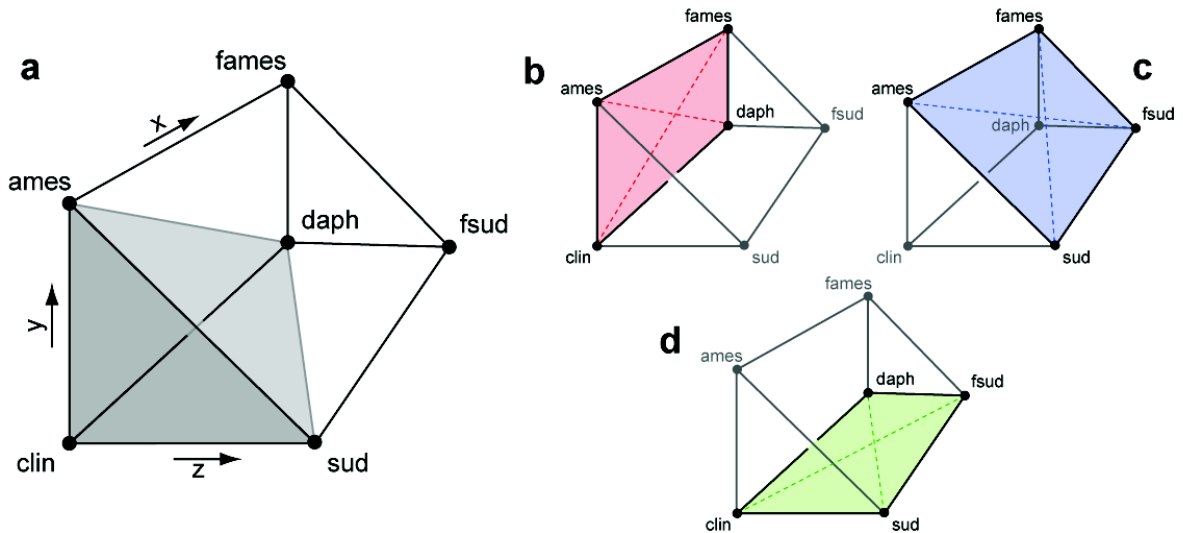


FIGURE 2.22 – Visualization of the chlorite composition space in the system FMASHO. (a) In this model, ames, clin, sud and daph are the independent end-members defining the shaded pyramidal volume (see text). The composition variable x ($x = X_{Fe}$) increases from ames to fames (also from sud to fsud and from clin to daph) corresponding to the FM substitution. The composition variable y ($y = X_{Al}^{M1}$) increases from clin to ames (also from daph to fames, from sud to ames and from fsud to fames) corresponding to the TS substitution. The last composition variable z ($z = X_{Vac}^{M1}$) increases from clin to sud (also from ames to sud, from daph to fsud and from fames to fsud). The internal reactions occur in the three rectangles (b) for the reaction (2.43), (c) for reaction (2.44) and (d) for reaction (2.45) (see text).

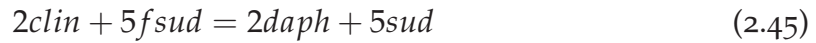
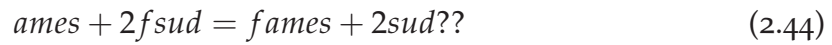
this study is to derive a new activity-composition model for chlorite that includes the sudoite end-member. The new model builds and expands upon the model of [Holland et al. \(1998\)](#) and is compatible with ([Holland et Powell 1998](#)) internally consistent thermodynamic data set. This model will be constrained from published experimental data on relevant phase equilibria and a new set of approximately 270 natural chlorite compositions for which the formation temperature is available. In addition, a new semi-empirical geothermometer for chlorite will be also derived that covers a wider range in temperatures than previous calibrations. In order to demonstrate the performance of the new chlorite activity-composition model, we will show several application examples that include pseudosection modeling, geothermometry using small-scale microprobe X-ray imaging, and fluid-mineral equilibria modeling.

2.3.3.2 New thermodynamic model for chlorite : $Chl(LWV)$

The chlorite solid solution model of [Holland et al. \(1998\)](#) considered the $Fe-Mg_{-1}$ substitution (FM), the Tschermak substitution (TS) $Al_{IV}Al_{VI}Si_{-1}(Mg,Fe)_{-1}$

and additionally order-disorder along the join between amesite and Al-free chlorite. Restricting our analysis to chlorite with $Si < 3$, these substitutions can be modeled with the four end-members clinochlore (*clin*), daphnite (*daph*), Mg-amesite (*ames*) and Fe-amesite (*fames*). The incorporation of octahedral vacancies (*V*) was assumed to result from the di/trioctahedral substitution (*DT*) $(Mg, Fe^{2+})_3V_{-1}Al_{-2}$, between the above trioctahedral end-members and the di-trioctahedral end-members sudoite and Fe-sudoite.

The extended solid solution model, called *Chl(LWV)* in the following, involves thus six end-members (Table 2.6, Fig. 2.22-a). From this full set of end-members, three internal reactions can be written (represented in Fig. 2.22-b, 2.22-c and 2.22-d respectively) :



From these reactions, only two are linearly independent, and two end-members in the selected set are compositionally dependent on the other end-member compositions, provided that the proportions of some end-members in the independent set can become negative. Following the approach of [Powell et Holland \(1999\)](#) and taking *ames*, *clin*, *daph* and *sud* as linearly independent end-members, the Gibbs free energy of *fames* and *fsud* can be derived from the reciprocal relationships :

$$\begin{aligned} G_{fames} = & G_{ames} + \frac{4}{5} G_{daph} - \frac{4}{5} G_{clin} \\ & + \frac{4}{5} W_{ames-daph} - \frac{4}{5} W_{ames-clin} - \frac{16}{25} W_{clin-daph} \end{aligned} \quad (2.46)$$

$$\begin{aligned} G_{fsud} = & G_{sud} - \frac{2}{5} G_{daph} - \frac{2}{5} G_{clin} \\ & + \frac{2}{5} W_{daph-sud} - \frac{2}{5} W_{clin-sud} - \frac{4}{25} W_{clin-daph} \end{aligned} \quad (2.47)$$

	T1(2)	T2(2)	M1(1)	M23(4)	M4(1)
Amesite-Mg	Si,Si	Al,Al	Al	Mg,Mg,Mg,Mg	Al
Amesite-Fe *	Si,Si	Al,Al	Al	Fe,Fe,Fe,Fe	Al
Clinocllore	Si,Si	Si,Al	Mg	Mg,Mg,Mg,Mg	Al
Daphnite	Si,Si	Si,Al	Fe	Fe,Fe,Fe,Fe	Al
Sudoite-Mg	Si,Si	Si,Al	V	Mg,Mg,Al,Al	Al
Sudoite-Fe *	Si,Si	Si,Al	V	Fe,Fe,Al,Al	Al

TABLE 2.6 – Site partitioning scheme used for the model Chl(LWV). *Dependent end-members (see text).

For phase equilibria computation using common petrological software packages, the thermodynamic properties of the dependent end-members are not required. However, generic non-linear Gibbs energy minimization codes such as GEM-Selektor (Kulik et al. in press, Wagner et al. in press) that find the amount and composition of stable phases by applying a set of Karush-Kuhn-Tucker conditions (one of these being a non-negativity constraint) require that the properties of dependent end-members in reciprocal solid solutions are explicitly defined. The compositions of the six end-members of chlorite can be plotted in a triangular prism showing two triangular faces, one with the Mg end-members *ames*, *clin*, *sud* and the second one with the Fe end-members *fames*, *daph* and *fsud* (Fig. 2.22).

Following common practice to determine the activities of each end-members, the site distribution is formulated in term of three linearly independent composition variables defined as follows :

$$\begin{aligned}
 x &= \frac{4 X_{fames} + 5 X_{daph} + 2 X_{fsud}}{4 X_{fames} + 5 X_{daph} + 2 X_{fsud} + 4 X_{ames} + 5 X_{clin} + 2 X_{sud}} \\
 &= \frac{Fe}{Fe + Mg} \\
 &= X_{Fe}
 \end{aligned} \tag{2.48}$$

$$y = X_{ames} + X_{fames} + \frac{1}{2}(X_{clin} + X_{daph} + X_{sud}) = X_{Al,M1} \tag{2.49}$$

$$z = X_{sud} = X_{V,M1} \tag{2.50}$$

These three compositional variables account for the chemical variability in the full composition space involving the selected set of chlorite end-members (x , y and z in Fig. 2.22-a). Assignment of site occupancies followed the approach of Vidal et al. (2001). The two tetrahedral $T1$ sites are assumed to be fully occupied by Si, and Si and Al may both occur on the two $T2$ sites. On the octahedral positions, Al preferentially occupies the $M4$ site, but may occur also in the $M1$ site and the four

M2M3 sites. Fe^{2+} and Mg^{2+} may occur in M1 and M2M3 sites with equipartitioning, and Vac is restricted to the M1 site (Vidal et al. 2001). According to this cation site repartition model, the resulting structural formula of chlorite is then $(Al)_1(Mg, Fe, Al)_4(Mg, Fe, Al, V)_1(Si, Al)_2Si_2O_{10}(OH)_8$. For a given composition of chlorite obtained from electron microprobe analysis, the compositional variables x , y and z are evaluated (see details in Appendix 1) to transform the end-member proportions (X_{ames} , X_{daph} , X_{clin} , X_{sud} , X_{fames} , X_{fsud}) into a set of independent end-member proportions (p_{ames} , p_{clin} , p_{daph} , p_{sud}) with the following equations :

$$p_{ames} = y \quad (2.51)$$

$$p_{ames} = 1 - y - z - x(1 - \frac{1}{5}y - \frac{3}{5}z) \quad (2.52)$$

$$p_{daph} = x(1 - \frac{1}{5}y - \frac{3}{5}z) \quad (2.53)$$

$$p_{sud} = z \quad (2.54)$$

All the chlorite compositions that have fractions of f_{ames} or f_{sud} , i.e. those that lie outside the shaded pyramidal volume in Fig. 2.22-a, involve negative proportions of one or more of the independent end-members. The ideal mixing activity of the independent end-members was calculated by on-site mixing of atoms (Powell et Holland 1993). Site fractions are obtained from composition variables as follows :

$$X_{Fe}^{M2M3} = x(1 - \frac{1}{2}z) \quad (2.55)$$

$$X_{Mg}^{M2M3} = (1 - x)(1 - \frac{1}{2}z) \quad (2.56)$$

$$X_{Al}^{M2M3} = \frac{1}{2}z \quad (2.57)$$

$$X_{Fe}^{M1} = x(1 - y - z) \quad (2.58)$$

$$X_{Mg}^{M1} = (1 - x)(1 - y - z) \quad (2.59)$$

$$X_{Al}^{M1} = y \quad (2.60)$$

$$X_V^{M1} = z \quad (2.61)$$

$$X_{Al}^{T2} = 1 - \frac{1}{2}(1 - y) \quad (2.62)$$

$$X_{Al}^{T2} = \frac{1}{2}(1 - y) \quad (2.63)$$

The ideal mixing activities are then obtained from the site fractions :

$$a_{ames} = (X_{Mg}^{M2M3})^4 X_{Al}^{M1} (X_{Al}^{T2})^2 \quad (2.64)$$

$$a_{clin} = 4(X_{Mg}^{M2M3})^4 X_{Mg}^{M1} X_{Al}^{T2} X_{Si}^{T2} \quad (2.65)$$

$$a_{daph} = 4(X_{Fe}^{M2M3})^4 X_{Fe}^{M1} X_{Al}^{T2} X_{Si}^{T2} \quad (2.66)$$

$$a_{sud} = 64(X_{Al}^{M2M3})^2 (X_{Mg}^{M2M3})^2 X_V^{M1} X_{Al}^{T2} X_{Si}^{T2} \quad (2.67)$$

The non-ideal part is expressed through macroscopic activity coefficients using the symmetric formalism (Holland et Powell 1996a,b) :

$$\begin{aligned} RT\ln(\gamma_{ames}) = & p_{clin}(1 - p_{ames})W_{ames-clin} + p_{daph}(1 - p_{ames})W_{ames-daph} \\ & p_{sud}(1 - p_{ames})W_{ames-sud} - p_{clin}p_{daph}W_{clin-daph} \\ & p_{clin}p_{sud}W_{clin-sud} - p_{daph}p_{sud}W_{daph-sud} \end{aligned} \quad (2.68)$$

$$\begin{aligned} RT\ln(\gamma_{clin}) = & p_{ames}(1 - p_{clin})W_{ames-clin} + p_{daph}(1 - p_{clin})W_{clin-daph} \\ & p_{sud}(1 - p_{clin})W_{clin-sud} - p_{ames}p_{daph}W_{ames-daph} \\ & p_{ames}p_{sud}W_{ames-sud} - p_{daph}p_{sud}W_{daph-sud} \end{aligned} \quad (2.69)$$

$$\begin{aligned} RT\ln(\gamma_{daph}) = & p_{ames}(1 - p_{daph})W_{ames-daph} + p_{clin}(1 - p_{daph})W_{clin-daph} \\ & p_{sud}(1 - p_{daph})W_{daph-sud} - p_{ames}p_{clin}W_{ames-clin} \\ & p_{ames}p_{sud}W_{ames-sud} - p_{clin}p_{sud}W_{clin-sud} \end{aligned} \quad (2.70)$$

$$\begin{aligned} RT\ln(\gamma_{sud}) = & p_{ames}(1 - p_{sud})W_{ames-sud} + p_{clin}(1 - p_{sud})W_{clin-sud} \\ & p_{daph}(1 - p_{sud})W_{daph-sud} - p_{ames}p_{clin}W_{ames-clin} \\ & p_{ames}p_{daph}W_{ames-daph} - p_{clin}p_{daph}W_{clin-daph} \end{aligned} \quad (2.71)$$

where W denotes the symmetric interaction parameters.

2.3.3.3 Model calibration

We apply the following strategy to calibrate the extended chlorite model described above. The initial standard state and symmetric interaction parameters were adopted from Holland et Powell (1998) and subsequent updates (Thermocalc dataset file *tcds55*). The standard state properties of sudoite were refined to be in agreement with the available experimental phase equilibria data (Vidal et al. 1992) and the interaction parameters involving sudoite were simultaneously refined using

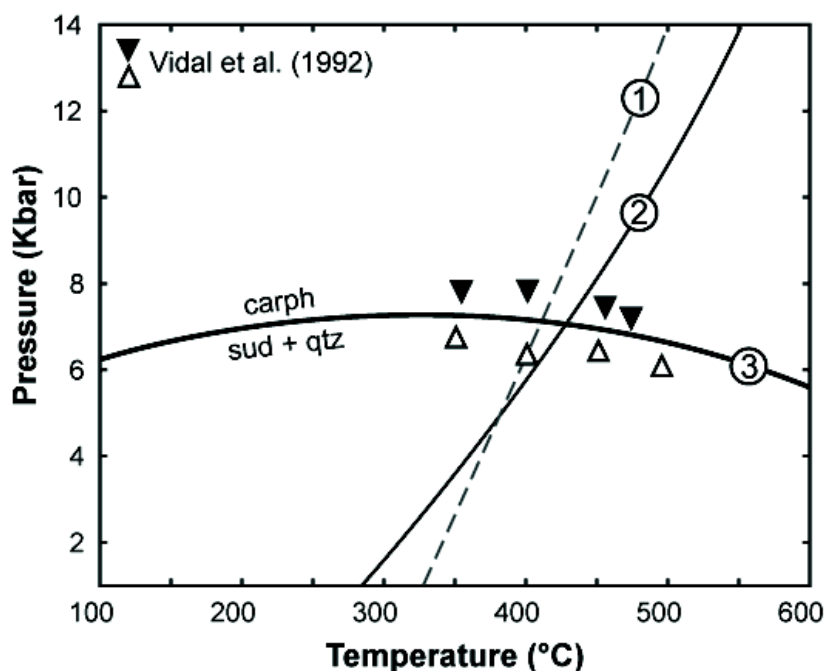


FIGURE 2.23 – Experimental brackets of [Vidal et al. \(1992\)](#) and the model curves of the equilibrium carpholite (*carph*) \rightleftharpoons sudoite (*sud*) + quartz (*qtz*) plotted using (1) enthalpy, entropy and heat capacity parameters from [Holland et Powell \(1998\)](#), (2) refined enthalpy and entropy with heat capacity parameters from [Holland et Powell \(1998\)](#), and (3) refined enthalpy and entropy and heat capacity parameters (Table 2)

natural data from the literature. All computations were performed using MEAMP (Multi-Equilibrium And Minimization Program), which is an unpublished Matlab-based software tool allowing to plot equilibria in P-T diagrams and to regress thermodynamic parameters using both experimental and natural data.

New sudoite molar To preserve consistency with the Holland-Powell thermodynamic dataset, the heat capacities, molar volumes, enthalpies, thermal expansions and compressibility parameters of *ames*, *clin*, *daph* were retained. In the revised dataset that was used here (*tcds55*), the entropies of *ames*, *clin* and *daph* are incremented by 20 J/K ([Coggon et Holland 2002](#)) compared to [Holland et Powell \(1998\)](#). The equilibrium curve for the reaction carpholite \rightleftharpoons sudoite + quartz obtained by using the standard thermodynamic properties from [Holland et Powell \(1998\)](#) (equilibrium 1 in Fig. 2.23), is clearly well outside of the experimental brackets of [Vidal et al. \(1992\)](#). Considering that the standard state thermodynamic properties for carpholite would predict equilibrium curves for several reactions involving carpholite that would be in excellent agreement with experimental brackets, it was necessary

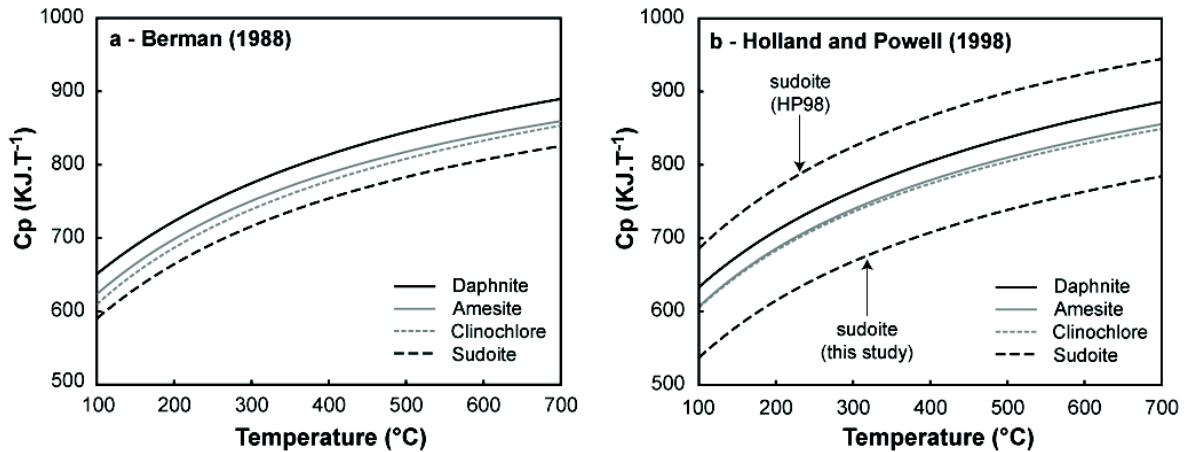


FIGURE 2.24 – Heat capacity of chlorite end-members estimated using (a) the method and coefficients from [Berman \(1988\)](#), and (b) the method and data use in the [Holland et Powell \(1998\)](#). The the heat capacity curves of sudoite have been plotted using the data from [Holland et Powell \(1998\)](#) and using the new heat capacity coefficients provided in Table 2.7

to refine the properties of sudoite. A simple adjustment of the enthalpy ($\Delta_f H_0$) and entropy (S_0) of sudoite did not result in better agreement with the experimental constrains, suggesting a problem with the heat capacity (C_p) coefficients for sudoite proposed by [Holland et Powell \(1998\)](#). The heat capacity coefficients of sudoite can only be obtained from estimation techniques, because no calorimetric data are available. The $C_p(T)$ function for sudoite was therefore estimated with the method of [Berman et Brown \(1985\)](#) and has been plotted in the range of 200 to 600°C along with $C_p(T)$ functions estimated for *clin*, *ames*, *fames* and *daph* (Fig. 2.24-a). At any temperature, we note from Figure 2.24-a that

$$C_{p_{sud}}(T_i) < C_{p_{clin}}(T_i) < C_{p_{ames}}(T_i) < C_{p_{daph}}(T_i) \quad (2.72)$$

The same relative order is observed when plotting the $C_p(T)$ functions of the same end-members from the Holland-Powell dataset, expect that the $C_p(T)$ of *sud* that is higher than that of *daph* (Fig. 2.24-b).

	$\Delta_f H$ (kJ)	S (JK ⁻¹)	V (kJKbar ⁻¹)	a (kJK ⁻¹)	$b(10^5)$ (kJK ⁻²)	c (kJK)	d (kJK ^{-1/2})
Sudoite-Mg	-8647.122	417	20.3	1.1049	1.1217	-6811.7	-10.1105

TABLE 2.7 – New molar thermodynamic properties (units : kJ, K, kbar) of sudoite derived in this study (see text). $\Delta_f H$ is the enthalpy of formation ; S is the entropy ; V the volume (all these properties are at 1 bar and 298.15K). a , b , c and d are the heat capacity coefficients.

Using the predicted heat capacity data and properties from [Holland et Powell \(1998\)](#) as initial guess, the enthalpy ($\Delta_f H_0$), entropy (S_0) and heat capacity coefficients of sudoite were simultaneously refined in order to (i) be consistent with Eq. (2.72), (ii) minimize the difference of the sudoite standard state properties compared to those listed in [Holland et Powell \(1998\)](#), and (iii) to locate the carpholite \rightleftharpoons sudoite + quartz equilibrium within the experimental brackets of [Vidal et al. \(1992\)](#). The resulting parameters are listed in Table 2.7, the equilibrium curve for the reaction carpholite \rightleftharpoons sudoite + quartz is plotted in Fig. 2.23 (bold curve, labelled 3), and the sudoite $C_p(T)$ function is plotted in the Fig. 2.23-b. The new entropy derived in our study differs by 18 kJ compared to that proposed in [Holland et Powell \(1998\)](#), which is consistent with the magnitude of the adjustment to other chlorite end-members (*ames*, *clin* and *daph*) that was applied by [Coggon et Holland \(2002\)](#) relative to [Holland et Powell \(1998\)](#).

Margules parameters on M1 The Fe-Mg mixing on M1 has been accepted to be slightly non-ideal as proposed by [Holland et al. \(1998\)](#), with $W_{clin-daph}$ at 2.5 kJ. This slight nonideality is inferred from fluid-mineral Fe-Mg partitioning data ([Holland et al. 1998](#)). We note that this low value is essentially compatible with the assumption of ideal to nearly ideal Fe-Mg mixing that was made by authors that developed activity-composition models for chlorite ([Vidal et al. 2001; 2005; 2006](#)) and dioctahedral mica ([Coggon et Holland 2002, Parra et al. 2002a, Dubacq et al. 2010](#)).

The value $W_{ames-clin}$ has been adopted as 18 kJ ([Holland et al. 1998](#)) and results in good agreement with the experiments of [Baker et Holland \(1996\)](#). Similarly, the $W_{ames-daph}$ has been fixed to 13.5 kJ, which is the value that is currently used in THERMOCALC in conjunction with the updated mineral standard state data. The small difference between Al-Mg and Al-Fe mixing energies results from the

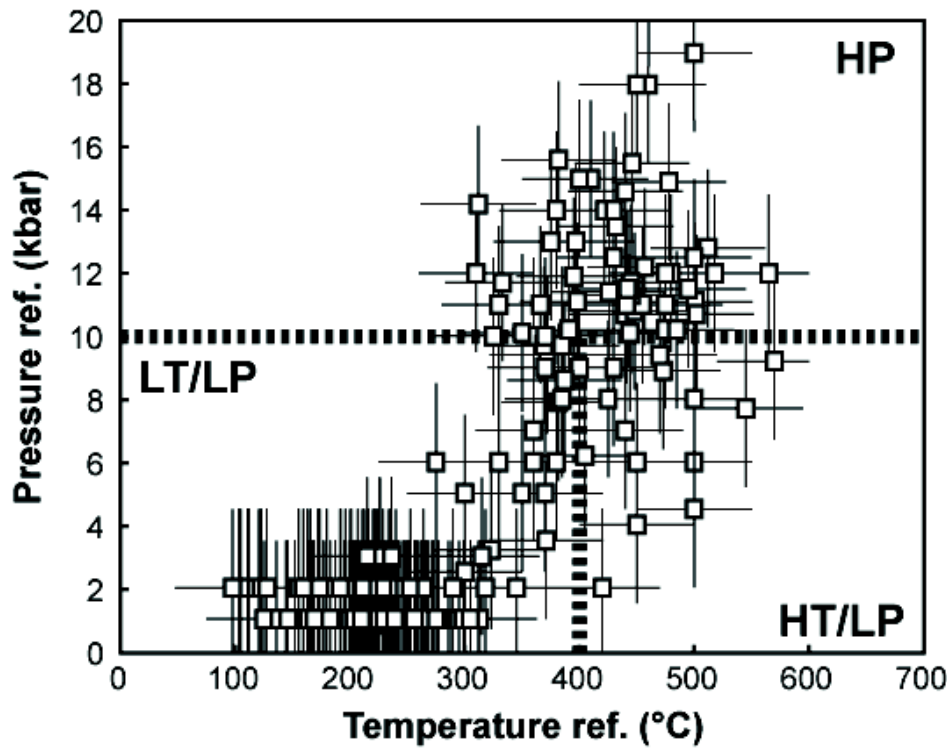
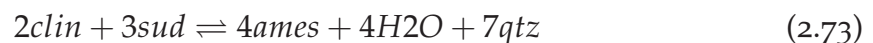


FIGURE 2.25 – Pressure-temperature conditions of the natural data used in the parameter regression. References for all data sources are given in 2.8

previous assumption of non-ideality in *Fe-Mg* exchange along the joint between *clin-daph* and *ames*. The values of the interaction parameters involving sudoite ($W_{ames-sud}$, $W_{clin-sud}$ and $W_{daph-sud}$) were simultaneously refined by using a set of natural chlorite compositional data in conjunction with published equilibrium conditions (P_{ref} , T_{ref}) between 100-600°C and 0-20 kbar (see list of references in Table 3 and the P-T plot in Fig. 4). The compositional variables x , y and z (Eq. 2.48, 2.49 and 2.50) were calculated from the chlorite structural formulae (Appendix 1). Analyses with small amounts of sudoite ($z < 0.045$) were removed from the original data set as suggested by Vidal et al. (2001). Finally, 271 published analyses of chlorite were selected for further use. The temperature of each chlorite was calculated using the position of the following equilibrium reaction involving chlorite, quartz and H_2O at the given pressure (P_{ref})



General range of P-T conditions	References
BT ($T < 400^{\circ}\text{C}$)	Cathelineau et Nieva (1985), Zang et Fyfe (1995), Schmidt et al. (1997), Baboury (1999) Vidal et al. (2001), Booth-Rea et al. (2002), Abad et al. (2003), Belmar et Morata (2005) Rolland et al. (2006), Serafimovski et al. (2006), Malasoma et Marroni (2007) Inoue et al. (2009), Shinjoe et al. (2009), Inoue et al. (2010), Lanari et al. (2012a) Cantarero et al. (2012)
HT/BP ($T > 400^{\circ}\text{C}$ $P < 10\text{kbar}$)	Goffé et Bousquet (1997), Hannula et al. (1999), Vidal et al. (1999), Hoisch (2000) Trotet et al. (2001), Vidal et al. (2001), Parra et al. (2002b), Moazzen (2004); Augier et al. (2005a), Calderon et al. (2005), Agard et al. (2006), Russo et al. (2006) Inoue et al. (2009)
HP ($P > 10\text{kbar}$)	Chopin (1979), Goffé et Bousquet (1997), Vidal et al. (1999), Agard et al. (2001b) Vidal et al. (2001), Parra et al. (2002b), Augier et al. (2005a)

TABLE 2.8 – *References of the analyses of minerals used for the regression (see text). The reference P-T conditions are plotted in figure 2.25.*

The non-ideal part of activity was described using a regular (symmetric) interaction parameter W that can be expressed as follow

$$W = a + bT + cP \quad (2.74)$$

The coefficients b and c were first fixed to zero and only the coefficient a was refined with the MEAMP program that uses a Nelder-Mead Simplex Method. A function calculates the sum of the square of residual $\Delta G_{\text{reaction}}$ calculated for each analysis at the P_{ref} and T_{ref} (temperature and pressure of equilibration) that are adopted from the original publications. By varying the selected parameters (here the a coefficients of $W_{\text{ames-sud}}$, $W_{\text{clin-sud}}$ and $W_{\text{daph-sud}}$), this square of the sum of residuals is minimized. As the first approach, a preliminary set of constant W parameters were extracted, which were used as input. Introducing pressure and temperature dependence would not detectably improve the fit to the natural data and all interaction parameters were accepted as constant. The calculated symmetric interaction parameters between sudoite and other chlorite end-members were found to be high and positive (see details in Table 4), with $W_{\text{ames-sud}} = 43.3 \text{ kJ}$, $W_{\text{clin-sud}} = 49.1 \text{ kJ}$ and $W_{\text{daph-sud}} = 43.4 \text{ kJ}$. Such high values are compatible with the observed miscibility gap between the natural di/tri and tri/tri-chlorite, which are found to coexist in low temperature low pressure (LT-LP) aluminous metapelites (e.g. Theye et al. 1992). The predicted difference between V-Mg and V-Fe mixing suggests a slight non-ideal Fe-Mg exchange, in good agreement with the interaction parameter proposed for Fe-Mg mixing on M1 by Holland et al. (1998) ($W_{\text{clin-daph}} = 2.5 \text{ kJ}$).

	W (J/mol)
$W_{\text{ames-clin}}$	18000 ⁽¹⁾
$W_{\text{ames-daph}}$	13500 ⁽¹⁾
$W_{\text{ames-sud}}$	43300 ⁽²⁾
$W_{\text{clin-daph}}$	2500 ⁽¹⁾
$W_{\text{clin-sud}}$	49100 ⁽²⁾
$W_{\text{daph-sud}}$	43400 ⁽²⁾

TABLE 2.9 – Non-ideal interaction parameters used in the model Chl(LWV) describing the non-ideal interactions on the site M1. $W = a + bT(K) + cP(\text{bar})$ (here $b = 0$ and $c = 0$, see text). (1) From Holland et al. (1998) and updates. (2) Adjusted in this study.

2.3.3.4 Results

The new standard state properties of *sud* and the solid solution parameters derived as explained above are summarized in Tables 2.7 and 2.8. Figure 2.26 shows that the temperatures (T_{calc}) estimated using Eq. (2.73) are in good agreement with the original temperature (T_{ref}) ($R^2 = 0.91$). The magnitude of data scatter observed in the 100-600°C temperature range is compatible with the uncertainties associated in the determination of the T_{ref} and P_{ref} data reported in the literature. Indeed, the chlorite-quartz equilibrium has a slope between 0.07 and 0.12 kbar K^{-1} , implying that the estimated temperature is dependent on pressure.

As discussed in the introduction, the composition of chlorite strongly depends on its formation temperature (Cathelineau 1988, Hillier et Velde 1991, Jowett 1991, de Caritat et al. 1993, Zang et Fyfe 1995, Baker et Holland 1996, Holland et al. 1998, Vidal et al. 2001; 2005; 2006, Inoue et al. 2009; 2010, Lanari et al. 2012a). This dependency is further illustrated using relationship between the composition variables (x , y , z), T_{calc} and the original P_{ref} data (Fig. 2.27). The first composition variable x (Eq. 2.48) does not systematically vary with T_{calc} and pressure (Fig. 6a), suggesting that x is mainly controlled by the bulk rock composition. The good correlation between T_{ref} and T_{calc} (Fig. 2.26) shows that our geothermometric calibration predicts the correct formation temperature for chlorite with X_{Mg} ranging from 0.10 to 0.85. The second composition variable y (Eq. 2.49) systematically increases with increasing temperature (Fig. 2.27-b). Because only the ames and fames chlorite end-members have two *Al* on *T2* and one *Al* in *M1*, the relationship between Al_{IV} and y is :

$$Al_{\text{IV}} = 1 + y \quad (2.75)$$

For comparison, empirical geothermometers based on the amount of Al_{IV} have

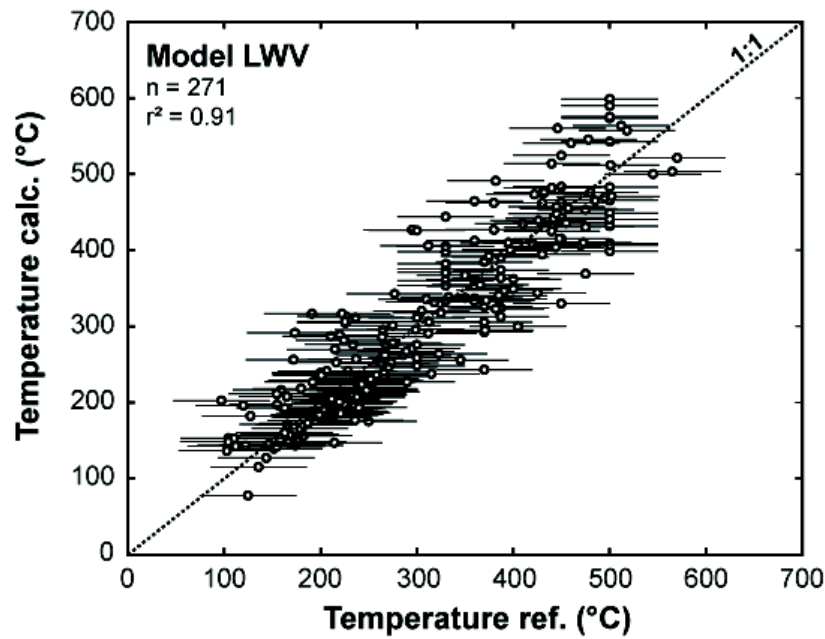


FIGURE 2.26 – Comparison between calculated and reference temperatures (temperature estimates from the original publications) of the natural samples that were used for regressing chlorite model parameters. In the absence of appropriate calculation of error propagation in the majority of the original publication, the errors bars on reference temperatures were set to an average value of $\pm 50^\circ\text{C}$. A total number of 271 natural analyses were finally used and the correlation coefficient for the correlation between calculated and reference temperature is 0.91

been plotted in the same diagram (lines in Fig. 2.27-b) using Eq. (2.75). The calibration of Cathelineau et Nieva (1985), Cathelineau (1988), Hillier et Velde (1991) predict different temperatures in the range 200-400°C. For instance, for a chlorite with $y = 0.15$, the calibrations Hillier et Velde (1991), Cathelineau et Nieva (1985) and Cathelineau (1988) predict, 220°C, 230°C and 310°C, respectively. The natural data have equilibrium temperatures between 180 and 500°C. This result demonstrates that the Al_{IV} content of chlorite is not an appropriate parameter for defining an universal chlorite geothermometer. In contrast, the third compositional parameter z (Eq. 2.50) shows a much better constrained relationship with temperature and pressure than do x and y . For a given pressure, the amount of vacancies increases with decreasing temperature and increasing pressure, as already shown by Vidal et al. (2001). An empirical calibration based on the amount of vacancies could reproduce the observed trends and thus be used as an empirical geothermometer (at given P) or, alternatively, as geobarometer (at given T).

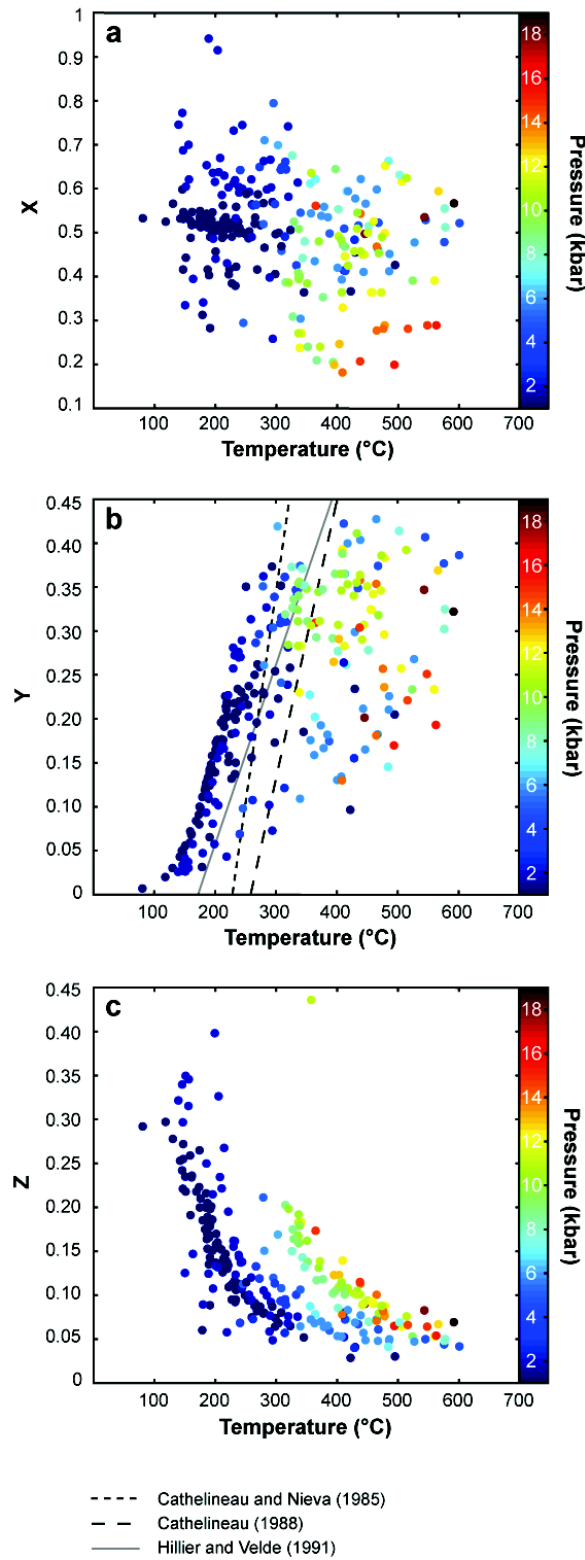


FIGURE 2.27 – Relationships between the different composition variables (a) x , (b) y and (c) z of chlorite minerals and the temperature calculated with the extended chlorite model. The color code of the data points denotes the equilibrium pressure, adopted from the original publications. Because the composition variable y is linearly correlated with x , the curves for three empirical chlorite thermometer calibrations (Cathelineau et Nieva 1985, Cathelineau 1988, Hillier et Velde 1991) were plotted as well. The data show that the number of vacancies (z) shows a well defined relationship with temperature for a given pressure.

2.3.3.5 A new semi-empirical geothermometer

The *Chl(LWV)* model described above has been developed for use in phase equilibria computation such as pseudosection modeling. The crystallization temperature of chlorite can be estimated from the equilibrium between chlorite, quartz and water (Eq. 2.73), but it requires calculation of $G(P, T)$ and the ideal and nonideal part of the activity coefficients (a_i and γ_i). Because many applications to field data are only interested in the chlorite formation temperature, we proposed in the following a simplified procedure (a semi-empirical geothermometer) based on the temperature dependence of Eq. (2.73). The logarithm of the equilibrium constant for Eq. (2.73) can be expressed as :

$$\ln(K) = \ln\left(\frac{a_{ames}^4}{a_{clin}^2 a_{sud}^3}\right) \quad (2.76)$$

in which a_{ames} , a_{clin} and a_{sud} are the ideal activities, which are defined in Eq. (2.64), (2.65) and (2.66), respectively. For the semi-empirical geothermometer, only the ideal part of the activity will be used. The error introduced by this simplification is comparatively small, because the regression of the activity-composition model showed that the symmetric interaction parameters do not require a temperature or pressure dependence. Therefore, the difference between the simplifying assumption of ideal mixing and the calibrated activity-composition model will amount to a constant term, when normalized by RT . However, the simplification will result in small differences between the semi-empirical model and the temperature prediction from of the nonideal *Chl(LWV)* model. Considering only the ideal part of activities, we adopt the general assumptions of Walshe (1986) and Inoue et al. (2009).

At thermodynamic equilibrium ($\Delta G_{reaction} = 0$) between chlorite, quartz and water, and neglecting ΔCp (which is likely not to change much with pressure and temperature), the logarithm of the equilibrium constant can be expressed as :

$$-\ln(K) = \frac{\Delta H^0 + (P - 1)\Delta V^0}{RT} + \frac{\Delta S^0}{R} \quad (2.77)$$

Figure 2.28-a shows a correlation diagram of $\ln(K)$ vs $1/T$ using the set of natural chlorite data and the temperatures calculated above (T_{calc}) with the *Chl(LWV)* model. The colors of the points denote the range of Pref. This diagram shows that

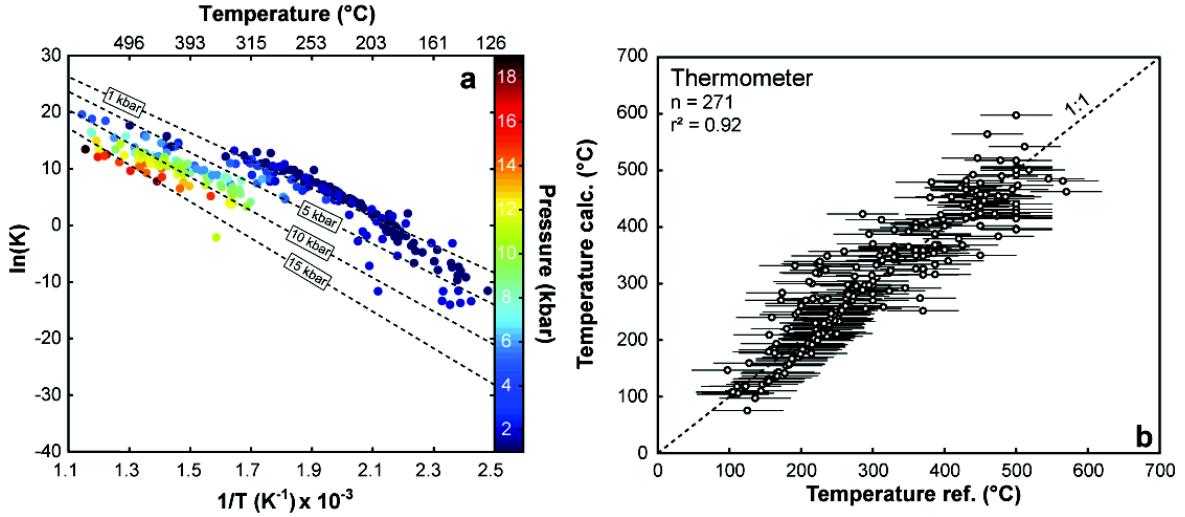


FIGURE 2.28 – Performance of a new semi-empirical chlorite geothermometer, (a) Correlation diagram illustrating the relationship between $1/T$ and the $\log K$ of Eq. (2.78). The color code of the data denotes the equilibrium pressure, and dashed lines are the regression curves at different pressures. (b) Comparison between calculated and reference temperatures for natural chlorite samples. The error bars for T were set to an average value of $\pm 50^\circ\text{C}$. A total number of 271 natural analyses were finally used and the correlation coefficient is 0.92.

$\ln(K)$ decreases with $1/T$ as predicted by Eq. (2.78), and further illustrates that $\ln(K)$ is significantly dependant on pressure. ΔH^0 , ΔV^0 and ΔS^0 have been estimated simultaneously by minimizing the temperature difference between T_{chl} estimated with Eq. (2.77) and T_{calc} estimated using the *Chl(LWV)* model. The regression yields the pressure and temperature dependence of $\ln(K)$ as :

$$-\ln(K) = \frac{203093 + 4996.99 P}{RT} + \frac{455.782}{R} \quad (2.78)$$

This relationship is plotted into the correlation diagram of $\ln(K)$ vs $1/T$ (Fig. 2.28-a) for pressures of 1 kbar, 5 kbar, 10 kbar and 15 kbar. The temperature of chlorite can then be calculated for a know $\ln(K)$ value using the relationship :

$$T_{Chlorite}(\text{°C}) = \frac{203093 + 4996.99 P(\text{kbar})}{-R \ln(K) - 455.782} - 273.15 \quad (2.79)$$

In order to verify the semi-empirical model, the temperatures calculated with Eq. (2.79) ($T_{Chlorite}$) were plotted against the reference temperatures. The good agreement between the original temperature estimates, the T_{calc} using the *Chl(LWV)* model and the $T_{chlorite}$ using Eq. (2.79) shows that this new calibration predicts the correct temperature over the range 100-500°C and 1-20 kbar. The chlorite tempera-

ture can be estimated using either (1) the full thermodynamic approach in conjunction with the estimation of the position of the chlorite-quartz-water equilibrium curve, or (2) using the semi-empirical relationship (Eq. 2.79) for this equilibrium.

The new semi-empirical thermometer uses an ideal activity model as proposed by Walshe (1986) and Inoue et al. (2009). Thorough comparison between $T_{chlorite}$ and the original T_{ref} shows that this assumption is a reasonably valid approach for estimating the temperature of chlorite formation. This approach cannot be used in the framework of the Holland-Powell internally consistent data set, because non-ideality is required to reproduce the solvus between chlorite and sudoite.

2.3.3.6 Applications and discussion

Phase diagram calculations The new solid solution model *Chl*(LWV) is compatible with the thermodynamic database of Holland et Powell (1998) and it can be used for phase diagram calculations such as pseudosection modeling. The model is compatible with the data structure of all major petrological packages, including THERMOCALC (Powell et al. 1998, Powell 2008), PERPLE_X (Connolly 2005; 2009, Connolly et Petrini 2002) and THERIAK (de Capitani and Petrakakis 2010), and has been included into the PERPLE_X program version 6.6.6. Details concerning the PERPLE_X coding can be found in the Appendix (Part. 2.3.3.10).

As discussed above, the occurrence and composition of chlorite minerals in diverse rocks is controlled by both the bulk rock composition and the equilibrium conditions. For certain bulk rock compositions, trioctahedral chlorite and sudoite have been observed to coexist in the same mineral assemblage. Sudoite is well known in sedimentary, diagenetic and hydrothermal environments and also described in low-grade aluminous metapelites (Goffé 1982, Fransolet et Schreyer 1984, Goffé et al. 1988, Franceschelli et al. 1989, Percival et Kodama 1989, Anceau 1992, Theye et al. 1992, Vidal et al. 1992, Billault et al. 2002). In retrogressed high-pressure low-temperature metapelites, assemblages involving sudoite + chlorite + phengite + quartz are found to form after the destabilization of the carpholite + chlorite + phengite \pm chloritoid assemblage.

For example, in eastern Crete sudoite is found in the phyllite-quartzite unit, mainly composed of low-grade metasediments (Theye et al. 1992). In this unit,

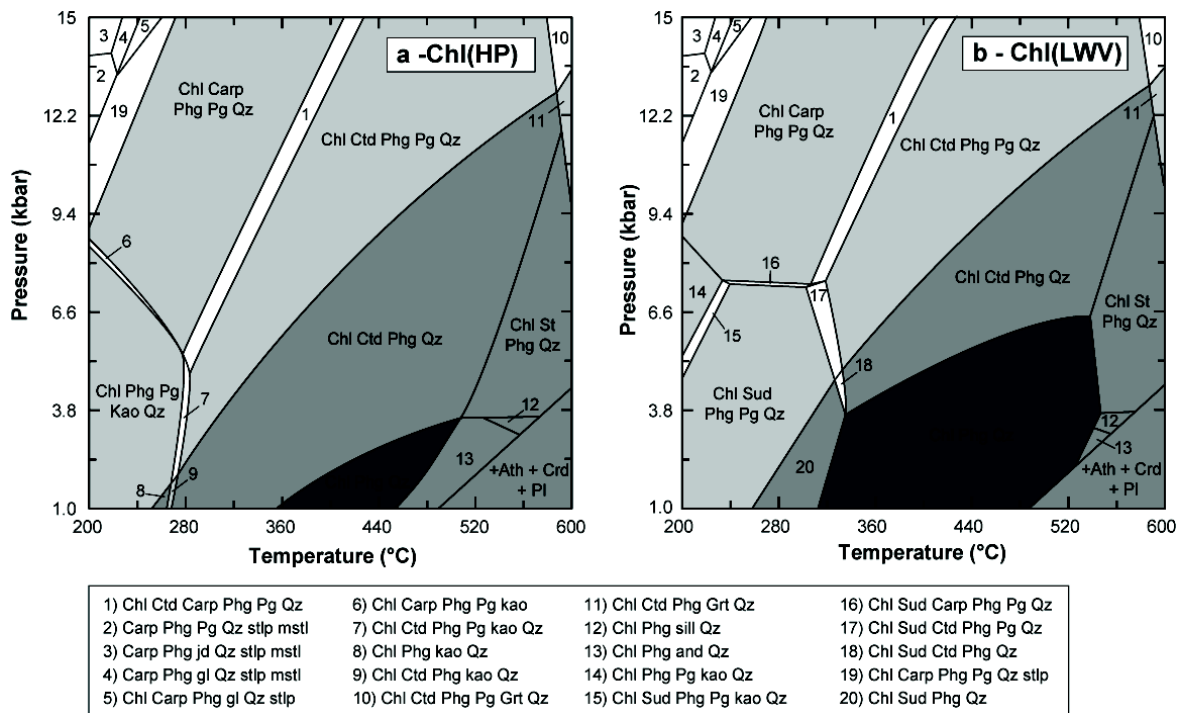


FIGURE 2.29 – Pseudosections calculated in the CaKFMASH system for the sample K84/204 of [Theye et al. \(1992\)](#). The pseudosections were calculated with PERPLE_X using chlorite solution models from (a) [Holland et Powell \(1998\)](#) and (b) this study. Mineral abbreviations : andalusite (And), carpholite (Carp), chlorite (Chl), chloritoid (Ctd), garnet (Gt), glaucophane (Gl), jadeite (Jd), kaolinite (Kao), Mg-stilpnomelane (Mstl), paragonite (Pg), phengite (Phg), quartz (Qz), sillimanite (Sill), stilpnomelane (Stlp), sudoite (Sud).

the peak metamorphic temperature-pressure conditions reached during the Alpine orogeny have been estimated at $300 \pm 50^\circ\text{C}$ and $8 \pm 3 \text{ kbar}$ ([Theye et Seidel 1992](#)). The sample K84/204 described by [Theye et al. \(1992\)](#) shows a green schist with the main mineral assemblage composed of quartz ($> 20\%$), sudoite ($< 20\%$), chlorite ($< 20\%$), phengite ($< 20\%$). Two P-T pseudosections were calculated in the CaKFMASH system using the solids solution models of [Coggon et Holland \(2002\)](#) for phengite, [Holland et Powell \(1998\)](#) for plagioclase, staurolite and garnet. Ideal mixing model was assumed for carpholite and chloritoid. The first pseudosection (Fig. 2.29-a) has been calculated using the *Chl(HP)* solid solution model ([Holland et al. 1998](#)) and the [Holland et Powell \(1998\)](#) thermodynamic standard state properties for sudoite. In this P-T pseudosection, only one chlorite that does not contain any structural vacancies is stable. A stability field with chlorite (13 wt% proportion), carpholite (4 wt%), phengite (8 wt%), paragonite (1 wt%) and quartz (74 wt%) occurs at high pressure. At lower pressure, the predicted stable assem-

blage is chlorite (15%), phengite (9%), paragonite ($< 1\%$), kaolinite (2%) and quartz (74%). When the modeling results are compared to the field data, two main problems are identified in this P-T pseudosection. First, sudoite is not predicted at low temperatures ($< 300^{\circ}\text{C}$) and low pressures ($< 7 \text{ kbar}$), which is in contrast to the observed mineral assemblage. Second, carpholite is predicted at 5.5 kbar and chloritoid at 250°C , which are unrealistically low limiting pressure and temperature conditions for these phases.

The second P-T pseudosection (Fig. 2.29-b) has been calculated using the new extended *Chl(LWV)* chlorite solid solution model and the new thermodynamic standard state properties for sudoite derived in this study. In contrast to the previous P-T pseudosection, two chlorite phases with different compositions coexist at low-pressure and low-temperature conditions. Sudoite-rich chlorite (3%) is stable along with chlorite (13%), phengite (9%), paragonite ($< 1\%$) and quartz (75%) between 200°C and 300°C and below 7.5 kbar . At higher pressures, sudoite becomes unstable and is replaced by carpholite (3%) in equilibrium with chlorite (14%), phengite (8%), paragonite (1%) and quartz (74%). This mineralogical change and the geometry of this reaction are in good agreement with experimental results (Vidal et al. 1992) and natural observations (Theye et Seidel 1992). Moreover, the chloritoid-in reaction occurs at more realistic conditions ($T > 320^{\circ}\text{C}$) than in the pseudosection calculated with the old chlorite model ($T > 260^{\circ}\text{C}$). The predicted pseudosection is in good agreement with the observations of Theye et al. (1992) in eastern Crete. The stability fields of carpholite and chloritoid are also in good agreement with field observations in western Crete and in the Peloponnese (see Theye et al. 1992, for details).

Geothermometry The new geothermometer can be used for a wide range of chlorite compositions (Fig. 2.27) in diverse geological environments such as sedimentary, hydrothermal and metamorphic systems. The semi-empirical calibration has been coded into XMapTools (Lanari et al. 2012b, <http://www.xmaptools.com>), a program for the X-ray image processing. The strategy for calculating the composition variables from a chlorite structural formula is outlined in Appendix (Part. 2.3.3.9).

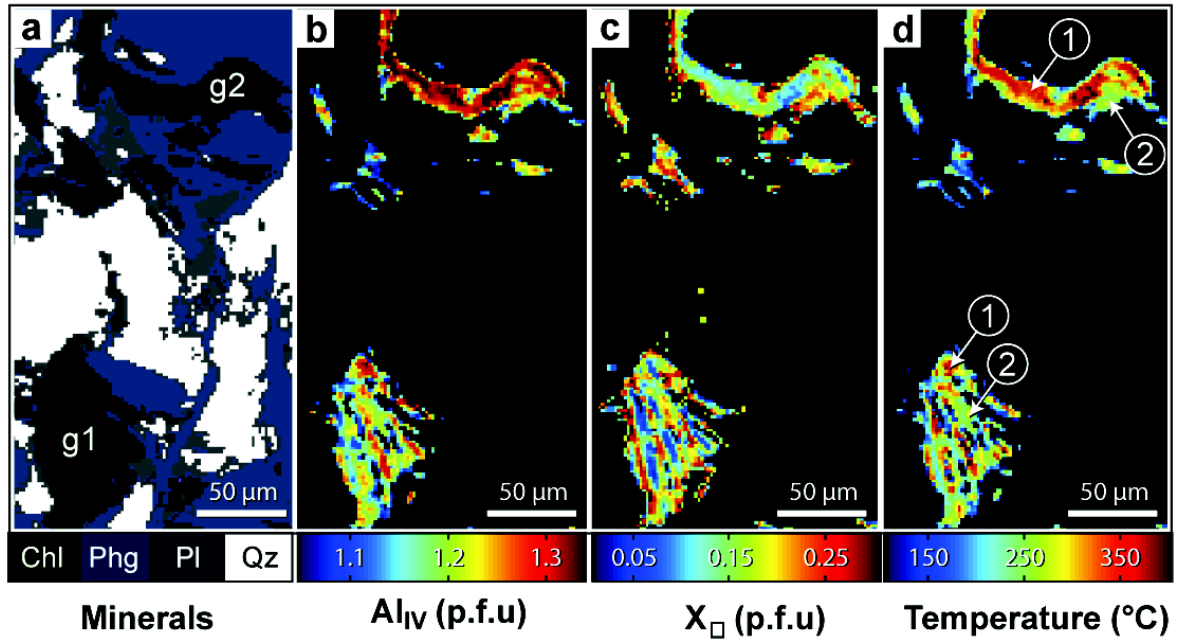


FIGURE 2.30 – Chlorite geothermometry applied to microprobe X-ray maps from [Lanari et al. \(2012a\)](#). (a) Mask-image in which each pixel is allocated to a mineral. (b) Compositional map for $X_{Al,IV}$ (per formula unit, p.f.u.) of chlorite pixels. (c) Compositional map of vacancies (V) of chlorite pixels. (d) Chlorite formation temperatures calculated from Eq. (2.78) for a pressure of 5 kbar. (1) are Hercynian detrital minerals (see details in [Lanari et al. 2012a](#)) with formation temperatures of 350-400°C, whereas (2) are chlorites recrystallized during Alpine metamorphism showing lower temperatures in the range 200-275°C.

In low-grade metamorphic terrains, one of the main challenges for deriving the P-T paths recorded by the rock is the distinction between detrital and neo-formed minerals, especially when the detrital minerals are partially recrystallized. For instance, in the western Alps the external part of the Briançonnais Zone known as the "Zone houillère" is made up of a stack of Carboniferous and Permian metasediments and volcanics. The metasediments are composed of organic-rich schist with intercalations of sandstones with a poorly defined mineralogy including detrital and neo-formed chlorite and K-white mica grains ([Gabalda et al. 2009](#), [Lanari et al. 2012a](#)). A chemical study of phyllosilicates was conducted by [Lanari et al. \(2012a\)](#) using X-ray mapping techniques [De Andrade et al. \(see 2006, for details about instrumental settings and standardization\)](#). Two distinct metamorphic events were identified, one Hercynian that is recorded in detrital minerals and a second Alpine event recorded in neo-formed minerals. Here we used a representative selection of the X-ray images from [Lanari et al. \(2012a\)](#) that were acquired on a typical thin-

section using the electron microprobe. We applied the following sequence of data processing operations (see details in [Lanari et al. submitted](#)) in XMAPTOOLS : (1) Pixels were allocated to a mineral using a statistical approach (mask-image in Fig. 2.30-a), (2) the raw X-ray maps were transformed into maps of oxide composition using selected point mode analyses as internal standards, (3) maps of oxide composition were transformed into maps of structural formulae (Fig. 2.30b, 2.30-c), and (4) crystallization temperatures of chlorite pixels (Fig. 2.30-c) were estimated using the new semi-empirical thermometer (Eq. 2.78 and Appendix (Part. 2.3.3.9)).

In the studied small-scale area, two chlorite grains are distinguished. The first grain labelled 'g1' in Fig. 2.30-a is a detrital grain with a size of 50 by 75 μm^2 and shows strong microfracturing. The second grain labelled 'g2' is a detrital grain with a size of 150 by 25 μm^2 and was kinked during the Alpine deformation event. Structural formulae maps of Al_{IV} and X_V are displayed in Figs. 2.30-b and 2.30-c, respectively. Both chlorite grains show a strong zoning their in Al_{IV} and X_V contents. These low-grade metamorphic chlorites exhibit a systematic decrease in Al_{IV} and an increase in X_V from core to rim. This negative correlation between Al_{IV} (increase with increasing T) and X_V (decrease with increasing T) contents is in good agreement with the trend in the natural data (Fig. 2.27-b, 2.27-c).

The chlorite formation temperature has been calculated for each chlorite pixel and the result is displayed in Fig. 2.30-d. Two distinct groups of chlorite temperatures were detected in this map. The first group (group 1 in Fig. 2.30-d) shows temperatures between 350 and 400°C and occur in the core of grain g2 or in bands in the g1 grains. In contrast, the rims of both grains (group 2 in Fig. 2.30-d) show systematically lower calculated formation temperatures between 200 and 275°C. The detrital part of the grains recorded crystallization temperature between 350 and 400°C and they partially recrystallized during the Alpine event at considerably lower temperature. This result is in very good agreement with the P-T paths proposed in [Lanari et al. \(2012a\)](#).

Fluid-mineral equilibria modeling The new chlorite activity-composition model has been used for modeling the composition of *NaCl*-bearing aqueous fluids in equilibrium with granitic rocks in the system Si-Al-Fe-Mg-Ca-Na-K-C-H-O-

Cl. Phase equilibria computations were performed with the high-precision GEM-SELEKTOR v.3 Gibbs free energy minimization code [Karpov et al. \(1997\)](#), [Kulik et al. \(in press\)](#), [Wagner et al. \(in press\)](#). The thermodynamic model is based on [Dolejs et Wagner \(2008\)](#), with additions for aqueous carbon species, carbonate minerals and their solid solutions. Thermodynamic data for minerals were taken from the internally consistent database of [Holland et Powell \(1998\)](#) and data for aqueous species came from the SUPCRT92 dataset and subsequent updates ([Shock et Helgeson 1988](#), [Shock et al. 1989; 1997](#), [Johnson et al. 1992](#), [Sverjensky et Helgeson 1997](#), [Tagirov et al. 1997](#), [Tagirov et Schott 2001](#)). This dataset reproduces measured mineral solubilities at elevated temperatures and pressures within their experimental uncertainty ([Holland et Powell 1998](#), [Hauzenberger et al. 2002](#), [Pak et al. 2003](#), [Wagner et al. in press](#)). Activity-composition relationships for mineral solid solutions were described by ideal, non-ideal symmetric and asymmetric models [Powell et Holland \(1993; 1999\)](#), [Holland et Powell \(1996b; 1998; 2003\)](#), [Coggon et Holland \(2002\)](#), [Dale et al. \(2005\)](#), and aqueous species activity coefficients were calculated with the extended Debye-Hueckel equation ([Helgeson et al. 1981](#)).

Fluid-mineral equilibria were calculated over the temperature range 100-600°C at 1 *kbar*, covering the late-magmatic to hydrothermal conditions of a shallow granitic intrusion. Calculations were performed for rock-buffered conditions (mass based fluid/rock ratio : 0.1) and at different salinities of 1, 2 and 5 mol/kg. The fluid/rock ratio changes slightly along the simulation path because of transfer of water between the fluid and the rock (changes in the stability of hydrous silicates), and dissolution and precipitation of minerals. The bulk rock composition was an average of the Soultz-sous-Forêts granite. Soultz-sous-Forêts is located in the Upper Rhine Graben in NE France, and hosts the European test site for geothermal energy utilization from enhanced geothermal systems. The hydrothermal alteration and fluid history of the Soultz-sous-Forêts site have been extensively studied, and indicate paleofluid circulation to at least 3-4 *km* depth penetrating into the crystalline basement ([Aquilina et al. 1997](#), [Komninou et Yardley 1997](#), [Cathelineau et Boiron 2010](#), [Fritz et al. 2010](#)).

Figure 2.31 summarizes the modeling results for the fluid salinity of 5 *mol/kg* over the temperature range 100-600°C, including total element solubilities and ma-

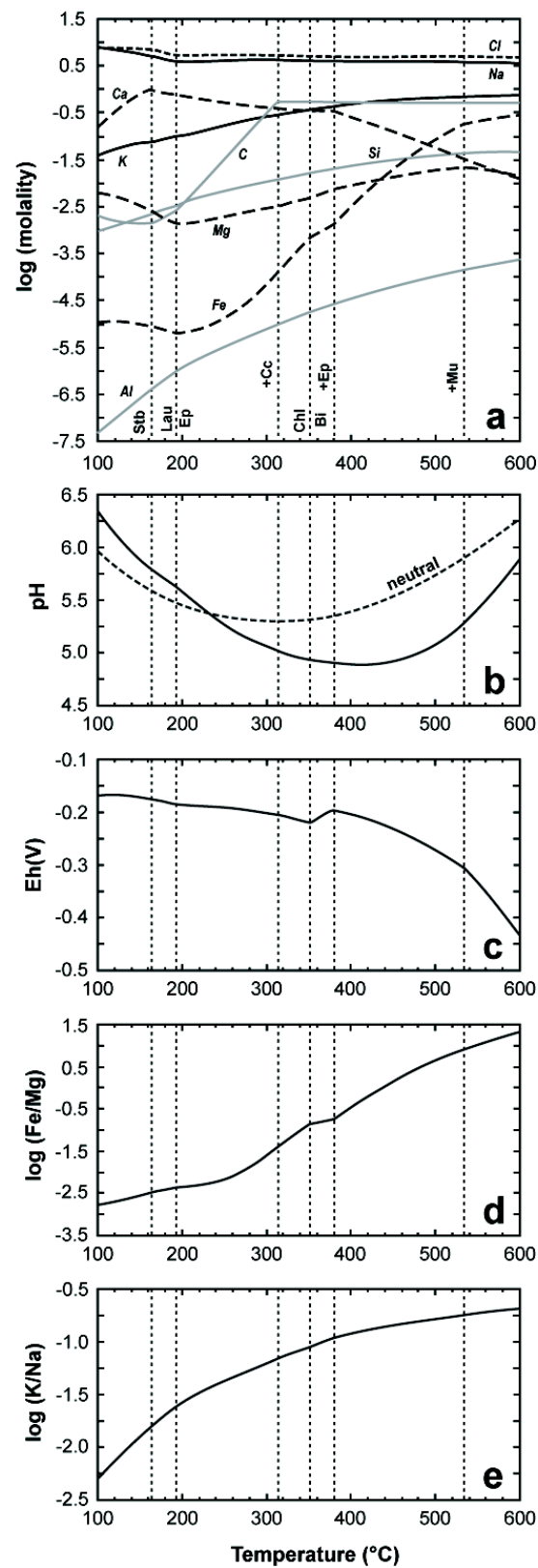


FIGURE 2.31 – Results of fluid-mineral equilibria modeling in the system Na-K-Ca-Mg-Fe-Al-Si-Cl-C-O-H, illustrating the temperature dependence of (a) total dissolved element molalities, (b) pH, (c) redox potential Eh, (d) Fe/Mg ratio and (e) K/Na ratio. Mineral abbreviations : muscovite (Mu), biotite (Bi), epidote (Ep), chlorite (Chl), calcite (Cc), laumontite (Lau), stilbite (Stb)

jor fluid parameters (pH , Eh , Fe/Mg and K/Na ratio). At high temperature, the initial mineral assemblage is K-feldspar, albite, biotite, quartz and hematite. With decreasing temperature, several mineral transformations occur that result in sharp changes in the element solubility curves (Fig. 2.31-a). Muscovite becomes stable at 530°C and epidote appears at 380°C. The biotite to chlorite transition is located at 350°C, and calcite is precipitated around 310°C. Low-temperature phase changes (below 200°C) involve the formation of zeolites (laumontite, stilbite) and the disappearance of epidote. Several first-order changes in fluid composition with decreasing temperature are observed. These include systematic decreases in silica and aluminum solubility, decrease in K concentration and K/Na ratio (Fig. 2.31-e), decrease in Fe and Mg solubility to about 200°C, decrease in the Fe/Mg ratio (Fig. 2.31-d), increase in Ca solubility to about 160°C, and increase in the redox potential Eh (Fig. 2.31-c). The pH decreases relative to neutral at high temperature, and increases below about 400°C (Fig. 2.31-b). The carbonate concentration is constant at high temperatures, but decreases substantially below about 310°C when calcite becomes stable. The solubility curves of Ca , Mg and Fe show a reversal in their trend at temperatures below 200°C, reflecting the formation of zeolite minerals. The modeling results for fluid salinities of 1 and 2 mol/kg show essentially the same sequence of mineral assemblages and solubility curves, with only minor shifts in the absolute values detectable. The predicted mineral assemblages at moderate to low temperatures are in reasonable agreement with those observed in hydrothermally altered granites at Soultz-sous-Forêts (Komninou et Yardley 1997, Fritz et al. 2010), except that our thermodynamic model does not account for clay minerals that are common low-temperature alteration phases.

2.3.3.7 Conclusions

An extended activity-composition model for di-trioctahedral in the FMASH system has been calibrated, which has been derived based on the Holland and Powell internally consistent thermodynamic dataset. The new model is formulated in terms of four linearly independent end-members, which are amesite, clinocllore, daphnite and sudoite, and accounts for Fe - Mg , Tschermaks and vacancy substitution. The ideal part of the activity of the chlorite end-members is described

with a mixing-on-site model and the nonideal part with a macroscopic symmetric formalism. The symmetric interaction parameters between sudoite and the other independent end-members have been simultaneously refined using a set of 271 published analyses of chlorite for which independent temperature estimates are available. The model was also calibrated using experimental data for the reaction $\text{carpholite} \rightleftharpoons \text{sudoite} + \text{quartz}$, which made it possible to refine standard state properties of sudoite. Update of the sudoite thermodynamic properties was required to reproduce the solvus between tri/trioctahedral chlorite and di/trioctahedral sudoite occurring in low-grade metapelites. Pressure-temperature pseudosections calculated with the new model predict mineral assemblages and modes for metapelites that are in very good agreement with natural assemblages. Based on the thermodynamic model, a new semi-empirical calibration was derived that can be used for chlorite geothermometry over the P-T range 100-500°C and 1-20 kbar. The empirical calibration has been included into the software package XMAPTOOLS that allows computing of chlorite formation temperature maps from electron-microprobe X-ray maps. The thermometer is useful for a large variety of chlorite, ranging from sedimentary to hydrothermal and metamorphic environments.

2.3.3.8 Acknowledgments

We would like to thank James Connolly (ETH Zurich), Eric Lewin, Emilie Janots and Nicolas Riel (ISTerre Grenoble) for helpful discussions. This work was financially supported by the Agence National pour la Recherche (ANR) ERD-Alps project and the Ecole doctorale Terre-Univers-Environnement travel grant.

2.3.3.9 Appendix : From structural formulae to composition variables

The calculation is based on a structural formula of chlorite (normalized on the basis of 14 oxygen atoms) where the concentrations of *Si*, *Ti*, *Al*, Fe^{2+} , Fe^{3+} , *Mg*, *Na*, *Ca*, and *K* are known in atoms per formula unit (p.f.u.). From the structural formula, the composition variables *x*, *y* and *z* (Eq. 2.48, 2.49 and 2.50, respectively) can be derived using the following approach :

$$(1) \\ XFe = \frac{Fe^{2+}}{Fe^{2+} + Mg}$$

$$x = XFe$$

(2)

$$Al_{IV} = 4 - (Si + Ti)$$

$$Al_{VI} = Al_{total} - Al_{IV}$$

$$R_1 = Na + K$$

$$V_{M1} = \frac{1}{2} (Al_{VI} - Al_{IV} + Fe^{3+} - R_1) \quad z = V_{M1}$$

(3)

$$Al_{M4} = 1 - Fe^{3+}$$

$$Al_{M23} = 2 V_{M1}$$

$$Al_{M1} = Al_{VI} - (Al_{M23} + Al_{M4})$$

$$y = Al_{M1}$$

2.3.3.10 Appendix : Coding of the the Chl(LWV) model for Perple_X

Chl(LWV)

7 | model type reciprocal, macroscopic formulation

2

3 2

fames_i fsud_i daph

ames sud_dqf clin

2 | 2 dependent endmembers

fames_i = 1 ames + 4/5 daph - 4/5 clin

fsud_i = 1 sud_dqf + 2/5 daph - 2/5 clin

o o o o o | endmember flags

| subdivision model for (ternary) site 1 (T2) :

o. 1. .1 o | range and resolution of X(Al_Si), imod = o -> cartesian subdivision

o. 1. .1 o | range and resolution of X(Al_Al), imod = o -> cartesian subdivision

| subdivision model for (ternary) site 2 (M2)

o. 1. .1 o | range and resolution of X(Fe), imod = o -> cartesian subdivision

begin_excess_function

w(clin ames) 18000. o. o.

w(clin daph) 2500. o. o.

w(clin sud_dqf) 49100. o. o.

w(daph ames) 13500. o. o.

w(daph sud_dqf) 43400. o. o.

w(ames sud_dqf) 43300. o. o.

```

end_excess_function

3 | 3 site configurational entropy model :

4 1. | 4 species on 1 M1 site
z(al,M1) = 1 ames
z(mg,M1) = 1 clin
z(fe,M1) = 1 daph

3 4. | 3 species on 4 M2+M3 sites
z(fe,m2+m3) = 1 daph
z(mg,m2+m3) = 1 clin + 1 ames + 1/2 sud_dqf

2 2. | 2 species on 2 T2 sites
z(al,T2) = 1 ames + 1/2 clin + 1/2 daph + 1/2 sud_dqf

end_of_model

```

2.3.3.11 Appendix : New sudoite thermodynamic standard state properties in 'hp02.ver'

```

sud_dqf EoS = 2 | H= -8647122.
MGO(2)AL2O3(2)SiO2(3)H2O(4)
Go = -7995205 So = 417.39 Vo = 20.3
c1 = 1104.9 c2 = .11217E-1 c3 = -6811700 c5 = -10110.5
b1 = .398E-4 b5 = -.398E-3 b6 = 870000 b7 = -130.5 b8 = 4
mo = 405000 m1 = 1.20881 m2 = -54

```

2.3.4 Logiciel 3 - MEAMP

Le logiciel MEAMP (Multi-Equilibrium And Minimization Program) a été utilisé pour ajuster le modèle Chl(LWV) présenté précédemment. Nous avons développé ce programme fonctionnant sous MATLAB© afin de pouvoir ajuster des paramètres thermodynamiques en utilisant des contraintes expérimentales ou des données naturelles. Une description de ce programme est disponible en annexe [A.2](#).

2.3.5 Discussion : formalisme de Holland et Powell, exemple des chlorites

Dans cette partie, nous allons discuter deux points particuliers du formalisme de Holland & Powell en utilisant toujours l'exemple des chlorites. Dans un premier temps, nous parlerons de l'extension du modèle Chl(LWV) aux chlorites siliceuses, avec un pôle Al-free-chlorite ([Holland et al. 1998](#)). Ce cas est particulièrement intéressant car le jeu de pôles purs proposé par ces auteurs ne va plus être constitué

uniquement de pôles purs chimiquement indépendants. Nous verrons que la solution proposée par [Holland et al. \(1998\)](#) est d'introduire un paramètre d'ordre et nous discuterons l'intérêt de ce paramètre pour les chlorites. Dans un deuxième temps, nous nous focaliserons sur les implications thermodynamiques de cette "relation interne" en étudiant la contrainte qu'elle impose aux propriétés standards de *fames*.

2.3.5.1 Extension du modèle aux chlorites siliceuses et paramètre d'ordre

Modèle simple ames + afchl + clin de Holland et al. (1998) Dans le modèle original de [Holland et al. \(1998\)](#), le champ de composition des chlorites est étendu vers le domaine des chlorites siliceuses ($Si > 3$) grâce à l'ajout d'un pôle pur de chlorite siliceuse appelée : Al-free-chlorite (*afchl*, $Si_4Mg_6O_{10}OH_8$). Dans le système magnésien *ames* + *afchl* + *clin* tel qu'il est décrit dans un premier temps par [Holland et al. \(1998\)](#), l'un des trois pôles purs est chimiquement dépendant des deux autres, car la réaction interne suivante intervient :



De plus, une composition de chlorite « ordonnée » (voir plus loin) se situe soit entre les pôles *clin* et *afchl* ($3 < Si < 4$ et donc $p_{ames} = 0$), soit entre les pôles *clin* et *ames* ($2 < Si < 3$ et donc $p_{afchl} = 0$). Cependant [Holland et al. \(1998\)](#) vont considérer ces trois pôles purs comme thermodynamiquement indépendants, en invoquant un modèle d'ordre-désordre, avec un paramètre d'ordre Q qui correspond à la proportion de *clin* ($Q = 2N = clin$ avec N la variable de composition, voir Fig. 2.32).

Contrairement au modèle Chl(LWV) où toutes les variables de compositions peuvent être calculées à partir d'une analyse de chlorite, [Holland et al. \(1998\)](#) proposent de recalculer, en utilisant une relation thermodynamique, la variable de composition N (et donc le paramètre d'ordre) : "To use this model for petrological calculations, the degree of order $Q = 2*N$ must first be determined for any composition y by solving equation (see here Eq. 2.80), and then the activities and activity coefficients can be

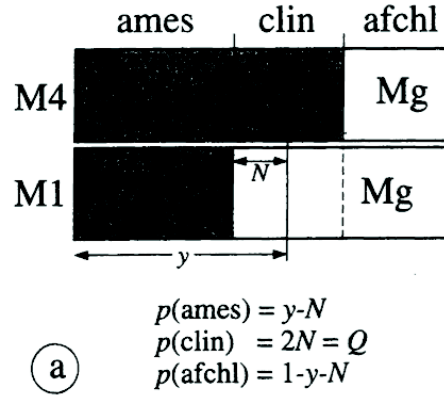


FIGURE 2.32 – Bloc diagramme des sites M1 et M4 de chlorite pour voir les relations entre les proportions de pôles purs, les variables de compositions y et N et le paramètre d'ordre Q d'après Holland et al. (1998)

calculated...".

$$0 = \Delta\mu_{\text{reaction}}^0 + A + 2NB + 2yC + RT \ln \frac{(1 - y + N)(y + N)}{(1 - y - N)(y - N)} \quad (2.81)$$

avec

$$A = 2W_{\text{afchl-clin}} - W_{\text{afchl-ames}} \quad (2.82)$$

$$B = W_{\text{afchl-ames}} - 2W_{\text{afchl-clin}} - 2W_{\text{clin-ames}} \quad (2.83)$$

$$C = W_{\text{clin-ames}} - W_{\text{afchl-clin}} \quad (2.84)$$

et

$$\Delta\mu_{\text{reaction}}^0 = 2\Delta\mu_{\text{clin}}^0 - \Delta\mu_{\text{ames}}^0 - \Delta\mu_{\text{afchl}}^0 \quad (2.85)$$

L'équation 2.81 est l'expression du potentiel chimique de la réaction interne (Eq. 2.80) égale à zéro. Cette astuce mathématique permet d'utiliser un jeu de pôles purs qui ne sont pas chimiquement indépendants en utilisant un paramètre d'ordre relié à un paramètre de composition et en résolvant la condition d'équilibre interne $\Delta\mu_{\text{reactionInterne}} = 0$ pour une température (et une pression) données.

Extension du modèle Chl(LWV) Le modèle étendu a été défini en choisissant cinq pôles purs indépendants : *ames*, *afchl*, *clin*, *daph* et *sud* et trois pôles purs dépendants : *fames*, *fafchl* et *fsud*. En suivant l'approche proposée précédemment à

partir des réactions internes, on peut dériver les expressions du potentiel chimique standard de *fames*, *fafchl* et *fsud* suivantes :

$$\begin{aligned}\mu_{fames}^0 &= \mu_{ames}^0 + \frac{4}{5} \mu_{daph}^0 - \frac{4}{5} \mu_{clin}^0 \\ &+ \frac{4}{5} W_{ames-daph} - \frac{4}{5} W_{ames-clin} - \frac{16}{25} W_{clin-daph}\end{aligned}\quad (2.86)$$

$$\begin{aligned}\mu_{fafchl}^0 &= \mu_{afchl}^0 + \frac{6}{5} \mu_{daph}^0 - \frac{6}{5} \mu_{clin}^0 \\ &- \frac{6}{5} W_{clin-afchl} - \frac{36}{25} W_{clin-daph} + \frac{6}{5} W_{daph-afchl}\end{aligned}\quad (2.87)$$

$$\begin{aligned}\mu_{fames}^0 &= \mu_{sud}^0 + \frac{2}{5} \mu_{daph}^0 - \frac{2}{5} \mu_{clin}^0 \\ &+ \frac{2}{5} W_{daph-sud} - \frac{2}{5} W_{clin-sud} - \frac{4}{25} W_{clin-daph}\end{aligned}\quad (2.88)$$

Les variables de compositions ont été définies de la manière suivante :

$$x = \frac{Fe}{Fe + Mg} = X_{Fe} \quad (2.89)$$

$$y = X_{fames} + X_{ames} + \frac{1}{2}(X_{clin} + X_{daph} + X_{fsud} + X_{sud}) = X_{Al,T2} \quad (2.90)$$

$$z = X_{fsud} + X_{sud} = X_{V,M1} \quad (2.91)$$

Pour une analyse de chlorite, les fractions de pôles purs (X_{fames} , X_{ames} , X_{clin} , X_{daph} , X_{sud} , X_{fsud} , X_{afchl} , X_{fafchl}) peuvent être transformées en un jeu de proportions de pôles purs indépendants (p_{ames} , p_{clin} , p_{daph} , p_{sud} , p_{afchl}) en utilisant les relations suivantes :

$$p_{ames} = y - N - \frac{1}{2}z \quad (2.92)$$

$$p_{afchl} = 1 - (y + N + \frac{1}{2}z) \quad (2.93)$$

$$p_{clin} = 2N - \frac{2}{5}x (3 - y - \frac{3}{2}z) \quad (2.94)$$

$$p_{daph} = \frac{2}{5}x (3 - y - \frac{3}{2}z) \quad (2.95)$$

$$p_{sud} = z \quad (2.96)$$

La fraction des éléments sur les différents sites est obtenue à partir des proportions de pôles purs indépendants :

$$X_{Fe,M23} = x (1 - \frac{1}{2}z) \quad (2.97)$$

$$X_{Mg,M23} = (1 - x) (1 - \frac{1}{2}z) \quad (2.98)$$

$$X_{Al,M23} = \frac{1}{2}z \quad (2.99)$$

$$X_{Fe,M1} = x \left(1 - y + N - \frac{1}{2}z\right) \quad (2.100)$$

$$X_{Mg,M1} = (1 - x) \left(1 - y + N - \frac{1}{2}z\right) \quad (2.101)$$

$$X_{Al,M1} = y - N - \frac{1}{2}z \quad (2.102)$$

$$X_{V,M1} = z \quad (2.103)$$

$$X_{Fe,M4} = x \left(1 - y - N - \frac{1}{2}z\right) \quad (2.104)$$

$$X_{Mg,M4} = (1 - x) \left(1 - y - N - \frac{1}{2}z\right) \quad (2.105)$$

$$X_{Al,M4} = y + N + \frac{1}{2}z \quad (2.106)$$

$$X_{Al,T2} = y \quad (2.107)$$

$$X_{Si,T2} = (1 - y) \quad (2.108)$$

Les expressions de l'activité idéale des pôles purs sont :

$$a_{ames} = (X_{Mg,M23})^4 X_{Al,M1} X_{Al,M4} (X_{Al,T2})^2 \quad (2.109)$$

$$a_{afchl} = (X_{Mg,M23})^4 X_{Mg,M1} X_{Mg,M4} (X_{Si,T2})^2 \quad (2.110)$$

$$a_{clin} = 4(X_{Mg}^{M23})^4 X_{Mg}^{M1} X_{Al,M4} X_{Al}^{T2} X_{Si}^{T2} \quad (2.111)$$

$$a_{daph} = 4(X_{Fe}^{M2M3})^4 X_{Fe}^{M1} X_{Al,M4} X_{Al}^{T2} X_{Si}^{T2} \quad (2.112)$$

$$a_{sud} = 64(X_{Al}^{M2M3})^2 (X_{Mg}^{M2M3})^2 X_V^{M1} X_{Al,M4} X_{Al}^{T2} X_{Si}^{T2} \quad (2.113)$$

La partie non idéale de l'activité est exprimée à travers des coefficients macroscopiques d'activité en utilisant un formalisme symétrique ([Holland et Powell 1996a;b](#)) :

$$\begin{aligned} RT \ln(\gamma_{ames}) = & p_{clin}(1 - p_{ames})W_{ames-clin} + p_{daph}(1 - p_{ames})W_{ames-daph} + \\ & p_{sud}(1 - p_{ames})W_{ames-sud} - p_{clin}p_{daph}W_{clin-daph} - \\ & p_{clin}p_{sud}W_{clin-sud} - p_{daph}p_{sud}W_{daph-sud} + \\ & p_{afchl}(1 - p_{ames})W_{ames-afchl} - p_{afchl}p_{clin}W_{afchl-clin} - \\ & p_{afchl}p_{daph}W_{afchl-daph} - p_{afchl}p_{sud}W_{afchl-sud} \end{aligned} \quad (2.114)$$

$$\begin{aligned}
RT\ln(\gamma_{afchl}) = & p_{ames}(1 - p_{afchl})W_{ames-afchl} + p_{clin}(1 - p_{afchl})W_{afchl-clin} + \\
& p_{daph}(1 - p_{afchl})W_{afchl-daph} + p_{sud}(1 - p_{afchl})W_{afchl-sud} - \\
& p_{ames}p_{clin}W_{ames-clin} - p_{ames}p_{daph}W_{ames-daph} - \\
& p_{ames}p_{sud}W_{ames-sud} - p_{clin}p_{daph}W_{clin-daph} - \\
& p_{clin}p_{sud}W_{clin-sud} - p_{daph}p_{sud}W_{daph-sud}
\end{aligned} \tag{2.115}$$

$$\begin{aligned}
RT\ln(\gamma_{clin}) = & p_{ames}(1 - p_{clin})W_{ames-clin} + p_{daph}(1 - p_{clin})W_{clin-daph} + \\
& p_{sud}(1 - p_{clin})W_{clin-sud} - p_{ames}p_{daph}W_{ames-daph} - \\
& p_{ames}p_{sud}W_{ames-sud} - p_{daph}p_{sud}W_{daph-sud} - \\
& p_{afchl}(1 - p_{clin})W_{afchl-clin} - p_{afchl}p_{ames}W_{ames-afchl} - \\
& p_{afchl}p_{daph}W_{afchl-daph} - p_{afchl}p_{sud}W_{afchl-sud}
\end{aligned} \tag{2.116}$$

$$\begin{aligned}
RT\ln(\gamma_{daph}) = & p_{ames}(1 - p_{daph})W_{ames-daph} + p_{clin}(1 - p_{daph})W_{clin-daph} + \\
& p_{sud}(1 - p_{daph})W_{daph-sud} - p_{ames}p_{clin}W_{ames-clin} - \\
& p_{ames}p_{sud}W_{ames-sud} - p_{clin}p_{sud}W_{clin-sud} - \\
& p_{afchl}(1 - p_{daph})W_{afchl-daph} - p_{afchl}p_{ames}W_{ames-afchl} - \\
& p_{afchl}p_{clin}W_{afchl-clin} - p_{afchl}p_{sud}W_{afchl-sud}
\end{aligned} \tag{2.117}$$

$$\begin{aligned}
RT\ln(\gamma_{sud}) = & p_{ames}(1 - p_{sud})W_{ames-sud} + p_{clin}(1 - p_{sud})W_{clin-sud} + \\
& p_{daph}(1 - p_{sud})W_{daph-sud} - p_{ames}p_{clin}W_{ames-clin} - \\
& p_{ames}p_{daph}W_{ames-daph} - p_{clin}p_{daph}W_{clin-daph} - \\
& p_{afchl}(1 - p_{sud})W_{afchl-sud} - p_{afchl}p_{ames}W_{ames-afchl} - \\
& p_{afchl}p_{clin}W_{afchl-clin} - p_{afchl}p_{daph}W_{afchl-daph}
\end{aligned} \tag{2.118}$$

avec W les paramètres d'interaction symétrique.

Calcul de N En supposant qu'une chlorite soit parfaitement ordonnée, on peut calculer une valeur de N_{theo} en utilisant les relations suivantes :

(1) Dans le cas $Si > 3$, alors $p_{afchl} > 0$ et $p_{ames} = 0$, ce qui signifie qu'en utilisant la relation : 2.102, on peut calculer N comme :

$$N_{theo} = y - \frac{1}{2}z \tag{2.119}$$

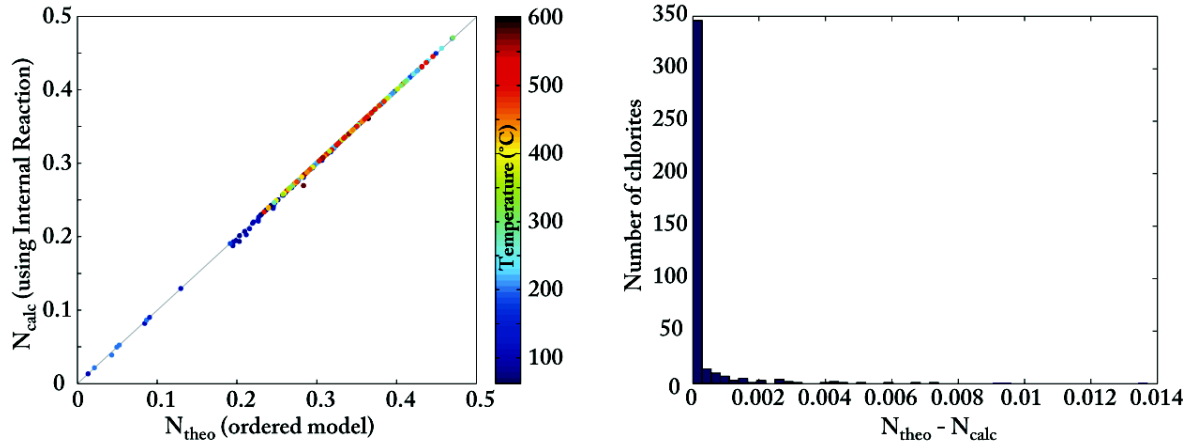


FIGURE 2.33 – Comparaison du N_{calc} ajusté pour que le potentiel chimique de la réaction interne soit nul et N_{theo} estimé en utilisant l'équation 2.119 ($Si > 3$) ou l'équation 2.120 ($Si < 3$).

(2) Dans le cas $Si < 3$, alors $p_{afchl} = 0$ et $p_{ames} > 0$, ce qui signifie qu'en utilisant la relation : 2.93, on peut calculer N de la manière suivante :

$$N_{theo} = 1 - y - \frac{1}{2}z \quad (2.120)$$

En suivant la même démarche que celle présentée dans Holland et al. (1998) et en utilisant les chlorites de la base de données présentée précédemment (Part. 2.3.3) auxquelles ont été ajoutées des données de BT ($Si > 3$) nous avons calculé pour chaque analyse les trois variables de compositions x (Eq. 2.89), y (Eq. 2.90) et z (Eq. 2.91). Dans un premier temps, le N_{calc} a été ajusté de manière à ce que le potentiel chimique de la réaction interne soit nul à la température de référence (T_{ref}) disponible pour chaque analyse. Puis dans un second temps, le N_{theo} a été estimé en supposant un modèle ordonné puis en utilisant soit l'équation 2.119 pour les chlorites avec un $Si > 3$, soit l'équation 2.120 pour les chlorites avec un $Si < 3$.

Les deux valeurs de N sont comparées sur la figure 2.33. Ce résultat montre que la valeur de N_{theo} est très proche de celle de N_{calc} avec 95% des différences inférieures à 0.001, ce qui signifie que quelque soit la température, les chlorites naturelles considérées dans notre base sont toujours ordonnées.

L'évolution de N avec la variable de composition Y et la température est présentée Fig. 2.34. Toutes les compositions des chlorites de la base de données sont

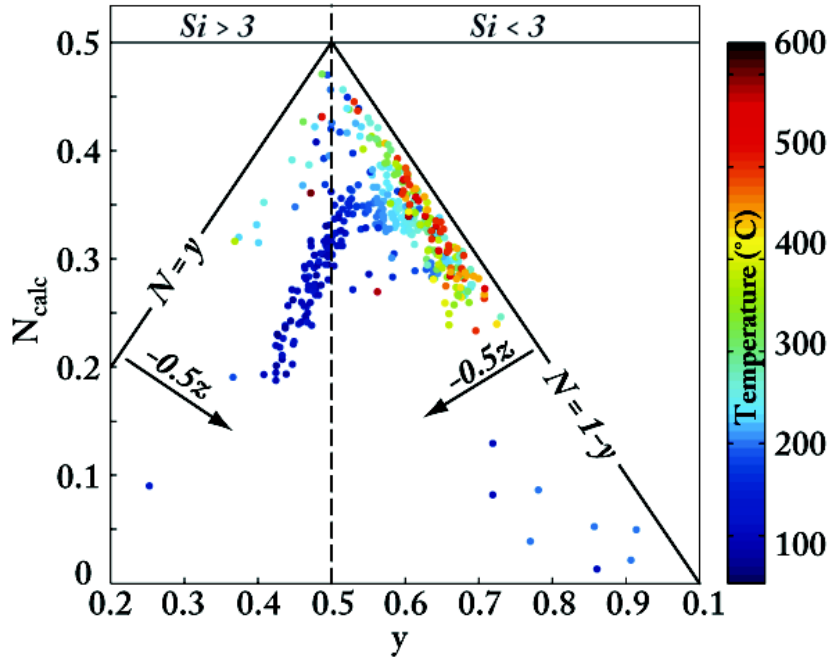


FIGURE 2.34 – Évolution de la variable de composition y en fonction de N_{calc} et de la température T_{ref} . La ligne pointillé sépare le domaine des chlorites siliceuses ($Si > 3$ et $y < 0.5$) des chlorites pauvres en silice ($Si < 3$ et $y > 0.5$).

tracées dans un triangle centré sur la valeur $y = 0.5$. Pour les chlorites avec $Si < 3$, la limite de composition est marquée par la relation $N = 1 - y$ qui provient de la relation d'ordre (Eq. 2.120). L'écart des compositions à cette relation identifiée notamment par Holland et al. (1998) à haute température est due à la présence du terme en $-\frac{1}{2}z$ (flèches sur la Fig. 2.34). Pour les chlorites avec $Si > 3$, la limite de composition est marquée par la relation $N = y$ qui provient de la relation d'ordre (Eq. 2.120). On remarque que cette fois l'écart en $-\frac{1}{2}z$ est plus important, indiquant que les chlorites riches en Si ont une teneur en sud plus importante, correspondant à des températures plus faibles (Fig. 2.34).

Conséquences sur l'équilibre chl + qtz + H_2O Si l'on considère uniquement les pôles purs magnésiens de chlorite, à l'équilibre avec le quartz et l'eau, on peut écrire les quatre réactions suivantes :





La réaction 2.121 est l'équilibre interne, la réaction 2.122 l'équilibre chl + qtz + H₂O utilisé précédemment dans le modèle Chl(LWV), et les réaction 2.123 et 2.124 les deux réactions chlorite + quartz impliquant le pôle pur *afchl*. Ces quatre équilibres ont été tracés pour une composition de chlorite donnée dans un diagramme pression température (Fig. 2.35). Pour trois variables de composition *x*, *y* et *z* données, la valeur de *N* avec 8 chiffres significatifs a été estimée en utilisant la procédure de Holland et al. (1998), c'est-à-dire en résolvant l'équilibre interne pour la température donnée. Lorsque l'on trace les quatre réactions dans un diagramme P-T en utilisant cette valeur de *N_{calc}*, elles se croisent en un point à la température *T_{ref}* (Fig. 2.35-a). Si maintenant l'on diminue le nombre de chiffres significatifs à 5, on remarque que cette très petite variation a un effet très important sur la position des réactions impliquant la *afchl* (Fig. 2.35-b). Par contre, la position de la courbe chlorite + quartz sans *afchl* (noté 2 sur la Fig. 2.35), ne change pas. Si l'on diminue encore le nombre de chiffres significatifs à 4, nombre utilisé par défaut par le programme MEAMP, les deux courbes chl + qtz + H₂O impliquant la *afchl* sont sorties de la fenêtre P-T et la réaction interne est à 760°C (Fig. 2.35-c).

Cette étude de sensibilité montre que pour étendre le modèle Chl(LWV) aux chlorites siliceuses, il faut re-calculer avec une grande précision la valeur de *N* en utilisant la position de la réaction interne. De plus, cette approche n'est pas totalement en phase avec la philosophie utilisée par Holland et Powell, qui consiste à prendre uniquement un jeu de pôles purs chimiquement indépendants. Enfin, cette technique pour estimer le paramètre d'ordre n'a, *a priori*, pas lieu d'être puisque notre calcul pour l'ensemble de la base de données montre que les chlorites naturelles sont très proches d'un modèle ordonné, quelque soit la température considérée. On notera que dans le cas où les chlorites sont parfaitement ordonnées (en respectant les relations 2.119 pour les chlorites avec un *Si* > 3 et 2.120 pour les chlorites avec un *Si* < 3), il est impossible de tracer la relation interne, le terme RTln(K) de la réaction interne serait infini.

Cette situation est provoquée par la présence dans le jeu de pôles purs du *clin*. En effet, l'absence de *clin* permettrait de définir directement une chlorite comme

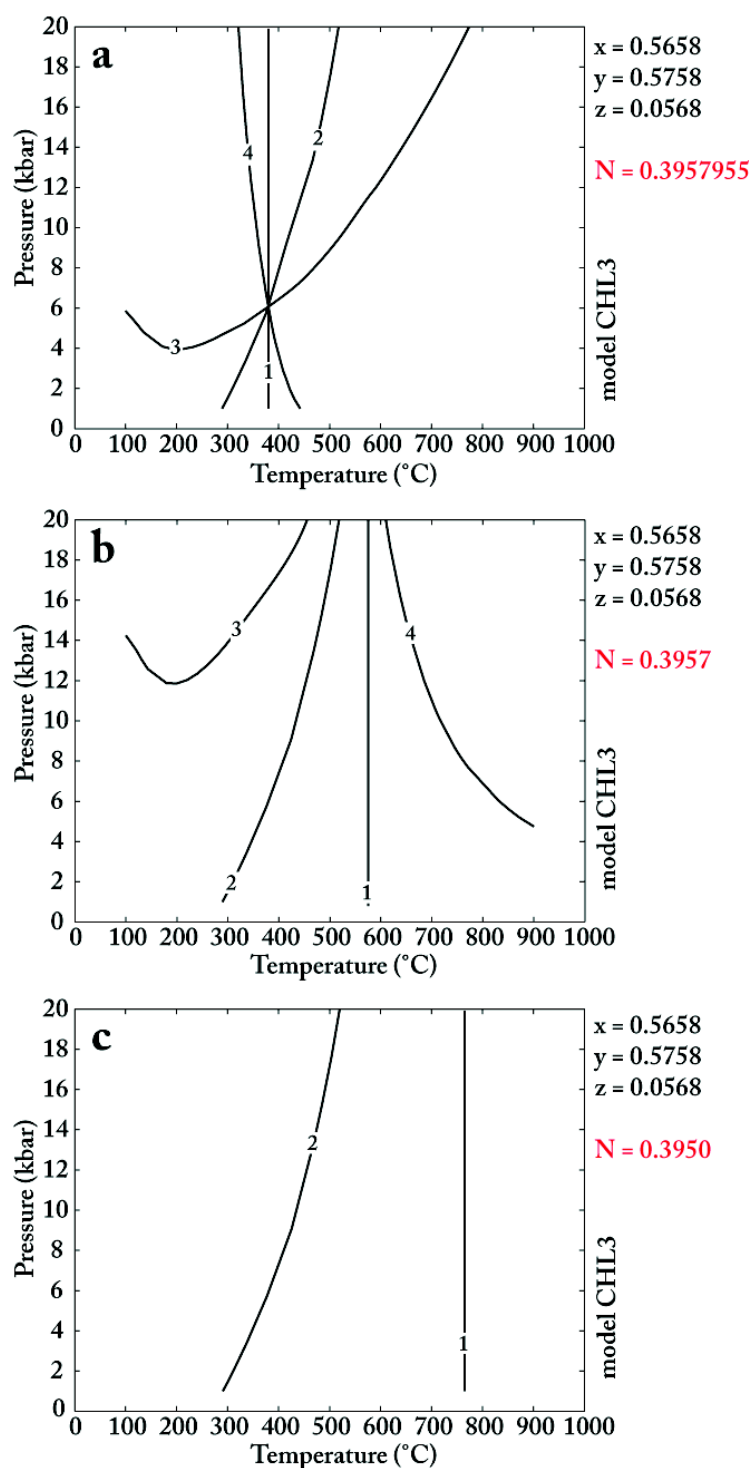


FIGURE 2.35 – Courbes $\text{Chl} + \text{Qtz} + \text{H}_2\text{O}$ et la réaction interne tracées pour une composition donnée de chlorite $x = 0.5658$, $y = 0.5758$ et $z = 0.0568$ et pour différents arrondis de la valeur de N . La valeur originale (en a) est la valeur calculée en utilisant la méthode décrite précédemment (voir texte). Les réactions notées (1), (2), (3) et (4) sur la figure correspondent respectivement aux réactions 2.121, 2.122, 2.123, 2.124 dans le texte. Nb : l'arrondi a été effectué en diminuant la valeur de N au fur et à mesure de la réduction du nombre de chiffres significatifs, car ce dernier ne peut pas être égal ou supérieur à la valeur limite de $1 - y - \frac{1}{2}z$, soit ici 0.3958. Si $N = 1 - y - \frac{1}{2}z$, alors le terme d'activité $\text{RTln}(a_{\text{fchl}})$ est infini et on ne peut pas tracer les réactions (1), (3) et (4).

une combinaison de *alfch*, *ames*, *sud* (et *daph* dans le système ferreux) donc sans aucune hypothèse sur le niveau d'ordre, et sans problème du calcul du p_{clin} .

2.3.5.2 Relations internes et propriétés standards

On a montré dans la description du formalisme (Part. 2.3.2.4) que pour simplifier les calculs thermodynamiques, en utilisant le formalisme de Holland et Powell, on peut calculer le μ_{fames}^0 du pôle pur chimiquement dépendant *fames* à partir des μ^0 des pôles purs indépendants (*ames*, *clin*, *daph*) en utilisant la condition d'équilibre :

$$\begin{aligned}\Delta\mu_{reaction} &= RT \ln \left[\frac{(X_{Fe,M1})^4 (X_{Mg,M2M3})^4}{(X_{Fe,M2M3})^4 (X_{Mg,M1})^4} \right] \\ &\quad + 4 \mu_{clin}^0 + 5 \mu_{fames}^0 - 4 \mu_{daph}^0 - 5 \mu_{ames}^0 \\ &\quad + 4 X_{Al,M1} (W_{Al-Fe} - W_{Al-Mg}) \\ &= 0\end{aligned}\tag{2.125}$$

ce qui revient à écrire, en faisant une hypothèse d'équipartition Fe du Mg sur les sites *M1* et *M2M3*, la relation interne suivante :

$$\begin{aligned}\mu_{fames}^0 &= \mu_{ames}^0 + \frac{4}{5} \mu_{daph}^0 - \frac{4}{5} \mu_{clin}^0 \\ &\quad + \frac{4}{5} W_{ames-daph} - \frac{4}{5} W_{ames-clin} - \frac{16}{25} W_{clin-daph}\end{aligned}\tag{2.126}$$

Dans cette relation, le terme d'interaction symétrique Δ_W ($\Delta_W = \frac{4}{5} W_{ames-daph} - \frac{4}{5} W_{ames-clin} - \frac{16}{25} W_{clin-daph}$) provient du formalisme macroscopique utilisé pour décrire l'activité non-idéale d'un pôle pur dépendant ou indépendant en fonction des proportions des pôles purs indépendants (c.f. annexe A.1.3).

La relation 2.125 indique que la relation interne est vérifiée quelque soit la composition de chlorite (à l'inverse de l'approche de Vidal et al. (2005), c.f. Part. 2.3.2.4). Elle impose donc des contraintes sur les propriétés standards du pôle pur dépendant *fames*. On peut donc utiliser cette relation interne (Eq. 2.126) pour recalculer les propriétés standards de *fames* (H^0f , S^0 , V^0 et coefficients C_p : a , b , c , d) à condition de connaître comment varie Δ_W avec la pression et la température. Pour le modèle *Chl(LWV)* présenté précédemment, les valeurs de W sont des constantes, car elles ne varient pas avec la pression et la température ($W_{ames-clin} = 18000$ J,

$W_{ames-daph} = 13000 \text{ J}$, $W_{clin-daph} = 2500 \text{ J}$). Il faut noter que dans cette hypothèse de l'indépendance des W à P et T :

$$S_{fames}^0 = S_{ames}^0 + \frac{4}{5} S_{daph}^0 - \frac{4}{5} S_{clin}^0 \quad (2.127)$$

$$V_{fames}^0 = V_{ames}^0 + \frac{4}{5} V_{daph}^0 - \frac{4}{5} V_{clin}^0 \quad (2.128)$$

$$Cp_{fames} = Cp_{ames} + \frac{4}{5} Cp_{daph} - \frac{4}{5} Cp_{clin} \quad (2.129)$$

et en ajoutant le terme en W à l'enthalpie :

$$\begin{aligned} H^0 f_{fames} &= H^0 f_{ames} + \frac{4}{5} H^0 f_{daph} - \frac{4}{5} H^0 f_{clin} \\ &= H^0 f_{ames} + \frac{4}{5} H^0 f_{daph} - \frac{4}{5} H^0 f_{clin} + \Delta_W \end{aligned} \quad (2.130)$$

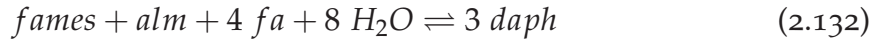
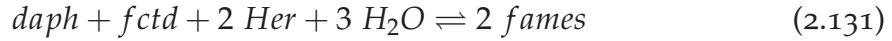
Ces relations sont intuitivement raisonnables et en accord avec les algorithmes de sommation d'oxydes utilisés pour prédire les entropies standards de phases non mesurées ou pour lesquelles il n'existe pas de contraintes expérimentales (e.g. [Holland 1989](#)). Il est intéressant de constater que cette approche donne généralement de bons résultats pour l'entropie et les Cp ([Berman et Brown 1985](#)) et des résultats moins bons pour l'enthalpie ([Chermak et Rimstidt 1989](#)). Cette dernière observation est également en accord avec la relation [A.29](#) qui indique que l'estimation de $H^0 f$ par sommation d'oxydes ne peut être précise qu'à la valeur de Δ_W . Il est donc nécessaire de connaître les valeurs des paramètres d'interaction pour estimer une $H^0 f$ par sommation d'oxydes. Les conclusions laissent entrevoir des pistes de recherche intéressantes comme par exemple l'estimation des W pour améliorer l'ajustement des $H^0 f$ par sommation d'oxydes.

Des propriétés standards de f_{ames} ont été calculées en utilisant les relations [2.127](#), [2.128](#), [2.129](#), [2.130](#), les propriétés thermodynamiques de la base de données [Holland et Powell \(1998\)](#), les mises à jours (c.f. Tab. [2.10](#)) et les valeurs de W du modèle Chl(LWV). Les propriétés standards de la f_{ames} dérivées pour cette étude sont différentes de 100 kJ pour $H^0 f$ et de 3 J.K^{-1} pour S^0 des propriétés standards estimées par [Vidal et al. \(2005; 2006\)](#). Il faut noter cependant que contrairement aux propriétés standards de f_{ames} de [Vidal et al. \(2005; 2006\)](#), nous n'avons ici pas utilisé de résultats expérimentaux obtenus dans le système FMASH. Or, de telles contraintes ont été obtenues par [Parra et al. \(2005\)](#).

	ref	H^0f (kJ)	S^0 (JK ⁻¹)	V^0 (kJKbar ⁻¹)	a (kJK ⁻¹)	$b(10^5)$ (kJK ⁻²)	c (kJK)	d (kJK ^{-1/2})
Amesite-Fe	this study	-7617.633	517.47	20.72	1.2417	1.08707	-4042.2	-11.41074
Amesite-Fe	VI	-7607.46	514.8	20.9				
Amesite-Mg	HP	-9034.44	410.0	20.52				
Amesite-Mg	VI	-9035.90	403.2	20.52				
Clinochlore	HP	-8912.41	430.5	21.09				
Clinochlore	VI	-8909.59	435.1	21.15				
Daphnite	HP	-7134.85	565.0	21.34				
Daphnite	VI	-7120.84	559.4	21.60				

TABLE 2.10 – Propriétés standards du pôle *fames* calculées à partir de la relation interne 2.126 (this study) et propriétés standards des pôles purs de chlorite *ames*, *clin* et *daph* d'après : HP : [Holland et Powell \(1998\)](#) + mises à jour ([Coggon et Holland 2002](#)) ; VI : [Vidal et al. \(2006\)](#).

Afin de tester les propriétés standards de *fames* que nous avons estimées avec la relation interne, nous avons considéré un modèle de solution solide pour les chlorites dans le système ferreux avec les pôles purs *fames* et *daph*. Puis nous avons tracé dans un champ P-T pour différentes valeurs de $Si_{chlorite}$ (pour un $W_{fames-daph}$ de 13500 J comme le $W_{ames-daph}$) les deux réactions suivantes encadrées par [Parra et al. \(2005\)](#) :



Les résultats sont reportés Fig. 2.36. Malheureusement, en utilisant les propriétés standards de *fames* calculées précédemment, ces réactions ne sont pas en accord avec les données expérimentales. Nous avons essayé d'ajuster les valeurs de $W_{fames-daph}$, mais pour la meilleure valeur trouvée ($W_{fames-daph} = 31kJ$), la position des deux réactions n'est toujours pas en accord avec [Parra et al. \(2005\)](#).

Ce résultat indique que les propriétés de *fames* calculées en respectant la condition d'équilibre interne et en utilisant les propriétés thermodynamiques standards de [Holland et Powell \(1998\)](#) ne sont pas adaptées et doivent donc être ajustées. Le formalisme de la relation interne imposant que ces propriétés standards dépendent de celles de *clin*, *daph* et *ames*, un nouvel ajustement du modèle dans son ensemble est donc nécessaire. Le changement de propriétés standards dans la base de données de [Holland et Powell \(1998\)](#) ne doit pas casser la cohérence interne de la base. Il est donc obligatoire d'ajuster l'ensemble des données thermodynamiques stan-

dards de tous les pôles purs ensembles, ce qui n'est possible que par les auteurs de la base de données qui disposent de la base de contraintes expérimentales.

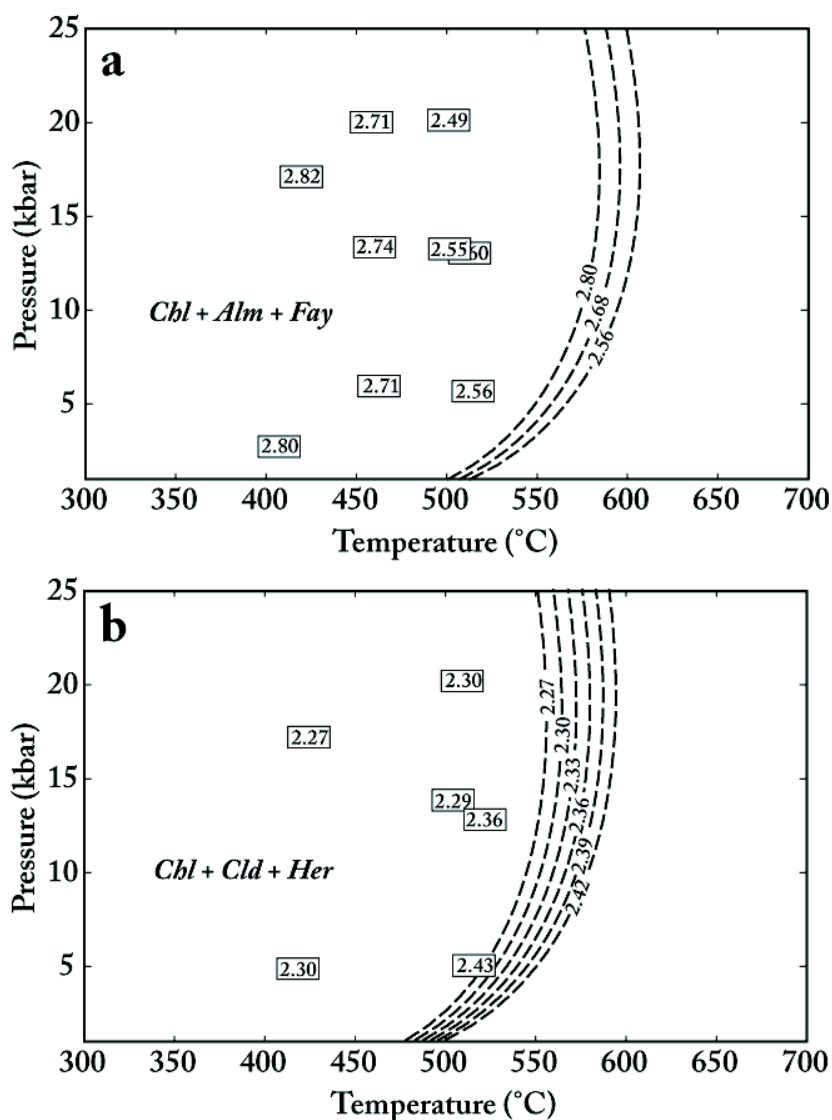


FIGURE 2.36 – Réactions (a) pour la réaction chlorite + almandin + fayalite (2.132) et (b) pour la réaction chlorite + chloritoïde + hercynite (2.131) tracées pour différentes teneurs de Si de chlorite. Les boîtes et les nombres sont les conditions expérimentales et les teneurs en Si des chlorites qui montrent l'écart le plus important avec la valeur de départ (d'après Parra et al. 2005).

2.4 CONCLUSIONS ET PERSPECTIVES

Nous avons vu dans ce chapitre que le développement de modèles de solutions solides pour les phyllosilicates compatibles avec la base de données de [Berman \(1988\)](#) et la technique des multi-équilibres fait des métapélites de bons candidats pour l'estimation des conditions P-T. Un exemple d'application a été proposé pour estimer les conditions P-T à partir d'assemblages chl + phg + qtz + H_2O dans des zones de failles. Nous avons présenté deux logiciels PTLINES et MULTIPLOT qui permettent de faire des calculs des multi-équilibres pour des compositions minérales données d'une paragenèse supposée à l'équilibre. Ces deux logiciels permettent d'appliquer "facilement" ces techniques à un nombre important de compositions et d'équilibres chimiques.

Dans un second temps, nous avons proposé un nouveau modèle de solution solide pour les chlorites compatible avec la base de données et le formalisme de [Holland et Powell \(1998\)](#). Ce modèle a été testé pour calculer des pseudosections ou pour modéliser des interactions fluide-roche. Enfin, un thermomètre empirique a également été proposé à des fins thermobarométriques en utilisant un modèle de solution solide idéal.

Nous avons, dans ce chapitre, identifié certains points qui peuvent constituer des pistes de recherches intéressantes :

(1) La calibration de [Vidal et al. \(2006\)](#) pour les chlorites pose des problèmes pour les chlorites de HT ($> 350-400^{\circ}C$) et il est nécessaire de calibrer un nouveau modèle en ajoutant une contrainte supplémentaire comme par exemple un pôle pur de ferri-sudoite.

(2) Le modèle Chl(LWV) a été contraint en utilisant les propriétés thermodynamiques standards de la base de données de [Holland et Powell \(1998\)](#) qui ne permettent pas de reproduire les résultats expérimentaux de [Parra et al. \(2005\)](#). Il est donc nécessaire de raffiner les propriétés standards des pôles purs de chlorite dans la base de données en particulier pour la daphnite. Les pôles magnésiens sont en effet contraints avec les contraintes expérimentales de [Baker et Holland \(1996\)](#). L'une

des question clef est de savoir s'il est possible d'utiliser des propriétés standards de *ames*, *clin* et *daph* et de recalculer des propriétés standards de *fames* afin d'être en accord à la fois avec les résultats expérimentaux de [Parra et al. \(2005\)](#) et de [Baker et Holland \(1996\)](#).

(3) Ce modèle pour les chlorites permet d'étendre l'application des pseudosections au domaine des basses températures. Il est maintenant nécessaire de calibrer un modèle commun pour les argiles et les micas, compatible avec la base de données de [Holland et Powell \(1998\)](#). Ce modèle a été dérivé, et est disponible en annexe de ce travail (Annexe [A.3](#)). Il est maintenant nécessaire de contraindre les différentes propriétés thermodynamiques standards et de solution solide en utilisant la base de données naturelles de [Dubacq et al. \(2010\)](#).

CARTOGRAPHIE CHIMIQUE

3

SOMMAIRE

3.1	IMAGERIE CHIMIQUE À L'ÉCHELLE DE LA LAME MINCE	119
3.2	ARTICLE 3 : XMAPTOOLS A MATLAB©-BASED GRAPHIC USER INTERFACE FOR MICROPROBE X-RAY IMAGES PROCESSING (SUBMITTED TO COMPUTERS AND GEOSCIENCES)	135
3.3	ARTICLE 4 : REE AND Hf DISTRIBUTION AMONG MINERAL PHASES IN THE CV-CK CLAN : A WAY TO EXPLAIN ϵ Hf HETEROGENEITIES IN CHUR (SUBMITTED TO GEOCHIMICA AND COSMOCHIMICA ACTA)	158
3.4	CONCLUSIONS ET PERSPECTIVES	194

Ce chapitre introduit la méthode d'imagerie chimique WDS à la microsonde et propose un logiciel pour traiter les données : XMAPTOOLS.

THIS chapter documents the chemical mapping techniques using a microprobe. The second part describes XMAPTOOLS, a software for the X-ray images processing.

3.1 IMAGERIE CHIMIQUE À L'ÉCHELLE DE LA LAME MINCE

★ *L'imagerie chimique quantitative permet d'identifier les variations de compositions (concentrations d'éléments) sur une petite surface d'un échantillon. Dans le cadre des roches métamorphiques, la transformation de ces images chimiques en micro-cartographies P-T permet de visualiser les variations spatiales, au moins en deux dimensions, de ces conditions d'équilibre et donc de les relier aux marqueurs structuraux, comme les marqueurs de la déformation. Pour atteindre cet objectif, il est nécessaire d'obtenir dans un premier temps des cartes de concentrations pour un jeu d'éléments chimiques.*

★ *Les travaux de De Andrade (2006) et De Andrade et al. (2006) ont permis de définir des conditions analytiques optimales pour faire de la cartographie quantitative à la microsonde en utilisant les spectromètres WDS, et de proposer une méthode de standardisation pour obtenir des cartes de concentrations élémentaires.*

★ *Dans cette partie introductive, nous allons proposer une description des méthodes classiquement utilisées pour l'imagerie chimique des roches en utilisant une microsonde électronique. Après avoir présenté les avantages de la cartographie WDS (en utilisant les spectromètres WDS, voir plus loin), nous présenterons le protocole d'acquisition recommandé à travers plusieurs exemples naturels des Alpes occidentales et des Alpes centrales.*

3.1.1 Microsonde électronique

Depuis son invention par le physicien français Raimond Castaing ([Castaing 1951](#)), la microsonde électronique (EPMA en Anglais pour : Electron Probe Micro-analyser.), également appelée "microsonde de Castaing", est couramment utilisée par les pétrographes pour estimer les compositions des phases minérales (e.g. [Potts et al. 2002](#)). Cette technique (schéma Fig. [3.1](#)) consiste à bombarder avec un faisceau focalisé d'électrons un échantillon de roche préalablement poli et métallisé, et d'analyser le spectre de rayons X qui est ré-émis par l'échantillon. Ce spectre est constitué de pics, ou raies, caractéristiques des différents éléments chimiques présents dans la partie analysée de l'échantillon. Deux types d'analyses peuvent être effectuées sur une microsonde électronique en utilisant soit le spectromètre EDS (Energy Dispersive Spectroscopy), soit les spectromètres WDS (Wavelength Dispersive Spectroscopy).

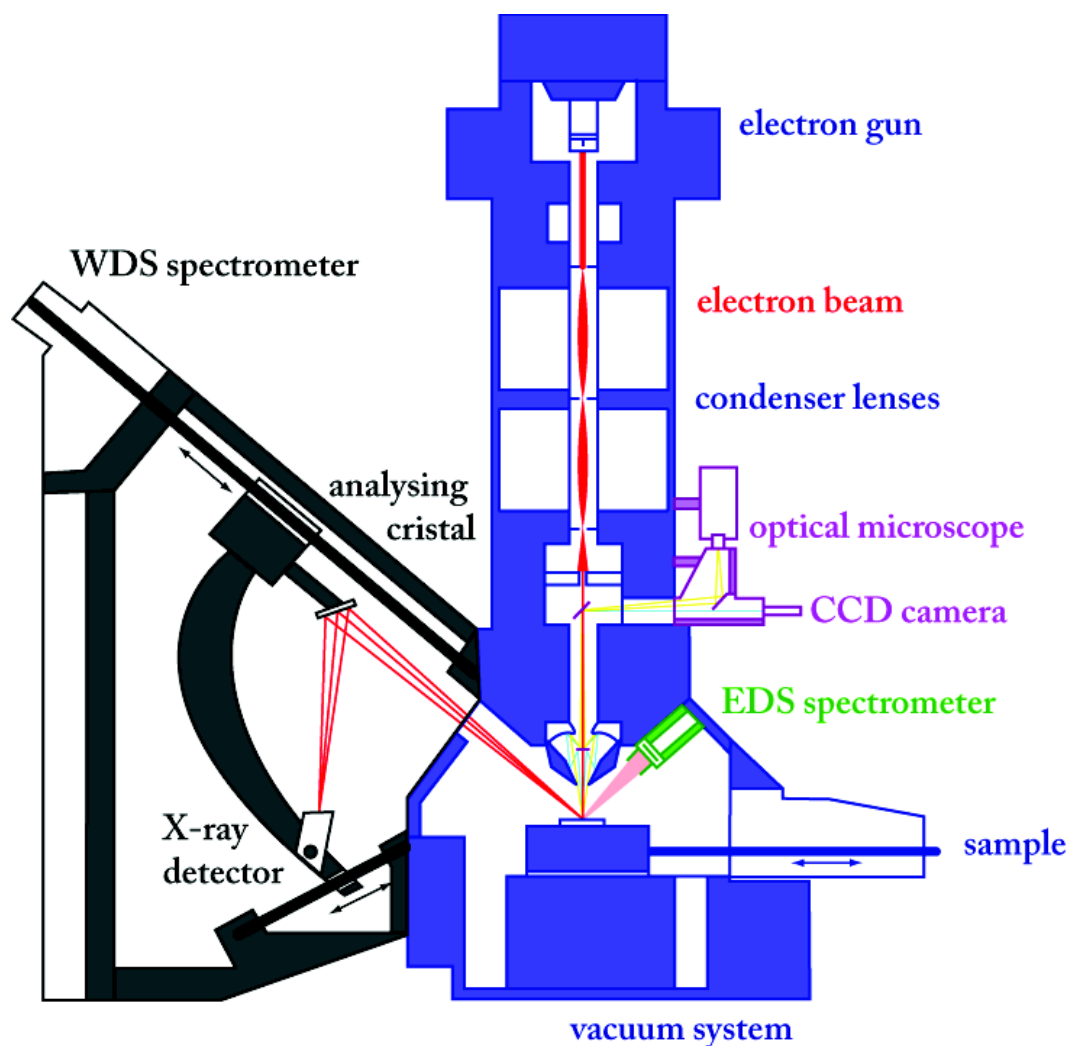


FIGURE 3.1 – Schéma explicatif du fonctionnement d'une microsonde électronique récente de type Cameca SX 100 ou JEOL 8200. La colonne est dessinée en bleu, le spectromètre WDS en noir, le spectromètre EDS en vert et le système microscope et caméra en mauve. Sur ce schéma, nous avons représenté qu'un seul spectromètre WDS.

Le spectromètre par dispersion d'énergie EDS possède un détecteur composé d'un semi-conducteur qui va produire des pics de tensions proportionnels à l'énergie du rayon X qui l'atteint. Une fois triés par intensité énergétique, ces pics de tensions vont permettre de produire un spectre qui est couramment utilisé pour détecter rapidement la présence ou non d'éléments dans la zone analysée. Les spectromètres par dispersion de longueur d'onde WDS quant à eux utilisent un cristal et les lois de diffraction pour séparer les rayons X en fonction de leur longueur d'onde. En plaçant le détecteur et le cristal à un certain angle par rapport à l'échantillon, on peut alors compter le nombre de rayons X, ou photons, émis par

l'échantillon pour une longueur d'onde particulière. Ce "nombre de coups" enregistré indique la présence d'un élément chimique et il est proportionnel, comme nous le verrons plus tard, à la concentration de cet élément. Dans la mesure où le spectromètre WDS est calé sur une longueur d'onde particulière, il n'est pas possible d'acquérir un spectre continu sans déplacer les miroirs. De ce fait, plusieurs spectromètres sont installés sur les microsondes afin d'optimiser le temps de mesure. Les microsondes électroniques récentes possèdent entre quatre et cinq spectromètres permettant de détecter huit à dix éléments en deux passages, c'est-à-dire avec un seul mouvement ou changement des miroirs. La comparaison entre les deux types de spectromètres montre que le capteur WDS a un meilleur rendement en conditions de cartographie, avec notamment une meilleure résolution spectrale, une meilleure limite de détection ainsi qu'un meilleur rapport signal sur bruit (De Andrade 2006, Holton 2012).

L'analyse quantitative de la concentration d'un élément requiert une calibration des spectromètres WDS. Pour ce faire, on utilise un standard dont la concentration $C_{std}^{élément}$ de l'élément est connue et dont on a mesuré l'intensité $I_{std}^{élément}$. On peut alors calculer la concentration $C_{ech}^{élément}$ de cet élément pour un échantillon à partir de la mesure de son intensité $I_{ech}^{élément}$, en utilisant la relation de Castaing (Castaing 1951) :

$$\frac{C_{ech}^{élément}}{C_{std}^{élément}} = k^{élément} \frac{I_{ech}^{élément}}{I_{std}^{élément}} \quad (3.1)$$

avec k un coefficient de correction qui corrige des effets de matrice engendrés par des phénomènes physiques, comme l'absorption et la fluorescence (par exemple la correction ZAF, voir Philibert et Tixier 1975, Heinrich 1966; 1987, Heinrich et Newbury 1991, Potts et al. 2002). k dépend notamment de l'élément, de la composition du standard et de sa densité.

Cette technique de standardisation est couramment utilisée pour les analyses ponctuelles "classiques". La microsonde est calibrée avant chaque séance pour tous les éléments mesurés afin de (1) paramétrer la position du miroir du spectromètre WDS sur le pic d'intensité et (2) de mesurer $I_{std}^{élément}$ et de définir $k^{élément}$. Les conditions analytiques "standards" le plus souvent utilisées sont les suivantes (Tab. 3.1). La tension du faisceau est généralement fixée à 15 KeV, valeur qui va contrôler la

	Tension	Intensité du faisceau	Temps comptage
Analyse ponctuelle "classique"	15 KeV	10-20 nA	30 s (mesure) + 10 s (temps morts)
Cartographie WDS	15 KeV	100 nA	0.3 s (mesure)

TABLE 3.1 – Conditions analytiques de la microsonde utilisées pour les analyses ponctuelles et pour la cartographie WDS

nature des éléments excitables ainsi que la taille de la poire d'analyse et donc la profondeur d'excitation sous le faisceau. Pour 15 KeV, la poire d'analyse est de $3 \mu\text{m}^3$ soit une largeur et une profondeur d'excitation légèrement supérieur au micron. Selon les microsondes et le type d'analyse, l'intensité du faisceau est choisie entre 10 et 20 nA. Enfin le temps de comptage est fixé à 20-30 secondes de mesure du signal et 10 secondes de mesure du bruit de fond. En raison de la limite du nombre de spectromètres WDS, une analyse ponctuelle nécessite un temps de mesure généralement compris entre 2 et 3 minutes. Cette durée standard permet d'acquérir les concentrations des différents éléments utilisés en pétrologie métamorphique (Si, Ti, Al, Fe, Mn, Mg, Ca, Na, K, Cr) avec une précision de 1%. Au cours d'une séance de 24h, on peut obtenir de cette manière entre 100 et 200 analyses ponctuelles.

3.1.2 Cartographie WDS

Comme le précise très justement [De Andrade \(2006\)](#) : "même si une séance d'analyse est ponctuée d'un bon nombre de mesures, on n'obtient au final qu'une vision très parcellaire de la chimie d'un échantillon". Pour mieux visualiser les variations chimiques au sein d'un échantillon, il est possible d'acquérir à la microsonde des cartes d'intensités en utilisant les spectromètres WDS. Dans ce cas, il s'agit de séries d'analyses effectuées le long d'une grille, fournissant des images de composition. Généralement, ces cartes sont constituées de 40.000 à 400.000 points de mesures, une mesure pour chaque pixel de l'image de composition. En utilisant les conditions d'analyses ponctuelles "classiques" décrites précédemment, la durée d'acquisition serait comprise entre 110 jours et 3 ans. Pour réduire ce temps d'analyse, il est possible de diminuer le temps de comptage pour chaque point. Mais ainsi, la précision de chaque mesure est également réduite. Une optimisation des conditions analytiques a été proposée par [De Andrade et al. \(2006\)](#), [De Andrade \(2006\)](#) conduisant à une augmentation de l'intensité du faisceau à 100 nA et à une réduction du temps de comptage à 300 ms par point (Tab. 3.1). Avec ces nouvelles

conditions, le temps d'acquisition des cartes de 40.000 à 400.000 points de mesure sera compris entre 6 et 60 heures.

Le fragment de roche à analyser est collé sur une lame de verre puis poli jusqu'à une épaisseur finale de $30\ \mu\text{m}$ (Fig. 3.2-a). Cette "lame mince" est étudiée dans un premier temps au microscope polarisant afin d'identifier les minéraux et les principales structures. La zone à cartographier est sélectionnée, avec une surface comprise entre $0,04\ \text{mm}^2$ (soit $200 \times 200\ \mu\text{m}^2$) et $10\ \text{mm}^2$ (soit $3,16 \times 3,16\ \text{mm}^2$). Elle dépend de la taille de la carte et du pas correspondant à la distance entre les points de la grille. La cartographie microsonde WDS est adaptée pour analyser des objets mesurant entre $10\ \mu\text{m}$ et plusieurs millimètres de largeur. D'autres méthodes de cartographie, non détaillées ici, ont été développées pour analyser des objets de taille supérieure, comme la cartographie EDS ou de fluorescence. C'est le cas par exemple de l'approche quantitative d'Ulrich (2010) qui permet d'obtenir des cartes chimiques et des images de phases de l'intégralité d'une lame mince ($30 \times 30\ \text{mm}^2$) et même plus (jusqu'à $6 \times 5\ \text{cm}$) en utilisant une microfluorescence X. Dans ce cas, la taille du faisceau sera comprise entre $30\ \mu\text{m}$ et $50\ \mu\text{m}$ et ne permettra donc pas d'identifier avec précision la géométrie d'objets de largeur inférieure à $300\ \mu\text{m}$.

Les conditions analytiques de 15 KeV, 100 nA, 300 ms, proposées par De Andrade et al. (2006) permettent d'acquérir à la microsonde des cartes d'intensités dans des temps raisonnables. Le logiciel fourni avec la microsonde permet d'exporter pour chaque élément mesuré un fichier contenant une matrice d'intensités (Fig. 3.2-b, valeurs en rouge). Afin d'étudier la chimie des différentes phases, il est nécessaire de transformer ces cartes d'intensités en cartes de concentrations ce qui correspond à une analyse de type "ponctuelle" pour chaque pixel.

3.1.3 Standardisation des cartes d'intensités

La transformation des mesures d'intensités en concentrations est possible en utilisant la relation de Castaing (Eq. 3.3). Pour la cartographie, le coefficient k n'est pas facile à estimer et une mauvaise contrainte de sa valeur peut vite introduire des biais importants dans le processus de standardisation. Comme nous l'avons vu précédemment, ce coefficient k est utilisé pour corriger les effets de matrices entre

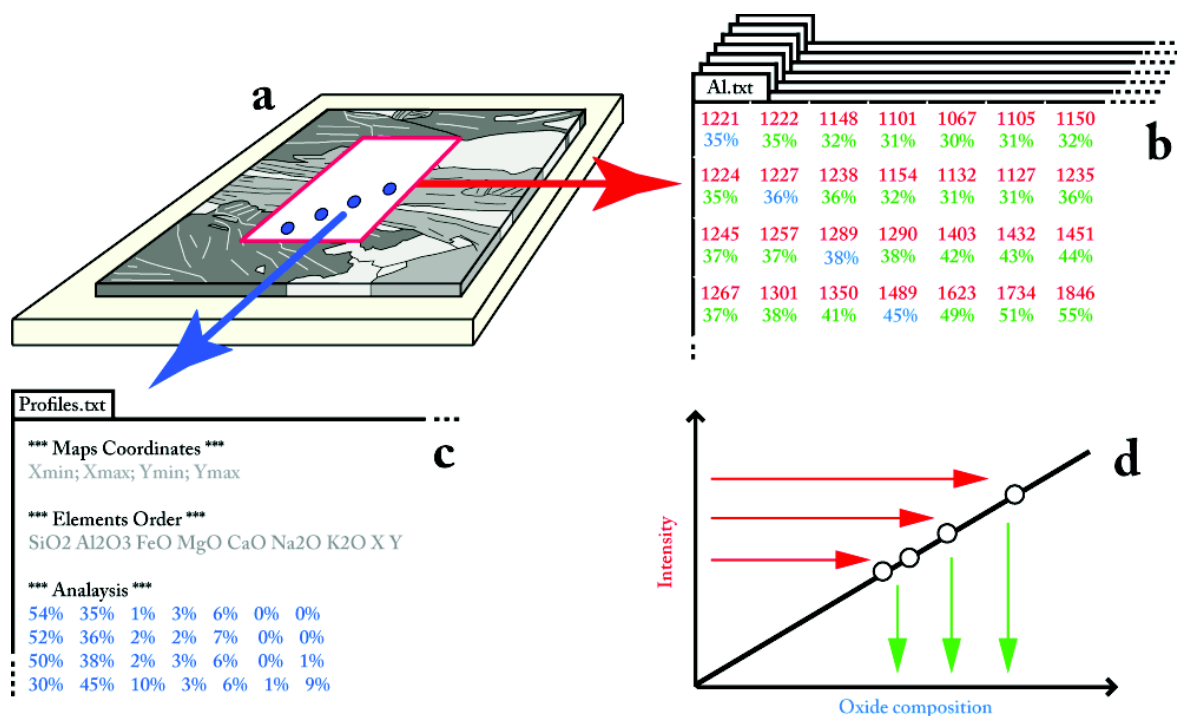


FIGURE 3.2 – Principe de cartographie microsonde et de standardisation des données brutes en utilisant des analyses ponctuelles comme standard. (a) Schéma d'une lame mince polie montée sur une plaque de verre. La zone cartographiée est en rouge et les analyses ponctuelles en bleu. (b) Fichiers de données d'intensités (valeurs en rouge). (c) Fichier de données des analyses ponctuelles. (d) Diagramme chimique : concentrations (poids d'oxydes) vs intensité. La droite de calibration permet de transformer les intensités (valeurs en rouge) en concentrations (valeurs en vert).

le minéral mesuré et le standard. Dans le cas où le minéral mesuré possède une composition très proche du standard utilisé, il est possible de négliger le paramètre k , ce qui revient à écrire la relation de Castaing simplifiée suivante (De Andrade et al. 2006, De Andrade 2006) :

$$C_{ech}^{élément} = C_{std}^{élément} \frac{I_{ech}^{élément}}{I_{std}^{élément}} \quad (3.2)$$

Afin que les compositions des standards soient similaires à celles de la zone mesurée, des analyses ponctuelles "classiques" peuvent être utilisées comme standard (De Andrade et al. 2006). Il est néanmoins nécessaire d'avoir différents standards pour chaque phase présente sur la portion d'échantillon analysée. Lors de la même séance microsonde, des analyses ponctuelles "classiques" sont acquises sur la zone cartographiée (Fig. 3.2-a et c, valeurs en bleu). Si l'on connaît les coordonnées de la carte et celles des analyses ponctuelles, il est possible de projeter chaque analyse sur un pixel de l'image chimique (Fig. 3.2-b, valeurs en bleu). Pour un jeu de pixels

donné, pour chaque élément, il est possible de définir une courbe de calibration dans un diagramme concentration *vs* intensité (Fig. 3.2-d). Cette relation va nous permettre de standardiser les cartes d'intensités en les transformant en cartes de concentrations (Fig. 3.2-b, valeurs en vert).

3.1.4 Avantages de la cartographie WDS

La cartographie WDS a l'avantage d'être plus performante que la cartographie EDS pour la quantification (détails dans [De Andrade 2006](#)). Cette dernière est quant à elle souvent utilisée par les pétrographes sur les Microscopes Electroniques à Balayage (MEB). Le détecteur EDS permet en effet, d'obtenir des images chimiques avec des durées d'acquisition beaucoup plus courtes. C'est pourquoi il est souvent utilisé à titre de "travail exploratoire" afin de repérer les zones d'intérêt d'une lame mince avant la séance de cartographie WDS.

C'est cette démarche qui a été suivie par [Dupuis \(2012\)](#) pour l'étude des grenats dans la Zone houillère briançonnaise en Savoie (France). Après une investigation au microscope polarisant, les différents grenats de la lame mince ont été cartographiés en utilisant l'EDS d'un MEB afin de détecter les éventuelles zonations chimiques. Un grain de grenat d'une taille de $400 \times 300 \mu m^2$ montre des variations de sa composition en Fe, Ca, Mn et Mg (Fig. 3.3). Ce grain semble être constitué de deux sous-grains, l'un au coeur et l'autre en bordure, avec des compositions chimiques relativement différentes. Le coeur est plus riche en Fe et plus pauvre en Ca et Mn que la bordure. L'intérêt de ces cartographies EDS est de caractériser très rapidement les phases minérales présentes et d'obtenir une première information sur les zonations chimiques.

Afin de mieux contraindre ces variations de composition dans le grenat, des cartes en mode WDS ont été acquises sur une partie du grain précédent (cadre rouge sur la Fig. 3.3-a) où le coeur semble montrer des variations de la teneur en Ca (Fig. 3.3-c). Ces analyses ont été réalisées sur une microsonde Cameca SX50 au Laboratoire d'Analyses Physiques et de Caractérisation des Matériaux de Lille. Les cartes chimiques d'une taille de 380×256 pixels ont été acquises en 10 heures avec un temps de comptage de 200 ms/point et un pas de $1 \mu m$. Avec la mesure des

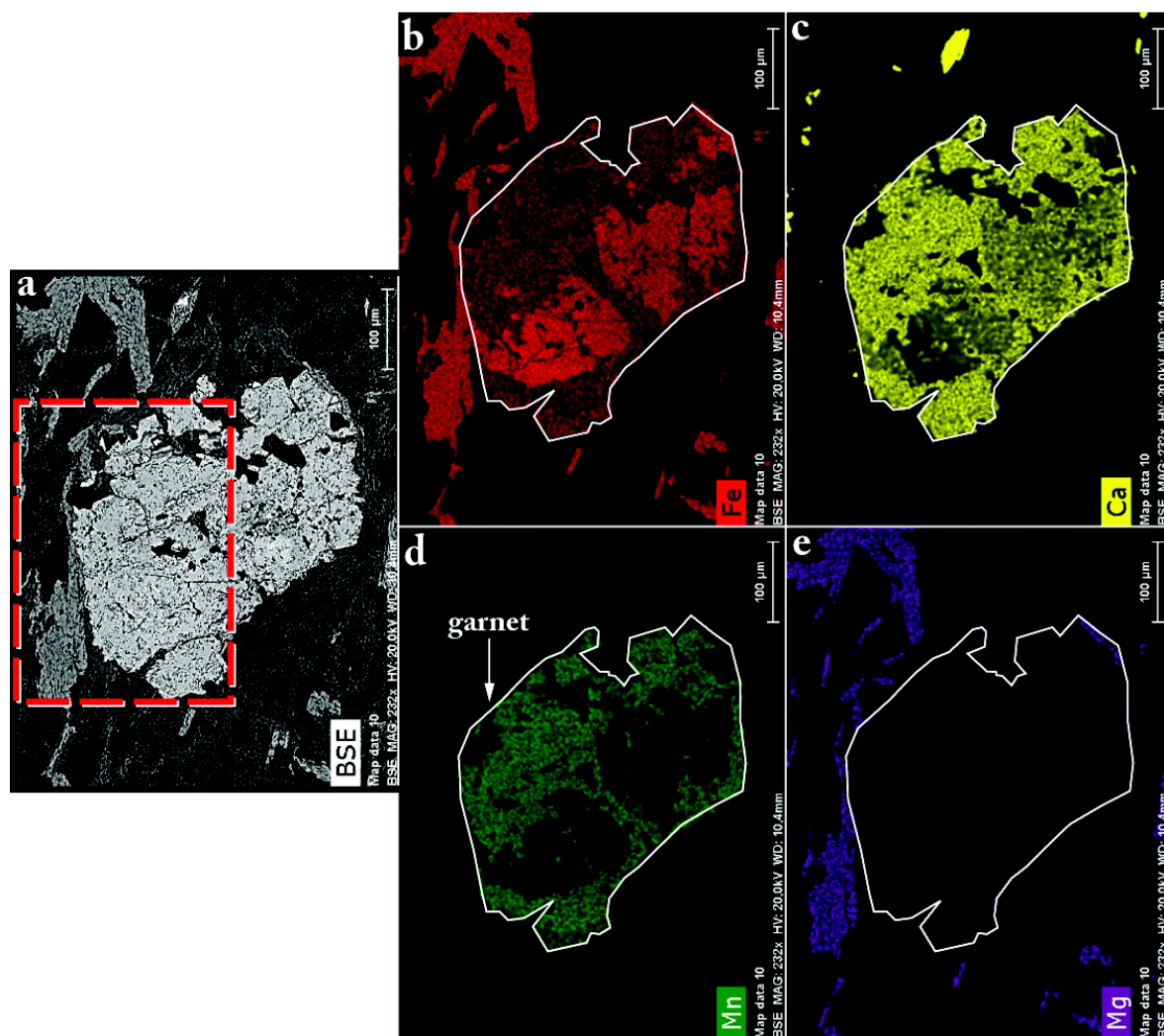


FIGURE 3.3 – Cartographie élémentaire au MEB. Exemple d'un grenat de la Zone houillère briançonnaise. Données : Dupuis (2012). (a) Image BSE (voir texte), (b) carte Fe, (c) carte Ca, (d) carte Mn, (e) carte Mg. Le grenat est entouré d'un trait blanc sur les cartographies élémentaires (b, c, d et e). La localisation de la cartographie microsonde WDS (Fig. 3.4) est indiquée en pointillés rouges.

analyses ponctuelles "classiques" pour standardiser les cartes chimiques, la durée d'acquisition totale a été d'environ 12 heures.

Les cartes d'intensités et les analyses ponctuelles ont été importées dans le logiciel XMAPTOOLS (décrit en détail dans la partie 3.2 et l'annexe A.4). Les valeurs d'intensités pour les pixels de grenat ont été transformées en concentrations (pourcentages de poids d'oxydes), puis en nombre d'atomes de formule structurale (*per formula unit*, p.f.u). La figure 3.4 (a, b, c et d) présente les cartes des proportions des quatre principaux pôles purs du grenat : grossulaire ($X_{gro} = Ca / (Ca + Fe^{2+} + Mn + Mg)$), almandin ($X_{alm} = Fe^{2+} / (Ca + Fe^{2+} + Mn + Mg)$), spessartine ($X_{spess} = Mn / (Ca + Fe^{2+} + Mn + Mg)$) et pyrope ($X_{pyr} = Mg / (Ca + Fe^{2+} + Mn + Mg)$). Ces cartes permettent de différencier plusieurs zonations dans le coeur et la bordure du grenat. Dans la partie du coeur, on retrouve la zonation en Ca (grossulaire) précédemment observée avec l'EDS. Cette fois-ci, on voit que le Fe montre une zonation inverse que celle du Ca. Pour le Mg et le Mn, la zonation est clairement différente. De plus, la teneur de pyrope dans le grenat varie entre 1 et 5% (Fig. 3.4-d), alors que le Mg n'était pas visible lors de la cartographie EDS (Fig. 3.3-c).

Un autre avantage des cartes de concentrations par rapport aux cartes d'intensités non standardisées réside dans la possibilité de tracer l'ensemble des compositions dans des diagrammes chimiques couramment utilisés par les pétrologues. Pour cet exemple, toutes les compositions des pixels de grenat ont été tracées dans un diagramme triangulaire almandin, spessartine, grossulaire (Fig. 3.4-e). Six différents groupes ont été sélectionnés sur le diagramme chimique et les pixels correspondants affichés avec les mêmes couleurs sur une nouvelle image (Fig. 3.4-f). Cette opération très facile à exécuter avec le module *TriPlot3D* du logiciel XMAP-TOOLS permet de définir et d'exporter des compositions moyennes pour chaque groupe du grenat avec la proportion correspondante (Tab. 3.2). Dans ce cas, on voit que le coeur détritique (Bocquet 1974, Bucher et al. 2003; 2004, Bucher et Bousquet 2007, Dupuis 2012) représente environ 22% de la surface totale du grain. La bordure alpine est plus riche en spessartine, ce qui est caractéristique des grenats de faible degré de métamorphisme. Les conditions du métamorphisme alpin ont en

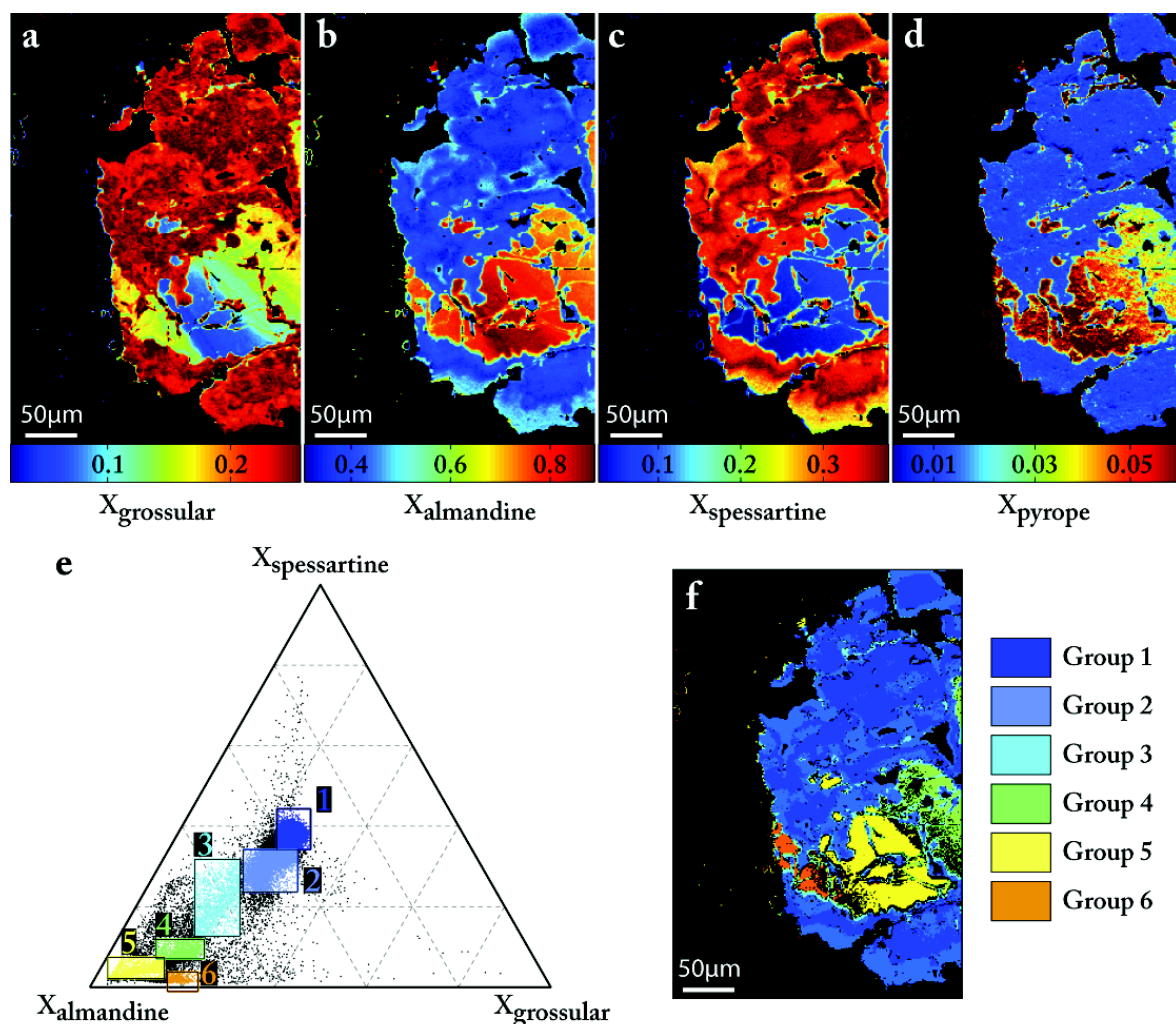


FIGURE 3.4 – Cartographie microsonde WDS et traitement chimique. Exemple d'un grenat de la Zone houillère briançonnaise. Données : Dupuis (2012). Cartes de compositions des pôles purs (a) grossulaire (b) almandin (c) spessartine (d) pyrope. (e) Diagramme triangulaire almandin, spessartine, grossulaire. Six différents groupes de pixels ont été sélectionnés (cadres) dans le diagramme chimique et sont représentés sur une carte (f).

effet été estimées à 370°C et 5 kbar (Bucher et al. 2003, Bucher et Bousquet 2007) pour cette zone.

Les avantages et inconvénients des deux méthodes de cartographie sont bien illustrés dans cet exemple. La cartographie EDS permet de caractériser rapidement les minéraux présents et de détecter d'éventuelles fortes zonations chimiques. La cartographie WDS permet d'obtenir des données plus précises grâce notamment à un meilleur seuil de détection. Chaque pixel de l'image en mode WDS sera traité après la standardisation comme une analyse ponctuelle.

	Grp1	Grp2	Grp3	Grp4	Grp5	Grp6
SiO ₂	37.17	37.06	37.36	36.92	36.23	36.82
Al ₂ O ₃	21.62	21.49	20.90	21.36	21.17	21.24
FeO	16.73	19.48	26.08	33.69	38.74	35.14
MnO	15.08	12.68	8.15	3.09	1.51	0.69
MgO	0.28	0.31	0.74	0.96	1.49	1.48
CaO	8.21	7.81	5.52	5.17	2.26	5.56
Na ₂ O	0.13	0.14	0.14	0.14	0.12	0.11
K ₂ O	0.10	0.11	0.11	0.10	0.09	0.09
Atom site distribution (12 anhydrous-oxygen basis)						
Si _{O/T}	3.00	3.00	3.04	2.96	2.93	2.96
Al _Y	2.06	2.05	2.00	2.02	2.02	2.01
Fe _X	1.13	1.32	1.77	2.26	2.62	2.36
Mg _X	0.03	0.04	0.09	0.11	0.18	0.18
Mn _X	1.03	0.87	0.56	0.21	0.10	0.05
Ca _X	0.71	0.68	0.48	0.44	0.20	0.48
Xalm	0.39	0.45	0.61	0.75	0.85	0.77
Xpyr	0.01	0.01	0.03	0.04	0.06	0.06
Xspess	0.36	0.30	0.19	0.07	0.03	0.02
Xgro	0.24	0.23	0.17	0.15	0.06	0.16
Proportions (%)	40.59	36.17	5.02	6.43	9.97	1.83

TABLE 3.2 – Compositions et formules structurales des différents groupes de grenat identifiés figure 3.4

3.1.5 Protocole d'acquisition et recommandations

Les acquisitions des images chimiques à la microsonde en mode WDS et des analyses ponctuelles nécessitent des précautions particulières qui seront détaillées ici. La méthodologie recommandée sera illustrée en utilisant les résultats de deux étudiants de Master 1 de Grenoble (Bernier 2011, Gardonio 2012) que j'ai co-encadrés avec Emilie Janots. L'échantillon étudié est une métapélite à chlorite, chloritoïde, phengite provenant de l'affleurement de Garvera (zone d'Urseren) dans les Alpes Centrales (Frey 1974; 1978, Frey et al. 1999, Frey et Ferreiro Mählmann 1999, Janots et al. 2011). L'acquisition des données a été effectuée en 2011 à l'Université de Lausanne (UNIL) sur une microsonde JEOL 8200. Les standards

utilisés pour calibrer les spectromètres WDS étaient le diopside pour le Si, Mg et Ca; l'andalousite pour l'Al; l'orthose pour le K; l'oxyde de titane pour le Ti; la fayalite pour le Fe et l'albite pour le Na. La tension du faisceau d'électrons était de 15 KeV et son intensité de 10 nA pour les analyses ponctuelles et 100 nA pour la cartographie WDS.

3.1.5.1 Image BSE, résolution et durée d'acquisition

La première étape consiste à acquérir une image BSE (Back-Scattered Electrons) avec une bonne résolution pour la zone d'intérêt (Fig. 3.5 a). Cette image va servir à repérer avec précision l'emplacement de la carte. Chaque pixel de l'image BSE correspond au nombre d'électrons qui atteignent le détecteur BSE. Ils sont rétrodiffusés par l'échantillon sous l'effet du faisceau. Ce nombre d'électrons est proportionnel au numéro atomique moyen de l'échantillon et donc à la masse moyenne atomique (Krinsley 1998, Goldstein 2003). Cette image BSE est traditionnellement représentée en niveaux de gris car elle enregistre seulement une information de masse qui est en fait une combinaison des masses de tous les éléments présents dans l'échantillon. Chaque minéral possède une masse différente qui est donc représenté avec une teinte particulière. Sur la figure 3.5 (a), les zones les plus blanches (signal fort) dans les baguettes de chloritoïde correspondent à des oxydes de titane qui sont les minéraux les plus lourds. Puis, on distingue le chloritoïde et la chlorite dans des teintes gris clair assez proche. Dans la matrice fine, les grains de phengite présentent des teintes gris foncé comme celles du quartz qui est ici le minéral le plus léger.

La zone analysée peut être repérée directement sur cette image BSE (cadre jaune sur la figure 3.5). Ici, il s'agit d'une zone de 500 μm de large et de 400 μm de haut. Comme la schistosité est constituée de grains de chlorite, phengite et quartz d'environ 10 à 20 μm de largeur, il faut un pas de 1 μm pour pouvoir travailler sur cette zone. En effet, à la bordure entre deux minéraux, les compositions de plusieurs pixels résulteront de mélanges entre les deux phases et ne seront pas exploitables par la suite. C'est pourquoi, il est recommandé pour une exploitation optimale, d'utiliser un pas 10 fois plus petit que la taille minimum des objets à analyser. Pour l'exemple utilisé ici, avec un pixel d'une surface de 1 μm^2 , la taille de l'image

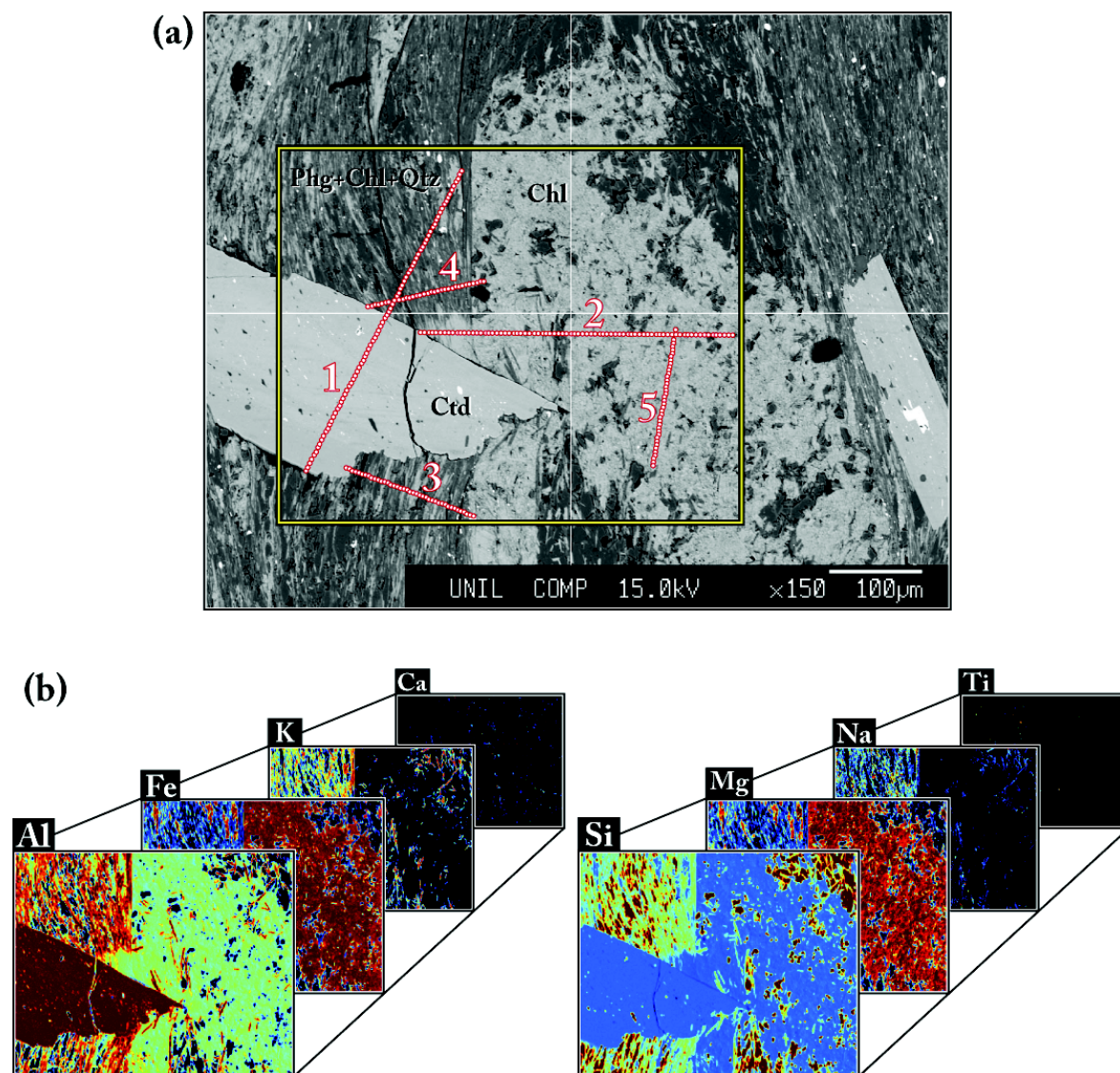


FIGURE 3.5 – Cartographie microsonde d'un échantillon de l'affleurement de Garvera (modifiée d'après [Bernier 2011](#), [Gardonio 2012](#)). (a) Image BSE de l'échantillon avec la zone cartographiée (cadre jaune) et les profils d'analyses ponctuelles (rouge, numérotés de 1 à 5). (b) Cartes d'intensités affichées avec le logiciel XMAPTOOLS.

chimique sera de 500×400 pixels. Il est important de noter que comme discuté précédemment, le volume de la poire d'analyse avec une tension à 15 KeV est d'environ $3 \mu m^3$ dans un standard de silicium. La largeur de cette poire d'analyse est de l'ordre du micron dans l'échantillon naturel. Il est donc tout à fait possible d'acquérir une carte avec un point tous les $1 \mu m$ avec un recouvrement qui sera "minimal".

3.1.5.2 Durée d'analyse

La durée totale d'acquisition (T_a) des cartes d'intensités WDS dépend de la taille de la carte (nombre de pixels, Nb_{pixels}), du temps de comptage par pixel (Tc) et du nombre de passages (Np) :

$$T_a(h) = \frac{Nb_{pixels} \times Tc(s) \times Np}{3600} \quad (3.3)$$

La durée totale d'acquisition pour les images élémentaires présentées sur la figure 3.5 (b) a été d'environ 33 heures.

3.1.5.3 Analyses ponctuelles pour la standardisation

La bonne acquisition des analyses ponctuelles est cruciale pour la transformation des cartes d'intensités en cartes de concentrations. Lors du traitement avec le logiciel XMAPTOOLS, il est nécessaire de replacer les analyses ponctuelles sur la carte avec la meilleure précision possible afin d'obtenir l'intensité du pixel correspondant à la concentration mesurée. Cette tâche n'est pas toujours facile, car la précision du déplacement du charriot de la sonde est généralement de l'ordre du μm et, si la lame n'est pas bien fixée au support, il peut y avoir des mouvements entre l'acquisition des cartes et celle des analyses ponctuelles.

Afin de faciliter l'étape de remplacement des profils sur les cartes d'intensités, il est préférable d'appliquer la stratégie suivante. (1) Les analyses ponctuelles sont acquises le long de lignes (points rouges sur la Fig. 3.5). (2) Les premier et dernier points de chaque profil sont situés sur une zone facilement repérable sur la carte chimique (inclusion, limite entre deux grains). Par exemple le profil 2 sur la figure 3.5 commence dans le chloritoïde juste à côté de la zone de fracture et finit dans une inclusion de phengite dans la chlorite. (3) Le pas entre chaque analyse ponctuelle

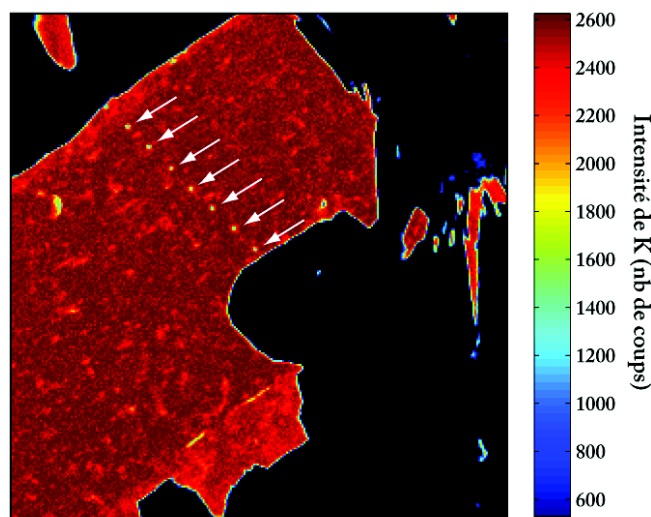


FIGURE 3.6 – Cartographie du K (intensité) dans des muscovites modifiée d'après [Dupuis \(2012\)](#). Les flèches blanches indiquent la position des points d'analyses ponctuelles.

d'une ligne ne doit pas être inférieur au pas de la carte. (4) Plusieurs profils doivent être acquis dans des directions différentes. (5) Notre expérience a montré qu'il est préférable d'avoir une vingtaine d'analyses pour chaque phase à quantifier lorsque les minéraux sont zonés. (6) Les positions des profils doivent être reportées avec la plus grande précision sur l'image BSE. (7) Pour la standardisation, il est recommandé de n'utiliser que les meilleures analyses ponctuelles ([Gardonio 2012](#)) qui ont des sommes de poids d'oxydes raisonnables. Il est donc nécessaire de filtrer les analyses avant de les utiliser comme standard.

Il est indispensable pour la phase de traitement de connaître les coordonnées de la carte et celles des profils. C'est pourquoi les deux types d'analyses sont acquis durant la même séance microsonde.

3.1.5.4 Discussion sur l'ordre d'acquisition

La procédure classique consiste à calibrer la microsonde en début de séance, à acquérir les analyses ponctuelles, puis les cartes d'intensités. Cet ordre peut poser un problème si l'intensité utilisée est trop élevée et que les éléments alcalins comme le K ou le Ca se sont volatilisés sous l'effet du faisceau. Le résultat est illustré sur la figure 3.6, où l'on distingue dans la carte d'intensité du K d'une muscovite la trace des analyses ponctuelles (flèches blanches). Pour cet exemple, 30% du K s'est

volatilisé lors de l'analyse. Dans ce cas, il est impossible de quantifier le K dans les muscovites car la courbe de calibration sera biaisée.

Lors de l'acquisition des analyses ponctuelles qui seront utilisées comme standard, il est donc fortement recommandé d'utiliser des courants faibles pour que les éléments alcalins ne se volatilisent pas. Une solution alternative consiste à acquérir tout d'abord les cartes d'intensités, puis les analyses ponctuelles. L'inconvénient est qu'il faut vérifier la calibration de la sonde après la séance de cartographie, ce qui est envisageable uniquement si les standards sont disponibles dans la microsonde sans avoir à changer le porte échantillon.

3.1.6 Traitement des données

Les cartes d'intensités extraites de la microsonde représentent des matrices de plus de 100.000 valeurs. La taille de ces cartes ne va pas permettre de traiter ces données avec un tableur comme Excel©. De plus, un grand nombre d'opérations est requis pour passer des cartes d'intensités aux cartes de pression et de température. C'est pourquoi [De Andrade \(2006\)](#) a développé un jeu de scripts Matlab© pour le traitement des cartes microsondes.

Ce traitement est un travail minutieux qui requiert une phase d'exploration afin de tirer un maximum d'informations scientifiques à partir des données disponibles. J'ai donc décidé de développer un logiciel avec une interface graphique, afin que l'utilisateur puisse se concentrer uniquement sur le traitement, sans avoir à manipuler le code. C'est ce logiciel, XMAPTOOLS, qui sera présenté en détail dans la partie suivante.

3.2 ARTICLE 3 : XMAPTOOLS A MATLAB©-BASED GRAPHIC USER INTERFACE FOR MICROPROBE X-RAY IMAGES PROCESSING (SUBMITTED TO COMPUTERS AND GEOSCIENCES)

★ *Le traitement des images chimiques mesurées à la microsonde et notamment leur standardisation, puis leur transformation en micro-cartographies P-T nécessite différentes étapes de calculs avec de grands jeux de données.*

★ *En utilisant une approche de Castaing simplifiée, De Andrade et al. (2006) ont montré qu'il est possible de transformer les images chimiques en cartes de concentrations.*

★ *Dans cette partie, nous allons décrire XMAPTOOLS, un logiciel que j'ai développé pour le traitement des données microsondes. Ce logiciel sera présenté sous la forme d'un article de Lanari et al. soumis à la revue Computers and Geosciences. Après une présentation détaillée des fonctions du programme, nous proposerons un exemple d'application tiré de l'étude de Lanari et al. (in press) exposée dans le chapitre 5.*

Cet article décrit en détail la version 1.5.2 de XMAPTOOLS, en particulier l'interface utilisateur et les différentes fonctionnalités disponibles (fonctions générales, options et fonctions thermobarométriques). Pour une description plus détaillée, une notice en Anglais est disponible dans l'annexe A.4. La dernière version du logiciel¹ est disponible en téléchargement gratuit sur notre site web <http://www.xmaptools.com>.



1. Actuellement la version en ligne est la v1.5.3 (01 septembre 2012)

XMapTools a Matlab©-based graphic user interface for microprobe X-ray images processing

Pierre Lanari², Olivier Vidal², Vincent De Andrade³, Benoît Dubacq⁴, Eric Lewin², Eugene Grosch⁵ and Stéphane Schwartz²

Submitted to Computers and Geosciences

Abstract - XMAPTOOLS is a MATLAB©-based graphical user interface program for electron microprobe X-ray images processing. This package available online, <http://www.xmaptools.com> includes general functions to identify the different mineral phases in thin section of rocks and to standardize raw microprobe measurements. An additional 50 functions are provided to calculate structural formulae from the standardized analyses and pressure-temperature conditions of crystallization, using multi-equilibrium thermobarometry and empirical thermobarometers from the literature. Two graphic user interface modules : CHEM2D and TRIPLOT3D are used to plot minerals compositions into binary and ternary diagrams. As an example, XMAPTOOLS is used to study a Himalayan eclogite sample from the Stak massif in north-Pakistan. The original high-pressure paragenesis made off omphacite and garnet has been destabilized into symplectites of plagioclase, clinopyroxene and amphibole during the retrograde path. Mineral compositions corresponding to 200,000 compositions yield estimates for the eclogitic pressure temperature path from 25 *kbar* to 9 *kbar*. As the pressure and the temperature were estimated for all the clinopyroxene pixels, pressure temperature maps were plotted and used to discuss the link between the equilibrium conditions of crystallization and the intergrowth microstructures. This example shows that XMAPTOOLS soft-

2. ISTERre, University of Grenoble 1, CNRS, 1381 rue de la Piscine, 38041 Grenoble, France

3. NSLS II, Brookhaven National Laboratory, SRX beamline, Bldg 817 Renaissance Road, Upton, New York 11973, USA.

4. Department of Earth Sciences, University of Cambridge, Downing Street, Cambridge CB2 3EQ, UK.

5. University of Bergen, Postboks 7800, NO-5020 Bergen, Norway

ware is very useful to study the chemical variation at the thin-section scale and to compute continuous pressure-temperature paths in zoned metamorphic rocks.

3.2.1 Introduction

Our understanding of the dynamics of orogens, subduction zones and lower crust critically relies on estimations of the pressure-temperature (P-T) conditions of crystallisation of mineral assemblages. If we derived the pressure (P) and temperature (T) at which an igneous or metamorphic rock equilibrated, we can determine a lot about where in the Earth the rock formed and how the rock formed. Thermobarometric tools such as multi-equilibrium thermobarometry (e.g. [Berman 1991](#)), pseudosections (e.g. [Holland et Powell 1998; 2011](#)) and empirical thermometers (e.g. [Cathelineau et Nieva 1985](#), [Schmidt 1992](#), [Waters et Martin 1993](#)) provide these estimates from the nature and composition of minerals present in the available rock samples. Previous work has shown that electron microprobe maps of the variations of composition can be used to shed light on the recrystallization history of samples showing various stages of re-equilibration along the retrograde path linked to major deformation events ([De Andrade et al. 2006](#), [Muñoz et al. 2006](#), [Vidal et al. 2006](#), [Yamato et al. 2007](#), [Lanari et al. 2012a](#), [Plunder et al. 2012](#), [Lanari et al. in press](#)). However, quantitative electron microprobe analyses require a standardisation of the number of collected photons (X-ray intensity). Point analysis including the standardization procedure of eight major elements (Si, Al, Mn, Mg, Fe, Na, Ca, K) under classical conditions (10 nA, 15 keV, 40 s) last about two minutes. This approach is therefore difficult to apply to chemical mapping, which is generally applied to samples heterogeneous on a 10 μm scale with maps typically containing about 150,000 pixels. [De Andrade et al. \(2006\)](#) showed that quantitative chemical maps can be obtained within a reasonable time by using a higher current intensity and a low counting time (100 to 300 ms/pixel), and a Castaing approach to standardize the measured concentrations using point analyses as internal standards. The Castaing approach assumes a relation of proportionality between X-ray intensity and relative abundance of an element in the same phase ([Castaing 1951](#)). As this relation neglects matrix effects such as absorption, electron scattering and fluorescence, it shows a better agreement if the standard point analysis and the mapped

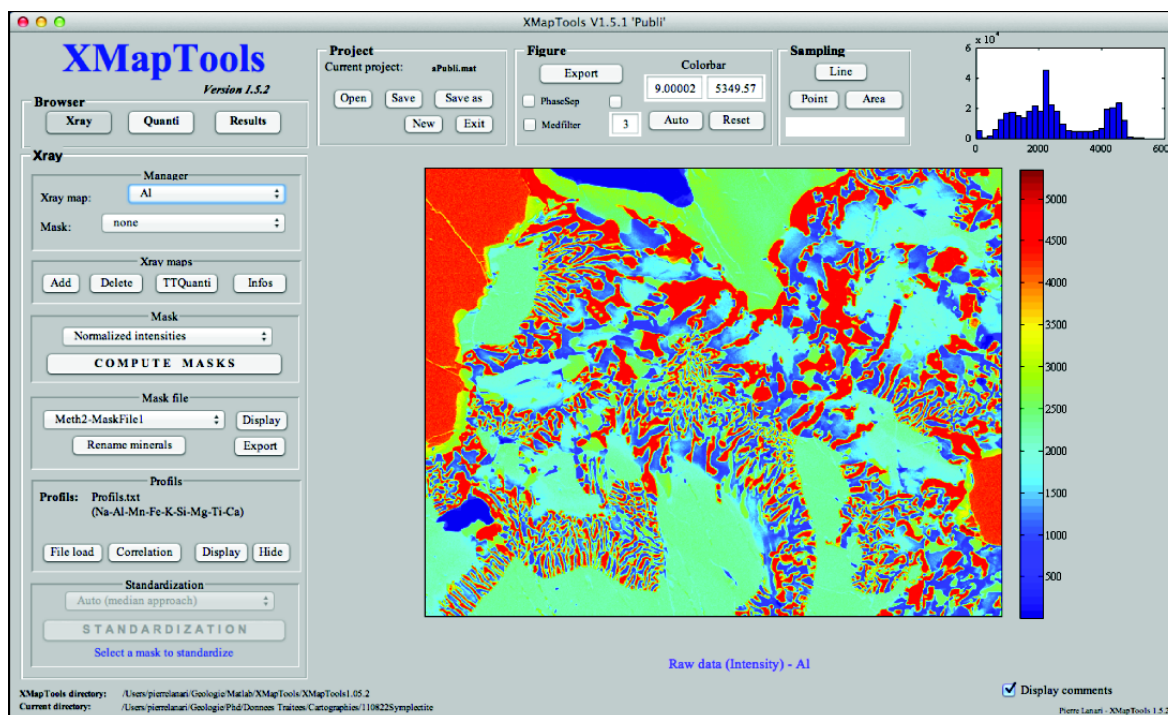


FIGURE 3.7 – XMAPTOOLS v1.5.2 graphic user interface. The displayed image is the raw Al-content map of the sample 'Eclogite' (see text for details) unit : number of recorded counts.

mineral are identical. Experience shows that at least 20 point analyses capturing most of the spatial chemical variability of each phase in the selected area of the sample are necessary for optimal standardisation of the raw map.

Here we propose a Matlab©-based Graphic User Interface (GUI) program named XMAPTOOLS that can be used 1) to separate automatically the mineral phases in the analysed sample, 2) to standardize raw X-ray intensities maps, 3) to calculate the structural formulae of the identified minerals (out of a selection of 12 usual minerals), 4) to plot the analyses into various classical chemical diagrams, and 5) to calculate P-T conditions of crystallisation using various empirical and semi-empirical thermobarometers. An example of application of the program to a retrogressed eclogite is presented below.

3.2.2 Description of the program

The XMAPTOOLS software (available at <http://www.xmaptools.com>) can be run with a MATLAB© version 7.5 release R2007b or later and it requires the statistics

toolbox for the k-means function. It uses a graphical interface named XMapTools.fig (Fig. 3.7) built using the MATLAB© Graphical User Interface Development Environment (GUIDE) tool. Each GUI components dragged with the GUIDE is associated to a callback function in the program file XMapTools.p, corresponding to a content-obscured version.

The program is structured into three main parts : Xray, Quanti and Results (Fig. 3.8) corresponding to three different step. In the first step Xray (Xray column in Fig. 3.8), the user adds the maps, automatically computes the masks, i.e. separates the different minerals, and identifies the mineral phases. The Standardization processing is the end of the Xray step. In the second step Quanti (Quanti column in fig. 3.8) the user transforms the standardized maps into maps of structural and into P-T maps using the computation tool. Results are investigated in the last step Results (Results column in Fig. 3.8) and plot of in binary and ternary diagrams. All the functions use for this processing are detailed below.

3.2.2.1 Raw data treatment (Xray)

Two types of data can be loaded in XMAPTOOLS : the raw data, X-ray intensity images corresponding to the number of collected photons for each pixel and the point analyses used as internal standards.

In both Cameca© and Jeol© microprobes, the raw data of chemical maps can be exported in ascii format such as *.txt file. One file is created for each measured element, containing header lines reporting information about analytical conditions and coordinates of the selected area, followed by a matrix of recorded X-ray intensity data, with one value for each element of each pixel of the map. After user removal of the header lines, the loading function of XMAPTOOLS reads the input files and creates X-ray intensity images. The loading function includes dead-time correction, which transforms the measured counting rates rate into true rate (see details in [De Andrade et al. 2006](#)).

Point analyses used for the standardization and their coordinates are other required inputs. Usually, these points analysis are made along different transects. The standard loading function reads a series of point analysis. The location of the

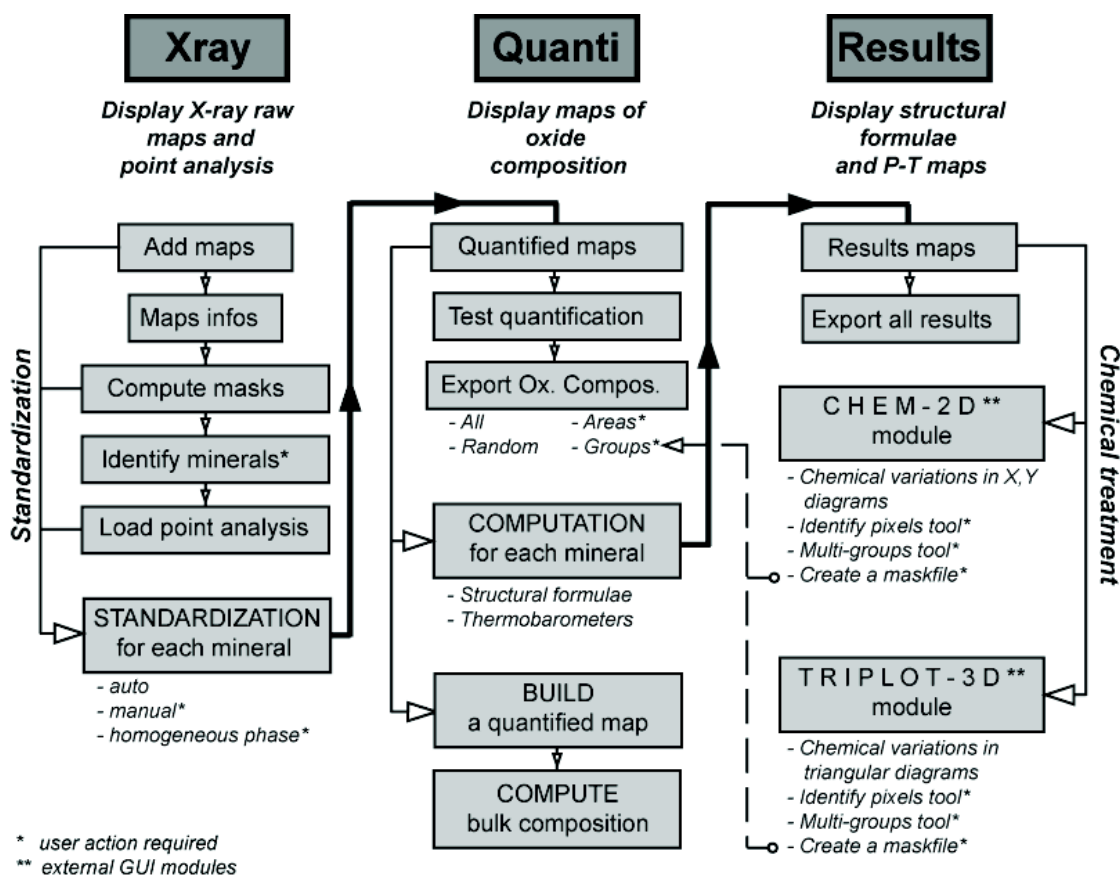


FIGURE 3.8 – XMapTOOLS operating diagram, resuming the main available functions. All steps marked with a star require user action. Light arrows indicate the way forward, bold-arrows the transition between the different sub-programs (Xray, Quanti, Results, see text), and the dashed arrows the available feedback.

point analyses are then projected onto the map, and the user can compare the X-ray intensities along the profiles measured by point analyses to the ones of the map. This comparison is useful to detect possible problems of location of profiles on the map, for example due to drifting of the stage during analysis. This comparison figure allows to test if the mapping and the point intensities are in good qualitative agreement, meaning that the point analyses used for the standardization are correctly projected.

Mask creating function This function creates a number of masks corresponding to the number of minerals identified in the mapped, where each mask is a matrix of logical numbers indexed on the coordinates of the composition map. The value of 1 is attributed to the pixels belonging to a given mineral phase, and 0 in the opposite case. This function allocates each individual pixel to one of the minerals phases.

The mask creating function uses the statistical analysis method k-means included in the MATLAB© statistics toolbox (see [De Andrade et al. 2006](#)). The user selects one pixel of each mineral on the chemical map as needed by k-means for initial guess. The compositions of these pixels are used as input data by the k-means function to define the starting cluster centroids. An iterative loop reassigns each pixel to the nearest cluster and then recalculates all the centroids until convergence, which corresponds to the minimization of the sum of point-to-centroid distances summed over all clusters ([Seber 1984](#), [Spath 1985](#)). Two approaches are available in XMAPTOOLS : the 'classical' and the 'normalized' approaches. Both of them use the K-means function, but with different X-ray intensities inputs. In the 'normalized' function, X-ray intensities of each element are normalized to their mean values, with the result that all elements have the same weight and only the variances are compared. In contrast, the X-ray intensities of each element in the 'classical' method are not normalized and depend on its concentration. Different masks can be derived using both methods. For a same sample, we recommend to test the two methods (see example in § [3.2.3.2](#)).

Standardization function This function transforms the X-ray intensities of all elements measured on pixels from each mask into oxide weight concentrations. The standardization of pixels requires calibration curves describing how X-ray intensities change with concentration ([Castaing 1951](#)). One calibration curve is calculated for each element in each phase from the intensity versus concentration relations constrained with point analyses. The calibration curves for Si in the different phases of the studied sample are shown in figure [3.8](#). For each mineral, the calibration curve is a line that can be drawn between the origin (zero intensity and concentration) and the central point of the cluster of the point analyses.

The standardization can be performed using one of the three methods available in XMAPTOOLS. The first method 'Auto' is fully automatic, and the cluster centroids are the arithmetic average values with the minimum standard deviation. The 'Manual' approach allows the user to define manually the cluster centroids and therefore the calibration curve. The last method 'Manual (homogeneous phase)' is adapted to homogeneous minerals such as quartz. The calibration curve is defined

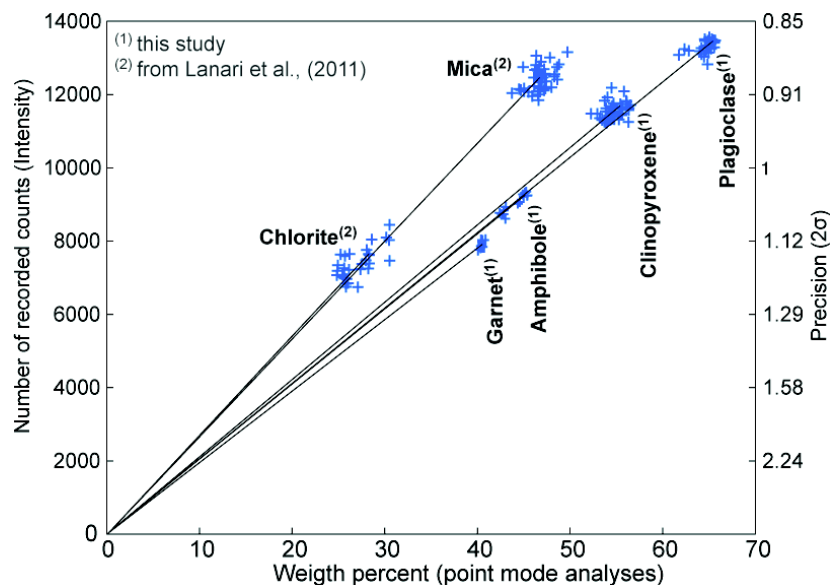


FIGURE 3.9 – Calibration curves for Si in different minerals defined using a median approach. The blue crosses correspond to high quality point oxide concentration and the raw intensity of the corresponding pixel. The precision is given depending from the intensity (% at 2σ see text).

by the mean values of X-ray intensities for the selected mineral and the user enters the corresponding concentration, e.g. 100% for SiO_2 in the case of quartz.

3.2.2.2 Calculations from quantified data (Quanti)

Once the masks have been defined and element concentrations have been estimated, structural formulae can be calculated and equilibrium conditions can be derived using empirical thermobarometers.

Structural formula functions Several structural formulae and atom site repartition models from literature were implemented in XMAPTOOLS (table 3.3). A general function is also available to calculate a structural formula on a given number of oxygen. This additional function is used to compute on each pixel the number of moles of elements per formula unit (p.f.u.).

Empirical thermobarometry functions XMAPTOOLS includes a wide range of thermobarometry functions. These methods were divided into two groups : the exchange reactions (Table 3.4) and thermobarometer functions (Table 3.5).

Group	Mineral (*)	End-members (**)	References
Chain silicates	Amphibole (23)	glaucofane (gl)	Holland et Blundy (1994)
		tremolite (tr)	Dale et al. (2000; 2005)
		f-tremolite (ftr)	Spear (1993)
		tschermakite (ts)	
		pargasite (parg)	
		cummingtonite (cum)	
		ferri-tschermakite (mfets)	
	Clinopyroxene (6)	jadeite (jd)	Spear (1993), Warren et Waters (2006)
		diopside (di)	
		hedenbergite (hed)	
		Ca-tschermak (cats)	
	Orthopyroxene (6)	Acmite (acm)	
		Enstatite (en)	Holland et Powell (1998)
	Chloritoid (6)	Ferrosilite (fs)	
		Mg-Tschermak (mgts)	
	Fe-chloritoid (fctd)		Vidal et al. (1999)
		Mg-chloritoid (mctd)	
	Mn-chloritoid (mnctd)		
	Staurolite (48)	Fe-staurolite (fst)	Holland et Powell (1998)
		Mg-staurolite (mst)	
	Mn-staurolite (mnst)		
	Epidote (12.5)	zoizite (zo)	Holland et Powell (1998)
		epidote (ep)	
	Cordierite (18)	Fe-epidote (fep)	
		cordierite (crd)	Holland et Powell (1998)
		Fe-cordierite (fcrd)	
		Mn-cordierite (mncrd)	
Ortho- and ring silicates	Garnet (12)	almandine (alm)	Spear (1993)
		pyrope (pyr)	
		spessartine (spe)	
		grossular (gro)	
Phyllosilicates	Olivine (4)	forsterite	Spear (1993)
		fayalite	
	Chlorite (14)	amesite (ames)	Holland et al. (1998)
		f-amesite (fames)	Vidal et al. (2001; 2005; 2006)
		daphnite (daph)	
		sudoite (sud)	
		chlorite-Mg (afchl)	
		chlorite-Fe (fafchl)	
	Micas (11)	celadonite (cel)	Coggon et Holland (2002)
		f-celadonite (fccl)	Parra et al. (2002a)
		muscovite (mus)	Dubacq et al. (2010)
		paragonite (par)	
Framework silicates	Feldspar (8)	margarite (marg)	
		phlogopite (phl)	
		f-phlogopite (fphl)	
		pyrophyllite (prl)	
		albite (ab)	Spear (1993)
		anortite (an)	
		microcline (mic)	

* Oxygen basis, ** abbreviation

TABLE 3.3 – List of solid solution models and associated end-members included in XMAPTools.

Method	Calibrations
Amphibole-Plagioclase	Holland et Blundy (1994), Blundy et Holland (1990)
Chlorite-Chloritoid	Vidal et al. (1999)
Garnet-Biotite	Goldman et Albee (1977), Holdaway et Lee (1977), Thompson (1976)
Garnet-Muscovite	Green et Hellman (1982), Krogh et Raheim (1978)
Garnet-Chlorite	Grambling (1990), Dickenson et Heweitt (1986)
Garnet-Amphibole	Korgh Ravna (2000a), Perchuk et al. (1985), Graham et Powell (1984)
Garnet-Cpx	Korgh Ravna (2000b), Ai (1994), Sengupta et al. (1989), Pattison et Newton (1989), Krogh (1988) Powell et Holland (1985), Dahl (1980), Ganguly (1979), Ellis et Green (1979), Mori et Green (1978) Raheim et Green (1974), Mysen et Heier (1972)

TABLE 3.4 – List of exchange reactions calibrations included in XMAPTOOLS

Min.	Thermometers	Barometers	Multi-equilibrium
Amp	Holland et Blundy (1994) - a	Anderson et Smith (1995)	Amphibole + plagioclase* P Schmidt (1992) T Holland et Blundy (1994)
	Holland et Blundy (1994) - b	Schmidt (1992)	Amphibole + plagioclase* + quartz* P Schmidt (1992) T Holland et Blundy (1994)
	Blundy et Holland (1990)	Johnson et Rutherford (1989) Johnson et Rutherford (1989) - P_{min} Johnson et Rutherford (1989) - P_{max} Hollister et al. (1987) Hammarstrom et Zen (1986)	
Chl	This study (§ 2.3.3) Inoue et al. (2009) Zang et Fyfe (1995) Jowett (1991) Hillier et Velde (1991) Cathelineau (1988) Kranidiotis et MacLean (1987) Cathelineau et Nieva (1985)		
Cpx		Waters (2002; 2003)	Cpx + garnet* + phengite* P Waters et Martin (1993), Waters (1996) T Korgh Ravna (2000b) or Ellis et Green (1979)
			Cpx + amphibole* + plagio* P Waters (2002; 2003) T Holland et Blundy (1994)
Phg		Massonne et Schreyer (1987)	
Grt	Creighton (2009) Kawasaki et al. (2011)		
Rt	Zack et al. (2004)		

* Fixed composition

TABLE 3.5 – List of empirical thermometers, barometers and Multi-equilibrium functions implemented in XMAPTOOLS. Abbreviations : Amp, amphibole ; Chl, chlorite ; Cpx, clinopyroxene ; Phg, phengite ; Grt, grenat ; Rt, rutile.

In exchange reactions, cations such as Fe^{2+} and Mg^{2+} are swapped between two minerals (Spear 1993). P-T conditions of equilibrium are derived from two distinct mineral compositions. XMAPTOOLS generates an image with the oxide weight percent compositions of the two minerals and allows the user to select pairs of pixels. The two selected compositions are used to estimate the equilibrium conditions. In the case of the exchange reactions the temperature is usually estimated for a given pressure because the exchange equilibrium is temperature-dependent. If the minerals show a metamorphic zoning not developed by diffusion and are in thermodynamic equilibrium, the variations of temperature conditions can be investigated using this approach. A set of mineral pairs is selected between the core and the rim of the two minerals providing a trend for the evolution of the temperature conditions. This trend shows if the crystallization occurs during the prograde path corresponding to an increase of temperature from the core to the rim or during the retrograde path corresponding to a decrease of temperature from the core to the rim.

The thermobarometers functions are 'pixel' thermobarometry and provide P, T, or P-T maps. In this case, equilibrium conditions were derived from only one composition with fixed variables such as other mineral composition, or P or T. Methods are listed in the table 3.5 and can be divided into three sub-groups : (1) The thermometers allows estimating the temperature, (2) the barometers the pressure, and (3) the thermobarometers that use multi-equilibrium techniques to derive both P and T maps. The multi-equilibrium approach use at least two equilibria implied by a given mineral assemblage to derive the equilibrium conditions (Berman 1991).

For example, the pressure of crystallisation of amphiboles can be estimated using an empirical barometer calibration based on the Al-content (e.g. Schmidt 1992). The temperature of amphibole in equilibrium with plagioclase can be also estimated with a semi-empirical calibration of the equilibrium : edenite + albite = richterite + anortite (Holland et Blundy 1994). The ideal and non-ideal parts of the amphibole activities are calculated automatically from the pixel compositions following the formalism described in the original publication. Using both calibrations together, this multi-equilibrium function ('Amp-PT (amp+pl)' in XMAPTOOLS)

predicts the P-T equilibrium conditions of amphibole compositions for a fixed plagioclase composition.

3.2.2.3 Chemical plots

The mineral compositions or end-members proportions can be plotted as a map or into chemical diagrams such as binary diagrams using the *Chem2D* module (Fig. 3.10), or ternary diagrams using the *TriPlot3D* module (Fig. 3.11). Both modules have a graphic interface in which the user can select the plotted variables and manage the figure axis. A density plot function is also available, which contours the cluster as a function of the analyse proportions.

Two selection functions 'identify pixels' and 'multi-groups' may be used to select points or ranges of composition in the diagrams, and the identification of the corresponding pixels on a map.

Several functions aim to create masks that correspond to matrix in which each pixel is allocated to a group. These masks are built from selections (identify pixel and multi-groups tools), or automatically using a clustering approach. The mask variable can be exported into mask file in ascii format (*.txt) and use in the 'Quanti' tab to export the average oxide composition corresponding to the selected pixels (see the dashed arrow in Fig. 3.9).

3.2.2.4 Others functions

All the results can be saved and previously saved projects can be loaded at any time using the functions 'save', 'save as' and 'load'.

Functions in the 'figure' window are dedicated to the management of the color bar such as the min and max values, the auto and reset buttons, and the phase separator button (PhaseSep in Fig. 3.7). The user can also export the main figure in different formats : *.fig, *.ai, *.eps, *.jpg, *.pcx, *.pbm, *.pdf, *.pgm, *.png, *.ppm, *.pkm and *.tif using the export button.

Functions in the 'sampling' window are used to select a subset of the data into the main displayed image. These functions are available for any displayed

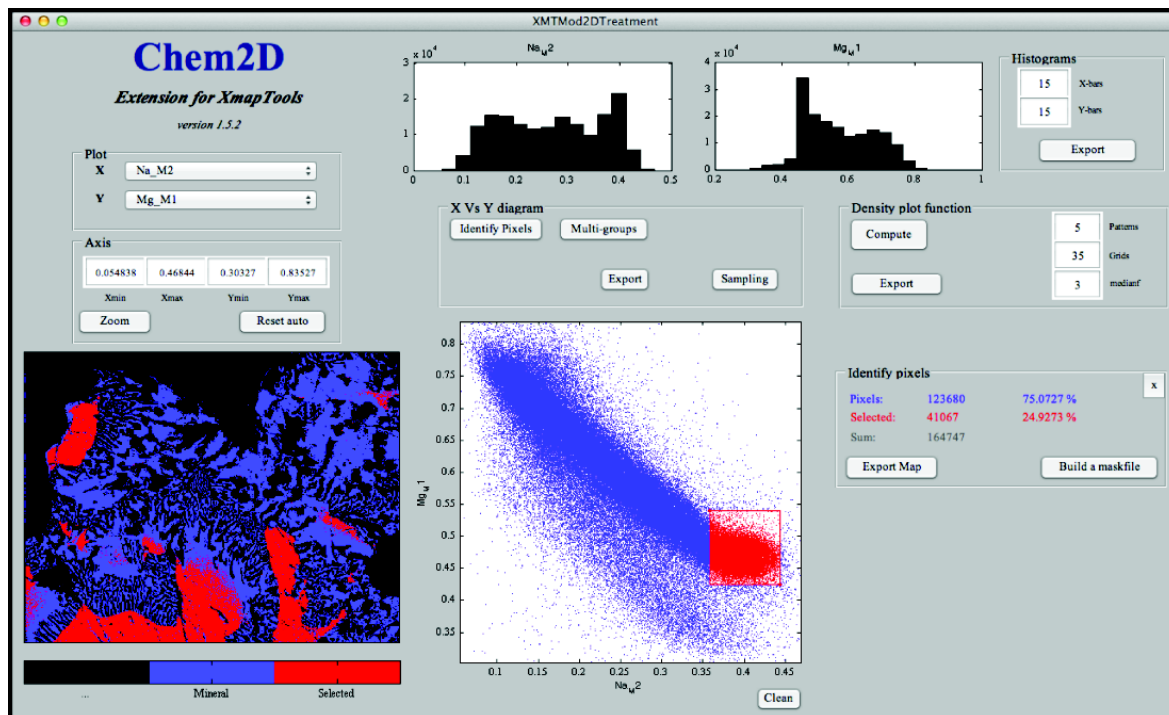


FIGURE 3.10 – XMAPTOOLS Chem2D module interface. The plotted diagram is Na_M2 vs Mg_M1 for clinopyroxene. Pixels with high Na-content were selected on the main diagram (red square) and plotted into a map (left, red pixels). The selected pixels of omphacite correspond to 25% of the clinopyroxene pixels (left, identify pixel window).

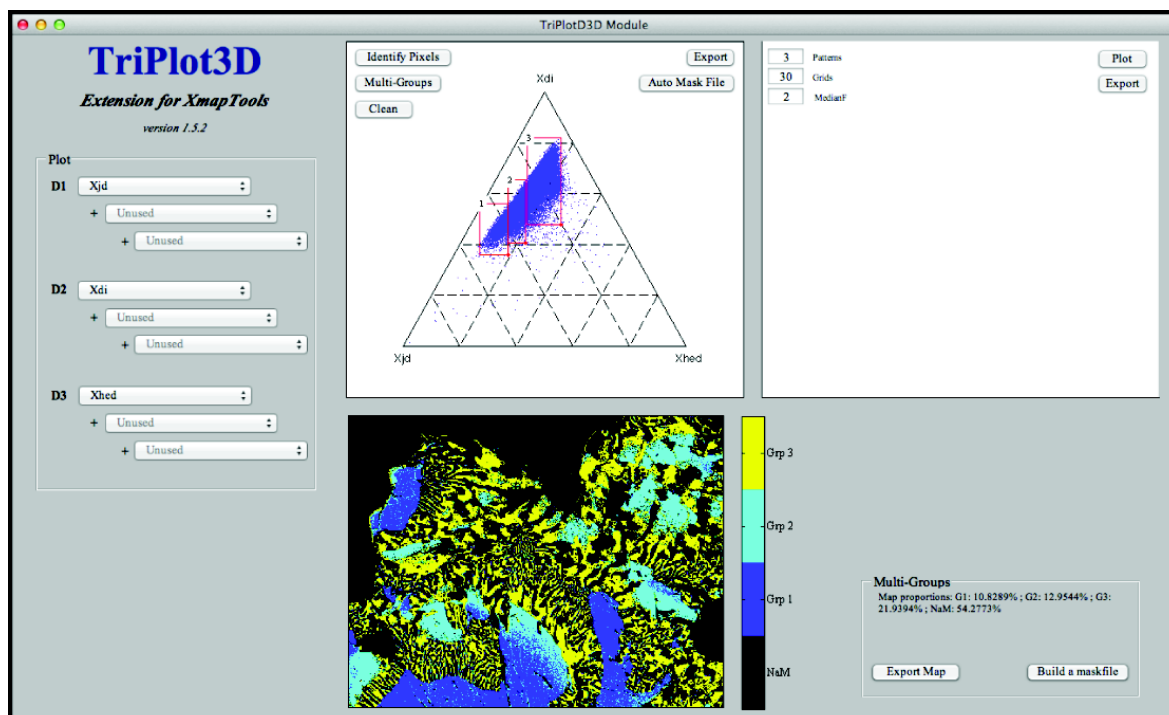


FIGURE 3.11 – XMAPTOOLS TriPlot3D module interface. The plotted triangular diagram is Xjadeite , Xdiopside , Xhedenbergite for clinopyroxene. Pixels with a high Xjadeite content were selected on the main diagram (red square) and plotted into a map (bottom, red pixels)

image (X-ray raw measurement, map of oxide compositions, structural formulae, equilibrium conditions maps). The selected data may be a pixel, a line or an area of pixels. This tool can be used for example to draw the composition variations of a mineral grain along a transect.

3.2.3 Tests and evaluation

The generation of structural formulae and P-T maps from microprobe analysis is an important tool for petrographic and geodynamic studies. Compositional maps were acquired on an eclogite sample from the Stak area, one of the three Himalayan high pressure to ultra high pressure (HP - UHP) continental massif (Guillot et al. 2008, Lanari et al. in press) of the NW Himalaya. The studied sample contains a well-preserved eclogitic assemblage constituted by garnet and Na-rich clinopyroxene (omphacite), which formed during the continental subduction. Omphacite, was subsequently retrogressed in Na-poorer clinopyroxene + plagioclase + amphibole symplectite. The last foliation is made up large amphiboles + biotite beds that developed during a strong collisional imprint associated with the hydration under crustal conditions (Lanari et al. in press).

3.2.3.1 Data acquisition

An area of 0.348 mm^2 ($520 \times 670 \text{ }\mu\text{m}^2$) located in a symplectite zone was mapped, which contains garnet, clinopyroxene, amphibole, plagioclase, Ti- and Fe-oxides. The data acquisition has been done at the Institute of Earth and Environmental Science in the University of Potsdam (Germany) using a JEOL JXA-8200 equipped with five wavelength-dispersive spectrometers. Mapping conditions were 15 keV accelerating voltage and 100 nA beam current, 1 μm beam diameter, 200 ms counting time and 1 μm step size. The X-ray intensities of Si, Ti, Al, Fe, Mg, Mn, Ca, Na and K were measured in two passes.

3.2.3.2 From X-ray intensities to map of composition

An image of the mineral phases created using the 'mask creating function' (see § 3.2.2.1) is shown in figure 3.12-a. The two methods for the mask creating function (classical and normalized) were tested and lead to similar estimates of the mine-

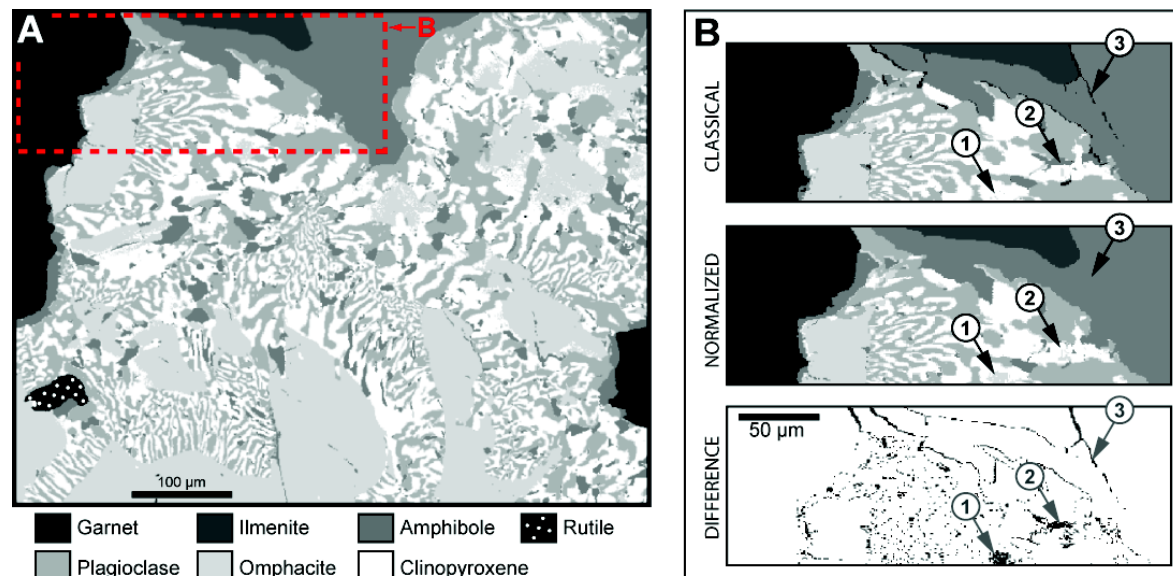


FIGURE 3.12 – Phase masks for the 'eclogite' sample (A) computed using the 'normalized' method (see text). The part used to compare the two available methods is marked using a dashed rectangle. (B) Comparison between methods 'classical' and 'normalized' with a difference image in which black pixels were the pixels not allocated to the same groups with both methods.

ral modal proportions except for garnet (Tab. 3.7). The difference for garnet is due to the erroneous allocation of the contours pixels around amphibole to the garnet mask when using the classical approach. This artefact may be corrected by creating an additional mask corresponding to the borders of the mineral or by using the normalized method. Additional differences between the 'normalized' and 'classical' approaches are shown in figure 3.12-b for a part of the map (dashed square in Fig. 3.12-a). For instance, the zone 1 in figure 3.12-b shows that omphacite is identified in the core of clinopyroxene using the 'normalized' method only. This is due to the normalization procedure because the difference between omphacite and clinopyroxene as seen by k-means results from small differences in their Na- and Mg-contents. These differences are not detected with the 'classical' method, which allocates more pixels to the clinopyroxene mask. The other examples (2 and 3 in Fig. 3.12) show that in some cases, the opposite effect is observed when variations occur in only one highly concentrated element, keeping the variations in low-concentrated elements at minimum. From this, we conclude that the two methods should be tested and we recommend to check the difference between the two results and to compute different mask-files with changing the number of phases.

	Normalized	Classical	Difference (%)
Ti-oxide	0.430	0.430	0.00
Garnet	7.000	7.700	9.09
Fe-Oxide	1.100	1.130	2.65
Amphibole	13.20	12.77	3.37
Plagioclase	21.26	21.52	1.21
Omphacite	30.97	29.88	3.65
Cpx	26.04	26.57	1.99

TABLE 3.6 – *Phases proportions estimated with XMAPTOOLS using available methods 'normalized' and 'classical'. The difference in percentage is an absolute difference.*

Standardization of the raw map was performed using the 'standardization function' (see § 3.2.2.1) with the 'Auto (median approach)' method. The calibration curves (see § 3.2.3.1 and graphical representation in fig. 3.9) were defined for clinopyroxene, garnet, amphibole and plagioclase.

Clinopyroxene structural formulae were calculated on a 6 oxygen-basis by distributing elements on tetrahedral ($T1$) and octahedral ($M1$, $M2$) sites. End-members proportions of jadeite, diopside, hedenbergite, acmite and Ca-tschermak (Table 3.3) were estimated according to the atom site repartition model of Spear (1993) and Warren et Waters (2006). The amphiboles structural formulae were calculated on a 23 oxygen-basis and elements were distributed on tetrahedral ($T1$, $T2$), octahedral ($M2$, $M13$, $M4$), and interlayer-like (A) sites. End-members proportions of glaucophane, tremolite, tschermakite, pargasite, cumingtonite, ferri-tschermakite (Table 3.3) were calculated according to the atom site repartition model of Dale et al. (2000; 2005). Structural formulae for garnet and plagioclase were respectively calculated on a 12 and 8 oxygen-basis following simple atom-site repartition models (see end-members list in table 3.3).

The transformation of oxide concentration maps into structural formulae maps highlights the relationship between atom-site composition and microstructures. The two chemical modules *Chem2D* and *TriPlot3D* were used to investigate the variations of clinopyroxene end-members proportions and structural formulae compositions. In figure 3.10, Na-rich clinopyroxene pixels were selected using the 'identify pixel' tool (§ 3.2.2.4) in the Na vs Mg diagram (red pixels). These Na-rich clinopyroxenes are omphacite and correspond to 25% of the total clinopyroxene pixels. Then, clinopyroxene pixels were divided into three groups using the 'multi-groups'

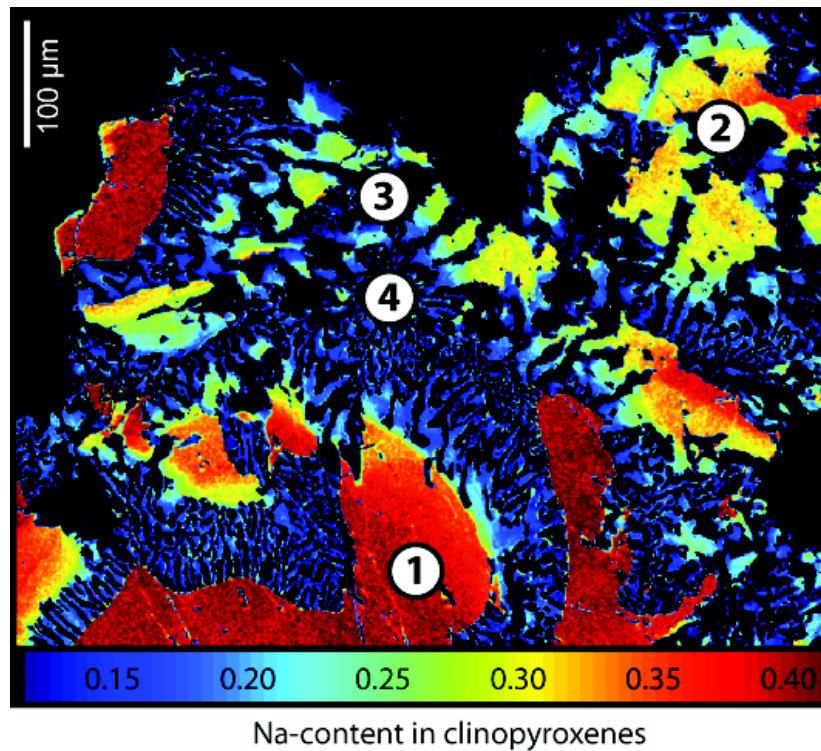


FIGURE 3.13 – Na-content of clinopyroxene (including omphacite). The different stages of crystallization (labelled 1 to 4) are discussed in the text.

tool into the jadeite-diposide-hedenbergite ternary diagram (blue, cyan and yellow pixels in Fig. 3.11).

The symplectite is known to nucleate on a grain boundary between two omphacite grains and to grow into the grain on one side, when the rock is sufficiently out of equilibrium to nucleate the product (Waters 2002; 2003). In the mapped area (Fig. 3.13), Na-rich clinopyroxene previously identified as omphacite shows high-Na content up to 0.4 p.f.u (zone 1 in Fig. 3.13). This primary omphacite (width > 100 μm) is destabilized into a first symplectite containing Na-poorer clinopyroxene, plagioclase and amphibole. Clinopyroxene in this first symplectite (zone 2 in fig. 3.13) crystallizes as broad lamellae (30-40 μm width) preserving the original shape of omphacite, but with a lower Na-content (0.35 to 0.28 p.f.u.) than the original omphacite grains. A second symplectite is observed in zone 3 of figure 3.13, which shows smaller clinopyroxene lamellae size (10-20 μm width) and Na-content (0.28 to 0.18 p.f.u.). The last symplectite has an even smaller clinopyroxene lamellae size (width < 10 μm) and Na-content (< 15 p.f.u.).

Raw data			Quantified data		
Element	Mean Intensity	Precision (% at 2σ)	Oxide	Composition	Error (2σ)
Si	11086	0.950	SiO ₂	54.718	0.528
Ti	93	10.35	TiO ₂	0.180	0.018
Al	2529	1.988	Al ₂ O ₃	9.690	0.194
Fe	631	3.981	FeO	4.529	0.176
Mg	1381	2.689	MgO	10.211	0.276
Ca	6486	1.242	CaO	16.379	0.206
Na	470	4.609	Na ₂ O	4.050	0.188
K	127	8.889	K ₂ O	0.020	0.002
			Structural formula		
				Composition	Error (2σ)
			Si_{T1}	1.962	0.010
			Al_{T1}	0.038	0.010
			Al_{M1}	0.371	0.010
			Mg_{M1}	0.546	0.014
			Fe_{M1}	0.136	0.005
			Ca_{M2}	0.629	0.008
			Na_{M2}	0.281	0.013
			X_{Mg}	0.801	0.008
			X_{Fe}	0.199	0.008
			X_{jd}	0.281	0.013
			X_{di}	0.546	0.014
			X_{hed}	0.136	0.005
			X_{cats}	0.019	0.005

TABLE 3.7 – Uncertainties resulting from microprobe acquisition on raw data and error-propagation using Monte-Carlo techniques on quantified data and structural formula for clinopyroxene. The precision at 2σ on raw data (in %) was estimated by XMAPTOOLS using the equation 3.4 (see text) on the average intensity of all the pixels of clinopyroxene. This uncertainty was propagated on the quantification process using a Monte-Carlo simulation with $n=100,000$ analyses. In the same way, the uncertainty was propagated on the structural formula calculation process (including atom-site repartition).

3.2.3.3 Precision and resolution of quantification

In the previous section, maps of structural formulae highlight variations in clinopyroxene related to the symplectite microstructures. Na-content in clinopyroxene decrease with the decreasing size of the symplectite (i.e. along time). The clinopyroxene solid solution includes jadeite the sodic end-member, while diopside hedenbergite and Ca-tschermak are calcic end-members. As the multiplicity of the $M2$ site is one and the $X_{Fe^{3+}} = 0$ (corresponding to $X_{acm} = 0$), the jadeite proportion is equal to the Na-content in clinopyroxene. Estimating the uncertainties associated with the structural formulae is needed to understand the implications linked to the chemical zoning.

The precision of microprobe measurement with our experimental protocol can be estimated using a Poisson law (De Andrade et al. 2006) :

$$P = \frac{1}{\sqrt{n}} \quad (3.4)$$

in which p is the precision (in % at 2σ), and n the number of recorded counts. The

mean intensities and precision measurements for each element (Si, Ti, Al, Fe, Mg, Ca, Na, K) of clinopyroxene pixels are listed in table 3.7. The precision measurements range from 0.95 % for Si to 10.35 % for Ti. The possible errors in the structural formula steaming from the analytical errors were estimated using a Monte Carlo method : 100,000 compositions of clinopyroxene were randomly simulated using a normal distribution from the mean intensity compositions (table 3.7). The simulated distributions were set in order to reproduce the measured precisions. The standardization process was performed for all the compositions using the calibration curves estimated above. The average oxide concentrations and structural formulae, and the associated standard deviations (2σ) are listed in Tab. 3.7. The average Na-content is estimated at 0.28 ± 0.01 p.f.u., which indicates that the compositional variations identified above (ranging from 0.41 to 0.13) are significant.

3.2.3.4 Combined P and T functions : P-T maps of Cpx

P-T maps were built using the combined P and T functions available in XMAPTOOLS (description in § 3.2.3.4 and list in table 3.4). At the thin section scale, two assemblages involving clinopyroxene are in equilibrium : the HP assemblage made of garnet, omphacite and phengite (in inclusion in garnet, not present in the mapped area) and the retrogressed assemblage with symplectite made of clinopyroxene, plagioclase and amphibole. These two parageneses were treated separately.

For the HP assemblage, P-T conditions of clinopyroxene pixels were estimated using the XMAPTOOLS function 'Cpx-P-T Rav (Omp-Gar-Phg)'. The pressure was estimated using the garnet, omphacite and phengite geobarometer of Waters et Martin (1993) and Waters (1996). The temperature was estimated using the garnet and omphacite geothermometer of Korgh Ravna (2000b). As only the clinopyroxene composition changes (see discussion in Lanari et al. in press), garnet and phengite compositions were fixed and P-T estimates were calculated for all the clinopyroxene compositions. For given compositions of garnet, omphacite and phengite, the function estimates first T_1 at a given P (P_{input}), and recalculates T_{n+1} and P_{n+1} until convergence (respectively 5°C and 0.1 kbar) between T_n and T_{n+1} and P_n and P_{n+1} .

For the symplectite, temperature was first estimated using the edenite-richterite

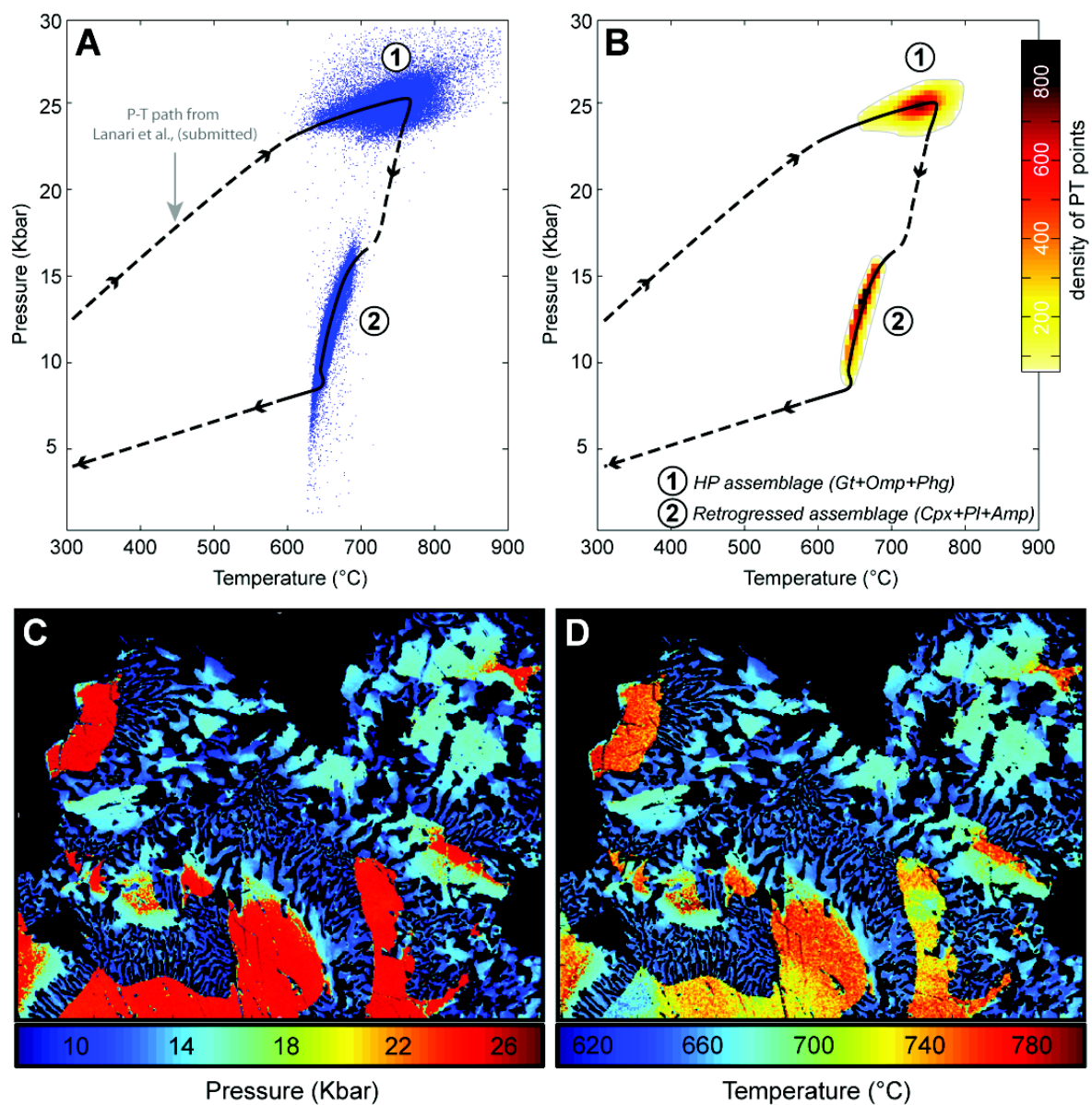


FIGURE 3.14 – P-T path and P-T maps of the Stak sample (from Lanari et al. in press) estimated from the compositions of clinopyroxenes.

calibration (Holland et Blundy 1994) with the composition of amphibole pixels for a fixed composition of plagioclase (function 'Amp-T HollandBlundy 1994a'). Temperature of amphibole was found to vary from 680°C in contact with Jd30% clinopyroxene to 640°C in contact with Jd10% clinopyroxene. Then, the pressure of clinopyroxene crystallization has been calculated using the calibration of Waters (2002; 2003) for the reaction : jadeite + tremolite \rightleftharpoons albite + edenite.

About 165,000 P-T calculations (one for each Cpx pixels) have been made, and the results have been plotted into binary diagrams (fig. 8a and 8b) using the module *Chem2D*, and into P and T maps (fig. 3.14 c and fig. 3.14 d). The density P-T diagram option (fig. 3.14 b) plotted using *Chem2D* module shows that the apparent deviation in pressure is composed of a small amount of points (< 1%). In contrast for the temperature, the density diagram shows a significant trend corresponding to the prograde evolution from 650°C to 750°C. This increase in T along the prograde path at constant pressure is confirmed by the distribution of temperature and pressure in map : The omphacite grains show a constant pressure at 25 kbar, but are zoned in temperature from 650°C in the old grain cores to 750°C in the old grain rims. Clinopyroxene in the symplectite shows a different trend with a decrease of both P and T with the increasing size of the intergrowths. This example is adapted to illustrate the importance of the mapping approach that allows to check for the relationships between P-T conditions and the microstructures.

3.2.4 Concluding remarks

(1) This paper describes in details XMAPTOOLS a MATLAB©-based GUI program for microprobe image processing. The current version is available from the website <http://www.xmaptools.com>. XMAPTOOLS requires Matlab© version 7.5 Release R2007b or later version. The current version also requires the Matlab© statistics toolbox. The main graphic interface is optimized for the different steps of processing with the separation into three tabs : 'Xray', 'Quanti' and 'Results'. In addition, two external modules *Chem2D* and *TriPlot3D* with independent graphic interfaces to plot chemical diagrams were provided.

- (2) XMAPTOOLS package includes 15 main functions used for the different processing steps. These functions are the base of XMAPTOOLS (see Fig. 3.9), from the raw data loading to the P-T maps. Additional functions such as save, save as and load are provided. The figure can be managed using the following functions : export, contrast, filters and sampling.
- (3) A set of 50 specific functions is included and will be regularly updated. These functions include structural formulae functions for the main minerals and empirical and semi-empirical geothermobarometers from the literature. Moreover, additionally functions make it possible to combine existing geothermometer and geobarometer for a given assemblage.
- (4) In order to illustrate the XMAPTOOLS using, we tested the program on an eclogite sample from the Stak massif (Pakistan, NW Himalaya). The precision and the resolution of the standardization were investigated using a Monte-Carlo simulation approach highlighting the high precision of the method. The study of the Na distribution in clinopyroxene shows that the estimated uncertainty is much smaller than the chemical variability, which allows detailed investigation of the compositional-structural-P-T relationships.
- (5) The quantitative mapping in wavelength dispersive mode (WDS) following the procedure of [De Andrade et al. \(2006\)](#) has a better precision than the classically qualitative mapping in energy dispersive mode (EDS).
- (6) XMAPTOOLS will be use for further developments. Future versions will include modules for the estimation of local bulk composition from quantified structural formulas maps. This specific point will be discussed in a forthcoming paper. The new version will be also updated with the addition of thermodynamic modelling tools (multi-equilibrium using all the reactions and pseudosection) in development.

3.2.5 Acknowledgments

We acknowledge A. Pourteau (Univ. Potsdam) for his assistance during the electron microanalysis. This work was supported by ANR-projects Cattel PAKSIS and ERD-Alps. We warmly thank B. Gardonio, F. Bernier, N. Riel, A. Robert, C. Martin, M. Munoz, F. Guillot, S. Guillot, B. Sauter for constructive comments and the test of the preliminary versions of XMAPTOOLS.

3.2.6 Appendix : User Notice

The XMAPTOOLS « user notice » document is available in the Annexe [A.4](#)

3.3 ARTICLE 4 : REE AND Hf DISTRIBUTION AMONG MINERAL PHASES IN THE CV-CK CLAN : A WAY TO EXPLAIN ϵ_{Hf} HETEROGENEITIES IN CHUR (SUBMITTED TO GEOCHIMICA AND COSMOCHIMICA ACTA)

★ *L'étude dans les chondrites, de la concentration et de la distribution en éléments de Terres Rares et en Hf, nécessite de connaître avec la plus grande précision les abondances modales des différentes phases.*

★ *L'utilisation des spectromètres WDS pour acquérir des images chimiques permet d'obtenir une meilleure limite de détection ainsi qu'une meilleure résolution pour identifier les variations chimiques dans un échantillon. Le logiciel XMAP-TOOLS présenté précédemment permet, à partir d'images chimiques, d'attribuer statistiquement chaque pixel à une phase minérale définie par l'utilisateur.*

★ *Dans cette partie, nous allons utiliser des images chimiques acquises sur des échantillons de chondrites et le logiciel XMAPTOOLS. L'objectif était d'identifier les différentes phases minérales en utilisant les modules chimiques CHEM2D et TRI-PLOT3D. Puis les abondances modales ont été calculées par le biais d'une approche statistique. Ces abondances ont servi à étudier l'évolution des concentrations en terres rares et en Hf, calculées en utilisant des bilans de masses. Ces résultats seront présentés sous la forme d'un article de Martin et al. soumis pour publication à la revue Geochimica and Cosmochimica Acta.*

REE and Hf distribution among mineral phases in the CV-CK clan : a way to explain ϵ Hf heterogeneities in CHUR

Céline Martin⁶, Vinciane Debaille⁷, Pierre Lanari⁸, Steven Goderist^{6,9}, Frank Vanhaecke⁹, Olivier Vidal⁸, Philippe Claeys⁶

To be submitted to Geochimica and Cosmochimica Acta

Abstract - Chondrites are among the most primitive objects in the Solar System and constitute the main building blocks of telluric planets. Among radiochronometers currently used for dating geological events, Sm-Nd ($\lambda^{147}\text{Sm} = 6.54 \times 10^{-12}\text{year}^{-1}$) and Lu-Hf ($\lambda^{176}\text{Lu} = 1.85 \times 10^{-11}\text{year}^{-1}$) are both composed of refractory and lithophile elements. They are thought to behave similarly as the parent elements (Sm and Lu) are generally less incompatible than the daughter elements (Nd and Hf) during geological processes. As such, their respective average isotopic compositions for the solar system are expected to be well defined by the average of chondrites, called Chondritic Uniform Reservoir. However, where the Sm-Nd isotopic system shows an actual spread of less than 4% in the average chondritic record, the Lu-Hf system shows a larger variational range of 28%. To better understand these different behaviors, this work examined the evolution of REE and Hf distribution among mineral phases during metamorphism of Karoonda-like (CK) and Vigarano-like (CV) carbonaceous chondrites. Trace-element patterns obtained for the first time in all the chondrite-forming minerals of a given class highlight many similarities between $\text{CV}_{\text{ox}}\text{B}$ and CK, suggesting that these chondrites groups could have a closely related origin. They also reveal that phosphates are not the main carrier of REE, contrary to what is usually assumed. Only 30 to 40%

6. Earth Science System, Vrije Universiteit Brussel, Pleinlaan 2, 1050 Brussels, Belgium

7. Laboratoire G-Time, Université Libre de Bruxelles, avenue F. Roosevelt 50, CP 160/02, 1050 Brussels, Belgium

8. ISTERre, University of Grenoble 1, CNRS, 1381 rue de la Piscine, 38041 Grenoble, France

9. Department of Analytical Chemistry, University of Ghent, Belgium

of Sm and Nd are stored in phosphates (at least in chondrites type 3 to 5) where they behave concomitantly. As such, they are not mobilized during early stages of metamorphism. The part of phosphate in Lu budget significantly decreases as the degree of metamorphism increases (30% for type 3 and 4, less than 1% in type 6). On the contrary, Hf is mainly hosted by silicates while phosphates do not contribute much to the Hf budget. These results indicate that the dichotomy of the main hosts of Sm, Nd and Lu on one hand and Hf on the other hand, and the resulting redistribution of Lu and Hf during metamorphism-linked recrystallization likely explain the heterogeneities observed in the CHUR for the Lu-Hf system.

3.3.1 Introduction

Chondrites represent the most primitive and undifferentiated meteorites. It is generally assumed that the Earth and other telluric planets in the inner solar system formed by chondrite accretion, after which they differentiated. As such, the average chondritic composition for lithophile and refractory elements, the Chondritic Uniform Reservoir (CHUR), serves as chemical reference for geochemical studies of the Earth and other planets. It also constitutes a reference for several radioactive isotopic systems, in particular ^{147}Sm - ^{143}Nd and ^{176}Lu - ^{176}Hf . Since the initial Earth is supposed to be chemically similar to CHUR, the evolution of the Bulk Silicate Earth should be close to that of the CHUR (Jacobsen et Wasserburg 1979). Knowing the initial composition of the Earth makes it possible to model the evolution of the terrestrial reservoirs (e.g. Jacobsen et Wasserburg 1979, Blichert-Toft et Albarède 1997). Recently, it appeared that while ϵNd values of chondrites are relatively homogeneous (-5.40 to $+2.73\epsilon$ units), ϵHf values display much larger scattering (-20.40 to $+5.87\epsilon$ units; Fig. 3.15). The ϵ notation is defined (example for Hf) as $\epsilon_{\text{Hf}} = \frac{(\frac{^{176}\text{Hf}}{^{177}\text{Hf}})_{\text{sample}} - (\frac{^{176}\text{Hf}}{^{177}\text{Hf}})_{\text{CHUR}}}{(\frac{^{176}\text{Hf}}{^{177}\text{Hf}})_{\text{CHUR}}} \times 1000$. In order to reduce the spread observed for the Lu-Hf system, Bouvier et al. (2008) suggested to calculate Hf CHUR values based only on type 3 chondrites, i.e. the less altered, either by aqueous alteration or by thermal metamorphism and thus the less chemically equilibrated. However, as planets are composed of chondrites of various metamorphic types, it is not satisfactory to simply dismiss the majority of chondrites to calculate their average composition.

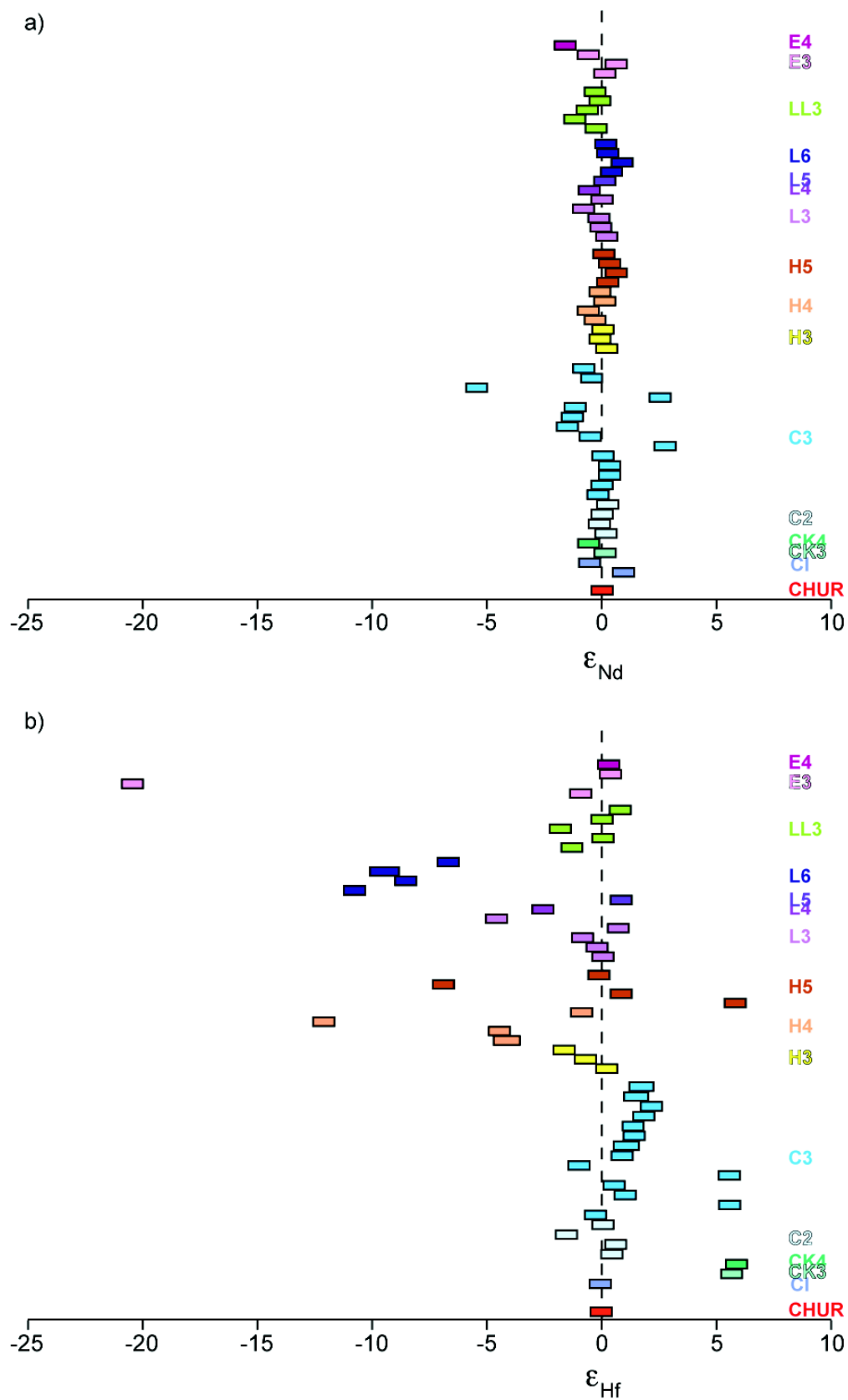


FIGURE 3.15 – Epsilon values in chondrites compared to CHUR. a) for Nd and b) for Hf. Values are from *Patchett et al. (2004)* and *Bouvier et al. (2008)*.

Rather it is imperative to document the reasons for the problematic behavior of the Lu-Hf system compared to Sm-Nd.

While little data are available on Rare Earth Element (REE) and Hf contents in some minerals in meteorites, no study has yet focused solely on the distribution of REE and Hf among mineral phases in the frame of the Sm-Nd/Lu-Hf dichotomy. It is usually assumed that phosphates bear the entire REE budget in ordinary chondrites (OC) and sulfides in enstatite chondrites (EC) (Bearley et Jones 1998, Yongheng et al. 1993). The only studies focusing on phosphates in OC so far show concentrations up to 130 ppm of Nd and 40 ppm of Sm, 4 ppm of Lu and less than 0.05 ppm of Hf (Amelin et Rotenberg 2004, Amelin 2005). The only study on REE content in sulfides in OC (Kong et al. 2000) concluded that the LREE content could be up to 3 ppm with decreasing values toward HREE (less than 0.12 ppm), while Hf contents were not measured. Similar analyses on carbonaceous chondrites (CV and CR, Mason et Martin 1974, Jacquet et al. 2012) showed low concentrations in olivines (0.01 to 0.1 times CI chondrites) and low-Ca pyroxene (0.1 to 0.5 times CI chondrites) but significantly higher values in high-Ca pyroxene (1 to 10 times CI chondrites). However, none of these studies have investigated the possible variations in REE and Hf contents during metamorphism, especially as some mineral phases may be replaced by new phases.

To address this issue, we selected a complete suite of CK chondrites because carbonaceous chondrites are among the most pristine material of the Solar System (Bearley 1997) and CK are the only carbonaceous meteorites that have undergone metamorphism, from type 3 to 6. This is important as higher metamorphic types (4 and higher) seems to be related to a larger dispersion in the Lu/Hf value (up to 28%, Patchett et al. (2004)), compared to lower metamorphic types (below type 4; 7% of variations) (Bouvier et al. 2008). As part of this study, we have also selected one CV3 chondrite, as the CK and CV chondrites are assumed to share a closely related origin and are informally referred to as the CV-CK clan, (Weisberg et al., 2006). The arguments in favor of a common origin include similar oxygen isotopes and resemblances in petrology and mineralogy (Greenwood et al. 2010). Indeed, CK represents the most oxidized chondrites (Kallemeyn et al. 1991) and

two among the three subgroups of CV are also oxidized (Allende-like $\text{CV}_{\text{ox}}\text{A}$ and Bali-like $\text{CV}_{\text{ox}}\text{B}$, [Weisberg et al. 1997](#)), and contain magnetite rather than native iron. However, [Richter et Neff \(2007\)](#) suggest that the presence of magnetite in CV_{ox} is due to aqueous alteration inside the parent body whereas in CK samples, the oxidation process responsible for magnetite occurs before agglomeration of the meteorite ([Rubin 1992](#)). Clearly, the idea of a unique parent body for CV and CK remains a matter of debate (e.g. [Richter et Neff 2007](#), [Greenwood et al. 2010](#), [Davidson et al. 2012](#), [Isa et al. 2012](#)).

The present work addresses the evolution of mineral-phases modal abundances during thermal metamorphism as well as the content of REE and Hf in mineral phases in CV3 and CK types 3 to 6. Mass balances are calculated for each sample and the distribution of REE and Hf among chondritic mineral phases will be discussed together with the possibility to link CVs and CKs to the same "clan".

3.3.2 Meteorites samples, preparation and analytical techniques

3.3.2.1 Samples preparation

Three samples of CK chondrites were selected among the collection of Antarctic meteorites from the NASA and National Institute of Polar Research of Tokyo (NIPR) collections to avoid weathering effects as much as possible. The samples Elephant Moraine 92002 (*EET92002* further) and Asuka-881277 (*A-881277*) are CK5. Yamato-82191 (*Y-82191*) represents the CK6. Three hot deserts meteorites were added to cover the whole range of metamorphic degrees : NWA 5956 as CK3, NWA5772 as CV3 and NWA 5798 as CK4.

Each sample was cut with diamond wire saw at the Université Libre de Bruxelles. No water or other fluid was used during sawing to avoid possible dissolution of some mineral phases, aqueous contamination or oxidation. Then, the obtained chondrites pieces ($< 2.5\text{ cm}$ in size) were then mounted in Epoxy resin and finally polished with ethanol, again to minimize oxidation

3.3.2.2 Analytical techniques

First, samples were observed by Scanning Electron Microscope (JEOL JSM-6400, Vrije Universiteit Brussel and JEOL JXA-8600, Université Libre de Bruxelles) to select areas as representative as possible of the bulk sample. Subsequently, compositional X-ray maps were acquired on the selected areas using an Electron Probe Micro-Analyzers (EPMA) CAMECA SX100 or CAMECA SXFive (Camparis, Université Pierre et Marie Curie, Paris 6, France) in wavelength dispersive mode (WDS spectrometers). The mapping conditions were 15 *keV* accelerating voltage, 100 *nA* beam current, 3 μm beam size and 100 *ms* counting time (following the procedure of [De Andrade et al. 2006](#)). Compositional X-ray maps were acquired for Si, Fe, Ca, Na, S, P, Ni, Cr and Mg. During the same microprobe session, high-quality point analyses (standard conditions : 15 *KeV*, 10 *nA*, 3 μm and 20 *s*) of all phases occurring in the scanned area were also performed. These analyses are used to transform the X-ray maps of composition into maps of element composition (wt%) using the software XMAPTOOLS v1.5.1 ([Lanari et al. 2012a](#); [in press](#)).

For the determination of the trace element contents, whole rock aliquots were carefully crushed in a dedicated agate mortar. Then, the powdered samples (45 to 95 *mg*) were digested in Teflon beakers in a mixture of HF and HNO₃ (2 :1). After evaporation, HCl was added to ensure digestion of oxides and dissolution of fluoride that might have formed during the HF step. The solutions were visually clear. After dilution, Ba, REE, Hf and Co were analyzed by ICP-MS (Element XR, ThermoFisher) at Gent University (Belgium). To monitor analytical reproducibility, geostandards BHVO-2 of the US Geological Survey (USGS), and SRM694 of the National Institute of Science and Technologies were dissolved and analyzed under the same conditions. Total reproducibility is better than 5% for REE and 10% for Hf. Data are presented in Table [3.8](#).

elements	BHVO-1 2G ¹	BHVO-2G (ICP-MS)	BHVO-2G (LA-ICP-MS)	NIST 694 ²	NIST 694 (ICP-MS)	BIR- 1G ¹	BIR-1G (LA-ICP-MS)	GSD- 1G ¹	GSD-1G (LA-ICP-MS)	Detection limits
Ba	131	132 ± 3.67	n.d.	111	102 ± n.d.	52	n.d.	40	n.d.	-
Co	44	45 ± 1.2	34.51 ± 11.65	98	91.88 ± 0.64	54.85 ± 0.61	54.85 ± 0.61	34.00 ± 0.20	31.09 ± 0.20	6.929 ± 2.72
La	15.2	15.5 ± 0.07	16.83 ± 0.64	98	91.88 ± 0.64	0.70 ± 0.17	0.70 ± 0.17	39.1 ± 0.20	40.55 ± 0.20	1.55 ± 0.073
Ce	37.6	39.0 ± 0.59	28.15 ± 2.24	26	23.31 ± 2.24	1.89 ± 0.17	2.30 ± 0.17	41.4 ± 0.37	40.05 ± 0.37	1.55 ± 0.063
Pr	5.35	5.49 ± 0.10	5.34 ± 0.20	n.d.	7.68 ± 0.20	0.37 ± 0.19	0.39 ± 0.19	45 ± 0.09	43.46 ± 0.09	1.59 ± 0.038
Nd	24.5	25.5 ± 0.77	21.65 ± 1.12	48	45.40 ± 1.12	2.37 ± 1.11	2.18 ± 1.11	44.7 ± 0.49	39.74 ± 0.49	1.83 ± 0.095
Sm	6.1	6.34 ± 0.19	5.84 ± 1.07	7.5	7.21 ± 1.07	1.09 ± 0.19	1.12 ± 0.19	47.8 ± 0.35	41.48 ± 0.35	2.91 ± 0.047
Eu	2.07	2.06 ± 0.01	2.25 ± 0.38	1.7	1.54 ± 0.38	0.52 ± 0.03	0.52 ± 0.03	41 ± 0.19	40.36 ± 0.19	2.05 ± 0.486
Gd	6.16	6.25 ± 0.13	5.95 ± 0.52	10.3	9.02 ± 0.52	1.85 ± 0.17	1.79 ± 0.17	50.7 ± 0.56	47.15 ± 0.56	2.60 ± 0.713
Tb	0.92	0.98 ± 0.03	0.86 ± 0.08	1.4	1.28 ± 0.08	0.35 ± 0.03	0.29 ± 0.03	47 ± 0.10	42.85 ± 0.10	2.20 ± 0.024
Dy	5.28	5.55 ± 0.14	5.53 ± 0.78	n.d.	8.52 ± 0.78	2.55 ± 0.24	2.68 ± 0.24	51.2 ± 0.65	48.89 ± 0.65	2.36 ± 0.053
Ho	0.98	1.01 ± 0.03	1.00 ± 0.12	2.2	2.07 ± 0.12	0.56 ± 0.07	0.49 ± 0.07	49 ± 0.13	47.94 ± 0.13	2.61 ± 0.034
Er	2.56	2.65 ± 0.07	2.46 ± 0.27	6.7	6.47 ± 0.27	1.7 ± 0.20	1.46 ± 0.20	40.1 ± 0.40	35.51 ± 0.40	2.82 ± 0.092
Tm	0.34	0.36 ± 0.01	0.31 ± 0.10	1	0.94 ± 0.10	0.24 ± 0.03	0.25 ± 0.03	49 ± 0.08	45.74 ± 0.08	3.05 ± 0.025
Yb	2.01	2.12 ± 0.06	2.09 ± 0.34	6	5.65 ± 0.34	1.64 ± 0.13	1.56 ± 0.13	50.9 ± 0.42	47.75 ± 0.42	3.43 ± 0.025
Lu	0.28	0.29 ± 0.01	0.28 ± 0.06	1	0.90 ± 0.06	0.25 ± 0.02	0.22 ± 0.02	51.5 ± 0.09	48.63 ± 0.09	2.59 ± 0.019
Hf	4.32	4.56 ± 0.12	4.41 ± 0.52	n.d.	0.40 ± 0.52	0.57 ± 0.00	0.43 ± 0.00	39 ± 0.19	36.92 ± 0.19	1.90 ± 0.082

¹ Jochum et Stoll (2008) ; ² Hollocher et al. (1995)

TABLE 3.8 – Geostandards analyses and detection limits (all values in ppm).

The in situ analyses of REE and Hf were performed using a New Wave Research UP₁₉₃HE ArF* excimer-based laser ablation system coupled to an Element XR (ThermoFisher) double-focusing sector field ICP-MS at Ghent University, Belgium. The following isotopes were determined : ^{24}Mg , ^{29}Si , ^{44}Ca , ^{47}Ti , ^{57}Fe , ^{59}Co , ^{139}La , ^{140}Ce , ^{142}Ce , ^{141}Pr , ^{144}Nd , ^{146}Nd , ^{147}Sm , ^{152}Sm , ^{153}Eu , ^{159}Tb , ^{163}Dy , ^{165}Ho , ^{166}Er , ^{169}Tm , ^{172}Yb , ^{174}Yb , ^{175}Lu , ^{178}Hf , ^{180}Hf . Analysis was performed via single spot (30 μm) ablation at a repetition rate of 10 Hz and a monitored energy density of 10 J/cm^2 on the sample surface. Using ^{47}Ti as internal standard, quantification was performed via external calibration versus several glass reference materials (USGS natural and synthetic glasses BHVO-2G, BIR-1G, and GSD-1G). Based on the standards and settings described, reproducibilities for the elements measured are typically between 5 and 10% RSD. The results obtained with Ti normalization were crosschecked with Ca or Mg normalization. The trace element concentration presented in part 3.3.3.2 represent the averages on n measurements and the errors were calculated as the standard deviation divided by \sqrt{n} . Detection limits (Tab. 3.8) were calculated for each analysis as the trace element concentrations in blank. The detection limits for Eu and Gd were significantly higher than for the other REE (one order of magnitude) and mineral concentrations were only sporadically measured for these two elements. Although presented in the In situ trace element data part (3.3.3.2) the data for these elements will not be used further for mass balance calculations or to interpret trace elements patterns.

Additionally, Nd and Sm were also measured in phosphates from EET92002 (the only sample with large enough phosphate crystals, 50-100 μm) by EPMA (CAMECA SX50, Camparis, Université Pierre et Marie Curie, Paris 6, France) using an acceleration voltage of 25 keV and a beam current of 500 nA . Each electron probe measurement represents the average of ten points analyzed within the same crystal.

3.3.3 Results

3.3.3.1 Samples petrology

Chemical variations within and between the phases present in the mapped areas were investigated using the modules CHEM2D and TRIPlot3D of XMAPTOOLS. The "Mask function" was used to allocate the pixels of the measured compositional map(s) to each of the occurring phases using a clustering approach (K-means method, details in [De Andrade et al. 2006](#)). After the pixel the mineral phases were contoured in a "mask image" allocation (see fig. [3.16-b](#), [3.16-d](#), [3.16-f](#), [3.16-h](#)), and their integrated surfaces and modal abundances were calculated. The modal abundances are presented as percentages of the mapped area (% m.a.) in the following. Two maps were acquired only on CK5 EET92002 and CK6 Y82191 to have an overview of the statistical representation.

In sample NWA 5956 (CK3), Back Scattered Electron (BSE) images reveal several chondrules of a maximum size of 300 μm , sometimes rimmed by or including opaque minerals (Fig. [3.16-a](#)) as well as smaller chondrules ($< 100 \mu\text{m}$) of opaque phases, embedded in the matrix. Fig. [3.16-b](#) presents the mask image obtained with XMapTools. The matrix, which is composed of a mixture of minerals with affinities to cronstedite, chrysotile and saponite, is the main component (63.76% m.a.). Mesostasis (9.90% m.a.) is found as interstitial phase inside the chondrules. Low-Ca pyroxene (15.44% m.a.) locally constitutes the main chondrule phase. The mapped area shows small (250 μm) olivine (5.20% m.a.), always as euhedral crystals and almost always within chondrules. Taenite (0.20% m.a.), generally weathered in lawrencite, is still present in the sample in close association with pyrrhotite (4.23% m.a.) and apatite (0.28% m.a.).

Large chondrules (1 – 2 mm) with euhedral olivine crystals (17.01% m.a.) and low-Ca pyroxene (25.42% m.a.) are visible in NWA 5772 (CV3). Mesostasis (8.67% m.a.) is found as interstitial phase in chondrules. The fine-grained matrix (47.28% m.a.) is made of phyllosilicates. The only accessory phase present is magnetite (1.60% m.a.) either as relatively large crystals (up to 150 μm length) inside the chondrules or as very small ones (few microns) distributed within the matrix. Considering that this sample contains magnetite, not native Fe, and that phyllo-

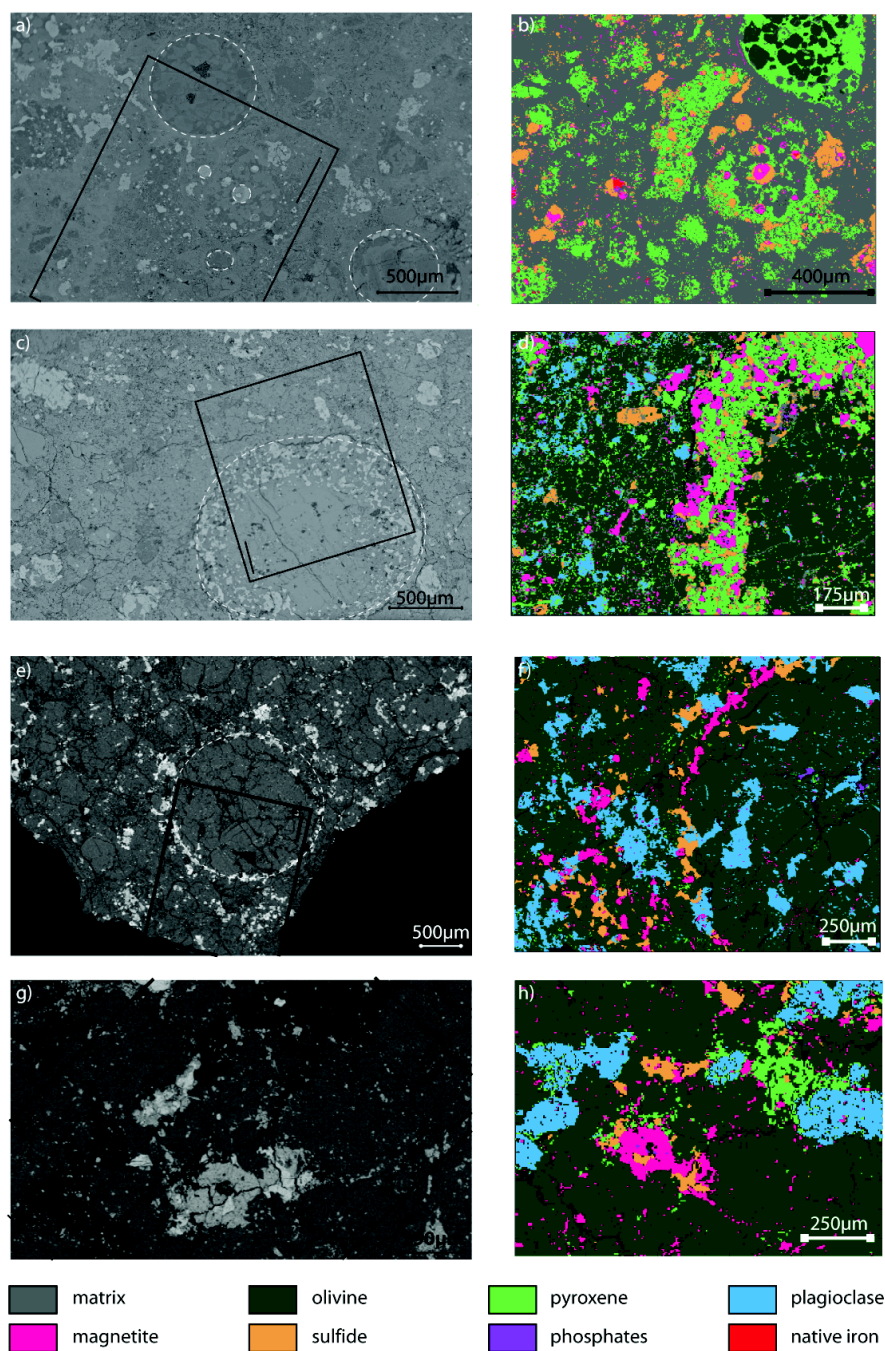


FIGURE 3.16 – a) BSE and b) mask image of CK3 NWA 5956, c) BSE and d) mask image of CK4 NWA 5798, e) BSE and f) mask image of CK5 EET92002, g) BSE and h) mask image of CK6 Y-82191. On BSE images, chondrules are highlighted with white dotted line and mask image area with black rectangle

silicates compose the matrix, it belongs to the Bali-like oxidized subgroup ($CV_{ox}B$), in agreement with classifications of [McSween \(1977\)](#) and [Weisberg et al. \(1997\)](#).

NWA 5798 represents the CK4 chondrites. Chondrules are scarce (Fig. 3.16-c) and overprinted by a rim of opaque phases and low-Ca pyroxene (14.76% m.a.), whereas the phyllosilicated matrix is almost totally (9.48% remaining) recrystallized into olivine (54.74% m.a.) and plagioclase (4.26% m.a.). High-Ca pyroxene (5.37% m.a.) is xenomorphous. Clusters of pentlandite (3.68% m.a.) and magnetite (7.28% m.a.) with exsolutions of ilmenite, together with merrillite (0.42% m.a.), either found in association with opaque minerals or as single crystals, are distributed throughout the matrix (Fig. 3.16-d).

In samples CK5 EET92002 and A-881277 the chondrules are barely discernible (Fig. 3.16-e). Olivine crystals ($79.02 \pm 2.11\%$ m.a.) are euhedral and large (up to $500 \mu m$). Xenomorphous plagioclase ($8.02 \pm 5.46\%$ m.a.) occurs both inside the chondrules and in the matrix whereas xenomorphous low-Ca pyroxene (2.39% m.a., only measurable in A-881277) and high-Ca pyroxene ($2.22 \pm 1.35\%$ m.a.) are usually found in the matrix. The size ranges from $30 \mu m$ for pyroxenes to $100 \mu m$ for plagioclase. Pentlandite ($4.40 \pm 1.84\%$ m.a.) and magnetite ($5.19 \pm 1.21\%$ m.a.) are again found in close association, locally surrounding chondrules (Fig. 3.16-e). Merrillite crystals ($0.64 \pm 0.42\%$ m.a.) display the largest sizes among all the CK chondrites studied ($50\text{-}100 \mu m$). They occur either in association with sulfide - magnetite or as single grains (Fig. 3.16-f).

Chondrite CK6 Y-82191 underwent the strongest metamorphism and the chondrules are not discernible (Fig. 3.16-g). Olivine ($73.05 \pm 2.85\%$), plagioclase ($9.03 \pm 1.97\%$ m.a.) and high-Ca pyroxene ($6.11 \pm 0.88\%$ m.a.) are xenomorphous whereas magnetite ($9.09 \pm 0.54\%$ m.a.) is either xenomorphous or present as framboidal crystals. Xenomorphous sulfides (pentlandite and pyrrhotite, $2.54 \pm 0.58\%$ m.a.) as well as small merrillite ($< 10 \mu m$, $0.08 \pm 0.00\%$ m.a.) are associated with magnetite (Fig. 3.16-h). Rare and small crystals of spinel ($< 1 \mu m$) occur in this sample.

	CV3 NWA 5772	CK3 NWA 5956	CK4 NWA 5798	CK4/5 Y-693	CK5 EET-92002	CK5 A-881277	CK6 Y-82191	
Co	80.216 ±	27.691 ±	12.324 ±	74.710 ±	n.d.	308.218 ±	105.518 ±	52.666 ±
La	0.189 ±	0.050 ±	0.005 ±	0.018 ±	0.258 ±	0.191 ±	0.136 ±	0.022 ±
Ce	0.479 ±	0.162 ±	0.016 ±	0.278 ±	0.478 ±	1.358 ±	0.959 ±	0.246 ±
Pr	0.025 ±	0.004 ±	0.001 ±	< d.l.	0.101 ±	0.037 ±	0.117 ±	0.033 ±
Nd	0.173 ±	0.073 ±	0.081 ±	< d.l.	0.607 ±	0.156 ±	0.165 ±	0.038 ±
Sm	0.060 ±	0.039 ±	< d.l.	< d.l.	0.259 ±	0.050 ±	0.084 ±	0.006 ±
Eu	< d.l.	< d.l.	0.208 ±	< d.l.	< d.l.	< d.l.	0.304 ±	
Gd	< d.l.	< d.l.	0.334 ±	< d.l.	0.520 ±	< d.l.	0.422 ±	0.025 ±
Tb	0.040 ±	0.002 ±	0.002 ±	0.006 ±	0.048 ±	0.023 ±	0.053 ±	0.008 ±
Dy	0.125 ±	0.030 ±	0.037 ±	0.009 ±	0.273 ±	0.080 ±	0.088 ±	0.015 ±
Ho	0.026 ±	0.014 ±	0.003 ±	0.064 ±	0.059 ±	0.025 ±	0.048 ±	0.002 ±
Er	0.087 ±	0.016 ±	0.013 ±	0.103 ±	0.329 ±	0.073 ±	0.126 ±	0.033 ±
Tm	0.027 ±	0.006 ±	0.000 ±	0.004 ±	0.053 ±	0.011 ±	0.002 ±	0.006 ±
Yb	0.202 ±	0.043 ±	0.034 ±	0.027 ±	0.438 ±	0.063 ±	0.015 ±	0.025 ±
Lu	0.021 ±	0.002 ±	0.000 ±	0.007 ±	0.077 ±	< d.l.	0.144 ±	0.005 ±
Hf	0.841 ±	0.554 ±	0.009 ±	0.048 ±	0.199 ±	0.037 ±	0.034 ±	0.026 ±
n	7	6	13	4	7	7	9	

n.d. : not determined, < d.l. : below detection limit, n = number of analyses

TABLE 3.9 – Olivine compositions (all values in ppm).

3.3.3.2 In situ trace-elements data

The REE and Hf contents are reported for magnetites, sulfides and silicates (two types of pyroxene, olivine, plagioclase and matrix) in all samples when the crystals are large enough to measure ($< 30 \mu m$). Due to the small size of the phosphate crystals, only two analyses were performed by Laser Ablation and two by EPMA

In olivine, the REE and Hf concentrations are similar (Tab. 3.9) for all CK chondrites and in CV3. They range from $607 \pm 169 \text{ ppb}$ for LREE (La-Sm) to 12 ppb for HREE (Tb-Lu ; Tab. 3.9). Hf contents usually range from 200 to 300 *ppb* in metamorphosed types whereas it is significantly lower in CK3 ($38 \pm 9 \text{ ppb}$) and significantly higher in CV3 ($841 \pm 554 \text{ ppb}$). In pyroxene, the REE contents vary according to the type of pyroxene. Low-Ca pyroxenes have REE contents similar to those of olivines, with a maximum of $324 \pm 96 \text{ ppb}$ of LREE and $7 \pm 1 \text{ ppb}$ of HREE. The Hf values show more scattering, from 129 to 529 *ppb* in CK chondrites and less than 50 *ppb* in CV3 chondrite. High-Ca pyroxenes from samples CK5 EET92002 and CK6 Y-82191 have higher contents for both REE and Hf, with values between 1 and 2 *ppm* (Tab. 3.9). High-Ca pyroxene from sample CK4 NWA 5798 presents lower values for MREE and HREE (500 *ppb* to 1.5 *ppm*). The matrix of type 3 chondrites is relatively rich in REE, with a maximum of $856 \pm 96 \text{ ppb}$ for LREE and a minimum of $42 \pm 11 \text{ ppb}$ for HREE, whereas Hf contents are close to 200 *ppb*. Plagioclase displays significant scattering of REE concentrations ; CK6 Y-82191 is the most enriched sample in LREE with values up to $1.825 \pm 0.385 \text{ ppm}$ whereas the other CK4-CK5 samples have values lower than 500 *ppb*. HREE range from 56 to 557 *ppb*, except for Dy in CK6 ($1.264 \pm 0.009 \text{ ppm}$). The Hf values in plagioclase are more homogeneous than the REE values in the different types of chondrite and range from 238 ± 103 to $437 \pm 207 \text{ ppb}$ (Tab. 3.9). It should be pointed out that the thin but elongated shape of the plagioclase renders analyses difficult considering the size of the laser beam. In addition, concentrations in plagioclase are often below to the detection limit of the LA-ICP-MS, explaining the data missing in Table 3.9.

Magnetites display significant concentration discrepancies, with high enrichment up to 5 *ppm* from La to Dy, and between 867 ± 128 to $135 \pm 23 \text{ ppb}$ for the other HREE for CV3 (NWA 5772). The CK4 (NWA 5798) and CK6 (Y-82191) values

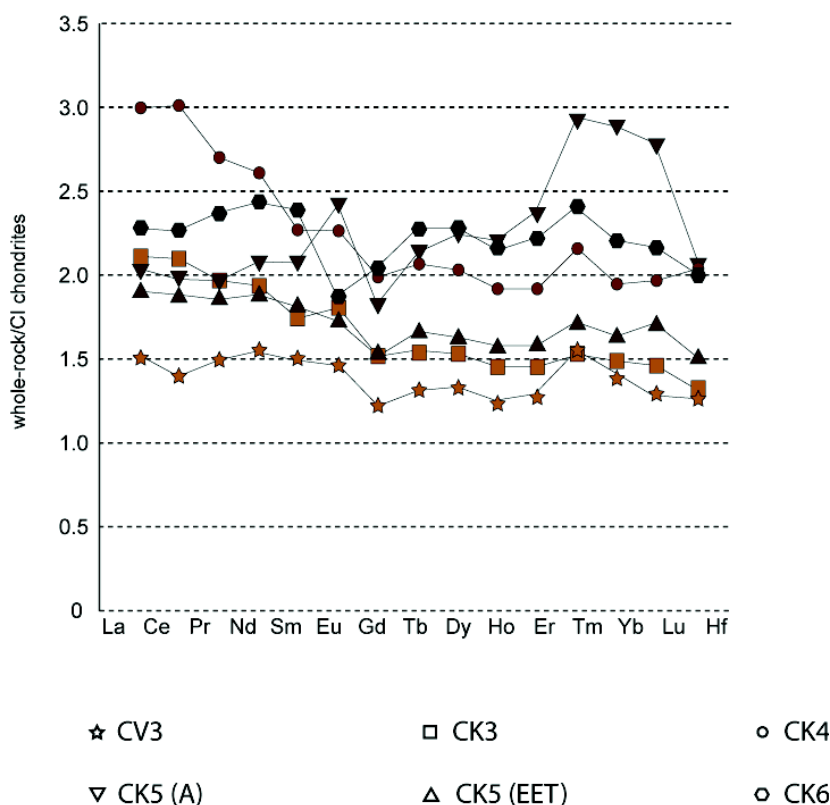


FIGURE 3.17 – Trace-element patterns on whole-rocks normalized to CI chondrites (Barrat et al. 2012).

range from 300 to 500 *ppb*, whereas CK5 samples (EET92002 and A-881277) appear less enriched (REE contents lower than 250 *ppb*). The Hf content in magnetite decreases notably from type 3 sample (400 *ppb*) to type 6 sample (below detection limit) with 300 *ppb* for type 4 and 75 *ppb* for type 5 samples (Tab. 3.9). Among the analyzed accessory minerals, sulfides have the lowest incompatible trace element contents. REE values often fall below detection limits and when measurable, they range from 17 *ppb* ($n = 1$) to 271 ± 44 *ppb*, except Ce which ranges from 100 to 500 *ppb*. In NWA 5798 (CK4), all the REE contents remain lower than 15 *ppb* (Tab. 3.9). Hafnium ranges from 11 ± 4 to 80 ± 12 *ppb*. Only one laser shot was possible on the small phosphate phases in NWA 5798 (CK4) and one in EET92002 (CK5). The results indicate that the contents are 2-3 times (for LREE and Hf) to 8-9 times (for HREE) higher in CK4 than in CK5, with respective values ranging from 3 to 80 *ppm* and from 0.4 to 30 *ppm* for the REE and 0.24 and 0.1 *ppm* for Hf (Tab. 3.9).

These data are in the same order of magnitude than those obtained by EPMA on EET92002 ($Nd = 82 \pm 37 \text{ ppm}$, $n = 2$ and $Sm = 42 \pm 33 \text{ ppm}$, $n = 2$).

3.3.3.3 Whole-rock analyses

All the CK samples are 1.5 to 2.5 times enriched in REE and Hf compared to CI chondrites (Fig. 3.17), except Tm, Yb and Lu in CK5 A-881277 that are almost 3 times larger than CI chondrites.

The REE and Hf concentration patterns (normalized to CI chondrites [Barrat et al. 2012](#)) are slightly less fractionated with increasing metamorphism. Indeed, CK3 and CK4 samples have (La/Yb)_N of respectively 1.43 and 1.55, whereas CK5 EET92002 has (La/Yb)_N of 1.18 and CK6 an almost flat pattern ((La/Yb)_N = 1.03). Sample CK5 A-881277 displays a singular behavior, with (La/Yb)_N = 0.71, that is likely due to the high enrichment of HREE in this sample.

Sample CV3 NWA 5772 is enriched 1.3 to 1.5 times compared to CI chondrites (Fig. 3.17) and displays an almost flat pattern with (La/Yb)_N = 1.09.

3.3.3.4 Mass balance calculations

Mass balance calculations are performed on all the samples and the recalculated totals in REE and Hf are compared to the WR values measured by ICP-MS (Tab. 3.10). The analytical errors on WR are up to 5% on REE and up to 10% for Hf. In the following, totals are therefore considered as satisfying when they are comprised, within error, between 95 and 105% for REE and 90 and 110% for Hf.

CV3	La	Ce	Pr	Nd	Sm	Eu	Gd	Tb	Dy	Ho	Er	Tm	Yb	Lu	Hf
olivine	9.00	9.43	2.97	4.02	4.44	/	/	13.86	6.27	6.39	7.04	11.60	14.57	10.71	104.46
±	2.39	3.20	0.45	1.70	0.04	/	/	0.37	1.52	1.00	1.29	2.48	3.06	1.27	68.63
low-Ca px	7.74	23.68	4.53	2.74	3.83	32.86	/	13.46	4.29	13.59	5.83	10.00	7.85	5.27	8.26
±	2.35	13.92	0.51	0.45	0.11	/	/	5.21	0.60	1.22	0.79	1.37	1.37	0.77	2.68
matrix	74.67	46.86	55.87	35.63	88.27	0.00	131.25	87.19	41.22	58.41	64.90	49.41	77.35	121.63	59.76
±	7.06	5.13	9.25	6.79	7.90	0.00	11.17	13.16	7.68	16.87	13.37	6.11	12.17	23.28	5.09
magnetite	23.34	25.59	10.68	11.13	9.38	15.19	10.64	9.74	6.08	5.91	6.59	5.83	4.32	6.54	4.57
±	5.96	11.17	2.29	2.78	4.05	2.61	1.55	2.69	1.89	2.86	0.95	2.31	1.21	1.11	0.91
Total	114.74	105.57	74.04	53.52	105.93	48.06	141.89	124.26	57.86	84.31	84.37	76.84	104.10	144.15	177.06
±	9.83	18.84	9.56	7.55	8.88	2.61	11.28	14.41	8.08	17.14	13.52	7.03	12.68	23.35	68.88

CK3	La	Ce	Pr	Nd	Sm	Eu	Gd	Tb	Dy	Ho	Er	Tm	Yb	Lu	Hf
olivine	0.48	0.23	0.49	0.81	0.75	/	0.00	1.17	1.35	0.92	0.91	0.67	1.69	1.72	1.40
±	0.05	0.06	0.01	0.47	0.10	/	0.00	0.17	0.50	0.18	0.29	0.71	0.71	0.14	0.32
low-Ca px	4.94	3.91	7.10	4.27	8.48	/	22.04	7.73	5.17	7.16	8.20	8.08	9.75	9.70	14.28
±	1.19	1.15	1.56	0.83	1.40	/	/	1.77	1.15	1.79	1.90	1.88	1.75	1.98	3.24
matrix	39.65	57.56	30.92	22.17	37.11	/	124.83	39.82	29.97	37.59	47.41	49.31	51.04	72.65	95.68
±	5.91	18.27	4.74	2.55	6.17	/	15.27	4.45	6.06	8.37	7.74	6.33	8.65	19.57	26.16
sulfure	0.40	0.71	0.66	/	/	/	/	3.85	0.93	0.71	0.52	/	/	/	2.42
±	0.07	0.18	0.13	/	/	/	/	/	/	/	0.08	/	/	/	0.36
phosphate*	22.18	17.66	21.83	21.64	26.76	25.04	30.25	/	/	/	33.29	31.27	27.21	24.65	0.49
Total	67.65	80.07	60.99	48.88	73.09	25.04	177.12	79.64	71.25	79.84	90.33	89.33	89.69	108.73	114.27
±	6.03	18.30	5.00	2.72	6.32	0.00	15.27	4.79	6.19	8.56	7.97	6.60	8.85	19.67	26.36

* values taken from CK4 NWA 5798

CK4	La	Ce	Pr	Nd	Sm	Eu	Gd	Tb	Dy	Ho	Er	Tm	Yb	Lu	Hf
olivine	9.10	36.80	16.48	8.28	/	86.65	44.80	19.40	7.45	0.00	20.64	22.66	18.72	57.74	49.80
±	1.40	8.20	0.56	1.59	/	/	/	4.17	0.97	0.00	/	4.41	4.40	7.35	10.69
low-Ca pyroxene	2.59	35.81	2.95	2.68	5.09	33.92	/	8.39	5.70	4.84	4.98	12.13	13.56	25.71	35.52
±	0.68	13.30	1.01	0.57	0.47	10.23	/	0.22	0.72	1.59	0.74	4.33	2.62	12.08	16.91
plagioclase	1.94	28.63	/	/	2.84	8.92	/	0.00	3.44	7.58	/	8.55	1.30	13.76	5.80
±	0.31	17.66	/	/	0.78	/	/	0.00	/	/	/	/	/	6.78	2.64
magnetite	5.03	7.03	1.27	3.42	12.52	14.97	11.16	2.90	4.78	4.21	5.19	/	6.40	/	10.27
±	1.07	3.70	0.42	1.15	5.44	1.84	/	1.47	2.04	2.35	/	/	2.40	/	3.96
sulfide	0.01	0.03	/	0.01	/	0.10	/	0.04	0.03	0.06	0.02	0.05	0.03	/	0.18
±	/	/	/	/	/	/	/	/	/	/	/	/	/	/	0.06
high-Ca pyroxene	3.01	4.94	7.28	4.80	9.44	11.39	15.48	10.52	9.37	6.75	8.90	6.75	12.13	2.33	24.46
phosphate	23.48	18.48	23.70	23.96	30.77	30.29	34.48	30.24	38.34	37.90	37.69	33.37	31.34	27.41	0.47
matrix*	4.12	5.91	3.29	2.41	4.19	/	13.95	4.36	3.33	4.18	5.26	5.16	5.77	7.92	8.78
Total	49.29	137.63	54.98	45.55	64.85	186.22	119.86	75.85	72.44	65.52	82.68	88.68	89.26	134.87	135.29
±	1.92	23.87	1.23	2.04	5.51	10.39	/	4.42	1.21	2.59	2.46	6.19	5.66	15.68	20.56

* values taken from CK3 NWA 5956

CK5 EET92002	La	Ce	Pr	Nd	Sm	Eu	Gd	Tb	Dy	Ho	Er	Tm	Yb	Lu	Hf
olivine	45.45	33.15	45.33	54.76	74.99	/	132.57	61.51	52.62	53.23	99.97	95.57	126.47	140.59	98.92
±	16.67	11.27	10.85	15.26	20.98	/	2.69	15.65	17.05	15.92	21.90	21.94	23.93	26.42	15.41
plagioclase	8.46	3.88	5.08	6.22	6.98	35.77	/	5.42	3.70	6.30	5.73	11.73	10.06	13.12	9.63
±	5.35	2.45	3.17	4.22	4.36	23.52	/	3.49	2.77	4.29	4.04	7.60	6.49	7.74	7.62
high-Ca pyroxene	4.51	4.72	4.02	6.68	7.15	5.02	8.06	8.03	8.77	8.48	12.33	9.81	9.25	12.07	19.91
magnetite	0.86	1.18	0.80	1.03	1.41	/	/	2.63	1.12	2.13	2.19	3.27	1.79	2.38	2.62
±	0.30	0.64	0.26	0.34	0.63	/	/	0.71	0.72	0.61	0.69	1.04	0.75	0.90	1.90
sulfide	1.96	1.82	1.45	2.01	2.35	/	5.03	1.65	1.91	2.22	3.11	3.67	3.76	4.03	1.55
±	0.48	0.41	0.35	0.50	0.40	/	0.79	0.45	0.40	0.49	0.65	0.79	0.81	0.75	0.23
phosphate	17.72	12.43	15.40	18.61	17.18	9.17	13.02	8.75	8.57	7.18	9.07	5.71	6.07	4.95	0.33
Total	78.96	57.19	72.07	89.30	110.07	49.96	158.67	87.99	76.69	79.52	132.42	129.75	157.41	177.15	132.96
±	17.52	11.56	11.31	15.84	21.44	23.52	2.80	16.06	17.29	16.51	22.29	23.26	24.81	27.56	17.30

* values taken from CK4 NWA 5798

CK5 A-881277	La	Ce	Pr	Nd	Sm	Eu	Gd	Tb	Dy	Ho	Er	Tm	Yb	Lu	Hf
olivine	31.47	89.02	15.88	12.81	12.47	/	/	23.06	11.12	15.94	7.11	11.89	10.24	/	32.41
±	5.78	54.39	4.40	4.92	0.75	/	/		1.25	2.43	1.36	2.35	2.41	/	6.32
plagioclase	3.89	50.07	2.60	0.00	1.03	19.17	/	1.39	3.06	1.24	/	2.02	3.59	/	5.24
±	0.51	39.64	1.30	0.00	0.50	/	/	/	/	0.14	/	0.24	/	/	2.40
magnetite	1.08	0.59	0.30	0.59	0.17	/	/	0.18	/	0.15	/	0.36	0.13	/	1.50
±	/	0.52	0.18	0.28	0.09	/	/	0.07	/	/	/	/	/	/	0.60
sulfide	1.52	1.52	0.51	1.86	/	/	/	0.00	0.50	0.90	1.38	3.44	1.30	/	2.28
low-Ca pyroxene*	0.49	0.55	0.38	0.85	0.44	/	/	0.00	0.70	0.00	1.06	0.83	1.10	2.21	1.93
high-Ca pyroxene*	6.36	6.74	5.75	9.16	9.32	5.42	10.08	9.46	9.57	9.10	12.45	8.71	7.84	11.25	21.73
Phosphate*	25.45	18.09	22.46	26.01	22.80	10.09	16.60	10.51	9.53	7.85	9.33	5.17	5.25	4.70	0.37
Total	70.26	166.57	47.88	51.27	46.23	34.69	26.68	44.60	34.49	35.17	31.34	32.42	29.45	18.16	65.46
±	5.80	67.31	4.60	4.92	0.91	/	/	0.07	1.25	2.44	1.36	2.36	2.41	0.00	6.79

* values are taken from CK5 EET92002

CK6	La	Ce	Pr	Nd	Sm	Eu	Gd	Tb	Dy	Ho	Er	Tm	Yb	Lu	Hf
olivine	18.64	50.75	38.12	10.65	16.95	205.80	74.35	45.55	11.30	28.70	25.22	39.55	28.22	46.03	56.46
±	3.19	13.31	10.80	2.54	1.49	11.12	6.00	7.13	2.03	2.01	6.85	7.13	5.22	6.98	11.69
high-Ca pyroxene	10.67	17.80	14.40	12.53	21.32	23.32	22.72	24.37	26.66	28.24	32.13	27.81	24.70	24.73	29.25
±	2.38	4.69	3.30	2.94	5.70	5.38	5.46	5.65	7.08	6.99	7.09	6.95	6.35	6.25	9.40
plagioclase	30.81	15.81	25.48	11.27	13.46	129.95	56.45	11.06	19.98	19.40	12.59	/	13.46	12.35	10.13
±	11.50	7.52	15.73	7.21	5.61	40.69	17.41	3.40	6.15	5.98	3.89	/	4.15	3.81	5.33
magnetite	6.32	31.39	5.94	4.13	14.91	/	/	5.72	3.96	/	3.52	5.63	5.05	11.27	/
±	1.53	26.54	1.13	3.32	6.36	/	/	0.64	0.54	/	0.94	3.15	0.42	0.95	/
sulfide	0.53	0.97	1.26	0.08	/	/	/	1.50	/	1.61	0.00	0.66	0.79	2.26	0.33
phosphate*	2.20	1.52	1.79	2.13	1.91	1.25	1.44	0.94	0.91	0.76	0.96	0.60	0.66	0.58	0.04
Total	69.18	118.24	86.99	40.80	68.55	360.31	154.95	89.14	62.82	78.72	74.42	74.25	72.87	97.22	96.20
±	12.27	30.98	19.39	8.84	10.32	205.80	74.35	45.55	11.30	28.70	25.22	39.55	9.22	10.16	15.92

* values taken from CK4 NWA 5798

TABLE 3.10 – Mass balance calculations

In CV3 and CK3 samples (Tab. 3.10), the phyllosilicate matrix bears more than 30% of the LREE and MREE and 40 to 90% of the HREE. In CV3, the remaining part is distributed among low-Ca pyroxene (up to 10% of the REE and even 23% of Ce), magnetite (25% for LREE decreasing toward 3-4% for HREE) and olivine (2-15% of the REE). Totals are too low for Pr, Nd, Dy and Tm (less than 80% retrieved), and too high for Lu ($144 \pm 23\%$). In CK3, the remaining is mainly found in phosphate (17-33% of the REE) and low-Ca pyroxene (up to 10% of the REE). Trace element values for phosphate is taken from CK4 NWA 5798 because even if this mineral is observed by SEM and on mask images, it could not be measured by laser ablation due to its small size ($< 10 \mu m$). In CK3, the totals are too low for all REE, except Ce and the heavy REE (from Er to Lu). This might be due the lack of REE measurements in mesostasis. Hf is mainly distributed among silicates in type 3 CK and CV chondrites. In CV3, the major part is found in olivine ($104 \pm 69\%$) and the remaining fraction occurs in the matrix ($60 \pm 5\%$) and low-Ca pyroxene ($8 \pm 3\%$). In CK3, $96 \pm 26\%$ are in the matrix and $14 \pm 3\%$ are in low-Ca pyroxene. The calculated totals fit within error in both cases : $177 \pm 69\%$ for CV3 and $114 \pm 26\%$ in CK3.

In CK4 NWA 5798 (Tab. 3.10), REE are mainly distributed among olivine (7-37%, except Lu, 60%) and phosphate (18-38%). The remaining part is found in high-Ca pyroxene (7-10% for the LREE and up to 12% for the HREE, except for Lu with less than 3%), low-Ca pyroxene (4% for the LREE, 5-8% for the MREE and 12-13% for the HREE, except 25% for Lu), plagioclase (up to 16%), residual matrix (6-9%, REE concentrations taken from CK3) and magnetite (2-16%). The part of Ce borne by silicates is significantly higher than other LREE, likely due to the two oxidation states of this element. Nevertheless, the total recalculated of Ce is reasonably satisfactory ($138 \pm 24\%$). For the other REE, the recalculated totals are outside the preferred range, with exception of Tm and Yb ($89 \pm 6\%$). They are too low (45-80%) for all the REE, except Lu that is too high ($135 \pm 16\%$). In this sample, Hf is mainly distributed among olivine (50%), high-Ca pyroxene (25%) and low-Ca pyroxene (35%). Lower amounts are distributed among magnetite (10%), matrix (9%) and plagioclase (6%). The total is slightly too high ($135 \pm 20\%$) but it could be explain by the start of matrix metamorphism (Hf value taken from CK3).

The CK5 samples highlight significant differences in their trace-element distribution (Table 3.10). In CK5 EET92002, the main carrier of REE is olivine (33 to 75%) and even close to 100% for Er ($100 \pm 22\%$), Tm ($96 \pm 22\%$) and Yb ($126 \pm 24\%$). Lu is slightly overestimated ($140 \pm 26\%$). Phosphate represents 12-19% of the LREE and decrease toward the HREE to 5%, whereas plagioclase, high-Ca pyroxene, sulfide and magnetite display an increasing contribution in the mass-balance toward the HREE : 4-8% LREE to 12-13% HREE in plagioclases, 4-7% LREE to 8-12% HREE in high-Ca pyroxene, lower than 2% for LREE to 4% in sulfide and $< 1\%$ LREE to 4% HREE in magnetite. Hf is distributed among olivine ($99 \pm 15\%$), high-Ca pyroxene (20%), plagioclase (6%), magnetite (2.7%) and sulfide (2.5%). The totals fall in the acceptable range for most of the REE, except Ce and Pr, which are too low (respectively $57 \pm 11\%$ and $72 \pm 11\%$) and the HREE, which are too high ($130 \pm 22\%$ to $177 \pm 26\%$) The recalculated total is also slightly too high for Hf ($133 \pm 16\%$). The overestimation of recalculated totals for HREE and Hf might be due to the high-Ca pyroxene, as only one measurement was carried out on this mineral. Moreover, some of the 'high-Ca pyroxenes' encountered in EET9202 could be a fine-grained mixture between high-Ca pyroxene and low-Ca pyroxene (possibly less enriched in REE and Hf, Table 3.9), hence explaining overestimation of the recalculated totals. CK5 A-881277 shows that the REE are distributed mainly among phosphate (18-25% of the LREE and 5-10% of the HREE) and olivine (7-30%, except Ce, $89 \pm 54\%$), while the remaining part is found in plagioclase and high-Ca pyroxene. Hafnium is mainly borne by olivine ($41 \pm 16\%$), plagioclase ($12 \pm 8\%$) and high-Ca pyroxene (12%). In this sample, calculated totals for trace elements are extremely low (20-50%) except for La ($77 \pm 7\%$, even out of satisfactory range), Ce ($167 \pm 67\%$) and Hf ($72 \pm 18\%$).

In the CK6 Y-191 sample, the main carriers of REE are silicates. Plagioclase bears 30% (LREE) to 12% (HREE), whereas olivine and high-Ca pyroxene bear respectively 11 to 50% and 10 to 28% of the REE. Magnetite also bears 4.5 to 15% of REE (except Ce : 32%). Olivine is the main Hf carrier (56%), followed by high-Ca pyroxene (29%) and plagioclase (10%). Totals are rather low, particularly for LREE (from $41 \pm 9\%$ (Nd) to $69 \pm 12\%$ (La), except Ce ($118 \pm 31\%$)). They are better, even

acceptable for HREE and Hf ($> 85\%$, in the acceptable range for Tb ($89 \pm 10\%$), Lu ($97 \pm 10\%$) and Hf ($96 \pm 16\%$)).

To summarize, totals recalculated by mass balances appear better for HREE and Hf than for LREE. The missing LREE are likely due to the higher incompatibility degree of these elements compared to that of the HREE. They are thus more sensitive to the 'nugget effect' of some micrometric or nanometric phases (e.g. spinels, ilmenite...) that could explain the missing masses. In the CK3 sample (unequilibrated), it can also be assumed that the selected area may not be entirely representative of the whole-rock. On the contrary, the mass balance is acceptable for almost all the REE (except Pr, Nd, Dy and Er) in the characterized CV3 sample, perhaps because it contains less mineral phases than the CK3 sample (respectively 5 and 9). Cerium could also display a significantly different distribution than its neighbors (La and Pr) most likely due to its two oxidation states.

Finally, the distribution of trace elements among minerals appears robust in all samples, except in CK5 A-881277. In this sample 50 to 80% of the REE budget is missing. This poor mass balance to be interpreted as the result of an unexpected and not observed mineral phase. In addition, this sample displays peculiar features such as a high enrichment in HREE ($(\text{La}/\text{Yb})_{\text{N}} = 2.17$), sulfide with elevated Co concentrations (12500 ppm), whereas the later ranges from 200 to 1000 ppm in other samples) not observed in the other samples. We thus assume that CK5 A-881277 experienced different conditions than the other CK meteorites presented in this paper.

3.3.3.5 Trace-element patterns

The trace element average concentrations of each mineral presented above are normalized to the recent trace-element abundances for CI chondrites of [Barrat et al. \(2012\)](#).

Olivines display slightly fractionated patterns (Fig. 3.18-a), enriched in HREE compared to LREE ($(\text{La}/\text{Yb})_{\text{N}} = 0.4$ to 0.7), except for CK5 A-881277 that is enriched in LREE compared to HREE ($(\text{La}/\text{Yb})_{\text{N}} = 2.17$). A slight negative Ce anomaly is detected in olivines of CK3 NWA 5956 and CK5 EET92002, whereas olivines in CK4

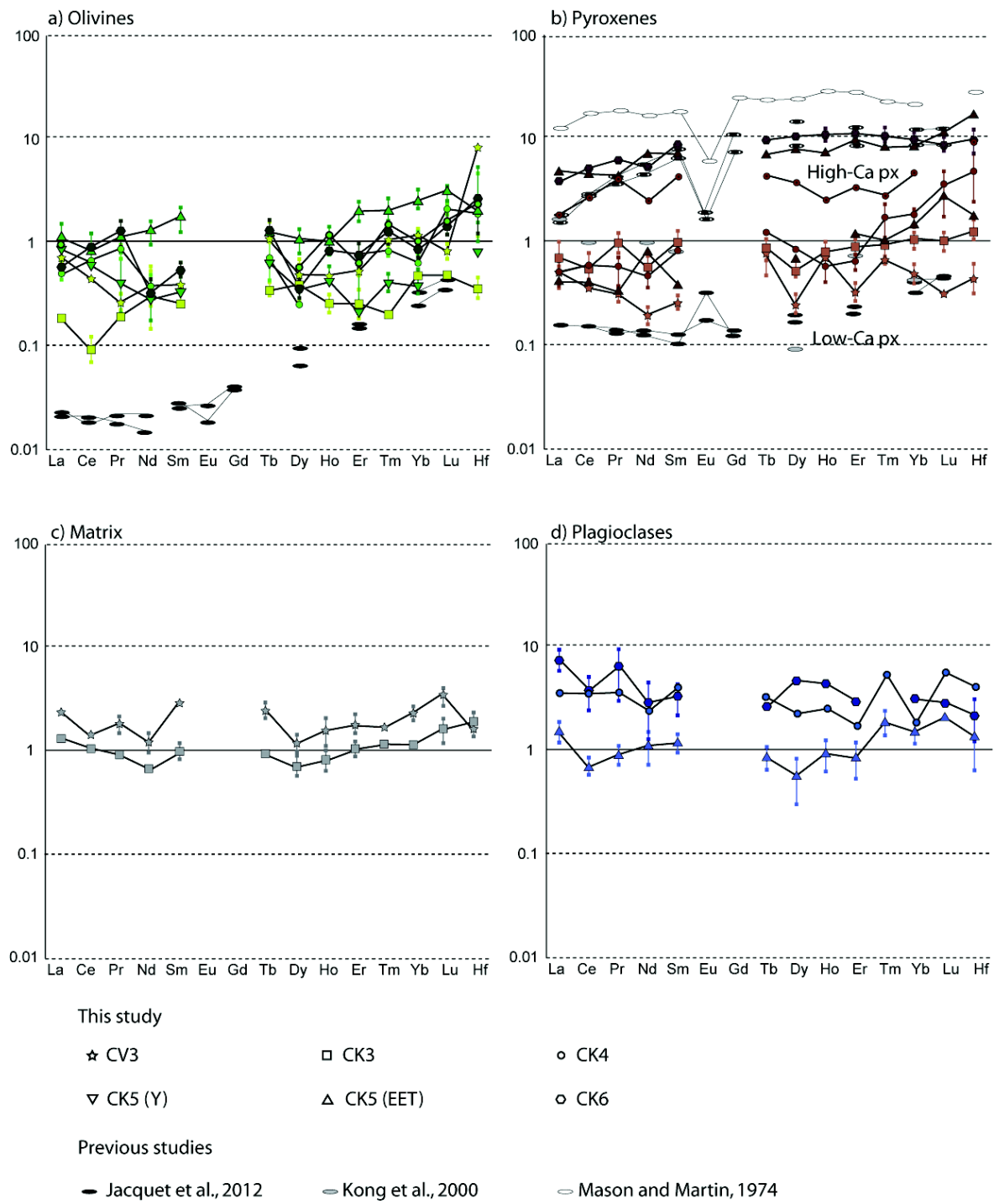


FIGURE 3.18 – Trace-element patterns on silicates normalized to CI chondrites (Barrat et al. 2012) and comparison with other published data. a) olivine, b) pyroxene, c) matrix and d) plagioclase.

NWA 5798, CK5 A-881277 and CK6 Y-191 patterns have a positive Ce anomaly. Except CK3 NWA 5956 that is 10 times to 2 times depleted in LREE and HREE respectively compared to CI chondrites, the other samples display values close to those of CI chondrites, slightly lower for LREE and slightly enriched (up to 3 times for Lu) for HREE (Fig. 3.18-a).

Low-Ca pyroxenes patterns also appear fractionated, with an increasing fractionation toward enrichment in HREE corresponding to an increase in metamorphic degree ($(La/Yb)_N$ ranging from 1.06 (CV3) to 0.31 (CK5); Fig. 3.18-b). High-Ca pyroxenes are also fractionated ($(La/Yb)_N$ ranges from 0.38 to 0.57) and samples CK5 EET92002 and CK6 Y-82191 are enriched in REE approximately ten times compared to low-Ca pyroxenes, i.e. 4-5 times (LREE) to ± 10 times (HREE) compared to CI chondrites. Sample CK4 NWA5798 is only 2 to 4 times higher in REE compared to CI chondrites, except Lu (0.88 times). The Hf values are about 10 to 15 times those of CI chondrites (Fig. 3.18-b). High-Ca pyroxene patterns do not display any Ce anomaly, together with the low-Ca pyroxene in found CK5 EET92002. On the contrary, low-Ca pyroxene patterns of CV3 NWA 5772 and CK4 5798 yield a significant positive Ce anomaly, and CK3 NWA 5956 displays a slight negative Ce anomaly.

Matrices present almost flat REE and Hf patterns ($(La/Yb)_N = 1.04$ (CV3) and 1.10 (CK3)) with a slight negative anomaly in Ce in CV3 NWA 5772 and a slight positive anomaly in Ce in CK3 NWA 5956. They are 2-3 times enriched in REE and Hf relative to whole-rock CI chondrites (Fig. 3.18-c).

Plagioclases have fractionated patterns enriched in LREE ($(La/Yb)_N > 2$ for CK4, and CK6), almost flat for CK5 EET92002 ($(La/Yb)_N = 0.98$) and even slightly enriched in HREE in CK5 A-881277 ($(La/Yb)_N = 0.76$). The enrichment is a factor 2 compared to CI chondrites. Only the CK5 EET92002 and CK6 samples are represented on figure 3.18-d due to the lack of values in CK4 and CK5 A-881277 (Table 3.9). They display a slight negative Ce anomaly.

Magnetites show strongly varying patterns between the samples (Fig. 3.19-a). Samples CV3 NWA5772 and CK5 A-881277 are very fractionated ($(La/Yb)_N = 6$). In

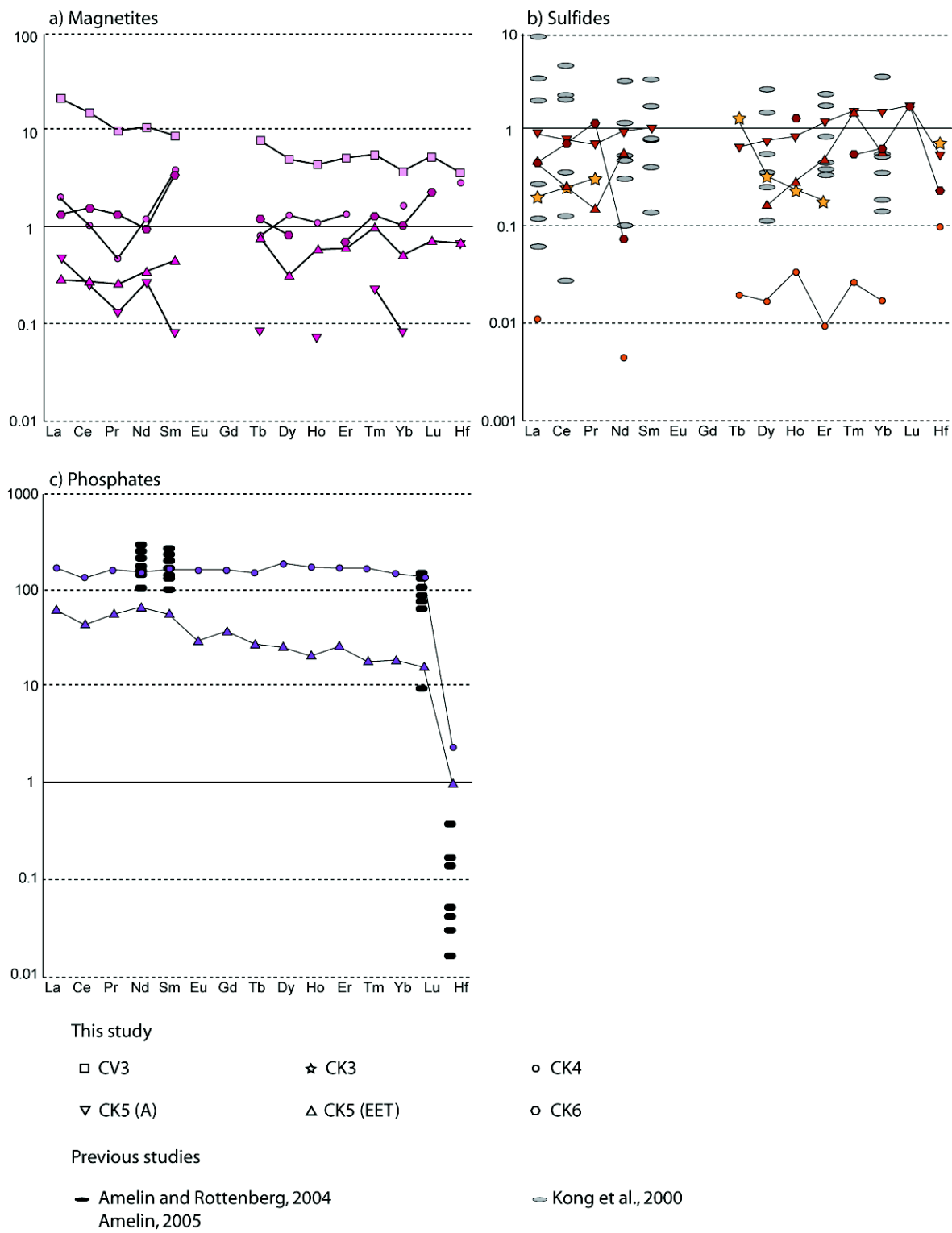


FIGURE 3.19 – Trace-element patterns on accessory phases normalized to CI chondrites (Barrat et al. 2012) and comparison with other published data. a) magnetite, b) sulfide, and c) phosphate.

CK4 NWA 5798 and CK6 Y-82191 are less fractionated ($(\text{La}/\text{Yb})_N = 1.2$) while CK5 EET92002 shows the opposite fractionation, in favor of HREE ($(\text{La}/\text{Yb})_N = 0.56$). The CV3 values range from being 22 (La) to 3-4 (HREE and Hf) times CI chondritic contents. CK4 NWA 5798 and CK6 Y-82191 not only have the same fractionation trend, but they also display similar degree of enrichment (1.5-2 times CI for LREE and 1.2-1.7 times CI for HREE). On the contrary, CK5 samples are lower than CI chondrites values (0.3 to 0.75 times for LREE and HREE respectively, for EET92002 and 0.5 to 0.08 times for LREE and HREE respectively, for A-881277). CK4 NWA 5798 and CK6 Y-191 display a slight positive Ce anomaly.

Sulfides display patterns fractionated towards higher HREE concentrations ($(\text{La}/\text{Yb})_N = 0.6$ to 0.8). They reach 0.1 (LREE) to 1 (HREE) times CI contents, with exception of CK5 EET92002 that is higher than 1 for HREE and CK4 NWA 5798 that is around 0.01. Hafnium ranges from 0.1 to 0.74 times CI values for all sample types (Fig. 3.19-b).

The two patterns obtained on phosphates display significant differences, but both have a slight negative anomaly in Ce (Fig. 3.19-c). In CK4 NWA 5798, the pattern is almost flat ($(\text{La}/\text{Yb})_N = 1.16$) and the contents are 130 to 170 times higher than in CI chondrites. The fractionation is higher in CK5 EET92002 ($(\text{La}/\text{Yb})_N = 3.42$) and the enrichment compared to CI chondrites is ± 60 times for the LREE and less than 20 times for the HREE (Fig. 3.19-c).

3.3.4 Discussion

In the present study, the effect of the evolution of mineralogy and modal abundances coupled with the evolution of REE and Hf distribution among different mineral phases during increasing metamorphism in CK chondrites is examined.

3.3.4.1 Mineralogy abundances and evolution during metamorphism

Matrices made of phyllosilicates and low-Ca pyroxene only exist in chondrites affected by low grades of metamorphism. Matrix modal abundances (% m.a.) are 47.3% (CV3) and 63.76% (CK3) in unequilibrated samples and decrease to less than

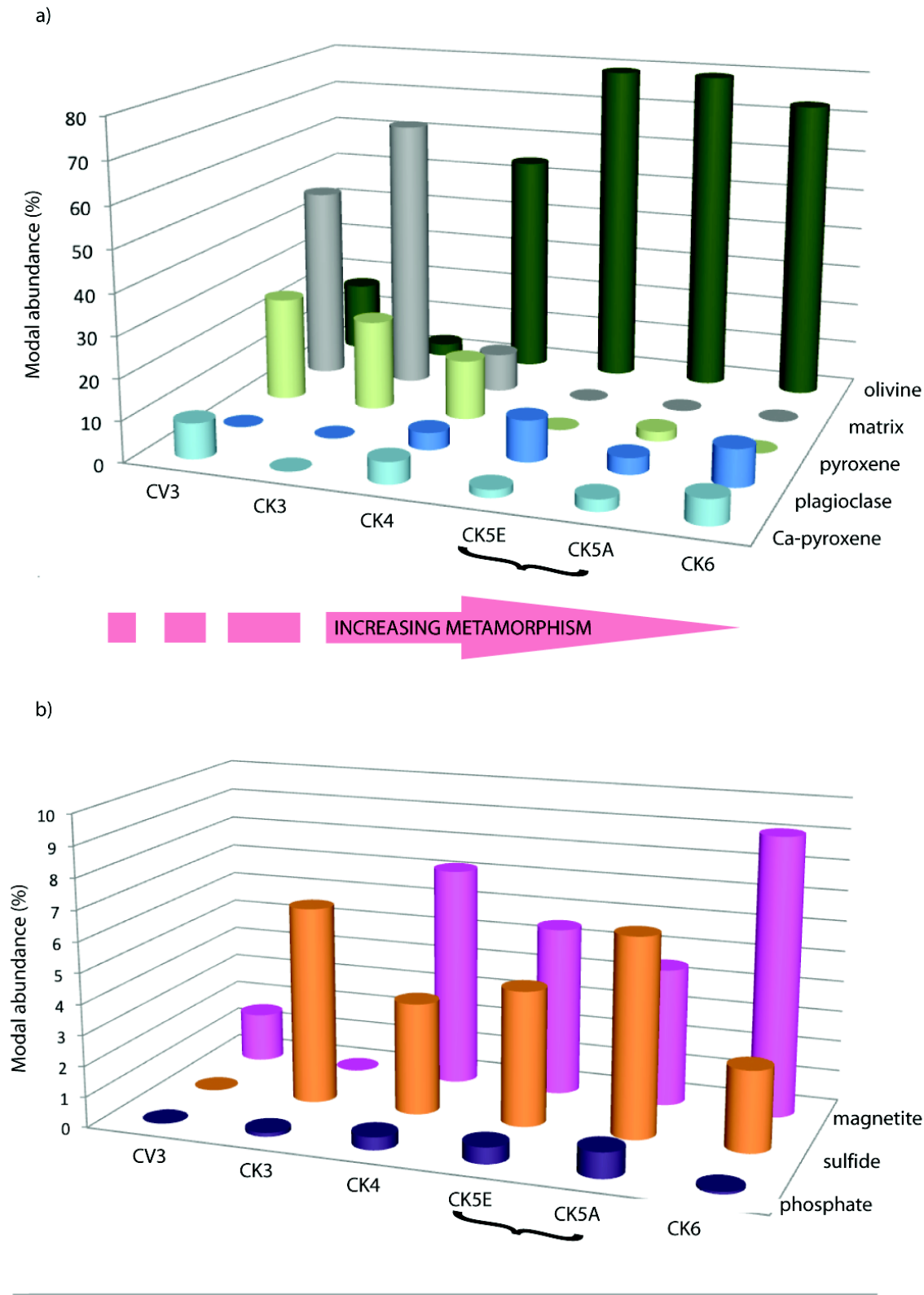


FIGURE 3.20 – Evolution of mineral abundances during thermal metamorphism. a) silicates and b) accessory phases.

10% in CK4 NWA 5798. The matrix completely disappears in higher grade of metamorphism (Fig. 3.20-a). The obtained values agree well with previously published data for CV chondrites (e.g. 50.0 to 51.3% m.a. in CV3_{oxB}, [McSween \(1977\)](#)) and CK chondrites (e.g. 57.7 to 86.7% m.a., [Richter et Neff \(2007\)](#)). Low-Ca pyroxene also displays a significant decrease from type 3 (25.42% m.a. and 15.42% m.a.) to type 6, where it is absent. It is still present in the CK4 sample (14.60%), low in CK5 A-881277 (2.39%) and totally absent in CK5 EET92002 (Fig. 3.20-a). High-Ca pyroxene does not display a clear evolution during metamorphism. It is less abundant in CK5 samples (2.86% m.a. in A-881277 and 1.90% m.a. in EET92002). The large occurrence of high-Ca pyroxene observed in this study, more particularly in CK4 samples in which total pyroxene is equal to 20% m.a., contrasts with the results of [Kallemeyn et al. \(1991\)](#) where low-Ca and high-Ca pyroxenes are described as minor to accessory phases. The fact that the mask images calculated with XMapTools allow to distinguish phases that appear similar on BSE pictures (such as two types of pyroxene or pyroxene and olivine) likely explains these differences, together with the absence of existing CK3 specimen in 1991. Olivine forms a minor phase in CK3 chondrite (5.20% m.a., almost only found in chondrules) while it reaches 17.01% m.a in CV3, where it is only observed in chondrules. In equilibrated chondrites, olivine represents 54.14% in CK4 sample and more than 70% in type 5 and 6. Plagioclase appears from type 4 and shows no clear evolution with metamorphism. It only remains as a minor phase (up to 10%).

Accessory phases do not display any significant evolution with increasing degree of metamorphism (Fig. 3.20-b). Ilmenite and spinel, which occur as exsolutions in magnetite were not quantified or analyzed, even by EPMA, due to their very small sizes ($\leq 1 \mu m$). Phosphate is the least abundant of the accessory phases. It is not observed in CV3, and ranges from 0.08% m.a. in CK6 to 0.83% m.a. in CK5 A-881277. Magnetite was not found in CK3, but a small amount of native Fe (0.20% m.a.), often altered into lawrencite, is observed. Magnetite represents only 1.60% m.a. in CV3 and ranges from 4.51 to 9.09% m.a. in metamorphosed CK samples. These values are compatible with those previous published (1.4 to 3.2% m.a. in CV3_{oxB}, in [McSween \(1977\)](#) and 1.2 to 8.1% m.a., average = 4.11%, n = 19 in CK,

in Geiger et Bischoff (1994)), even if the present values are slightly higher in CK chondrites (average = 6.93%, $n = 7$). Sulfide was not observed in CV3 sample and it ranges from 2.64 in CK6 to 6.46% m.a. in CK5 A-881277. The only sulfide present in all studied samples is pentlandite, except in CK6, where pyrrhotite is also found.

The mineralogical opaque species observed in this study agree with previous studies (McSween 1977, Kallemeyn et al. 1991, Geiger et Bischoff 1994, Righter et Neff 2007), however the modal abundances could be significantly different. The results of this study concur with those of Righter et Neff (2007), who described opaque assemblages in CK chondrites ranging from 3.5 to 18% m.a. While Geiger et Bischoff (1994) described a maximum modal abundance of opaque phases of 1.3% m.a., but usually lower than 0.1% m.a.. The difference between the results of Geiger et Bischoff (1994) and this study might be related to the acquisition method. They used an image processing system coupled with polarizing optical microscope whereas XMapTools involves EPMA X-ray maps. The latter, measured using WDS spectrometers, is expected to produce a more accurate and reliable determination of very small phases (minimal size 3-5 μm).

3.3.4.2 Are phosphates the key to explain Lu-Hf whole-rock discrepancies ?

Phosphates are usually considered to be the main carrier of REE in ordinary chondrites (Brearley 1997). Therefore, it is assumed that their recrystallization during metamorphism can lead to Lu/Hf heterogeneities (Bouvier et al. 2008). In the present study, we investigated the REE and Hf distribution among minerals in the only metamorphized suite of carbonaceous chondrites. The amount of phosphate in CK chondrites is low (0.08 to 0.83%), with no clear evolution of abundance during metamorphism (the highest abundance is found in CK5 and the lowest in CK6). Two phosphate species are observed : apatite or Cl-apatite in CK3 and merillite in all the other samples. They either represent mineralogical evolution of phosphate during metamorphism or the natural variability in chondritic samples. The REE and Hf concentrations obtained in CK phosphates in this study and the values already published for Sm and Nd (Amelin et Rotenberg 2004) and Lu and Hf (Amelin 2005) on OC (H5, L/LL4, L4, L5) are compared. The values obtained

for Nd and Sm on CK4 phosphate are in good agreement with those previously published, whereas they are slightly lower for CK5 EET92002 (Fig. 3.20-c). In terms of Lu, the present data are in the same range as ordinary chondrites, whereas Hf in CK chondrites appears at least two times higher than in OC, i.e. equal or higher to CI content.

This study shows that phosphates do not appear to be the main carrier of REE in CK and CV chondrites although it still constitutes an important contributor. Indeed phosphate bear up to 30% of Sm and 26% of Nd, but the matrix in CK3 also bears up to 40% of Sm and 22% of Nd. These values even reach 90% for Sm and 36% for Nd in the CV3 sample, in which no phosphate is observed (Fig. 3.21-a, 3.21-b). Olivine in CK5 EET92002 also bears up to 75% of Sm and 55% of Nd. Thus, the Sm and Nd fraction stored in phosphate likely escapes redistribution as they show no clear evolution with increasing metamorphism, while the Sm and Nd part borne by silicates is redistributed during metamorphism. In the CK6 sample, Sm and Nd are only borne by silicates and magnetite (less than 2.5% in phosphate) and it is assumed that Sm and Nd are almost totally redistributed during CK6 recrystallization. In CK3 and CK4 samples, 25 to 27% of Lu is actually borne by phosphate, but matrix in CK3 as well as olivine and pyroxene in CK4 account for more than 50% of the Lu fraction (Fig. 3.21-c). No phosphate is observed in the CV3 sample, and the CV3 matrix bears a significant part of Lu ($122 \pm 23\%$). Similarly to Sm and Nd, phosphate does not appear to be the main carrier of Lu. In higher metamorphic grades, the fraction of Lu borne by phosphate falls below 10%. The remaining fraction is distributed among silicates (CK5) and silicates and magnetite (CK6). Similar to the LREE, a significant, even major, part of Lu is redistributed during metamorphism. Interestingly, the decrease of the Lu fraction borne by phosphate during metamorphism is not due to the decline of merrillite modal abundance (0.42% m.a. in CK4 and 0.64% m.a. in CK5, Fig. 3.21-c) but rather to diminishing Lu concentrations in phosphate (one order of magnitude lower in CK5 than in CK4, Tab. 3.9). The fraction of Hf borne by phosphate is always negligible (less than 0.5%, Fig. 3.21-d). Whatever the chondrite type and class, Hf is essentially concentrated in matrix (CK3) and in olivine, and low- and high-Ca pyroxenes. Considering that

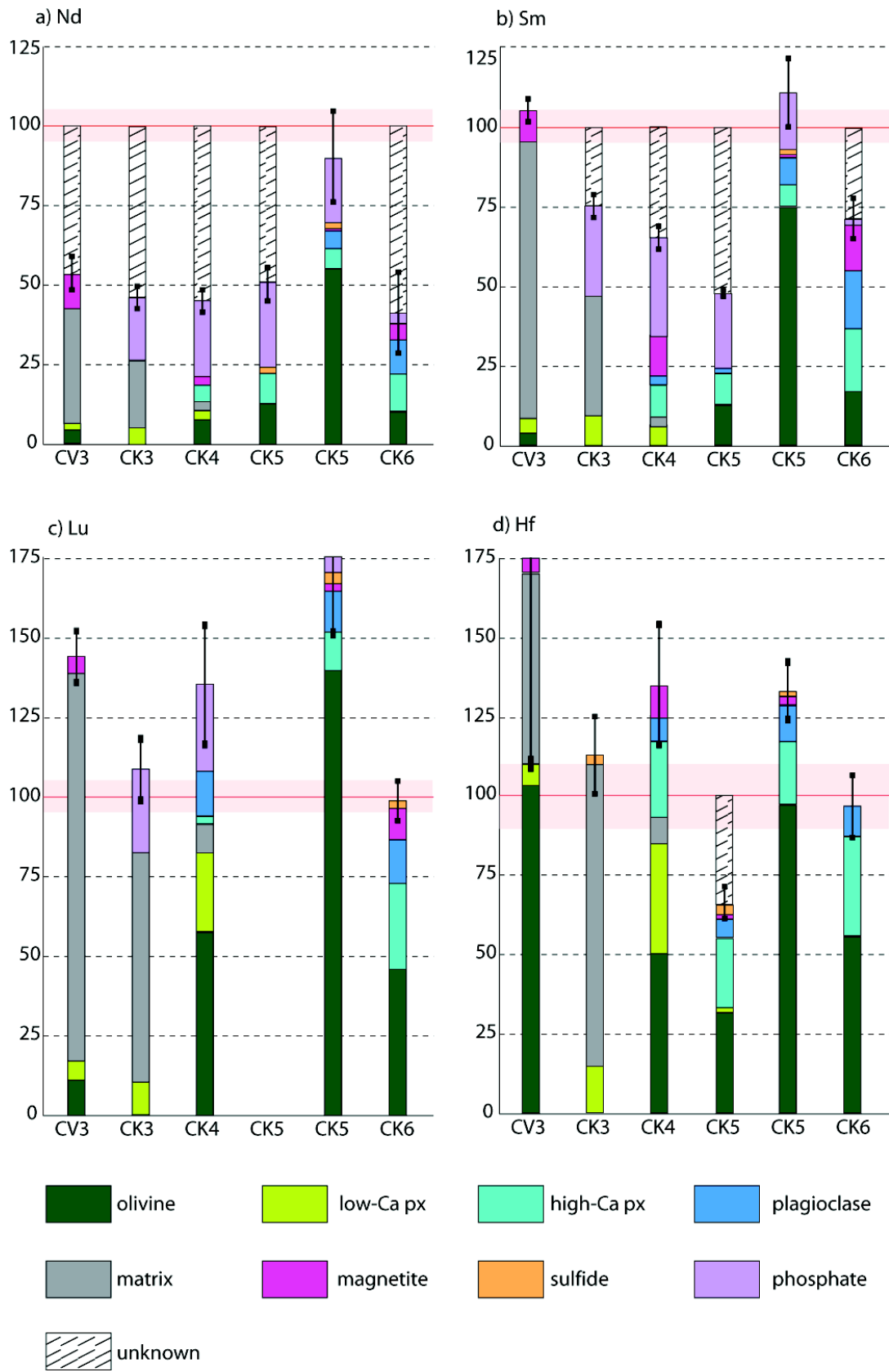


FIGURE 3.21 – a) Nd, b) Sm, c) Lu and d) Hf distribution among minerals phases in CV_{ox}B and CK chondrites.

metamorphism induces low-Ca pyroxene and matrix breakdown in parallel with an olivine modal abundance increase, Hf is significantly re-distributed during metamorphism.

Up to 30% of Sm and Nd are stored in phosphates at least in type 3 to 5, and therefore are not significantly redistributed during metamorphism. This behavior may explain the robustness of the Sm-Nd isotopic system in chondrites. On the contrary, Lu and more particularly Hf are mostly borne by different silicates and consequently they are redistributed during metamorphism - induced recrystallization. This dichotomy in the distribution, together with the fact that the same minerals carry both Sm and Nd while Lu and Hf are mainly borne by different phases, could explain the discrepancies observed for ϵHf values.

3.3.4.3 Have CK and CV chondrites a close origin ?

The idea that CV and CK chondrites could share a similar origin is based on both their resemblances in mineralogy / petrology and their similar oxygen isotopes ([Greenwood et al. 2010](#)). In addition, some CV samples are oxidized ([McSween 1977](#)).

REE measurements were carried out on high-Ca pyroxene from Allende (CV3_{oxA}) by spark-source mass spectrometer ([Mason et Martin 1974](#)). The first measurements by LA-ICPMS on olivine and pyroxene of carbonaceous chondrites (Vigarano (CV3R) and Renazzo (CR2)) are from [Jacquet et al. \(2012\)](#).

The comparison between CV3_{oxB} and CK minerals highlight that olivine from CV3_{oxB} NWA 5772 possesses LREE contents equivalent to those of CK (e.g. resp. $189 \pm 50 \text{ ppb}$ and $119\text{-}258 \text{ ppb}$ of La, Tab. 3.9) and also rather similar in HREE (e.g. resp. $21 \pm 2 \text{ ppb}$ and b.l.d - 77 ppb of Lu, Tab. 3.9), with the noticeable exception of the CK3 (La = $46 \pm 5 \text{ ppb}$ and Lu = 12 ppb , Tab. 3.9). The comparison of CI-normalized pattern of CV3_{oxB} olivine to that occurring in more reduced carbonaceous chondrites, such as CV3R and CR2 ([Jacquet et al. \(2012\)](#), replaced on Fig. 3.18-a) shows significantly different features. The REE patterns are more fractionated in reduced chondrites ((La/Yb)_N = 0.1) than in oxidized ones ((La/Yb)_N = 0.7). LREE contents of reduced carbonaceous chondrites are very low (0.02 times

CI) and only their HREE values are close to the lowest of CK chondrites (CK3 and CK5 A881277).

Pyroxene patterns of $CV3_{oxB}$ and CK are similar to those obtained on CV3R and CR2 [Jacquet et al. \(2012\)](#). REE and Hf contents are significantly higher in high-Ca pyroxene than in low-Ca pyroxene (about one order of magnitude). No difference between oxidized and reduced lithologies could be highlighted, except a possible different degree of enrichment in LREE (Fig. 3.18-b). Some data already obtained on high-Ca pyroxene from Allende ($CV3_{oxA}$) show a similar shape pattern ($(La/Yb)_N = 0.61$, Fig. 3.18-b) but are 12 to 26 times higher than CI chondrites ([Mason et Martin 1974](#)). However, this result derives from a unique chondrule using a methodology (crushing, heavy liquors separation and spark source mass spectrometer) that significantly differs from the present study. To obtain an idea of pyroxene patterns in other classes of chondrites, the comparison is done with the unique data coming from enstatite crystals of the Bishunpur ordinary chondrite (LL3, [Kong et al. \(2000\)](#), Fig. 3.18-b).

$CV3_{oxB}$ and CK display similar REE patterns in olivine, whereas CVR and CR are slightly different. No difference is observed in pyroxene patterns, regardless of the oxidized states of the carbonaceous chondrites. The major argument to refute the fact that CK and CV belong to a unique clan is oxidation conditions (water alteration in parent body for CV_{ox} (e.g. [Krot et al. 2004](#)) and the oxidizing area in the nebulae before agglomeration for CK ([Rubin 1992](#))). The similarities of REE patterns of olivine in oxidized and in reduced samples suggest that redox conditions might affect on the incorporation of REE into olivine. In this case $CV3_{oxB}$ and CK could have experienced similar oxidation conditions. This argument has to be considered as a significant clue for a closely related origin of CV and CK chondrites.

These results highlight two other arguments in favor of a closely related origin of CV and CK. First, the associations of magnetite and sulfide observed in CK chondrites ([Rubin 1992](#), , this study) are also observed in $CV3_{oxB}$ ([McSween 1977](#)). Second, the trace element distribution among minerals of $CV3_{oxB}$ NWA 5772 is

closer to those of metamorphized CK than those of CK3, particularly for olivine (Table 3.10).

3.3.5 Summary and Conclusions

The study of the REE and Hf distribution in five CK and one CV_{ox}B samples demonstrates that phosphates do not represent the main carrier of REE in CC but silicates.

First, we observed a decoupling between the distribution of the LREE (Sm and Nd), Lu (HREE) and Hf (HFSE). Up to 40% of Sm and Nd are actually borne by phosphates in low-grade metamorphism (type 3 to 5), the remaining being essentially found in silicates (matrix in type 3, and in this order, olivine, pyroxenes and plagioclase - when existing - in higher metamorphic grades). In type 6, less than 2% of Sm and Nd are borne by phosphates, and the LREE are distributed among high-Ca pyroxene, and plagioclase and olivine (in this order). Lutetium is also significantly borne by phosphates (20-30%) in CK chondrites with very low grades of metamorphism (type 3 and 4), but less than 5% of Lu are found in phosphates in type 5 and less than 1% in type 6. The remaining part is borne by matrix in type 3 and by olivine, low-Ca pyroxene and plagioclase (in this order) in type 4. In higher grade of metamorphism, the main carrier is olivine and to a lesser extent plagioclase and high-Ca pyroxene. Magnetite can also contain a non-negligible part of REE in type 6 CK chondrites (e.g. 15% Sm and 12% Lu). Hafnium is only borne by silicate phases, regardless of the metamorphic grade. In type 3, the main host is matrix, whereas Hf is distributed among olivine and high-Ca pyroxene in higher grades of metamorphism.

Since a significant part (40%) of Sm and Nd are actually stored in phosphates up to type 5, these elements escape redistribution with increasing metamorphism. However, almost 60% of these elements can be redistributed inside the silicate phases when they (re)crystallized during metamorphism. The larger part of Sm and Nd is transferred from phosphates into silicates (and magnetite) between type 5 and 6. Importantly, Sm and Nd behave similarly during recrystallization and are therefore not decoupled. Such a feature likely minimizes the discrepancies of Nd isotopic va-

lues in CHUR. On the contrary, Lu and Hf are decoupled at least in low grade of metamorphism (type 3 and 4). Up to 30% of Lu is stored in phosphates in low metamorphic grades, however this amount significantly decreases in type 5 ($< 5\%$) and 6 ($< 1\%$). Most of Lu is redistributed from phosphates to all the silicate phases (and magnetite in type 6) with increasing metamorphism. Hafnium is mainly stored in two minerals (olivine and high-Ca pyroxene) in equilibrated CK chondrites. These differences in Lu and Hf behavior probably create major heterogeneities in Lu/Hf ratios among different types of chondrites, and consequently leads to the observed variations in the Hf isotopic values of CHUR. Thus, the evolution/recrystallization of phosphates during metamorphism alone cannot explain the discrepancies observed in Hf CHUR values. This is truly the different behavior of Lu and Hf during metamorphism that is the clue to this heterogeneity.

To conclude, the study of REE and Hf distribution among mineral phases in CK and CV chondrites highlights that :

- (1) the main host of REE and Hf are not phosphates but silicates, even if up to 40% of Sm and Nd and 30% of Lu are stored in phosphates in low grade of metamorphism.
- (2) Sm and Nd are (re)distributed among the same mineral phases during metamorphism. This coupling preserves the Sm/Nd ratio, and consequently the uniformity of Nd CHUR values.
- (3) Lu and Hf are not borne by the same minerals. Lu is redistributed from phosphate to silicate phases with increasing degree of metamorphism, while Hf is stored in olivine and high-Ca pyroxene in types 4 to 6. This decoupling can create major discrepancies in the Lu/Hf ratio, and can thus explain the heterogeneity observed in Hf CHUR values.
- (4) CV and CK chondrites could belong to a unique clan and share a common origin, as suggested by [Weisberg et al. \(2006\)](#). Although this is still largely deba-

ted, our results on CK and CV3_{oxB} highlight clear resemblances in REE patterns. Further studies of CV3_{oxA} samples could elucidate this conundrum.

3.3.6 Acknowledgments

The authors acknowledge Oscar Steenhaut (VUB) and Alain Bernard (ULB) for SEM analyses, Michel Fialin and Frédéric Couffignal for EPMA analyses, and Andrei Izme for assistance with laser ablation analyses. C.M. is grateful to Fabien Kuntz for having given pieces of NWA 5772 sample. This work benefited from funding of BELSPO funding (SAMBA and BELAM programs) and the InBev-Baillet Latour Antarctica Fellowship. Ph. C and F. V. thank Research Foundation Flanders (FWO) for grant G.A078.11 and G.0021.11. S.G. is a postdoctoral fellow of the Research Foundation - Flanders (FWO).

3.4 CONCLUSIONS ET PERSPECTIVES

Dans ce chapitre, nous avons présenté une technique de quantification des images chimiques acquises en utilisant les spectromètres WDS (De Andrade et al. 2006) à la microsonde. Puis, nous avons proposé XMAPTOOLS, un logiciel pour le traitement de ces cartographies. Un premier exemple d'application a été proposé sous la forme d'un article de Martin et al. et d'autres seront proposés dans les deux chapitres à venir consacrés aux applications (Alpes (Chap. 4) et Himalaya (Chap. 5)). XMAPTOOLS est un logiciel qui est appelé à évoluer dans les années à venir, avec notamment l'ajout de nouvelles fonctions et de nouveaux modules. Ces perspectives de développement peuvent être regroupées selon trois principaux axes :

- (1) *L'ajout de nouvelles méthodes « classiques » de thermobarométrie.* Une petite partie des calibrations disponibles dans la littérature ont été incluses dans le logiciel en fonction des besoins rencontrés. L'ajout de nouveaux thermomètres, baromètres et thermobaromètres interviendront au fur et à mesure des mises à jour.
- (2) *L'ajout d'un module permettant de faire des calculs thermodynamiques.* Ce module doit permettre de tracer des réactions chimiques, en utilisant les bases de données thermodynamiques de Holland et Powell (1998) ou de Berman (1988). Ce module est actuellement en cours de développement à partir d'une adaptation des logiciels MULTIPLOT et MEAMP. Il permettrait de sélectionner directement des compositions de minéraux sur les cartes microsonde et d'essayer de reconstruire les conditions P-T en traçant tous les équilibres intervenant entre les différentes phases.
- (3) *L'ajout d'un module pour calculer des composition locales.* On a vu que XMapTools permettait pour chaque phase de transformer les cartes d'intensités mesurées à la microsonde en cartes de compositions chimiques. À partir de ces cartes, il est possible de recalculer la compositions moyenne d'une partie de la zone d'étude, en tenant compte des zonations chimiques, ce qui est impossible en combinant simplement des abondances modales et des analyses ponctuelles. Un exemple de cartes de compositions est proposé figure 3.22 pour les éléments Si, Ca, Al et Mg (unité, nombre de moles).

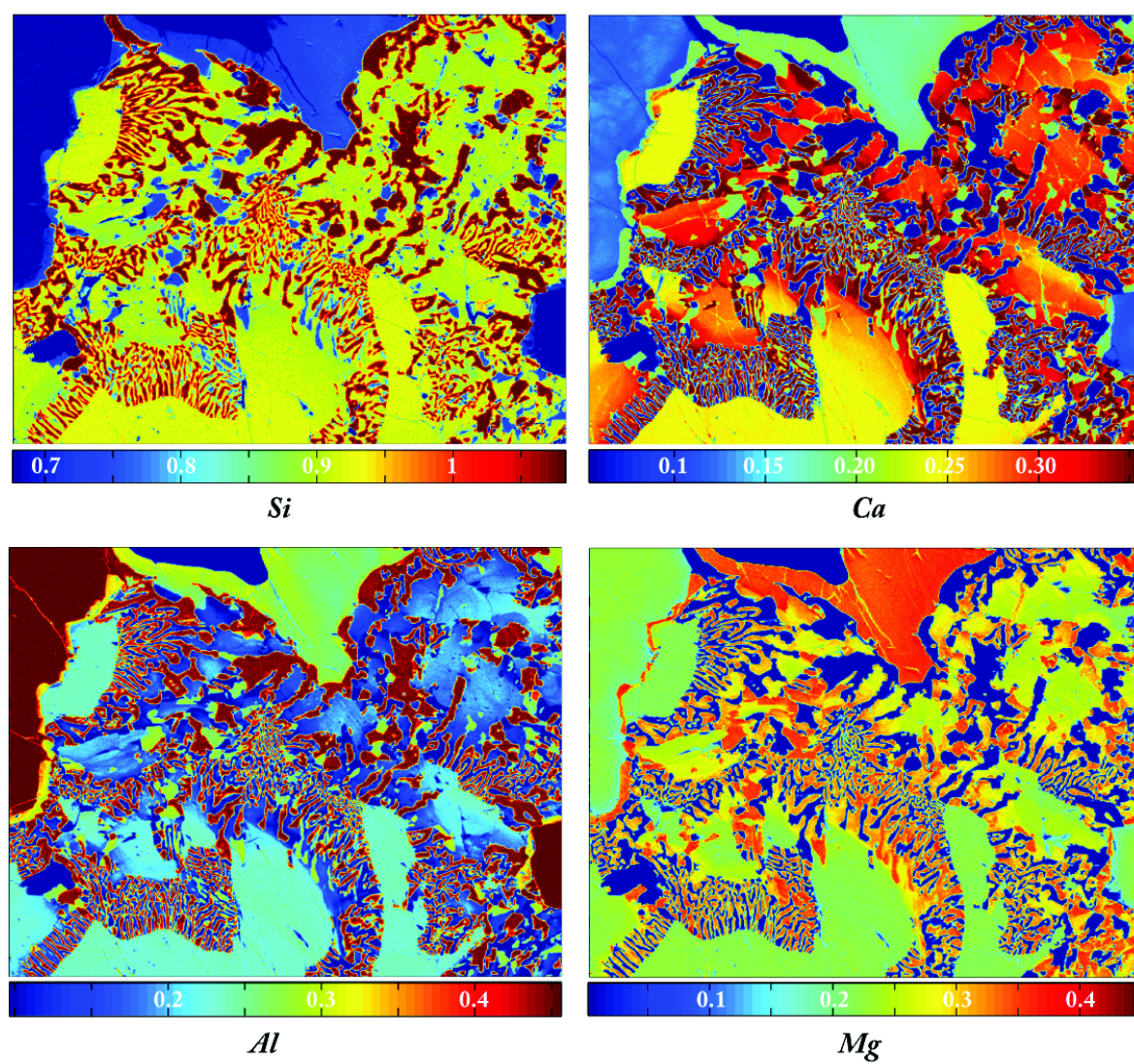


FIGURE 3.22 – Exemple de cartes de compositions "assemblées". Unité : nombre de moles. Échantillon : éclogite du massif de Stak (données de Lanari et al. in press)

APPLICATION AUX ALPES OCCIDENTALES

4

SOMMAIRE

4.1	INTRODUCTION : LES ALPES OCCIDENTALES	199
4.2	ETUDE DES UNITÉS BRIANÇONNAISES	210
4.3	PREMIERS RÉSULTATS SUR L'ÉTUDE DU COMPLEXE DES SCHISTES LUSTRÉS DU QUEYRAS	260
4.4	SYNTHÈSE ET PERSPECTIVES	283

CE chapitre est consacré à la cartographie des conditions P-T-t- ϵ enregistrées par les roches métamorphiques des zones internes des Alpes occidentales en associant imagerie chimique, étude d'équilibres locaux et datations $^{40}\text{Ar}/^{39}\text{Ar}$.

IN this chapter we study the P-T-t- ϵ evolution of the metamorphic rocks in the internal zones of the Western Alps using thermodynamic modeling, chemical mapping and $^{40}\text{Ar}/^{39}\text{Ar}$ dating techniques.

4.1 INTRODUCTION : LES ALPES OCCIDENTALES

★ *La reconstruction des modèles géodynamiques de l'évolution d'une chaîne de montagne nécessite de connaître les trajets P-T-t qu'ont subi les différentes unités tectono-métamorphiques de la chaîne.*

★ *La chaîne alpine est la chaîne de montagne la plus étudiée au monde et un grand nombre de données P-T(-t) sont disponibles dans la littérature. Dans la partie occidentale de la chaîne, de nombreux travaux ont été menés sur l'étude des trajets P-T-t dans les massifs les plus orientaux qui présentent la plus forte empreinte métamorphique (Ambin, Dora Maira, Grand Paradis, Schistes lustrés, Vanoise et Viso). Par exemple, la partie la plus à l'Ouest des zones internes présente beaucoup moins de données précises, en raison de la faible empreinte du métamorphisme alpin.*

★ *Dans cette partie introductive, après une brève présentation des zones internes des Alpes occidentales, nous proposerons une liste non-exhaustive des grands travaux menés dans la partie occidentale de la chaîne. Dans un deuxième temps, nous décrirons la stratégie mise en place pour apporter de nouvelles données P-T(-t) pour certaines zones peu contraintes, afin d'affiner les modèles géodynamiques disponibles.*

4.1.1 Généralités sur la partie occidentale de la chaîne alpine

La chaîne alpine est typiquement une chaîne de subduction-collision (e.g. [Hamilton 1969](#), [Coney 1970](#), [Dewey 1970](#), [Beaumont et al. 1996](#)) qui résulte de la convergence, depuis le Crétacé Supérieur, entre l'Afrique et l'Europe. Cette convergence a entraîné la fermeture par subduction et obduction de trois paléo-domaines à croûte continentale amincie et/ou à croûte océanique : les domaines valaisan, briançonnais et liguro-piémontais ([Ernst 1971](#)). Il en résulte à l'actuel, un édifice complexe de nappes et d'écailles plissées lors de différents événements tectoniques associés à la subduction, puis à la collision.

Cette étude est focalisée sur l'arc alpin occidental (Fig. [4.1](#)) qui est une petite partie d'un arc plus vaste qui inclut les Alpes centrales et orientales, et également les Carpathes (e.g. [Lallemant et al. 2005](#)). Dans cette partie de la chaîne, on dis-

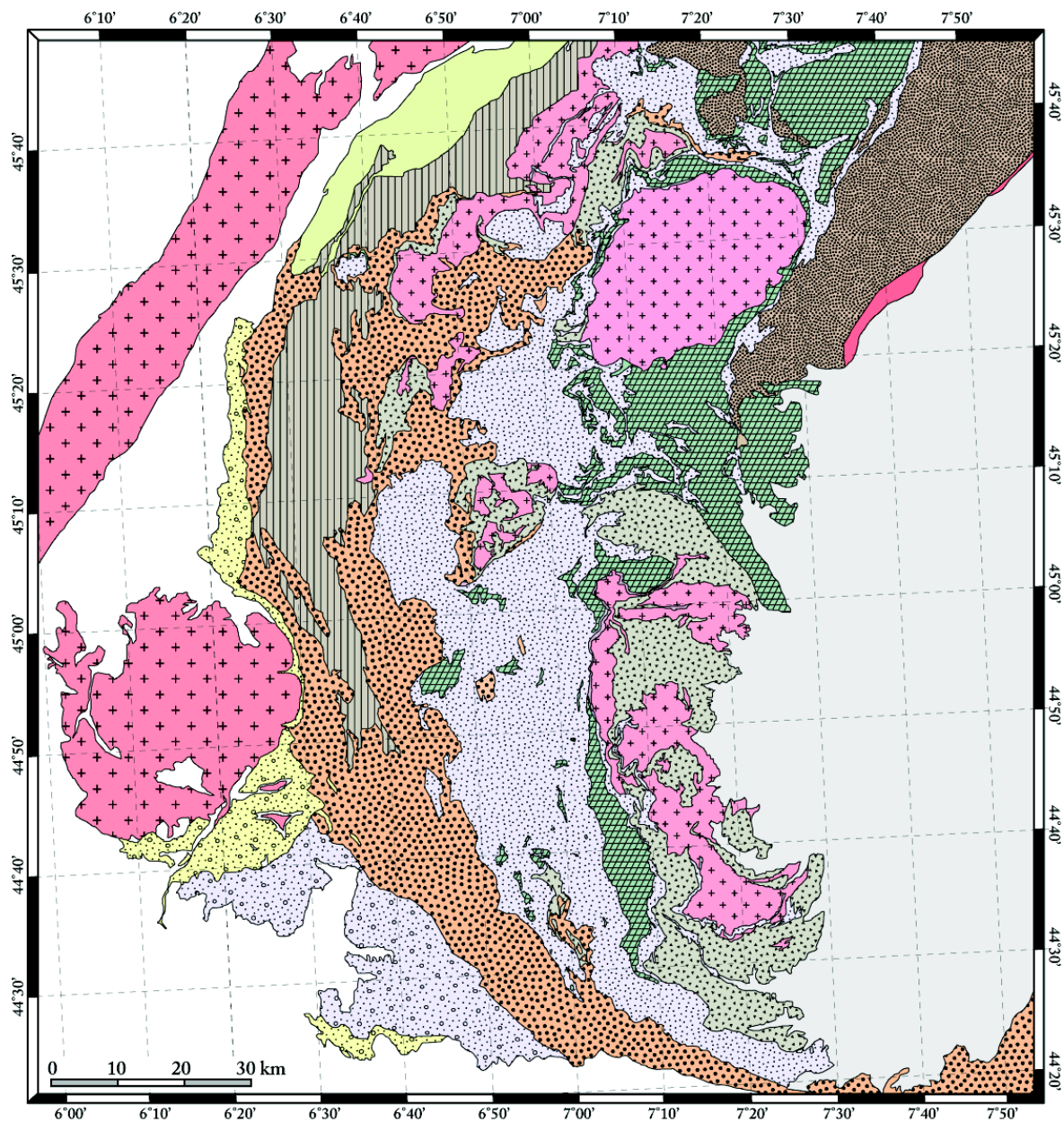
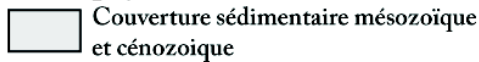


FIGURE 4.1 – Carte géologique des Alpes occidentales franco-italiennes (modifiée d'après *Debelmas 1980, Kerckhove et al. 1980, Tricart 2003, Bousquet et al. 2008, Gabalda et al. 2009, Schwartz et al. 2009, Lanari et al. 2012a, Dumont et al. 2012*). La légende est disponible figure 4.2.

Zones alpines

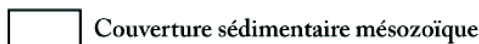
origines paléo-géographiques

« Avant-pays »

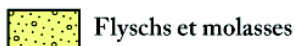


Afrique

Zone Externe non métamorphique (Delphino-Helvétique)



paléomarge européenne proximale

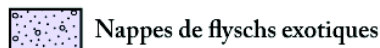


bassins d'avant-chaine



paléomarge européenne proximale

Zones Internes non métamorphiques



océan



paléomarge africaine

Zones Internes métamorphiques

Zone Valaisane

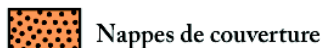


domaine Valaisan

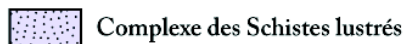
Zone Briançonnaise



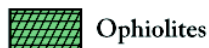
paléomarge européenne



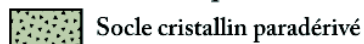
Zone Piémontaise



océan



Socle cristallin anté-alpin



paléomarge européenne



Zone Austro-Alpine

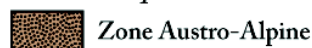


FIGURE 4.2 – Légende de la carte géologique présentée figure 4.1. Les figurés ont été classés par zones alpines "classiques" en mentionnant en italique les origines paléo-géographiques. Sur ces figures, les nappes piémontaises issues de la marge distale ont été reportées avec les nappes de couverture briançonnaise.

tingue sur des arguments tectoniques, métamorphiques, paléontologiques et lithostratigraphiques, plusieurs unités principales (Fig. 4.1). Les Alpes occidentales sont classiquement divisées en deux zones distinctes séparées par un accident majeur, le Front pennique (Fig. 4.3).

À l'ouest du Front pennique, affleurent les unités externes de la zone delphino-helvétique. Elles sont constituées des massifs cristallins externes et de leur couverture sédimentaire mésozoïque et correspondent à la paléo-marge européenne proximale. Localement, elles sont recouvertes par des flyschs et molasses des bassins d'avant chaînes tertiaires.

À l'est du Front pennique, on entre dans les zones internes. Dans les Alpes, les zones internes d'origine européennes sont dites penniques par opposition aux zones internes austro-alpines et apuliennes. Juste après le franchissement du Front pennique, au Nord de Moutiers (Fig. 4.4), on rencontre une première suture soulignée par la zone valaisane. Elle témoigne de la présence d'un paélo-domaine océanique (ou constitué de croûte continentale très amincie pour cette portion), l'océan Valaisan. Au Sud de Moutiers, cette suture valaisanne n'est pas présente et localement, affleurent des unités internes non métamorphiques comme les épaisses séries de flyschs exotiques qui sont séparées des unités métamorphiques briançonnaises par un chevauchement majeur : le Front briançonnais (Fig. 4.3). La zone Briançonnaise est constituée de nappes de couvertures reposant sur un socle cristallin anté-alpin avec dans la partie la plus externe la présence entre les deux d'une série permo-carbonifères constituant la zone houillère briançonnaise. La zone briançonnaise est séparée des unités océaniques liguro-piémontaises des Schistes lustrés par le Front des Schistes lustrés (Fig. 4.3), ancien front chevauchant qui localement est rétrocharié vers l'Est (Tricart 1984). Ces unités océaniques constituées de sédiments et de masses ophiolitiques (e.g. Tricart 1973, Lagabrielle 1987, Philippot 1988, Schwartz 2000, Agard 1999) forment la deuxième suture de la chaîne résultant de la fermeture de l'océan liguro-piémontais. Plus à l'Est affleurent les massifs cristallins internes piémontais de Dora Maira et du Grand Paradis, puis dans la partie Nord, les unités austro-alpines et sud-alpines, séparées de l'avant-pays ita-

lien par la ligne insubrienne qui correspond à la limite tectonique orientale de la chaîne (Fig. 4.3).

4.1.2 Bref historique des études géologiques des Alpes françaises

La chaîne Alpine est la chaîne la plus étudiée au monde (Coward et Dietrich 1989) et les premières "observations géologiques" relatées remontent à plus de 150 ans. Nous allons dresser ici un bref historique des travaux et avancées majeurs sur les Alpes internes françaises. Ceci va nous permettre de situer notre travail dans la perspective de l'étude de la chaîne alpine.

4.1.2.1 Stratigraphie et déformations alpines

Dans la partie méridionale des Alpes internes occidentales, les premières observations rapportent l'existence de formations sédimentaires qui reposent sur des "terrains primitifs" (Gueymard 1830). Plus tard, Lory (1864) établit une première stratigraphie dans le Briançonnais et propose de subdiviser d'Ouest en Est l'ensemble de la chaîne en 4 zones distinctes : (1) les massifs cristallins externes, (2) la zone subbriançonnaise, le flysch des Aiguilles d'Arves et celui de l'Embrunais-Ubaye regroupés avec le Briançonnais occidental, (3) la Zone Houillère briançonnaise, et (4) le Briançonnais central et oriental regroupé avec les Schistes lustrés. Ces zones diffèrent de celles que nous avons proposées précédemment. La raison principale est l'absence, à l'époque, du concept de nappes, rendant impossible la compréhension de la géométrie des différents ensembles. Ce n'est que cinquante ans plus tard, à la suite des travaux de Termier (1891), Bertrand (1894), Kilian (1899; 1903), Argand (1916), Kilian et al. (1923), qu'apparaît la notion fondamentale de recouvrement et donc la distinction entre les "vrais Schistes lustrés" à ophiolites et certaines unités du Briançonnais interne. Ces auteurs sont également les premiers à proposer des modèles tectoniques impliquant des nappes de charriage. Au début du XX^e siècle, des études tectono-stratigraphiques approfondies, sous la forme d'un travail de cartographie, sont menées. Il en découle un nouveau découpage des nappes briançonnaises à l'Est et au Sud-Est du Pelvoux (Gignoux 1938, Debelmas 1955). À partir des années 1970, de nombreux travaux d'inventaire à l'échelle de

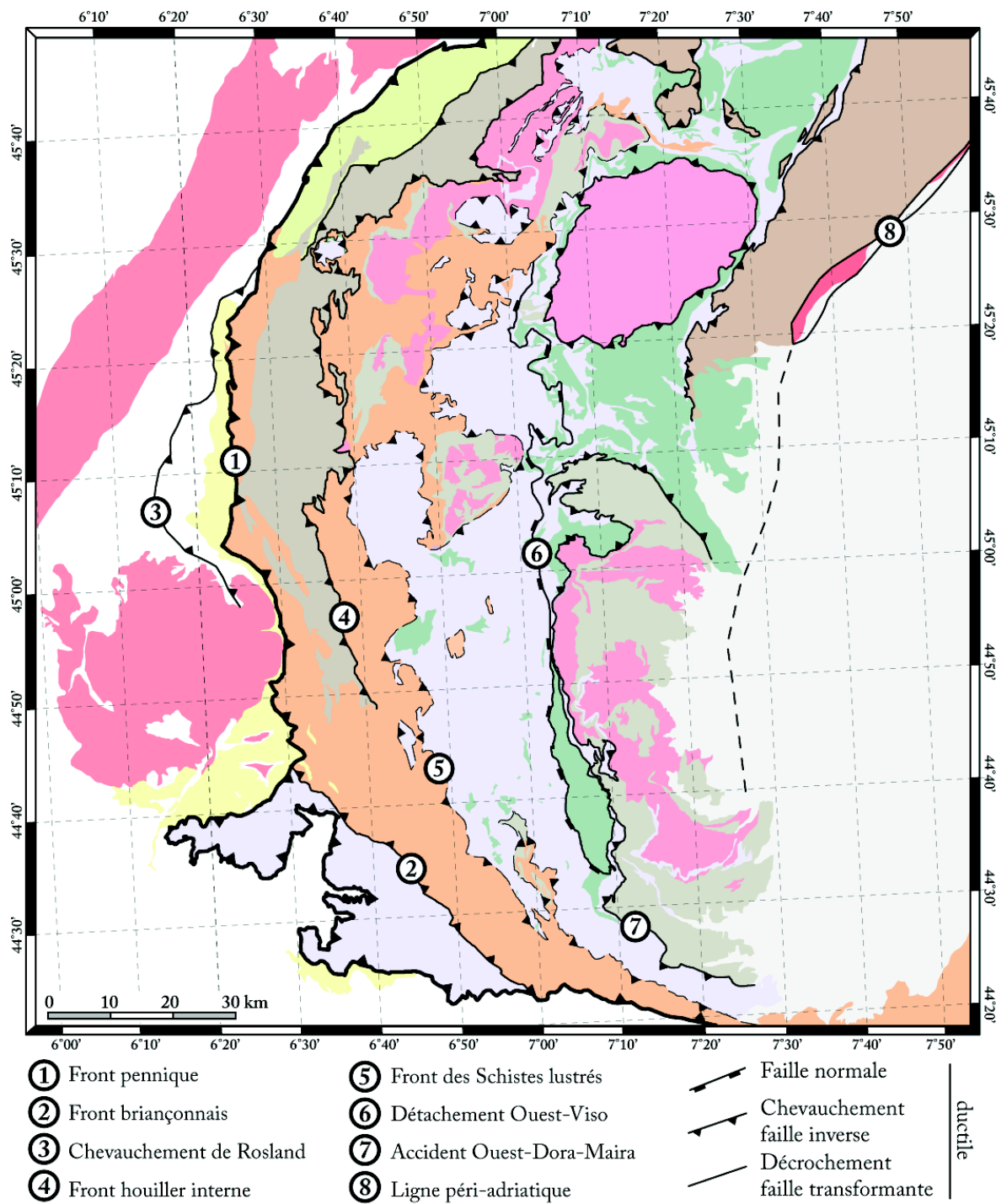


FIGURE 4.3 – Carte tectonique simplifiée des Alpes occidentales franco-italiennes. Les couleurs utilisées pour la cartographie des unités géologiques sont les mêmes que celles de la figure 4.2.

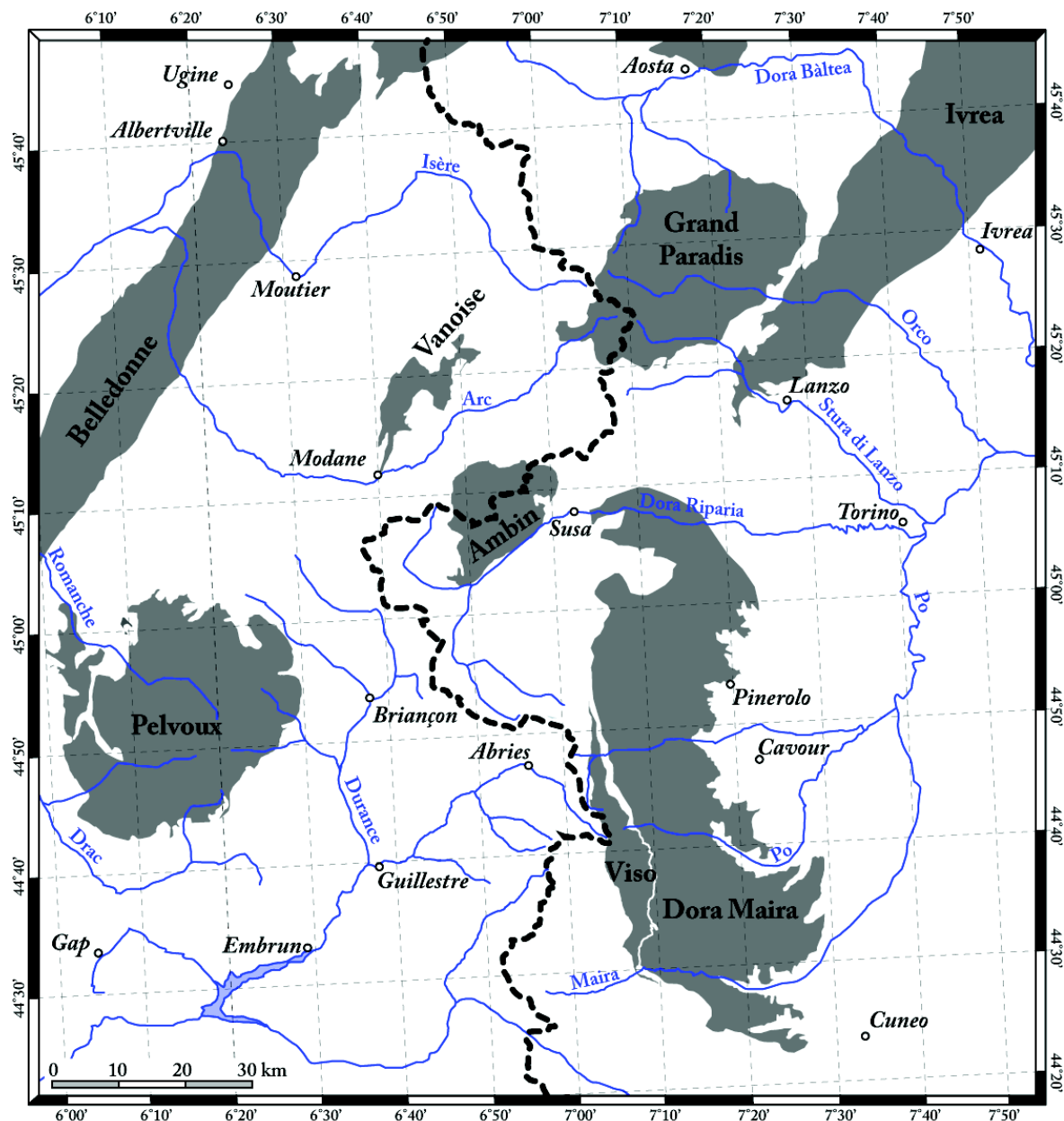


FIGURE 4.4 – Carte horo-hydrographique des Alpes occidentales franco-italiennes. Les principaux massifs sont représentés en gris sur la carte. La ligne pointillée noire est la frontière franco-italienne qui souligne la ligne de partage des eaux.

massifs¹ ont eu pour objectif de compléter ce travail de cartographie tout en réalisant une étude détaillée des structures de déformation alpines. C'est notamment l'objectif principal des travaux de thèses de [Bertrand \(1966\)](#), [Vialon \(1966\)](#), [Tricart \(1980\)](#), [Fabre \(1982\)](#), [Jaillard \(1984\)](#), [Detraz \(1984\)](#), [Baudin \(1987\)](#), [Guillot \(1987\)](#) dans les unités d'origine continentale (Briançonnais et massifs cristallins internes) et de [Nicolas \(1966\)](#), [Fudral \(1973\)](#), [Tricart \(1973\)](#), [Caron \(1977\)](#), [Deville \(1987\)](#), [Lagabrielle \(1987\)](#) dans les unités d'origine océanique (Piémontais).

4.1.2.2 Métamorphisme

L'étude du métamorphisme dans les Alpes occidentales débute par les travaux précurseurs en Vanoise (Fig. 4.4) d'[Ellenberger \(1958; 1963\)](#) avec notamment la mise en évidence du caractère syn-tectonique du métamorphisme alpin. Quelques années plus tard, plus à l'Ouest dans la zone houillère briançonnaise, [Fabre \(1961\)](#) distingue clairement des métamorphismes polyphasés respectivement alpin et anté-alpin. Suite à l'apparition du concept de tectonique des plaques ([Morgan 1968](#)), [Ernst \(1971\)](#) propose un premier modèle reliant le métamorphisme alpin de haute pression au phénomène de subduction de matériel océanique sous une plaque continentale. L'identification de paragenèses éclogitiques dans des roches d'origine continentale dans la zone de Sesia-Lanzo ([Dal Piaz et al. 1972](#), [Compagnoni et Maffeo 1973](#)) sont l'origine du concept de subduction continentale. Dix ans plus tard, la découverte de la coésite dans les unités continentales de Dora Maira par [Chopin \(1984\)](#) permet d'introduire le concept de ultra-haute pression (UHP) et prouve qu'une partie de la croûte continentale de la paléo-marge briançonnaise a été entraînée à une centaine de kilomètres de profondeur dans la subduction ([Gillet et al. 1984](#)). Dans la partie occidentale de la chaîne, de nombreuses thèses portant sur des études du métamorphisme à l'échelle de massifs viendront compléter le jeu des données disponibles. On citera ici notamment les travaux de [Caron \(1970\)](#), [Goffé \(1975\)](#), [Chopin \(1979\)](#), [Robert \(1979\)](#), [Balleivre \(1986\)](#). La première synthèse "moderne" du métamorphisme est effectuée par [Bocquet \(1974\)](#), puis par [Saliot \(1978\)](#) qui propose une carte de la distribution des minéraux index et fournit un

1. C'est-à-dire sur une zone d'une cinquantaine de km^2 , souvent délimitée par des vallons ou des lieux-dits, comme par exemple [Fudral \(1973\)](#) qui travaillât "entre le vallon du torrent du Cornet d'Arêches et le hameau des Chapieux".

grand nombre d'analyses chimiques, discutant ainsi l'évolution des compositions de minéraux à l'échelle de la chaîne. Toutes ces nouvelles données sur le métamorphisme ainsi que les premières données radiochronologiques ont permis l'apparition de modèles tectono-métamorphiques (e.g. [Caby et al. 1978](#), [Gillet et al. 1986](#)).

4.1.2.3 Études récentes

À la fin du XX^e siècle, le travail de cartographie est achevé et les grandes structures ainsi que les principales phases de déformation ont été identifiées à l'exception de la partie Sud des Schistes lustrés qui sera récemment complétée par [Tricart \(2003\)](#). Grâce à ces données structurales et aux données métamorphiques et radiochronologiques, de nombreux modèles apparaissent pour essayer d'expliquer l'évolution tectono-métamorphique de la chaîne. Ces tentatives ont mis en évidence des contradictions et donc la nécessité de ré-entreprendre des études fines dans plusieurs zones de la chaîne. C'est pourquoi, au cours des quinze dernières années, de nouveaux travaux de thèse ont été conduits sur l'étude du métamorphisme dans les Alpes françaises ([Bousquet 1998](#), [Agard 1999](#), [Schwartz 2000](#), [Ceriani 2001](#), [Ganne 2003](#), [Le Bayon 2005](#), [Yamato 2006](#), [Gerber 2008](#), [Gabalda et al. 2009](#), [Angiboust 2011](#)). Ces travaux coïncident également avec l'apparition de nouveaux outils thermobarométriques et radiochronologiques (e.g. [Holdaway et Mukhopadhyay 1993](#)).

La répartition du métamorphisme à l'échelle de la chaîne est aujourd'hui bien connue comme le montre la carte synthétique de [Oberhänsli et al. \(2004\)](#) (Fig. 4.5). Une synthèse similaire des âges du métamorphisme Schistes bleus enregistré durant la subduction a été récemment proposée par [Berger et Bousquet \(2008\)](#). Ces deux synthèses mettent en évidence une absence de données dans certaines zones de la terminaison Sud qui résulte, soit des lithologies qui sont défavorables, soit de l'absence de minéraux index. Ce travail s'inscrit dans la continuité des études présentées précédemment et résulte de la nécessité de compléter les données P-T et radiochronologiques pour la branche Sud de l'Arc, afin de raffiner les modèles tectono-métamorphiques. L'objectif a été d'appliquer les techniques de microcartographie et de thermodynamique présentées précédemment (Chap 2 et 3) ainsi que des méthodes de datation $^{40}\text{Ar}/^{39}\text{Ar}$ sur phengite pour proposer des trajets

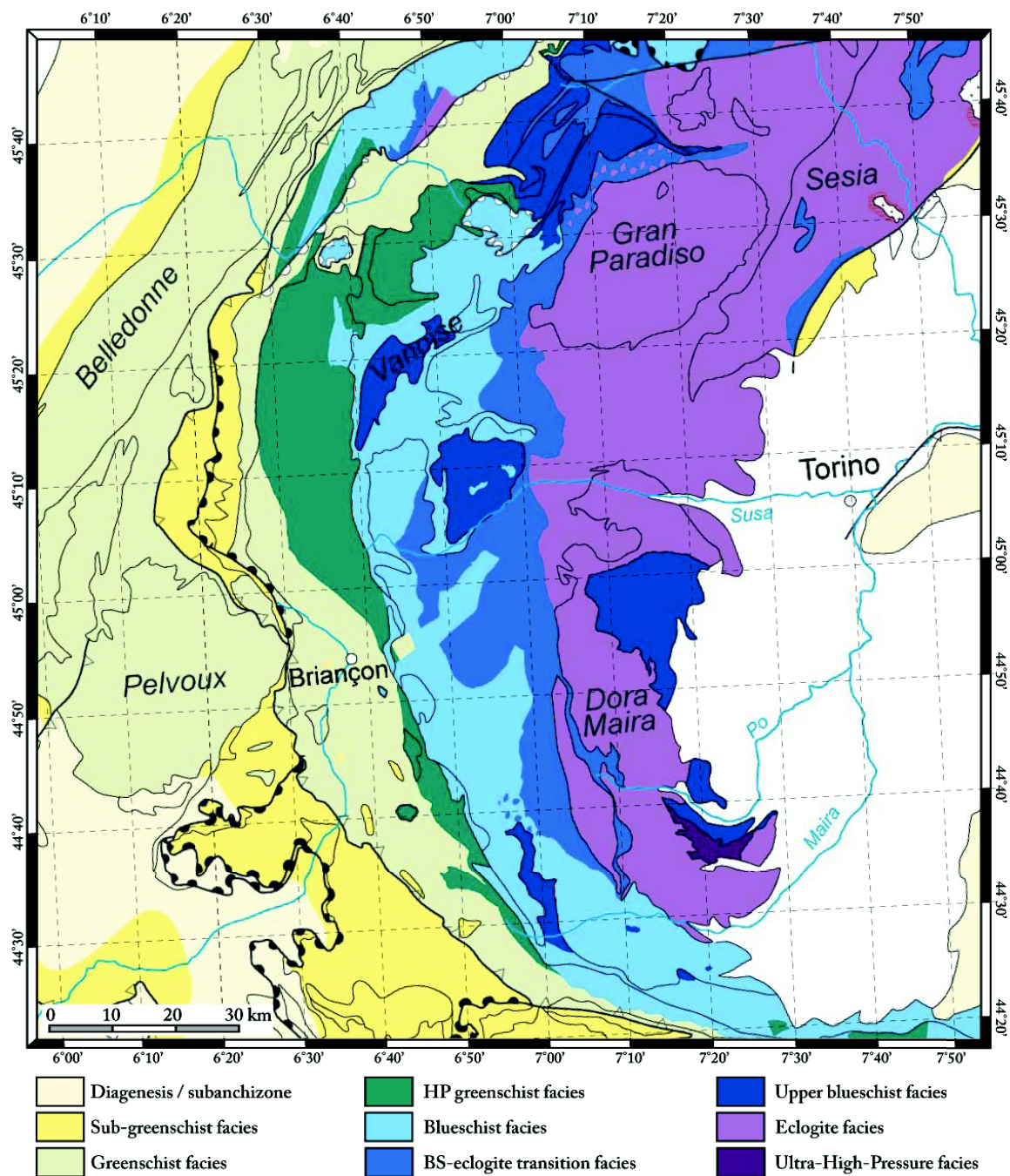


FIGURE 4.5 – Carte du métamorphisme dans les Alpes occidentales modifiée d'après Oberhänsli et al. (2004).

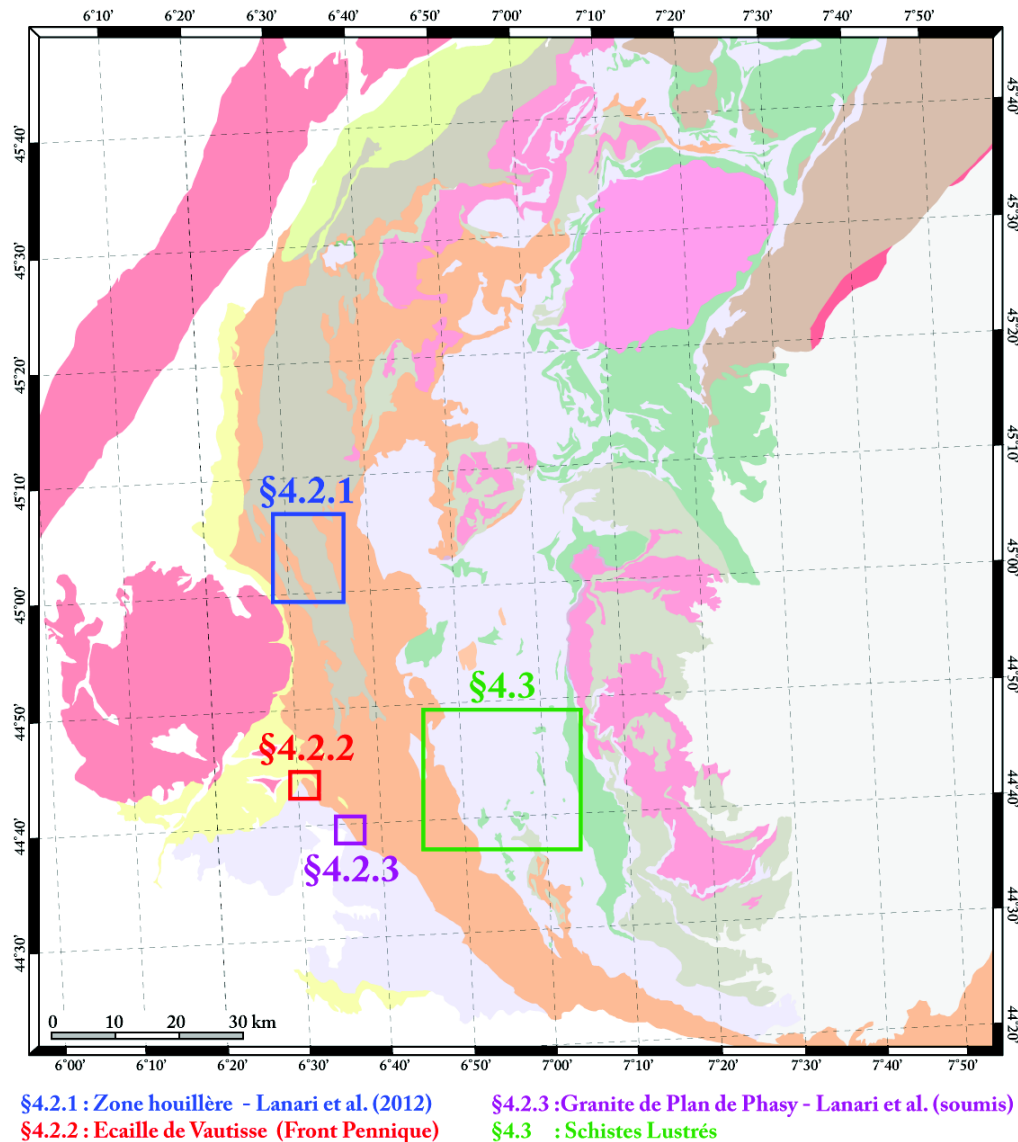


FIGURE 4.6 – Localisation des différentes zones d'étude traitées dans la suite. Les couleurs utilisées pour la cartographie des unités géologiques sont les mêmes que celles de la figure 4.2.)

P-T- ϵ -t de secteurs qui en sont actuellement dépourvus. Nous avons donc focalisé nos efforts sur les parties de la chaîne où, faute de méthodes adaptées, il n'y avait pas d'estimations précises disponibles.

Dans un premier temps, nous allons traiter des unités d'origine continentale de la zone briançonnaise (Part 4.2, c.f. Fig. 4.6), puis sur le complexe des Schistes lustrés du Queyras (Part. 4.3, c.f. Fig. 4.6).

4.2 ÉTUDE DES UNITÉS BRIANÇONNAISES

★ *Les unités les plus externes de la Zone briançonnaise ont enregistré un métamorphisme alpin dans le faciès des Schistes verts. Il est donc difficile d'estimer des trajets P-T en utilisant des approches conventionnelles.*

★ *Dans la Zone briançonnaise au Sud de la vallée de la Maurienne, aucune estimation P-T précise n'est disponible, ni pour la zone Houillère, ni pour les nappes de couverture.*

★ *Dans cette partie, nous allons proposer la caractérisation des trajets P-T- ϵ (-t) de trois secteurs clefs de la partie méridionale de la Zone briançonnaise : La Zone houillère dans la haute vallée de la Clarée ; les nappes briançonnaises au niveau de l'écaille de Vautisse et un fragment de socle briançonnais : le « Granite de Plan de Phasy ».*

4.2.1 Introduction

La Zone briançonnaise s'étend depuis le front pennique jusqu'au front des Schistes lustrés pour sa partie externe et apparaît en fenêtre sous les Schistes lustrés pour sa partie la plus interne (Fig. 4.1).

4.2.1.1 Données disponibles sur le métamorphisme

Les données sur le métamorphisme disponibles dans la Zone briançonnaise au Sud de la vallée de la Maurienne sont des données peu précises qui proviennent de la présence de minéraux index comme la lawsonite (Saliot 1978, Caby 1996, Frey et Ferreiro Mählmann 1999, Goffé et al. 2004, Bousquet et al. 2008). Des estimations précises à la fois de la pression et de la température sont disponibles uniquement dans les parties les plus internes de la Zone briançonnaise comme par exemple dans le massif d'Acceglio (Schwartz et al. 2000) ou d'Ambin (Ganne et al. 2005; 2007).

4.2.1.2 Stratégie

Pour affiner les modèles d'évolutions géodynamiques pour la Zone briançonnaise, nous avons focalisé nos efforts sur la partie la plus occidentale de cette zone

qui ne possédait pas d'estimation précise des conditions P-T. Les unités briançonnaises potentiellement riches en phyllosilicates cristallisés durant le métamorphisme alpin ont été systématiquement échantillonnées. Finalement, trois secteurs clefs ont été retenus pour une étude thermobarométrique, couplé pour deux d'entre avec une étude radiochronologique.

Nous allons dans une première partie proposer une étude détaillée des conditions du métamorphisme dans la branche Sud de la Zone houillère briançonnaise (secteur de la Haute Vallée de la Clarée au Nord de Névache). Les résultats de ce travail seront présentés sous forme d'un article de [Lanari et al. \(2012a\)](#) publié dans la revue *Journal of Geodynamics*. Nous avons réalisé une étude combinée de la température maximale du métamorphisme (T_{max}) alpin, enregistrée par la matière carbonée présente dans les métapélites (e.g. [Beyssac et al. 2002](#)), et une analyse détaillée d'un échantillon de grès micacé, afin de reconstruire les conditions P-T enregistrées par les minéraux. Nous avons utilisé des images chimiques acquises à la microsonde et le logiciel XMAPTOOLS pour différencier les phyllosilicates détritiques et ceux cristallisés (ou recristallisés) lors du métamorphisme alpin. À partir de ces différentes chimies, les conditions de cristallisation des chlorites et des phengites ont été estimées en combinant différentes techniques de multi-équilibres disponibles dans la littérature (e.g. [Vidal et al. 2006](#), [Dubacq et al. 2010](#)). Les conditions du pic de pression du métamorphisme alpin ont été estimées à $371 \pm 26^\circ\text{C}$ and $3.5 \pm 1.4 \text{ kbar}$. Ces résultats sont cohérents avec la température maximale de $283 \pm 50^\circ\text{C}$ obtenue avec l'étude Raman de la matière carbonée dans le même échantillon. Ces premières estimations P-T pour cette zone faiblement métamorphique ont permis, en les combinant avec les résultats de la littérature, disponibles pour les zones les plus internes de la chaîne, de proposer un schéma d'évolution géodynamique de la paléo-marge briançonnaise durant la subduction continentale alpine.

Dans une deuxième partie, nous présenterons les résultats obtenus au niveau de l'écaille de Vautisse (Vallée de Dormillouse). Des analyses ponctuelles de chlorites et de phengites acquises à la microsonde électronique ont permis d'identifier les conditions P-T enregistrées par les minéraux alpins (e.g. $278 \pm 50^\circ\text{C}$ et

3.5 ± 2.4 kbar). Dans un deuxième temps, des grains de phengites ont été extraits et l'un d'entre eux daté en utilisant la technique $^{40}\text{Ar}/^{39}\text{Ar}$.

Dans une dernière partie, nous présenterons les conditions P-T-t obtenues pour un échantillon provenant du « granite de Plan-de-Phasy ». Les résultats seront présentés sous forme d'un article de Lanari et al. soumis à la revue *Terra Nova*. Cette écaille de socle appelée « granite de Plan-de-Phasy » (Kerckhove et Piboule 1999) est pincée dans le Chevauchement briançonnais frontal et affleure dans la vallée de la Durance à l'Ouest de Guillestre (Fig. 4.4 et 4.6) sur le hameau de Plan-de-Phasy. Dès la fin du XIV^{e} siècle, Kilian et Termier (1898) décrivent cette unité comme un granite mylonitisé par analogie avec certains granites du Pelvoux. Ces auteurs proposent que ce granite provienne du socle cristallin briançonnais anté-Houiller de la zone interne. Plus tard, après l'identification de la faille normale de la Durance, Debelmas (1955) propose que le granite de Plan-de-Phasy soit une écaille de socle cristallin de la zone externe mise à l'affleurement par le jeu normal de la faille. Plus récemment, notamment étonnés de l'absence de Houiller entre le prétendu socle et sa couverture permo-triassique, Kerckhove et Piboule (1999) proposent que le granite de Plan-de-Phasy soit en réalité une arkose appartenant à la semelle anté-anisienne. Pour essayer de mieux comprendre cette unité et sa signification géodynamique, nous avons réalisé une étude de terrain combinée à une étude pétrographique des phyllosilicates afin d'estimer le trajet P-T-t. Les phengites cristallisées pour des conditions HP-LT ont été séparées à la main en utilisant une loupe binoculaire. Après irradiations, les grains sélectionnés ont été datés en utilisant la technique $^{40}\text{Ar}/^{39}\text{Ar}$ et donnent un âge de cristallisation à 45.85 ± 1.06 Ma. Les résultats de cette étude ont permis d'affiner le modèle d'évolution géodynamique de la paléo-marge briançonnaise durant la subduction continentale alpine.

4.2.2 Article 5 : Diachronous evolution of the alpine continental subduction wedge : Evidence from P-T estimates in the Briançonnais Zone houillère (France - Western Alps) (Published in Journal of Geodynamics).

Diachronous evolution of the alpine continental subduction wedge : Evidence from P-T estimates in the Briançonnais Zone houillère (France - Western Alps)

Pierre Lanari^a, Stéphane Guillot^a, Stéphane Schwartz^a, Olivier Vidal^a, Pierre Tricart^a, Nicolas Riel^a, Olivier Beyssac^b

Journal of Geodynamics, Vol. 56-57 pp. 39-54 (2012)

doi :10.1016/j.jog.2011.09.006

Abstract - The study of continental subduction processes requires detailed Pressure Temperature (P-T) paths to understand the kinematic of burial and exhumation of continental units. In the French Western Alps, the Briançonnais zone is a remnant of the continental subduction wedge. P-T conditions have been estimated in its most internal parts, but there is a lack of data in the western part, known as the "Zone houillère". This Briançonnais Zone houillère is classically divided into two sub-units : the upper and lower Houiller units. This study focuses on both of these in the Clarée valley, north of Briançon. In this low-grade metamorphic terrain, estimation of P-T history is complicated because there are few adapted methods and these rocks have a poor metamorphic mineralogical content, including detrital metamorphic minerals inherited from their hercynian history. Therefore, to acquire accurate P-T estimates a multi-method approach is required, involving qualitative and quantitative Raman Study of Carbonaceous Material (RSCM), chemical analysis from quantified X-ray maps and thermodynamic modelling of chlorites and K-white micas. Such multi-approach P-T estimates on a sandstone sample allow distinguishing hercynian peak metamorphic conditions of $371 \pm 26^{\circ}\text{C}$ and $3.5 \pm 1.4 \text{ kbar}$ and alpine peak metamorphic conditions of $275 \pm 23^{\circ}\text{C}$ and $5.9 \pm 1.7 \text{ kbar}$. These results are consistent with our RSCM and T_{max} estimates. Raman study conducted on organic-rich schist samples shows an eastward increase of the alpine T_{max} in the upper Houiller unit, from 280 to 300 °C across the Briançonnais Zone houillère. In contrast, carbonaceous material included in detrital

grains of muscovite in the sandstone exhibits higher temperatures. This hercynian T_{max} is estimated using thermodynamic modelling at 376 ± 50 °C. According to these results and previous work in more internal parts of the Briançonnais zone, a geodynamic reconstruction is proposed, which is characterized by a diachronous evolution of the Briançonnais zone involved in alpine continental subduction at different times. The geothermal gradient in the Briançonnais zone changes from 8°C/km during early continental subduction, to 40°C/km during the collisional event at about 35-30 *Ma*. The intermediate gradient of 15°C/km estimated in the Briançonnais Zone houillère suggests that this unit was buried later, than the more internal Briançonnais units, after 40 *Ma*.

Keywords - Continental subduction ; P-T path ; low-grade metamorphism ; geodynamic ; Western Alps

4.2.2.1 Introduction

Since the discovery of UHP mineral parageneses in continental rocks in the Alps and in Norway (Chopin 1984, Smith 1984), the concept of continental subduction has been thoroughly investigated worldwide (e.g. Guillot et al. (2009) for a review). One of the main open questions concerns the size of exhumed continental units during their syn-collisional evolution. Young et al. (2007) recently proposed that only large-scale units (hundreds of km^2) can be exhumed. In the French Western Alps, the Briançonnais zone is a remnant of the continental subduction wedge. This domain outcrops in a 1200 km^2 area, sandwiched between the oceanic subduction paleo-wedge (Piedmont internal zone) and the collision paleo-wedge (external zone). This configuration makes it a strategic area for understanding the thermal evolutions and therefore the continental subduction processes. Several studies have been conducted over the last ten years, which were aimed at constraining the evolution of Pressure-Temperature (P-T) conditions of the internal parts of the wedge such as the Vanoise and Ambin massifs of the Briançonnais Zone, during the Alpine orogeny (Ganne 2003, Ganne et al. 2003; 2005; 2007, Gerber 2008, Strzeczynski et al. 2012). In contrast, the metamorphic evolution of the external part of the Briançonnais Zone, known as the "Zone houillère", remains largely unconstrained (Gabalda

et al. 2009). P-T conditions recorded by the Briançonnais Zone houillère during alpine continental collision are not well established. This low-metamorphic-grade terrain consists of a stack of Carboniferous and Permian metasediments and volcanics. Metasediments are composed of organic-rich schist and sandstone levels with a poor and monotonous mineralogy (mostly phyllosilicates), which have hampered P-T estimates using classical thermobarometric approaches.

The first metamorphic conditions derived in the Briançonnais Zone houillère were empirical estimates from index mineral occurrences (see the lawsonite example (Saliot 1978, Frey et al. 1999, Goffé et al. 2004, Bousquet et al. 2008)). More recently, Ceriani et al. (2003) estimated both temperature and pressure in the Saint-Martin de Belleville area using the K-white mica b-cell method, combined with illite crystallinity and fission-track analysis. They proposed a temperature of 280–300°C at a pressure of 3.5 *kbar*. Further south in the Arc valley (Fig. 4.7), Gabalda et al. (2009) conducted a detailed study of thermal metamorphism using RSCM thermometry (Raman Study of Carbonaceous Material). This method (see §4.2.2.4) provides the maximal temperature (T_{max}) reached by a sample during metamorphism. The study of Gabalda et al. (2009) exhibited an eastward increasing T_{max} trend from $346 \pm 50^\circ\text{C}$ to $389 \pm 50^\circ\text{C}$. The authors suggested these T_{max} are most likely Alpine in age, based on the presence of lawsonite in the median and eastern part of the Briançonnais Zone houillère (Frey et al. 1999, Goffé et al. 2004). However, the occurrence of lawsonite at such temperatures would imply a pressure higher than 8–10 *kbar* (Spear 1993), which is not compatible with the estimation of Ceriani et al. (2003). Furthermore, Zircon Fission Track (ZFT) analysis in the western part of the Arc valley, and further north (same location as that studied by Ceriani et al. (2003)), provided ages between 70 *Ma* and 90 *Ma* (Fügenshuh et Schmid 2003, Ceriani et al. 2003). These ages, which are intermediates between Hercynian and Alpine ages, indicate incomplete Tertiary annealing, as there is no evidence of a cretaceous metamorphic event in the Briançonnais Zone houillère. The upper thermal limit of the zircon partial-annealing zone thus provides an estimate about the maximum temperature reached during the alpine event. Depending of the zircon type (amount of α -damage), the upper limit of the zircon partial-annealing tempe-

perature varies from 240°C (Brandon et al. 1998, Bernet 2009) to 300°C (Tagami et al. 1998). The temperatures obtained by Gabalda et al. (2009) in the western part of their transect in the Briançonnais Zone houillère are higher than the experimentally determined zircon annealing temperatures. They are most likely overestimated by about 50°C. This review of metamorphic data in the Briançonnais Zone houillère reveals a great paucity of P-T data, and an apparent incompatibility between the different available estimates. All metamorphic domains along a transect from the Pelvoux external crystalline massif to the Dora Maira internal crystalline massif are well documented (Agard et al. 2001a; 2002, Ganne 2003, Ganne et al. 2003; 2005; 2007, Schwartz et al. 2007, Gerber 2008, Simon-Labric et al. 2009, Strzeczynski et al. 2012) except for the Briançonnais Zone houillère. Therefore we focus our investigation on the Briançonnais Zone houillère in the Clarée valley to the south of the area studied by Gabalda et al. (2009).

P-T estimates in low-grade metamorphic terrains are difficult; we propose a multi-approach metamorphic study here, which consists of a combination of chemical mapping, thermodynamic modelling and RSCM thermometry. Chemical mapping allows the identification of pre-alpine, inherited detrital minerals and new metamorphic minerals growing during the alpine orogeny. It requires measurement of quantified maps of composition using the method proposed by De Andrade et al. (2006). The P-T conditions of metamorphism were estimated from the composition of chlorites and K-white micas in equilibrium (Vidal et Parra 2000, Vidal et al. 2005; 2006, Dubacq et al. 2010). In the present study, the combination of chemical mapping and multi-equilibrium calculations allows construction of a well-resolved P-T path. Unfortunately, the application of such approaches is complex and time-consuming. For this reason, only a single sample has been studied. The results are compared with RSCM thermometry conducted in the Clarée Valley on a large set of samples to estimate the T_{max} of metamorphic events (Beyssac et al. 2002).

The aim of this study is (1) to propose a multi-method approach to estimate P-T conditions in low-grade metamorphic terrains with detrital mineral fractions, (2) to establish a structural cross-section across the Briançonnais Zone houillère between the Pelvoux external crystalline massif and the internal Briançonnais zone (AA' in

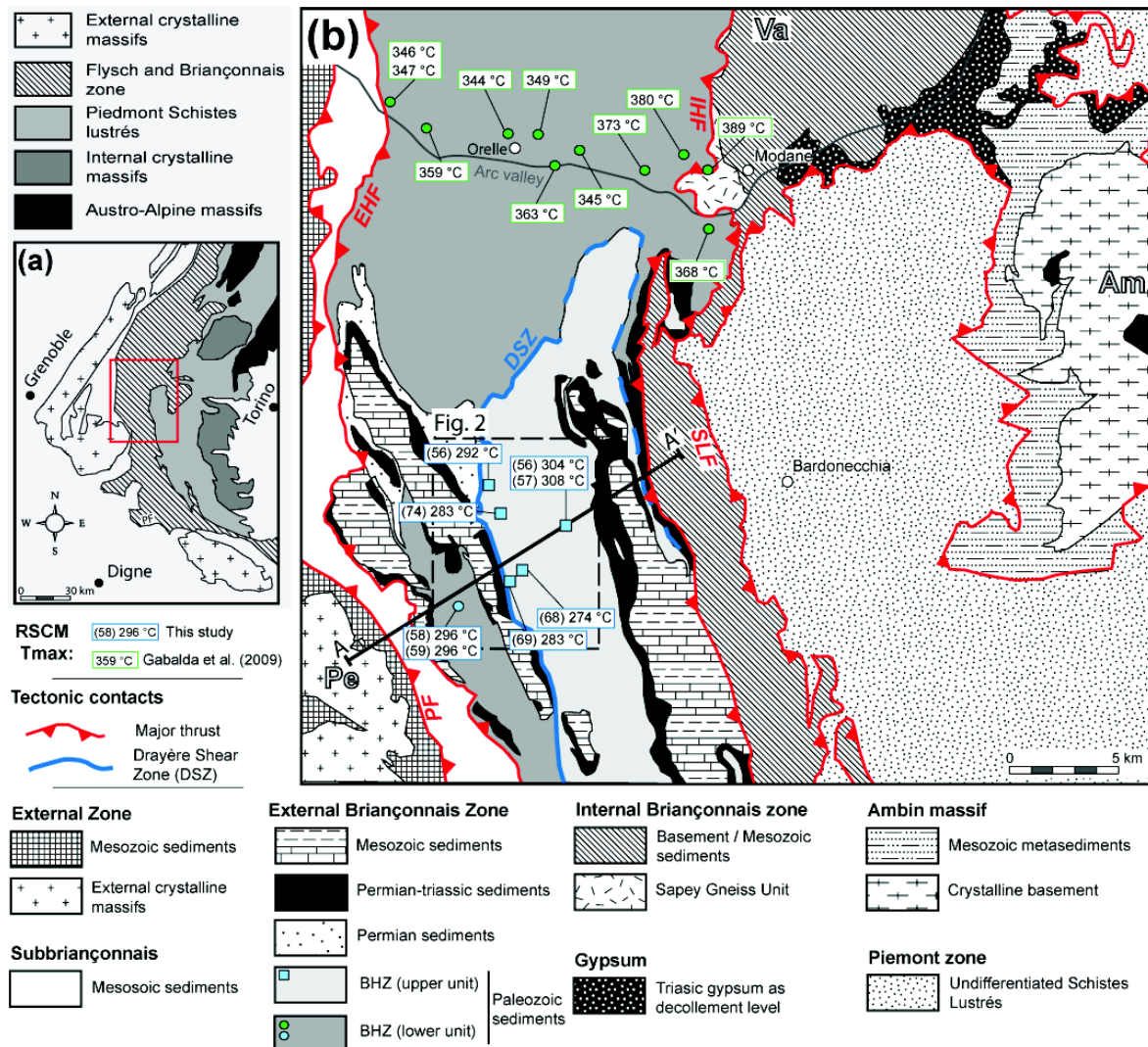


FIGURE 4.7 – Geological map of (a) the western Alps; (b) The Briançonnais zone between the Pelvoux and Ambin massifs modified after Barfèty et al. (2006a), Ford et al. (2006), Gabalda (2008), Gabalda et al. (2009). RSCM Tmax estimates in the Briançonnais Zone houillère from this study and Gabalda et al. (2009), are shown with an absolute incertitude of ± 50 °C. Symbols refer to the stratigraphic unit (square for the upper houiller unit and circle for the lower houiller unit). PF : Penninic Front; EHF : External Houiller Front; DSZ : Drayere Shear Zone; IHF : Internal Houiller Front; SLF : Schistes lustrés Front. Am : Ambin; Pe : Pelvoux; Va : Vanoise. The detailed map (b) is located in the sketch map (a.)

Fig. 4.7) and (3) to compare structure, microstructures and P-T estimates at the local and regional scales in order to discuss the burial and exhumation dynamics of the Briançonnais zone.

4.2.2.2 Geological setting

Regional geology

In the core of the Western alpine arc, the internal metamorphic zones consist of a stack of oceanic and continental-margin derived nappes (e.g. [Graciansky et al. \(2010\)](#) with references therein). This nappe stack results from Mesozoic-Cenozoic convergence between the European and African continental plates, accommodated by subduction and collision processes (see [Schmid et Kissling \(2000\)](#) for a review). Oceanic units (Piedmont Schistes lustrés nappes and associated ophiolites) are derived from the Ligurian segment of the Mesozoic Tethyan ocean. Their complex structure results from severe syn-collisional refolding of the subduction wedge ([Tricart et Schwartz 2006](#), [Lardeaux et al. 2006](#)) and presents an eastward increasing in metamorphic gradient temperature ([Rolland et al. 2000](#), [Schwartz 2000](#), [Agard et al. 2001a](#), [Gabalda et al. 2009](#), [Schwartz et al. 2009](#)). The ocean-derived zone is currently sandwiched between Austroalpine (African) and European nappe stacks. Within the latter, the Briançonnais zone is classically divided into two sub-zones ([Barf  ty et al. 2006a](#)) separated by the Internal Houiller Front (IHF in Fig. 4.7). To the West, the external Briançonnais zone presents relatively comprehensive Mesozoic sedimentary series with a Carboniferous substratum : the Briançonnais Zone houill  re. This unit exhibits low-grade alpine metamorphism ([Salot 1978](#), [Caby 1996](#), [Le Fur 1998](#), [Frey et al. 1999](#), [Goff   et al. 2004](#)). To the east, the internal Briançonnais zone presents a thinner Mesozoic sedimentary cover on top of a basement consisting of pre-Carboniferous metamorphic terrains (like the Ambin massif in Fig. 4.7).

The Briançonnais Zone houill  re is classically divided into the upper and the lower Houiller units (Fig. 4.7), both constituted by polygenetic conglomerates, sandstones, organic-rich schists and anthracite levels intruded by volcanic sills and dykes ([Mercier et Beaudoin 1987](#), [Barf  ty et al. 2006b](#)). The Dray  re shear zone se-

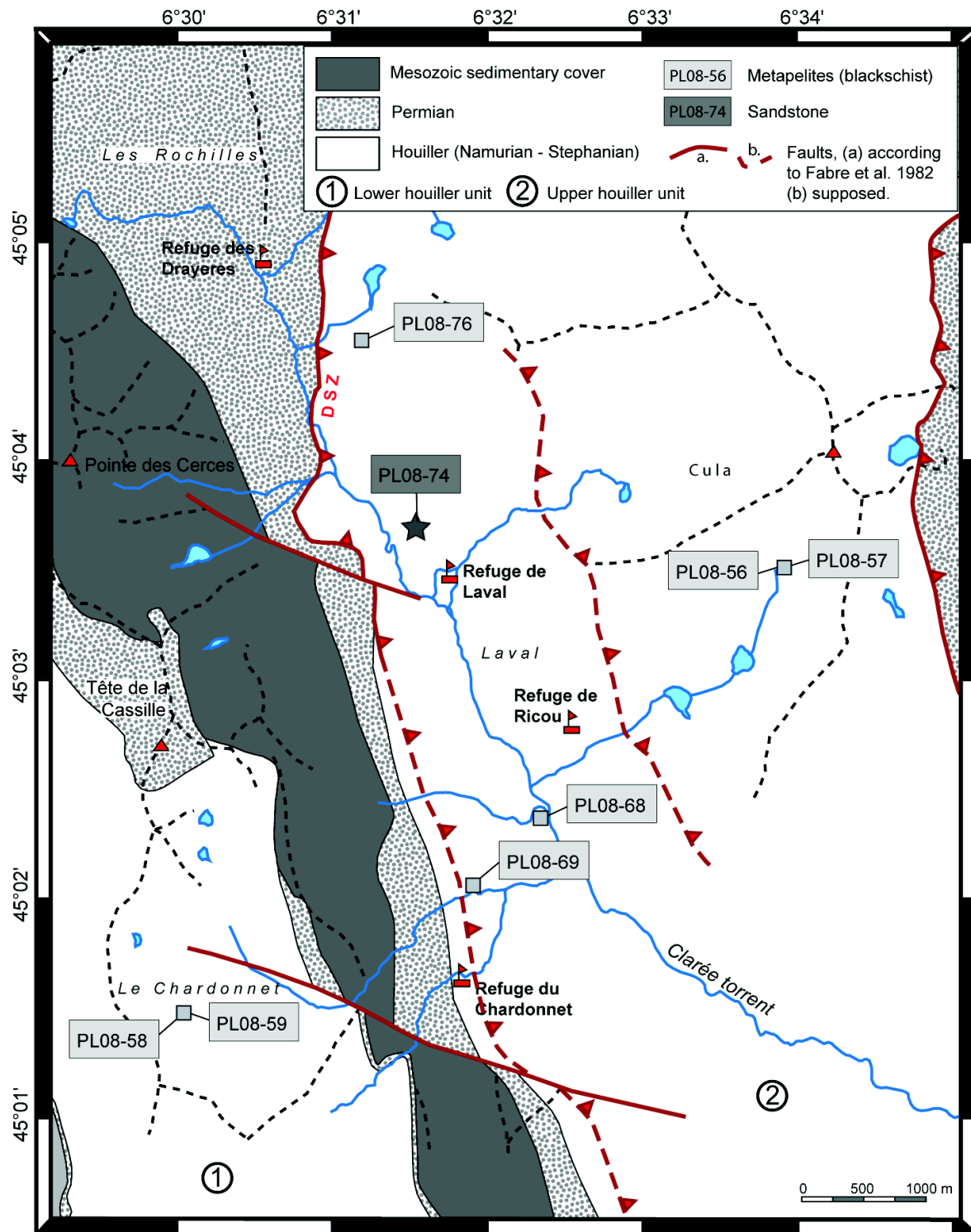


FIGURE 4.8 – Simplified geological map of the Clarée valley area modified after *Fabre (1982)*, *Fabre et al. (1982)*. All samples used in the RSCM study (squares) and for P-T estimates based on X-ray mapping (star) are located in the map. This study is confined to the Namurian-Stephanian formations. DSZ, Drayères Shear Zone.

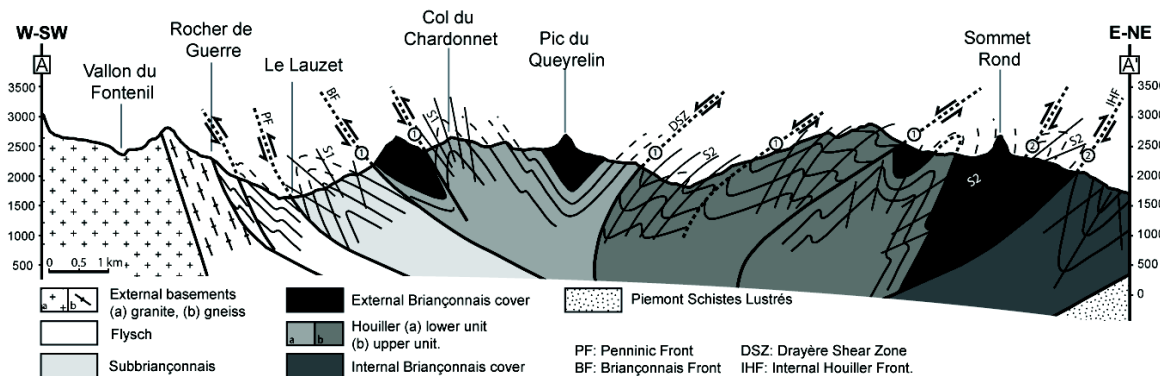


FIGURE 4.9 – Structural cross-section across the external and internal zones of the western Alps (A-A' section in Fig. 4.8), north of Briançon modified after [Fabre et al. \(1982\)](#), [Caby \(1996\)](#), [Barf  ty et al. \(2006a;b\)](#). Note the fan-shape structure of the Brian  onnais zone. Fault movements are indicated with the associated tectonic phase (1 or 2). PF : Penninic Front ; EHF : External Houiller Front (corresponding here to the Brian  onnais Front) ; DSZ : Dray  re Shear Zone ; IHF : Internal Houiller Front.

parates the upper and lower Houiller units. Along this fault, stretching lineations and shear bands indicate a ductile extensional regime ([Caby 1996](#)). [Fabre \(1982\)](#) also noted that the Dray  res shear zone is probably superimposed on an inherited Palaeozoic fault. The Dray  re shear zone was defined in the Clar  e valley (eastern bank of the Clar  e river, Fig. 4.8) and the continuity further north remains poorly defined. The northern part of the contact between upper and lower Houiller units (dashed line in Fig. 4.7) appears as a stratigraphic contact ([Bertrand et al. 1996](#)). The disappearance of the lower Houiller unit further north is associated with a southern axial plunge of folds in both Houiller units ([Fabre et al. 1982](#), [Caby 1996](#)), which corresponds to gradually deeper crustal levels exposed northward ([Ceriani 2001](#)).

Structural evolution of the Brian  onnais Zone houill  re

For a long time the Brian  onnais Zone houill  re has been described as a fan structure ([Kilian 1903](#), [Fabre 1982](#), [Detraz 1984](#), [Caby 1996](#), [Ceriani 2001](#)). In effect, the external Houiller front exhibits a top-to-the-west thrusting direction, and the internal Houiller front a top-to-the-east thrusting (i.e. backthrusting) direction (Figs. 4.7 and 4.9). This simple fan shape accounts for some of the main structural features such as km-size recumbent folds facing toward the west in the western part and toward the east in the eastern part. Just to the south, in the Brian  onnais sedi-

mentary cover nappes, [Tricart \(1984\)](#) demonstrated that after initial nappe stacking associated with a first foliation development, two main shortening events occurred : (1) west-directed folding and thrusting linked to activity of the Briançonnais frontal thrust and (2) east-verging folding and top-to-the-east thrusting, associated with "back-thrusting" of the Briançonnais zone onto the Piedmont Schistes lustrés complex. These Oligocene post-nappe shortening phases were followed by ductile then brittle extension from the Neogene onwards ([Tricart et Schwartz 2006](#)).

The most recent model by [Bertrand et al. \(1996\)](#) proposed an alternative scenario comprising three compressional stages, followed by a late extensional one (Table 4.1) based on observations in the lower Houiller unit further north. The *D1* deformation event is characterized by an intense and penetrative *S1* schistosity ([Ceriani 2001](#)), oriented sub-parallel to *S0* in strongly deformed layers. Several authors have interpreted this event resulting from the initial piling up of different thrust sheets ([Tricart 1980; 1984](#), [Fabre et al. 1982](#), [Detraz 1984](#), [Aillères et al. 1995](#), [Bertrand et al. 1996](#), [Gabalda et al. 2009](#)). The kinematic interpretation of *D1* event is not easy, because there is no associated stretching lineation, while evidences of duplication ([Fabre et al. 1982](#)) or *F1* isoclinal folds are extremely scarce ([Bertrand et al. 1996](#), [Ceriani 2001](#)). The *D2* event develops large-scale *F2* recumbent folds associated with the *S2* regional schistosity. In the middle to eastern part of the Briançonnais Zone houillère, *S2* consistently dips to the West. The *D3* event is strongly localized and *F3* folds correspond to multi-scale low amplitude bending of *S2* foliation. These *F3* folds are associated with a sub-horizontal *S3* schistosity ([Aillères et al. 1995](#), [Bertrand et al. 1996](#), [Caby 1996](#)). [Bertrand et al. \(1996\)](#) suggest that this *D3* event, which shows a top-to-the west vergence, is responsible for the fan geometry of the Briançonnais Zone houillère. In effect, the apparent eastward facing of the *F2* folds may be due to the bending of *D2* structures around large-scale *F3* folds. This polyphased story showing a top-to-the west vergence, has already been described by [Fabre et al. \(1982\)](#), but without detailed interpretation.

Studied area - the Clarée valley

HF	Lower Houiller Unit (Bertrand et al. 1996)	Lower Houiller Unit (Chardonnet Sector this study)	DSZ	Upper Houiller Unit (this study)
D4	Late extensional stage			
D3	Km-size F3 folds			
D2	West-dipping S2 schistosity and recumbent F2 folds facing toward east.	Large-scale rotation	Folding	Km-size F2 folds facing toward east with axial planar S2 schistosity
D1	Top-to-the W-NW thrusting	Schistosity S1 with km-size isoclinal folds	Top-to-the W-NW thrusting	Schistosity S1 with km-size isoclinal folds

TABLE 4.1 – Correlation table showing the deformation history for both, faults and tectonic units. HF : Houiller Front ; DSZ : Drayère shear zone.

The studied area is located in the Clarée valley (Fig. 4.8), 20 km NNW of the town of Briançon. There, excellent outcropping conditions offer the opportunity to study both the upper and lower houiller units. The area west of the Drayère shear zone exhibits lower houiller unit with fragments of its related Mesozoic cover involved in the Queyrellin and the "Aiguillette du Lauzet" synclinal folds (Fig. 4.9). The axial surfaces of these km-size folds display a fanshape, which is in part linked to proximity of the external houiller front. Only one penetrative schistosity S1, with a steep dip to the east, is visible in less competent layers. In contrast, in the upper houiller unit east of the Drayère shear zone, intense ductile deformation is displayed by m to km-size recumbent folds, associated with top-to-the east shearing. The first schistosity S1 is penetrative and turns within the F2 folds, which present an axial plane S2 schistosity dipping to the west (Fig. 4.9). In this area, the S1 schistosity is sub-parallel to S0.

In the Clarée valley, the Briançonnais Zone houillère commonly presents only two deformation phases (Table 4.1). The first phase, D1, is linked to the westward propagation of thrusting activity associated with the Drayère shear zone (noted 1 in Fig. 4.9). Along this shear zone, higher grade metamorphic rocks overthrust lesser grade metamorphic rocks, implying that D1 event corresponds to the exhumation of Briançonnais Zone houillère units. The second phase, D2, is related to the "backthrusting" phase, with top-to-the east shearing. This event involved folding of the Drayère shear zone as illustrated in Fig. 4.9. In the Rochille sector (Permian series in the NW corner of Fig. 4.8) a third deformation phase, D3, with top-to-the west horizontal shearing has been identified by Fabre et al. (1982). The sequence of

Sample	Rock	Longitude	Latitude	Altitude	n	Ra1	Std	Tmax°C	1 σ , °C
PLo8-56	Schist	933065	2015423	2662	11	0.62	0.01	304	5.14
PLo8-57	Schist	933111	2015375	2660	13	0.62	0.01	308	4.14
PLo8-58	Schist	928110	2011307	2570	14	0.61	<0.01	296	1.21
PLo8-59	Schist	928096	2011309	2576	12	0.61	0.01	296	2.89
PLo8-68	Schist	931201	2012867	1904	16	0.59	0.01	274	4.18
PLo8-69	Schist	930796	2012499	2081	17	0.60	0.01	283	2.06
PLo8-74	Sandstone	929840	2015915	2114	10	0.60	0.01	283	4.09
PLo8-76	Schist	929333	2017315	2379	15	0.61	0.01	292	2.32

TABLE 4.2 – *Samples and associated results using RSCM. Longitude and latitude are provided in Lambert II étendu. Results include the average and standard deviation of n spectra $Ra1$ area ratios of Lahfid et al. (2010). The 1σ error is provided for each T_{max} estimate and it must not exceed 8°C (Beyssac et al. 2007)*

events presented here does not differ significantly from those proposed previously.

4.2.2.3 Sampling

The Briançonnais Zone houillère in the Clarée Valley exhibits essentially two useful types of lithologies : organic-rich schists and sandstones. The latter are rich in detrital minerals. For this study, eight samples were collected (Fig. 4.8 and Table 4.2). Seven samples are organic-rich schists and are characterized by a high content of carbonaceous materials (CM) and various amounts of phyllosilicates, small grain of quartz and feldspars. The carbonaceous material consists of microcrystal agglomerates (framboids) underlining the schistosity, with sizes between $8000\ \mu\text{m}^2$ and $40,000\ \mu\text{m}^2$. A few detrital minerals ($< 1\%$) are found as flake-shaped muscovites with width less than $5\ \mu\text{m}$. Organic-rich schist samples are spread over the area with two samples in the "Le Chardonnet" sector in the lower houiller unit and eight samples in the upper houiller unit (Fig. 4.8). For this study, this upper houiller unit is divided into two sectors, the "Laval" sector and "Cula" sector further west (Fig. 4.8).

The last sample (PL08-74, star in Fig. 4.8) is a sandstone from the "Laval" sector. It has a high content of detrital minerals such as chlorite and micas. Some flakes of detrital muscovite and chlorite are visible in thin section (Fig. 4.10b) and identified as H minerals in Fig. 4.12 and Fig. 4.13 ($H1$ and $H2$). This sample exhibits two schistositities ($S1$ and $S2$ in Figs. 4.12 and 4.13) and comes from the hinge zone of an east-verging $F2$ fold in the upper houiller unit, close to the Drayère shear zone. The CM content is lower than that of the organic-rich schists. Carbonaceous

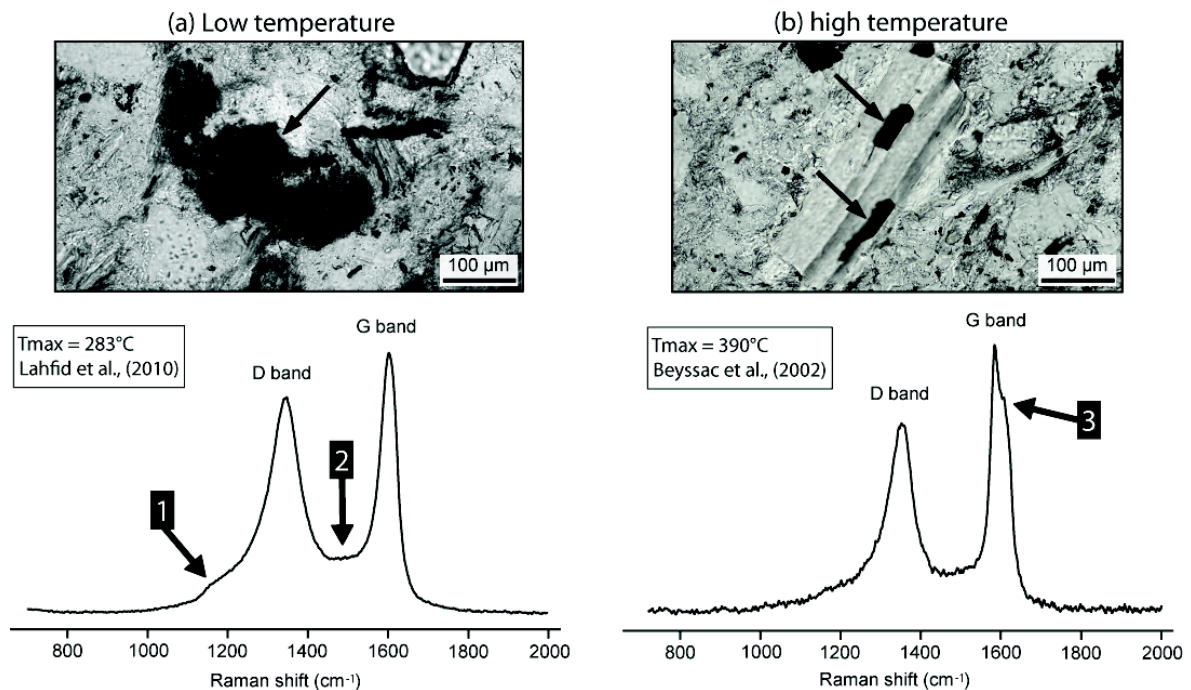


FIGURE 4.10 – Selection of representative first-order region of Raman spectra from sample PL08-74 sample (cf. Table 4.2). (a) Low-temperature CM is microcrystal aggregates. Spectra exhibit low-temperature characteristics, such as the D4 shoulder around 1200 cm^{-1} [1] and a widely developed D3 band around 1500 cm^{-1} [2]. In this case the thermometer of Lahfid et al. (2010) has been used (see text). (b) High temperature CM in inclusion within muscovites. HT spectra exhibit a D2 band shoulder close to 1620 cm^{-1} indicating a large graphite band. In this case, the thermometer of Beyssac et al. (2002) has been used (see text).

material appears in microcrystals agglomerates (Fig. 4.10a) and is included within detrital minerals like muscovites (Fig. 4.10b). Inclusions of CM have flake shapes of $500\text{-}1000\text{ }\mu\text{m}^2$, and lie in muscovite cleavage planes.

Different methods have been used to analyse these samples. RSCM thermometry has been performed on organic-rich samples in order to estimate the maximal temperature (T_{max}). RSCM thermometry allows reconstructing the thermal structure of an orogen during their metamorphic thermal peak (Beyssac et al. 2002; 2007, Negro et al. 2006, Gabalda et al. 2009, Lahfid et al. 2010). Our data provide the first results from the upper houiller unit. Unfortunately RSCM thermometry provides only the T_{max} and advanced investigations are required to estimate both P and T and to build consistent P-T paths. Thermodynamic computations were realized on the sandstone sample with a high detrital mineral content to construct P-T paths. The combination of both methods provides an excellent framework to study low-grade metamorphic areas.

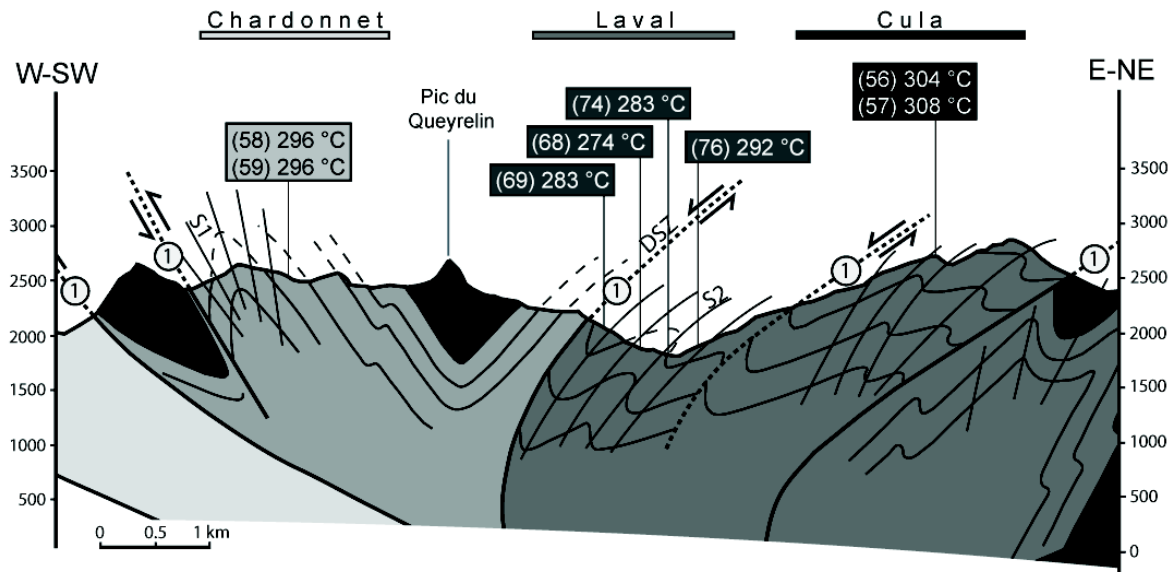


FIGURE 4.11 – Detailed cross-section of the Briançonnais houiller zone (upper and lower houiller unit) including RSCM T_{max} estimations using the method of [Lahfid et al. \(2010\)](#) (see text). Legend is the same as Fig. 4.9, and sectors refer to Fig. 4.8.

4.2.2.4 Analytical and thermobarometric methods

Raman spectrometry of carbonaceous material

Organic matter present in rocks is gradually transformed into CM during regional metamorphic processes. This progressive graphitization process can be used for the estimation of peak temperature (T_{max}) reached by the studied sample ([Beysac et al. 2002; 2003b](#)). The degree of graphitization is controlled by temperature during regional metamorphism ([Beysac et al. 2002; 2003a](#)). Moreover, graphitization is an irreversible process, so that retrograde metamorphic reactions do not affect the temperature estimates. This thermometer is based on the quantification of the degree of ordering of CM using the $R2$ area ratio between the graphite G band and the $D1$ and $D2$ defect bands ($R2 = D1/[G + D1 + D2]$) extracted from the Raman spectra ([Beysac et al. 2002](#)). [Beysac et al. \(2002\)](#) showed that the $R2$ ratio is linearly correlated with the T_{max} of the metamorphic cycle ($T_{max} (^{\circ}\text{C}) = -445.R2 + 641$). This correlation may be used as a thermometer with an intrinsic error calibration of 50°C due to the petrological data used for calibration, but lower relative accuracy of about 15°C ([Beysac et al. 2004](#)).

For T_{max} below 330°C , the Raman spectra of CM are different with two addi-

tional bands ($D3$ and $D4$), which require a different fitting procedure (Lahfid et al. 2010). Lahfid et al. (2010) performed a systematic study of the evolution of the Raman spectrum of CM in low-grade metamorphic rocks in the Glarus Alps (Switzerland). They showed that the Raman spectrum of CM exhibits a significant evolution in the relative contributions of the different bands with increasing T in the range 200–350°C. A new ratio $Ra1$ ($RA1 = [D1 + D4] / [D1 + D2 + D3 + D4 + G]$) quantifying the degree of ordering of CM is linearly correlated with increasing T (T_{max} (°C) = $(Ra1 - 0.3758) / 0.0008$) in the case of the Glarus Alps. Using this correlation, which is not a universal calibration (see discussion in Lahfid et al. (2010)) may provide first-order insights in the thermal evolution of rocks in the Zone houillère briançonnaise, which are characterized by a similar protolith and geological setting.

All Raman spectra have been measured following the procedure of Beyssac et al. (Beyssac et al. 2002; 2003b; 2007). Polished thin sections were used and analyses were performed through a transparent adjacent mineral. The most common mineral used is quartz, because it does not have Raman bands in the studied range. Raman spectra were obtained using a Renishaw InVIA Reflex microspectrometer (IMPC, Université Pierre et Marie Curie, Paris) with a 514-nm argon laser. The laser power at the surface was set around 1 mW. This laser was focused on the sample using a DMLM Leica microscope with a 100× objective (numerical aperture = 0.85). The signal was filtered by edge filters and finally dispersed using a 1800 lines/mm grating to be analysed by a Peltier cooled RENCAM CCD detector. The Raman spectrometer was calibrated with a silicon standard. For each sample, 10–20 spectra (noted n in Table 4.2) were recorded with 2×60 s acquisition times. The fitting procedure (Beyssac et al. 2002; 2007, Lahfid et al. 2010) was performed using the software PEAKFIT v4.

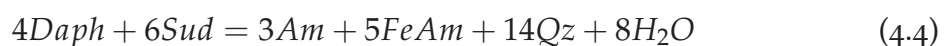
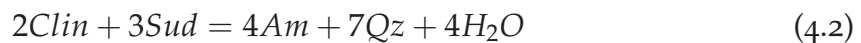
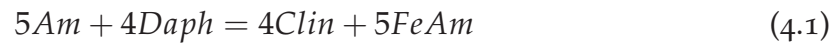
EPMA point analyses and X-ray map of composition

Electron probe microanalyser (EPMA) point analyses were made with common calibration at conditions of 15 keV and 10 nA. In order to study the relationship between phyllosilicate composition and rock structure, quantitative maps of composition were also acquired and standardized according to the procedure of De An-

drade et al. (2006). The mapping conditions were 15 keV and 100 nA, with a counting time of 300 ms per grid point. These conditions enable to measure a map of 450×450 pixels ($> 2,000,000$ analyses) with a total measurement time of around 33 h. For each mineral, a series of pixels was measured in point mode, and results were used as internal standards to transform the map of photon intensity into maps of elements concentration. EPMA analyses of the PL08-74 sandstone sample were performed at Université Pierre et Marie Curie (CAM Paris), using a CAMECA SX100 instrument. Standards used were diopside (Si, Mg, Ca), orthose (Al, K), Mn-TiO₃ (Mn, Ti), garnet (Fe) and albite (Na). The beam size diameter was routinely set at 2 μ m. The raw composition maps were transformed into quantitative maps using high quality point analyses of all phases present in the mapped area (De Andrade et al. 2006). This was achieved using our Matlab-GUI software (XMapTools 1.04, <http://www.xmaptools.com>) that can be used to treat the raw analyses and display the results as binary or ternary plots. This software was also used to calculate the crystallization temperatures of chlorite (one estimated temperature per chlorite pixel) and pressures from of phengite².

Chlorite-quartz-water thermometer

With increasing grade of metamorphism, chlorite shows increasing Al_{IV} (Cathelineau et Nieva 1985, Cathelineau 1988, Hillier et Velde 1991, Zang et Fyfe 1995) and decreasing vacancy contents (Cathelineau et Nieva 1985, Vidal et al. 2001). The observed evolution of composition with temperature can be modeled with the following equilibria (Vidal et al. 2005; 2006) :



where clinocllore (*Clin*), Mg-amesite (*Am*), Fe-amesite (*FeAm*), daphnite (*Daph*), and sudoite (*Sud*) are end-members of chlorite coexisting with quartz (*Qz*) and

². This function is not available in the XMapTools 1.05 version (see §3), but you can use the program MultiPlot

water (H_2O). The temperature locations of the equilibria (4.1)-(4.4) depend on the activity of the *Clin*, *Daph*, *Sud* and amesite end-members as well as the activity of water. At fixed water activity and pressure, an increase in sudoite component (increase in vacancies) and *Clin* + *Daph* components (increase in Si) leads to a shift in the equilibria at lower temperatures, consistent with numerous empirical thermometers based on the amount of Al_{IV} in chlorite (Cathelineau et Nieva 1985, Cathelineau 1988, Hillier et Velde 1991, Inoue et al. 2009). Vidal et al. (2005; 2006) suggested that a simultaneous estimation of Fe^{3+} in chlorite and equilibrium temperature for the Chl-Qtz- H_2O assemblage can be performed using criterion based on the convergence of equilibria (4.1)-(4.4) at a given pressure, which is achieved for a minimal $XFe^{3+} = (Fe^{3+} / Fe_{tot})$ of chlorite. For a given chlorite composition (and thus end-member activities), Fe^{3+} is increased until convergence of (4.1)-(4.4) is obtained at given pressure. This method has been validated qualitatively by comparing estimated values of XFe^{3+} with XANES measurements (Vidal et al. 2006, Muñoz et al. 2006). Temperature and XFe^{3+} were estimated at a fixed pressure of 4 kbar and a water activity equal to 1. Convergence was considered to be achieved when the temperature difference between all equilibria (4.1)-(4.4) was less than 30°C. This value was adopted in order to take into account the cumulative uncertainties stemming from errors in the thermodynamic data of the chlorite end-members, solid solution properties and the analytical uncertainties.

Phengite-quartz-water thermometry

Following the earlier work of Velde (1965), Massonne et Schreyer (1987) proposed a relationship between pressure and Si content per formula unit (pfu) of phengites for the system $K_2O - MgO - Al_2O_3 - SiO_2 - H_2O$ (KMASH) for K-white-mica coexisting with K-feldspar, quartz and phlogopite. These studies indicated that at fixed bulk-rock composition, the extent of the Tschermak substitution and therefore the Si content of phengite increases with pressure. At low temperature, the Si content of dioctahedral mica is also controlled by the pyrophyllitic substitution, which is responsible for an increase of Si and a decrease of interlayer content (IC, excluding interlayer water) with decreasing T (Bishop et Bird 1987, Cathelineau

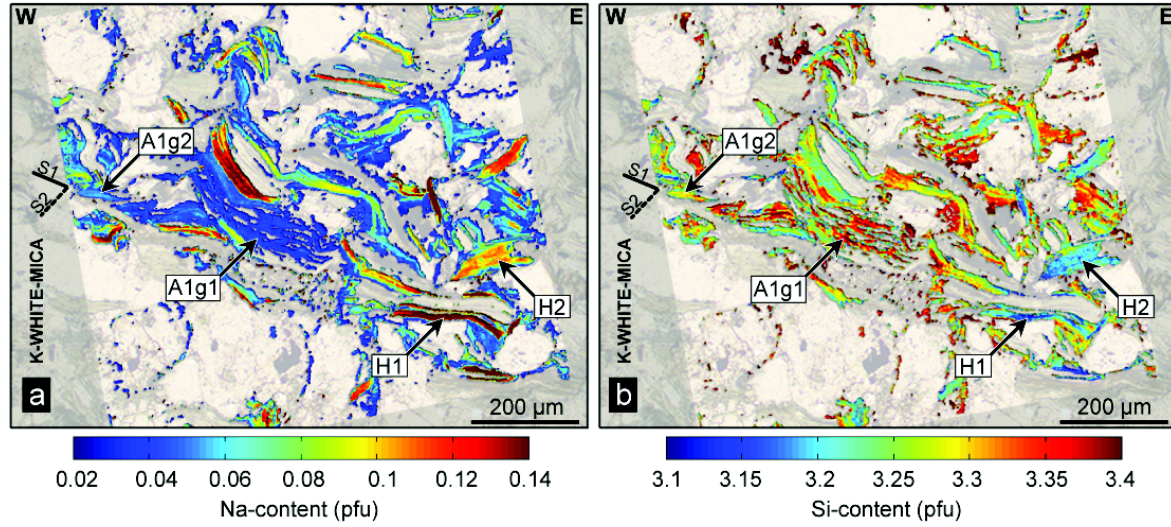
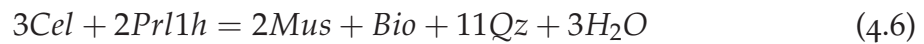


FIGURE 4.12 – (a) Si-content (pfu) and (b) Na-content (pfu) compositional maps of K-white-micas from sample PL08-74. Mica types noted by arrows (H1, H2, A1 and A2) are discussed in the text.

1988, Agard et al. 2000, Parra et al. 2002b;a, Battaglia 2004). The vacant sites of LT and LP illites are partially hydrated (Loucks 1991, Drits et McCarty 2007, Vidal et Dubacq 2009, Dubacq et al. 2010, Vidal et al. 2010). Dubacq et al. (2010) proposed a formalism that involves dehydrated micas and hydrated pyrophyllite-like thermodynamic end-members to model these compositional variations as a function of T and P. The equilibrium conditions of quartz + water + K-mica is represented by a P-T line along which the interlayer water content varies. The P-T location of this line can be calculated from equilibrium conditions of the following equilibria :



where celadonite (*Cel*), pyrophyllite (*Prl*), pyrophyllite.1H₂O (*Prl1h*), muscovite (*Mus*) and biotite (*Bio*) are solid solution components of the mica phase. Dubacq et al. (2010) showed that the mica-quartz-water equilibrium could be used as a barometer at given temperature conditions (e.g. from chlorite-quartz-water thermometry, see above).

4.2.2.5 Thermobarometric results

T_{max} estimates

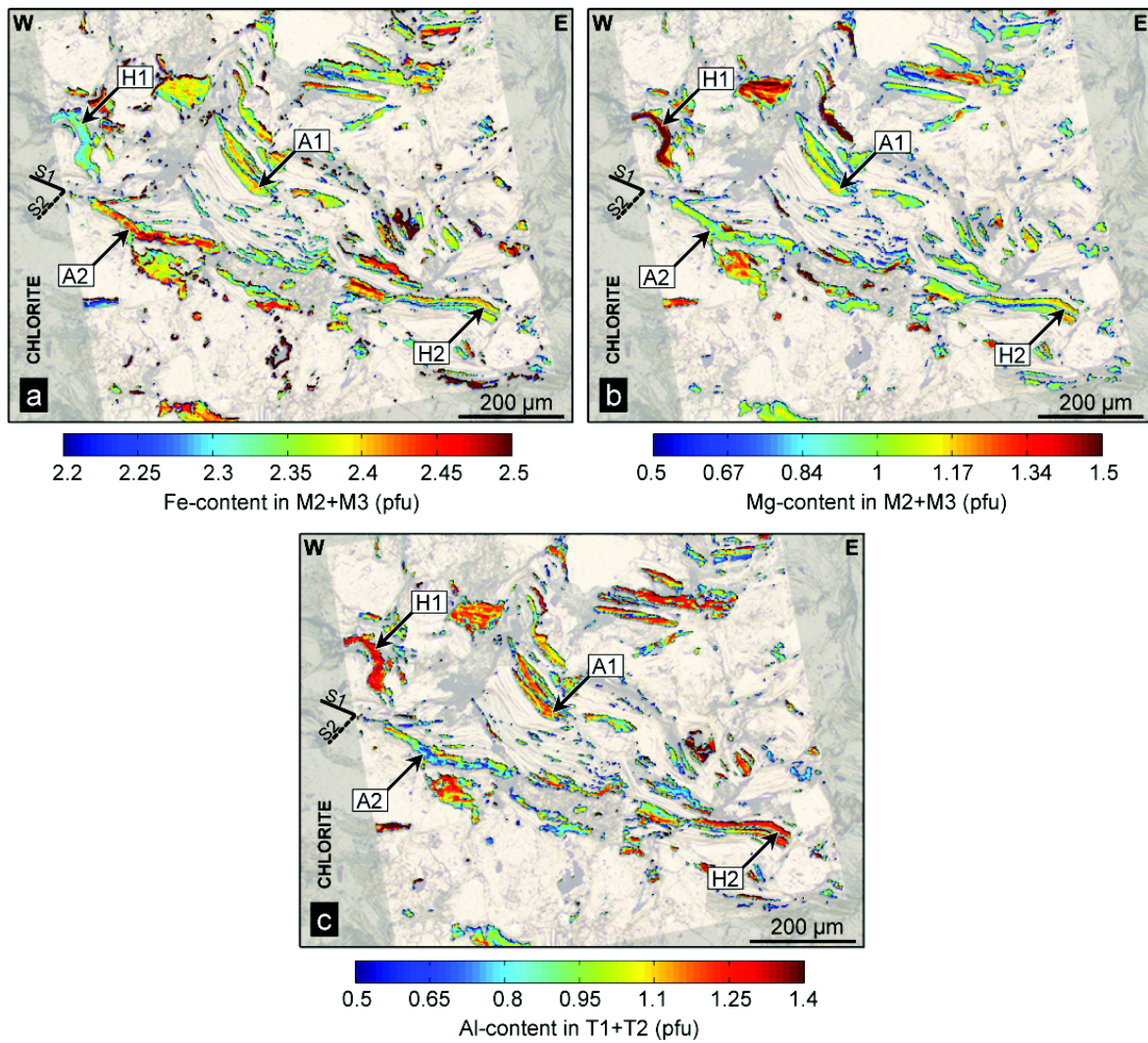


FIGURE 4.13 – (a) Al-content (pfu), (b) Mg-content in M2+M3 (pfu) and (c) Fe-content in M2+M3 (pfu) compositional maps of chlorites from sample PL08-74. Chlorite types noted by arrows (H1, H2, A1 and A2) are discussed in the text

Two types of spectra were obtained from CM measured through different transparent minerals (Fig. 4.10). The first type, measured through quartz, presents features characteristic of $T_{max} < 330^{\circ}\text{C}$ (Lahfid et al. 2010) : the D band exhibits a shoulder close to 1200 cm^{-1} and the region between the D and G bands exhibits high intensity, indicating the presence of a well-developed D3 band. An average $T_{max} = 283^{\circ}\text{C}$ ($1\sigma = 4^{\circ}\text{C}$) was obtained from these spectra when applying the calibration proposed by Lahfid et al. (2010) using the ratio $Ra1$ (PL08-74 in Table 4.2). The second type of spectra measured through detrital muscovite and chlorite (Fig. 4.10-b) have different shapes and exhibit a shoulder on the G band, the D2 band defined by Beyssac et al. (2002). A temperature of 390°C was calculated from three

spectra (Fig. 4.10b) measured in detrital muscovite with $1\sigma = 4^\circ\text{C}$. The large difference between the temperatures obtained by RSCM using CM included in quartz or in phyllosilicate will be discussed later.

In organic-rich schist samples, spectra are characteristic of low- temperature conditions and the thermometer of Lahfid et al. (2010) provides values of $T_{max} < 310^\circ\text{C}$. Results are summarized in Table 4.2 and projected in a cross section of the Briançonnais Zone houillère (Fig. 4.11). From west to east, the estimated T_{max} were around 296°C , 283°C and 306°C for the "Chardonnet", "Laval" and "Cula" areas, respectively. These results show that T_{max} are roughly constant in the Briançonnais Zone houillère with variations $< 30^\circ\text{C}$.

Chemical variations and geothermometry

K-white-micas Detrital Hercynian grains are commonly observed in low-grade metasediments. In our case, large flakes of detrital micas (noted *H* in fig. 4.12) are preferentially re-oriented in the *S*₁ plane and sometimes kinked by *S*₂. However, microstructural criteria are not sufficient to distinguish hercynian and alpine mica grains. In contrast, several generations of K-white-mica can be clearly distinguished from their contrasted compositions. The most important compositional variations of mica derived from the X-ray map involve the Na and Si contents (Figs. 4.12 and 4.14). Compositional maps highlight the coexistence of Si-poor and Na-rich mica grains (*H*₁ and *H*₂ in Fig. 4.12) with Si-rich and Na-poor mica grains (*A*_{1g}₁ and *A*_{1g}₂ in Fig. 4.12). Detrital mica (*H*) were divided into two groups according to their Na-content : *H*₁ micas have Na-content ranging from 0.15 to 0.2 *pfu* and *H*₂ from 0.07 to 0.13 *pfu*. The most Si-rich micas (*A*), show Na- content lower than 0.07 *pfu*. They were also split into two groups : *A*_{1g}₁ for Si-contents between 3.45 and 3.32 *pfu* and *A*_{1g}₂ for Si- contents between 3.32 and 3.15 *pfu* (Fig. 4.14-b).

The phengite-quartz-water method of Dubacq et al. (2010) was applied to each pixel of mica groups (*H*₁, *H*₂, *A*_{1g}₁ and *A*_{1g}₂) selected on the X-ray map. For each pixel of mica, a P-T line was calculated ; the results are plotted in Fig. 4.16a. *H*₁ and *H*₂ groups show temperatures at 330°C and 375°C ($P = 4 \text{ kbar}$), respectively.

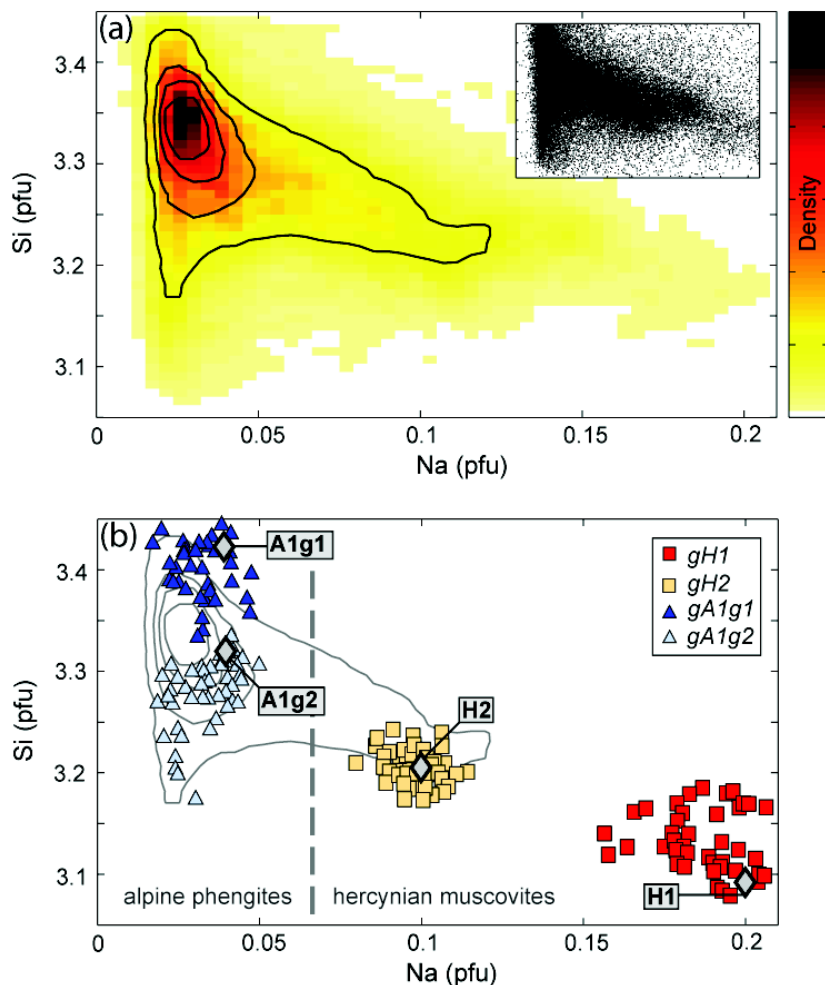


FIGURE 4.14 – Chemical analysis of K-white micas in Na-Si space (pfu). (a) Density map of all micas analysis on the X-ray map. (b) Chemical evolutions for four groups of pixels selected manually on the map (see location in Fig. 4.11) and plotted : gH1 (dark squares) Na-rich muscovites ; gH2 (light squares) Na-intermediate muscovites ; gA1g1 (dark triangles) Si-rich phengites and gA1g2 (light triangles) low-Si phengites. Representative analyse of each groups (K-white-micas : H1, H2, A1g1 and A1g2 ; grey diamonds) are listed in Table 4.4.

In contrast, A1 mica shows temperatures lower than 300°C at the same pressure. Detrital *H* micas have a low Si-content and are identified as hercynian muscovites. Some detrital grains exhibit a zonation in Na-content decreasing from core to rim (see *H2* in Fig. 4.12-a). The phengite-quartz-water method shows a decrease in the estimated temperature correlated with a decrease in Na-content (*H1* and *H2* groups in Fig. 4.16-a). This zoning indicates that hercynian muscovites crystallized during cooling (hercynian exhumation).

Micas belonging to the *A* group have higher Si-contents (above 3.25 pfu) and are identified as alpine phengites. Well-developed phengites are zoned and exhibit

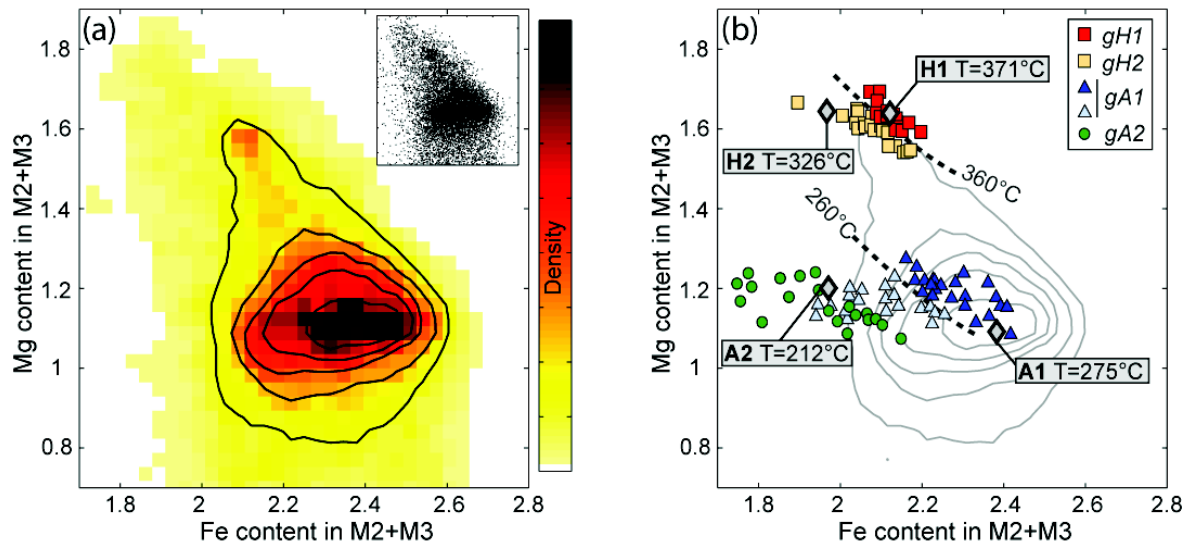


FIGURE 4.15 – Chemical analysis of chlorites in Fe-Mg space (pfu, considering the M2-M3 octahedral sites). (a) Density map of all chlorite analysis on the X-ray map. (b) Chemical evolutions for five groups selected manually on the map (see location in fig. 4.12) : gH1 (dark squares) Hercynian chlorites, which have crystallization temperature above 360°C, gH2 (light squares) Hercynian low-temperature Hercynian chlorites, between 300°C and 360°C, gA1g1 (dark triangles) Alpines chlorites, which have crystallization temperature between 260°C and 300°C, gA1g2 (light triangles), low-temperature Alpine chlorites, with temperatures between 200°C and 260°C and gA2 (dark circles), late chlorites, which have crystallization temperature below 200°C. Representative analyse of each groups (Chlorites : H1, H2, A1g1, A1g2 and A2, grey diamonds) are listed in Table 4.3.

a decrease in their Si content from core to rim (see A1g1 core in Fig. 4.12-b). This result shows that A phengites crystallized during the alpine retrogression path under decreasing pressure conditions. This zonation is confirmed by the phengite-quartz-water method, which shows a decrease in estimated pressures for a fixed temperature (close to 260°C) between A1g1 and A1g2 mica groups.

Chlorites Similarly to mica, flakes of detrital chlorite are easily identified using microstructural criteria. They are preferentially reoriented in the S1 schistosity and kinked (H1 in Fig. 4.13). Chlorite also shows chemical variations (Figs 4.13 and 4.15). H1 and H2 chlorites show higher (Mg + Fe)-contents than A1 and A2 chlorite. Both H1 and H2 chlorites have high Al_{IV} contents ranging from 1.2 to 1.4 pfu, and they present a zonation with decreasing Mg from core to rim. The separation in two groups H1 and H2 is based on the Mg and Fe variations. Indeed, from core to rim, H chlorites exhibit a decrease of the (Mg + Fe) content (Table 4.3 and Fig. 4.13). The A1 and A2 chlorites are poorer in Mg (1.2 pfu) and show a decrease

	Chlorite				
	H1	H2	A1	A2 g1	A2 g2
SiO ₂	24.23	24.99	24.43	25.73	28.89
TiO ₂	0	0	0	0	0
Al ₂ O ₃	22.44	22.18	21.36	21.52	20.93
FeO _{total}	26.59	26.79	32.46	30.03	26.08
MnO	0	0	0	0	0
MgO	11.47	11.63	7.44	8.3	7.88
CaO	0	0	0	0	0
Na ₂ O	0	0	0	0	0
K ₂ O	0	0	0	0	0
Atom site distribution (14 anhydrous oxygen basis including Fe ³⁺)					
Si _(T1+T2)	2.66	2.7	2.71	2.78	3.09
Al _(T2)	1.34	1.3	1.29	1.22	0.91
Al _(M1)	0.24	0.23	0.14	0.14	0.13
Mg _(M1)	0.3	0.28	0.3	0.23	0.18
Fe ²⁺ _(M1)	0.34	0.3	0.29	0.22	0
V _(M1)	0.12	0.19	0.27	0.41	0.69
Mg _(M2+M3)	1.64	1.64	1.09	1.2	1.09
Fe ²⁺ _(M2+M3)	2.12	1.97	2.38	1.97	1.52
Al _(M2+M3)	0.24	0.39	0.53	0.83	1.39
Al _(M4)	0.98	0.83	0.67	0.48	0.33
Fe ³⁺ _(M4)	0.02	0.17	0.33	0.52	0.58
Mg _(M4)	0	0	0	0	0.09
XFe ³⁺	1	7	11	19	25
Temperature (°C)	371*	323*	275*	212*	106**

* Vidal et al. (2006) Pinit = 4 kbar)

** Inoue et al. (2009) with fixed X.Fe³⁺

TABLE 4.3 – Selection of quantified analysis and structural formulae of chlorites which location are indicated in Fig. 4.12. Chlorites H1, H2, A1 and A2g1 temperatures has been estimated using chlorite-quartz-water thermometry for a given pressure of 4 kbar. X.Fe³⁺ is estimated by the model and correspond to the minimum amount of Fe³⁺. A2g2 chlorite has high Si-content ($Si > 3$) and temperature has been calculated using the thermometer of Inoue et al. (2009) with reasonable value of Fe³⁺ fixed.

in Fe-content from 2.3 pfu for A1 (dark triangles in Fig. 4.15-b) to 1.9 pfu for A2 (circles in Fig. 4.15-b).

The chlorite-quartz-water method of Vidal et al. (2005; 2006) has been applied to all pixels of chlorite groups (H1, H2, A1, A2) from the X-ray map. The results for representative analyses of the A1, A2, H1 and H2 compositions are listed in Table 4.3. Temperature estimates for H1 and H2 chlorites range between 360-390°C and 300-360°C, respectively. In contrast, A1 and A2 chlorites show lower temperatures ranging from 300°C to 100°C (Fig. 4.16-b). Some A chlorites exhibit a decrease of the Fe-content from core to rim associated to a temperature decrease (between A1 and A2 groups). These variations allow displaying the 260°C isograd in the Fe-Mg chemical space. Temperatures of the Si-richest chlorites ($Si > 3$ pfu) could not be calculated with the solid-solution model of Vidal et al. (2006), which is relevant for chlorite with $Si < 3$ only. For these compositions, the temperatures were esti-

	Mica			
	H1	H2	A1g1	A1g2
SiO_2	40.55	45.57	49.86	47.56
TiO_2	0	0	0	0
Al_2O_3	40.95	31.55	27.23	28.76
FeO_{total}	1.61	1.94	2.89	3.59
MnO	0	0	0.16	0.2
MgO	1.55	0.83	2.39	1.45
CaO	0.06	0.05	0.06	0.05
Na_2O	1.33	0.75	0.31	0.32
K_2O	6.19	8.56	9.6	9.48
Atom site distribution (11 anhydrous oxygen basis)				
$Si_{(T1+T2)}$	3.08	3.21	3.42	3.32
$Al_{(T2)}$	0.92	0.79	0.58	0.68
$Al_{(M1)}$	1.84	1.83	1.62	1.68
$Mg_{(M1)}$	0.1	0.07	0.23	0.13
$Fe_{(M1)}$	0.06	0.1	0.15	0.19
$V_{(M2+M3)}$	0.89	0.97	0.98	0.97
$Mg_{(M2+M3)}$	0.07	0.01	0.01	0.01
$Fe_{(M2+M3)}$	0.04	0.02	0.01	0.02
$K_{(A)}$	0.6	0.77	0.84	0.84
$Na_{(A)}$	0.2	0.1	0.04	0.04
$V_{(A)}$	0.2	0.13	0.12	0.12

TABLE 4.4 – Selection of quantified analysis and structural formulas of mica, which location are indicated in 4.16.

mated with the chlorite thermometer of Inoue et al. (2009), for $(XFe^{3+})_{chlorite}$ 0.25. This value was inferred from the $T - XFe^{3+}$ evolution calculated for the higher temperature chlorite with the approach of Vidal et al. (2005; 2006).

P-T estimates

P-T conditions were estimated from the intersection of the Mica-Qtz- H_2O (Fig. 4.16-a) and Chl-Qtz- H_2O (Fig. 4.16-b) equilibria. H1 and H2 phyllosilicates yield metamorphic conditions at $371 \pm 26^\circ C$, 3.5 ± 1.4 kbar and $326 \pm 19^\circ C$ and 3.2 ± 1.1 kbar, respectively (Fig. 4.17-a). The equilibrium conditions of the Alpine assemblage A1g1 and A2g1 were estimated at $275 \pm 23^\circ C$, 5.9 ± 1.7 kbar and $260 \pm 18^\circ C$, 2 ± 1.2 kbar, respectively (Fig. 4.17-b). Late chlorites with high Si-content ($> 3pfu$) crystallized at lower temperature between $200^\circ C$ and $100^\circ C$. Assuming a geothermal gradient of $40^\circ C/km$ (see Section 4.2.2.6), the pressure conditions at such temperature is less than 2 kbar. The combination of these results pleads for an early and rapid isothermal exhumation stage followed by a later stage of slow and almost isothermal exhumation.

4.2.2.6 Discussion

Characterization of hercynian and alpine metamorphic conditions

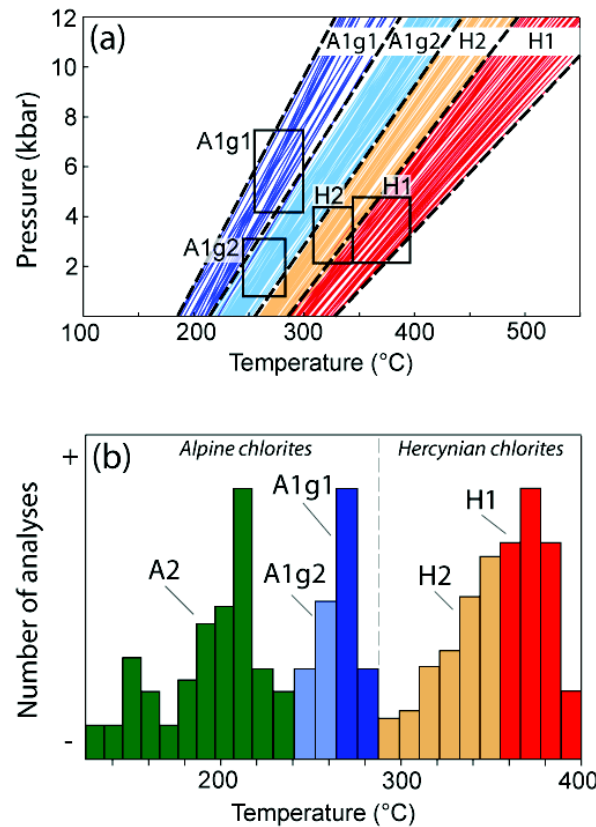


FIGURE 4.16 – a) K-white-mica P-T estimates (lines) using the method of Dubacq et al. (2010). Boxes are constructed using the results of the chlorite thermometer (b). For a given temperature, pressure has been estimated along the corresponding K- white-mica P-T equilibrium lines. The deviation proposed (see text) is the maximum possibility in pressure and temperature to combine both methods. (b) Reconstruction of chlorite temperatures pseudo-distribution (without vertical scale) from histograms of each group.

Microstructural criteria and chemical analyses, associated with thermodynamic modelling, point out distinctions between A (A1 + A2) and H (H1 + H2) metamorphic minerals (Fig. 4.14, for K- white mica and Fig. 4.15, for chlorite). P-T conditions are associated with specific mineral chemistries such as low Si-content in H muscovites and high Mg-content in H chlorites. A retrogressive path is evidenced using mineral zoning, starting at a metamorphic peak of $371 \pm 26^\circ\text{C}$ and $3.5 \pm 1.4 \text{ kbar}$ (Fig. 4.17-a). H minerals are detrital minerals deposited in sandstone levels of the Carboniferous basins during erosion of the hercynian metamorphic belt. Part of the detrital phyllosilicates is preserved during the alpine metamorphic overprint, while new phyllosilicates crystallized. The high Si^{4+} content in phengites cores (A1g1 in Fig. 4.12-b) constitutes an argument to propose HP-LT peak conditions at $275 \pm 23^\circ\text{C}$ and $5.9 \pm 1.7 \text{ kbar}$ (Fig. 4.17-b). A (A1 + A2) phengites are interpreted as related to Alpine metamorphism. Alpine metamorphic conditions peak calculated

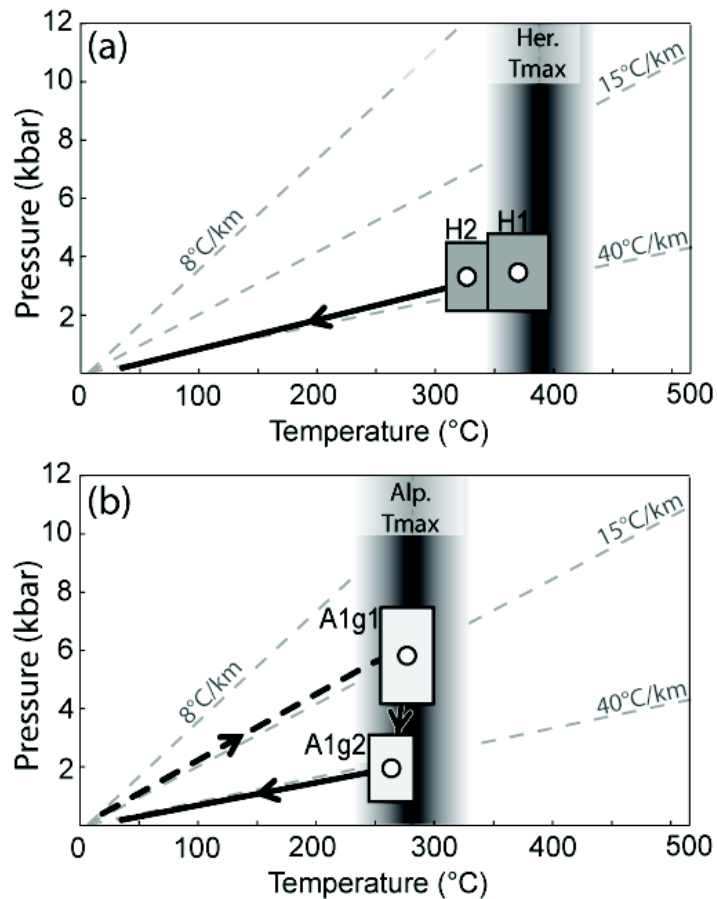


FIGURE 4.17 – P-T paths using P-T estimation of chlorite and K-white-mica (boxes) and T_{max} estimation using RSMC study (gradation). Here T_{max} is the hercynian T_{max} of $393 \pm 50^\circ\text{C}$ obtained on included CM in sample PL08-74 using the method of [Beyssac et al. \(2002\)](#). Alp. T_{max} is the Alpine T_{max} obtained from CM in the sample PL08-74 using the method of [Lahfid et al. \(2010\)](#). Typical geothermal gradients of subduction (8°C/km) and collision (40°C/km) as well as an intermediate gradient (15°C/km) are also shown.

for the upper houiller unit (275°C and 6 kbar) are consistent with the presence of lawsonite as described by [Fabre et al. \(1982\)](#).

Identification of two types of CM in the Briançonnais Zone houillère

Two methods have been used depending on the type of CM : that of [Beyssac et al. \(2002\)](#) for high temperatures ($> 330^\circ\text{C}$) and that of [Lahfid et al. \(2010\)](#) for low temperatures ($< 330^\circ\text{C}$). In our case, this point merits a specific discussion. Both types of CM occur in the same sample based on the shape of the spectra and the microstructural location (Fig. 4.10). As previously underlined, muscovites are Hercynian and record higher-temperature metamorphism compared to the alpine metamorphic phengites. The CM preserved as inclusions in detrital minerals (muscovite and

Mg-rich chlorite) record a hercynian high-temperature T_{max} above 330°C. In spite of the small number of analyses ($n = 3$), the T_{max} of 390°C has a low dispersion ($1\sigma = 4^\circ\text{C}$). Moreover, this estimate of T_{max} is consistent with the thermodynamic modelling results on *H* muscovite. The estimated temperature peak using Mg-rich chlorite and muscovite is $371 \pm 26^\circ\text{C}$. Using the intrinsic T_{max} uncertainty to 50°C provided by [Beyssac et al. \(2002\)](#), the RSCM result is of $390 \pm 50^\circ\text{C}$. Both results are in accordance and provide a range for the location of the Hercynian metamorphic peak between 350°C and 400°C. It is important to note that we also found three high-temperature CM spectra in organic-rich schist samples. Their T_{max} are identical and close to 390°C. Thus, "detrital" CM, recording HT metamorphism is present in small amounts ($< 1\%$) in organic-rich schists. This last observation confirms that the different spectra reflect true T_{max} differences related to two distinct metamorphic events.

The second type of CM is located in a different microstructural position. It consists of framboidal aggregates that were always analysed through transparent minerals. In this case, the spectra shape is characteristic of temperatures below 330°C (fig. 4.10 a). We used the correlation observed by [Lahfid et al. \(2010\)](#) to estimate T_{max} lower than 310°C in the Briançonnais Zone houillère. In contrast to the previous case, this low- T_{max} CM dominates in both organic-rich schist and sandstone lithologies (99% of CM in organic-rich schists). As the CM in the organic-rich schist deposits is preserved in Carboniferous basins, they did not record the strong late hercynian thermal event ([Frey et al. 1999](#)), thus this T_{max} must necessarily be Alpine in age. In the Chardonnet sector, the two analysed samples provide similar T_{max} ($296 \pm 3^\circ\text{C}$, see Table 4.2). The same trend is observed in the Cula sector, with a slight variation of 4°C between both samples (Table 4.2). In the Laval sector, the average T_{max} is 283°C . The main conclusion is that the alpine T_{max} in the Briançonnais Zone houillère is nearly constant along our section.

P-T-t constraints in the Briançonnais Zone

The new estimates of Alpine peak metamorphic conditions at $275 \pm 23^\circ\text{C}$ and $5.9 \pm 1.7 \text{ kbar}$ complement the available data along this transect. Previous work

has provided P-T estimates for the most internal Briançonnais zone (Ganne et al. 2003; 2007, Gerber 2008, Strzeczynski et al. 2012). In the Briançonnais stack of sedimentary cover thrust sheets, the metamorphic peak was reached at 12 *kbar* and 300°C (Gerber 2008), while estimates for the Ambin basement suggest 15-18 *kbar* and 500°C (Ganne et al. 2007, Gerber 2008).

The absolute age of *D1* was constrained throughout the Briançonnais zone by step-heating and laser ablation dating on K- white mica (Ganne 2003, Berger et Bousquet 2008, Gerber 2008). The measured ages show a wide range between 40 and 55 *Ma* with a peak at ca. 50 *Ma* for the internal parts of the Zone briançonnaise. This age-range reflects the crystal-chemical zonation of the micas. The age of *D2*, associated with west-verging kinematics is better constrained ranging between 37 *Ma* and 32 *Ma* (Ganne et al. 2007, Strzeczynski et al. 2012). Other estimates on associated shear zones further north (Entrelor Shear Zone) indicated similar ages (Freeman et al. 1997). The *D2* ages are interpreted as the youngest limit for greenschist facies metamorphism (Ganne et al. 2007). This event occurred at low-pressure conditions and is associated with a decrease of both pressure and temperature, indicating a relatively low exhumation rate. The end of the metamorphic evolution is constrained by Apatite Fission Track (AFT) analysis. In the Briançonnais Zone houillère, AFT ages decrease from 27 to 32 *Ma* near Briançon (Tricart et al. (2007) and references therein) to 18 *Ma* in the northern part in the Arc Valley (Fügenschuh et Schmid 2003, Malusà et al. 2005), and 8-10 *Ma* in southern Aosta Valley, to 6 *Ma* in the northern Aosta Valley (Malusà et Vezzoli 2006). This south to north younging of ages suggests that exhumation was partitioned in the Briançonnais Zone houillère. In the studied sector, AFT ages are comparatively old (up to 31.7 *Ma*) indicating final exhumation since the onset of the so-called "collision phase". The transition between continental subduction and collision is characterized by the underthrusting of european continental crust below the propagating penninic thrust from 34 to 28 *Ma* (Sanchez et al. 2011, Simon-Labric et al. 2009). Considering the east-west transect studied here, variations in AFT ages also suggest an east-west diachronic exhumation. The Ambin basement is well documented with AFT ages between 18 and 23 *Ma* (see Tricart et al. (2007) for references). The Schistes lustrés

display general east-west younging AFT ages between 22 and 9 *Ma* (Schwartz et al. 2007). The studied transect between the Briançonnais Zone houillère and the Dora Maira massif displays an eastward decrease in AFT ages from 30 *Ma* in the Briançonnais Zone houillère to 22 *Ma* in the eastern part of the Schistes lustrés, 19 *Ma* in the Ambin basement, and 9 *Ma* in the Monviso units. These observations indicate that final exhumation is strongly diachronous along our transect in the internal zones, and migrates from west to east during Oligocene-Miocene times.

Geodynamic model for the Briançonnais Zone during Eocene-Oligocene times

A possible kinematic reconstruction of this part of the western Alps during Eocene-Oligocene times (between 50 and 30 *Ma*) is proposed in Fig. 4.18. During the 50-45 *Ma* time interval peak P-T conditions were reached in both the Ambin basement and Vanoise cover at depths between 40 and 60 *km*. At that time, the Briançonnais Zone houillère was not yet involved in the continental subduction. Peak pressure conditions were established in the Schistes lustrés complex before 62-55 *Ma* (Agard et al. 2002). At 50 *Ma*, the Schistes lustrés units were already partly exhumed (see Agard et al. (2001a)). Note that P-T estimates in the Schistes lustrés for this event (D2 in Agard et al. (2001a)) show a metamorphic gradient consistent with the gradient in the Briançonnais zone of 8-10°C/*km*.

In the 40-37 *Ma* time interval, the Ambin basement and Vanoise cover units were exhumed from 18 and 24 *km* depths, respectively. At the same time, the Briançonnais Zone houillère reached P-T peak conditions of 6 *kbar* and 275°C. The geothermal gradient was higher than 15°C/*km*, resulting from crustal thickening and lower convergence rates (Handy et al. 2010). The frontal thrust moved to the west with activation of the Briançonnais frontal thrust (D1 event in the Briançonnais Zone Houillère, Fig. 4.9). The Drayère shear zone was also active and drove the exhumation of the upper houiller unit.

The final stage in our reconstruction has been drawn for early Oligocene time (34-30 *Ma* in Fig. 4.18). The exhumation rate was very rapid in the Briançonnais zone, as illustrated by AFT ages close to 30 *Ma*. This exhumation, related to the

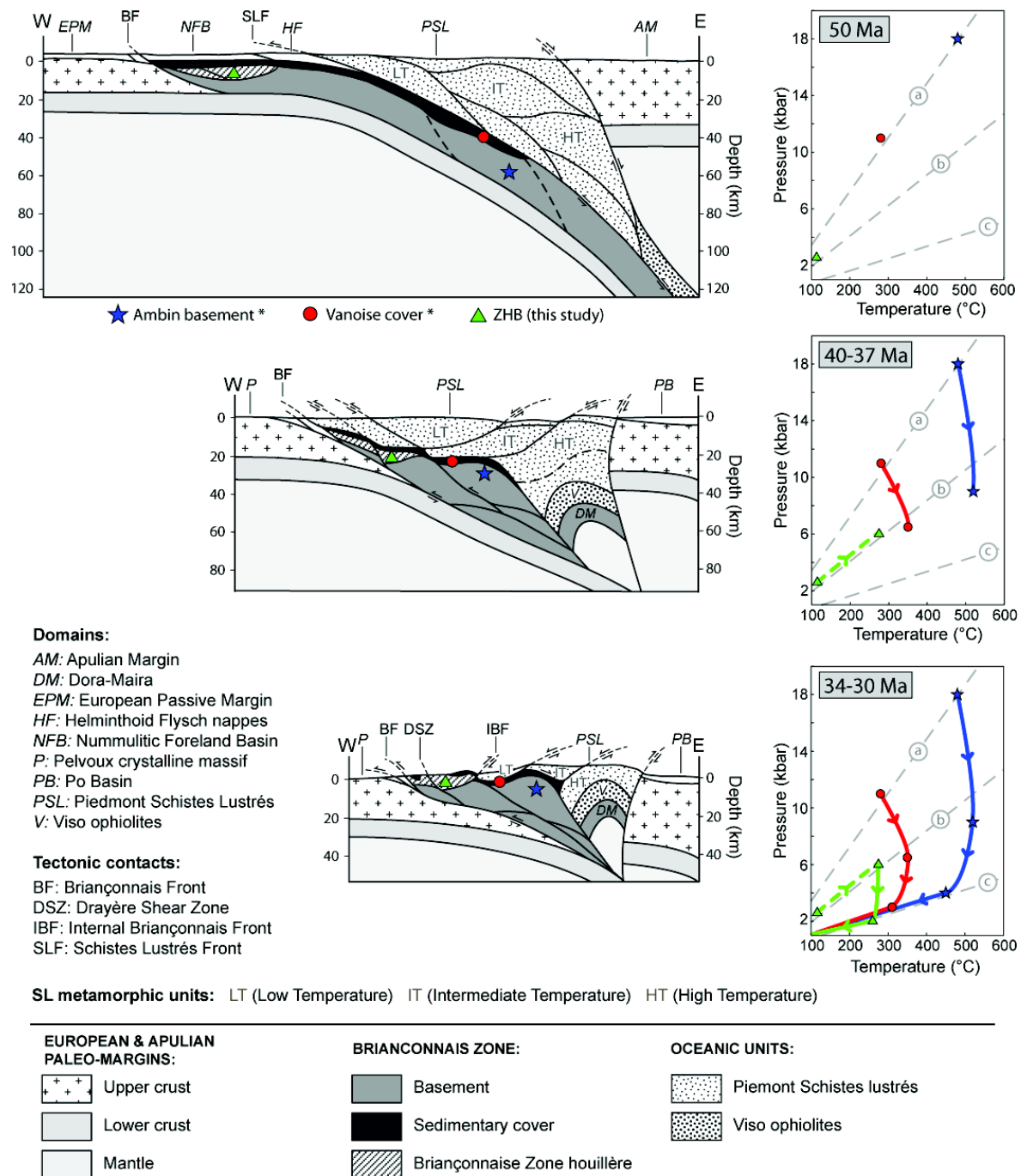


FIGURE 4.18 – Possible kinematic reconstruction of this part of the Western Alps from Eocene to Oligocene (modified from [Gabalda \(2008\)](#)) with associated P-T paths for Ambin basement and Vanoise cover ([Gerber \(2008\)](#), see text) and the Briançonnais Zone houillère (this study). The geometry of the accretionary prism is from geophysical investigations in a paleo-accretionary complex in the Chilean forearc ([Glodny et al. 2005](#)). Geothermal gradient of (a) 8°C/km, (b) 15°C/km and (c) 40°C/km are also shown

Briançonnais front activity that involves the underthrusting of the Pelvoux by crustal thickening (Simon-Labric et al. 2009), was associated with a high erosion rate. Doming of the Briançonnais basement accompanied the top-to-the-east movement observed in the upper houiller unit. It is probably during this event (*D2* in the upper Houiller unit, Fig. 4.9) that westward tilting of the Drayère shear zone took place and that the Briançonnais zone acquired its fan structure. All units recorded P-T conditions along a metamorphic collisional gradient of 40°C/km. This view is compatible with AFT ages that display diachronous exhumation across the belt. At 30 Ma, exhumation was almost ended in the Briançonnais Zone houillère, but not in the innermost parts of the Alpine belt (Ambin, Monviso areas).

This kinematic reconstruction implies a crustal segmentation into small thrust sheets during exhumation of continental bodies. P-T paths of each unit exhibit, as discussed above, diachronous burial and exhumation processes. The edification of this continental wedge requires small-size units with a width less than 30 km. In contrast to results from Young et al. (2007) in Norway, this study highlights that the continental crust cannot remain coherent during metamorphism and exhumation in the Alps.

Multi-method approach for P-T estimates in low-grade metamorphic terrains

This study shows that a detailed metamorphic analysis of low-grade metamorphic terrains can be conducted using the presented multi-method approach. Combining large-scale T_{max} estimates from RSCM thermometry and local P-T estimate from chemical mapping and quantitative thermometry enables distinguishing between Hercynian and alpine metamorphic events. Use of quantitative chemical mapping is essential to obtain a large number of analyses and to identify chemical zoning. Distinguishing between detrital and newly grown metamorphic minerals is not possible using conventional methods such as optical microscopy. Partial recrystallization occurs in such P-T conditions in the presence of metamorphic fluids (see Putnis et Austrheim (2010) and references therein). P-T estimates were realized using the multi-equilibrium thermodynamic approach based on available solid solution models (Vidal et al. 2005; 2006, Dubacq et al. 2010). In contrast to pseudo-

sections used for higher metamorphic conditions, these methods do not required knowledge of bulk rock composition. Nevertheless, the composition of recrystallized chlorites and phengites are strongly dependent on the bulk rock and the fluid composition (work in progress), therefore the chemical diagrams provided here cannot be easily transposed to other examples.

This study is also an example of a comparison between RSCM thermometry and multi-equilibrium techniques. Resulting estimates of the thermal peak are consistent between both methods for the alpine and hercynian metamorphic events.

4.2.2.7 Conclusion

In this contribution, a multi-method approach was used to quantify P and T conditions in a low-grade metamorphic terrain : the Briançonnais Zone houillère. Quantified microprobe maps associated with thermodynamic modelling allowed distinguishing, in the same sample, alpine metamorphic chlorite and phengite (*A* minerals) and hercynian derived detrital chlorite and muscovite (*H* minerals). This study reports the first quantification of metamorphic conditions recorded by detrital minerals and newly grown minerals in the same composite texture of a metasedimentary rock. This study highlights the importance of the use of phengite and chlorite minerals to derive P-T paths in different metamorphic domains, even at very low temperatures. P-T results show convincing correlations between RSCM thermometry and thermodynamic analysis and provided P-T estimates of the alpine metamorphic peak of $275 \pm 23^{\circ}\text{C}$ and $5.9 \pm 1.7 \text{ kbar}$ in the upper Houiller unit. Our T_{max} estimates between 275°C and 300°C are compatible with ZFT data available in the lower Houiller unit further north. This thermal shape likely results from a top-to-the-NW *D1* thrusting event. The subsequent *D2* event is associated with a top-to-the-east shearing and "backtrusting" of the Briançonnais zone onto the Piedmont Schistes lustrés. In contrast, the *H* minerals show that Hercynian peak conditions were hotter at $371 \pm 26^{\circ}\text{C}$ and $3.5 \pm 1.4 \text{ kbar}$.

These data give rise to a refined geodynamic model of this alpine transect during Eocene-Oligocene times. The results clearly show diachronous burial and exhumation dynamics for different parts of the Briançonnais Zone, which highlights

the complexity evolution of the continental wedge. This study clearly shows a segmentation of crustal units into relatively small thrust sheets, contrary to some models arguing for large-scale exhumation (e.g. [Young et al. \(2007\)](#)).

4.2.2.8 Acknowledgments

Authors would like to sincerely thank G. Gosso (University of Milano) and an anonymous reviewer for their helpful comments, J.M. Lardeaux (University of Nice) and R. Stephenson (University of Aberdeen) for efficient editorial handling. We acknowledge contributions of other members of the Grenoble ISTERre lab and especially : Mathias Bernet, Peter van der Beek, Emilie Janots, Thierry Dumont, Arnaud Pêcher. We warmly thank F. Couffignal (CAMPARIS) for EPMA facilities access and help, B. Dubacq (University of Cambridge) for thermodynamic help and Peter van der Beek (ISTERre) for English corrections. The Raman microspectrometer at IMPMC Paris has been funded by the ANR JCJC program (project GeoCARBONS, PI O. Beyssac). This work was funded by the ERD-Alps ANR project.

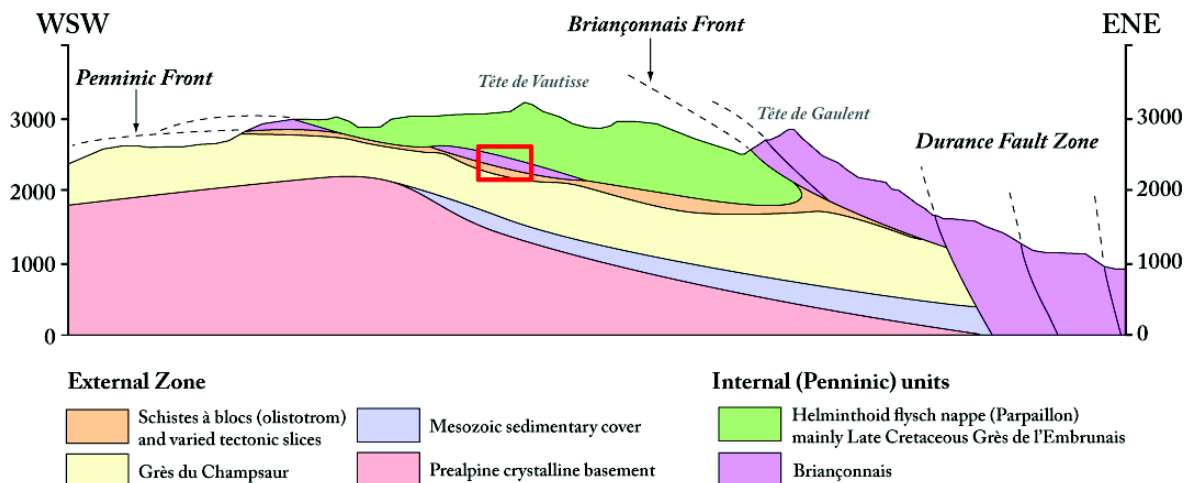


FIGURE 4.19 – Coupe géologique simplifiée au niveau des têtes de Vautisse et de Goulent. La position des échantillons utilisés pour l'étude P-T-t est reportée sur la coupe (cadre rouge).

4.2.3 Etude des micas blancs de l'écaille de Vautisse

L'étude des roches de la Zone houillère présentée précédemment a montré qu'il est possible de distinguer quatre événements métamorphiques dans les chlorites et les micas blancs en utilisant des images chimiques acquises à la microsonde, le logiciel XMAPTOOLS et les calibrations chl + qtz + H₂O (Vidal et al. 2006) et phg + qtz + H₂O (Dubacq et al. 2010). Cependant, l'âge du pic de pression ne peut pas être estimé en utilisant des méthodes de datation ⁴⁰Ar/³⁹Ar sur phengites, car ces dernières résultent de la recristallisation de muscovites détritiques (Lanari et al. 2012a). Comme les conditions métamorphiques à l'Alpin sont très faibles avec une température inférieure à 300°C, aucune surcroissance n'a été détectée autour des minéraux accessoires détritiques.

Afin de confirmer le modèle proposé (4.18), nous avons essayé d'obtenir un âge "absolu" du pic de pression pour l'affleurement de « l'écaille de Vautisse » situé plus au Sud dans la vallée de Dormillouse (Fig. 4.6). Sur le flanc Sud de cette vallée, sous la crête des Ubernaus, affleure une lentille de Briançonnais pincée dans le front pennique, entre l'épaisse série des Grès du Champsaur et celle du Flysch à Helminthoïdes (Fig. 4.19). Cette écaille briançonnaise d'une cinquantaine de mètres d'épaisseur est constituée d'un niveau de Trias dolomitique (Schytien) surmonté de schistes noirs probablement Eocènes.

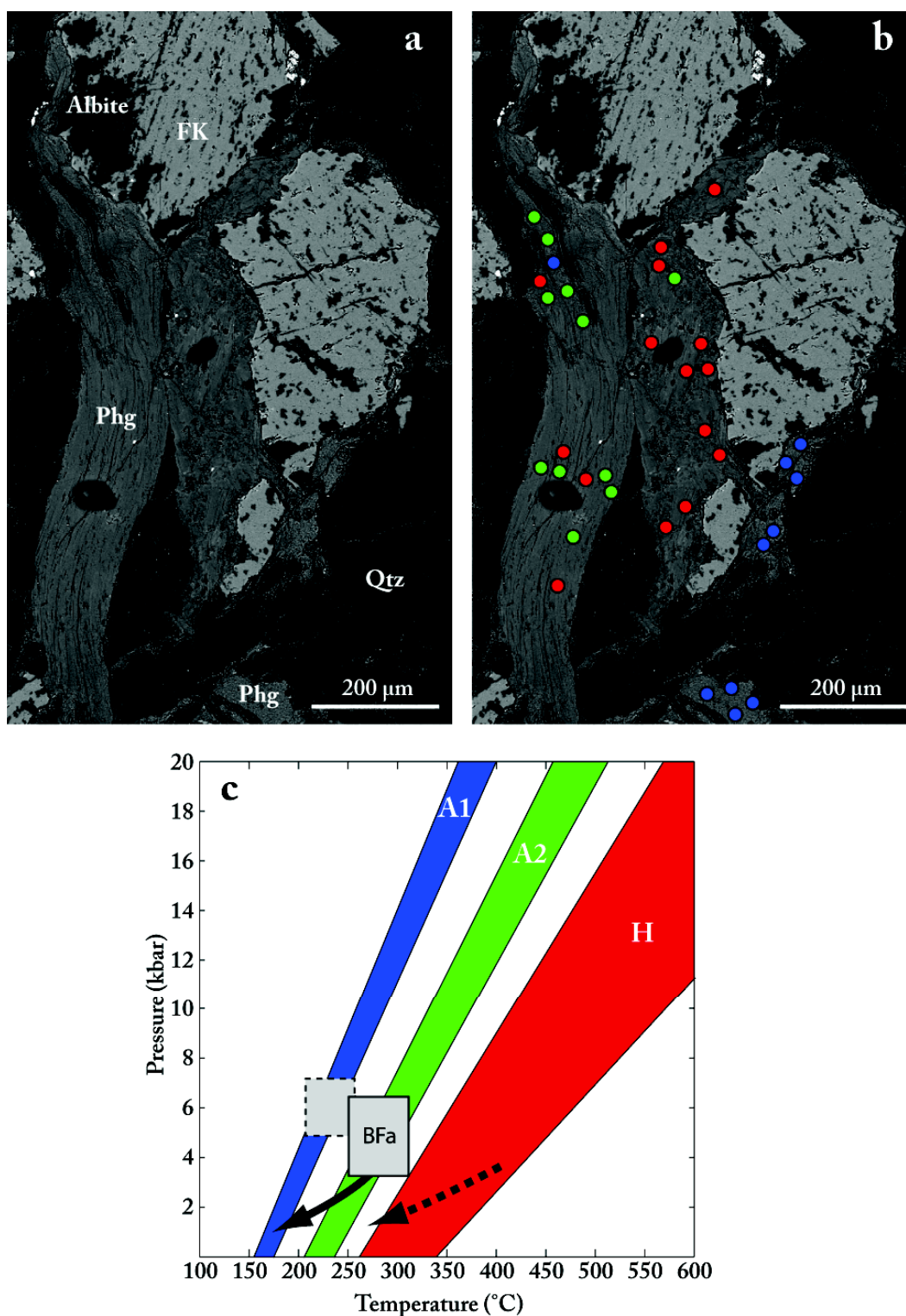


FIGURE 4.20 – Étude des micas blancs de l'écaïlle de Vautisse (Echantillon PL09_18). (a) image BSE de muscovite détritique hercynienne partiellement recrystallisée en phengite alpine. (b) Analyses ponctuelles utilisées pour tracer les équilibres $\text{Phg} + \text{Qtz} + \text{H}_2\text{O}$. Les couleurs du point correspondent aux différents groupes (A1, A2 et H1). (c) Équilibres $\text{Phg} + \text{Qtz} + \text{H}_2\text{O}$ tracés pour les différents groupes. Les conditions prédites pour les micas détritiques (groupe H) sont similaires à celles estimées dans la zone houillère.

Deux échantillons PL09_18 et PL09_21 ont été prélevés dans le premier banc de grès à la base de la série de Flysch à Helminthoïdes (cadre rouge sur la Fig. 4.19). Cette zone de contact entre les schistes noirs Eocènes et le flysch montre une importante déformation en cisaillement avec une linéation d'étirement associée orientée N-S. Ces deux échantillons ont été analysés à la microsonde afin de caractériser les conditions P-T associées à cette linéation. En lame mince, ces échantillons sont composés de quartz, feldspath, muscovites et parfois de rares chlorites. Les muscovites détritiques (notées H sur la figure 4.20-c) ont des valeurs de Si^{4+} faibles autour de 3,10 p.f.u. Elles sont partiellement recristallisées en phengites alpines (notées A2 sur la figure 4.20-c) avec des taux de Si^{4+} supérieurs entre 3,25 et 3,35 p.f.u. La phengite alpine cristallise également à partir de la déstabilisation du Feldspath (noté A1 sur la Fig. 4.20-d) avec des teneurs en Si^{4+} très élevées entre 3,55 et 3,60 p.f.u. Les lignes d'équilibres $phg + qtz + H_2O$ Dubacq et al. (2010) sont similaires à celles prédites pour la Zone houillère à l'exception de la phengite notée ici A1 provenant de la déstabilisation des feldspaths et non observée dans les grès de la Zone houillère (Lanari et al. 2012a).

Les rares chlorites identifiées et analysées sont systématiquement associées aux phengites notées A2. Les températures calculées avec la méthode $chl + qtz$ (Vidal et al. 2006) sont comprises entre 250 et 280°C. Les pressions calculées avec la méthode $phg + qtz$ Dubacq et al. (2010) pour cette gamme de température sont comprises entre 3,5 et 4,5 kbar. Ces pressions sont plus faibles que celles de la Zone houillère (6 kbar). Cette différence de 2 kbar est expliquée par des positions structurales différentes. L'échantillon de l'écaille de Vautisse appartenant aux nappes briançonnaises est en position structurale plus haute que ceux de la Zone houillère.

Les échantillons ont été broyés et tamisés pour récupérer uniquement les fractions inférieures au millimètre. Les mono-grains et agrégats de phengites alpines ont été séparés précautionneusement à la main en utilisant une loupe binoculaire. Cette opération a été menée en prenant garde de ne pas sélectionner de muscovite détritique, facilement distinguable des phengites à la loupe binoculaire. Les grains sélectionnés ont été irradiés 70h (J1), puis 10h (J2 et J3) dans le réacteur nucléaire de l'Université de McMaster à Hamilton (Canada). Le grain présentant la

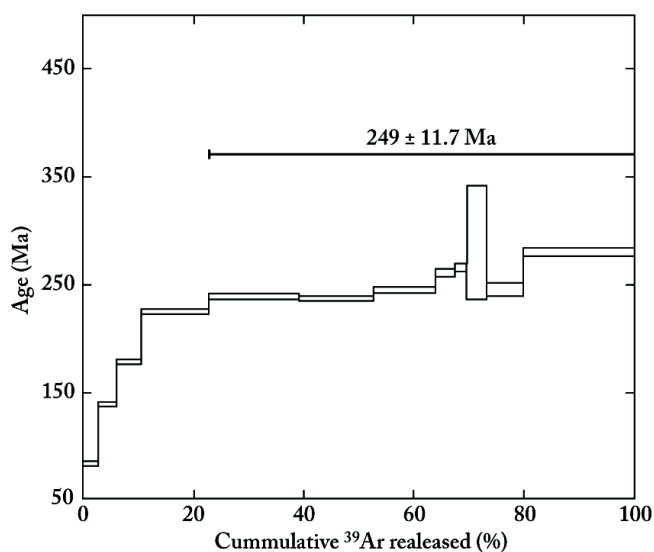


FIGURE 4.21 – Spectre $^{40}\text{Ar}/^{39}\text{Ar}$ d'un mica blanc de l'échantillon PLog_21

plus grande chance de ne pas contenir de muscovite détritique a été analysé au laboratoire GeoAzur de l'Université de Nice en utilisant un laser 50W SYNRAD CO₂ associé à un spectromètre de masse VG3600.

Le spectre $^{40}\text{Ar}/^{39}\text{Ar}$ montre un plateau à $249 \pm 11 \text{ Ma}$ (Fig. 4.21). Cet âge correspond à un âge intermédiaire entre les épisodes hercynien (e.g. 300 Ma) et alpin (e.g. 50-30 Ma) ce qui est symptomatique d'une non remise à zéro totale de l'âge $^{40}\text{Ar}/^{39}\text{Ar}$ lors de l'épisode alpin. Ce résultat provient du fait que la phengite cristallise par remplacement d'une muscovite détritique hercynienne et que même si ce remplacement semble total, en l'absence d'une déformation importante, l'âge $^{40}\text{Ar}/^{39}\text{Ar}$ n'est pas remis à zéro (Sanchez et al. 2011). Afin de dater par $^{40}\text{Ar}/^{39}\text{Ar}$ les phengites de l'épisode alpin, il est nécessaire de sélectionner un échantillon dans une zone ayant subi une forte déformation.

4.2.4 Article 6 : P-T-t estimation of syn-kinematic strain in low-grade rocks (< 300°C) using thermodynamic modelling and $^{40}\text{Ar}/^{39}\text{Ar}$ dating techniques : example of the Plan-de-Phasy shear zone (Briançonnais Zone, Western Alps). (Submitted to Terra Nova)

P-T-t estimation of syn-kinematic strain in low-grade rocks ($< 300^{\circ}\text{C}$) using thermodynamic modelling and $^{40}\text{Ar}/^{39}\text{Ar}$ dating techniques : example of the Plan-de-Phasy shear zone (Briançonnais Zone, Western Alps).

Pierre Lanari³, Yann Roland⁴, Stéphane Schwartz³, Olivier Vidal³, Stéphane Guillot³, Pierre Tricart³, Thierry Dumont³

submitted to Terra Nova

Abstract - Pressure-Temperature-time estimates of the syn-kinematic deformation at the pressure peak conditions reached during shallow underthrusting of the Briançonnais in the Alpine subduction zone was achieved by thermodynamic modelling and $^{40}\text{Ar}/^{39}\text{Ar}$ dating in the Plan-de-Phasy granite unit (SE of the Pelvoux Massif, Western Alps). The dated phengites crystallized syn-kinematically in a shear zone indicating top-to-the NW motion. By combining quantitative mapping techniques and multi-equilibrium methods we estimate the conditions of crystallization of phengites at $270 \pm 50^{\circ}\text{C}$ and $8.1 \pm 2 \text{ kbar}$ at $45.85 \pm 1.06 \text{ Ma}$. This P-T-t estimate associated to data from the literature allows to precise the timing and the geometry of the Alpine continental subduction. We propose that Briançonnais continental units were scalped on top of the continental slab during ongoing continental subduction and exhumed continuously till collision at ca. $32 - 30 \text{ Ma}$, with evidence of further partial hydrothermal reequilibration at 13 Ma .

4.2.4.1 Introduction

Estimation of burial and exhumation rates and subsequent building of consistent geodynamic models of continental subduction processes and orogenic evolution are based on our knowledge of Pressure-Temperature-time (P-T-t)

3. ISTERre, University of Grenoble 1, CNRS, 1381 rue de la Piscine, 38041 Grenoble, France

4. Géosciences Azur, UMR7329-CNRS, UNS, 28 Av. Valrose, BP 2135, 06103 Nice, France

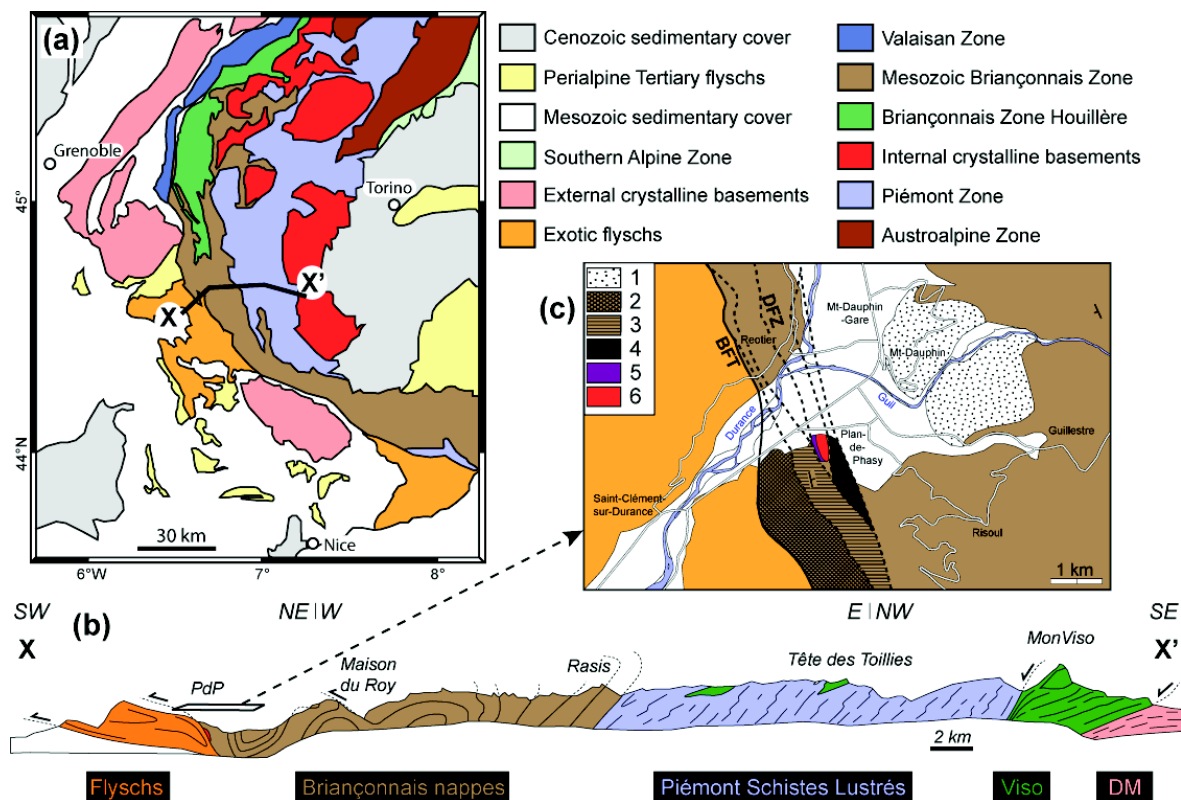


FIGURE 4.22 – Geological framework including (a) a schematic map of the Western Alps modified after (Bousquet *et al.* 2008) and Dumont *et al.* (2012). (b) EW section across the internal zones modified from Lardeaux *et al.* (2006). (c) Detailed map of the Guillestre - Plan-de-Phasy area. 1, Quaternary conglomerats; 2, Eocene Flysch noir; 3, Triassic marble; 4, Triassic Gypsum; 5, Permo-Triassic metasediments; 6 and PdP, Plan-de-Phasy "granite" basement. BFT, Briançonnais Frontal Thrust (bold line); DFZ Durance Fault Zone (dashed lines)

paths recorded by the different units across mountain belts (e.g. Rolland *et al.* 2012). In order to estimate P-T-t conditions of metamorphic rocks, we need to link P-T estimates with "absolute" ages. This goal can be easily achieved in well equilibrated high-grade metamorphic rocks for which several methods are available to estimate P-T conditions such as pseudosections (e.g. Connolly 2005) and several dating techniques such as $^{40}\text{Ar}/^{39}\text{Ar}$ and *U-Pb* (McDougall *et al.* Harrison 1988). Unfortunately for low-grade metamorphic samples ($< 300^\circ\text{C}$) P-T estimates and mineral dating are both challenging. Low-grade quartzo-feldspathic rocks ($< 300^\circ\text{C}$) are devoid of index minerals and the critical paragenesis is made of chlorite, K-rich white micas and quartz.

However, a multi-method approach using multi-equilibrium techniques allows

estimating the P-T conditions recorded by the rocks from chlorite and phengite compositions (Lanari et al. 2012a, and references therein). Further, phengite can be dated using $^{40}\text{Ar}/^{39}\text{Ar}$ approach, but one of the key issues involved in the interpretation of $^{40}\text{Ar}/^{39}\text{Ar}$ of ages is to know whether the age reflects crystallization age or cooling age (Di Vincenzo 2004, and references therein). As the closure temperature of phengite is higher than 400°C (McDougall et Harrison 1988), low-grade newly-formed phengites below 400°C must provide crystallization ages. Indeed recent developments of the $^{40}\text{Ar}/^{39}\text{Ar}$ dating method on phengite grains show that it is possible to determine the age of phengite crystallization related to deformation events in low-grade temperature shear zones (Kirschner et al. 1996, Corsini et al. 2004, Simon-Labric et al. 2009, Rolland et al. 2009, Sanchez et al. 2011).

After more than a century of investigations, the Alps still represent a natural laboratory to study geodynamic convergent processes in mountain belts (e.g. Bousquet et al. 2008). In the Briançonnais Zone of the French Western Alps (Fig. 4.22-a, Fig. 4.22-b) a small tectonic slice of phengite bearing gneiss known as the "Plan-de-Phasy granite" is pinched in the Briançonnais Frontal Thrust (Tricart 1984, Kerckhove et Piboule 1999) which recorded a top-to-the west tectonic motion during the Early Oligocene corresponding to the development of collision stage (Simon-Labric et al. 2009, Dumont et al. 2012). In the Plan-de-Phasy granite, this latter event is superimposed on subduction tectono-metamorphic event underlined by older phengite minerals. The study of this early paragenesis will allow investigating the tectono-metamorphic history of the Briançonnais continental margin during Alpine continental subduction.

4.2.4.2 Geological setting

In the core of the Western Alps, the internal metamorphic zones are made of a stack of oceanic and continental units recording an eastward increase in metamorphic conditions (Saliot 1978, Rolland et al. 2000, Agard et al. 2001a, Goffé et al. 2004, Bousquet et al. 2008, Gabalda et al. 2009, Schwartz et al. 2009). This orogenic wedge is constituted by the Piedmont zone, which represents different levels of the paleo-subduction zone with preserved low thermal gradient ($5 - 8^\circ\text{C}/\text{km}$) representing the subduction dynamics (e.g. Lardeaux et al. 2006). From top to bottom (i) unme-

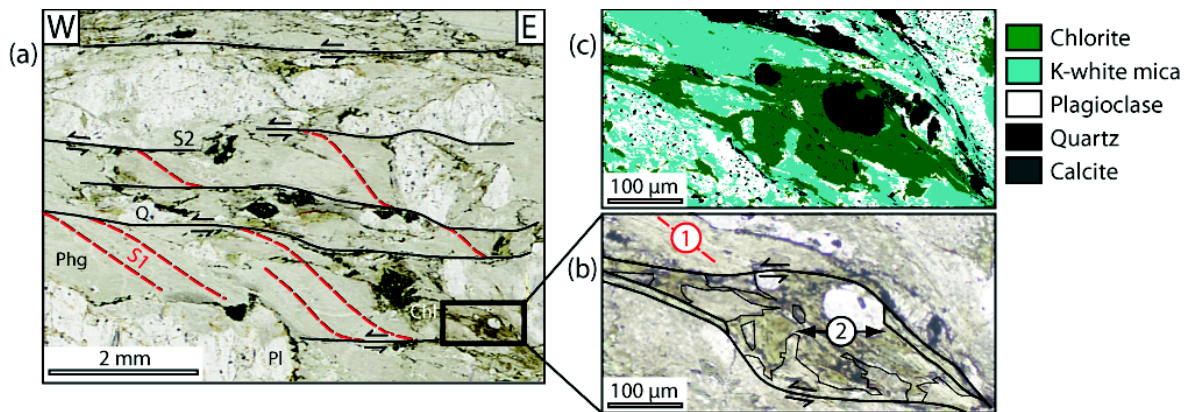


FIGURE 4.23 – Plan-de-Phasy granite sample : (a) Photomicrograph at the thin section scale showing the two schistositities S1 (red dashed lines) and S2 (black lines). Chl, chlorite; Q, quartz; Phg, phengite; Pl, plagioclase. (b) Photomicrograph zoom. (c) Mask image in which all the pixels of the chemical map were allocated to one mineral (see text)

tamorphosed obducted (Chenaillet) ophiolite rests upon (ii) the Queyras "Schistes lustrés", which represent a fossil sedimentary accretionary wedge developed under blueschist facies conditions during late Paleocene-Early Eocene subduction of the Tethys ocean [Agard et al. \(2002\)](#). This blueschist domain lies structurally above (iii) the eclogitic Monviso ophiolites. Eclogitic metagabbros occur as boudins in a matrix of serpentinites or highly deformed meta-basalts corresponding to the deep subduction channel developed at the base of the accretionary wedge ([Schwartz et al. 2001](#), [Angiboust et al. 2011](#)). Structurally below, (iv) the Briançonnais zone outcrops as tectonic windows (Fig. 4.22). Close to Guillestre, in the studied area (Fig. 4.22-b), the Upper Briançonnais Zone is made of a stack of late Palaeozoic to Mesozoic sediments (e.g. [Tricart 1984](#)) that suffered upper greenschist facies conditions ($275 \pm 23^{\circ}\text{C}$ and $5.9 \pm 1.7 \text{ kbar}$) during Alpine metamorphism ([Caby 1996](#), [Lanari et al. 2012a](#)).

The Plan-de-Phasy granite is a 300 m wide highly-deformed and recrystallized Hercynian gneiss slice exhibiting top-to-the-NW and W sense of shear, surrounded by Permian to Triassic metasediments and gypsum lenses pinched in the Briançonnais Frontal Thrust. This formerly ductile shear zone is reactivated by the active extensional-strike slip Durance Fault Zone ([Tricart et al. 1996](#)) in more brittle conditions (Fig. 4.22-c).

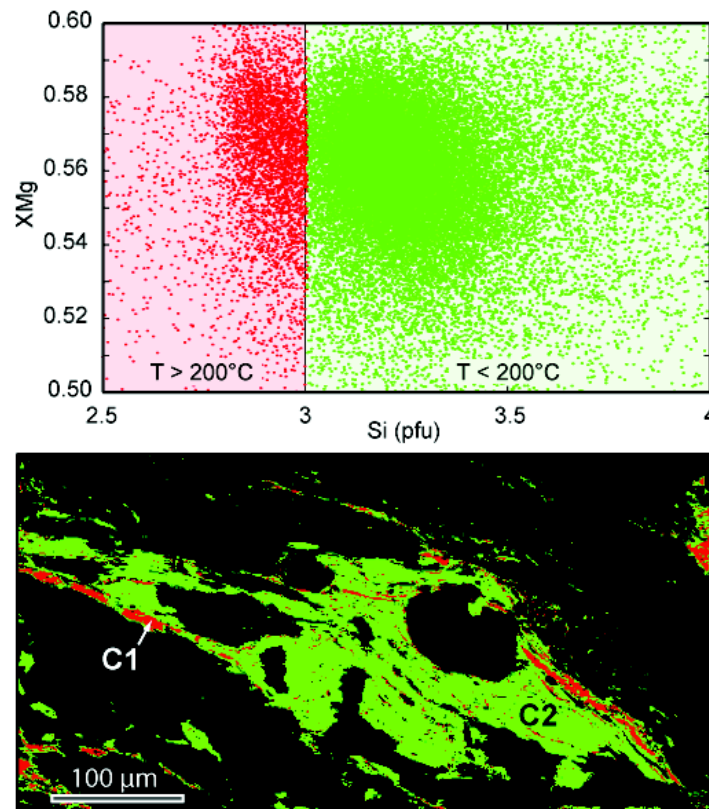


FIGURE 4.24 – Chemical analysis of chlorite compositions plotted into a binary diagram Si (p.f.u.) vs XMg (top). The corresponding pixels were plotted into a map (bottom)

4.2.4.3 Petrological and chemical studies

Oriented samples were collected in the Plan-de-Phasy granit unit. At the thin section scale, the only visible assemblage is made of K-rich white mica + chlorite + quartz + plagioclase + calcite (Fig. 4.23-a). Two generations of micas were identified using structural and chemical criteria : (1) multi-mm K-white micas belong to the first one and crystallized during top to the N-NW shearing event corresponding to S1 schistosity (red lines in Fig. 4.23-a). (2) K-white mica grains are sheared during a top to the W deformation event and associated to chlorite crystallization, it corresponds to a narrow recrystallization zone S2 along C surfaces (black lines Fig. 4.23-a).

We selected a small area ($1100 \times 560 \mu\text{m}^2$) in which the two schistosités (S1-S2) are present with chlorite growing in a S2 tensile crack (Fig. 4.23-b). This area was chemically mapped at the Institute of Earth and Environmental Sciences, Potsdam University using a JEOL JXA-8200 electron microanalyser in wavelength dispersive

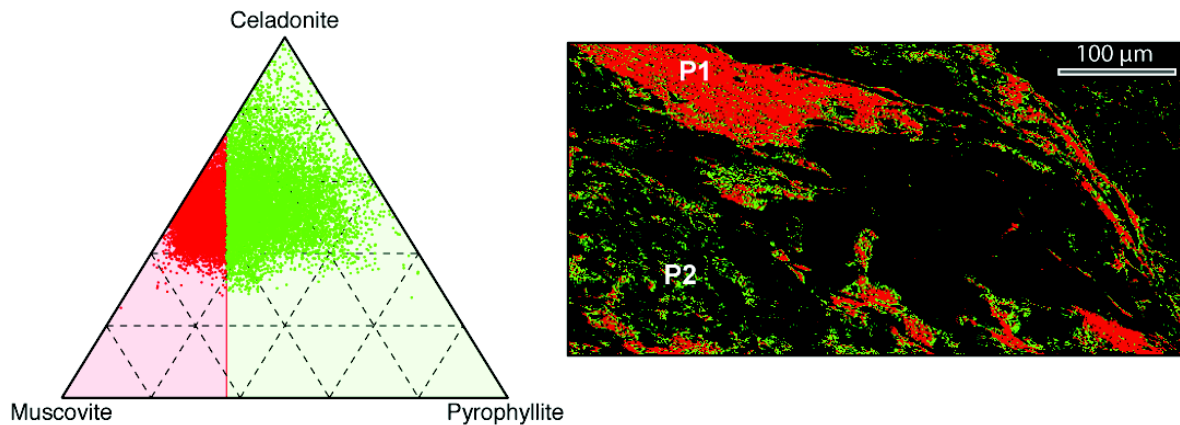


FIGURE 4.25 – Chemical analysis of K-white mica compositions plotted into a ternary diagram muscovite, celadonite, pyrophyllite (top). The corresponding pixels were plotted into a map (bottom)

mode. Analytical conditions for the mapping were 15 KeV accelerating voltage, 100 nA, specimen current and 300 ms of counting time (De Andrade et al. 2006) and a step of 2 μm. During the same microprobe session, punctual analyses were acquired along transects on the same area. Analytical conditions were 15 KeV, 10 nA, 45 s and 1 μm. The X-ray map processing was achieved using the program XMAPTOOLS (Lanari et al. 2012b). The different minerals were identified from the chemical maps (Fig. 4.23-c). Punctual analyses were projected into the X-ray maps and used as standard to transform them into maps of oxide compositions. Maps of structural formulae were calculated and the compositions plotted into chemical diagrams (Fig. 4.24 and 4.25). Chlorite compositions do not show large variation in the Mg content with XMg ($XMg = Mg^{2+} / (Mg^{2+} + Fe^{2+})$) ranging between 0.54 and 0.58 (Fig. 4.24-a). In contrast, two groups of chlorite compositions can be distinguished based on the Si-content. The first group C1, in red in the figure 4.24, corresponds to chlorite with $Si < 3$ per formula unit (p.f.u.). The second group C2, in green in the figure 4.24, corresponds to chlorite with $Si > 3$ p.f.u. The C2 chlorite group generally shows a large number of octahedral vacancies and crystallized at lower temperature (Inoue et al. 2009). The C1 chlorite minerals crystallized in the S1 schistosity while the C2 chlorite group underlines the late recrystallization S2 along C-planes (Fig. 4.24-b).

Chlorite		Phengite	
	C1		P1
SiO ₂	27.21	SiO ₂	53.14
Al ₂ O ₃	18.97	Al ₂ O ₃	23.14
FeO	21.87	FeO	4.22
MnO	0.31	MnO	0.04
MgO	17.36	MgO	4.55
CaO	0.10	CaO	0.07
Na ₂ O	0.03	Na ₂ O	0.41
K ₂ O	0.17	K ₂ O	10.03
Atom site distribution (Atom site distribution (14 Ox.))		Atom site distribution (Atom site distribution (11 Ox.))	
Si(T ₁ +T ₂)	2.88	Si(T ₁ +T ₂)	3.55
Al(T ₂)	1.12	Al(T ₂)	0.44
Al(M ₁)	0.12	V(M ₁)	0.93
Mg(M ₁)	0.49	Mg(M ₁)	0.04
Fe ₂ +(M ₁)	0.35	Fe ₂ +(M ₁)	0.02
V(M ₁)	0.042	Al(M ₂ +M ₃)	1.37
Mg(M ₂ +M ₃)	2.24	Mg(M ₂ +M ₃)	0.41
Fe(M ₂ +M ₃)	1.58	Fe(M ₂ +M ₃)	0.21
Al(M ₂ +M ₃)	0.11	K(A)	0.85
Al(M ₄)	1.00	Na(A)	0.05
Fe ₃ +(M ₄)	0.00	V(A)	0.08

TABLE 4.5 – Average composition of Chlorite C1 and phengite P1.

Phengite compositions were plotted into a ternary diagram : Muscovite ($Si_3Al_3V_1K_1O_{10}(OH)_2$), celadonite ($Si_4Al_1V_1(Mg, Fe)_1K_1O_{10}(OH)_2$) and pyrophyllite ($Si_4Al_2V_2O_{10}(OH)_2$) and are also divided into two groups (Fig. 4.25). The first group *P1* belongs to the *S1* schistosity. This group does not show any chemical zoning. Thus, the average composition of this group (Tab. 1 and *P1* in Fig. 4.25) was calculated using all the selected pixels in red in the figure 4.25. The second group *P2* is composed of pixels showing celadonite-rich and pyrophyllite-rich compositions (Fig. 4.25a) and are formed from the destabilization of plagioclase and *P1* phengite (green pixels in Fig. 4.25-b). This destabilization occurs during the *D2* event or maybe later under hydrothermal conditions.

4.2.4.4 P-T estimates

We used a multi-equilibrium approach (Berman 1991) as previously detailed in Lanari et al. (2012a) to derive the P-T conditions of crystallization of chlorite and phengite. Si-poor chlorite composition ($Si < 3$) in equilibrium with quartz and water, allows us to estimate the *D1* temperature using the calibration of Vidal et al. (2006). For the Si-rich chlorite group (*D2*), we use the new calibration of Inoue et al. (2009) that includes a $(Si)_4$ end-member : Al-free-chlorite. From a phengite composition, we can estimate a P-T line along which phengite is in equilibrium with quartz and water using the calibration of Dubacq et al. (2010). The intersection between the temperature estimates from chlorite thermometry and the P-T line

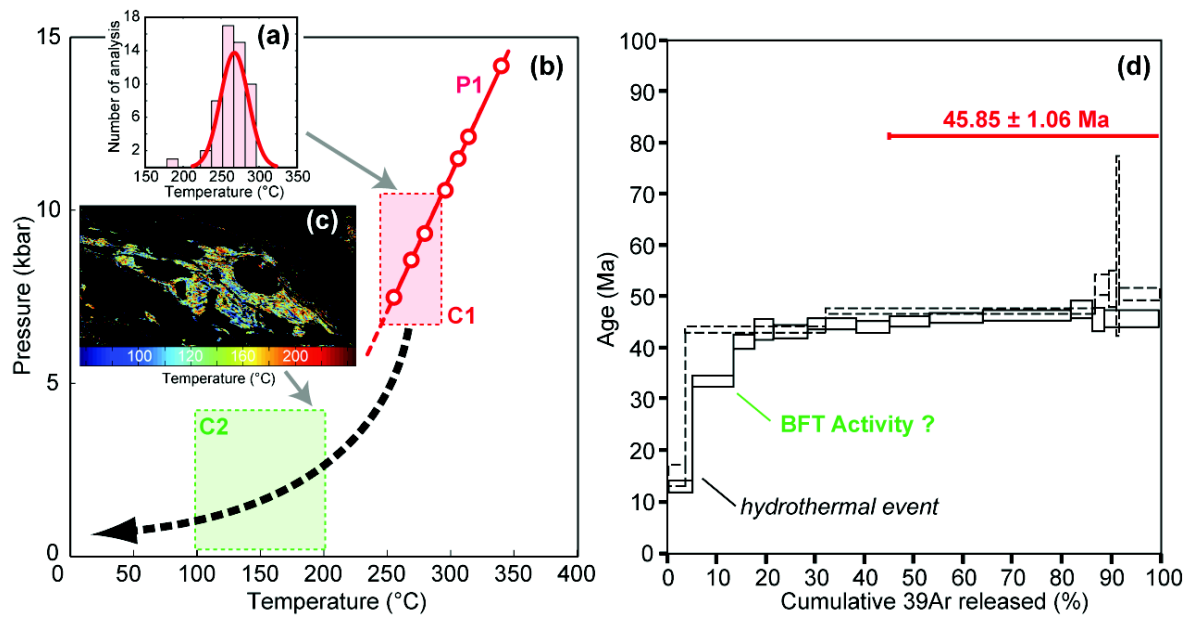


FIGURE 4.26 – *P-T-t* estimate of the metamorphic peak in the Plan-de-Phasy granite. (a) Temperature of Si-poor chlorite compositions calculated using the calibration of [Vidal et al. \(2006\)](#). (b) *P-T* diagram showing the *P-T* line of phengite P1 and the temperature range of C1 chlorite compositions. (c) Temperature map of Si-rich chlorite compositions calculated with the calibration of [Inoue et al. \(2009\)](#). (d) $^{40}\text{Ar}/^{39}\text{Ar}$ spectra of P1 phengite. Age is shown at 2?.

estimated with phengite constrains the chlorite-phengite *P-T* equilibrium ([Lanari et al. 2012a](#)).

Temperatures of a selection of C1 chlorites (white arrow C1 in Fig. 4.24) were calculated for an input pressure of 7 *kbar* and plotted into the figure 4.26-a. Temperatures range between 240°C and 300°C and provide an average temperature of $270 \pm 25^\circ\text{C}$. The *P-T* equilibrium line of the P1 phengite was calculated and allows estimating the pressure at 8.1 ± 2 *kbar* for a temperature of 270°C (Fig. 4.26-b). The temperature map of C2 chlorite group has been calculated and show temperatures ranging between 100°C and 200°C (Fig. 4.26-c). The phengite equilibrium line cannot be used, as the C2 chlorites are not in equilibrium with phengite.

4.2.4.5 Ar-Ar phengite dating

As the P1 phengite grains crystallized during the D1 metamorphic event, the dating could provide an absolute age of the first deformation event in the Briançonnais nappes. Phengite grains less than 500 μm were separated by hand-picking

under a binocular microscope. The selected grains were irradiated for 10h in the nuclear reactor at McMaster University in Hamilton (Canada) in position 5c along with Fish Canyon sanidine monitor (28.03 ± 0.08 Ma, Jourdan et al. (2004)). The estimated errors of $^{40}\text{Ar}^*/^{39}\text{ArK}$ ratio range between $\pm 0.1\%$ (2σ), and $\pm 0.6\%$ (2σ) in the volume where the samples were included. Phengite grain datings were undertaken by step heating with a 50 W CO₂ Synrad 48-5 continuous laser beam and the measurement of isotopic ratios was realized with a VG3600 mass spectrometer at Geoazur (detailed method in Jourdan et al. 2004). The two Ar-Ar spectra exhibit a slight staircase shape in low temperature steps, likely featuring hydrothermal alteration (e.g. Rolland et al. 2008), and a flat high temperature part providing an age of crystallization of 45.85 ± 1.06 Ma (Fig. 4.26-d, table in supplementary material).

4.2.4.6 Discussion and geodynamic implications

In this study, the Alpine pressure peak reached by the Plan-de-Phasy granite during *D1* low-temperature metamorphic event is calculated at $270 \pm 25^\circ\text{C}$ and 8 ± 1.2 kbar was dated at 45.85 ± 1.06 Ma. The *D1* phengite growth was syn-kinematic as shown by textural S-C fabrics and absence of any compositional zoning, so the calculated age is an age of crystallization during to the top to N to NW shear zone activity. Phengite minerals were destabilized during the retrogressed path into celadonite-rich and phengite-rich micas or clays. This destabilization probably occurred during the *D2* event, i.e. during the Briançonnais Frontal Thrust activity. Further north, in the underthrust External Pelvoux crystalline massif, Simon-Labric et al. (2009) showed that this *D2* event occurs between 34 and 30 Ma, and could explain part of the Ar loss. Finally, the low temperature Ar loss reflects alteration, probably related with hydrothermal activity (as is clearly evidenced in the field). The two dated grains show a first step age of 13 ± 2 Ma. This (maximum) age is in good agreement with apatite fission-track age of 11.7 ± 1.2 Ma obtained by Schwartz (2000) in the same unit and interpreted as partial to total annealing of samples by hydrothermal fluids Tricart et al. (2007). This thermal fluid system was linked to the onset of Durance normal fault activity and are analogous to those that currently feed the active hot springs along the fault zone at Plan-de-Phasy (Fig. 4.22-c).

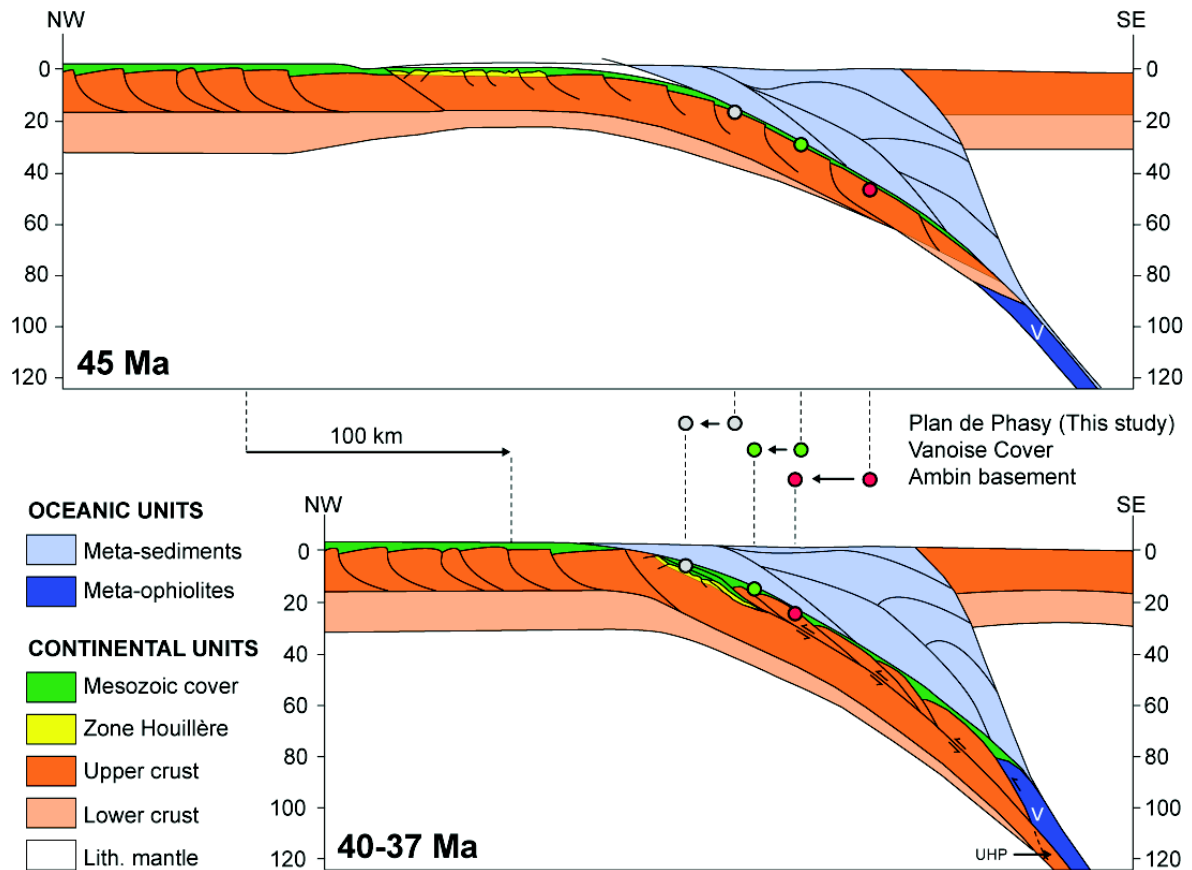


FIGURE 4.27 – Possible kinematic reconstruction of this part of the Western Alps from Eocene to Oligocene (modified from Lanari et al. 2012a). V, Viso.

According to our new results and the available P-T-t in the literature Ganne et al. (2007), Gerber (2008), Gabalda et al. (2009), Lanari et al. (2012a), Strzeczynski et al. (2012), we propose to integrate the Plan-de-Phasy granite in the framework of the Briançonnais zone evolution during Eocene time (Figure 4.27). At 50-45 Ma, a major D1 top to the NW HP-LT tectono-metamorphic event corresponding to the pressure peak is recorded in the internal Briançonnais zones, in the Vanoise sedimentary cover (Gerber 2008, Strzeczynski et al. 2012) and in the Ambin gneissic basement (Ganne et al. 2007). Considering the relatively cold geothermal gradient of this D1 tectono-metamorphic event (ca. 8-10°C/km) this event was related to the continental subduction of the Briançonnais zone (Ganne et al. 2007, Lanari et al. 2012a, Strzeczynski et al. 2012)). In the external Briançonnais zone, the Plan-de-Phasy unit also recorded a top-to-the-NW tectonic event at 45.85 ± 1.06 Ma along a relatively cold apparent geotherm of 11°C/km. This suggests that the Plan-de-

Phasy unit could have been initially rooted within the Internal Briançonnais zone. The absence of any carboniferous sediments symptomatic of the Briançonnais Zone Houillère between the Plan-de-Phasy granite basement and its Permian to Triassic sediments cover confirms that this unit has an Internal Briançonnais origin (Fig. 4.27-a). Assuming a convergence rate of 1.5 km/Ma during Eocene time (Handy et al. 2010), we can reconstruct the geometry of the Briançonnais continental subduction at 40-37 Ma (Fig. 4.27-b). Most of the Internal Briançonnais units are partly exhumed at that time (Ganne et al. 2007, Gerber 2008, Strzeczynski et al. 2012) except the most external units such as the Briançonnais Zone Houillère (Lanari et al. 2012a). Exhumation of the Internal Briançonnais units resulted in the scrapping off the basement-cover transition while the continental subduction still continued. The HP-LT units scalped at the top of the continental slab form a stack of continental units in front of the active continental subduction corresponding to the future Briançonnais Frontal Thrust (Fig. 4.27-b). The final emplacement of the Plan-de-Phasy in its present-day position is related to Briançonnais Frontal Thrust activity at ca. 32-30 Ma (Simon-Labric et al. 2009, Dumont et al. 2012).

4.2.4.7 Conclusion

In this work we show that it is possible to depict the tectono-metamorphic evolution of low grade chlorite-phengite bearing lithologies involved in shear zones in order to pinpoint the main kinematic events and corresponding P-T-t path. Here, we provide insights for the fossilization of shallow activity of the Alpine subduction zone and underthrusting of Briançonnais continental crust at ca. 46 Ma. Such a detailed metamorphic approach and associated geochronological study is only possible in highly-deformed sample in which phengite grains are neo-crystallized.

4.2.4.8 Acknowledgements

This study was supported by the ANR ERD-Alps (Erosion and Relief Development in the western Alps). Support from S. Gallet during Ar-Ar analysis and data processing is warmly thanked.

4.3 PREMIERS RÉSULTATS SUR L'ÉTUDE DU COMPLEXE DES SCHISTES LUSTRÉS DU QUEYRAS

★ *La reconstruction des trajets P-T-t enregistrés par les métasédiments nécessite de pouvoir relier estimations P-T et données radiochronologiques pour les différents épisodes de déformation.*

★ *À l'inverse de la partie plus au Nord, les Schistes lustrés du Queyras n'ont pas de contrainte radiochronologique sur les principales phases de déformation ductile liées à la subduction. Les conditions P-T, dans cette partie du paléo-prisme océanique, ont été estimées en utilisant les roches basiques (Schwartz, 2000) et seule la chronologie de l'histoire tardive est bien contrainte (e.g. Schwartz et al. 2009).*

★ *Dans cette partie, nous allons exposer les premiers résultats obtenus sur deux affleurements des Schistes lustrés du Queyras. Nous avons combiné une approche micro-cartographique et de multi-équilibres pour estimer les conditions P-T et des datations $^{40}\text{Ar}/^{39}\text{Ar}$ sur phengites pour contraindre l'âge des différentes générations de structures.*

4.3.1 Introduction

4.3.1.1 Schistes lustrés du Queyras

Le complexe des Schistes lustrés est constitué d'abondants volumes de sédiments océaniques de nature variées (calcschistes, marbres, quartzites) déposés entre le Jurassique et le Crétacé supérieur (Lagabrielle 1987) et de masses ophiolotiques constituées de serpentines, métagabros et prasinites (Schwartz 2000). L'ensemble de ces formations ont été affectées par de nombreux événements tectoniques syn-sédimentation (e.g. Lemoine 1980) et post-sédimentation (e.g. Lagabrielle 1987) qui compliquent la compréhension du complexe dans son ensemble.

L'étude de la déformation dans le complexe des Schistes lustrés du Queyras permet de mettre en évidence trois épisodes majeurs de déformation syn-schisteux

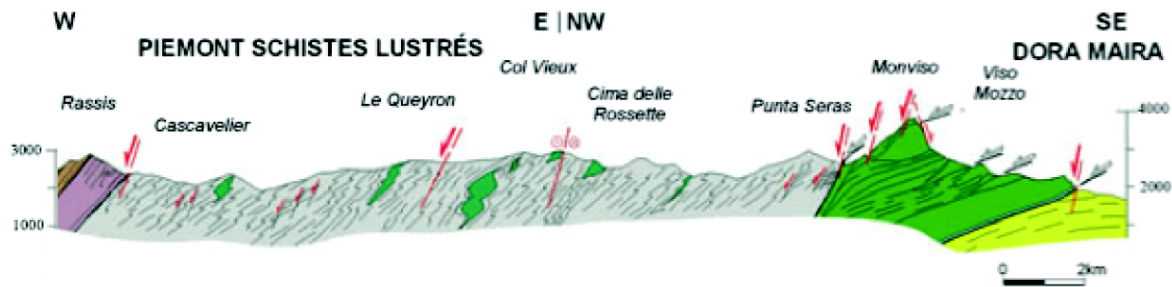


FIGURE 4.28 – Coupe à travers les Schistes lustrés du Queyras, le massif du Viso modifiée d'après Lardeaux et al. (2006)

affectant un plan de foliation précoce (e.g. Caron et al. 1973, Tricart et Schwartz 2006).

Le complexe des Schistes lustrés du Queyras est structuré par un plan d'aplatissement principal qui présente un pendage Ouest compris entre 20 et 40° (Fig. 4.28). Ce plan, noté ici S2 est localement associé à des plis à vergence Sud. Cette S2 est un plan de foliation associé à un métamorphisme dans le faciès des Schistes bleus, qui contient une linéation minérale L2 (Fig. 4.29) correspondant probablement à une réorientation par étirement d'une linéation plus ancienne.

Des charnières de plis précoces P1 ont été localement préservés (Fig. 4.29). Ces plis à flancs parallèles possèdent des axes orientés globalement E-W et résultent d'une déformation cisailante avec une vergence vers le Nord (Schwartz 2000).

Le plan d'aplatissement principal S2 est repris par une phase de déformation D3 associé à un métamorphisme dans le faciès des Schistes verts. Elle est exprimée par des plis P3, avec des axes généralement orientés N-S (Fig. 4.29), et qui sont associés à une tectonique E-W donc post 35 – 32 Ma (e.g. Dumont et al. 2012). Une schistosité S3 localement crénelante se développe dans le coeur des plis P3.

L'ensemble de ces structures ductiles est repris par un épisode d'extension à la transition ductile/fragile marqué par l'apparition de fentes à quartz. Dans un deuxième temps, l'ensemble des structures ont été basculées vers l'Ouest en raison de l'exhumation du massif cristallin interne de Dora-Maira (e.g. Tricart et al. 2007, Schwartz et al. 2009).

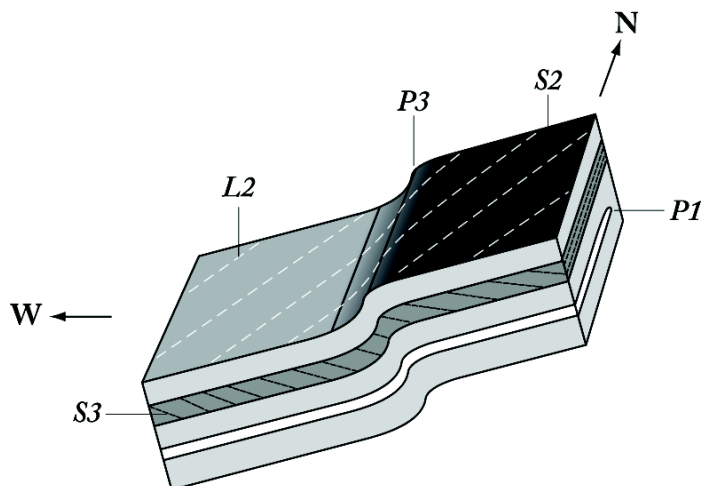


FIGURE 4.29 – Schéma des structures de déformations ductiles rencontrées dans le complexe des Schistes lustrés du Queyras. P, plis ; S, foliation/schistosité ; L, linéation minérale

4.3.1.2 Métamorphisme

Les Schistes lustrés du Queyras présentent une évolution spatiale progressive des conditions dans le faciès des Schistes bleus. Quatre domaines ont été identifiés par [Schwartz \(2000\)](#) avec un pic de pression qui évolue de 300°C et 8 *kbar* à l'Ouest à 450°C et 13 *kbar* à l'Est. Ces estimations ont été effectuées à partir des assemblages observés dans les roches basiques des ensembles ophiolitiques. Contrairement à la partie Nord (e.g. [Agard et al. 2001a; 2002](#)), les Schistes lustrés du Queyras ne possèdent pas d'estimations radiochronologiques précises des différentes phases de déformations présentées précédemment. Les âges obtenus plus au Nord sont difficilement transposables à la branche Sud, car les phases de déformations identifiées dans les deux zones sont difficiles à relier.

4.3.1.3 Stratégie

Afin de déterminer les conditions P-T-t des différentes phases de déformation, nous avons appliqué les techniques de micro-cartographie et de multi-équilibres à deux métapélites des Schistes lustrés du Queyras en réalisant en parallèle des datations $^{40}\text{Ar}/^{39}\text{Ar}$ sur phengites. Dans un premier temps, nous allons présenter les résultats d'une étude Raman de la matière carbonée qui a servi à calculer la T_{max} enregistrée par les métasédiments de la zone et à préciser le découpage des

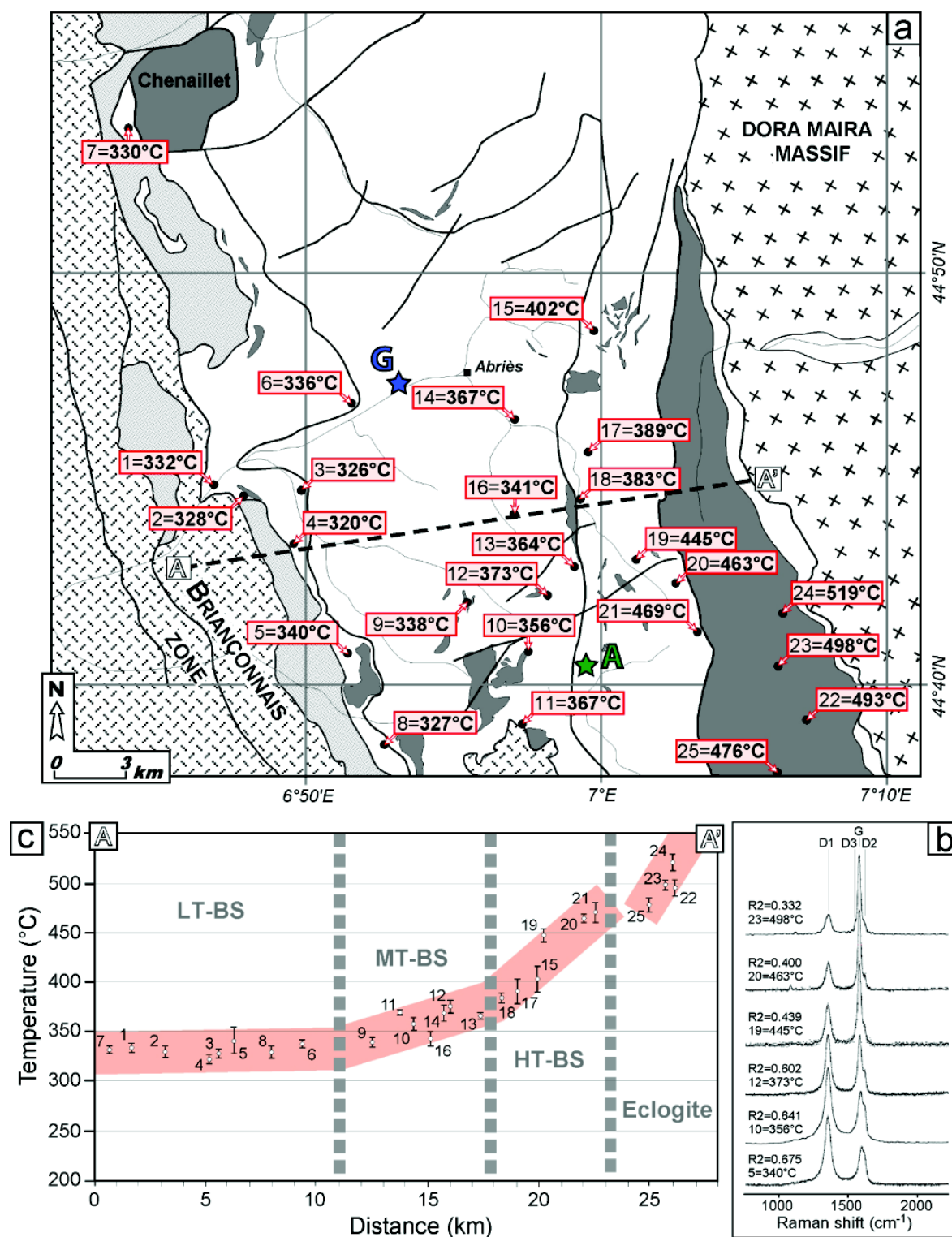


FIGURE 4.30 – Etude Raman de la matière carbonée dans les métasédiments des Schistes lustrés du Queyras. (a) carte des T_{max} . G : Gouret ; A : Arkose de Roca Nera. (b) évolution des spectres Raman de la matière carbonée d'Ouest (bas) en Est (haut). (c) Vue en coupe. Les Schistes lustrés ont été divisés en trois groupes de températures : LT-BS (Low Température - Blueschist) ; MT-BS (Median Température - Blueschist) et HT-BS (High Température - Blueschist).

unités métamorphiques. Puis nous détaillerons les premiers résultats thermobarométriques et radiochronologiques obtenus pour un affleurement situé dans la zone de moyenne température (Affleurement du Gouret) et pour un affleurement situé dans la zone de haute température (Affleurement de l'Arkose de Roca Nera).

4.3.2 Etude Raman de la matière carbonée

L'étude, en utilisant la spectrométrie Raman de la matière carbonée, est basée sur le degré de graphitisation de la matière organique durant le métamorphisme. Le phénomène de graphitisation correspond à une transformation de la matière organique en matière carbonée et est dépendant de la température maximale atteinte lors du métamorphisme (Beyssac et al. 2002; 2003b;a; 2004; 2007, Lahfid et al. 2010). Les analyses ont été réalisées à l'ENS-Lyon en utilisant un appareil Horiba Jobin-Yvon LabRam HR800. L'échantillon a été excité en utilisant un laser argon avec une longueur d'onde de 514 nm. Nous avons utilisé un microscope OlympusTM BX30 avec un objectif $\times 100$ couplé au spectromètre. Le temps de mesure était de 120 s réparti en deux cycles d'acquisitions. Le spectromètre a été calibré avant chaque séance d'analyse avec un standard de silice. Le traitement des spectres a été réalisé en utilisant le programme Peakfit[©].

La température maximale (T_{max}) obtenue par RSCM sur les métasédiments des Schistes lustrés du Queyras correspond à la température maximale associée à la mise en place des unités durant le processus de subduction. Notre étude montre une évolution des T_{max} d'Ouest en Est depuis 340°C jusqu'à 498°C (Fig. 4.30). Ces données thermiques sont cohérentes avec le découpage métamorphique de la zone d'étude proposée par Tricart et al. (2004). L'unité Schistes bleus de basse température présente des T_{max} inférieures à 340°C. L'unité Schistes bleus de moyenne-température présente des T_{max} de 356 à 373°C. L'unité Schistes bleus de HT présente des T_{max} de 402 à 463°C. Enfin, l'unité éclogitique du Viso a enregistré une T_{max} supérieure à 475°C compatible avec les données de Angiboust et al. (2011).

sample	Long. (N)	Lat. (E)	n	R2 mean	Std	Tmax (°C) mean	1 σ
Queyras Schistes lustrés Low-Temperature Blueschist							
1	44.7578	6.7918	10	0.694	0.019	332.3	8.33
2	44.7109	6.8138	10	0.703	0.024	328.3	10.47
3	44.7526	6.8320	10	0.707	0.021	326.5	9.55
4	44.7255	6.8432	9	0.722	0.021	319.6	9.28
5	44.6801	6.8702	13	0.675	0.036	340.5	15.95
6	44.7848	6.8784	14	0.686	0.017	335.9	7.44
7	44.8904	6.7233	9	0.700	0.020	330.0	6.70
8	44.6413	6.8942	8	0.707	0.026	326.7	11.88
9	44.6738	6.9405	10	0.683	0.020	337.5	8.94
Queyras Schistes lustrés Medium-Temperature Blueschist							
10	44.6753	6.9906	11	0.641	0.027	355.9	11.94
11	44.6443	6.9929	12	0.616	0.036	367.5	4.45
12	44.7013	7.0048	11	0.602	0.027	373.1	12.05
13	44.7410	7.0288	11	0.622	0.015	364.3	6.45
14	44.7783	6.9783	7	0.615	0.035	367.5	15.57
16	44.7389	6.9679	13	0.673	0.032	341.3	14.39
Queyras Schistes lustrés High-Temperature Blueschist							
15	44.8147	7.0288	11	0.537	0.052	401.9	23.16
17	44.7586	7.0343	6	0.566	0.079	388.9	22.58
18	44.7350	7.0310	11	0.581	0.022	382.6	9.87
19	44.7117	7.0705	10	0.439	0.028	445.5	12.44
20	44.7010	7.0996	12	0.400	0.022	462.8	9.67
21	44.6881	7.1162	10	0.386	0.044	469.1	19.78
Monviso Eclogite							
22	44.6426	7.1771	6	0.332	0.036	493.3	16.00
23	44.6704	7.1687	11	0.321	0.020	498.2	9.10
24	44.6939	7.1549	12	0.273	0.037	519.5	16.35
25	44.5953	7.1467	10	0.371	0.033	475.9	14.00

TABLE 4.6 – Liste des échantillons et résultats obtenus en utilisant la spectrométrie Raman sur la matière carbonnée. La T_{max} a été calculée en utilisant la calibration de [Beyssac et al. \(2002\)](#). La dispersion importante observée, supérieure à 7°C, provient du fait que les analyses ont été acquises sur des fragments de roches avec plus de 70% de matière carbonnée et non sur des lames minces polies à travers un minéral transparent.

4.3.3 Zone MT-BS : Affleurement du Gouret

L’affleurement du Gouret est situé dans la vallée du Guil (rive droite) entre les communes d’Aiguilles et d’Abriès (noté G sur la Fig. 4.30) au niveau du Pont du Camping du Gouret. Dans les talwegs orientés N-S, sont visibles les plis *P1* couchés à vergence N ou S associés à une schistosité *S1* (Fig. 4.31). Dans la falaise orientée E-W, on distingue la schistosité principale *S2* qui est pentée vers l’Ouest et qui est plissée par des plis *P3* avec localement une schistosité de crénulation *S3* indiquant une vergence Ouest (Fig. 4.31). Ces plis présentent une forte dispersion de leurs axes qui résulte de charnières à axes courbes symptomatiques d’une forte composante en aplatissement, en plus de l’étirement E-W (voir Caron 1974, Schwartz 2000, Fig. 4-7-b et Fig. 4-8).

Deux échantillons de métapélites alumineuses ont été prélevés sur cet affleurement, le premier au niveau des anciens plis *P1* (*PL10-G-S1*) et le second dans la schistosité principale *P2* (*PL10-G-S2*). Des lames minces ont été découpées dans l’échantillon en préservant l’orientation originale mesurée sur le terrain. Puis un fragment de chaque échantillon a été broyé afin d’extraire par tri sous une loupe binoculaire les grains de phengites pour datation. Cette technique permet de sélectionner les grains appartenant à une seule schistosité. Pour cet affleurement, nous allons présenter uniquement l’échantillon de la *S2*, car comme nous le verront dans la partie sur les âges (Part. 4.3.5) les phengites de la schistosité *S1* ont recristallisé durant l’épisode de déformation *D2*.

L’échantillon *PL10-G-S2* a été analysé à la microsonde au Laboratoire Magmas et Volcans de l’Institut de Physique du Globe de Clermont-Ferrand en utilisant une CAMECA SX50 avec quatre spectromètres. Les conditions d’analyse étaient de 15 keV, 100 nA et 300 ms pour la cartographie et de 15 keV, 10 nA et 20 + 10 s pour les analyses ponctuelles. Les données brutes ont été traitées avec le logiciel XMAPTOOLS (Chap. 3). Les différentes phases minérales ont été identifiées grâce aux images chimiques, puis chaque pixel de l’image a été attribué à l’une de ces phases en utilisant une approche statistique. Ensuite, les cartes d’intensités mesurées à la microsonde ont été transformées en cartes de concentrations (pourcentages de poids d’oxydes), puis en cartes de formules structurales (p.f.u.) en utilisant les fonctions disponibles

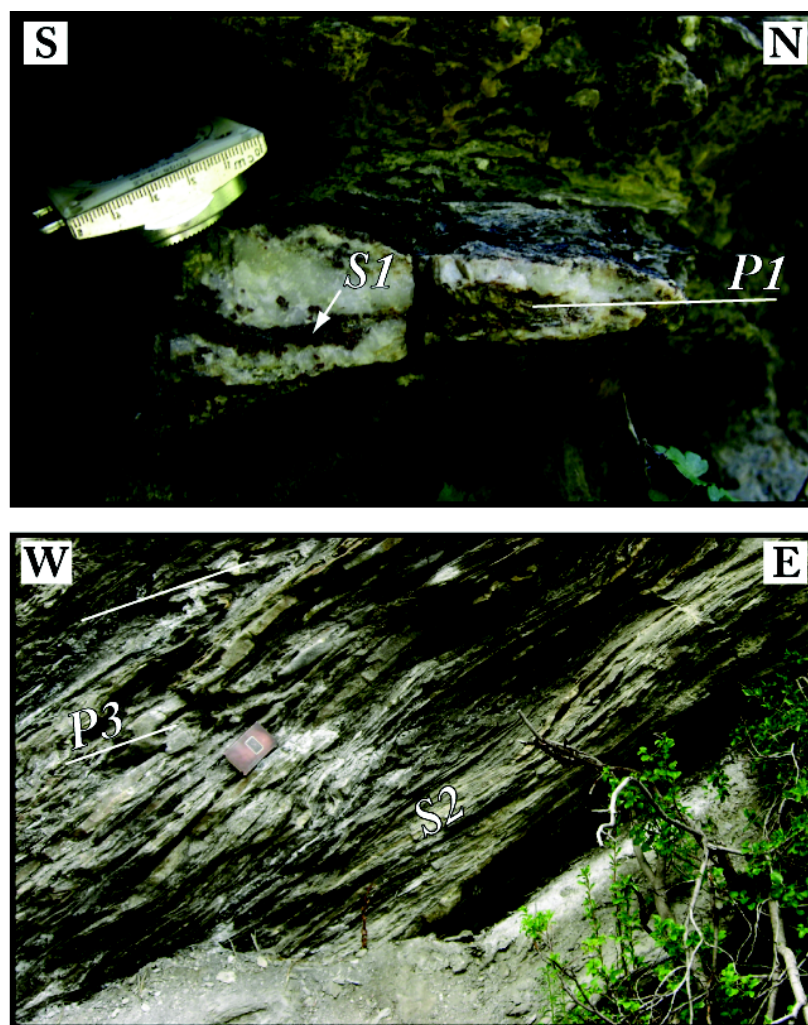


FIGURE 4.31 – Photos des deux générations de plis observés à l’affleurement du Gouret. Photo du haut : pli P1 et schistosité S1. Photo du bas : Schistosité S2 et plis P3.

dans le logiciel. L’étude chimique des différents minéraux a été réalisée en utilisant le module TriPlot3D.

4.3.3.1 Etude minéralogique

L’échantillon PL10-G-S2 est constitué d’une unique paragenèse à chlorite, phengite et quartz (Fig. 4.32) avec, par endroits, des zones riches en calcite (non visibles sur la Fig. 4.32). Deux orientations minérales ont été détectées dans les grains de phengites et de chlorites, l’une principale qui correspond à la S2 décrite précédemment (pentée vers l’Ouest, c.f. Fig. 4.32) et l’autre plus ancienne, notée S1, orientée perpendiculairement à S2 (Fig. 4.32-c).

Les compositions de tous les pixels de chlorites ont été reportées dans un dia-

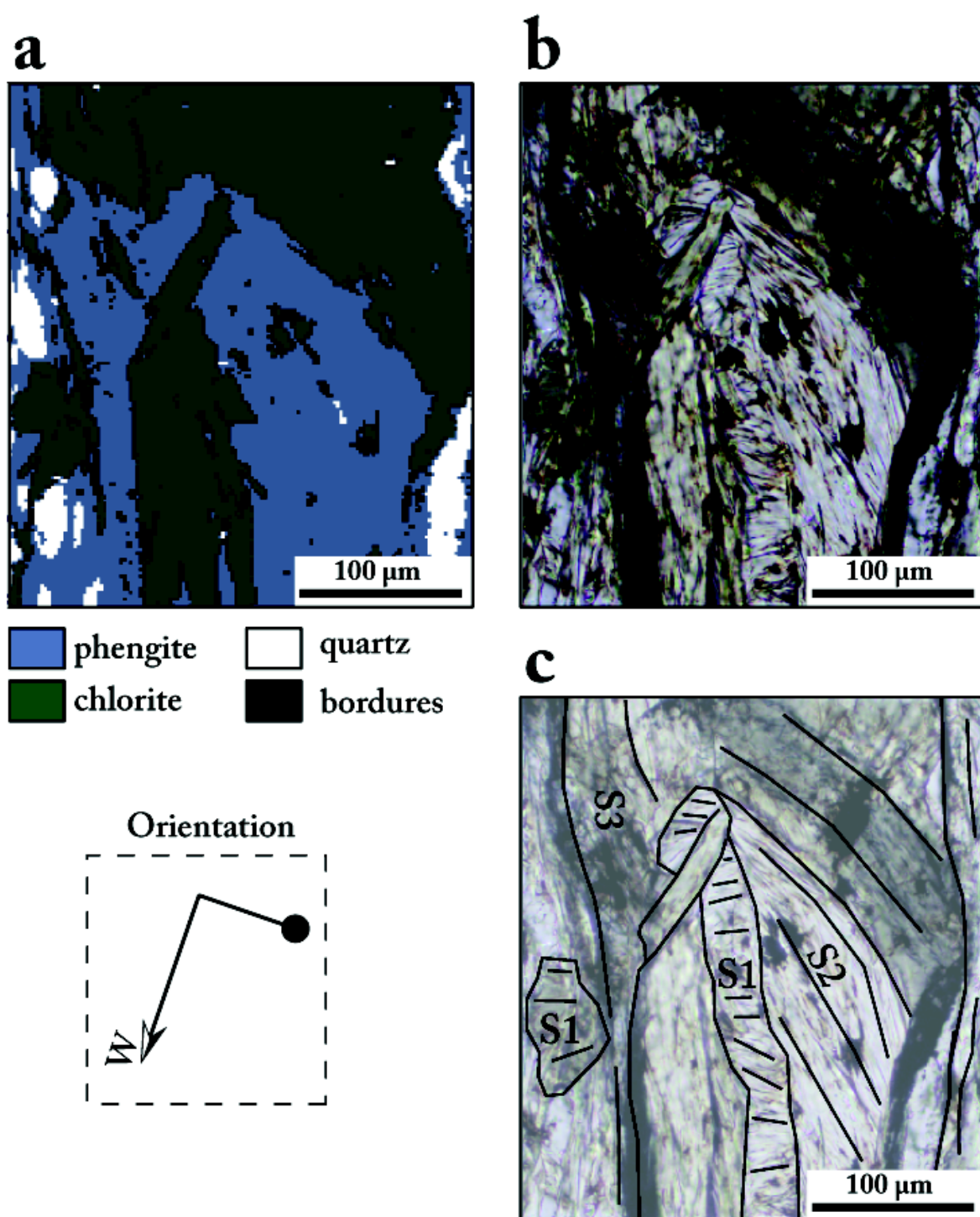


FIGURE 4.32 – Zone de la lame mince de l'échantillon PL10-G-S2 (Gouret) étudiée à la microsonde. (a) Image des différentes phases minérales générées avec XMAPTOOLS. Un groupe "bordures" a été utilisé pour classifier les pixels qui résultent d'un mélange entre une composition de chlorite et une de phengite. (b) Photographie de la zone cartographiée en lumière polarisée non analysée. (c) Schéma avec les différentes schistosités S1, S2 et S3.

gramme triangulaire *ame*, *clin* + *daph*, *sud* en utilisant un $XFe^{3+} = 0.1$ qui est la proportion minimum de Fe^{3+} nécessaire au calcul de la formule structurale. La composition des chlorites est relativement homogène avec une composition moyenne ame_{42} ($clin+daph$)₄₂ et sud_{16} (Fig. 4.33-a). La faible dispersion est due aux variations des valeurs de XMg ($XMg = Mg/(Mg + Fe^{2+})$) entre 0.34 pour le grain aligné dans la S1 et 0.28 pour ceux appartenant à la S2 (Fig. 4.33-b).

Les compositions de tous les pixels de phengites ont été reportées dans un diagramme triangulaire *mus*, *celn* *prl* (Fig. 4.33-c). À l'inverse des chlorites, les compositions des phengites ne sont pas homogènes et ont été divisées en trois groupes, notés M1, M2 et M3 sur la figure 4.33-c, sur le critère de la teneur en X_{cel} et X_{mus} . Les pixels correspondant aux différentes sélections ont été affichés sur une carte en utilisant le même code couleur (Fig. 4.33-d). Les compositions notées M1, les plus riches en X_{cel} , sont localisées au coeur des différents grains de phengite orientés selon la S1 ou la S2 (Fig. 4.32-c et Fig. 4.33-d). Les compositions notées M2 sont localisées en bordure de ces grains. Les compositions notées M3, les plus riches en X_{mus} , sont situées à la limite entre les différents grains et dans les grains appartenant à la S3 (Fig. 4.32-c).

4.3.3.2 Etude thermobarométrique

La température moyenne du groupe C1 a été estimée à $334 \pm 50^\circ\text{C}$ en utilisant les compositions d'une sélection de chlorites et la méthode chl+qtz+H₂O de Vidal et al. (2006). Cette température a été calculée à 7 kbar pour un pourcentage de Fe^{3+} minimum de 12% prédit, en accord avec la quantité minimale de 10% estimée précédemment. La température des chlorites riches en Mg et des chlorites plus riches en Fe ne sont pas distinguables. Afin de vérifier ce résultat, une carte de température a été calculée en utilisant la calibration que nous avons proposé dans l'article de Lanari et al. (Chap. 2) avec en 10% de Fe^{3+} qui est la quantité minimum requise pour calculer une formule structurale. La température moyenne des chlorites est dans ce cas de $332 \pm 50^\circ\text{C}$ (Fig. 4.34-c) en accord avec les résultats du thermomètre de Vidal et al. (2006). Les températures estimées sont comprises entre 300°C et 350°C.

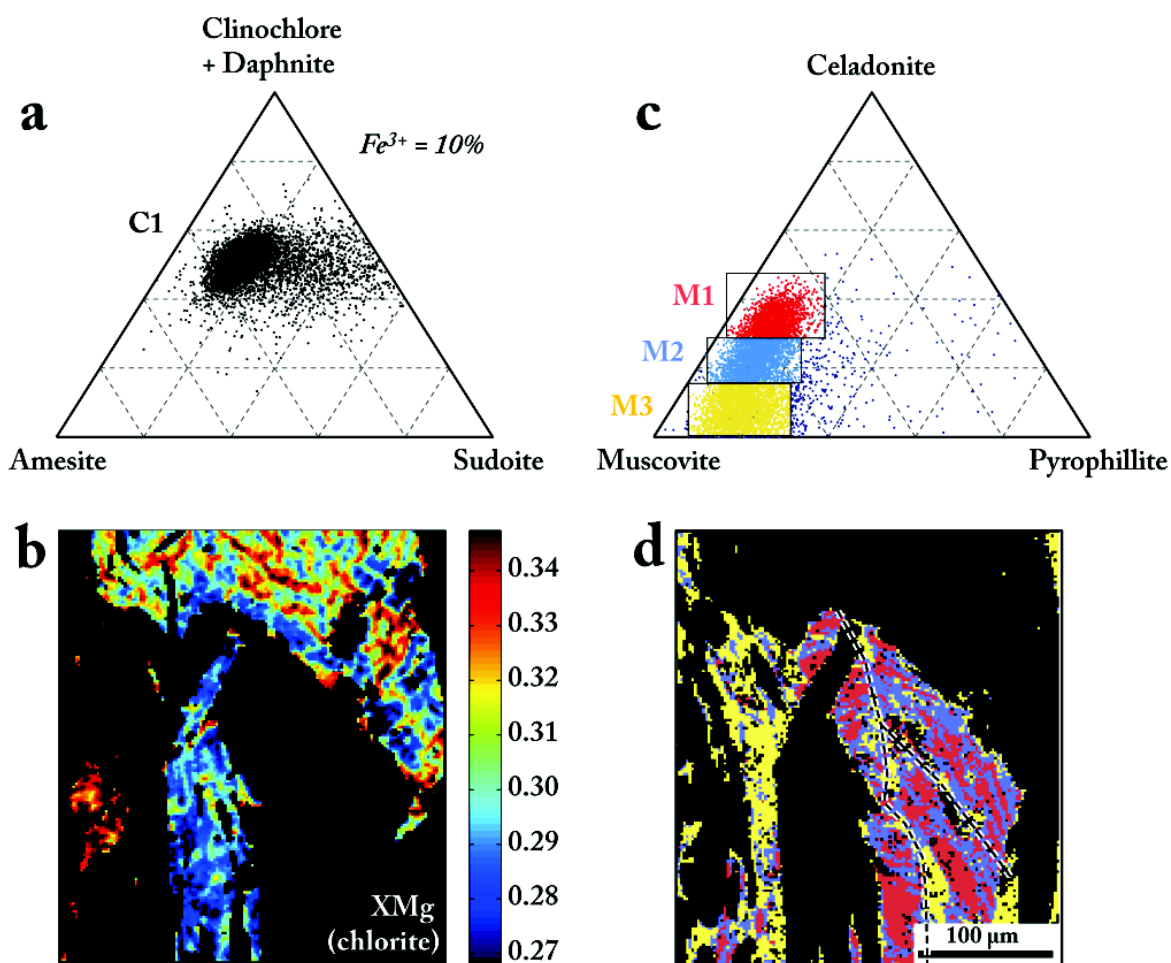


FIGURE 4.33 – Étude chimique des chlorites et des micas de l'échantillon PL10-G-S2 (Gouret). Tous les pixels de l'image chimique ont été reportés dans des diagrammes triangulaires en utilisant le module TriPlot3D de XMAPTOOLS. (a) Diagramme triangulaire ames, clin + daph, sud pour les chlorites. Les formules structurales ont été calculées avec 10% de Fe^{3+} . Un seul groupe de chlorites a été identifié (en noir). La température moyenne de ce groupe calculée avec la méthode $\text{chl} + \text{qtz} + \text{H}_2\text{O}$ de Vidal *et al.* (2006) est de $334 \pm 50^\circ\text{C}$ (voir texte). (b) Carte du XMg ($\text{XMg} = \text{Mg} / (\text{Mg} + \text{Fe}^{2+})$) dans les chlorites. (c) Diagramme triangulaire mus, cel, prl pour les phengites. Trois groupes de phengites ont été distingués en fonction de la teneur en cel (rouge, jaune, bleu). Les pixels correspondant ont été reportés sur la carte en (d). Les lignes en pointillés marquent les limites entre les différents grains de phengites identifiés en utilisant l'image en lumière polarisée non analysée (Fig. 4.32).

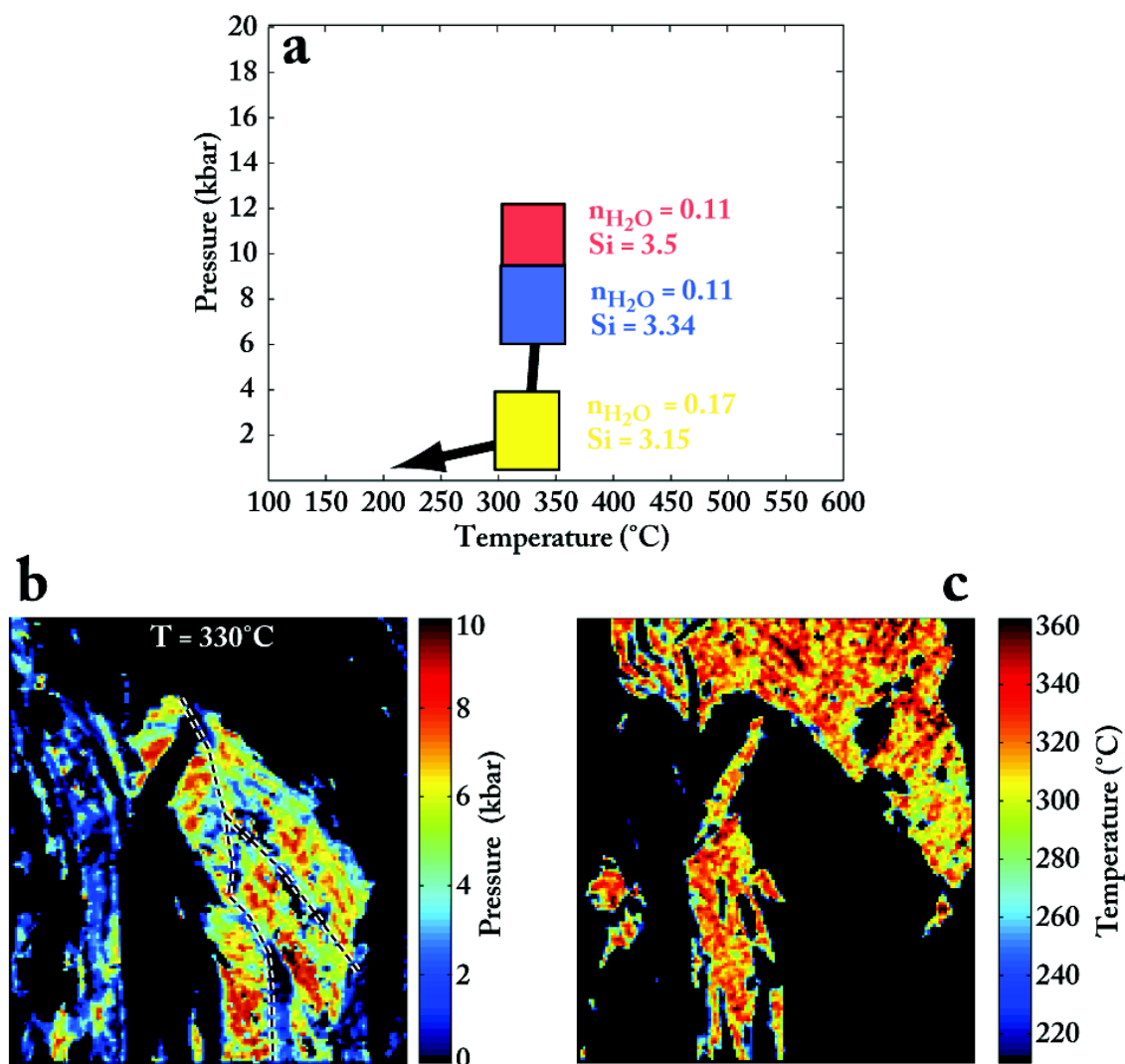


FIGURE 4.34 – Reconstruction du trajet P-T pour l'échantillon Gouret. (a) Chemin P-T. Les différentes boîtes correspondent aux différents événements de croissance des phengites. Pour chaque cas, la composition moyenne en Si (p.f.u.) est fournie ainsi que la quantité d'eau interfoliaire prédite par le modèle $\text{phg} + \text{qtz} + \text{H}_2\text{O}$ de Dubacq et al. (2010). (b) Carte de la pression de cristallisation des phengites calculées à la température de 330°C, tirée de l'étude des chlorites. (c) Carte des températures de chlorites estimées en utilisant la calibration de Lanari et al. (Chap 2) pour 10% de Fe^{3+}

Comme la température enregistrée dans les chlorites ne varie pas, la pression de chaque composition de phengite a été estimée en utilisant la position de l'équilibre $\text{chl} + \text{qtz} + \text{H}_2\text{O}$ à une température de 330°C . La carte des pressions de phengites est reportée sur la figure 4.34-b. Les phengites du groupe M1 cristallisent à $10,1 \pm 2,5 \text{ kbar}$ et ont une valeur moyenne de $\text{Si}^{4+} = 3,50 \text{ p.f.u.}$ La quantité d'eau en position interfoliaire dans les phengites prédite avec le modèle de Dubacq et al. (2010) est $n\text{H}_2\text{O} = 0,11 \text{ p.f.u.}$ (Fig. 4.34-a). Pour le groupe M2 les phengites cristallisent à $7,7 \pm 2,5 \text{ kbar}$ pour une valeur moyenne de $\text{Si}^{4+} = 3,34 \text{ p.f.u.}$ et pour la même quantité d'eau interfoliaire prédite $n\text{H}_2\text{O} = 0,11 \text{ p.f.u.}$ (Fig. 4.34-a). Enfin, les phengites du groupe M3 cristallisent à $2,4 \pm 2,4 \text{ kbar}$ pour une valeur moyenne de $\text{Si}^{4+} = 3,15 \text{ p.f.u.}$ plus faible, mais une quantité d'eau interfoliaire prédite plus importante $n\text{H}_2\text{O} = 0,17 \text{ p.f.u.}$ (Fig. 4.34-a).

Les conditions de pression enregistrées par les phengites sont cohérentes avec les variations de chimie mises en évidence précédemment. Les phengites orientées perpendiculairement à la S2 et celles dans la S2, montrent exactement la même tendance, avec un coeur HP et une diminution de la pression vers les bordures. Ce résultat montre que les phengites alignées perpendiculairement à la S2 ont été entièrement recristallisées durant l'épisode D2 tout en préservant cette orientation initiale. Comme les phengites de la schistosité S2 sont principalement composées des deux groupes chimiques M1 et M2 (Fig. 4.34-d), la phase D2 correspond au début de l'exhumation avec une diminution de la pression de $10,1 \pm 2,5$ à $7,7 \pm 2,5 \text{ kbar}$ pour une température de $334 \pm 50^\circ\text{C}$. Les phengites du dernier groupe M3 cristallisent à $325 \pm 50^\circ\text{C}$ et $2,4 \pm 2,4 \text{ kbar}$ qui sont des conditions typiques de la transition ductile/fragile. Ces conditions sont associées à la phase D3 identifiée sur le terrain et en lame mince (Fig. 4.32-c). En utilisant les résultats des trois groupes de phengites et la température moyenne des chlorites, un trajet P-T synthétique a été reporté sur la figure 4.34.

4.3.4 Zone HT-BS : Arkose de Roca Nera

L'affleurement de l'arkose de Roca Nera étudié se situe sur le versant italien du Col Agnel, entre le sommet du col et le village de Chianale (noté A sur la Fig. 4.30). Comme à l'affleurement du Gouret, on distingue des plis couchés *P1* à vergence N et une schistosité principale *S2* globalement pentée vers l'Ouest. Localement, les plis *P3* ne sont pas visibles. À l'échelle pluri-centimétrique, les niveaux les plus grossiers d'arkose sont boudinés avec l'apparition, entre deux boudins, de veines à chlorite + calcite + quartz (Fig. 4 de Schwartz et al. 2009). Cet épisode de double boudinage est l'expression d'un épisode extensif qui intervient dans le faciès des Schistes verts à la transition fragile/ductile, durant la collision (Schwartz et al. 2009).

Deux échantillons ont été prélevés sur cet affleurement, le premier au niveau des anciens plis *P1* (*PL10-A-S1*) et le second dans la schistosité principale *P2* pentée vers l'Ouest (*PL10-A-S2*). Des lames minces ont été découpées dans les échantillons en notant les orientations originales. Puis, pour chaque échantillon, un fragment a été broyé et les phengites ont été triées à la main sous une loupe binoculaire.

L'échantillon *PL10-A-S1* a été analysé au Laboratoire Magmas et Volcans de l'Institut de Physique du Globe de Clermont-Ferrand en utilisant une microsonde CAMECA SX50 avec quatre spectromètres. Les conditions d'analyses étaient de 15 keV, 10 nA et 20 + 10 s. Une série d'analyses ponctuelles de chlorite et de mica ont été acquises afin d'estimer les conditions P-T de la phase D1. Dans les coeurs de plis *P1*, on trouve une paragenèse à chlorite + mica + paragonite préservée. Les conditions P-T ont été estimées en utilisant des analyses ponctuelles et les équilibres chl + qtz + H₂O et phg + qtz + H₂O (Vidal et al. 2006, Dubacq et al. 2010). Nous avons pu estimer une condition moyenne P-T à 289 ± 50°C et 9,95 ± 2,5 kbar (travail en cours). L'acquisition d'images chimiques sur cet échantillon serait nécessaire afin de distinguer d'éventuelles zonations et donc un trajet P-T prograde (c.f âges, Part. 4.3.5).

L'échantillon *PL10-A-S2* a été analysé à l'Institute of Earth and Environmental Science de l'Université de Postdam en utilisant une JEOL JXA-8200 avec cinq

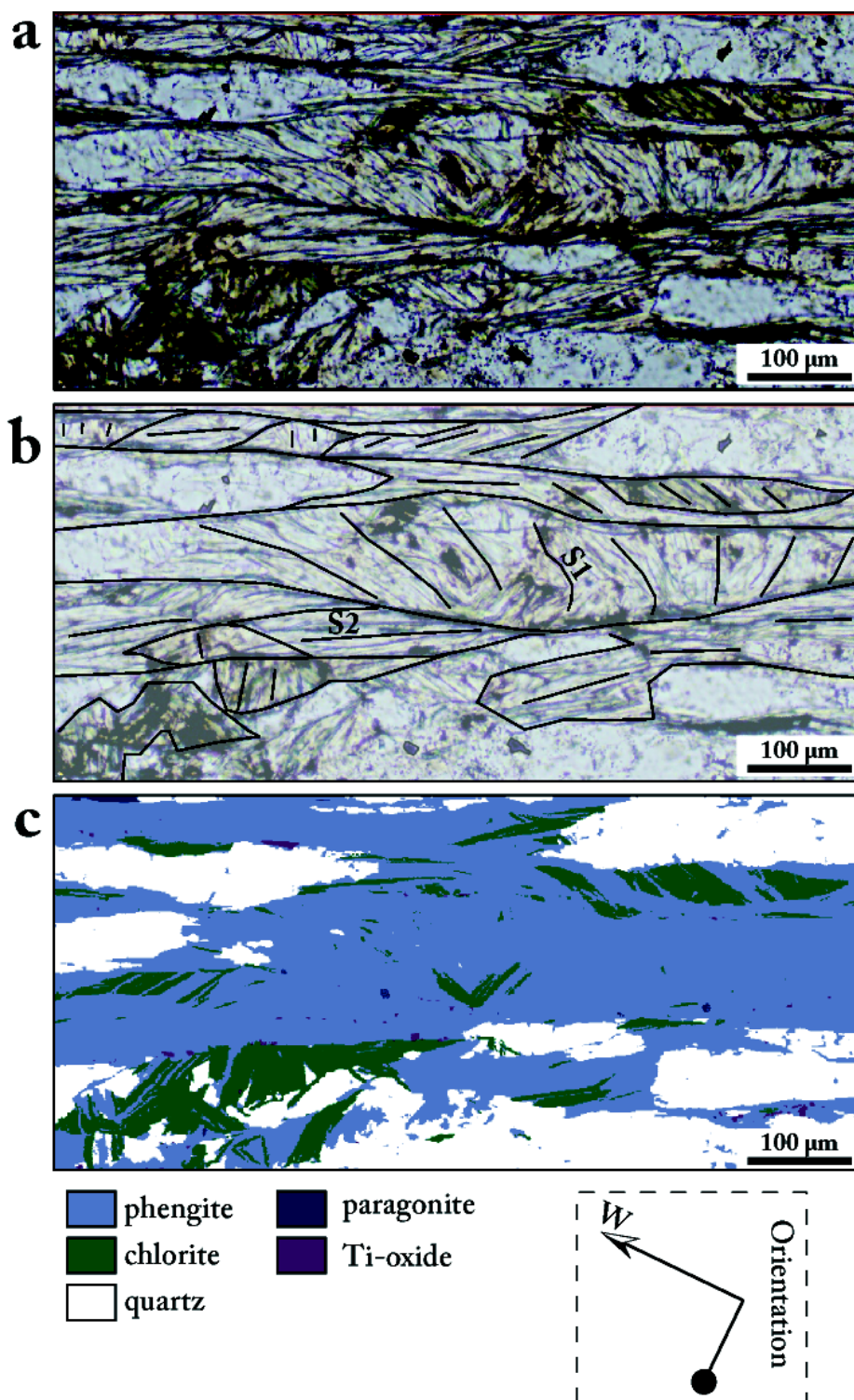


FIGURE 4.35 – Zone de la lame mince de l'échantillon PL10-A-S2 (Arkose de Roca Nera) étudiée à la microsonde. (a) Photographie de la zone cartographiée en lumière polarisée non analysée. (b) Schéma avec les différentes schistosités. (c) Image des différentes phases minérales générée avec XMapTools.

spectromètres. Les conditions d'analyses étaient de 15 keV, 100 nA et 300 ms pour la cartographie et de 15 keV, 10 nA et 20 + 10 s pour les analyses ponctuelles. Les données brutes ont été traitées avec le logiciel XMAPTOOLS (Chap. 3). Les différentes phases minérales ont été identifiées grâce aux images chimiques, puis chaque pixel de l'image a été attribué à l'une de ses phases en utilisant une approche statistique. Les données brutes ont été transformées en cartes de concentrations (pourcentages de poids d'oxydes), puis en cartes de formules structurales (p.f.u.) en utilisant les fonctions disponibles dans le logiciel. L'étude chimique des différents minéraux a été réalisée en utilisant le module TriPlot3D.

4.3.4.1 Etude Minéralogique

L'échantillon PL10-A-S2 présente une paragenèse à chlorite + phengite + quartz \pm paragonite \pm oxyde de titane (Fig. 4.35). Il est constitué d'alternance de lits à phyllosilicates et de quartz. Deux orientations minérales ont été détectées dans les phengites, l'une marquant la schistosité principale S2 et une autre orientation notée S1, perpendiculaire à S2 (Fig. 4.35).

Les compositions des pixels de chlorites ont été reportées dans un diagramme triangulaire *ame*, *clin* + *daph*, *sud*. Deux groupes de compositions notés C1 et C2 ont été distingués en fonction de la teneur en X_{ames} (Fig. 4.36-a). La fraction de X_{sud} reste constante dans les deux groupes à environ $0,1 \pm 0,05$. La large dispersion observée indique que les deux groupes de chlorites n'ont probablement pas les mêmes proportions de Fe^{3+} . Les pixels correspondant aux différents groupes chimiques ont été reportés sur la figure 4.36-c. On voit que les chlorites C1 présentent plusieurs orientations parallèles ou perpendiculaires à S2, mais semblent généralement associées à la S2, les chlorites C2 étant plus tardives.

Les compositions des pixels de phengites ont été reportées dans un diagramme triangulaire *mus*, *cel*, *prl* (Fig. 4.36-b). Deux groupes de compositions M1 et M2 ont été identifiés, basés sur la teneur en X_{mus} et en X_{cel} . Les pixels correspondant à ces deux groupes chimiques ont été représentés sur la figure 4.36-c. Les phengites M1, les plus enrichies en *cel* sont alignées dans la S1 et semblent à l'équilibre localement

avec les chlorites C1. À l'inverse les phengites M2 plus riches en X_{mus} sont situées dans les grains perpendiculaires à la S2.

4.3.4.2 Circulation fluide et recristallisation tardive

Les phengites notées M2 sur la figure 4.36 sont orientées perpendiculairement à la S2 et semblent donc plus anciennes. Cependant, si l'on considère la teneur en *cel* et donc la quantité de *Si*, elles semblent cristalliser à des pressions plus faibles et donc plus tardivement dans le cas d'un trajet rétrograde. Une carte du Na (unité p.f.u.) dans les phengites est disponible figure 4.37. Les phengites orientées perpendiculairement à la S2 (notées M2 précédemment) ont des teneur en Na plus importantes que les phengites qui marquent la S2. Comme le Na est localisé à la limite des grains, il peut provenir de la circulation de fluides enrichis qui favorisent la recristallisation de phengites précoces. Les zones riches en Na correspondent aux zones de circulations de fluides qui pourraient intervenir lors d'un épisode de double boudinage comme cela a été décrit par [Schwartz et al. \(2009\)](#). Les anciennes phengites associées à S1 ont donc été entièrement recristallisées tardivement. Il est nécessaire, pour valider cette hypothèse, de comparer les conditions de cristallisation prédites pour ces phengites M2 avec les conditions obtenues par [Schwartz et al. \(2009\)](#) pour l'épisode de double boudinage.

4.3.4.3 Etude thermobarométrique

Les températures moyennes des groupes C1 et C2 ont été estimées en utilisant la méthode chl + qtz + H_2O de [Vidal et al. \(2006\)](#) sur une sélection d'analyses réalisées sur la carte. Les températures calculées sont $419 \pm 50^\circ\text{C}$ pour le groupe C1 et $363 \pm 50^\circ\text{C}$ pour le groupe C2 avec des proportions de Fe^{3+} respectivement de 4% et 20%.

La pression des phengites a été estimée pour les températures des deux groupes de chlorites en utilisant les équilibres phg + qtz + H_2O calculés avec la calibration de [Dubacq et al. \(2010\)](#). Les zones correspondant aux équilibres phg + qtz + H_2O des sélections de phengites M1 et M2 ont été reportées sur la figure 4.38. La pression moyenne des phengites M1 estimée pour une température de $419 \pm 50^\circ\text{C}$ est de $15,4 \pm 2,5 \text{ kbar}$ et la quantité d'eau interfoliaire $nH_2O = 0,12$. La pression

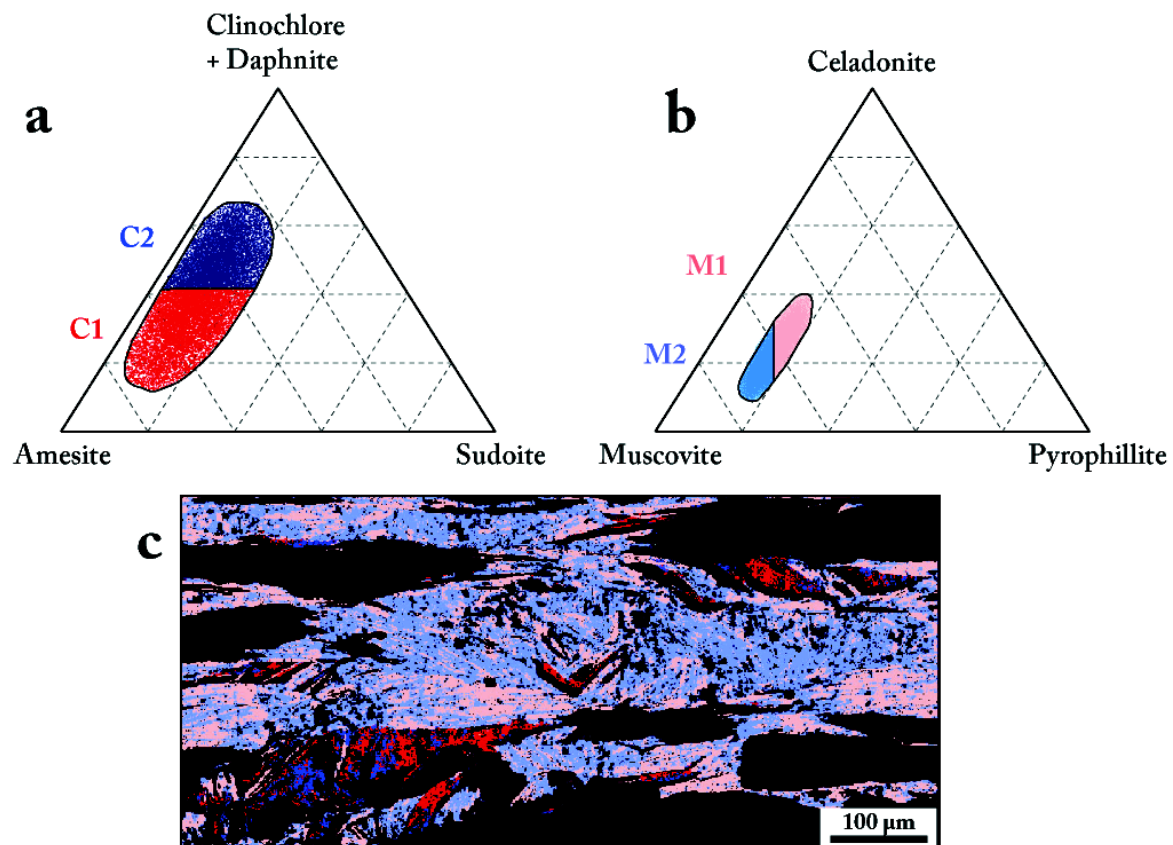


FIGURE 4.36 – Étude chimique des chlorites et des micas de l'échantillon PL10-A-S2 (Arkose de Roca Nera). Après une série de filtres, tous les pixels de l'image chimique ont été reportés dans des diagrammes triangulaires en utilisant le module `TriPlot3D` de `XMAPTOOLS`. (a) Diagramme triangulaire ames, clin + daph, sud pour les chlorites. Deux groupes de chlorites C1 et C2 ont été distingués en fonction de la teneur en X_{ames} . La température moyenne de ses groupe calculée avec la méthode chl+qtz+H₂O de Vidal et al. (2006) est de $412 \pm 50^\circ\text{C}$ pour C1 et $343 \pm 50^\circ\text{C}$ pour C2 (voir texte). (b) Diagramme triangulaire mus, cel, prl pour les phengites. Deux groupes de phengites M1 et M2 ont été distingués en fonction de la teneur en cel (rouge, bleu). (d) Carte des différents groupes de chlorites et de phengites. Les couleurs utilisées sont les mêmes que pour les figures (a) et (b).

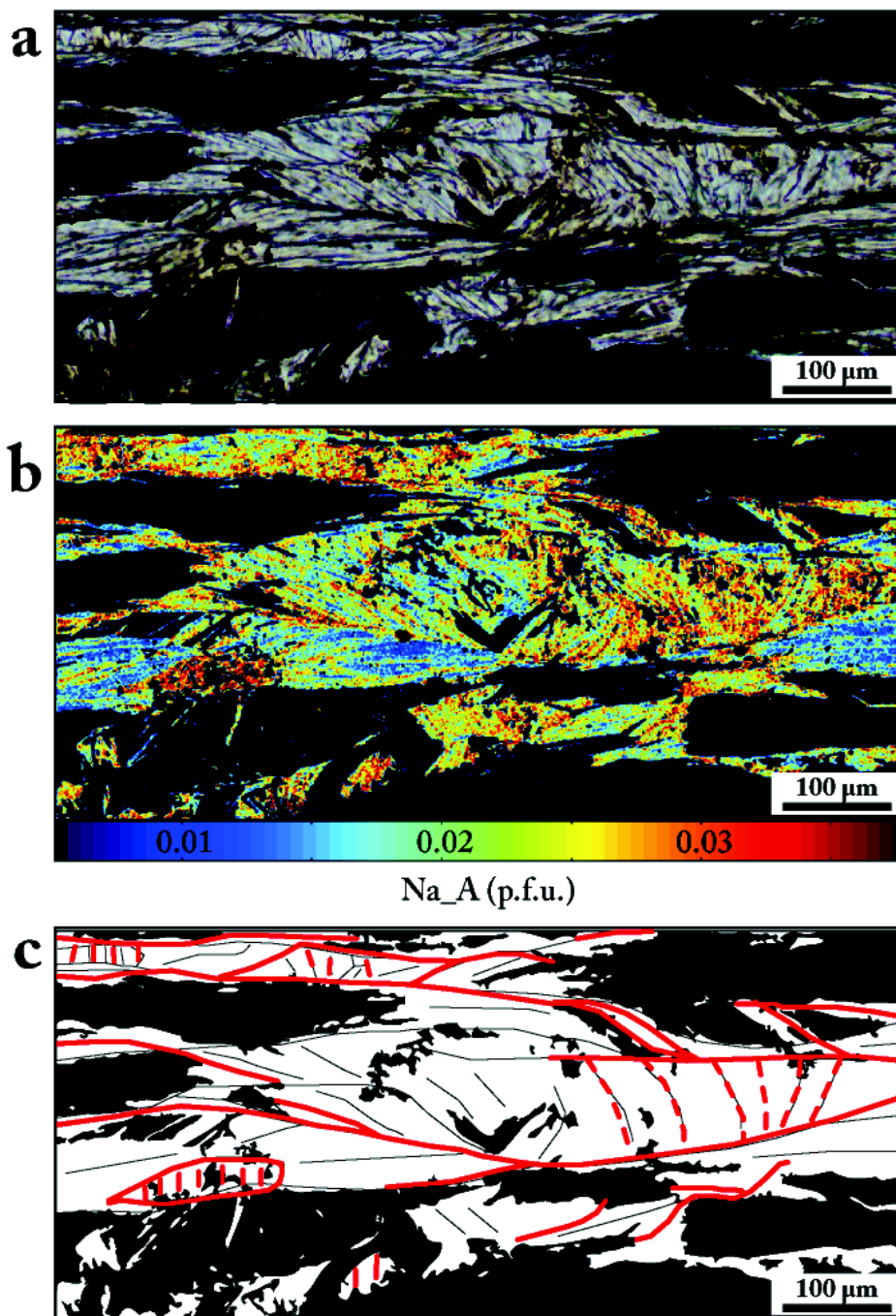


FIGURE 4.37 – (a) Photographie des phengites en lumière polarisée non analysée avec un filtre noir qui masque les autres minéraux. (b) Carte du Na dans les phengites (p.f.u.). Dans ce cas, le Na est utilisé comme traceur des fluides tardifs qui permettent une recrystallisation des phengites à la transition ductile/fragile. (c) Schéma de circulation des fluides (traits rouges). Ces circulations sont localisées à la limite entre les grains. Les traits en pointillés montrent les zones où la recrystallisation est maximale, en raison de l'extension associée à l'épisode de double boudinage.

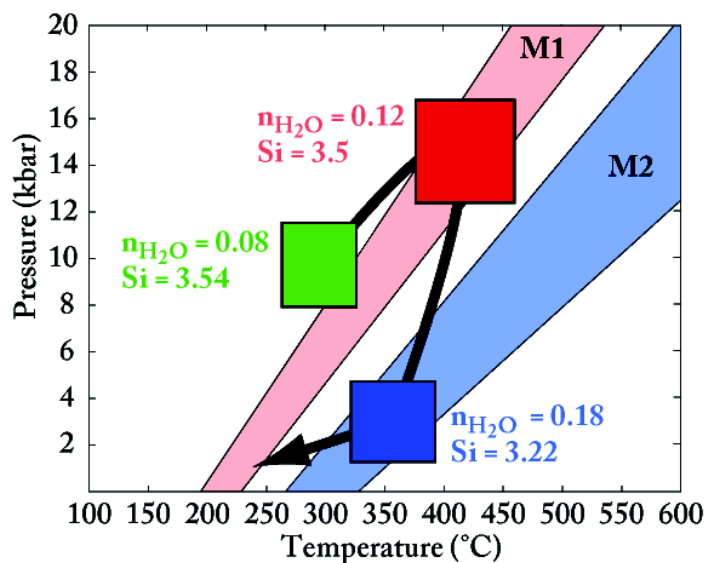


FIGURE 4.38 – Trajet P-T complet enregistré par l'unité de l'arkose de Roca Nera dans les Schistes lustrés. Le cadre vert correspond à l'estimation P-T réalisée pour l'échantillon PL10-A-S1. Les cadres rouges et bleus (ainsi que les équilibres chl + qtz + H₂O) correspondent aux estimations réalisées pour l'échantillon PL10-A-S2. Les zones claires (rouges et bleues) correspondent aux équilibres phg + qtz + H₂O (voir texte).

moyenne des phengites M2 estimée pour une température de $363 \pm 50^\circ\text{C}$ est de $3,1 \pm 2,5 \text{ kbar}$ et $n\text{H}_2\text{O} = 0,18$. Ces résultats sont en accord avec la diminution de la quantité moyenne de Si dans les phengites de 3,5 p.f.u. pour M1 à 3,22 p.f.u. pour M2. L'augmentation de $n\text{H}_2\text{O}$ prédite dans les phengites M2 est associée à l'augmentation du Na mesurée précédemment. Ces deux résultats sont cohérents avec des circulations tardives de fluides hydrothermaux durant un épisode extensif.

Un trajet P-T synthétique est reporté figure 4.38. Il a été construit en combinant les estimations des échantillons PL10-A-S1 et PL10-A-S2. Les chlorites et les phengites de la schistosité S1 préservée dans les plis P1 ont enregistré la phase prograde du métamorphisme HP/BT avec des conditions à $285 \pm 50^\circ\text{C}$ et $9,95 \pm 2,5 \text{ kbar}$ correspondant à un gradient géothermique froid de $10^\circ\text{C}/\text{km}$. Le pic de pression à $419 \pm 50^\circ\text{C}$ et $15,40 \pm 2,5 \text{ kbar}$ est enregistré par les phengites qui marquent la schistosité S2, associée au début de l'exhumation (diminution progressive du Si du coeur vers la bordure). Cet épisode dans le faciès des Schistes bleus correspond toujours à un gradient géothermique froid de $8^\circ\text{C}/\text{km}$ ce qui montre que le gradient

géothermique reste stable entre ces deux événements. Le dernier épisode enregistré par les phengites et les chlorites est associé à une importante circulation de fluides, qui a entraîné la recristallisation des phengites et des chlorites orientées perpendiculairement à la *S2* lors d'un épisode extensif à la transition fragile/ductile dans le faciès des Schistes vert, à $363 \pm 50^\circ\text{C}$ et $3,10 \pm 2,5 \text{ kbar}$. Ces conditions plus tardives correspondent à un gradient géothermique beaucoup plus chaud de $37^\circ\text{C}/\text{km}$, typique d'un gradient de collision. Cette dernière estimation P-T est en accord avec celles réalisées par [Schwartz et al. \(2009\)](#), en utilisant les températures des chlorites contenues dans les veines de quartz et la technique des inclusions fluides. On peut donc ici relier la phase *D3* à la phase de double boudinage qui, d'après [Schwartz et al. \(2009\)](#), intervient tardivement après 27 *Ma*. Cet âge post 30 *Ma* est cohérent avec le gradient géothermique chaud enregistré. Cette phase *D3* intervient avant l'épisode de basculement dû à la mise en place du dôme de Dora-Maira sous l'effet de l'indentation du corps d'Ivrea (e.g. [Schwartz et al. 2009](#)).

4.3.5 Nouvelles données radiochronologiques

La procédure utilisée pour préparer et dater les grains de phengites des échantillons *PL10-G-S1*, *PL10-G-S2*, *PL10-A-S1* et *PL10-A-S2* est la même que celle décrite dans l'article de Lanari et al. (Part. 4.2.4) sur le « granite de Plan-de-Phasy ». Les spectre $^{40}\text{Ar}/^{39}\text{Ar}$ ainsi que des trajets P-T-t sont reportés sur la figure 4.39 pour les affleurements du Gouret et de l'Arkose de Roca Nera. Comme les températures de cristallisation des phengites caractérisées précédemment sont toutes inférieures à 420°C , tous les âges $^{40}\text{Ar}/^{39}\text{Ar}$ obtenus sont considérés comme des âges de cristallisation et non pas comme des âges de refroidissement.

4.3.5.1 Affleurement du Gouret - zone MT-BS

Schistosité ancienne *S1* Un grain de phengite de l'échantillon *PL10-G-S1*, prélevé dans un pli *P1* associé à une tectonique de vergence N a été daté. Le spectre $^{40}\text{Ar}/^{39}\text{Ar}$ montre un plateau avec un âge calculé à $40,51 \pm 2,29 \text{ Ma}$ (Fig. 4.39-a).

Schistosité principale *S2* Deux grains de phengites de l'échantillon *PL10-G-S2*, prélevés dans la foliation principale ont été datés. Les spectres $^{40}\text{Ar}/^{39}\text{Ar}$ montrent

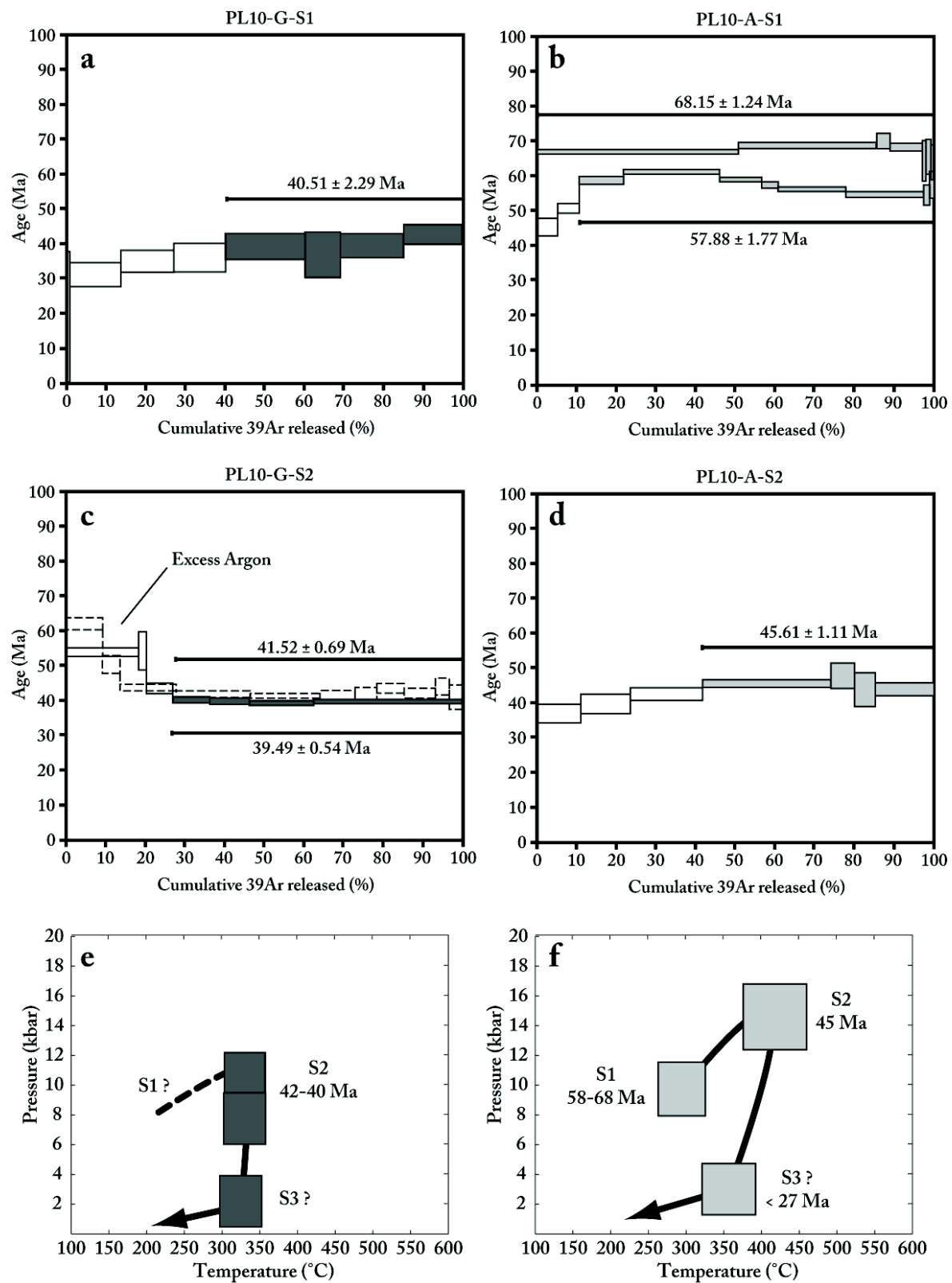


FIGURE 4.39 – Spectres $^{40}\text{Ar}/^{39}\text{Ar}$ pour les différents échantillons de l'unité des Schistes lustrés et trajets P-T-t. (a), (c), (e) Affleurement du Gouret. (b), (d), (f) Affleurement de l'Arkose de Roca Nera.

deux plateaux bien définis avec des âges calculés à $41,52 \pm 0,69 \text{ Ma}$ et $39,49 \pm 0,54 \text{ Ma}$ (Fig. 4.39-c). Les premiers paliers montrent des âges plus vieux dans les deux cas, symptomatiques d'un excès d'Argon en bordure des grains. Cet excès d'Argon peut être relié à l'événement de recristallisation tardif des bordures des phengites que nous avons précédemment associé à la phase D3.

Interprétation Les âges des phengites appartenant à la S1 et à la S2 sont les mêmes, aux incertitudes près, autour de 40 Ma . Ce résultat peut être expliqué par une forte recristallisation des phengites durant le début de l'exhumation et donc associé à un épisode de déformation important. Les âges de la S1 ont donc été remis à zéro durant la phase D2 à $42 - 40 \text{ Ma}$ (Fig. 4.39-e) et ne peuvent pas être identifiés pour cet affleurement.

4.3.5.2 Affleurement de l'Arkose de Roca Nera - zone HT-BS

Schistosité ancienne S1 Deux grains de phengites de l'échantillon PL10-A-S1, prélevés dans un pli P1 à vergence N ont été datés. Le spectre $^{40}\text{Ar}/^{39}\text{Ar}$ montre deux plateaux avec des âges calculés à $68,15 \pm 1,24 \text{ Ma}$ et $57,88 \pm 1,77 \text{ Ma}$ (Fig. 4.39-b).

Schistosité principale S2 Un grain de phengite de l'échantillon PL10-A-S2, prélevé dans la foliation principale S2 a été daté. Le spectre $^{40}\text{Ar}/^{39}\text{Ar}$ montre un plateau à $45,61 \pm 1,11 \text{ Ma}$ (Fig. 4.39-d).

Interprétation Les âges des phengites appartenant à la S1 à $58-68 \text{ Ma}$ sont plus vieux que l'âge de la phengite de la S2 à 45 Ma . À l'inverse de l'affleurement précédent, les phengites préservées dans la S1 dans les coeurs des plis P1 montrent des âges vieux et des conditions P-T de HP/BT du trajet prograde.

4.4 SYNTHÈSE ET PERSPECTIVES

4.4.1 Méthodologie

Les estimations P-T et P-T-t proposées pour les unités océaniques des Schistes lustrés et les unités continentales du Briançonnais montrent que les techniques combinées de micro-cartographie et de multi-équilibres avec des datations Ar/Ar permettent d'obtenir des données précises dans des zones pour lesquelles il y avait une absence de contraintes. L'approche micro-cartographique est particulièrement utile, car elle permet de valider les hypothèses d'équilibres et de relier les variations chimiques aux différentes phases de déformation.

4.4.2 Synthèse

Des nouveaux trajets P-T-t ont été présentés pour deux affleurements clefs des Schistes lustrés du Queyras, le premier se situe dans la zone de MT (affleurement du Gouret) et le second dans la zone de HT (affleurement de l'Arkose de Roca Nera). L'âge de la phase D1, associée à l'enfouissement, a été contraint à 58 – 68 *Ma* dans l'unité de HT avec un âge de D2 plus récent à $45,61 \pm 1,11$ *Ma*. Dans la zone de MT, les phengites précoces de la S1 n'ont pas préservé d'âges progrades en raison d'une recristallisation à 40 *Ma* en même temps et aux mêmes conditions P-T que les phengites de la S2 (Fig. 4.39-b et 4.39-d). L'âge de la S2 a pu être estimé au niveau des deux affleurements et montre que le début de l'exhumation est plus vieux de 3 à 5 *Ma* dans la zone de HT à l'Est que dans la zone de BT à l'Ouest. Ce résultat indique que l'exhumation des différentes unités dans les Schistes lustrés du Queyras n'est pas synchrone et commence dans les zones qui ont enregistré les conditions P-T les plus élevées. Le deuxième résultat majeur de cette étude est la caractérisation du trajet prograde pour l'unité de l'Arkose de Roca Nera. Cet enfouissement correspond à un saut de pression de 5 *kbar* soit 15 *km* en 16 *Ma*, ce qui donne une vitesse verticale d'enfouissement moyenne de l'ordre de 1 *cm/an* (Fig. 4.40).

Pour la paléo-marge continentale Briançonnaise, nous avons mis en évidence un écaillage précoce de la partie orientale de la croûte continentale, marqué par l'acti-

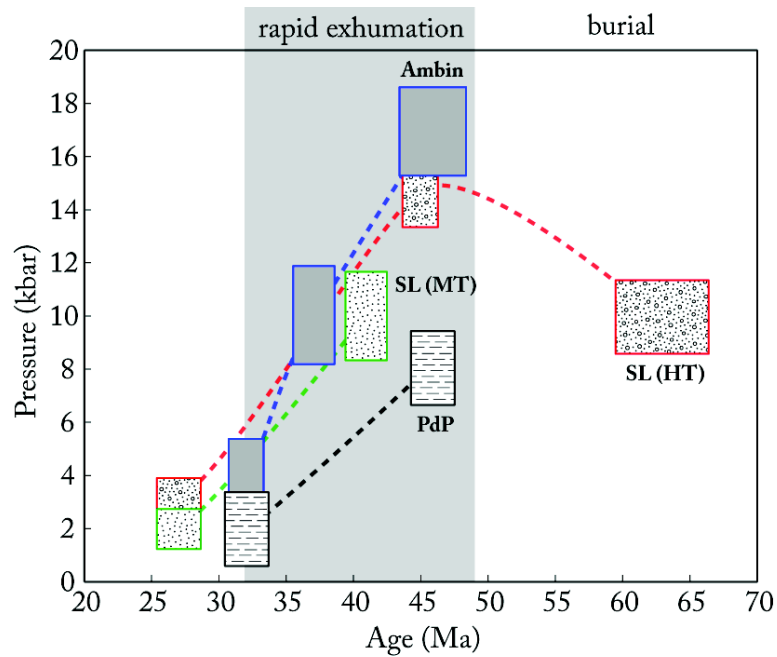


FIGURE 4.40 – Chemins P - t pour différentes unités des Schistes lustrés (SL(MT) et LS(HT) cette étude) et du Briançonnais (PdP, Plan de Phasy cette étude ; Ambin ([Ganne et al. 2005; 2007](#), [Gerber 2008](#))).

vation de zones de cisaillement qui naissent dès 46 Ma . Cette phase majeure à vergence N marque le début de l'exhumation (Fig. 4.41). La partie la plus occidentale du Briançonnais, caractérisée par la présence de la zone houillère, est impliquée plus tard dans la subduction continentale, durant l'exhumation des massifs plus internes ([Lanari et al. 2012a](#)).

Durant la période 65-45 Ma l'unité HT des Schistes lustrés enregistre un enfouissement avec une vitesse verticale de 1 cm/an . Cette vitesse est compatible avec la vitesse horizontale de 1,9 cm/an proposée par [Handy et al. \(2010\)](#), grâce aux reconstructions tectoniques, pour un angle de subduction d'environ 30° . Les nouveaux résultats mettent en évidence que l'exhumation des unités océaniques débute à 45 Ma pour les zones de MT. Cette exhumation est donc synchrone avec le début de l'exhumation des unités d'origine continentale les plus internes (e.g. [Lanari et al. 2012a](#)). L'étude des Schistes lustrés du Queyras montre que pour la chaîne Alpine occidentale, l'exhumation n'intervient pas par un processus d'épaississement à la base du prisme océanique durant la subduction océanique (modèle classique de [Platt 1986](#)), mais intervient durant un épisode d'écaillage crustal de

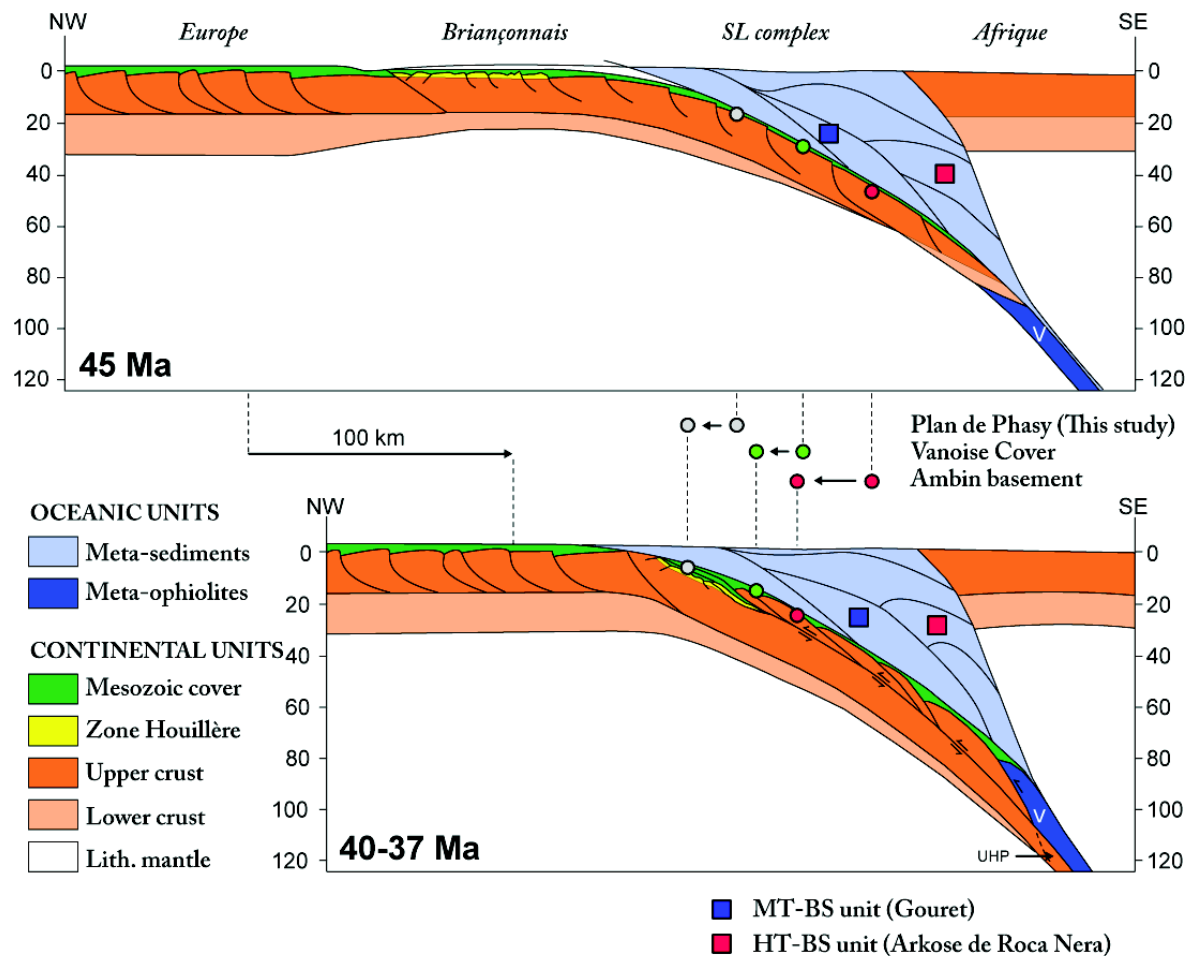


FIGURE 4.41 – Possible kinematic reconstruction of this part of the Western Alps from Eocene to Oligocene (modified from Lanari et al. 2012a). V, Viso.

la marge passive pendant la subduction continentale. Cet événement majeur observable dans toute cette partie de la chaîne peut être lié à un changement dans l'angle de la subduction causé par l'entrée en subduction de la paléo-marge briançonnaise. Cet événement marque le début d'une période d'exhumation rapide dans les zones internes (e.g. Ford et al. 2006, et Fig. 4.40), associée à une tectonique de vergence N-S (Dumont et al. 2012) qui perdurera jusqu'à la collision avec la plaque européenne à 32 Ma (e.g. Simon-Labric et al. 2009).

4.4.3 Perspectives

Les résultats présentés dans ce chapitre permettent de compléter les données P-T et P-T-t disponibles à l'échelle des Alpes occidentales (Fig. 4.42 et Tab. 4.7). Les T_{max} résultant de l'étude de la matière carbonée en utilisant la spectrométrie Raman ont également été reportées sur la carte générale (Fig. 4.43). Cette synthèse montre l'évolution E-W des conditions du métamorphisme (ici de la température) Rolland et al. (e.g. 2000), Schwartz (e.g. 2000), Oberhänsli et al. (e.g. 2004), Gabalda et al. (e.g. 2009). Il est maintenant nécessaire d'intégrer l'ensemble de ces données P-T, P-T-t, ou T_{max} dans un même modèle géodynamique afin d'expliquer l'évolution de la chaîne, en particulier la transition entre une dynamique de subduction N-S et une dynamique de collision E-W autour de 33-30 Ma. L'utilisation de la modélisation numérique en 3D semble être une piste intéressante pour répondre à ce genre de questions et pour tester plusieurs évolutions possibles. De plus, les reconstructions géodynamiques nécessitent de connaître avec la plus grande précision la géométrie actuelle de la chaîne. Le projet d'imagerie sismique CIFALPS en cours de réalisation le long de la transversale Zone externe - Briançonnais - Schistes lustrés du Queyras - Viso - Dora Maira permettra dans l'année à venir d'apporter de nouvelles contraintes sur la géométrie actuelle de la chaîne et donc d'affiner les modèles de reconstructions géodynamiques.

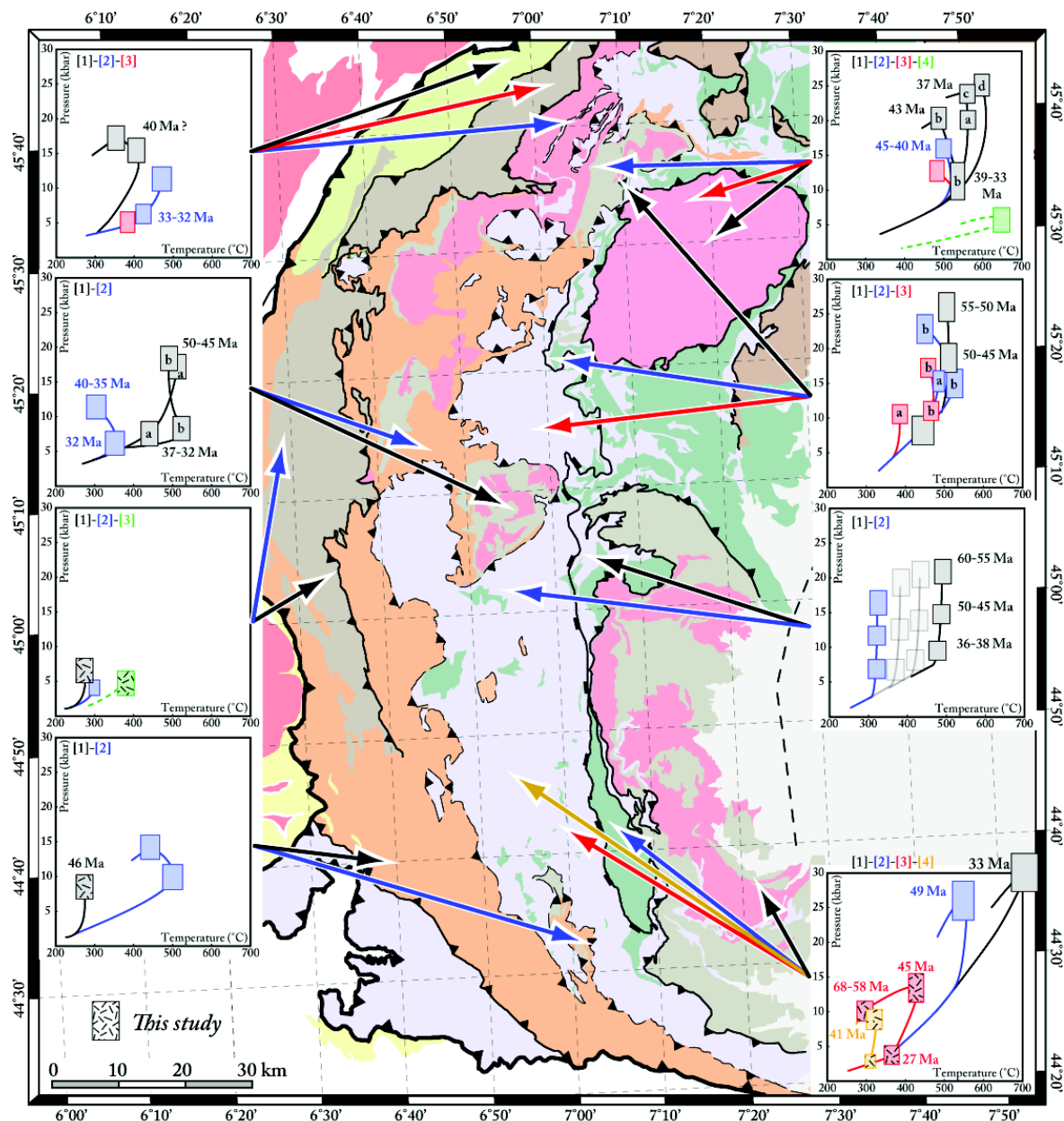


FIGURE 4.42 – Synthèse des données métamorphiques à l'échelle des Alpes internes occidentales. Les références utilisées pour construire la figure sont disponibles dans le tableau 4.7. Les boîtes représentant les estimations P-T issues de ce travail ont été représentées avec un figuré.

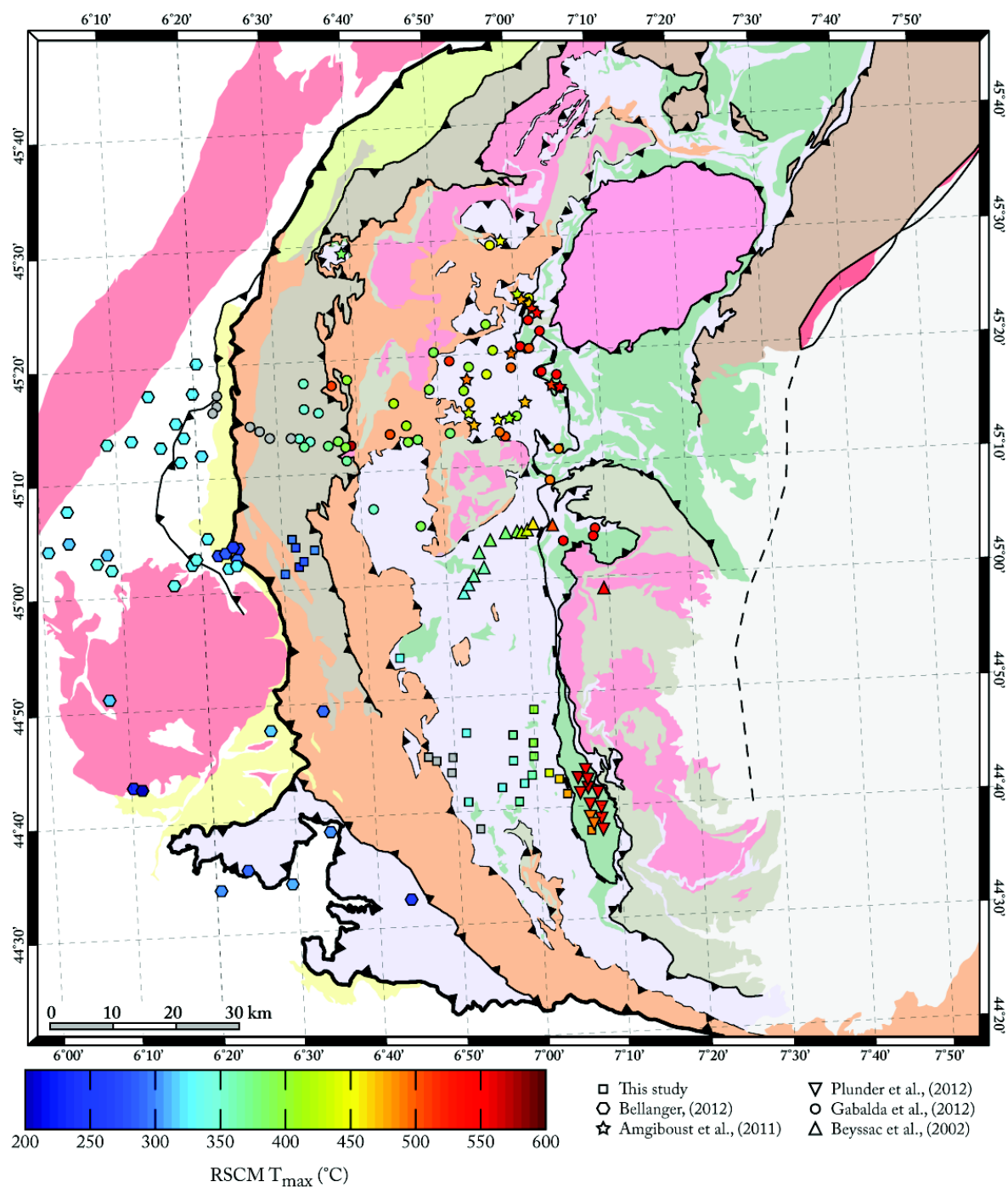


FIGURE 4.43 – Carte de synthèse à l'échelle des Alpes occidentales des T_{\max} obtenues en étudiant la matière carbonée par spectroscopie Raman (Beyssac et al. 2002, Gabalda et al. 2009, Plunder et al. 2012, Angiboust et al. 2011, Lanari et al. 2012a, Bellanger 2012).

Grand Paradis		
[1]	P-T	(a) Rolland et al. (2000) (b) Le Bayon et al. (2006)
	t	(c) Gabudianu Radulescu et al. (2009), Gasco et al. (2010) (d) Rosenbaum et al. (2012)
[2]	P-T	Meffan-Main et al. (2004), Rosenbaum et al. (2012), Gabudianu Radulescu et al. (2009)
	t	Guillot et al. (2012), Bucher et al. (2003)
[3]	P-T	Bucher (2003)
	t	Le Bayon et Ballèvre (2006)
Valaisan		
[1]	P-T	Goffé et Bousquet (1997), Bousquet et al. (2002)
	t	from Wiederkehr et al. (2009) (Central Alps)
[2]	P-T	Bucher et al. (2003), Bucher et Bousquet (2007)
	t	Bucher (2003)
[3]	P-T	Bucher et al. (2003), Bucher et Bousquet (2007)
SL - Maurienne		
[1]	P-T	Bucher et al. (2003)
	t	Bucher (2003)
[2]	P-T	(a) Rolland et al. (2000) (b) Plunder et al. (2012)
[3]	P-T	(a) Rolland et al. (2000) (b) Plunder et al. (2012)
Ambin-Vanoise		
[1]	P-T	(a) Ganne (2003), (b) Gerber (2008)
	t	Ganne (2003), Gerber (2008)
[2]	P-T	Ganne (2003), Strzeczynski (2006), Gerber (2008), Strzeczynski et al. (2012)
	t	Strzeczynski et al. (2012)
SL - Italie		
[1] + [2]	P-T	Agard et al. (2001a)
	t	Agard et al. (2002)
Zone houillère		
[1]	P-T	Lanari et al. (2012a)
[2]	P-T	Ceriani et al. (2003)
[3]	P-T	Lanari et al. (2012a)
Queyras-V-DM		
[1]	P-T	Chopin et al. (1991)
	t	Duchene et al. (1997)
[2]	P-T	Messiga et al. (1999), Schwartz et al. (2001), Angiboust et al. (2011)
	t	Duchene et al. (1997)
[3]	P-T	this study
	t	this study
[4]	P-T	this study
	t	this study

TABLE 4.7 – Liste des références des conditions P-T et P-T-t reportées sur la Fig. 4.42.

APPLICATION À L'HIMALAYA

5

SOMMAIRE

5.1	INTRODUCTION : ÉCLOGITES ET HIMALAYA	293
5.2	ARTICLE 7 : DECIPHERING HIGH-PRESSURE METAMORPHISM IN COLLISIONAL CONTEXT USING MICROPROBE-MAPPING METHODS : APPLICATION TO THE STAK ECLOGITIC MASSIF (NW HIMALAYA). (IN PRESS, GEOLOGY)	298

CE chapitre est consacré à l'étude du chemin P-T enregistré par une éclogite himalayenne du massif de Stak en utilisant le logiciel XMAPTOOLS.

IN this chapter the program XMAPTOOLS was used to calculate the P-T path recorded by an eclogite sample from the Stak massif (NW Himalaya).

5.1 INTRODUCTION : ÉCLOGITES ET HIMALAYA

★ *L'étude du métamorphisme de HP-UHP enregistré par les unités continentales des chaînes de montagne de type subduction-collision est importante car elle permet de contraindre l'évolution géodynamique de la marge continentale durant la subduction. Cependant l'identification de l'épisode éclo­gitique et la reconstruction du trajet P-T peut s'avérer difficile si la rétro­morphose, lors de la collision, a entraîné la recristallisation quasi-totale des anciennes paragé­nèses.*

★ *Trois massifs HP-UHP ont été identifiés le long de la chaîne himalayenne, deux dans la syntaxe N-W (Kaghan et Tso Morari) et un dans la partie centrale (Ama Drime). Le massif de Stak, au Pakistan, a été identifié comme un quatrième massif éclo­gitique, mais sans contrainte précise sur les conditions du trajet HP/BT.*

★ *Dans cette partie introductive, nous allons présenter brièvement la chaîne himalayenne puis le massif de Stak, ainsi que la stratégie mise en place pour reconstruire le chemin P-T à partir d'un échantillon éclo­gitique.*

5.1.1 Chaîne himalayenne et éclo­gites

La chaîne himalayenne résulte du mouvement relatif vers le Nord de la plaque indienne (e.g. [White et Lister 2012](#)) qui a entraîné la fermeture par subduction océanique de l'océan téthysien puis sa collision avec la plaque asiatique ([Dewey 1970](#), [McKenzie et Sclater 1971](#), [Desio 1977](#), [Sengör 1979](#)). L'âge du premier contact entre l'Inde et l'Asie a été contraint en utilisant les datations du métamorphisme de haute pression (HP) enregistré durant la subduction continentale ([de Sigoyer et al. 2000](#), [Kaneko et al. 2003](#), [Leech et al. 2005](#), [Parrish et al. 2006](#), [Riel et al. 2008](#), [Riel 2008](#)) et l'étude du timing de l'érosion et de la sédimentation ([Searle et al. 1987](#), [Searle et Rex 1988](#), [Guillot et al. 2003](#), [Aitchison et al. 2007](#)). La variabilité des méthodes employées et des âges obtenus entre 65 Ma et 45 Ma marque la difficulté de définir la notion de collision en terme d'enregistrements paléo-magnétiques, sédimentologiques, tectoniques et métamorphiques (e.g. [Guillot et al. 2003](#)).

L'étude du métamorphisme de haute pression est important, car il permet de reconstituer l'âge du début de la subduction continentale en connaissant l'âge du

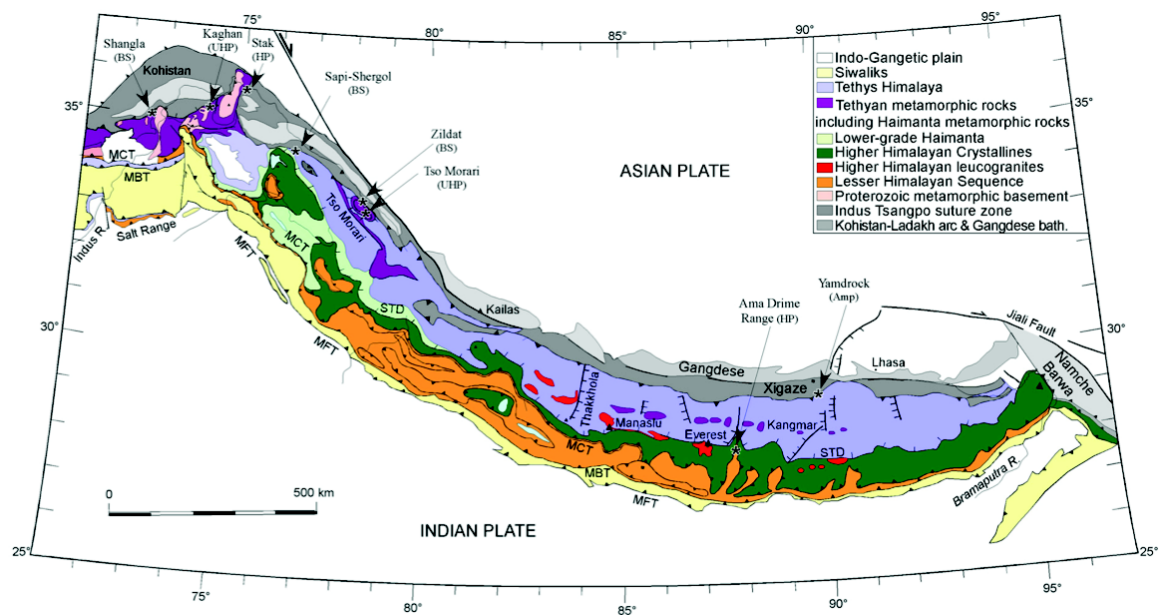


FIGURE 5.1 – Carte géologique de l'Himalaya d'après [Guillot et al. \(2008\)](#). Les étoiles montrent les emplacements des massifs éclogitiques. BS : blueschist unit ; Amp : amphibolitic unit ; HP : high-pressure unit, UHP : ultrahigh-pressure unit.

pic de pression, la profondeur et la vitesse de convergence. Pour le massif du Tso Morari dans le N-W de la chaîne (Fig. 5.1), cet âge a été estimé à 57 Ma par [Leech et al. \(2005\)](#). Ces reconstitutions sont indispensables pour reconstruire avec le plus de précision la géométrie de la paléo-marge Nord indienne (e.g. [Guillot et al. 2007](#)). Cependant, à l'inverse des Alpes (chapitre 4), le métamorphisme associé à la subduction est difficile à étudier en raison d'une intense phase de rétro-morphose durant la collision ([Guillot et al. 2008](#)).

Depuis la première description pétrologique des éclogites par [Hauy \(1822\)](#) ces roches ont été très décrites dans de nombreuses chaînes de montagnes (voir les synthèses de [Godard 2001](#), [Guillot et al. 2009](#)). Comme nous l'avons vu dans le chapitre 2, [Eskola \(1915; 1921\)](#) définit un champ éclogitique qui s'étend à haute pression (HP), c'est-à-dire pour des pressions supérieures à 15 kbar (Fig. 2.1). La découverte de la coésite dans les quartzites à pyrope de Dora Maira dans les Alpes occidentales par [Chopin \(1984\)](#) a permis d'introduire le terme de ultra-haute pression (UHP). C'est la première fois que l'on démontrait que la croûte continentale pouvait être entraînée, lors de la subduction, à plus de 100 km de profondeur dans

le manteau. Depuis une trentaine d'années, l'identification de ces massifs HP et UHP a été un enjeu majeur afin de mieux comprendre l'évolution géodynamique de ces zones de convergence.

Le long des 2.000 *km* de la chaîne Himalayenne, seulement quatre massifs éclo­gitiques appartenant tous au "Greater Himalayan Sequence" ont été découverts. Dans la partie Est, le massif de l'Ama Drime (Lombardo et al. 1998, Lombardo et Rolfo 2000, Groppo et al. 2007), et dans la partie Ouest, les massifs de Kaghan (Chaudhry et Ghazanfar 1987, Spencer et al. 1990, O'Brien et al. 1999; 2001) et du Tso Moriri (Guillot et al. 1995; 1997, de Sigoyer et al. 2000). Un cinquième massif éclo­gitique à Stak dans le Nord du Pakistan a été décrit par Le Fort et al. (1997), mais la rétro­morphose très marquée n'a pas permis de préciser les conditions du pic du métamorphisme. Des échantillons en provenance de ce massif ont été étudiés par Riel et al. (2008), Riel (2008).

5.1.2 Massif de Stak

Le massif de Stak se situe dans la vallée de l'Indus à mi-chemin entre les villes de Skardu et de Gilgit dans la zone du Cachemire au Nord-Ouest du Pakistan (Fig. 5.1 5.3). Géologiquement, l'unité éclo­gitique de Stak, est positionnée sur le flanc Est du massif cristallin du Nanga Parbat, pincée entre les roches plutoniques de l'arc du Kohistan-Ladakh et des gneiss et orthogneiss constitutifs du massif du Nanga-Parbat. L'unité d'une centaine de mètres de large est formée d'un mélange de paragneiss, d'orthogneiss, de marbres et de boudins de roches basiques éclo­gitisés (Fig. 5.2). Cette association lithologique est typique d'une marge continentale intrudée par un volcanisme basique.

Structuralement, l'ensemble de l'unité est fortement plissé par deux phases majeures : une première isoclinale syn-foliation et une seconde phase à plis asymétriques à vergence S-E reprenant la foliation. La première phase de plissement est attribuée à l'événement éclo­gitique, alors que la seconde est associée à l'exhumation du massif du Nanga-Parbat (Riel 2008) et plisse la zone de contact entre le massif du Nanga-Parbat et l'arc du Kohistan-Ladakh.



FIGURE 5.2 – Panorama de l’affleurement des roches éclogitiques du massif de Stak (Photos © N. Riel)

5.1.3 Straté­gie

La partie suivante sera consacrée à l'étude pétrologique et métamorphique d'une petite zone d'une lame mince d'un échantillon d'éclogite provenant du massif de Stak. Cet échantillon montre une paragé­nèse de HP-UHP à grenat, omphacite et phengite. Cette assem­blage est déstabilisé en symplectite à clinopyroxene, amphibole et plagioclase. Enfin, est surimposée une paragé­nèse plus tardive à amphibole et biotite qui est associée à la collision himalayenne et à la mise en place du dôme du Nanga Parbat. Nous allons proposer un chemin P-T composé d'environ 200.000 points P-T qui a été automatiquement calculé en utilisant le logiciel XMAPTOOLS (chapitre 3) et des images chimiques acquises à la microsonde. Pour chaque paragé­nèse identifiée précédemment, nous avons utilisé une approche de type "multi-équilibres", mais en utilisant des calibrations empiriques pour calculer la position des équilibres chimiques. Le trajet P-T proposé est également compatible avec une pseudosection calculée par minimisation d'énergie en utilisant le logiciel THERIAK-DOMINO. Ces résultats montrent que le massif de Stak est un nouveau massif éclo­gitique avec un trajet P-T comparable à ceux de Kaghan et du Tso Morari, ce qui permet de supposer la présence d'une large province de HP à UHP dans la partie NW de la chaîne himalayenne. Cette étude sera présentée sous la forme d'un article de Lanari et al. (in press) en cours de publication dans la revue *Geology*.

5.2 ARTICLE 7 : DECIPHERING HIGH-PRESSURE METAMORPHISM IN COLLISIONAL CONTEXT USING MICROPROBE-MAPPING METHODS : APPLICATION TO THE STAK ECLOGITIC MASSIF (NW HIMALAYA). (IN PRESS, GEOLOGY)

★ *La reconstruction de trajets P-T de l'épisode de HP à UHP pour les roches ayant subi une forte rétro-morphose dans le faciès des amphiboles n'est pas facile en utilisant des approches classiques.*

★ *Le massif de Stak au Pakistan (NW Himalaya) a été identifié comme un quatrième massif éclogitique, mais en raison de la forte empreinte collisionnelle, le pic de pression et le trajet P-T n'ont pas pu être contraints.*

★ *Dans cette partie, nous allons utiliser des techniques de micro-cartographie pour essayer de contraindre un chemin P-T le plus continu possible de l'histoire éclogitique d'un échantillon du massif de Stak. Nous allons présenter les résultats sous la forme d'un article de Lanari et al. (in press) accepté pour publication dans la revue Geology.*

Deciphering high-pressure metamorphism in collisional context using microprobe-mapping methods : Application to the Stak eclogitic massif (NW Himalaya)

Pierre Lanari¹, Nicolas Riel¹, Stéphane Guillot¹, Olivier Vidal¹, Stéphane Schwartz¹, Arnaud Pêcher¹, and Keiko H. Hattori²

in press - Geology

Abstract - The Stak massif, northern Pakistan, is a newly recognized occurrence of eclogite formed by the subduction of the northern margin of the Indian continent in the NW Himalayas. Although this unit was extensively retrogressed during the Himalayan collision, records of the high-pressure (HP) event as well as a continuous pressure-temperature (PT) path were assessed from a single thin section using a new multi-equilibrium method. This method uses microprobe X-ray compositional maps of garnet and omphacitic pyroxene followed by calculations of $\sim 200,000$ P-T estimates using appropriate thermobarometers. The Stak eclogite underwent prograde metamorphism, increasing from 650°C and 2.4 GPa to the peak conditions of 750°C and 2.5 GPa, then retrogressed to 700-650°C and 1.6-0.9 GPa under amphibolite-facies conditions. The estimated peak metamorphic conditions and PT path are similar to those of the Kaghan and Tso Moriri high- to ultra-high-pressure (HP-UHP) massifs. We propose that these three massifs define a large HP to UHP province in NW Himalaya, comparable to the Dabie-Sulu province in China and the Western Gneiss province in Norway.

Key Words - Metamorphism ; Eclogite ; Himalaya ; Microprobe ; XMapTools

1. ISTerre, University of Grenoble 1, CNRS, 1381 rue de la Piscine, 38041 Grenoble, France

2. Department of Earth Sciences, University of Ottawa, Ottawa, Ontario K1N 6N5, Canada.

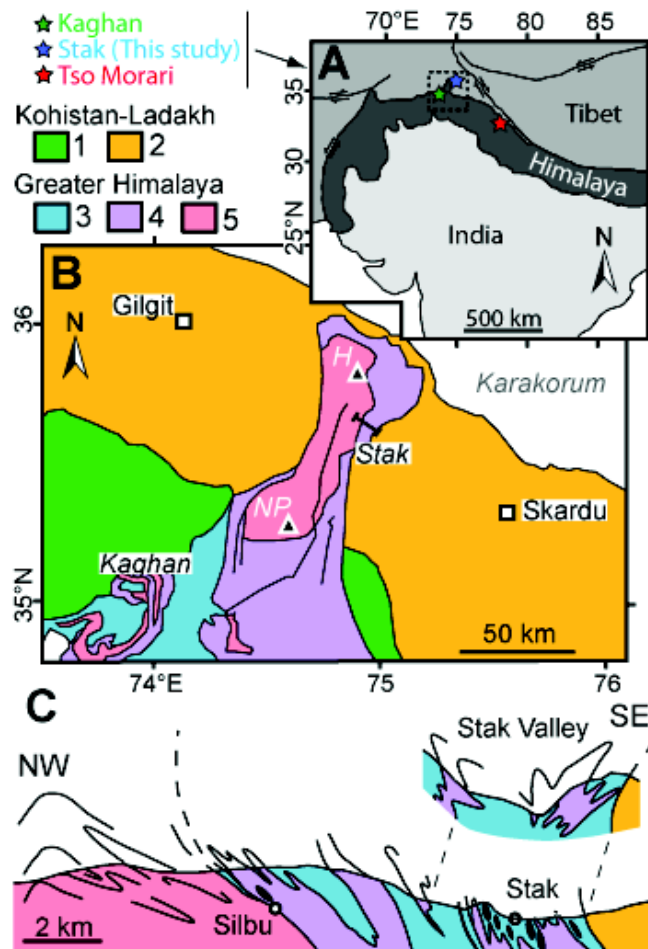


FIGURE 5.3 – Schematic geological maps (A) of the N India and Himalaya area, (B) of the NW Himalayan massif, modified from [Pêcher et al. \(2008\)](#) with locations of known eclogitic massifs (Tso Morari, Kaghan and Stak) (NP, Nanga Parbat; H, Haramosh), and (C) cross section through the Stak massif. Geological units : 1, Amphibolites (Kohistan) and Chilas complex (Ladakh); 2, Undifferentiated Kohistan and Ladakh units (volcano and metasediments, batholiths and Eocene volcanics); 3, Neotethyan sedimentary group; 4, Higher Himalayan Crystallines and paleozoic intrusives; 5, basement gneiss.

5.2.1 Introduction

The recent discovery of micro-diamond and coesite inclusions in rocks previously considered as collision-type granulites ([Kotkova et al. 2011](#)) suggests that evidence for subduction-related metamorphism is commonly obliterated during late collisional events. [Le Fort et al. \(1997\)](#) considered that the Stak massif in northern Pakistan (Fig. 5.3) is a retrogressed eclogitic massif, but the pervasive retrogression made it difficult to evaluate the peak metamorphic conditions, which were only constrained to be $> 1.3 \text{ GPa}$ and $> 610^\circ\text{C}$. We report a new approach invol-

ving X-ray mapping of a single thin section, $520 \times 670 \mu\text{m}^2$ in size, which yielded information to determine a detailed P-T path. This path is similar to those of eclogitic units of Kaghan and Tso Morari ($\sim 150 \text{ km}$ and $\sim 500 \text{ km}$ from the Stak massif, respectively), which suggests the presence of a large HP to UHP province in the NW Himalayas.

5.2.2 Geological setting and sample description

The Stak area is located in the Indus valley of northwest Skardu, Pakistan (Fig. 5.3). High pressure rocks are exposed on the northern edge of the Indian continental plate within the Main Mantle Thrust, between the Ladakh arc to the south and the Nanga Parbat Haramosh gneisses (Higher Himalayan Crystallines) to the north (Fig. 5.3 b). These units (weakly metamorphosed garnet-free amphibolites of the Ladakh arc, strongly metamorphosed metasedimentary rocks of the Nanga Parbat, and felsic gneisses of the Nanga Parbat core) are imbricated in tight, multiphase folds up to a km-scale with superimposed NNE-SSW and E-W trends. Mafic dikes that originally intruded the sedimentary rocks form metric to decametric eclogitic boudins within the felsic gneisses in an area $\sim 2 \text{ km}$ wide by $\sim 10 \text{ km}$ long, with poorly delineated boundaries (Guillot et al. 2008) this area is defined as the Stak massif. Our investigation focused on these eclogitized mafic boudins which contain layers of small rounded garnet and omphacitic pyroxene. The cores are rimmed by hydration products of amphibole and biotite formed during the Himalayan collision. SHRIMP dating on zircon yielded scattered Himalayan ages between 70 and 50 Ma (Riel et al. 2008).

Samples show evidence for three deformation events, with each represented by a specific paragenesis. An early paragenesis (P_1) consists of garnet with phengite inclusions and relict omphacitic pyroxene in small areas ($< 1 \text{ mm}^2$) in the matrix. Omphacite is partially replaced by symplectic intergrowths of secondary pyroxene, plagioclase and amphibole (Fig. 5.4). The foliation associated with P_1 is defined by the preferred orientation of omphacite and garnet. A later paragenesis (P_2) is composed of millimetric amphibole and biotite in discontinuous layers along the

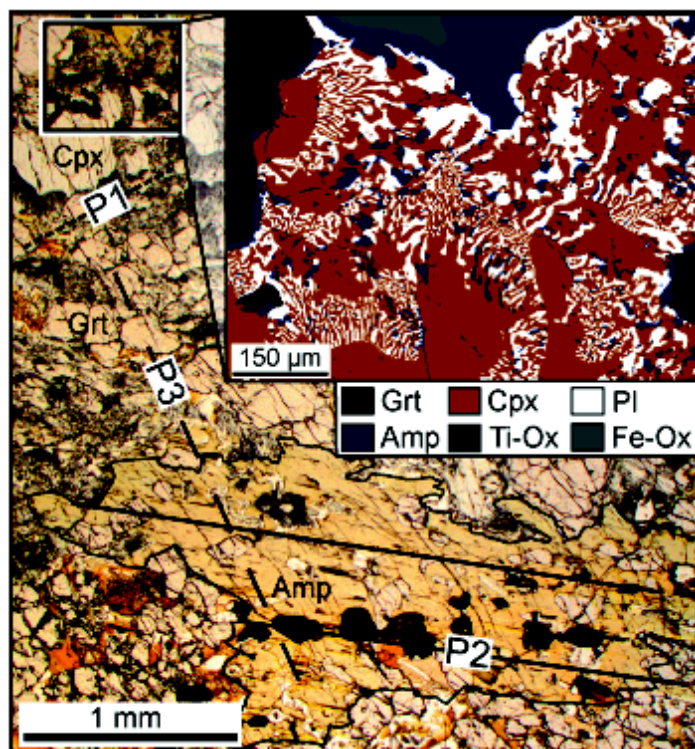


FIGURE 5.4 – Photomicrograph showing the texture of the studied sample. Three main parageneses were identified (labeled P1, P2 and P3, see text). The inset shows the mapped area. Grt, garnet; Cpx, clinopyroxene; Pl, plagioclase; Amp, amphibole; Ti-Ox, Ti-oxide and Fe-Ox, Fe-oxide.

main foliation (Fig. 5.4). The third paragenesis (P3) consists of calcite and chlorite, which developed at the expense of garnet along fractures.

5.2.3 Microprobe mapping and treatment methods

A JEOL JXA-8200 electron probe microanalyser at the Institute of Earth and Environmental Science, Potsdam University, was used to acquire spot analyses and X-ray compositional maps in wavelength dispersive mode (De Andrade et al. 2006, Lanari et al. 2012a). Analytical conditions for spot analyses were 15 KeV accelerating voltage 10 nA specimen current. Standards used were Fe_2O_3 (Fe), $MnTiO_3$ (Mn, Ti), diopside (Mg, Si), orthoclase (Al, K), anorthite (Ca) and albite (Na). The compositional mapping of 350,000 pixels over an area of $520 \times 670 \mu m^2$ was carried out at 200 ms per pixel (see De Andrade et al. 2006, Lanari et al. 2012a, for detailed statistical evaluation). Higher specimen current of 100 nA was employed for mapping. During the mapping, spot analyses were also conducted along profiles in the analyzed area. The data were then used to calibrate the X-ray compositional maps.

The X-ray compositional maps were treated using a Matlab©-based software XMapTools which identifies mineral phases and their locations from X-ray images (Lanari et al. 2012b). In the program, the raw data were converted to quantitative concentrations using the results of spot analyses (one for each phase in the sample), and a structural formula was calculated for each pixel of the mapped area. Each mineral is separated into different compositional groups (for example, clinopyroxene is divided into four subgroups based on the Na and Fe contents). Finally, P-T conditions were calculated in XMapTools using empirical and semi-empirical thermobarometers.

5.2.4 Chemical and thermobarometry results

Garnet shows similar compositions from core to rim ($Alm_{48} Prp_{32-33} Grs_{17-19} Sp_{s1}$) with the exception of a thin (15 μm) rim that contains low pyrope (29 %) and grossular (16 %) contents, and higher almandine and spessartine contents. The rim likely formed by reactions with amphibole during the late *P3* event. Phengite enclosed in garnet has intermediate Si-contents, 3.28 per formula unit (p.f.u.). Four groups of clinopyroxene were identified. Primary clinopyroxene has high jadeite contents ($jd_{41}-jd_{40}$ corresponding to omphacite) and shows an increase in Fe from 0.07 p.f.u. in the core to 0.19 p.f.u. in the rim. The primary clinopyroxene is further divided into two subgroups based on the Fe-contents; 0.07-0.13 and 0.13-0.19 p.f.u. The secondary clinopyroxene in symplectite is divided into two subgroups; one with high jadeite contents ($Jd_{30}-Jd_{25}$), the second with low jadeite contents ($Jd_{25}-Jd_{10}$). This decrease in jadeite content correlates with the decreasing width of intergrowths. Plagioclase in symplectites has similar compositions from core (Ab_{87}) to rim (Ab_{85}). Three groups of amphibole were identified. The first group comprises small grains (10-30 μm) in the symplectite and has low Fe^{3+} content in M1 (0.48 ± 10 p.f.u.) and a high Na content in A (0.54 ± 0.6 p.f.u.). The second group has a larger grain size ($> 100 \mu m$) and shows higher Fe^{3+} content in M1 (0.70 ± 15 p.f.u.) and lower Na content in A (0.39 ± 15 p.f.u.). The third group occurs as corona on gar-

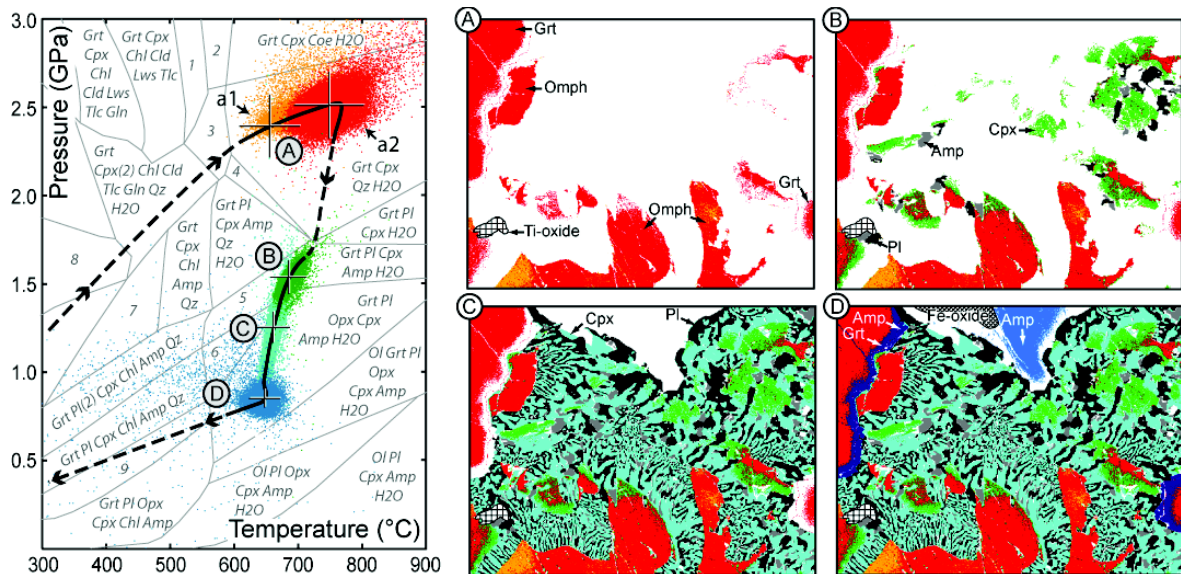


FIGURE 5.5 – P-T grid showing the estimated path of the Stak eclogite and associated P-T maps (for assemblages A, B, C, and D). The colors in the maps correspond to those of the fields in the P-T diagram. The P-T path (thick black solid and dashed line) is based on 200,000 P-T estimates (colored dots) using empirical and semi-empirical thermobarometers on a simplified pseudosection grid (see Supplementary Material for the detailed grid). The error bars were estimated from the uncertainty in electron microprobe data using a Monte-Carlo simulation (see Supplementary Material). Grt, garnet; Cpx, clinopyroxene; Qz, quartz; Coe, coesite; Pl, plagioclase; Amp, amphibole; Ol, olivine; Chl, chlorite; Opx, orthopyroxene; Cld, chloritoid; Tlc, talc; Lws, lawsonite; Gln, glaucophane. Complementary assemblages : 1 : Grt Cpx Chl Lws Tlc H₂O ; 2 : Grt Cpx Lws Coe H₂O ; 3 : Grt Cpx Cld Tlc Qz H₂O ; 4 : Grt Cpx Pl Qz H₂O ; 5 : Grt Pl Cpx Amp Qz H₂O ; 6 : Grt Pl Opx Cpx Amp Qz H₂O ; 7 : Grt Cpx Chl Amp Qz Pl Gln ; 8 : Grt Pl Cpx (2) Cld Amp Gln Qz ; 9 : Grt Pl Opx Cpx Chl Amp Qz.

net (Fe^{3+} in M1 0.54 p.f.u. and Na in A 0.30 p.f.u.). Detailed composition data are provided in the Supplementary Material³ (§ 5.2.7).

Pressure and temperature conditions were estimated for the different paragenetic sequences outlined above. The first assemblage labeled (A) in Figure 5.5 is composed of garnet, omphacite, and phengite. Since omphacite shows a range in Fe content, the P-T conditions were estimated using varying omphacite compositions and fixed garnet and phengite compositions. The calculation used the composition of phengite with the highest Si content and the average composition of garnet. The calculation used the garnet-omphacite thermometer of Korch Ravna (2000b), which is the latest calibration, and the garnet-omphacite-phengite barometer of Waters et

3. GSA Data Repository item 20012xxx, details of mineral groups and pseudosection is available online at www.geosociety.org/pubs/ft2012.htm, or on request from editing@geosociety.org or Documents Secretary, GSA, P.O. Box 9140, Boulder, CO 80301, USA.

[Martin \(1993\)](#) and [Waters \(1996\)](#). The calculated P-T conditions are plotted in a P-T diagram and the pixels (ca. 200,000) are shown in the mapped area (Fig. 5.5 A). Omphacite crystallization started at 650°C and 2.4 *GPa* ("a1", orange-colored field in Fig. 5.5) and continued to form during the peak metamorphic conditions of 750°C and 2.5 *GPa* ("a2", red colored field in Fig. 5.5).

The symplectite of clinopyroxene, amphibole and plagioclase is a breakdown product of omphacite ([Waters 2003](#)). This retrogressed assemblage is divided into two based on crystal sizes in the symplectite; they are labelled (B) and (C) in Figure 5.5. Clinopyroxene grains in the symplectite assemblage (B) are larger and occur together with amphibole and plagioclase on the rims of relict omphacite. The second symplectite assemblage (C) has a smaller grain size. The P-T conditions reflecting this textural change were calculated using equilibria involving pyroxene, plagioclase and amphibole in the absence of quartz. The temperature was first estimated from the distribution of Na and Ca between plagioclase and hornblende using the edenite-richterite calibration of [Holland et Blundy \(1994\)](#). The estimated temperatures vary from 680°C where plagioclase is in contact with Jd30% clinopyroxene to 640°C in contact with Jd10% clinopyroxene. Pressure was estimated with fixed composition of amphibole and plagioclase for the defined temperature ranges using the calibration of [Waters \(2002; 2003\)](#) based on the reaction : jadeite + tremolite = albite + edenite, involving clinopyroxene, plagioclase and amphibole. Activities of end-members were calculated for amphibole and clinopyroxene following the models of [Dale et al. \(2000\)](#) and [Holland \(1990\)](#), respectively. Activity of plagioclase was assumed to be ideal. The P-T estimates and the corresponding pixels are also plotted in Figure 5.5 B and 5.5 C. Our results show that clinopyroxene with plagioclase and amphibole in the symplectite crystallized under P-T conditions varying from 1.5 *GPa* and 680°C (assemblage B) to 1 *GPa* and 650°C (assemblage C).

The late assemblage (D in Fig. 5.5) includes large grains of amphibole (P2 in Fig. 5.4) and biotite, minor Fe-oxides and quartz. The P-T conditions for the assemblage were estimated using the edenite-richterite calibration of [Holland et Blundy \(1994\)](#) and the barometer of [Schmidt \(1992\)](#). Although the Schmidt barometry is

designed for granitic rocks, the observed mineral assemblage is similar to that of granitoids. The results (blue pixels in Fig. 5.5 D) show the crystallization of large amphibole grains at 650°C and 0.85 GPa. Such conditions are common during collisional events. The Fe-Mg exchange thermometer of [Korh Ravna \(2000a\)](#) yielded temperatures ranging from 510 to 460°C for the crystallization of amphibole on the rims of garnet, which corresponds to the latest stage of exhumation.

To complement the P-T estimates, pseudosections were calculated in the NCF-MASHO system using various software packages including *Perple_X*. Since different programs yielded similar results, the pseudosections were made with *Theriak-Domino* ([De Capitani et Petrakakis 2010](#)) using the thermodynamic database of [Berman \(1988\)](#). The first attempt was made using the bulk-rock composition data, but the results did not match the observed mineral abundances and mineral compositions of garnet under the HP conditions. The result indicates that the metamorphic reactions were not controlled by the bulk rock composition. Therefore, the composition in a small area was calculated with *XMapTools* from the observed mineral compositions and abundance (50% garnet and 50% omphacite) based on the X-ray maps. The pseudosection calculated from this local bulk composition agrees well with the observed mineral compositions at pressures ranging from 2.5 to 1 GPa along the P-T path prior to hydration of the rocks at pressures about 0.9 GPa.

5.2.5 Metamorphic and tectonic implications

The calculated P-T evolution shows that omphacite and garnet started to crystallize near the end of the prograde path, from ~650°C and 2.4 GPa to up to the peak conditions at 750°C and 2.5 GPa (Fig. 5.5). During this period, garnet did not significantly change its composition, as predicted by similar compositions of garnet ($Alm_{50} Prp_{33} Grs_{16}$) at 650°C - 2.4 GPa and at 750 °C - 2.5 GPa) in the pseudosection (detailed grid in Supplementary Material § 5.2.7). The absence of coesite in the Stak eclogite is consistent with the estimated peak pressure, which is below the stability field of coesite (Fig. 5.5). Symplectite intergrowth is associated with hydration, which resulted in the crystallization of amphibole. The pseudosec-

tion (Fig. 5.5) shows the upper stability limit of amphibole at about 1.6 *GPa* and 700°C, which is in good agreement with the highest pressure for amphibole obtained by empirical barometers. The observed clinopyroxene compositions are also consistent with the calculated pseudosections. Clinopyroxene has a decreasing Na content, from 0.32 p.f.u. at 1.5 *GPa* and 680°C to 0.22 p.f.u. at 1.3 *GPa* and 660°C.

In summary, despite a pervasive overprint, a continuous P-T path was obtained for minerals in a single thin section from the Stak massif based on microprobe mapping data. The new approach uses the bulk compositions of small areas, the P-T conditions responsible for reactions in the small area, and microtextures, such as symplectite to determine the reaction path; the estimated P-T path (Fig. 5.5) indicates that the growth of clinopyroxene, plagioclase and amphibole symplectite continued during the retrograde path (1.6-0.9 *GPa*) at the expense of omphacite. This study shows the usefulness of evaluating the effective bulk compositions responsible for microtextural reactions; such data, combined with mineral compositions, provide quantitative thermobarometric information, even for pervasively retrogressed rocks. Furthermore, this work reveals that the Stak massif had a metamorphic evolution similar to that of the well preserved Kaghan and Tso Moriri HP to UHP massifs in NW Himalayas (Guillot et al., 2008). Therefore, we propose that the Stak massif is another example of continental eclogitic metamorphism in the NW Himalayas, and suggest that the entire NW margin of the Indian continent records continental subduction (Fig. 5.6).

Worldwide, the size of UHP domains varies widely (e.g. review by Guillot et al. 2009). The Dora Maira UHP unit in the Western Alps covers a surface area less than 25 *km*². In contrast, the Mesozoic metamorphic domain in China forms an essentially continuous HP-UHP terrane extending more than 4000 *km*, from Quinlin-Dabie to the Sulu belt (Yang et al. 2003). Similarly, the Western Gneiss Region in Norway forms a continuous HP-UHP unit covering over 400 × 200 *km*² (Young et al. 2007). In the Himalayas, three recognized HP-UHP units (Kaghan, Stak and Tso Morai; Fig. 5.3) likely form a HP-UHP terrane that is partly covered by the Kohistan-Ladakh arc and metamorphic Tethyan series. Its dimension is ~500 *km*

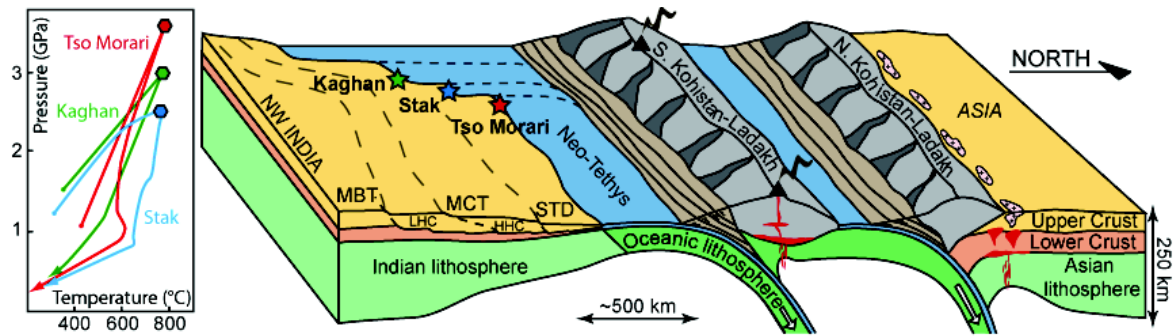


FIGURE 5.6 – Schematic section of the western Himalayas during closure of the Neo-Tethys at the Paleocene-Eocene boundary, and the P-T paths for the three eclogitic units : Stak (this study), Kaghan and Tso-Morari (modified after [Guillot et al. 2008](#)). MBT, Main Boundary Thrust ; LHC, Lower Himalayan Thrust ; MCT, Main Central Thrust ; HHC, High Himalayan Crystalline ; STD, South Tibetan detachment.

long and 150 km wide (Fig. 5.6), which is comparable in size to the Western Gneiss Region in Norway and the Dabie-Sulu belt in China.

5.2.6 Acknowledgments

We acknowledge A. Pourteau (Univ. Potsdam) for his assistance during the authors' electron microanalysis. This work was supported by ANR-projects Cattel PAKSIS and ERD-Alps. The paper was greatly improved by constructive comments from N. Arndt, M. Leech and two anonymous reviewers.

5.2.7 Supplementary material

5.2.7.1 Uncertainties on P-T estimates

The error on P-T estimates depends on the analytical uncertainties of compositions of minerals (i.e. the uncertainty of the microprobe analysis). The P-T scatter resulting from the variation of compositions can be calculated with a Monte-Carlo technique. The precision of the data is element dependent, and can be estimated using a Poisson law (Details in [De Andrade et al. 2006](#)). Each assemblage (a1, a2, B, C and D) is treated separately using average compositions given below (Table DR1 for clinopyroxene and DR2 for amphiboles). A Gaussian error distribution (with $1\sigma = 1\%$ (SiO_2); 10% (TiO_2); 2% (Al_2O_3); 4% (FeO); 2% (MgO); 1% (CaO); 5% (Na_2O) and 9% (K_2O) relative) for all major oxides was randomly sampled about the nominal weight percentage composition. For each case (assemblages a1, a2, B, C and D), 100.000 permutations lead to the simulation of 100.000 mineral compositions. The set of simulated compositions generated was used to compute 100.000 P-T points. The average P and T and associated standard deviation (1σ) calculated from P-T points are used to compute a P-T ellipse in which the size (2σ with a 95% confidence level) represents the resolution on P-T estimate (cross reported on Fig. 5.5). The second source of error, resulting from the uncertainties associated with the thermodynamic data, is difficult to estimate here from the empirical and semi-empirical thermobarometers. The temperature dependency of standard state properties is negligible for thermometers and the P dependency is negligible for barometers. Finally the cumulative P and T uncertainties are probably not larger than those of P-T calculation using a full thermodynamic approach, with unreliable thermodynamic data or incomplete solid solution models (as it is still the case for amphibole). These uncertainties have only a systematic effect on the absolute position (shift in temperature and/or pressure) of the P-T points, and not on their relative positions.

5.2.7.2 Supplementary figures

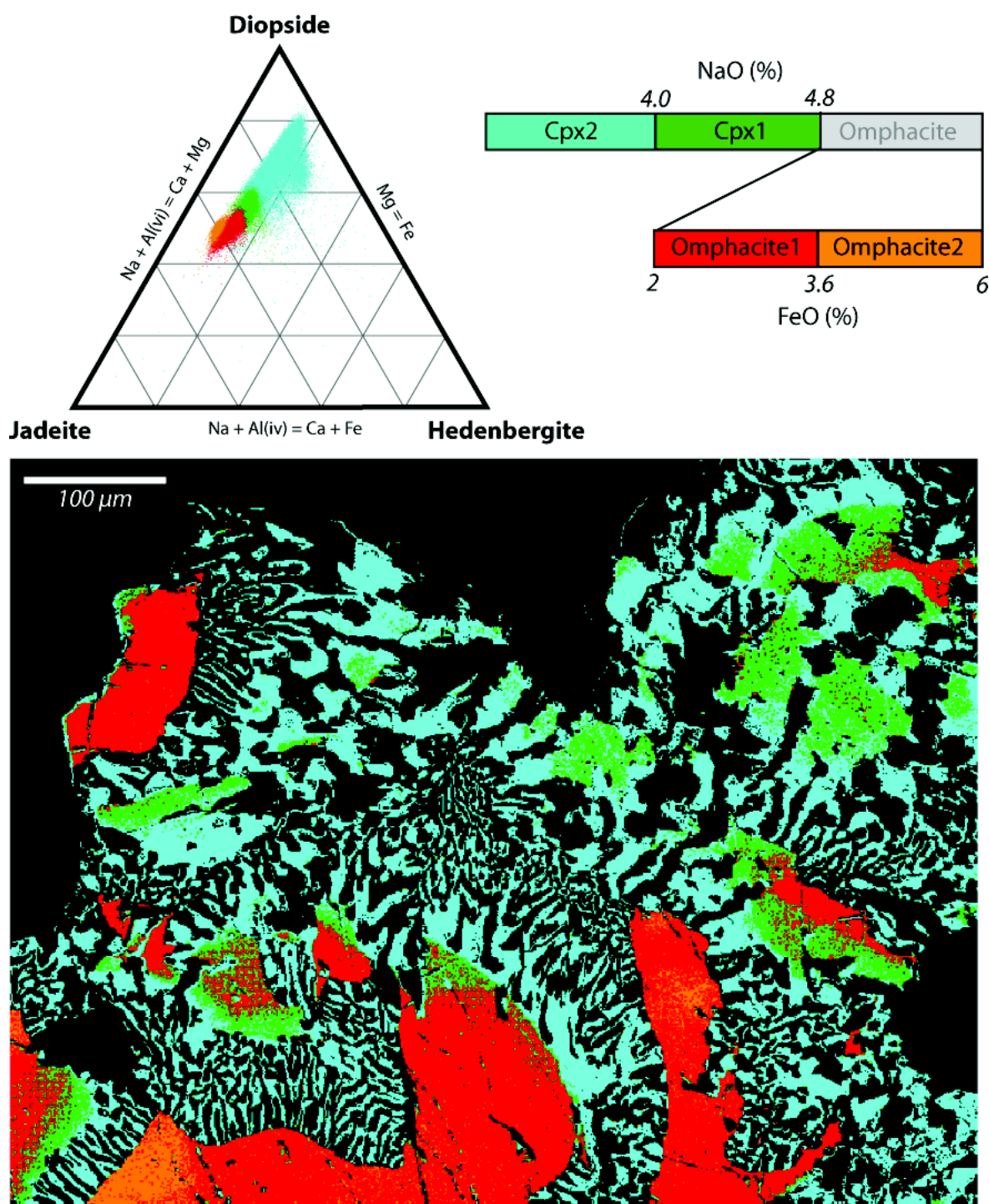


FIGURE 5.7 – Composition of clinopyroxene at individual pixels plotted in a ternary diagram of hedenbergite-jadeite-diopside. They are grouped into four based on the contents of Na_2O and FeO ; high Fe-omphacite (orange), low Fe omphacite (red), high Na Cpx1 (green) and low Na Cpx2 (cyan). Representative analyses for each clinopyroxene groups were provided in table DR1. Colors used to plot the pixels of different groups are the same as used in the fig. 5.5 of the manuscript and correspond to the P-T conditions.

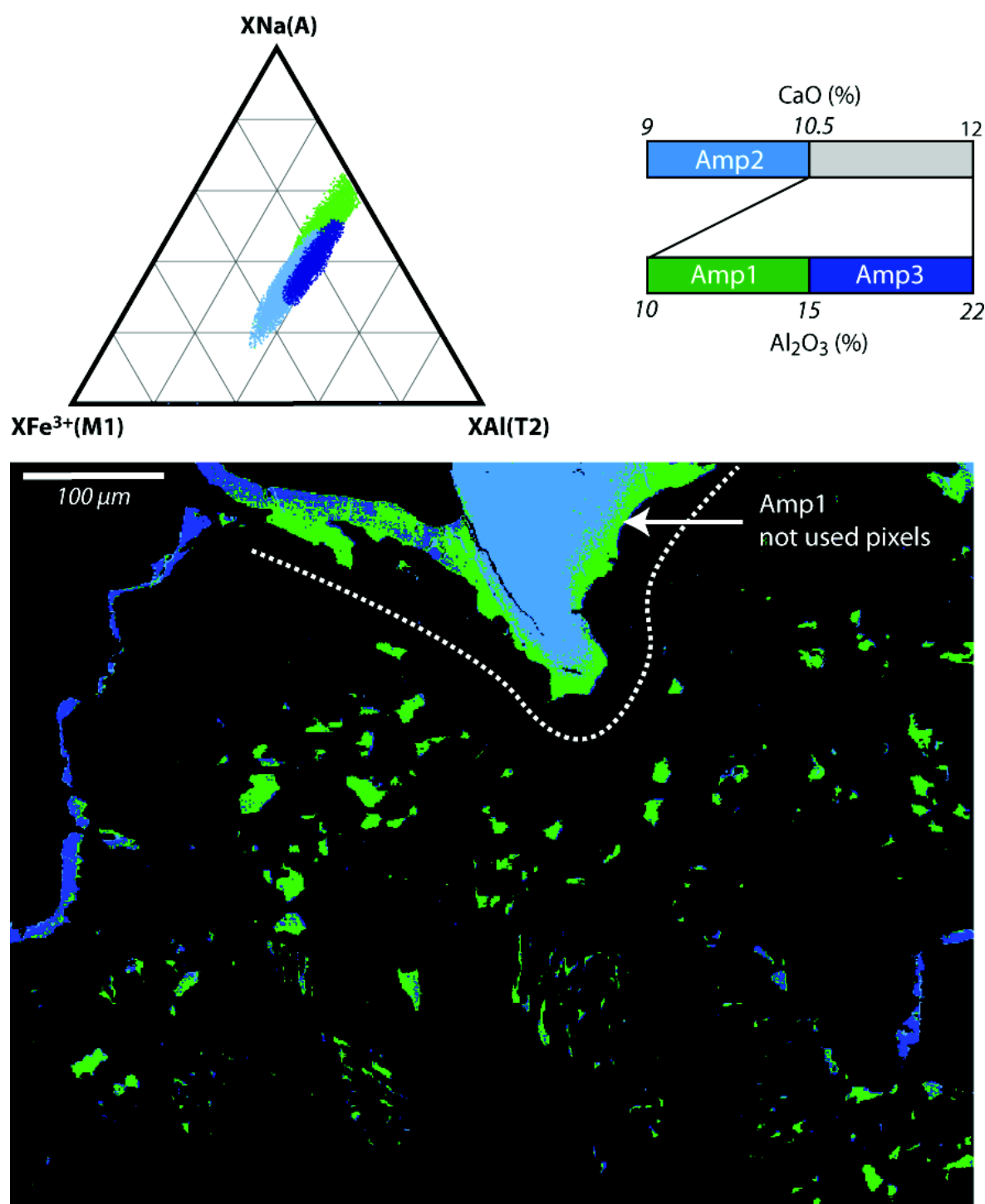


FIGURE 5.8 – Distribution of different groups of amphibole based on the individual compositions of small areas (pixel). The compositional groups are displayed in the ternary diagram XFe^{3+} in M1, XNa in A and XAl in T2 (see Table DR2) and into a map with the same colors. Two main groups are distinguished; high Ca amp1 (green) and low Ca amp2 (cyan). The Ca-rich amphibole is further grouped into, low Al amphibole (amp1, green) and high Al amphibole (amp3, navy blue). Representative composition for each amphibole group is provided in Table DR2. Note that the amp2 rims noted ?not used pixels? were not used to estimate the P-T conditions because these pixels are mixture composition between Amp1 and Amp2.

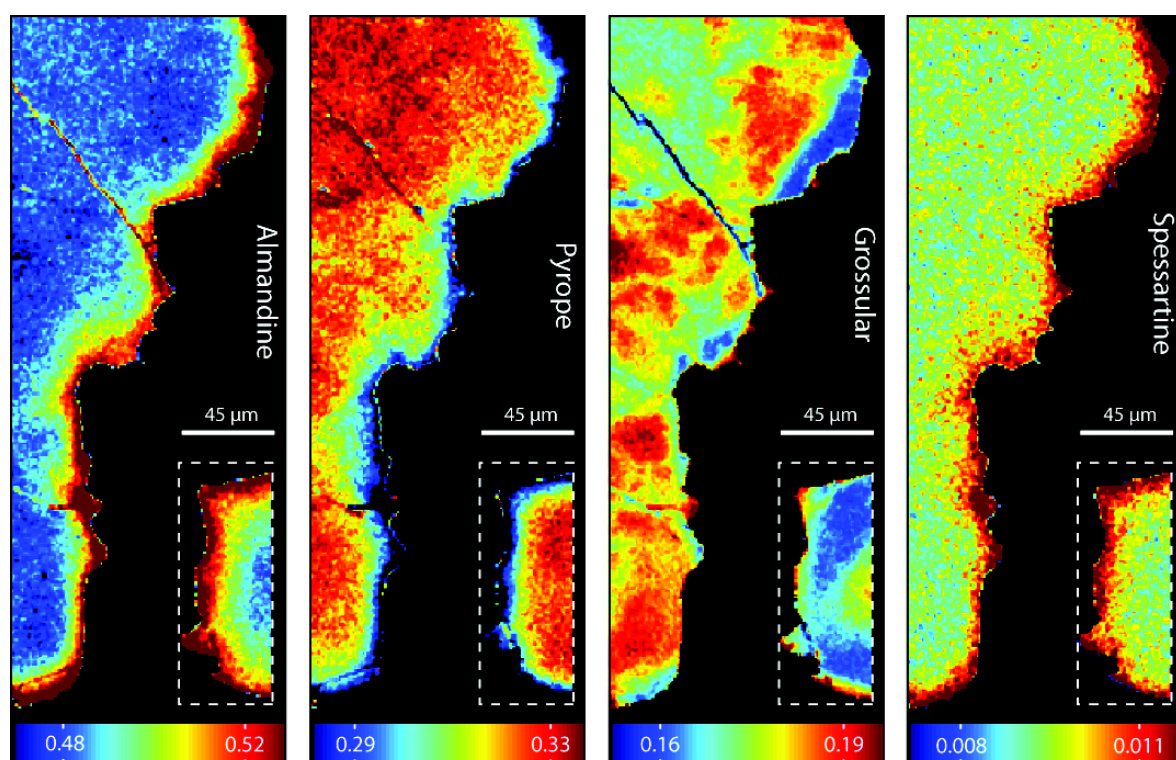


FIGURE 5.9 – Composition maps of garnet (reconstructing with the two garnet of the selected area) showing the fraction of end-members of garnet : Almandin , Pyrope, Grossular, Spessartine. The average composition of garnet is provided in the Table DR₃.

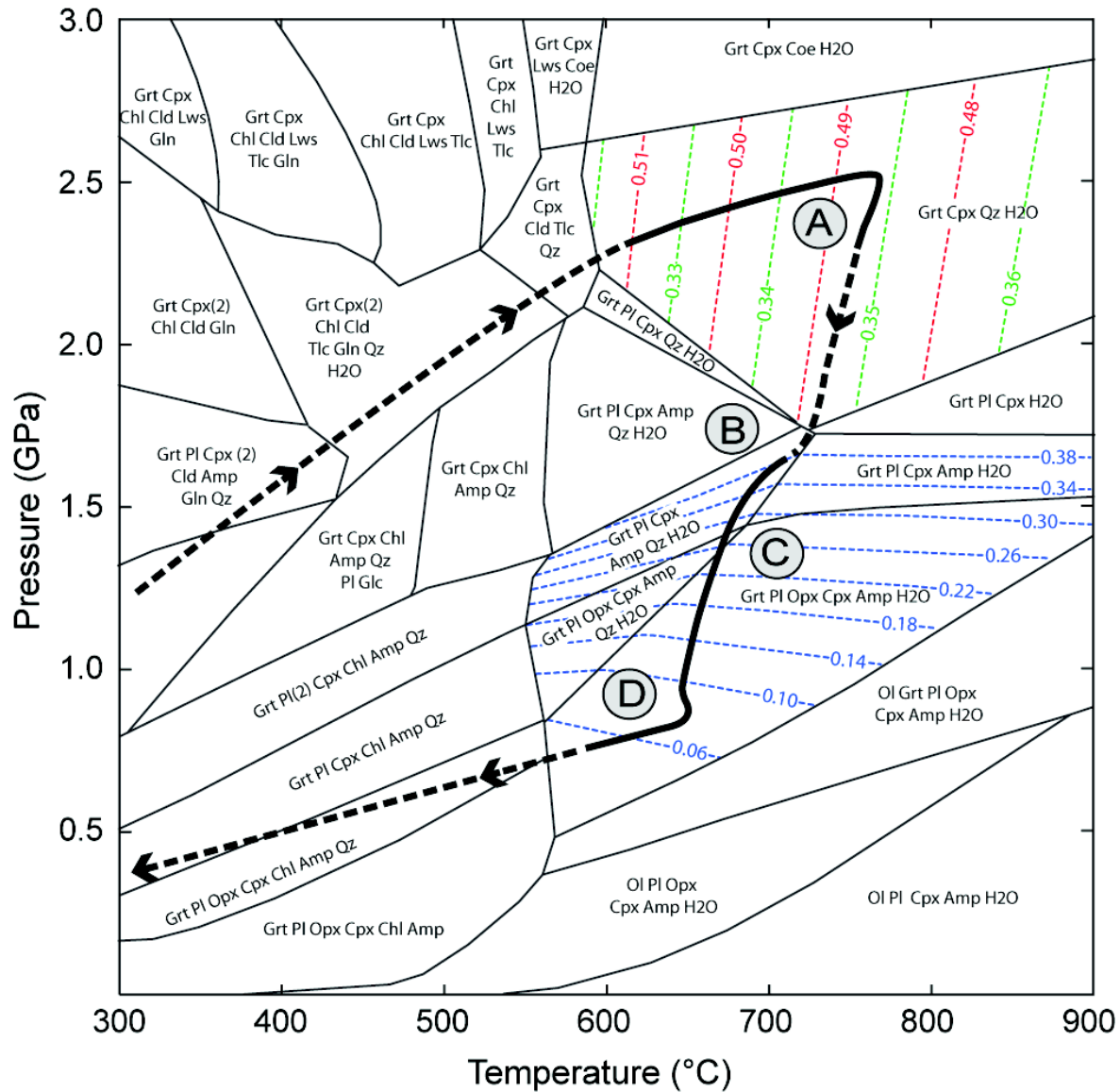


FIGURE 5.10 – Pseudosection computed from the local bulk composition (atomic fraction) : Si(0.8) Al(0.327) Fe(0.188) Mg(0.225) Ca(0.182) Na(0.097) O(?) H(0.1), in the system NCFMASHO using Teriak-Domino software. The proposed P-T path is shown by thick dashed black curves and solid curve (P-T path proposed in the Fig. 5.5 of the manuscript, the solid part is well defined). Iso-pletes for almandine component (X_{alm}) in red dashed lines, those for pyrope component (X_{pyr}) in green dashed lines and those for jadite component (X_{jad}) in clinopyroxene in blue dashed line were added. Grossular component (X_{gr}) is homogeneous in the field labeled A ($X_{gr} = 0.16$). Abbreviations used : Grt, Garnet ; Cpx, Clinopyroxene ; Qz, Quartz ; Coe, Coesite ; Pl, Plagioclase ; Amp, Amphibole ; Ol, Olivine ; Chl, Chlorite ; Opx, Orthopyroxene ; Cld, Chloritoid ; Tlc, Talc ; Lws, Lawsonite ; Gln, Glaucophane. A, B, C and D labels refer to the steps proposed in the manuscript (see Fig. 5.5). The measured bulk rock composition (atomic fraction) is : Si(0.78) Al(0.31) Fe(0.16) Mg(0.228) Ca(0.181) Na(0.100).

5.2.7.3 Supplementary tables

	Omp1	Omp2	Cpx1	Cpx2
SiO ₂	55.55	54.94	54.13	54.41
Al ₂ O ₃	12.01	11.92	10.09	6.81
FeO	3.35	4.11	4.60	4.89
MnO	0.03	0.03	0.03	0.03
MgO	8.84	8.88	9.94	12.19
CaO	13.65	13.82	16.07	18.68
Na ₂ O	5.76	5.60	4.36	2.64
K ₂ O	0.02	0.02	0.02	0.02
Formula based on 6 oxygen.				
Si(T1)	1.97	1.96	1.95	1.97
Al(T1)	0.03	0.04	0.05	0.03
Al(M1)	0.48	0.46	0.38	0.26
Mg(M1)	0.47	0.47	0.53	0.66
Fe(M1)	0.10	0.12	0.14	0.15
Ca(M2)	0.52	0.53	0.62	0.72
Na(M2)	0.40	0.39	0.30	0.19
XMg	0.82	0.79	0.79	0.82
XFe	0.18	0.21	0.21	0.18

TABLE 5.1 – Representative compositions and structural formulae of clinopyroxene. XMg = atomic ratio of Mg/(Mg + Fe²⁺) and XFe = atomic ratio of Fe/(Mg + Fe²⁺).

	Amp1	Amp2	Amp3
SiO ₂	44.61	44.63	43.36
Al ₂ O ₃	13.74	13.62	15.77
FeO	10.34	10.55	9.97
MnO	0.05	0.05	0.05
MgO	14.31	14.14	13.91
CaO	11.25	10.03	11.20
Na ₂ O	3.00	3.13	3.07
K ₂ O	0.52	0.93	0.54
Formula based on 23 oxygen.			
Si(T1)	4	4	4
Si(T2)	2.33	2.33	2.14
Al(T2)	1.67	1.67	1.86
Al(M2)	0.63	0.61	0.78
Mg(M2)	0.63	0.49	0.48
Fe(M2)	0.26	0.20	0.19
Fe3(M2)	0.48	0.70	0.54
Mg(M13)	2.06	2.01	2.07
Fe(M13)	0.83	0.84	0.83
Ca(M4)	1.71	1.52	1.70
Na(M4)	0.29	0.48	0.30
Na(A)	0.54	0.39	0.54
Vac(A)	0.46	0.61	0.46
XMg	0.71	0.70	0.71
XFe	0.29	0.30	0.29
XFe ³⁺	0.39	0.56	0.46

TABLE 5.2 – Representative compositions and structural formulae of amphibole. XMg = atomic ratio of Mg/(Mg + Fe²⁺); XFe = atomic ratio of Fe/(Mg + Fe²⁺); XFe³⁺ = Fe³⁺/(Fe²⁺ + Fe³⁺) and Vac(A) is the vacancy in the A site.

	Grt
<i>SiO</i> ₂	39.26
<i>Al</i> ₂ <i>O</i> ₃	22.85
<i>FeO</i>	23.05
<i>MnO</i>	0.46
<i>MgO</i>	8.52
<i>CaO</i>	6.58
<i>Na</i> ₂ <i>O</i>	0.04
<i>K</i> ₂ <i>O</i>	0.01
Formula based on 12 oxygen.	
<i>Si</i> (<i>O</i> / <i>T</i>)	2.97
<i>Al</i> (<i>Y</i>)	2.04
<i>Fe</i> (<i>X</i>)	1.46
<i>Mg</i> (<i>X</i>)	0.96
<i>Mn</i> (<i>X</i>)	0.03
<i>Ca</i> (<i>X</i>)	0.53
<i>XFe</i>	0.49
<i>XMg</i>	0.32
<i>XMn</i>	0.01
<i>XCa</i>	0.18

TABLE 5.3 – Representative composition and structural formula of garnet. *XMg* = atomic ratio of *Mg*/(*Mg* + *Fe*²⁺ + *Mn* + *Ca*); *XFe* = atomic ratio of *Fe*/(*Mg* + *Fe*²⁺ + *Mn* + *Ca*); *XMn* = atomic ratio of *Mn*/(*Mg* + *Fe*²⁺ + *Mn* + *Ca*) and *XCa* = atomic ratio of *Ca*/(*Mg* + *Fe*²⁺ + *Mn* + *Ca*).

	Mica
<i>SiO</i> ₂	48.64
<i>Al</i> ₂ <i>O</i> ₃	27.91
<i>FeO</i>	1.13
<i>MnO</i>	0.00
<i>MgO</i>	3.37
<i>CaO</i>	0.00
<i>Na</i> ₂ <i>O</i>	0.05
<i>K</i> ₂ <i>O</i>	11.34
Formula based on 12 oxygen.	
<i>Si</i> (<i>T</i> ₁ + <i>T</i> ₂)	3.31
<i>Al</i> (<i>T</i> ₂)	0.69
<i>Vac</i> (<i>M</i> ₁)	1.00
<i>Mg</i> (<i>M</i> ₁)	0.00
<i>Fe</i> ₂ + (<i>M</i> ₁)	0.00
<i>Al</i> (<i>M</i> ₂ + <i>M</i> ₃)	1.55
<i>Mg</i> (<i>M</i> ₂ + <i>M</i> ₃)	0.38
<i>Fe</i> (<i>M</i> ₂ + <i>M</i> ₃)	0.07
<i>K</i> (<i>A</i>)	0.98
<i>Na</i> (<i>A</i>)	0.01
<i>Vac</i> (<i>A</i>)	0.01

TABLE 5.4 – Representative composition and structural formula of mica. *Vac* is vacancy.

	Plagioclase
SiO_2	62.40
Al_2O_3	19.12
FeO	0.60
MnO	0.01
MgO	1.03
CaO	5.54
Na_2O	8.14
K_2O	0.09
Formula based on 8 oxygen.	
Si	2.86
Al	1.03
Na	0.72
Ca	0.27
K	0.01

TABLE 5.5 – Representative composition and structural formula of plagioclase.

CONCLUSION GÉNÉRALE

6

Au cours de ma thèse, j'ai développé plusieurs outils et techniques pour l'estimation des trajets P-T en combinant des approches d'imagerie chimique et de multi-équilibres. Puis dans un deuxième temps, ces outils ont été utilisés pour reconstituer l'histoire P-T d'échantillons métamorphiques des Alpes et de l'Himalaya.

Nous avons montré que les phyllosilicates sont de bons candidats pour l'estimation des trajets P-T dans les métapélites en utilisant la technique des multi-équilibres avec la base de données de [Berman \(1988\)](#). Les calculs d'équilibres thermodynamiques peuvent être réalisés en utilisant les deux logiciels proposés : PT-LINES et MULTIPLOT. Nous avons mis en évidence, grâce à de nombreux tests sur des échantillons naturels, certaines limites du modèle pour les chlorites de [Vidal et al. \(2006\)](#) à HT, qui soulignent la nécessité d'augmenter le nombre de contraintes avec, notamment, l'ajout de nouveaux pôles purs. Dans un deuxième temps, nous avons proposé un modèle de solution solide pour les chlorites tri/trioctahédriques et di/trioctahédriques, compatible avec la base de données et le formalisme de [Holland et Powell \(1998\)](#) et permettant de calculer des pseudosections ou encore de modéliser des interactions fluide/roche. À des fins thermobarométriques, un thermomètre a été proposé, basé sur la température de l'équilibre chl + qtz + H₂O à une pression donnée, en supposant un modèle d'activité idéale.

Nous avons présenté le Logiciel XMapTools. Il permet, en utilisant une équation de Castaing simplifiée (e.g. [De Andrade et al. 2006](#)), de standardiser des images chimiques, acquises à la microsonde avec les spectromètres WDS en cartes de concentrations, puis de les transformer en micro-cartographies P-T, en utilisant une approche de type multi-équilibres. Cette technique présente de nombreux avantages pour les études thermobarométriques, notamment en permettant de relier, à l'échelle de la lame mince, les variations de chimie et des conditions P-T avec les différentes phases de déformation. Les applications en Sciences de la Terre ne se limitent pas aux roches métamorphiques et nous avons proposé un exemple de l'étude des abondances modales des différentes phases dans les météorites.

Les outils et techniques présentés ont été utilisés pour reconstruire des trajets P-T d'unités métamorphiques de deux chaînes de montagnes de type subduction-collision, les Alpes et l'Himalaya. Pour la première, nous avons proposé des trajets P-T et des trajets P-T-t pour des zones où, jusqu'ici, faute de lithologies favorables, les conditions du métamorphisme et/ou les âges étaient peu contraints. Nous avons vu que l'association de la technique des multi-équilibres avec l'imagerie chimique permet de proposer des conditions P-T pour les différentes paragenèses identifiées. Cette étude fine a même permis de distinguer un trajet P-T enregistré dans des minéraux détritiques, en partie préservés lors du métamorphisme alpin. Cette étude pétrologique a été occasionnellement associée à une identification par spectrométrie Raman des T_{max} (enregistrées par la matière carbonée) et à des datations $^{40}\text{Ar}/^{39}\text{Ar}$ sur phengites. L'ensemble de ces nouvelles données, pour les unités d'origines continentale et océanique, a permis de mettre en évidence le couplage entre l'exhumation du prisme océanique et l'écaillage crustal de la plaque continentale subduite. Cet événement majeur, intervenant à 45 Ma, a probablement été causé par le changement de l'angle de la subduction, lié à la subduction de la paléo-marge briançonnaise. Puis nous avons étudié une éclogite himalayenne ayant subi une importante rétro-morphose dans le faciès des amphiboles, lors de la collision. Nous avons montré qu'il est possible de reconstituer un trajet P-T « continu » pour l'épisode de HP, à partir d'images chimiques en utilisant XMapTools et des calibrations empiriques.

Tous ces travaux mettent en évidence les apports de l'approche micro-cartographique pour la reconstruction des trajets P-T (et donc des modèles géodynamiques), mais également pour l'étude des processus de cristallisation des minéraux. En effet, il est possible, en la combinant avec des approches d'estimations P-T inverses, d'obtenir une image dynamique du métamorphisme. À l'inverse, les pseudosections sont calculées pour une composition donnée, souvent la composition de la roche totale. Cependant, la cristallisation de certains minéraux au cours du trajet P-T peut entraîner un changement de la composition « effective » (disponible pour cristalliser de nouveaux minéraux). Une pseudosection n'est donc valable en théorie que pour un instant, une pression et une température donnés, pour une

paragénèse parfaitement équilibrée pour laquelle on a utilisé la composition. Les cartes de concentrations obtenues après la standardisation permettent de calculer des compositions « locales » de micro-domaines, que l'on suppose à l'équilibre thermodynamique. Ces compositions peuvent être utilisées, pour chaque paragénèse supposée à l'équilibre, pour calculer par minimisation d'énergie une pseudosection et comparer l'assemblage observé avec celui prédit (ainsi que les compositions des minéraux) et ainsi déterminer des conditions P-T. Plusieurs grilles, avec des typologies différentes, seront donc obtenues pour chaque assemblage et non une seule grille permettant de reconstituer un trajet P-T. La micro-cartographie permet donc de faire le lien entre les approches d'estimation P-T directes et inverses, en les utilisant conjointement. Cependant, dans la pratique, ce couplage nécessite, pour la minimisation d'énergie, des modèles de solutions solides capables de pouvoir reproduire l'ensemble des compositions observées, ce qui n'est pas le cas à l'heure actuelle pour certaines solutions solides à l'image des amphiboles ou encore des micas.

BIBLIOGRAPHIE

- Abad I., Nieto F., Peacor D. R., et Velilla N. 2003. Prograde and retrograde diagenetic and metamorphic evolution in metapelitic rocks of Sierra Espuna (Spain). *Clay Minerals*, 38 : 1–23. (Cité page 85.)
- Agard P. 1999. Evolution métamorphique et structurale des métapélites océaniques dans l’orogène Alpin : l’exemple des Schistes lustrés des Alpes occidentales (Alpes cottiennes). *Thèse, Université d’Orsay*, pp. 278. (Cité pages 202 et 207.)
- Agard P., Goffé B., Touret J. L. R., et Vidal O. 2000. Retrograde mineral and fluid evolution in high-pressure metapelites (schistes lustrés unit, western alps). *Contributions to Mineralogy and Petrology*, 140 : 296–315. (Cité page 229.)
- Agard P., Jolivet L., et Goffé B. 2001a. Tectonometamorphic evolution of the Schiste Lustrés complex : implications for the exhumation of HP and UHP rocks in the Western Alps. *Bulletin de la Societe Geologique de France*, 172 : 617–636. (Cité pages 216, 218, 240, 251, 262 et 289.)
- Agard P., Monié L., Jolivet L., et Goffé B. 2002. Exhumation of the Schistes Lustrés complex : in-situ laser probe $^{40}\text{Ar}/^{39}\text{Ar}$ constraints and implications for the Western Alps. *Journal of Metamorphic Geology*, 20 : 599–618. (Cité pages 216, 240, 252, 262 et 289.)
- Agard P., Monié P., Gerber W., Omrani J., Molinaro M., Meyer B., Labrousse L., Vrielynck B., Jolivet L., et Yamato P. 2006. Transient, synobduction exhumation of Zagros blueschists inferred from P-T, deformation, time, and kinematic constraints : Implications for Neotethyan wedge dynamics. *Journal of Geophysical Research*, 111 : B11401. (Cité page 85.)
- Agard P., Vidal O., et Goffé B. 2001b. Interlayer and Si content of phengite in HP-LT carpholite-bearing metapelites. *Journal of Metamorphic Geology*, 19 : 479–495. (Cité pages 66 et 85.)
- Ai Y. 1994. A revision of the garnet-clinopyroxene Fe^{2+} Mg exchange geothermometer. *Contributions to Mineralogy and Petrology*, 115 : 467–473. (Cité pages 21 et 144.)
- Aillères L., Bertrand J. M., Macaudière J., et Champenois M. 1995. Structure de la zone Houillère Briançonnaise (Alpes Françaises), tectonique néoalpine et conséquences sur l’interprétation des Zones Penniques Frontales. *Comptes Rendu Académie des Sciences Paris*, 321 : 247–254. (Cité page 221.)
- Aitchison J. C., ali J. R., et Davis A. M. 2007. When and where did India and Asia collide? *Journal of Geophysical Research*, 112, B05423. (Cité page 293.)
- Amelin Y. 2005. Meteorite Phosphates Show Constant ^{176}Lu Decay Rate Since 4557 Million Years Ago. *Science*, 310 : 839–841. (Cité pages 162 et 186.)
- Amelin Y. et Rotenberg E. 2004. Sm-Nd systematics of chondrite. *Earth and Planetary Science Letters*, 223 : 267–282. (Cité pages 162 et 186.)

- Anadon P., Colombo F., Esteban M., Marzo M., Robles P., M. S. ans Santanach, et Solé-Sugranyes L. 1979. Evolución tectonoestratigráfica de los Catalánides. *Acta Geológica Hispánica*, 14 : 242–270. (Cité page 45.)
- Anceau A. 1992. Sudoite in some Visean (Lower Carboniferous) K-bentonites from Belgium. *Clay Minerals*, 27 : 283–292. (Cité page 91.)
- Anderson J. L. et Smith D. R. 1995. The effects of temperature and f_{O_2} on the Al-in-hornblende barometer. *American Mineralogist*, 80 : 549–559. (Cité page 144.)
- Angiboust S. 2011. Couplages profonds et comportement de la lithosphère océanique dans les zones de subduction : approches pétrologique et thermomécanique. *Thèse, Université Pierre et Marie Curie, Paris 6*. (Cité page 207.)
- Angiboust S., Langdon R., Agard P., Waters D. J., et Chopin C. 2011. Eclogitization of the Monviso ophiolite (W. Alps) and implications on subduction dynamics. *Journal of Metamorphic Geology*, 30 : 37–61. (Cité pages 252, 264, 288 et 289.)
- Aquilina L., Pauwels H., Genter A., et Fouillac C. 1997. Water-rock interaction processes in the Triassic sandstone and the granitic basement of the Rhine Graben : Geochemical investigation of a geothermal reservoir. *Geochimica et Cosmochimica Acta*, 61 : 4281–4295. (Cité page 96.)
- Argand E. 1916. Sur l’Arc des Alpes Occidentales. *Eclogae Geologicae Helvetiae*, 14 : 145–191. (Cité page 203.)
- Augier C., Agard P., Monié P., Jolivet L., Robin C., et Booth-Rea G. 2005a. Exhumation, doming and slab retreat in the Betic Cordillera (SE Spain) : in situ $^{40}\text{Ar}/^{39}\text{Ar}$ ages and P-T-d-t paths for the Nevado-Filabride complex. *Journal of Metamorphic Geology*, 23 : 357–381. (Cité pages 75 et 85.)
- Augier R., Booth-Rea G., Agard P., Martínez-Martínez J.M., Jolivet L., et Azañón J.M. 2005b. Exhumation constraints for the lower Nevado-Filabride Complex (Betic Cordillera, SE Spain) : a Raman thermometry and Twerqu multiequilibrium thermobarometry approach. *Bulletin de la Societe Geologique de France*, 176 : 403–416. (Cité pages 4 et 75.)
- Baboury D. 1999. Origine volcanogène des veines aurifères riches en sulfures de la mine Géant Dormant, Abitibi. *PhD thesis, Université du Québec à Chicoutimi*. (Cité page 85.)
- Baker J. et Holland T. J. B. 1996. Experimental reversals of chlorite compositions in divariant $\text{MgO-Al}_2\text{O}_3\text{-SiO}_2\text{-H}_2\text{O}$ assemblages. *American Mineralogist*, 81 : 676–684. (Cité pages 26, 66, 73, 75, 83, 86, 115 et 116.)
- Ballevre M. 1986. Collision continentale et chemins P-T. L’unité pennique du Grand Paradis (Alpes occidentales). *Thèse, Université de Rennes 1*. (Cité page 206.)
- Barfétý J.C., Polino R., Mercier D., Caby R., et Fourneaux J.C. 2006a. Carte géologique de la France au 1/50 000ème ; feuille de névache-bardonecchia-modane. *Feuille, Orléans*, pp. 799. (Cité pages 217, 218 et 220.)
- Barfétý J.C., Polino R., Mercier D., Caby R., et Fourneaux J.C. 2006b. Notice explicative de la feuille névache-bardonecchia-modane à 1/50,000. *BRGM Feuille, Orléans*, pp. 160. (Cité pages 218 et 220.)

- Barrat J. A., Zanda B., Moynier F., Bollinger C., Liorzou C., et Bayon G. 2012. Geochemistry of CI chondrites : Major and trace elements, and Cu and Zn Isotopes. *Geochimica et Cosmochimica Acta*, 83 : 79–92. (Cité pages [172](#), [173](#), [179](#), [180](#) et [182](#).)
- Barrow G. 1912. On the geology of the lower deeside and the southern highland border. *Proc. Geol. Assoc.*, 23 : 268–273. (Cité page [14](#).)
- Battaglia S. 2004. Variations in the chemical composition of illite from five geothermal fields : a possible geothermometer. *Clay Minerals*, 39 : 501–510. (Cité page [229](#).)
- Baudin T. 1987. Etude géologique du massif du Ruitor (Alpes Franco-Italiennes) : Evolution structurale d'un socle briançonnais. *Thèse, Université Scientifique et Médicale de Grenoble*. (Cité page [206](#).)
- Bearley A. J. et Jones R. H. 1998. Chondritic meteorites. *Reviews in Mineralogy*, 36. (Cité page [162](#).)
- Beaumont C., Ellis S., et Hamilton J. 1996. Mechanical model for subduction-collision tectonics of Alpine-type compressional orogens. *Geology*, 24 : 675–678. (Cité page [199](#).)
- Bellanger M. 2012. Evolution géodynamique de la marge dauphinoise à la latitude des massifs cristallins externe de Belledonne/Grandes Rousses/Ecrins-Pelvoux. *Thèse, Université d'Orléan*. (Cité page [288](#).)
- Belmar M. et Morata D. 2005. Nature and P-T-t constraints of very low-grade metamorphism in the Triassic-Jurassic basins, Coastal Range, central Chile. *Revista geológica de Chile*, 32 : 189–2005. (Cité page [85](#).)
- Benson S. W. 1968. Thermochemical kinetics. *John Wiley and Sons, New York*, pp. 223. (Cité page [360](#).)
- Berger A. et Bousquet R. 2008. Subduction-related metamorphism in the Alps : review of isotopic ages based on petrology and their geodynamic consequences. *Geological Society of London*, 298 : 117–144. (Cité pages [207](#) et [239](#).)
- Berman R. G. 1988. Internally-consistent thermodynamic data for minerals in the system Na₂O-K₂O-CaO-MgO-FeO-Fe₂O₃-Al₂O₃-SiO₂-TiO₂-H₂O-CO₂. *Journal of Petrology*, 29 : 445–522. (Cité pages [6](#), [22](#), [26](#), [30](#), [66](#), [67](#), [82](#), [115](#), [194](#), [306](#), [319](#) et [359](#).)
- Berman R. G. 1990. Mixing properties of Ca-Mg-Fe-Mn garnets. *American Mineralogist*, 75 : 328–344. (Cité page [30](#).)
- Berman R. G. 1991. Thermobarometry using multi-equilibrium calculations : a new technique with petrological applications. *Canadian Mineralogist*, 29 : 833–855. (Cité pages [4](#), [21](#), [23](#), [25](#), [26](#), [30](#), [31](#), [137](#), [145](#) et [255](#).)
- Berman R. G. 2007. WinTWQ (version 2.3) a software package for performing internally-consistent thermobarometric calculations. *Geological Survey of Canada, open file 5462*, pp. 41. (Cité page [30](#).)
- Berman R. G. et Brown T. 1984. A thermodynamic model for multicomponent melts, with application to the system CaO-Al₂O₃-SiO₂. *Geochimica et Cosmochimica Acta*, 48 : 661–678. (Cité pages [30](#) et [31](#).)

- Berman R. G. et Brown T. 1985. Heat capacity of minerals in the system Na₂O-K₂O-CaO-MgO-FeO-Fe₂O₃-Al₂O₃-SiO₂-TiO₂-H₂O-CO₂ : representation, estimation, and high temperature extrapolation. *Contributions to Mineralogy and Petrology*, 89 : 168–183. (Cité pages 30, 82, 112 et 359.)
- Bernet M. 2009. A field-based estimate of the zircon fission-track closure temperature. *Chemical geology*, 259 : 181–189. (Cité page 216.)
- Bernier F. 2011. Equilibrage des chlorites-micas-chloritoïdes dans des métasédiments du faciès schiste vert : étude de l’affleurement de Garvera (zone d’Urseren, Alpes centrales). *Mémoire, Université Joseph-Fourier Grenoble 1.*, pp. 35. (Cité pages 129 et 131.)
- Bertrand J. M. 1966. Etude géologique de la partie française du massif du Grand Paradis (Région de Bonneval sur Arc, Vanoise orientale). *Thèse, Université de Paris*, pp. 128. (Cité page 206.)
- Bertrand J. M., Aillères L., Gasquet D., et Macaudière J. 1996. The Pennine Front zone in Savoie (Western Alps) a review and new interpretations from the Zone Houillère Briançonnaise. *Eclogae Geol. Helv.*, 89 : 297–320. (Cité pages 220, 221 et 222.)
- Bertrand M. 1894. Etude dans les Alpes françaises. Structure en éventail, massifs amygdaloïdes et métamorphisme. Schistes lustrés de la zone centrale. *Bulletin de la Société Géologique de France*, 22 : 66–162. (Cité page 203.)
- Beyssac O., Bollinger L., Avouac J. P., et Goffé B. 2004. Thermal metamorphism in the lesser Himalaya of Nepal determined from Raman spectroscopy of carbonaceous material. *Earth and Planetary Science Letters*, 225 : 231–241. (Cité pages 225 et 264.)
- Beyssac O., Brunet F., Petitet J. P., Goffé B., et Rouzaud J. N. 2003a. Experimental study of the microtextural and structural transformations of carbonaceous materials under pressure and temperature. *European Journal of Mineralogy*, 15 : 937–951. (Cité pages 225 et 264.)
- Beyssac O., Goffé B., Chopin C., et Rouzaud N. 2002. Raman spectra of carbonaceous material in metasediments : a new geothermometer. *Journal of Metamorphic Geology*, 20 : 859–871. (Cité pages 211, 216, 224, 225, 226, 230, 237, 238, 264, 265 et 288.)
- Beyssac O., Goffé B., Petitet J. P., Froigneux E., Moreau M., et Rouzaud J. N. 2003b. On the characterisation of disordered and heterogeneous carbonaceous materials by Raman spectrometry. *Spectrochimica Acta*, 59 : 2267–2276. (Cité pages 225, 226 et 264.)
- Beyssac O., Simoes M., Avouac J. P., Farley K. A., Chen Y. G., et Goffé B. 2007. Late Cenozoic metamorphic evolution and exhumation of Taiwan. *Tectonics*, 26 (TC6001) : 32. (Cité pages 223, 224, 226 et 264.)
- Billault V., Beaufort D., Patrier-Mas P., et Petit S. 2002. Crystal chemistry of Fe-sudoites from uranium deposits in the Athabasca basin (Saskatchewan, Canada). *Clays and Clay Minerals*, 50 : 70–81. (Cité page 91.)
- Bishop B. P. et Bird D. K. 1987. Variation in sericite compositions from fracture zones within the Coso Hot Springs geothermal system. *Geochimica et Cosmochimica Acta*, 51 : 1245–1256. (Cité page 228.)

- Blichert-Toft J. et Albarède F. 1997. The Lu-Hf isotope geochemistry of chondrites and the evolution of the mantle-crust system. *Earth and Planetary Science Letters*, 148 : 243–258. (Cité page 160.)
- Blundy J. et Holland T. J. B. 1990. Calcic amphibole equilibria and a new amphibole-plagioclase geothermometer. *Contributions to Mineralogy and Petrology*, 104 : 208–224. (Cité page 144.)
- Bocquet J. 1974. Etude minéralogiques et pétrologiques sur les métamorphismes d'âge alpin dans les alpes françaises. *Thèse, Université Scientifique et Médicale de Grenoble*. (Cité pages 127 et 206.)
- Booth-Rea G., Azañón J. M., Goffé B., Vidal O., et Martínez-Martínez J. M. 2002. High-pressure, low-temperature metamorphism in Alpujarride Units of southeastern Betics (Spain). *Comptes Rendus de l'Académie des Sciences de Paris*, 334 : 857–865. (Cité page 85.)
- Bousquet R. 1998. L'exhumation des roches métamorphiques de haute pression - basse température : de l'étude de terrain à la modélisation numérique. Exemple de la fenêtre de l'Engadine et du domaine valaisan dans les Alpes Centrales. *Thèse, Université d'Orsay*, Orsay, pp. 200. (Cité page 207.)
- Bousquet R., Goffé B., Vidal O., Oberhänsli R., et Patriat M. 2002. The tectono-metamorphic history of the Valaisan domain from the Western to the Central Alps : New constraints on the evolution of the Alps. *GSA Bulletin*, 114 : 207–225. (Cité page 289.)
- Bousquet R., Oberhänsli R., Goffé B., Wiederkehr M., Koller F., Schmid S. M., Schuster R., Engi M., Berger A., et Martinotti G. 2008. Metamorphism of metasediments at the scale of an orogen : a key to the Tertiary geodynamic evolution of the Alps. In Siegesmund, S., Fügenschuh, B. and Froitzheim, N. (eds) *Tectonic Aspects of the Alpine-Dinaride-Carpathian System*; Geological Society, London, Special Publications, 298 : 393–411. (Cité pages 200, 210, 215, 250 et 251.)
- Bouvier A., Vervoort J. D., et Patchett P. J. 2008. The Lu-Hf and Sm-Nd isotopic composition of CHUR : Constraints from unequilibrated chondrites and implications for the bulk composition of terrestrial planets. *Earth and Planetary Science Letters*, 273 : 48–57. (Cité pages 160, 161, 162 et 186.)
- Brandon M. T., Roden-Tice M. K., et Garver J. I. 1998. Late Cenozoic exhumation of the Cascadia accretionary wedge in the Olympic Mountains, northwest Washington State. *GSA Bulletin*, 110 : 985–1009. (Cité page 216.)
- Brearley A. J. 1997. Disordered biopyriboles, amphibole, and talc in the Allende meteorite : Products of nebular or parent body aqueous alteration? *Science*, 276 : 1103–1105. (Cité pages 162 et 186.)
- Bryndzia L. T. et Scott L. D. 1987. The composition of chlorite as a function of sulfur and oxygen fugacity ; an experimental study. *American Journal of Science*, 287 : 50–76. (Cité page 26.)
- Bucher S. 2003. The Briançonnais units along the ECORS-CROP transect (Italian-French Alps) : structures, metamorphism and geochronology. *Thèse, Université de Basel, Suisse*, pp. 169. (Cité page 289.)

- Bucher S. et Bousquet R. 2007. Metamorphic evolution of the Briançonnais units along the ECORS-CROP profile (Western Alps) : new data on metasedimentary rocks. *Swiss Journal of Geosciences*, 100 : 227–242. (Cité pages 127, 129 et 289.)
- Bucher S., Schmid S. M., Bousquet R., et Fugenschuh B. 2003. Late stage deformation in a collisional orogen (Western Alps). Nappe refolding, back thrusting or normal faulting. *Terra Nova*, 15 : 109–117. (Cité pages 127, 129 et 289.)
- Bucher S., Ulardic C., Bousquet R., Ceriani S., Fugenschuh B., Gouffon Y., et Schmid S. M. 2004. Tectonic evolution of the Briançonnais units along a transect (ECORS-CROP) through the Italian-French Western Alps. *Eclogae Geologicae Helvetiae*, 97 : 321–345. (Cité page 127.)
- Caby R. 1996. Low-angle extrusion of high-pressure rocks and the balance between outward and inward displacements of Middle Penninic units in the western Alps. *Eclogae Geol. Helv.*, 89 : 229–267. (Cité pages 210, 218, 220, 221 et 252.)
- Caby R., Kienast J. R., et Saliot P. 1978. Structure métamorphique et modèle d'évolution tectonique des Alpes occidentales. *Rev. Géogr. Phys. Géol. Dyn.*, 20 : 307–322. (Cité page 207.)
- Calderon M., Galaz G., Tascon G., Ramirez C., Luca R., Zenk M., Brandelik A., et Hervé F. 2005. Metamorphic P-T constraints for non-coaxial ductile flow of Jurassic pyroclastic deposits : Key evidence for the closure of the Rocas Verdes Basin in Southern Chile. *6th International Symposium on Andean Geodynamics (ISAG 2005, Barcelona)*. (Cité page 85.)
- Cantarero I., Lanari P., Vidal O., Alias G., Travé A., et Baqués V. 2012. Evolution of the Vallès fault from chlorite and mica equilibrium. *VIII Congreso Geológico de España*. (Cité pages 7, 49, 50 et 85.)
- Cardellach E., Canals A., et Grandia F. 2002. Recurrent hydrothermal activity induced by successive extensional episodes : the case of the Berta F-(Pb-Zn) vein system (NE Spain). *Ore Geology Review*, 22 : 133–141. (Cité pages 42 et 46.)
- Caron J. M. 1970. Contribution à l'étude géologique de la région de sestrière (Alpes Cottiennes, Italie). *Thèse, Université d'Orsay, Orsay*, pp. 188. (Cité page 206.)
- Caron J. M. 1974. Les glissements synschisteux, reflets dans les Schistes lustrés de mouvements de socle ? (exemple dans les Alpes cottiennes septentrionales, France et Italie). *Géologie Alpine*, 50 : 45–55. (Cité page 266.)
- Caron J. M. 1977. Lithostratigraphie et tectonique des Schistes lustrés dans les Alpes cottiennes septentrionales (France et Italie). *Bulletin de la Société Géologique de France*, 7 : 255–263. (Cité page 206.)
- Caron J. M., Schumacher F., et Tricart P. 1973. Chronologie et évolution longitudinale des structures dans les Schistes lustrés des Alpes cottiennes (France et Italie). *Bulletin des Sciences géologiques*, 26 : 245–258. (Cité page 261.)
- Castaing R. 1951. Application des sondes électroniques à une méthode d'analyse ponctuelle chimique et cristallographique. *Thèse, Université de Paris*. (Cité pages 119, 121, 137 et 141.)
- Cathelineau M. 1988. Cation site occupancy in chlorites and illites as function of temperature. *Clay Minerals*, 23 : 471–485. (Cité pages 73, 74, 75, 86, 87, 88, 144, 227 et 228.)

- Cathelineau M. et Boiron M. C. 2010. Downward penetration and mixing of sedimentary brines and dilute hot waters at 5 km depth in the granite basement of Soultz-sous-Forêts (Rhine graben, France). *Comptes Rendus Geosciences*, 342 : 560–565. (Cité page 96.)
- Cathelineau M et Nieva D. 1985. A chlorite solid solution geothermometer the Los Azufres (Mexico) geothermal system. *Contributions to Mineralogy and Petrology*, 91 : 235–244. (Cité pages 73, 74, 85, 87, 88, 137, 144, 227 et 228.)
- Ceriani S. 2001. A combined study of structure and metamorphism in the frontal Penninic units between the Arc and Isère valley (Western Alps) : implications for the geodynamic evolution of the Western Alp. *Phd, Basel*, pp. 196. (Cité pages 207, 220 et 221.)
- Ceriani S., Fugenschuh B., Potel S., et Schmid S. 2003. Tectono-metamorphic evolution of the Frontal Penninic units of the Western Alps : correlation between low-grade metamorphism and tectonic phases. *Swiss Bull. Miner. Petrol.*, 83 : 111–131. (Cité pages 215 et 289.)
- Chatterjee N. D., Krüger R., Haller G., et Olbricht W. 1998. The bayesian approach to an internally consistent thermodynamic database : theory, database, and generation of phase diagrams. *Contributions to Mineralogy and Petrology*, 133 : 149–168. (Cité page 22.)
- Chaudhry M. N. et Ghazanfar M. 1987. Geology, structure and geomorphology of Upper Kaghan valley, Northwestern Pakistan. *Geological Bulletin University of Punjab*, 22 : 13–57. (Cité page 295.)
- Chermak J. A. et Rimstidt J. D. 1989. Estimating the thermodynamic properties (DGf and DHf) of silicate minerals at 298 K from the sum of polyhedral contributions. *American Mineralogist*, 74 : 1023–1031. (Cité page 112.)
- Chopin C. 1979. De la Vanoise au massif du Grand Paradis, une approche pétrographique et radiochronologique de la signification géodynamique du métamorphisme de haute pression. *Thèse, Université Pierre et Marie Curie, Paris 6*, pp. 145. (Cité pages 85 et 206.)
- Chopin C. 1984. Coesite and pure pyrope in high-grade blueschists of the Western Alps. *Contributions to Mineralogy and Petrology*, 86 : 107–118. (Cité pages 206, 214 et 294.)
- Chopin C., C. Henryn, et Michard A. 1991. Geology and petrology of the coesite-bearing terrain, Dora Maira massif, Western Alps. *European Journal of Mineralogy*, 3 : 263–291. (Cité page 289.)
- Chopin C. et Schreyer W. 1983. Magnesiochloritoid and magnesiochloritoid : Two index minerals of pelitic blueschists and their preliminary phase relations in the model system MgO-Al₂O₃-SiO₂-H₂O. *American Journal of Science*, 283 : 72–96. (Cité page 26.)
- Coggon R. et Holland T. J. B. 2002. Mixing properties of phengitic micas and revised garnet-phengite thermobarometers. *Journal of Metamorphic Geology*, 20 : 683–696. (Cité pages 66, 81, 83, 92, 96, 113 et 143.)
- Compagnoni R. et Maffeo B. 1973. Jadeite-bearing metagranites l.s. and related rocks in the Mount Mucrone Area (Sesia-Lanzo Zone, Western Italian Alps). *Schweizerische mineralogische und petrographische Mitteilungen*, 53 : 355–378. (Cité page 206.)
- Coney P. J. 1970. The geotectonic cycle and the new global tectonics. *Geological Society of America Bulletin*, 81 : 739–748. (Cité pages 3 et 199.)

- Coney P. J. 1972. Cordilleran tectonics and North American plate motions. *American Journal of Science*, 272 : 462–465. (Cité page 3.)
- Connolly J. A. D. 1990. Multivariable phase-diagrams - an algorithm based on generalized thermodynamics. *American Journal of Science*, 290 : 666–718. (Cité pages 5, 67 et 68.)
- Connolly J. A. D. 2005. Computation of phase equilibria by linear programming : A tool for geodynamic modeling and its application to subduction zone decarbonation. *Earth and Planetary Science Letters*, 236 : 524–541. (Cité pages 5, 67, 68, 75, 91 et 250.)
- Connolly J. A. D. 2009. The geodynamic equation of state : What and how. *Geochemistry Geophysics Geosystems*, 10, Q10014. (Cité pages 5, 67, 68, 75 et 91.)
- Connolly J. A. D. et Kerrick D. M. 1987. An algorithm and computer program for calculating composition phase diagrams. *CALPHAD*, 11 : 1–55. (Cité pages 5, 67 et 68.)
- Connolly J. A. D. et Petrini K. 2002. An automated strategy for calculation of phase diagram sections and retrieval of rock properties as a function of physical conditions. *Journal of Metamorphic Geology*, 20 : 697–708. (Cité pages 75 et 91.)
- Corsini M., Ruffet G., et Caby R. 2004. Alpine and late-hercynian geochronological constraints in the Argentera Massif (Western Alps). *Eclogae Geologicae Helvetiae*, 97 : 3–15. (Cité page 251.)
- Coward R. A. et Dietrich D. 1989. Alpine tectonics – an overview. In “Alpine tectonic”, Special publication, 45 (eds. Coward, M., Dietrich, D. and Park, R. G.). *Geol. Soc.*, pages 1–29. (Cité page 203.)
- Creighton S. 2009. A semi-empirical manganese-in-garnet single crystal thermometer. *Lithos*, 112 : 177–182. (Cité page 144.)
- Dahl P.S. 1980. The thermal-compositional dependence of Fe²⁺ Mg distributions between coexisting garnet and pyroxene : applications to geothermometry. *American Mineralogist*, 65 : 866. (Cité pages 21 et 144.)
- Dal Piaz G. V., Hunziker J. C., et Martinotti G. 1972. La zona Sesia-Lanzo e l'evoluzione tettonico-metaorfica delle Alpi Nordoccidentali interne. *Mem. Soc. Geol. It.*, 11 : 433–460. (Cité page 206.)
- Dale J., Holland T. J. B., et Powell R. 2000. Hornblende–garnet–plagioclase thermobarometry : a natural assemblage calibration of the thermodynamics of hornblende. *Contributions to Mineralogy and Petrology*, 140 : 353–362. (Cité pages 143, 150 et 305.)
- Dale J., Powell R., White W. M., Elmer F., et Holland T. J. B. 2005. A thermodynamic model for Ca–Na clinoamphiboles in Na₂O–CaO–FeO–MgO–Al₂O₃–SiO₂–H₂O–O for petrological calculations. *Journal of Metamorphic Geology*, 23 : 771–791. (Cité pages 96, 143 et 150.)
- Davidson J., Lauretta D. S., et D. L. S. 2012. Compositional variations in silicate phases within the CV and CK carbonaceous. *Lunar and Planetary Science Conference. The Woodlands, Texas*. (Cité page 163.)
- De Andrade V. 2006. De l'imagerie chimique à la micro-cartographie Pression-Température-Déformation : évolution minéralogique et transport de matière dans des systèmes en déséquilibre thermomécanique. *Thèse, Université Joseph Fourier of Grenoble*. (Cité pages 4, 26, 50, 52, 61, 121, 122, 124, 125 et 134.)

- De Andrade V, Vidal O, Lewin E, O'Brien P, et Agard P. 2006. Quantification of electron microprobe compositional maps of rock thin sections : an optimized method and examples. *Journal of Metamorphic Geology*, 24 : 655–668. (Cité pages 4, 7, 94, 122, 123, 124, 137, 139, 141, 152, 156, 164, 167, 194, 216, 226, 227, 254, 302, 309 et 319.)
- De Capitani C. et Brown T. 1987. The computation of chemical equilibrium in complex systems containing non-ideal solutions. *Geochimica et Cosmochimica Acta*, 51 : 2639–2652. (Cité pages 30, 67 et 68.)
- De Capitani C. et Petrakakis K. 2010. The computation of equilibrium assemblage diagrams with Theriak/Domino software. *American Mineralogist*, 95 : 1006–1016. (Cité pages 30, 67, 68, 75 et 306.)
- de Caritat P., Huchon P., et Walshe J. L. 1993. Chlorite geothermometry ; a review. *Clays and Clay Minerals*, 41 : 219–239. (Cité pages 73, 74, 75 et 86.)
- de Sigoyer J., Chavagnac V., Blichert-Toft J., Villa M., Luais B., Guillot S., Cosca M., et Mascle G. 2000. Dating the Indian continental subduction and collisional thickening in the northwest Himalaya : multichronology of the Tso Moriri eclogites. *Geology*, 28 : 487–490. (Cité pages 293 et 295.)
- Debelmas J. 1955. Les zones subbriançonnaises et briançonnaises occidentales entre Val-louise et Guillestre (Hautes-Alpes). *Mémoires S. carte géologique de la France*, pp. 171. (Cité pages 203 et 212.)
- Debelmas J. 1980. Carte géologique de la France au 1/250 000 : Feuille d'Annecy. *BRGM Feuille, Orléans*. (Cité page 200.)
- Desio A. 1977. The occurrence of blueschists between the middle Indus and the Swat Valleys as an evidence of subduction (North Pakistan). *Accademia Nazionale dei Lincei*, 8 : 1–9. (Cité page 293.)
- Detraz G. 1984. Etude géologique du bord interne de la zone Houillère Briançonnaise entre la vallée de l'Arc et le massif de Peclet-Polset (Alpes de Savoie). *Thèse - Université scientifique et médicale de Grenoble*, pp. 163. (Cité pages 206, 220 et 221.)
- Deville E. 1987. Etude géologique en Vanoise orientale (Alpes occidentales françaises, Savoie). De la naissance à la structuration d'un secteur de la paléomarge européenne et de l'océan Téthysien : aspects stratigraphiques, pétrographiques et tectoniques. *Thèse, Université de Savoie*, pp. 297. (Cité page 206.)
- Dewey J. M., J. F. and Bird. 1970. Mountain belts and the new global tectonics. *Journal of Geophysical Research*, 75 : 2625–2647. (Cité pages 3, 199 et 293.)
- Di Vincenzo G. 2004. The Relationship between Tectono-metamorphic Evolution and Argon Isotope Records in White Mica : Constraints from in situ ^{40}Ar - ^{39}Ar Laser Analysis of the Variscan Basement of Sardinia. *Journal of Petrology*, 45 : 1013–1043. (Cité page 251.)
- Dickenson M. et Hewett D. 1986. A garnet-chlorite geothermometer. *Geological Society of America ; Abstract*, 18 : 584. (Cité page 144.)
- Dolejs D. et Wagner T. 2008. Thermodynamic modeling of non-ideal mineral-fluid equilibria in the system Si-Al-Fe-Mg-Ca-Na-K-H-O-Cl at elevated temperatures and pressures : Implications for hydrothermal mass transfer in granitic rocks. *Geochimica et Cosmochimica Acta*, 72 : 526–553. (Cité page 96.)

- Dorogokupets P. I., Karpov I. K., Lashkevich V. V., Naigebauer V. A., et Kazmin L. A. 1988. Isobaric-isothermal potentials of minerals, gases and aqueous species in the "Selektor" program package. In : *Physicochemical models in geochemistry* (eds. Kiselev A.I. and Karpov I.K.), Nauka Publ., Novosibirsk,, pages 124–147. (Cité page 361.)
- Drits V. A. et McCarty D. K. 2007. The nature of structure-bonded H₂O in illite and leucophyllite from dehydration and dehydroxylation experiments. *Clays and Clay Minerals*, 55 : 45–58. (Cité pages 29, 33, 34 et 229.)
- Dubacq B. 2008. Thermodynamique des phyllosilicates de basse température : de l'approche macroscopique à la simulation atomistique. *Thèse, Université Joseph-Fourier de Grenoble*, pp. 253. (Cité pages 4, 26 et 49.)
- Dubacq B., Vidal O., et De Andrade V. 2010. Dehydration of dioctahedral aluminous phyllosilicates : thermodynamic modelling and implications for thermobarometric estimates. *Contributions to Mineralogy and Petrology*, 159 : 159–174. (Cité pages 4, 27, 28, 29, 33, 34, 37, 39, 42, 43, 55, 83, 116, 143, 211, 216, 229, 231, 236, 242, 245, 247, 255, 271, 272, 273 et 276.)
- Duchene S., Blichert-Toft J., Luais B., Lardeaux J. M., Télouk P., et Albarède F. 1997. The Lu-Hf dating of Alpine eclogites. *Nature*, 387 : 586–589. (Cité page 289.)
- Dumont T., Schwartz S., Guillot S., Simon-Labric T., Tricart P., et Jourdan S. 2012. Structural and sedimentary records of the Oligocene revolution in the Western Alpine arc. *Journal of Geodynamics*, 56-57 : 18–38. (Cité pages 200, 250, 251, 259, 261 et 285.)
- Dupuis M. 2012. Macro et microstructure de l'éventail briançonnais. *Mémoire, Université de Lille 1*. (Cité pages 125, 126, 127, 128 et 133.)
- Ellenberger F. 1958. Etude géologique du pays de Vanoise. *Mémoire explic. carte géol. Fr.*, pp. 161. (Cité page 206.)
- Ellenberger F. 1963. La Vanoise, un géanticlinal métamorphique. *Mémoire HS soc. géol. Fr.*, 2 : 383–393. (Cité page 206.)
- Ellis D. J. et Green D. H. 1979. An experimental study of the effect of Ca upon garnet-clinopyroxene Fe-Mg exchange equilibria. *Contributions to Mineralogy and Petrology*, 71 : 13–22. (Cité pages 21 et 144.)
- Ernst W.G. 1971. Metamorphic zonation on presumably subducted lithospheric plates from Japan, Californie and the Alps. *Contributions to Mineralogy and Petrology*, 34 : 43–59. (Cité pages 199 et 206.)
- Eskola P. 1915. Om sambandet mellan kemisk och mineralogisk sammansättning hos orijärvitraktens metamorfa bergarter. *Bull. Comm. geol. Finl.*, 44. (Cité pages 14 et 294.)
- Eskola P. 1921. The mineral facies of rocks. *Norsk Geologisk Tidsskrift*, 6 : 143–194. (Cité pages 14 et 294.)
- Fabre J. 1961. Contribution à l'étude de la zone houillère en Maurienne et en Tarentaise (Alpes de Savoie). *Mémoire BRGM*, pp. 315. (Cité page 206.)
- Fabre R. 1982. Le paléozoïque briançonnais au Nord de Névache : analyse des déformations alpines dans un secteur axial de la zone briançonnaise. *Thèse - Université scientifique et médicale de Grenoble*, pp. 397. (Cité pages 206, 219 et 220.)

- Fabre R., Gidon M., et Tricart P. 1982. La structure du paléozoïque de la zone briançonnaise axiale au Nord de Névache. *Géologie Alpine*, 58 : 31–52. (Cité pages 219, 220, 221, 222 et 237.)
- Ford M., Duchene S., Gasquet D., et Vanderhaegue O. 2006. Two-phase orogenic convergence in the external and internal SW Alps. *Journal of the Geological Society, London*, 163 : 815–826. (Cité pages 217 et 285.)
- Franceschelli M., Mellini M., et Memmi I. 1989. Sudoite, a rock-forming mineral in Verucano from the Northern Apennines (Italy) and the sudoite-chloritoid-pyrophyllite assemblage in prograde metamorphism. *Contributions to Mineralogy and Petrology*, 101 : 274–279. (Cité page 91.)
- Fransolet A. et Schreyer W. 1984. Sudoite, di/trioctahedral chlorite : A stable low-temperature phase in the system $\text{MgO-Al}_2\text{O}_3\text{-SiO}_2\text{-H}_2\text{O}$. *Contributions to Mineralogy and Petrology*, 86 : 409–417. (Cité page 91.)
- Freeman S. R., Inger S., Butler R. W. H., et Cliff R. A. 1997. Dating deformation using Rb-Sr in white mica : Greenschist facies deformation ages from the Entrelor shear zone. *Tectonics*, 16 : 57–76. (Cité page 239.)
- Frey M. 1974. Alpine Metamorphism of Pelitic and Marly Rocks of the Central Alps. *SMPM*, 54 : 489–506. (Cité page 129.)
- Frey M. 1978. Progressive Low-Grade Metamorphism of a Black Shale Formation, Central Swiss Alps, with Special Reference to Pyrophyllite and Margarite Bearing Assemblages. *Journal of Petrology*, 19 : 95–135. (Cité page 129.)
- Frey M., Desmond J., et Neubauer F. 1999. The new metamorphic map of the Alps ; 1 : 500000 ; 1 : 1000000. *Schweizerische mineralogische und petrographische Mitteilungen*, 79 : 230. (Cité pages 129, 215, 218 et 238.)
- Frey M. et Ferreiro Mählmann R. 1999. Alpine metamorphism of the Central Alps. *Schweizerische mineralogische und petrographische Mitteilungen*, 79 : 135–154. (Cité pages 129 et 210.)
- Frey M., Saunders J., et Schwander H. 1988. The mineralogy and metamorphic geology of low grade metasediments, Northern Range, Trinidad. *Geological Society of London*, 145 : 563–575. (Cité page 27.)
- Fritz B., Jacquot E., Jacquemont B., Baldeyrou-Bailly A., Rosener M., et Vidal O. 2010. Geochemical modeling of fluid-rock interactions in the context of the Soultz-sous-Forêts geothermal system. *Comptes Rendus Geosciences*, 342 : 653–667. (Cité pages 96 et 98.)
- Fudral S. 1973. Contribution à l'étude de l'unité de Moutier (zone des brèches de Tarantaise) entre le vallon du torrent du Cormet d'Arêches et le hameau des Chapieux (Savoie) - Alpes françaises. *Thèse, Université Scientifique et Médicale de Grenoble*, pp. 141. (Cité page 206.)
- Fügenschuh B. et Schmid S.M. 2003. Late stages of deformation and exhumation of an orogeny constrained by fission-track data : a case study in the western alps. *GSA Bulletin*, 115 : 1425–1440. (Cité pages 215 et 239.)
- Gabalda S. 2008. Processus d'exhumation dans les alpes occidentales : modélisation géométrique et reconstitution géodynamique sur la transversale chartreuse-maurienne, une approche multi-échelle. *Phd thesis*, pp. 175. (Cité pages 217 et 241.)

- Gabalda S., Beyssac O., Jolivet L., Agard P., et Chopin C. 2009. Thermal structure of a fossil subduction wedge in the western alps. *Terra Nova*, 21 : 28–34. (Cité pages 94, 200, 207, 214, 215, 216, 217, 218, 221, 224, 251, 258, 286 et 288.)
- Gabudianu Radulescu I., Rubatto D., Gregory C., et Compagnoni R. 2009. The age of HP metamorphism in the Gran Paradiso Massif, Western Alps : A petrological and geochronological study of "silvery micaschists". *Lithos*, 110 : 95–108. (Cité page 289.)
- Ganguly J. 1979. Garnet and clinopyroxene solid solutions, and geothermometry based on Fe-Mg distribution coefficient. *Geochimica et Cosmochimica Acta*, 43 : 1021–1029. (Cité pages 21 et 144.)
- Ganne J. 2003. Les domes de socles HP-BT dans le domaine Pennique des Alpes nord-occidentales (massifs d'Ambin et de Vanoise Sud) : modalités de leur exhumation. *Thèse, Université de Savoie*, pp. 309. (Cité pages 207, 214, 216, 239 et 289.)
- Ganne J., Bertrand J. M., et Fudral S. 2005. Fold interference pattern at the top of basement domes and apparent vertical extrusion of HP rocks (Ambin and South Vanoise massifs, Western Alps). *Journal of structural geology*, 27 : 553–570. (Cité pages 210, 214, 216 et 284.)
- Ganne J., Bertrand J. M., Fudral S., Marquer D., et Vidal O. 2007. Structural and metamorphic evolution of the Ambin massif (western Alps) : toward a new alternative exhumation model for the Briançonnais domain. *Bulletin de la Société Géologique de France*, 178 : 437–458. (Cité pages 210, 214, 216, 239, 258, 259 et 284.)
- Ganne J., Bussy F., et Vidal O. 2003. Multi-stage garnet in the internal Briançonnais basement (Ambin Massif, Savoy) : new petrological constraints on the blueschist-facies metamorphism in the Western Alps and tectonic implications. *Journal of Petrology*, 44 : 1281. (Cité pages 4, 75, 214, 216 et 239.)
- Ganne J., De Andrade V., Weinberg R. F., Vidal O., Dubacq B., Kagambega N., Naba S., Baratoux L., Jessell M., et Allibon J. 2012. Modern-style plate subduction preserved in the palaeoproterozoic west african craton. *Nature*, 5 : 60–65. (Cité pages 4 et 75.)
- Gardonio B. 2012. Estimation des conditions P-T dans des métasédiments ; étude de l'affleurement de Garvera (zone d'Ureseren, Alpes centrales). *Mémoire, Université Joseph-Fourier Grenoble 1*. (Cité pages 129, 131 et 133.)
- Gasco I., Borghi A., et Gattiglio M. 2010. Metamorphic evolution of the Gran Paradiso Massif : A case study of an eclogitic metagabbro and a polymetamorphic glaucophane-garnet micaschist. *Lithos*, 115 : 101–120. (Cité page 289.)
- Geiger T. et Bischoff A. 1994. Formation of opaque minerals in CK chondrites. *Planetary and Space Science*, 43 : 485–498. (Cité page 186.)
- Gerber W. 2008. Evolution tectono-métamorphique du briançonnais interne : comportement du socle et de sa couverture dans un contexte de subduction continentale profonde. *Phd, Université Pierre et Marie Curie (Paris)*, pp. 306. (Cité pages 207, 214, 216, 239, 241, 258, 259, 284 et 289.)
- Ghiorso M. S. et Sack R. O. 1995. Chemical mass transfer in magmatic processes iv. a revised and internally consistent thermodynamic model for the interpolation and extrapolation of liquid-solid equilibria in magmatic systems at elevated temperatures and pressures. *Contributions to Mineralogy and Petrology*, 119 : 197–212. (Cité page 22.)

- Gignoux M. 1938. Description géologique du bassin supérieur de la durance. *Travaux du laboratoire de la Faculté des Sciences de l'Université de Grenoble*, 21. (Cité page 203.)
- Gillet P., Choukroune P., Ballèvre M., et Davy P. 1986. Thickening history of the western alps. *Earth and Planetary Science Letters*, 78 : 44–52. (Cité page 207.)
- Gillet P., Ingrin J., et Chopin C. 1984. Coesite in subducted continental crust : P-T history deduced from an elastic model. *Earth and Planetary Science Letters*, 70 : 426–436. (Cité page 206.)
- Giorgetti G., Goffé B., Memmi I., et Nieto F. 1998. Metamorphic evolution of Verrucano metasediments in northern Apennines : new petrological constraints. *European Journal of Mineralogy*, 10 : 1295–1308. (Cité page 27.)
- Glodny J., Lohrmann J., Echtler H., Grafe K., Seifert W., Collao S., et Figueroa O. 2005. Internal dynamics of a paleoaccretionary wedge : insights from combined isotope tectonochronology and sandbox modelling of the South-Central Chilean forearc. *Earth and Planetary Science Letters*, 231 : 23–39. (Cité page 241.)
- Godard G. 2001. Eclogites and their geodynamic interpretation : a history. *Journal of Geodynamics*, 32 : 165–203. (Cité page 294.)
- Goffé B. 1975. Etude structurale et pétrographique du versant occidental du massif paléozoïque de Chasseforêt (Vanoise méridionale). *Thèse, Université d'Orsay, Orsay*, pp. 186. (Cité page 206.)
- Goffé B. 1982. Définition du faciès Fe-Mg carpholite-chloritoid, un marqueur du métamorphisme de HP-BT dans les métasédiments alumineux. *Phd, Université de Paris VI*. (Cité page 91.)
- Goffé B et Bousquet R. 1997. Ferrocarpholite, chloritoïde et lawsonite dans les métapélites des unités du Versoyen et du Petit St Bernard (zone valaisanne, Alpes occidentales). . *Schweizerische mineralogische und petrographische Mitteilungen*, 77 : 137–147. (Cité pages 85 et 289.)
- Goffé B., Michard A., Kienast J. R., et Le Mer O. 1988. A case of obduction-related high pressure, low temperature metamorphism in upper crustal nappes, Arabian continental margin. Oman : P-T paths and kinematic interpretation. *Tectonophysics*, 151 : 363 :386. (Cité page 91.)
- Goffé B., Schwartz S., Lardeaux J. M., et Bousquet R. 2004. Explanatory notes to the map : metamorphic structure of the Alps western and Ligurian Alps. *Mitt. Osterr. Miner. Ges.*, 149 : 125–144. (Cité pages 210, 215, 218 et 251.)
- Goldman D. et Albee A. 1977. Correlation of Mg/Fe partitioning between garnet and biotite with O18/O16 partitioning between quartz and magnetite. *American Journal of Science*, 277 : 761. (Cité page 144.)
- Goldstein J. 2003. Scanning electron microscopy and x-ray microanalysis. *Kluwer Academic and Plenum Publishers*, pp. 689. (Cité page 130.)
- Gottschalk M. 1997. Internally consistent thermodynamic data for minerals in the system SiO₂-TiO₂-Al₂O₃-Fe₂O₃-CaO-MgO-FeO-K₂O-Na₂O-H₂O-CO₂. *European Journal of Mineralogy*, 9 : 175–223. (Cité page 22.)

- Graciansky P. C., Roberts D. G., et Tricart P. 2010. The Western Alps. From Rift to Passive Margin to Orogenic Belt : An Integrated Geoscience Overview. *Elsevier*, pp. 429. (Cité page 218.)
- Graham C. et Powell R. 1984. A garnet-hornblende geothermometer : calibration, testing, and application to the Pelona Schist, Southern California. *Journal of Metamorphic Geology*, 2 : 13–31. (Cité page 144.)
- Grambling J. A. 1990. Internally-consistent geothermometry and H₂O barometry in metamorphic rocks : the example garnet-chlorite-quartz. *Contributions to Mineralogy and Petrology*, 105 : 617–628. (Cité page 144.)
- Green D. H. et Hellman P. 1982. Fe-Mg partitioning between coexisting garnet and phengite at high pressure, and comments on a garnet-phengite geothermometer. *Lithos*, 15 : 253–266. (Cité pages 66 et 144.)
- Greenwood R. C., Franchi I. A., Kearsley A. T., et Alard O. 2010. The relationship between CK and CV chondrite. *Geochimica et Cosmochimica Acta*, 74 : 1684–1705. (Cité pages 162, 163 et 189.)
- Groppo C., Lombardo B., Rolfo F., et Pertusati P. 2007. Clockwise exhumation path of granulitized eclogites from the Ama Drime range (Eastern Himalayas). *Journal of Metamorphic Geology*, 25 : 51–75. (Cité page 295.)
- Grosch E. G., Vidal O., Abu-Alam T., et McLoughlin N. 2012. PT-Constraints on the metamorphic evolution of the Paleoproterozoic Kromberg type-section, Barberton Greenstone Belt, South Africa. *Journal of Petrology*, 53 : 513–545. (Cité pages 4, 49, 52 et 75.)
- Gueymard E. 1830. Sur la minéralogie et la géologie du département des Hautes-Alpes. *Rapport, Grenoble*. (Cité page 203.)
- Guggenheim E.A. 1966. Statistical thermodynamics. *Oxford University Press, London*, pp. 184. (Cité pages 30, 31, 67 et 69.)
- Guillot F. 1987. Géologie de l'Antépermien de Vanoise septentrionale (zone briançonnaise interne, Savoie, France). *Thèse, Université des Sciences et Technologie de Lille 1*, pp. 280. (Cité page 206.)
- Guillot F., Bertrand J.M., Bussy F., Lanari P., L. Cosma, et Pin C. 2012. Early variscan i-type pluton in the pre-alpine basement of the western alps : The ca. 360 Ma cogne diorite (nw-italy). *Lithos*, in press. (Cité page 289.)
- Guillot S., de Sigoyer J., Lardeaux J. M., et Mascle G. 1997. Eclogitic metasediments from the Tso Moriri area (Ladakh, Himalaya) : evidence for continental subduction during India-Asia convergence. *Contributions to Mineralogy and Petrology*, 128 : 197–212. (Cité page 295.)
- Guillot S., Garzanti E., Baratoux D., Marquer D., Mahéo G., et de Sigoyer J. 2003. Reconstructing the total shortening history of the NW Himalaya. *Geochemistry Geophysics Geosystems*, 4 : 22. (Cité page 293.)
- Guillot S., Hattori K., Agard P., Schwartz S., et Vidal O. 2009. Exhumation processes in oceanic and continental subduction contexts : a review. In : Lallemand, S., Funiciello, F. (Eds.), Subduction Zone Dynamics. *Springer-Verlag, Berlin Heidelberg*, pages 175–204. (Cité pages 214, 294 et 307.)

- Guillot S., Lardeaux J. M., Mascle G., et Colchen M. 1995. Un nouveau témoin du métamorphisme de haute-pressure dans la chaîne himalayenne : les éclogites rétro-morphosées du Dome du Tso Moriri (Est Ladakh, Himalaya). *Comptes Rendus de l'Académie des Sciences de Paris*, 320 : 931–936. (Cité page 295.)
- Guillot S., Mahéo G., de Sigoyer J., Hattori K., et Pêcher A. 2008. Tethyan and Indian subduction viewed from the Himalayan high-to ultrahigh-pressure metamorphic rocks. *Tectonophysics*, 451 : 225–241. (Cité pages 148, 294, 301 et 308.)
- Guillot S., Replumaz A., Hattori K., et Strzeczynski P. 2007. Initial geometry of western Himalaya an Ultra-High pressure metamorphic evolution. *Journal of Asian Earth Sciences*, 30 : 557–564. (Cité page 294.)
- Haas J. L. et Fisher J. R. 1976. Simultaneous evaluation and correlation of thermodynamic data. *American Journal of Science*, 276 : 525–545. (Cité pages 30 et 359.)
- Halter W. H., Williams-Jones A. E., et Kontak D. J. 1998. Modeling fluid-rock interaction during greisenization at the East Kemptville tin deposit : implications for mineralization. *Chemical geology*, 150 : 1–17. (Cité page 73.)
- Hamilton W. 1969. Mesozoic California and the underflow of Pacific mantle. *Geological Society of America Bulletin*, 80 : 2409–2430. (Cité pages 3 et 199.)
- Hammarstrom J. et Zen E. 1986. Aluminum in hornblende ; an empirical igneous geobarometer. *American Mineralogist*, 71 : 1297–1313. (Cité page 144.)
- Handy M. R., Schmid S. M., Bousquet R., Kissling E., et Bernoulli D. 2010. Reconciling plate-tectonic reconstruction of Alpine Tethys with the geological-geophysical record of spreading and subduction in the Alps. *Earth Sciences Review*, 102 : 121–158. (Cité pages 240, 259 et 284.)
- Hannula K., Lackey J., Mattox E., Mcgrath G., Onasch E., et Werteim J. 1999. Syn-tectonic pluton intrusion during contractional deformation : microstructural and metamorphic evidence from the aureole of the Acadian Victory Pluton, north-eastern Vermont, USA. *Journal of Metamorphic Geology*, 17 : 271–286. (Cité page 85.)
- Harvey B. et Tracy R. J. 1996. Petrology. *Freeman*, 2nd ed., pp. 375. (Cité page 14.)
- Hauy R. J. 1822. Traité de Minéralogie, Seconde édition. *Bachelier et Huzard, Paris*. (Cité page 294.)
- Hauzenberger C. A., Baumgartner L. P., et Pak T. M. 2002. Experimental study on the solubility of the “model”-pelite assemblage albite + K-feldspar + andalusite + quartz in supercritical chloride-rich aqueous solutions at 0.2 GPa and 600 °C. *Geochimica et Cosmochimica Acta*, 65 : 4493–4507. (Cité page 96.)
- Heinrich K. F. J. 1966. X-ray Optics and Microanalysis. Eds R. Castaing, P. Deschamps and J. Philibert (Paris : Hermann), pages 159–67. (Cité page 121.)
- Heinrich K. F. J. 1987. Mass absorption coefficients for electron probe analysis. Ed. J. D. Brown And R.H. Packwood (London Ont. : Univ. W. Ontario), pages 67–119. (Cité page 121.)
- Heinrich K. F. J. et Newbury D. E. 1991. Electron probe quantitation. *Plenium press, New York*. (Cité page 121.)

- Helgeson H. C., Delany J. M., Nesbitt H. W., et Bird D.K. 1978. Summary and critique of the thermodynamic properties of rock-forming minerals. *American Journal of Science*, 278 : 1–229. (Cité pages 30 et 360.)
- Helgeson H. C., Kikham D. H., et Flowers G. C. 1981. Theoretical prediction of the thermodynamic behavior of aqueous electrolytes at high pressures and temperatures. IV. Calculation of activity coefficients, osmotic coefficients, and apparent molal and standard and relative partial molal properties to 600 °C and 5 KB. *American Journal of Science*, 281 : 1249–1516. (Cité page 96.)
- Hillier S. et Velde B. 1991. Octahedral occupancy and chemical composition of diagenetic (low-temperature) chlorites. *Clay Minerals*, 26 : 149–168. (Cité pages 73, 74, 75, 86, 87, 88, 144, 227 et 228.)
- Hodges K. V. et McKenna L. W. 1987. Realistic propagation of uncertainties in geologic thermobarometry. *Journal of Metamorphic Geology*, 3 : 343–370. (Cité pages 49 et 50.)
- Hoisch T. 2000. Conditions of metamorphism in lower-plate rocks at Bare Mountain, Nevada - implications for extensional faulting. Geological and geophysical characterization studies of Yucca Mountain, Nevada : A potential high-level radioactive-waste repository. *US Geological Survey - Digital Data Series*, 58 : 1–23. (Cité page 85.)
- Holdaway M. J. et Lee S. 1977. Fe-Mg cordierite stability in high-grade pelitic rocks based on experimental theoretical and natural observations. *Contributions to Mineralogy and Petrology*, 63 : 175–198. (Cité page 144.)
- Holdaway M J et Mukhhopadhyay B. 1993. Geothermobarometry in pelitic schists : A rapidly evolving field. *American Mineralogist*, 78 : 681–693. (Cité page 207.)
- Holland T., Baker J., et Powell R. 1998. Mixing properties and activity-composition and relationships of chlorites in the system MgO-FeO-Al₂O₃-SiO₂-H₂O. *European Journal of Mineralogy*, 10 : 395–406. (Cité pages 6, 66, 67, 73, 75, 76, 83, 85, 86, 92, 101, 102, 103, 107, 108, 109 et 143.)
- Holland T. J. B. 1989. Dependence of entropy on volume for silicate and oxide minerals : A review and a predictive model. *American Mineralogist*, 74 : 5–13. (Cité pages 67 et 112.)
- Holland T. J. B. 1990. Activities of components in omphacitic solid solutions. *Contributions to Mineralogy and Petrology*, 105 : 446–453. (Cité page 305.)
- Holland T. J. B. et Blundy J. 1994. Non-ideal interactions in calcic amphiboles and their bearing on amphibole-plagioclase thermometry. *Contributions to Mineralogy and Petrology*, 116 : 433–447. (Cité pages 143, 144, 145, 155 et 305.)
- Holland T. J. B. et Powell R. 1996a. Thermodynamics of order–disorder in minerals. 1 : symmetric formalism applied to minerals of fixed composition. *American Mineralogist*, 81 : 1413–1424. (Cité pages 67, 69, 80, 105 et 363.)
- Holland T. J. B. et Powell R. 1996b. Thermodynamics of order–disorder in minerals. 2 : symmetric formalism applied to solid solutions. *American Mineralogist*, 81 : 1425–1437. (Cité pages 67, 69, 80, 96, 105 et 363.)
- Holland T. J. B. et Powell R. 1998. An internally consistent thermodynamic data set for phases of petrological interest. *Journal of Metamorphic Geology*, 16 : 309–343. (Cité pages 5, 7, 18, 22, 30, 65, 66, 67, 68, 69, 75, 76, 80, 81, 82, 83, 91, 92, 96, 112, 113, 115, 116, 137, 143, 194, 319, 360, 361, 367 et 372.)

- Holland T. J. B. et Powell R. 2003. Activity-composition relations for phases in petrological calculations : an asymmetric multicomponent formulation. *Contributions to Mineralogy and Petrology*, 145 : 492–501. (Cité pages 67, 69 et 96.)
- Holland T. J. B. et Powell R. 2011. An improved and extended internally consistent thermodynamic dataset for phases of petrological interest, involving a new equation of state for solids. *Journal of Metamorphic Geology*, 29 : 333–383. (Cité pages 22 et 137.)
- Hollister L. S., Grissom G., Peters E., Stowell H., et Sisson V. 1987. Confirmation of the empirical correlation of Al in hornblende with pressure of solidification of calc-alkaline plutons. *American Mineralogist*, 72 : 231. (Cité page 144.)
- Hollocher K., Fakhry A., et Ruiz J. 1995. Trace element determination for USGS basalt BHVO-1 and NIST standard reference materials 278, 688 and 694 by Inductively Coupled Plasma-Mass Spectrometry. *Geostandards Newsletter*, 19 : 35–40. (Cité page 165.)
- Holton Y. 2012. Is Energy-Dispersive Spectroscopy in the SEM a Substitute for Electron Probe Microanalysis ? *Microscopy and Analysis*, 141 : 54–57. (Cité page 121.)
- Hower J et Mowatt TC. 1966. The mineralogy of illites and mixed-layer illite/montmorillonites. *American Mineralogist*, 51 : 825–854. (Cité pages 33, 34 et 38.)
- Hynes A. et Forest R. C. 1988. Empirical garnet-muscovite geothermometry in low grade metapelites, Selwyn Range (Canadian Rockies). *Journal of Metamorphic Geology*, 8 : 89–124. (Cité page 66.)
- Inoue A., Kurokawa K., et Hatta T. 2010. Application of chlorite geothermometry to hydrothermal alteration in Toyoha geothermal system, southwestern Hokkaido, Japan. *Resource Geology*, 60 : 52–70. (Cité pages 73, 85 et 86.)
- Inoue A., Meunier A., Patrier-Mas P., Rigault C., Beaufort D., et Vieillard P. 2009. Application of chemical geothermometry to low-temperature trioctahedral chlorites. *Clays and Clay Minerals*, 57 : 371–382. (Cité pages 60, 61, 73, 74, 85, 86, 89, 91, 144, 228, 234, 235, 254, 255 et 256.)
- Isa J., Rubin A. E., et Wasson J. T. 2012. Bulk compositions of CV and CK chondrites : support for a lcosc relationship. *Lunar and Planetary Science Conference. The Woodlands, Texas*. (Cité page 163.)
- Jacobsen S. B. et Wasserburg G. J. 1979. The mean age of mantle and crustal reservoirs. *Journal of Geophysical Research*, 84 : 7411–7427. (Cité page 160.)
- Jacquet E., Gounelle M., et alard O. 2012. Trace-element microdistribution in carbonaceous chondrite chondrules. *Lunar and Planetary Science Conference. The Woodlands, Texas*. (Cité pages 162, 189 et 190.)
- Jaillard E. 1984. Etude géologique des unités briançonnaises de Vanoise occidentale au sud-ouest de Pralognan (Savoie) : Evolution sédimentaire et structurale. *Thèse, Université Joseph-Fourier de Grenoble*, pp. 211. (Cité page 206.)
- Janots E., Berger A., et Engi M. 2011. Physico-chemical control on the REE minerals in chloritoid-grade metasediments from a single outcrop (Central Alps, Switzerland). *Lithos*, 121 : 1–11. (Cité page 129.)

- Jenkins D. M. et Chernovsky J. V. 1986. Phase equilibria and crystallochemical properties of Mg-chlorites. *American Mineralogist*, 71 : 924–936. (Cité page 26.)
- Jiang W., Peacor D. R., et Essene E. J. 1992. Muscovite- and R1 illite-smectite-kaolinite intergrowth in the Eocene McAdams sandstone : Nonexistence of hydro-muscovite and implications for illite metastability. *Geological Society of America ; Abstract*, 24 : 71. (Cité page 27.)
- Jiang W. T., Peacor D. R., et Essene E. J. 1994. Clay minerals in the McAdams sandstone, California : implications for substitution of H_3O^+ and H_2O and metastability of illite. *Clays and Clay Minerals*, 42 : 35–45. (Cité pages 33 et 38.)
- Jochum K. P. et Stoll B. 2008. Reference materials for elemental and isotopic analyses by LA-(MC)-ICP-MS : Successes and outstanding needs. *Mineralogical Association of Canada*. (Cité page 165.)
- Johnson J. W., Oelkers E. H., et Helgeson H. C. 1992. SUPCRT92 : a software package for calculating the standard molal thermodynamic properties of minerals, gases, aqueous species, and reactions from 1 to 5000 bars and 0 to 1000 °C. *Computers and Geosciences*, 18 : 899–947. (Cité page 96.)
- Johnson M. et Rutherford M. 1989. Experimental calibration of the aluminum-in-hornblende geobarometer with application to Long Valley caldera (California) volcanic rocks. *Geology*, 17 : 837–841. (Cité page 144.)
- Jourdan S., Féaux G., Bertrand H., Kampunzu A. B., Tshoso G., Le Gall B., Tiercelin J., et Capiez P. 2004. The Karoo triple junction questioned : evidence for Jurassic and Proterozoic $^{40}Ar/^{39}Ar$ ages and geochemistry of the giant Okavango dyke swarm (Botswana). *Earth and Planetary Sciences Letters*, 222 : 989–1006. (Cité page 257.)
- Jowett E.C. 1991. Fitting iron and magnesium into the hydrothermal chlorite geothermometer : Gac/mac/seg. *Joint Annual Meeting (Toronto, May 27-29, 1991) Program with Abstracts*. (Cité pages 73, 74, 86 et 144.)
- Juez-Larré J. 2003. Post Late Paleozoic tectonothermal evolution of the northeastern margin of Iberia, assessed by fission-track and (U- Th)/He analyses. A case history from the Catalan Coastal Ranges. *Phd thesis, Vrije Universiteit*, pp. 200. (Cité pages 45 et 46.)
- Kallemeyn G. W., Rubin A. E., et Wasson J. T. 1991. The compositional classification of chondrites : V. The Karoonda (CK) group of carbonaceous chondrites. *Geochimica et Cosmochimica Acta*, 55 : 881–892. (Cité pages 162, 185 et 186.)
- Kaneko Y., Katayama I., Yamamoto H., Misawa K., Ishikawa M., Rehman H. U., Kausar A., et Shiraishi K. 2003. Timing of Himalayan ultrahigh-pressure metamorphism : sinking rate and subduction angle of the Indian continental crust beneath Asia. *Journal of Metamorphic Geology*, 21 : 589–599. (Cité page 293.)
- Karpov I. K., Chudnenko K. V., et Kulik D. A. 1997. Modeling chemical mass transfer in geochemical processes : Thermodynamic relations, conditions of equilibria, and numerical algorithms. *American Journal of Science*, 297 : 767–806. (Cité page 96.)
- Kawasaki T., Nakano N., et Osanai Y. 2011. Osumilite and a spinel + quartz association in garnet-sillimanite gneiss from Rundvagshetta, Lützow-Holm Complex, East Antarctica. *Gondwana Research*, 19 : 430–445. (Cité page 144.)

- Kerckhove C., Barféty J. C., Bogdanoff S., et Lemoine M. 1980. Carte géologique de la France au 1/250 000 : Feuille de Gap. *BRGM Feuille, Orléans*. (Cité page 200.)
- Kerckhove C. et Piboule M. 1999. The Plan de Phazy Granite, near Guillestre (Briançonnais zone in the Durance area of the french-italian western Alps) : a hundred years old myth. *Geologie Alpine*, 75 : 117–122. (Cité pages 212 et 251.)
- Kilian M. W. 1899. La zone du Briançonnais. Essai de synthèse tectonique. *Ass. Fr. pour l'Avenir des Sciences*, 28 : 403. (Cité page 203.)
- Kilian M. W. 1903. Sur le rôle des charriages dans les Alpes delphino-provençales et sur la structure en éventail des Alpes briançonnaises. *Compte Rendu Académie des Sciences Paris*, 137 : 536–537. (Cité pages 203 et 220.)
- Kilian M. W., Blanchet F., Moret L., et Roch E. 1923. Contribution à la connaissance du terrain houiller de la zone intra-alpine française. *Travaux du laboratoire de la Faculté des Sciences de l'Université de Grenoble*, 13. (Cité page 203.)
- Kilian M. W. et Termier P. 1898. Note sur divers types pétrographiques et sur le gisement de quelques roches éruptives des Alpes françaises. *Bulletin de la Societe Geologique de France*, 26 : 357–361. (Cité page 212.)
- Kirschner D. L., Cosca M., Masson H., et Hunziker J. C. 1996. Staircase $40/\text{Ar}39$ Ar spectra of fine-grained white mica : Timing and duration of deformation and empirical constraints on argon diffusion. *Geology*, 24 : 747–750. (Cité page 251.)
- Kohn M. J. 1993. Uncertainties in differential thermodynamic (Gibbs' method) P–T paths. *Contributions to Mineralogy and Petrology*, 113 : 24–39. (Cité page 49.)
- Kohn M. J. et Spear F. S. 1991a. Error propagation for barometers : 1. Accuracy and precision of experimentally located end-member reactions. *American Mineralogist*, 76 : 128–137. (Cité page 49.)
- Kohn M. J. et Spear F. S. 1991b. Error propagation for barometers : 2. Application to rocks. *American Mineralogist*, 76 : 138–147. (Cité pages 49 et 50.)
- Komninou A. et Yardley B. W. D. 1997. Fluid-rock interaction in the Rhine Graben : A thermodynamic model of the hydrothermal alteration observed in deep drilling. *Geochimica et Cosmochimica Acta*, 61 : 515–531. (Cité pages 96 et 98.)
- Kong P., Deloule E., et Palme H. 2000. REE-bearing sulfide in Bishunpur (LL3.1), a highly unequilibrated ordinary chondrite. *Earth and Planetary Science Letters*, 177 : 1–7. (Cité pages 162 et 190.)
- Korh Ravna K. 2000a. Distribution of Fe^{2+} and Mg between coexisting garnet and hornblende in synthetic and natural systems : an empirical calibration of the garnet-hornblende Fe-Mg geothermometer. *Lithos*, 53 : 265–277. (Cité pages 144 et 306.)
- Korh Ravna K. 2000b. The garnet clinopyroxene Fe^{2+} Mg geothermometer : an updated calibration. *Journal of Metamorphic Geology*, 18 : 211–219. (Cité pages 21, 144, 153 et 304.)
- Kotkova J., O'Brien P., et Ziemann M. A. 2011. Diamond and coesite discovered in Saxony-type granulite : Solution to the Variscan garnet peridotite enigma. *Geology*, 39 : 667–670. (Cité page 300.)

- Kranidiotis P. et MacLean W. H. 1987. Systematics of chlorite alteration at the Phelps Dodge massive sulfide deposit, Matagami, Quebec. *Economic Geology and the Bulletin of Society of Economic Geologists*, 82 : 1898–1911. (Cité pages 73, 74 et 144.)
- Krinsley D. H. 1998. Backscattered scanning electron microscopy and image analysis of sediments and sedimentary rocks. *Cambridge University Press*. (Cité page 130.)
- Krogh E. J. 1988. The garnet-clinopyroxene Fe-Mg geothermometer - a reinterpretation of existing experimental data. *Contributions to Mineralogy and Petrology*, 99 : 44–48. (Cité pages 21 et 144.)
- Krogh E. J. et Raheim A. 1978. Temperature and pressure dependence of Fe-Mg partitioning between garnet and phengite, with particular reference to eclogites. *Contributions to Mineralogy and Petrology*, 66 : 75–80. (Cité page 144.)
- Krot A. N., Petaev M. I., Russel S. S., Itoh S., Fagan T. J., Yurimoto H., Chizmadia L., Weisberg M. K., Komatsu M., Ulyanov A. A., et Keil K. 2004. Amoeboid olivine aggregates and related objects in carbonaceous chondrites : records of nebular and asteroid processes. *Chemie der Erde - Geochemistry*, 64 : 185–239. (Cité page 190.)
- Kulik D. et Wagner T. 2005. Temperature corrections of standard molar thermodynamic properties of condensed substances and gases using data in DComp records of GEM-Selektor. *GEM-Selektor On-Line Documentation in PDF format*. (Cité page 361.)
- Kulik D. et Wagner T. 2008. Pressure corrections for standard molar thermodynamic properties of condensed substances and fluids using data from DComp records of GEM-Selektor. *GEM-Selektor On-Line Documentation in PDF format*. (Cité page 361.)
- Kulik D. A., Wagner T., Dmytrieva S. V., Kosakowski G., Hingerl F. F., Chudnenko K. V., et Berner U. in press. GEM-Selektor geochemical modeling package : Revised algorithm and GEMS3K numerical kernel for coupled simulation codes. *Computational Geosciences*. (Cité pages 5, 67, 78 et 96.)
- Lacroix B., Charpentier D., Buatier M., Vennemann T., Labaume P., Adatte T., Trave A., et Dubois M. 2012. Formation of chlorite during thrust fault reactivation. Record of fluid origin and P-T conditions in the Monte Perdido thrust fault (southern Pyrenees). *Contributions to Mineralogy and Petrology*, 163 : 1083–1102. (Cité page 49.)
- Lagabrielle Y. 1987. Les ophiolites : Marqueurs de l'histoire tectonique des domaines océaniques. Le cas des Alpes franco-italiennes (Queyras, Piémont) comparaison avec les ophiolites d'Antalya (Turquie) et du Coast Range de Californie. *Thèse, Université de Bretagne occidentale*. (Cité pages 202, 206 et 260.)
- Lahfid A., Beyssac O., Deville E., Negro F., Chopin C., et Goffé B. 2010. Evolution of the Raman spectrum of carbonaceous material in low-grade metasediments of the Glarus Alps (Switzerland). *Terra Nova*, 22 : 354–360. (Cité pages 223, 224, 225, 226, 230, 231, 237, 238 et 264.)
- Laird J. 1988. Chlorites : Metamorphic petrology. *Reviews in Mineralogy*, 19 : 405–453. (Cité page 73.)
- Lallemant S., Huchon P., Jolivet L., et Prouteau G. 2005. Convergence lithosphérique. *Vuibert Ed.*, pp. 182. (Cité page 199.)

- Lanari P., Guillot S., Schwartz S., Vidal O., Tricart P., Riel N., et Beyssac O. 2012a. Diachronous evolution of the alpine continental subduction wedge : Evidence from P-T estimates in the Briançonnais Zone houillère (France-Western Alps). *Journal of Geodynamics*, 56-57 : 39-54. (Cité pages [4](#), [8](#), [41](#), [49](#), [65](#), [73](#), [75](#), [85](#), [86](#), [94](#), [95](#), [137](#), [164](#), [200](#), [211](#), [245](#), [247](#), [251](#), [252](#), [255](#), [256](#), [258](#), [259](#), [284](#), [285](#), [288](#), [289](#) et [302](#).)
- Lanari P., Riel N., Guillot S., Vidal O., Schwartz S., Pêcher A., et Hattori K. in press. Deciphering high-pressure metamorphism in collisional context using microprobe-mapping methods : Application to the Stak eclogitic massif (NW Himalaya). *Geology*. (Cité pages [8](#), [49](#), [50](#), [135](#), [137](#), [148](#), [153](#), [154](#), [164](#) et [195](#).)
- Lanari P., Vidal O., De Andrade V., Dubacq B., Lewin E., et Schwartz S. submitted. XMap-Tools a Matlab-based graphic user interface for microprobe X-ray images processing. *Computers and Geosciences*. (Cité page [95](#).)
- Lanari P., Vidal O., Schwartz S., Riel N., Guillot S., et Lewin E. 2012b. Deciphering P-T paths in metamorphic rocks involving zoned minerals using quantified maps (XMap-Tools software) and thermodynamics methods : Examples from the Alps and the Himalaya. *Geophysical Research Abstracts*, 14 : 10605. (Cité pages [93](#), [254](#) et [303](#).)
- Lardeaux J. M., Schwartz S., Tricart P., Paul A., Guillot S., Béthoux N., et Masson F. 2006. A crustal-scale cross-section of the south-western Alps combining geophysical and geological imagery. *Terra Nova*, 18 : 412-422. (Cité pages [218](#), [250](#), [251](#) et [261](#).)
- Le Bayon B. 2005. Evolution structurale et métamorphique d'une croûte continentale subductée (Grand Paradis, Alpes occidentales). *Thèse, Université de Rennes 1*, pp. 385. (Cité page [207](#).)
- Le Bayon B. et Ballèvre M. 2006. Deformation history of a subducted continental crust (Gran Paradiso, Western Alps) : continuing crustal shortening during exhumation. *Journal of Structural Geology*, 28 : 793-815. (Cité page [289](#).)
- Le Bayon B., Pitra P., Ballevre M., et Bohn M. 2006. Reconstructing p-t paths during continental collision using multi-stage garnet (gran paradiso nappe, western alps). *Journal of Metamorphic Geology*, 24 : 477-496. (Cité page [289](#).)
- Le Fort P., Guillot S., et Pêcher A. 1997. HP metamorphic belt along the Indus suture zone of NW Himalaya : New discoveries and significance. *Comptes Rendus de l'Académie des Sciences-Series IIA-Earth and Planetary Science*, 325 : 773-778. (Cité pages [295](#) et [300](#).)
- Le Fur F. 1998. Etude structurale et cinématique d'un réseau alpin de veines de quartz (Plan Bouchet-Zone Houillère Briançonnaise). *Géologie Alpine*, 75 : 187-190. (Cité page [218](#).)
- Leech M., Singh S., Jain A. K., Klemperer S. L., et Manickavasagam R. M. 2005. The onset of India-Asia continental collision : early, steep subduction required by timing of UHP metamorphism in the western Himalaya. *Earth and Planetary Science Letters*, 234 : 83-97. (Cité pages [293](#) et [294](#).)
- Lemoine M. 1980. Sepentinites ; gabbros and opicalcites in the Piemont-Ligurian domain of the Western Alps : possible indicators of oceanic fracture zones and associated sepen-tinite protusion in the Jurassic-Cretaceous Tethys. *Archives des Sciences de Genève*, 33 : 1655-1668. (Cité page [260](#).)

- Lieberman J. et Petrakakis K. 1991. TWEEQU thermobarometry : Analysis of uncertainties and application to granulites from western Alaska and Austria. *Canadian Mineralogist*, 29 : 857–887. (Cité pages 4, 23, 25, 31 et 50.)
- Lombardo B., Pertusati P., Rolfo F., et Visona D. 1998. First report of eclogites from the E Himalaya : implications for the Himalayan orogeny. *Memorie di Scienze Geologiche*, 50 : 67–68. (Cité page 295.)
- Lombardo B. et Rolfo F. 2000. Two contrasting eclogite types in the Himalayas : implications for the Himalayan orogeny. *Journal of Geodynamics*, 30 : 37–60. (Cité page 295.)
- Lory C. 1864. Description géologique du dauphiné. *Rapport, Paris, Grenoble*. (Cité page 203.)
- Loucks R. R. 1991. The bound interlayer H₂O content of potassic white micas ; muscovite-hydromuscovite-hydropyrophyllite solutions. *American Mineralogist*, 76 : 1563–1579. (Cité pages 33, 38 et 229.)
- Mäder U. K., Percival J. A., et Berman R. G. 1994. Thermobarometry of garnet - clinopyroxene - hornblende granulites from the Kapuskasing structural zone. *Canadian Journal of Earth Sciences*, 31 : 1134–1145. (Cité pages 30, 31, 67 et 69.)
- Maier K. K., C. G. and Kelley. 1932. An equation for the representation of high-temperature heat content data. *Journal of the American Chemical Society*, 54 : 3243–3246. (Cité pages 30 et 359.)
- Malasoma A. et Marroni M. 2007. HP/LT metamorphism in the Volparone Breccia (Northern Corsica, France) : evidence for involvement of the Europe/Corsica continental margin in the Alpine subduction zone. *Journal of Metamorphic Geology*, 25 : 529–545. (Cité page 85.)
- Malusà M.G., Polino R., Zattin M., Bigazzi G., Martin S., et Pianna F. 2005. Miocene to present differential exhumation in the Western Alps : insights from fission track thermochronology. *Tectonics*, 24 : 1–23. (Cité page 239.)
- Malusà M.G. et Vezzoli G. 2006. Interplay between erosion and tectonics in the Western Alps. *Terra Nova*, 18 : 104–108. (Cité page 239.)
- Margules M. 1895. Uben due Zusammensetzung der gesättigten Dampfes con Mischungen. *Sitzungsber Wien Akad*, 104 : 1243–1278. (Cité pages 30, 31 et 67.)
- Mason B. et Martin P. M. 1974. Minor and trace element distribution in melilite and pyroxene from the Allende meteorite. *Earth and Planetary Science Letters*, 22 : 141–144. (Cité pages 162, 189 et 190.)
- Massonne H. J. 1989. The upper thermal stability of chlorite-quartz : an experimental study in the system MgO-Al₂O₃-SiO₂-H₂O. *Journal of Metamorphic Geology*, 7 : 567–581. (Cité pages 26 et 66.)
- Massonne H. J. et Schreyer W. 1986. High-pressure syntheses and X-ray properties of white micas in the system K₂O-MgO-Al₂O₃-SiO₂-H₂O. *Neues Jahrb Mineral Abh*, 153 : 177–215. (Cité page 27.)
- Massonne H. J. et Schreyer W. 1987. Phengite geobarometry based on the limiting assemblage with k-feldspar, phlogopite, and quartz. *Contributions to Mineralogy and Petrology*, 96 : 212–224. (Cité pages 144 et 228.)

- Massonne H. J. et Szpurka Z. 1997. Thermodynamic properties of white micas on the basis of high-pressure experiments in the systems K_2O - MgO - Al_2O_3 - SiO_2 - H_2O . *Lithos*, 41 : 229–250. (Cité pages 27 et 66.)
- McDougall I. et Harrison T. M. 1988. Geochronology and thermochronology by the $^{40}Ar/^{39}Ar$ method. *New York, Oxford University Press*, pp. 212. (Cité pages 250 et 251.)
- McKenzie D. et Sclater J. G. 1971. The evolution of the Indian Ocean since the Late Cretaceous. *Geophysical Journal International*, 24 : 437–528. (Cité page 293.)
- McSween J. H. Y. 1977. Petrographic variations among carbonaceous chondrites of the Vigarano type. *Geochimica et Cosmochimica Acta*, 41 : 1777–1790. (Cité pages 169, 185, 186, 189 et 190.)
- Meffan-Main S., Cliff R. A., Barnicoat A. C., Lombardo B., et Compagnoni R. 2004. A Tertiary age for Alpine high-pressure metamorphism in the Gran Paradiso massif, Western Alps : a Rb–Sr microsampling study. *Journal of Metamorphic Geology*, 22 : 267–281. (Cité page 289.)
- Mercier D. et Beaudoin B. 1987. Revision du carbonifère briançonnais : Stratigraphie et évolution du bassin. *Géologie Alpine, Mémoires H.S.*, 13 : 25–31. (Cité page 218.)
- Messiga B., Kienast J. R., G. Rebayn, Riccardi P., et Tribuzio R. 1999. Cr-rich magnesiochloritoid eclogites from the Monviso ophiolites (Western Alps, Italy). *Journal of Metamorphic Geology*, 17 : 287–299. (Cité page 289.)
- Moazzen M. 2004. Chlorite-chloritoid-garnet equilibria and geothermometry in the Sanandaj-Sirjan metamorphic belt, southern Iran. *Iranian Journal of Sciences and Technologies*, 28 : 1–14. (Cité page 85.)
- Morgan W. J. 1968. Rises, Trenches, Great Faults, and Crustal Block. *Journal of Geophysical Research*, 73 : 1959–1982. (Cité page 206.)
- Mori T. et Green D. H. 1978. Laboratory duplication of phase equilibria observed in natural garnet lherzolites. *Journal of Geology*, 86 : 83–97. (Cité pages 21 et 144.)
- Mountain B. W. et Williams-Jones A. E. 1995. Mass transfer and the path of metasomatic reactions in mesothermal gold deposits : an example from Flambeau Lake, Ontario. *Economic Geology*, 91 : 302–321. (Cité page 73.)
- Muñoz M., De Andrade V., Vidal O., Lewin E., Pascarelli S., et Susini J. 2006. Redox and speciation micromapping using dispersive X-ray absorption spectroscopy : Application to iron in chlorite mineral of a metamorphic rock thin section. *Geochemistry Geophysics Geosystems*, 7 : 11. (Cité pages 137 et 228.)
- Mysen B. O. et Heier K. S. 1972. Petrogenesis of eclogites in high grade metamorphic gneisses, exemplified by the Hareidland eclogite, western Norway. *Contributions to Mineralogy and Petrology*, 36 : 73–94. (Cité pages 21 et 144.)
- Negro F., Beyssac O., Goffé B., Saddiqi O., et Bouybaouene M. 2006. Thermal structure of the Alboran Domain in the Rif (northern Morocco) and the Western Betics (southern Spain). Constraints from Raman spectroscopy of carbonaceous material. *Journal of Metamorphic Geology*, 24 : 309–327. (Cité page 224.)

- Nicolas A. 1966. Interprétation des ophiolites piémontaises entre le Grand Paradis et la Dora Maira : conséquences paléogéographiques et structurales. *Thèse, Université Scientifique et Médicale de Grenoble*, pp. 295. (Cité page 206.)
- Nieto F., Mellini M., et Abad I. 2010. The Role of H_2O in the Crystal Structure of Illite. *Clays and Clay Minerals*, 58 : 238–246. (Cité pages 33, 34, 36, 37, 38 et 39.)
- Oberhänsli R., Bousquet R., Engi M., Goffé B., Gosso G., Handy M. R., Koller F., Lardeaux J. M., Polino R., Rossi R., Schuster, Schwartz S., et Spalla I. 2004. Metamorphic structure of the alps. *Commission for the Geological Map of the World (CGMW), Paris*. (Cité pages 207, 208 et 286.)
- O'Brien P., Zotov N., et Law R. 1999. First discovery of coesite in the Kaghan eclogites (Pakistan) ; implications for Himalayan evolution. *Terra Nova*, 2 : 109–111. (Cité page 295.)
- O'Brien P., Zotov N., Law R., Khan A. M., et Jan M. Q. 2001. Coesite in Himalayan eclogite and implication for models of India–Asia collision. *Geology*, 29 : 435–438. (Cité page 295.)
- Pak T. M., Hauzenberger C. A., et Baumgartner L. P. 2003. Solubility of the assemblage albite + K-feldspar + andalusite + quartz in supercritical aqueous chloride solutions at 650 °C and 2 kbar. *Chemical geology*, 200 : 377–393. (Cité page 96.)
- Parra T. 2001. Les équilibres Chlorite-Phengite. De l'étude de la lame mince aux calculs des trajets pression-température. *Thèse, Université d'Orsay, Orsay*. (Cité page 26.)
- Parra T., Vidal O., et Agard P. 2002a. A thermodynamic model for Fe-Mg dioctahedral K white micas using data from phase-equilibrium experiments and natural pelitic assemblages. *Contributions to Mineralogy and Petrology*, 143 : 706–732. (Cité pages 4, 27, 28, 38, 41, 83, 143 et 229.)
- Parra T., Vidal O., et Jolivet L. 2002b. Relation between the intensity of deformation and retrogression in blueschist metapelites of Tinos Island (Greece) evidenced by chlorite-mica local equilibria. *Lithos*, 63 : 41–66. (Cité pages 4, 75, 85 et 229.)
- Parra T., Vidal O., et Theye T. 2005. Experimental data on the Tschermak substitution in Fe-chlorite. *American Mineralogist*, 90 : 359–370. (Cité pages 28, 112, 113, 114, 115 et 116.)
- Parrish R. R., Groug M. P., S. J. an Searle, et Waters D. 2006. Plate velocity of ultrahigh-pressure eclogites in the Pakistan Himalaya. *Geology*, 34 : 989–992. (Cité page 293.)
- Patchett P. J., Vervoort J. D., Sederlund U., et Slaters V. J. M. 2004. Lu,Hf and Sm,Nd isotopic systematics in chondrites and their constraints on the Lu,Hf properties of the Earth. *Earth and Planetary Science Letters*, 222 : 29–41. (Cité pages 161 et 162.)
- Pattison D. R. M. et Newton R. C. 1989. Reversed experimental calibration of the garnet-clinopyroxene Fe-Mg exchange thermometer. *Contributions to Mineralogy and Petrology*, 101 : 87–103. (Cité pages 21 et 144.)
- Pêcher A., Seeber L., Guillot S., Jouanne F., Kausar A., Latif M., Majid A., Mahéo G., Mugnier J. L., Rolland Y., van der Beek P., et Van Melle J. 2008. Stress field evolution in the northwest Himalayan syntaxis, northern Pakistan. *Tectonics*, 27-TC6005. (Cité page 300.)
- Perchuk L., Aranovich L. Y., Podlesskii K., Lavrent'eva I., Gerasimov V., Fed'kin V., Kitsul V., Karsakov L., et Bernikov N. 1985. Precambrian granulites of the Aldan shield, eastern Siberia, USSR. *Journal of Metamorphic Geology*, 3 : 265–310. (Cité page 144.)

- Percival S. et Kodama H. 1989. Sudoite from Cigar Lake, Saskatchewan. *Canadian Mineralogist*, 27 : 633–641. (Cité page 91.)
- Philibert J. et Tixier R. 1975. Physical aspects of electron microscopy and microbeam analysis. *Siegel B. M. and Beaman, D. R., eds, J. Wiley, New York*, pp. 333. (Cité page 121.)
- Philippot P. 1988. Déformation et éclogitisation progressives d'une croûte océanique subductée : Le Monviso, Alpes occidentales. Contraintes cinématiques durant la collision alpine. *Thèse, Université de Montpellier*, pp. 269. (Cité page 202.)
- Platt J. 1986. Dynamics of orogenic wedges and the uplift of high-pressure metamorphic rocks. *Geological Society of America Bulletin*, 97 : 1037–1053. (Cité page 284.)
- Plissart G., Femenias O., Maruntiu M., Diot H., et Demaiffe D. 2009. Mineralogy and geothermometry of grabbro-derived listevenites in the Tisovita-Iutu ophiolite, Southwestern Romania. *Canadian Mineralogist*, 47 : 81–105. (Cité page 49.)
- Plunder A., Agard P., Dubacq B., Chopin C., et Bellanger M. 2012. How continuous and precise is the record of P-T paths. Insights from combined thermobarometry and thermodynamic modelling into subduction dynamics (Schistes Lustrés, W. Alps). *Journal of Metamorphic Geology*, pages 1–24. (Cité pages 137, 288 et 289.)
- Potts P. J., Bowles J. F., Reed S. J., et Cave R. 2002. Microprobe Techniques in the Earth-Science. *The Mineralogical Society Series Editor ; Chapman and Hall*, pp. 419. (Cité pages 119 et 121.)
- Powell R. 1985. Regression diagnostics and robust regression in geothermometer/geobarometer calibration : the garnet-clinopyroxene geothermometer revisited. *Journal of Metamorphic Geology*, 3 : 231–243. (Cité page 21.)
- Powell R. 2008. On thermobarometry. *Journal of Metamorphic Geology*, 26 : 155–179. (Cité pages 3, 22, 67, 68, 75 et 91.)
- Powell R. et Holland T. J. B. 1985. An internally consistent thermodynamic dataset with uncertainties and correlations : 1 : Methods and a worked example. *Journal of Metamorphic Geology*, 3 : 327–342. (Cité page 144.)
- Powell R. et Holland T. J. B. 1988. An internally consistent thermodynamic dataset with uncertainties and correlations : 3 application methods, worked examples and a computer program. *Journal of Metamorphic Geology*, 6 : 173–204. (Cité pages 67 et 68.)
- Powell R. et Holland T. J. B. 1993. On the formulation of simple mixing models for complex phases. *American Mineralogist*, 78 : 1174–1180. (Cité pages 31, 67, 69, 79, 96 et 363.)
- Powell R. et Holland T. J. B. 1994. Optimal geothermometry and geobarometry. *American Mineralogist*, 79 : 120–133. (Cité pages 67 et 68.)
- Powell R. et Holland T. J. B. 1999. Relating formulations of the thermodynamics of mineral solid solutions : Activity modeling of pyroxenes, amphiboles, and micas. *American Mineralogist*, 84 : 1–14. (Cité pages 77, 96 et 362.)
- Powell R., Holland T. J. B., et Worley B. 1998. Calculating phase diagrams involving solid-solution via non-linear equations, with examples using THERMOCALC. *Journal of Metamorphic Geology*, 16 : 577–588. (Cité pages 67, 68, 75 et 91.)

- Price J. G. 1985. Ideal site mixing in solid solutions, with an application to two-feldspar geothermometry. *American Mineralogist*, 70 : 696–701. (Cité pages 30, 31, 67 et 69.)
- Putnis A. et Austrheim H. 2010. Fluid-induced processes : metasomatism and metamorphism. *Geofluids*, 10 : 254–269. (Cité page 242.)
- Raheim A. et Green D. H. 1974. Experimental determination of the temperature and pressure dependence of the Fe-Mg partition coefficient for coexisting garnet and clinopyroxene. *Contributions to Mineralogy and Petrology*, 48 : 179–203. (Cité pages 21 et 144.)
- Ransom B. et Helgeson H. 1993. Compositional end- members and thermodynamic components of illite and dioctahedral aluminous smectite solid-solutions. *Clays and Clay Minerals*, 41 : 537–550. (Cité page 36.)
- Riel N. 2008. Caractérisation Pression-Température-Temps d'un massif éclogitique Himalayen. *Mémoire M2R, Université Joseph-Fourier Grenoble 1.*, pp. 30. (Cité pages 293 et 295.)
- Riel N., Hattori K., Guillot S., Rayner N., Davis N., Latif M., et Kausar A. 2008. SHRIMP zircon ages of eclogites in the Stak massif, northern Pakista. *Himalayan Journal of Sciences*, 5 : 119–120. (Cité pages 293, 295 et 301.)
- Righter K. et Neff K. E. 2007. Temperature and oxygen fugacity constraints on CK and R chondrites and implications for water and oxidation in the early solar system. *Polar Science*, 1 : 25–44. (Cité pages 163, 185 et 186.)
- Rimmelé G., Parra T., Goffé B., Oberhänsli R., Jolivet L., et Candan O. 2006. Exhumation paths of high-pressure-low-temperature metamorphic rocks from the lycian nappes and the Menderes massif (sw turkey) : a multi-equilibrium approach. *Journal of Petrology*, 46 : 641–669. (Cité pages 4, 50 et 75.)
- Robert D. 1979. Contribution à l'étude géologique de la haute vallée de l'Arc (Région de Bonneval, Savoie). *Thèse, Université Pierre et Marie Curie, Paris* 6. (Cité page 206.)
- Robie R. A. et Hemingway B. S. 1995. Thermodynamic properties of minerals and related substances at 298.15 K and 1 bar (105 pascals) pressure and at higher temperatures. *U. S. Geological Survey Bulletin*, 2131 : 461. (Cité page 22.)
- Robie R. A., Hemingway B. S., et Fisher J. R. 1978. Thermodynamic Properties of Minerals and Related Substances at 298.15 K and 1 Bar Pressure and at Higher Temperatures. *U. S. Geological Survey Bulletin*, 1452 : 456. (Cité page 360.)
- Rolland Y., Carrio-Schaffhauser E., Sheppard S., Pêcher A., et Esclauze L. 2006. Metamorphic zoning and geodynamic evolution of an inverted crustal section (Karakorum margin, N Pakistan), evidence for two metamorphic events. *International Journal of Earth Sciences*, 95 : 288–305. (Cité page 85.)
- Rolland Y., Cox S. F., et Corsini M. 2009. Constraining deformation stages in brittle-ductile shear zones from combined field mapping and $^{40}\text{Ar}/^{39}\text{Ar}$ dating : the structural evolution of the Grimsel Pass area (Aar massif, Swiss Alps). *Journal of Structural Geology*, 31 : 1377–1394. (Cité page 251.)
- Rolland Y., Lardeaux J. M., Guillot S., et Nicollet C. 2000. Syn-convergence extension, vertical pinching and contrasted metamorphic units on the Western edge of the Gran Paradiso massif (French-Italian Alps). *Geodinamica Acta*, 13 : 133–148. (Cité pages 218, 251, 286 et 289.)

- Rolland Y., Lardeaux J. M., et Jolivet L. 2012. Deciphering orogenic evolution. *Journal of Geodynamics*, 56-57 : 1-6. (Cité page 250.)
- Rolland Y., Rossi M., Cox S. F., Corsini M., Mancktelow N., Pennacchioni G., Fornari M., et Boullier A. M. 2008. $^{40}\text{Ar}/^{39}\text{Ar}$ dating of syn-kinematic white mica : insights from fluid-rock reaction in low-grade shear zones (Mont Blanc Massif) and constraints on timing of deformation in the NW External Alps. In : Wibberley C.A.J., Kurtz W., Imber J., Holdsworth R.E. and Colletini C. (eds). *The Internal Structure of Fault Zones : Implications for Mechanical and Fluid-Flow Properties*. Geological Society of London Special Publications, 299 : 293-315. (Cité page 257.)
- Rosenbaum G., Menegon L., Glodny J., Vasconcelos P., Ring U., Massironi M., Thiede D., et Nasipuri P. 2012. Dating deformation in the Gran Paradiso Massif (NW Italian Alps) : Implications for the exhumation of high-pressure rocks in a collisional belt. *Lithos*, 144-145 : 130-144. (Cité page 289.)
- Rubin A. E. 1992. A shock-metamorphic model for silicate darkening and compositionally variable plagioclase in CK and ordinary chondrites. *Geochimica et Cosmochimica Acta*, 56 : 1705-1714. (Cité pages 163 et 190.)
- Russo S., Cutrupia D., Di Bella M., et Minutoli C. 2006. High-pressure metamorphism in southern Calabria, Italy : the Cardeto chlorite-garnet metapelites. *Periodico di Mineralogia*, 75 : 23-42. (Cité page 85.)
- Saccocia P. J. et Seyfried W. 1994. The solubility of chlorite solid solutions in 3.2wt% from 300-400 °C, 500 bars. *Geochimica et Cosmochimica Acta*, 58 : 567-585. (Cité page 26.)
- Salot P. 1978. Le métamorphisme dans les Alpes françaises. *Thèse, Université d'Orsay, Orsay*, pp. 183. (Cité pages 206, 210, 215, 218 et 251.)
- Sanchez G., Rolland Y., Corsini M., Oliot E., Goncalves J., P. an Schneider, Verati C., J.M. Lardeaux, et Marquer D. 2011. Dating low-temperature deformation by $^{40}\text{Ar}/^{39}\text{Ar}$ on white mica, insights from the Argentera-Mercantour Massif (SW Alps). *Lithos*, 125 : 521-536. (Cité pages 239, 248 et 251.)
- Saravanan C. S., Mishra B., et Jairam M. S. 2009. P-T conditions of mineralization in the Jonnagiri granitoid-hosted gold deposit, eastern Dharwar Craton, southern India : Constraints from fluid inclusions and chlorite thermometry. *Ore Geology Review*, 36 : 333-349. (Cité page 49.)
- Schmid S.M. et Kissling E. 2000. The arc of western Alps in the light of geophysical data on deep crystal structures. *Tectonics*, 19 : 62-85. (Cité page 218.)
- Schmidt D., Schmidt S., Mullis J., Ferreira Mählmann R., et Frey M. 1997. Very low grade metamorphism of the Tavayanne formation of western Switzerland. *Contributions to Mineralogy and Petrology*, 129 : 385-403. (Cité page 85.)
- Schmidt M. W. 1992. Amphibole composition in tonalite as a function of pressure : an experimental calibration of the Al-in-hornblende barometer. *Contributions to Mineralogy and Petrology*, 110 : 304-310. (Cité pages 137, 144, 145 et 305.)
- Schmidt M. W. 1998. La deshydratation dans les zones de subduction et le recyclage des matériaux crustaux dans le manteau. *HDR, Université Blaise-Pascal, Clermont Ferrand*. (Cité page 27.)

- Schwartz S. 2000. La zone piémontaise des Alpes occidentales : un paléo-complexe de subduction. Arguments métamorphiques, géochronologiques et structuraux. *Thèse/Phd, Université Claude Bernard, Lyon*, pp. 392. (Cité pages 202, 207, 218, 257, 260, 261, 262, 266 et 286.)
- Schwartz S., Allemand P., et Guillot S. 2001. Numerical model of the effect of serpentinites on the exhumation of eclogitic rocks : insights from the Monviso ophiolitic massif (Western Alps). *Tectonics*, 42 : 193–206. (Cité pages 252 et 289.)
- Schwartz S, Lardeaux J. M., et Tricart P. 2000. La zone d'Acceglio (Alpes cottiennes) : un nouvel exemple de croûte continentale éclogitisée dans les Alpes occidentales. *Comptes Rendu Académie des Sciences Paris*, 330 : 859–866. (Cité page 210.)
- Schwartz S., Lardeaux J. M., Tricart P., Guillot S., et Labrin E. 2007. Diachronous exhumation of HP-LT metamorphic rocks from south-western Alps : evidence from fission-track analysis. *Terra Nova*, 19 : 133–140. (Cité pages 216 et 240.)
- Schwartz S., Tricart P., Lardeaux J. M., Guillot S., et Vidal O. 2009. Late tectonic and metamorphic evolution of the Piedmont accretionary wedge (Queyras Schistes lustrés, western Alps) : evidences for tilting during Alpine collision. *GSA Bulletin*, 121 : 502–518. (Cité pages 200, 218, 251, 261, 273, 276 et 280.)
- Searle D. J. W., M. P. an Cooper et Rex A. J. 1988. Collision tectonics of the Ladakh—Zaskar Himalaya. *Philosophical Transactions of the Royal Society of London. Series A, Mathematical and Physical Sciences*, 326 : 117–150. (Cité page 293.)
- Searle M. P., Windley B. F., Coward M. P., Cooper D. J. W., Rex A. J., Rex D., Li T., Xiao X., Jan M. Q., Thakur V. C., et Kumar S. 1987. The closing of Tethys and the tectonics of the Himalaya. *Geological Society of America Bulletin*, 98 : 678–701. (Cité page 293.)
- Seber G. 1984. *Multivariate Observations*. Hoboken, NJ : John Wiley and Sons, Inc. (Cité page 141.)
- Sengör A. M. C. 1979. Mid-Mesozoic closure of Permo-Triassic Tethys and its implications. *Nature*, 279 : 590–593. (Cité page 293.)
- Sengupta P., Dasgupta S., Bhattacharya P. K., et Hariya Y. 1989. Mixing behavior in quaternary garnet solid solution and an extended Ellis and Green garnet-clinopyroxene geothermometer. *Contributions to Mineralogy and Petrology*, 103 : 223–227. (Cité pages 21 et 144.)
- Serafimovski T., Dolenec T., et Tasev G. 2006. Actinolite-phengite-chlorite metasomatites from the Toranica Pb-Zn ore deposit in Macedonia. *Materials and Geoenvironment*, 53 : 445–453. (Cité page 85.)
- Shinjoe H., Goto A., Kagitani M., et Sakai C. 2009. Ca-Al hydrous silicates in the chlorite-grade pelitic schists in Sanbagawa metamorphic belt and a petrogenetic analysis in the model mixed-volatile system. *Journal of Mineral Petrology Sciences*, 104 : 263–275. (Cité page 85.)
- Shock E. L. et Helgeson H. C. 1988. Calculation of the thermodynamic and transport properties of aqueous species at high pressures and temperatures : Correlation algorithms for ionic species and equation of state predictions to 5 kb and 1000 °C. *Geochimica et Cosmochimica Acta*, 52 : 2009–2036. (Cité page 96.)

- Shock E. L., Helgeson H. C., et Swerjensky D. A. 1989. Calculation of the thermodynamic and transport properties of aqueous species at high pressures and temperatures : Standard partial molal properties of inorganic neutral species. *Geochimica et Cosmochimica Acta*, 53 : 2157–2183. (Cité page 96.)
- Shock E. L., Sassani D. C., Willis M., et Sverjensky D. A. 1997. Inorganic species in geological fluids : Correlations among standard molal thermodynamic properties of aqueous ions and hydroxide complexes. *Geochimica et Cosmochimica Acta*, 61 : 907–950. (Cité page 96.)
- Simon-Labric T., Rolland Y., Dumont T., Heymes T., Authemayou C., Corsini M., et Fornari M. 2009. $^{40}\text{Ar}/^{39}\text{Ar}$ dating of Penninic Front tectonic displacement (Western Alps) during the Lower Oligocene (31–34 Ma). *Terra Nova*, 21 : 127–136. (Cité pages 216, 239, 242, 251, 257, 259 et 285.)
- Smith D.C. 1984. Coesite in clinopyroxene in the Caledonides and its implication for geodynamics. *Nature*, 310 : 641–644. (Cité page 214.)
- Spath H. 1985. Cluster dissection and analysis : theory, FORTRAN programs, examples. *New York : Halsted Press*. (Cité page 141.)
- Spear F. S. 1993. Metamorphic phase equilibria and pressure-temperature-time paths. *Mineralogical Society of America, Washington, D. C.*, pp. 799. (Cité pages 3, 20, 31, 69, 143, 145, 150 et 215.)
- Spencer D. A., Ramsay J., Spencer-Cervato C., Pognante U., Chaudry M. N., et Ghazanfar M. 1990. High pressure (eclogite facies) metamorphism in the Indian plate, Northwestern Himalaya, Pakistan. In *Proceeding of the Second Pakistan Geological Congress - Geological Bulletin University of Peshawar*, 23 : 87–100. (Cité page 295.)
- Staudigel H. et Schreyer W. 1977. The upper thermal stability of clinochlore, $\text{Mg}_5\text{Al}[\text{Si}_3\text{Al}_{10}](\text{OH})_8$, at 10–35 kbar $\text{P}(\text{H}_2\text{O})$. *Contributions to Mineralogy and Petrology*, 61 : 187–198. (Cité page 26.)
- Strzeczynski P. 2006. Tectono-metamorphic evolution and 3D modelling along the Lyon Torino railway project (Maurienne, Alps). *Thèse, Université de Lyon*. (Cité page 289.)
- Strzeczynski P., Guillot S., Leloup P. H., Arnaud N., Vidal O., Ledru P., Courrioux G., et Darmendrail X. 2012. Structural-metamorphic and ^{40}Ar - ^{39}Ar analysis in the Briançonnais zone (Modane Aussois area, Lyon Turin transect, Western Alps). Integration in the Alpine framework. *Journal of Geodynamics*, 56–57 : 55–75. (Cité pages 214, 216, 239, 258, 259 et 289.)
- Sverjensky E. L., D. A. an Shock et Helgeson H. C. 1997. Prediction of the thermodynamic properties of aqueous metal complexes to 1000 °C and 5 kb. *Geochimica et Cosmochimica Acta*, 61 : 1359–1412. (Cité page 96.)
- Tagami T., Ito H., et Nishimura S. 1998. Thermal annealing characteristics of spontaneous fission tracks in zircon. *Chemical geology*, 80 : 159–169. (Cité page 216.)
- Tagirov B. et Schott J. 2001. Aluminum speciation in crustal fluids revisited. *Geochimica et Cosmochimica Acta*, 65 : 3965–3992. (Cité page 96.)

- Tagirov B., Zotov A. V., et Akinfiyev N. N. 1997. Experimental study of dissociation of HCl from 350 to 500 °C and from 500 to 2500 bars. Thermodynamic properties of HCl(aq). *Geochimica et Cosmochimica Acta*, 61 : 4267–4280. (Cité page 96.)
- Tarantola A., Mullis J., Guillaume D., Dubessy J., Capitani C., et Adbelmoula M. 2009. Oxidation of CH₄ to CO₂ and H₂O by chloritization of detrital biotite at 270 °C in the external part of the Central Alps, Switzerland. *Lithos*, 112 : 497–510. (Cité page 49.)
- Termier P. 1891. Etude sur la constitution géologique du massif de la Vanoise (Alpes de Savoie). *Bulletin Service de la Carte Géologique de France*, 2 : 367–513. (Cité page 203.)
- Theye T. et Seidel E. 1992. Petrology of low-grade high-pressure metapelites from the External Hellenides (Crete, Peloponnese). A case study with attention to sodic minerals. *European Journal of Mineralogy*, 3 : 343–366. (Cité pages 92 et 93.)
- Theye T., Seidel E., et Vidal O. 1992. Carpholite, sudoite and chloritoid in low-grade high-pressure metapelites from Crete and the Peloponnese, Greece. *European Journal of Mineralogy*, 4 : 487–507. (Cité pages 67, 85, 91, 92 et 93.)
- Thompson A. 1976. Mineral reactions in pelitic rocks : II. Calculation of some P-T-X(Fe-Mg) phase relations. *American Journal of Science*, 276 : 425–454. (Cité page 144.)
- Tricart P. 1973. Les Schistes lustrés du Haut-Cristillan. Analyse tectonique d'un secteur externe du domaine piémontais (Alpes occidentales, France). *Thèse, Université Louis Pasteur, Strasbourg*, pp. 191. (Cité pages 202 et 206.)
- Tricart P. 1980. Tectoniques superposées dans les Alpes occidentales au Sud du Pelvoux. Evolution structurale d'une chaîne de collision. *Thèse, Institut de Géologie, Strasbourg*, pp. 407. (Cité pages 206 et 221.)
- Tricart P. 1984. From passive margin to continental collision - a tectonic scenario for the western alps. *American Journal of Science*, 284 : 97–120. (Cité pages 202, 221, 251 et 252.)
- Tricart P. 2003. Carte géologique de la France au 1/50 000ème; Feuille d'Aiguille - Col Saint-Martin. *BRGM Feuille, Orléans*. (Cité pages 200 et 207.)
- Tricart P., Bouillin J. P., Dick P., Moutier L., et Wing C. 1996. Le faisceau de failles de haute-Durance et le jeu distensif du front Briançonnais au SE du Pelvoux (Alpes occidentales). *Comptes Rendus de l'Académie des Sciences de Paris*, 323 : 251–257. (Cité page 252.)
- Tricart P. et Schwartz S. 2006. A north-south section across the Queyras Schistes Lustrés (Piedmont zone, Western Alps) : syn-collision refolding of a subduction wedge. *Eclogae Geol. Helv.*, 99 : 429–442. (Cité pages 218, 221 et 261.)
- Tricart P., Schwartz S., Sue C., et Lardeaux J. M. 2004. Evidence of synextension tilting and doming during final exhumation from analysis of multistage faults (Queyras Schistes lustrés, Western Alps). *Journal of Structural Geology*, 26 : 1633–1645. (Cité page 264.)
- Tricart P., van der Beek P., Schwartz S., et Labrin E. 2007. Diachronous late-stage exhumation across the western Alpine arc : constraints from apatite fission-track thermochronology between the Pelvoux and Dora-Maira Massifs. *Geological Society of London*, 164 : 163–174. (Cité pages 239, 257 et 261.)
- Trotet F., Vidal O., et Jolivet L. 2001. Exhumation of Syros and Sifnos metamorphic rocks (Cyclades, Greece). New constraints on the P-T paths. *European Journal of Mineralogy*, 13 : 901–920. (Cité pages 4, 75 et 85.)

- Ulrich M. 2010. Péridotites et serpentinites du complexe ophiolitique de la Nouvelle-Calédonie. *Thèse, Université de Nouvelle Calédonie*, pp. 212. (Cité page [123](#).)
- Velde B. 1965. Phengite micas ; synthesis, stability, and natural occurrence. *American Journal of Science*, 263 : 886–913. (Cité page [228](#).)
- Verlaguet A., Goffé B., Brunet F., Poinssot C., Vidal O., Findling N., et Menut D. 2011. Metamorphic veining and mass transfer in a chemically closed system : a case study in Alpine metabauxites (western Vanoise). *Journal of Metamorphic Geology*, 29 : 275–300. (Cité page [49](#).)
- Vialon P. 1966. Etude géologique du massif cristallin Dora-Maira Alpes cotiennes internes - Italie. *Thèse, Université Scientifique et Médicale de Grenoble*, pp. 281. (Cité page [206](#).)
- Vidal O., De Andrade V., Lewin E., Munoz M., Parra T., et Pascarelli S. 2006. P-T-deformation-Fe³⁺/Fe²⁺ mapping at the thin section scale and comparison with XANES mapping : application to a garnet-bearing metapelite from the Sambagawa metamorphic belt (Japan). *Journal of Metamorphic Geology*, 24 : 669–683. (Cité pages [3](#), [4](#), [24](#), [27](#), [28](#), [29](#), [32](#), [41](#), [42](#), [44](#), [49](#), [51](#), [52](#), [53](#), [54](#), [55](#), [59](#), [73](#), [75](#), [83](#), [86](#), [112](#), [113](#), [115](#), [137](#), [143](#), [211](#), [216](#), [227](#), [228](#), [234](#), [235](#), [242](#), [245](#), [247](#), [255](#), [256](#), [269](#), [270](#), [273](#), [276](#), [277](#), [319](#) et [363](#).)
- Vidal O. et Dubacq B. 2009. Thermodynamic modelling of clay dehydration, stability and compositional evolution with temperature, pressure and H₂O activity. *Geochimica et Cosmochimica Acta*, 73 : 6544 – 6564. (Cité pages [33](#), [34](#) et [229](#).)
- Vidal O., Dubacq B., et Lanari P. 2010. Comment on "the role of H₃O⁺ in the crystal structure of illite by Nieto, F., Melini, M., Abad, I.". *Clays and Clay Minerals*, 58 : 717–720. (Cité pages [7](#), [29](#) et [229](#).)
- Vidal O., Goffé B., Bousquet R., et Parra T. 1999. Calibration and testing of an empirical chloritoid-chlorite Mg-Fe exchange thermometer and thermodynamic data for daphnite. *Journal of Metamorphic Geology*, 17 : 25–39. (Cité pages [21](#), [26](#), [85](#), [143](#) et [144](#).)
- Vidal O., Goffé B., et Theye T. 1992. Experimental study of the stability of sudoite and magnesiocarpholite and calculation of a new petrogenetic grid for the system FeO–MgO–Al₂O₃–SiO₂–H₂O. *Journal of Metamorphic Geology*, 10 : 603–614. (Cité pages [26](#), [66](#), [80](#), [81](#), [83](#), [91](#), [93](#) et [372](#).)
- Vidal O. et Parra T. 2000. Exhumation paths of high-pressure metapelites obtained from local equilibria for chlorite-phengite assemblages. *Geological Journal*, 35 : 139–161. (Cité pages [27](#), [38](#), [49](#), [50](#) et [216](#).)
- Vidal O., Parra T., et Trotet F. 2001. A Thermodynamic Model for Fe-Mg Aluminous Chlorite Using Data from Phase Equilibrium Experiments and Natural Pelitic Assemblages in the 100 to 600 C, 1 to 25 kb Range. *American Journal of Science*, 301 : 557. (Cité pages [4](#), [26](#), [27](#), [28](#), [66](#), [73](#), [75](#), [78](#), [79](#), [83](#), [84](#), [85](#), [86](#), [87](#), [143](#), [227](#) et [363](#).)
- Vidal O., Parra T., et Vieillard P. 2005. Thermodynamic properties of the Tschermak solid solution in Fe-chlorite : Application to natural examples and possible role of oxidation. *American Mineralogist*, 90 : 347–358. (Cité pages [4](#), [24](#), [27](#), [28](#), [41](#), [55](#), [59](#), [70](#), [73](#), [75](#), [83](#), [86](#), [111](#), [112](#), [143](#), [216](#), [227](#), [228](#), [234](#), [235](#), [242](#) et [363](#).)
- Wagner T., Kulik D. A., Hingerl F. F., et Dmytrieva S. V. in press. GEM-Selektor geochemical modeling package : TSolMod library and data interface for multicomponent phase models. *Canadian Mineralogist*. (Cité pages [5](#), [67](#), [78](#) et [96](#).)

- Walshe J. L. 1986. A six-component chlorite solid solution model and the conditions of chlorite formation in hydrothermal and geothermal systems. *Economic Geology*, 81 : 681–703. (Cité pages 73, 74, 89 et 91.)
- Warren C. et Waters D. 2006. Oxidized eclogites and garnet-blueschists from Oman : P–T path modelling in the NCFMASHO system. *Journal of Metamorphic Geology*, 24 : 1–20. (Cité pages 143 et 150.)
- Waters D. 1996. The Garnet-Cpx-Phengite barometer. Recommended calibration and calculation method, updated 1 March 1996. <http://www.earth.ox.ac.uk/davewa/research/eclogite/ecbarcal.html> 1. (Cité pages 144, 153 et 305.)
- Waters D. 2002. Clinopyroxene-Amphibole-plagioclase symplectites in Norwegian eclogites : microstructures, chemistry and the exhumation P–T path. *Mineralogical Society, Winter Conference, Derby*. (Cité pages 144, 151, 155 et 305.)
- Waters D. 2003. P–T paths from Cpx-Hbl-Pl symplectites, updated 22 February 2003. <http://www.earth.ox.ac.uk/davewa/research/eclogites/symplectites.htm>. (Cité pages 144, 151, 155 et 305.)
- Waters D. et Martin H. 1993. Geobarometry in phengite-bearing eclogites. *Terra Nova*, 5 : 410–411. (Cité pages 137, 144, 153 et 304.)
- Weisberg M. K., McCoy T. J., et Krot A. N. 2006. Systematics and Evaluation of Meteorite Classification. *Meteorites and the early Solar System II. The University of Arizona Pres.* (Cité page 192.)
- Weisberg M. K., Prinz M., et Clayton T. K., R. N. and Mayeda. 1997. Cv3 chondrites ; three subgroups, not two meteoritics. *Earth and Planetary Science Letters*, 32 : 138–139. (Cité pages 163 et 169.)
- White L. T. et Lister G. S. 2012. The collision of India with Asia. *Journal of Geodynamics*, 56–57 : 7–17. (Cité page 293.)
- Wiederkehr M., Sudo M., Bousquet R., Berger A., et Schmid S. M. 2009. Alpine orogenic evolution from subduction to collisional thermal overprint : The $^{40}\text{Ar}/^{39}\text{Ar}$ age constraints from the Valaisan Ocean, central Alps. *Tectonics*, 28. (Cité page 289.)
- Worley B. et Powell R. 2000. High-precision relative thermobarometry : theory and a worked example. *Journal of Metamorphic Geology*, 18 : 91–101. (Cité page 49.)
- Yamato P. 2006. Des contraintes pour les zones de convergences : Confrontation des données du métamorphisme et des modélisations numériques thermomécaniques - Applications aux Alpes et à l'Oman. *Thèse, Université Pierre et Marie Curie, Paris 6*, pp. 259. (Cité page 207.)
- Yamato P., Agard P., Goffé B., De Andrade V., Vidal O., et Jolivet L. 2007. New, high-precision P–T estimates for Oman blueschists : implications for obduction, nappe stacking and exhumation processes. *Journal of Metamorphic Geology*, 25 : 657–682. (Cité pages 4, 75 et 137.)
- Yang J., Wu Z., Dobrzhinetskaya L. F., Grenn H. W., Pei W., Shi R., Wu C., Wooden C., Zhang J., Wan Y., et Li H. 2003. Discovery of metamorphic diamonds in central China : an indication of a >4000-km-long zone of deep subduction resulting from multiple continental collisions. *Terra Nova*, 15 : 370–379. (Cité page 307.)

- Yongheng C., Daode W., et Pernicka E. 1993. REE and other trace element chemistry of oldhamite (CaS) in the Qingzhen chondrite (EH3) and their genetic implications. *Chinese Journal of Geochemistry*, 12 : 317–327. (Cité page 162.)
- Young D. Y., Hacker B. R., Andersen T. B., et Corfu F. 2007. Prograde amphibolite facies to ultrahigh-pressure transition from Nordfjord, western Norway : implications for exhumation tectonics. *Tectonics*, 26 : 1–15. (Cité pages 214, 242, 244 et 307.)
- Zack T., Moraes R., et Kronz A. 2004. Temperature dependence of Zr in rutile : empirical calibration of a rutile thermometer. *Contributions to Mineralogy and Petrology*, 148 : 471–488. (Cité page 144.)
- Zang W. et Fyfe W. S. 1995. Chloritization of the hydrothermally altered bedrock at the Igarape Bahia gold deposit, Carajas, Brazil. *Mineralium Deposita*, 30 : 30–38. (Cité pages 73, 74, 85, 86, 144 et 227.)

ANNEXES



SOMMAIRE

A.1	THERMODYNAMIQUE	359
A.2	LOGICIEL MEAMP	367
A.3	MODÈLE CLAY	373
A.4	XMAPTOOLS - USER NOTICE	395
A.5	ARTICLES SUPPLÉMENTAIRES	443

A.1 THERMODYNAMIQUE

A.1.1 Calcul de G^0 (formalisme de Berman et Brown)

Le potentiel chimique d'une phase peut s'écrire de la manière suivante en utilisant la convention de Berman et Brown ($G^0 = H^0 - T \times S^0$) :

$$\mu_i = H_i^0 + \int_{T_0}^T C_p dT + \int_{P_0}^P V dP - T(S_i^0 + \int_{T_0}^T \frac{C_p}{T} dT) + RT \ln(a_i) \quad (\text{A.1})$$

La capacité calorifique à P et T données ($C_p(P,T)$) d'un composant est estimée en utilisant l'équation polynomiale de [Berman et Brown \(1985\)](#) qui est une troncature des équations de [Maier \(1932\)](#), [Haas et Fisher \(1976\)](#) :

$$C_p(P, T) = k_1 + k_2 T^{-0.5} + k_3 T^{-2} + k_4 T^{-3} \quad (\text{A.2})$$

avec k_1, k_2, k_3 et k_4 les coefficients C_p disponibles dans la base de données [Berman \(1988\)](#). On peut donc calculer les deux intégrales nécessaires au calcul du potentiel chimique (Eq. [A.1](#)) :

$$\int_{T_0}^T C_p dT = k_1(T - T_0) - 2 k_2(\sqrt{T} - \sqrt{T_0}) - k_3\left(\frac{1}{T} - \frac{1}{T_0}\right) - \frac{k_4}{2}\left(\frac{1}{T^2} - \frac{1}{T_0^2}\right) \quad (\text{A.3})$$

et

$$\begin{aligned} \int_{T_0}^T \frac{C_p}{T} dT = & k_1(\ln(T) - \ln(T_0)) + 2 k_2\left(\frac{1}{\sqrt{T}} - \frac{1}{\sqrt{T_0}}\right) \\ & - \frac{k_3}{2}\left(\frac{1}{T^2} - \frac{1}{T_0^2}\right) - \frac{k_4}{3}\left(\frac{1}{T^3} - \frac{1}{T_0^3}\right) \end{aligned} \quad (\text{A.4})$$

Le volume du composant à P et T données ($V(P, T)$) est calculé en utilisant une fonction simple pour les solides de [Berman \(1988\)](#) :

$$V(P, T) = V^0[1 + v_1(T - T_0) + v_2(T - T_0)^2 + V_3(P - P_0) + v_4(P - P_0)^2] \quad (\text{A.5})$$

avec V^0 le volume à 1 bar et 20°C et V_1, V_2, V_3 et V_4 les coefficients de volume disponibles dans la base de données [Berman \(1988\)](#). Cette expression de $V(P,T)$ permet de calculer l'intégrale suivante nécessaire au calcul du potentiel chimique :

$$\begin{aligned} \int_{P_0}^P V dP = & (V^0 + (V_1 V^0)(T - T_0) + (V_2 V^0)(T - T_0)^2)(P - P_0) \\ & + (V_3 V^0)\left(\frac{P^2}{2} - P_0 P + \frac{P_0^2}{2}\right) \\ & + (V_4 V^0)\left(\frac{P^3}{3} - P^2 P_0 + P_0^2 P - \frac{P_0^3}{3}\right) \end{aligned} \quad (\text{A.6})$$

A.1.2 Calcul de G^0 (formalisme de Holland et Powell)

Dans un système chimique à n éléments, le potentiel chimique standard $\mu^0 = G(P, T)$ d'un composé peut s'écrire de la manière suivante en utilisant la convention de Benson-Helgeson (Benson 1968, Helgeson et al. 1978) :

$$\mu^0 = G^0 - (T - T_0) \times S^0 + \int_{T_0}^T C_p dT + \int_{P_0}^P V dP - T \int_{T_0}^T \frac{C_p}{T} dT \quad (\text{A.7})$$

avec

$$G^0 = H^0 - T_0 \left(S^0 - \sum_{i=1}^n v_i S_i \right) \quad (\text{A.8})$$

avec v_i le nombre d'éléments i de la phase et S_i les coefficients d'entropie standard des éléments chimiques.

L'expression A.7 peut également s'écrire de la manière suivante :

$$\mu^0 = G^0 + \Delta G_T + \Delta G_P \quad (\text{A.9})$$

avec ΔG_T l'incrément de l'énergie libre standard de Gibbs à une pression P_0 de 1 bar entre la température de référence T_0 et une température T :

$$\Delta G_T = -(T - T_0) \times S^0 + \int_{T_0}^T C_p dT - T \int_{T_0}^T \frac{C_p}{T} dT \quad (\text{A.10})$$

et ΔG_P l'incrément à une température T_0 de 298 K entre une pression de référence P_0 et une pression P :

$$\Delta G_P = \int_{P_0}^P V dP \quad (\text{A.11})$$

Nous allons maintenant décrire séparément ces deux incréments ΔG_T et ΔG_P :

(1) La capacité calorifique à P et T données ($C_p(P, T)$) d'un composant est estimée en utilisant l'équation polynomiale de Robie et al. (1978), également utilisée par Holland et Powell (1998) :

$$C_p(P, T) = a + bT + cT^{-2} + dT^{-0.5} \quad (\text{A.12})$$

avec a , b , c et d les coefficients de C_p disponibles dans la base de données de Holland et Powell (1998). On peut donc calculer les deux intégrales nécessaires au calcul du potentiel chimique standard :

$$\int_{T_0}^T C_p dT = a(T - T_0) + b\left(\frac{T^2}{2} - \frac{T_0^2}{2}\right) - c\left(\frac{1}{T} - \frac{1}{T_0}\right) + 2d(\sqrt{T} - \sqrt{T_0}) \quad (\text{A.13})$$

et

$$\int_{T_0}^T \frac{C_p}{T} dT = a(\ln(T) - \ln(T_0)) + b(T - T_0) - \frac{c}{2} \left(\frac{1}{T^2} - \frac{1}{T_0^2} \right) - 2d \left(\frac{1}{\sqrt{T}} - \frac{1}{\sqrt{T_0}} \right) \quad (\text{A.14})$$

En combinant les équations A.10, A.13 et A.14 l'incrément de l'énergie libre de Gibbs ΔG_T devient :

$$\Delta G_T = -S_0(T - T_0) - T \sum_i (M_i K_i) \quad (\text{A.15})$$

avec K_i les coefficients C_p (respectivement a , b , c et d) et M_{n_i} les termes de la fonction de Temkin-Shwarzman (e.g. Dorogokupets et al. 1988, Kulik et Wagner 2005) :

$$M_1 = T \ln\left(\frac{T}{T_0}\right) - T + T_0 \quad (\text{A.16})$$

$$M_2 = \frac{1}{2}(T - T_0)^2 \quad (\text{A.17})$$

$$M_3 = \frac{(T - T_0)^2}{2 T \times T_0^2} \quad (\text{A.18})$$

$$M_4 = \frac{2(\sqrt{T} - \sqrt{T_0})^2}{\sqrt{T_0}} \quad (\text{A.19})$$

soit :

$$\Delta G_T = -S_0(T - T_0) - a M_1 - b M_2 - c M_3 - d M_4 \quad (\text{A.20})$$

(2) Le volume du composant à P et T données ($V(P, T)$) est calculé en utilisant une relation basée sur l'équation d'état de Murnaghan EoS (e.g. Holland et Powell 1998, Kulik et Wagner 2008) :

$$V(P, T) = V(P_0, T) \left[1 - \frac{4P}{K_T + 4P} \right]^{\frac{1}{4}} \quad (\text{A.21})$$

avec

$$V(P_0, T) = V^0 [1 + a^0(T - T_0) - 20 a^0(\sqrt{T} - \sqrt{T_0})] \quad (\text{A.22})$$

et

$$K_T = K_0(1 - 1.5 \cdot 10^{-4}(T - T_0)) \quad (\text{A.23})$$

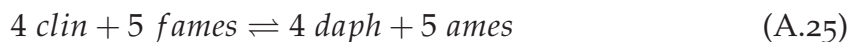
On peut donc calculer ΔG_P comme l'intégrale $\int_{P_0}^P V dP$ (Eq. A.24) :

$$\Delta G_P = \frac{V(P_0, T) \times K_T}{3} \left[\left(1 + \frac{4P}{K_T} \right)^{\frac{3}{4}} - 1 \right] \quad (\text{A.24})$$

A.1.3 Réactions internes et relations internes

Une des hypothèses majeures du formalisme utilisé par Holland et Powell est que le $\Delta\mu_{reaction}$ des réaction internes est égal à zéro pour n'importe quelle condition de pression et de température. L'implication de cette hypothèse sur le calcul des propriétés standard des pôles purs chimiquement dépendants a été discutée dans la discussion du chapitre 2 (Part. 2.3.5). L'une des conséquences directes de cette hypothèse est qu'il faut trouver une méthode pour exprimer le μ_{fames}^0 tel que pour la réaction interne $\Delta\mu_{reaction} = 0$. Une méthode matricielle a été proposée par Powell et Holland (1999) pour estimer le μ_{fames}^0 en utilisant une "relation interne". Nous allons détailler ici une autre procédure pour estimer l'expression de cette "relation interne". Nous espérons que cette approche sera plus concrète pour le lecteur.

Nous avons vu dans le manuscrit qu'entre les quatre pôles purs de chlorite amesiteMg (*ames*), clinochlore (*clin*), daphnite (*daph*) et amesiteFe (*fames*) intervient la réaction interne suivante :



ce qui signifie qu'il est possible d'exprimer la composition chimique de *fames* en fonction des compositions de *daph*, *ames* et *clin* :

$$\text{fames} = \frac{4}{5}\text{daph} + \text{ames} - \frac{4}{5}\text{clin} \quad (\text{A.26})$$

On peut écrire le potentiel chimique de la réaction interne (Eq. A.25) comme :

$$\Delta\mu_{reaction} = \sum_{i=1}^n v_i \mu_i \quad (\text{A.27})$$

ce qui revient à écrire que,

$$\Delta\mu_{reaction} = \sum_{i=1}^n v_i (\mu_i^0 + RT \ln(a_{ideale_i}) + RT \ln(\gamma_i)) \quad (\text{A.28})$$

ou encore,

$$\Delta\mu_{reaction} = \Delta\mu_{reaction}^0 + \Delta RT \ln(a_{ideale_{reaction}}) + \Delta RT \ln(\gamma_{reaction}) \quad (\text{A.29})$$

ce qui revient à traiter le problème en trois parties distinctes : la partie standard, la partie d'activité idéale et la partie d'activité non-idéale.

(1) L'activité idéale des pôles purs *fames*, *ames*, *clin* et *daph* peut être calculée en utilisant un modèle ionique grâce aux relations suivantes (détails dans la partie 2.3.3) :

$$a_{fames} = (X_{Fe,M2M3})^4 X_{Al,M1} (X_{Al,T2})^2 \quad (A.30)$$

$$a_{ames} = (X_{Mg,M2M3})^4 X_{Al,M1} (X_{Al,T2})^2 \quad (A.31)$$

$$a_{clin} = 4(X_{Mg,M2M3})^4 X_{Mg,M1} X_{Al,T2} X_{Si,T2} \quad (A.32)$$

$$a_{daph} = 4(X_{Fe,M2M3})^4 X_{Fe,M1} X_{Al,T2} X_{Si,T2} \quad (A.33)$$

avec $(X_{i,j})^q$ la fraction de l'élément *i* sur le site *j* de multiplicité *q* (c.f. Eq. 2.14). On peut donc écrire le terme $\Delta RT \ln(a_{ideale_{reaction}})$ de la réaction interne de la manière suivante :

$$\Delta RT \ln(a_{ideale_{reaction}}) = RT \ln \left[\frac{(a_{daph})^4 (a_{ames})^5}{(a_{clin})^4 (a_{fames})^5} \right] \quad (A.34)$$

On peut substituer les expressions des activités idéales (A.30, A.31, A.32 et A.33), ce qui donne après simplification :

$$\Delta RT \ln(a_{ideale_{reaction}}) = RT \ln \left[\frac{(X_{Fe,M1})^4 (X_{Mg,M2M3})^4}{(X_{Fe,M2M3})^4 (X_{Mg,M1})^4} \right] = 0 \quad (A.35)$$

Cette relation est nulle, si et seulement si, il y a équipartition du Fe^{2+} et du *Mg* sur les différents sites cristallins (soit $X_{Fe,M1} = X_{Fe,M2M3} = 1 - X_{Mg,M1} = 1 - X_{Mg,M2M3}$), hypothèse souvent utilisée pour les chlorites (e.g. Vidal et al. 2001; 2005; 2006).

(2) Pour calculer le terme macroscopique d'activité non-idéale d'un pôle pur *i* en utilisant un formalisme symétrique pour un jeu de *n* pôles indépendants, on utilise la relation suivante (Holland et Powell 1996a;b, Powell et Holland 1993) :

$$RT \ln(\gamma_i) = \sum_1^n -(c_1 - p_1) (c_2 - p_2) W_{12} \quad (A.36)$$

avec c_1 et c_2 les coefficients de la réaction qui définit les pôles purs en fonction du jeu de pôles purs indépendants, dont les proportions sont p_1 et p_2 , et W_{12} le paramètre régulier entre les deux pôles purs indépendants (ou paramètre de Margules).

Pour le pôle pur *ames*, par exemple, qui appartient au jeu des trois pôles purs choisis comme indépendants, on peut écrire la réaction suivante, qui définit sa composition en fonction du set de pôles purs indépendants :

$$1 \text{ ames} = 1 \text{ ames} + 0 \text{ clin} + 0 \text{ daph} \quad (\text{A.37})$$

ce qui, en appliquant la relation A.36, permet d'obtenir le terme macroscopique $RT\ln(\gamma_{ames})$ suivant :

$$\begin{aligned} RT\ln(\gamma_{ames}) &= (1 - p_{ames}) p_{clin} W_{ames-clin} \\ &\quad + (1 - p_{ames}) p_{daph} W_{ames-daph} \\ &\quad - p_{clin} p_{daph} W_{clin-daph} \end{aligned} \quad (\text{A.38})$$

De la même manière, on peut calculer les termes macroscopiques des deux autres pôles indépendants :

$$\begin{aligned} RT\ln(\gamma_{clin}) &= p_{ames} (1 - p_{clin}) W_{ames-clin} \\ &\quad + p_{daph} (1 - p_{clin}) W_{daph-clin} \\ &\quad - p_{ames} p_{daph} W_{ames-daph} \end{aligned} \quad (\text{A.39})$$

$$\begin{aligned} RT\ln(\gamma_{ames}) &= p_{ames} (1 - p_{daph}) W_{ames-daph} \\ &\quad + p_{clin} (1 - p_{daph}) W_{clin-daph} \\ &\quad - p_{ames} p_{clin} W_{ames-clin} \end{aligned} \quad (\text{A.40})$$

Pour le pôle *fames* qui est le pôle pur chimiquement dépendant, on peut écrire la réaction suivante, qui définit sa composition en fonction du jeu de pôles purs indépendants :

$$1 \text{ fame} = 1 \text{ ames} - \frac{4}{5} \text{ clin} + \frac{4}{5} \text{ daph} \quad (\text{A.41})$$

ce qui, en appliquant la relation A.36, permet d'obtenir le terme macroscopique $RT\ln(\gamma_{ames})$ suivant :

$$\begin{aligned} RT\ln(\gamma_{ames}) &= (1 - p_{ames}) \left(\frac{4}{5} + p_{clin} \right) W_{ames-clin} \\ &\quad - (1 - p_{ames}) \left(\frac{4}{5} - p_{daph} \right) W_{ames-daph} \\ &\quad + \left(\frac{4}{5} + p_{clin} \right) \left(\frac{4}{5} - p_{daph} \right) W_{clin-daph} \end{aligned} \quad (\text{A.42})$$

On peut donc calculer le $\Delta RT \ln(\gamma_{reaction})$ comme :

$$\begin{aligned} \Delta RT \ln(\gamma_{reaction}) &= \sum_{i=1}^n v_i (RT \ln(\gamma_i)) \\ &= 4 RT \ln(\gamma_{clin}) + 5 RT \ln(\gamma_{fames}) - 4 RT \ln(\gamma_{daph}) \\ &\quad - 5 RT \ln(\gamma_{ames}) \end{aligned} \quad (A.43)$$

En substituant dans cette équation les termes macroscopiques calculés précédemment (Eq. A.38, A.39, A.40 et A.42) et après simplification, on obtient :

$$\Delta RT \ln(\gamma_{reaction}) = 4 W_{ames-daph} - 4 W_{ames-clin} - \frac{16}{5} W_{clin-daph} \quad (A.44)$$

ce qui, en d'autres termes, signifie que l'expression macroscopique de l'activité non-idéale de $RT \ln(\gamma_{fames})$ est égale à une combinaison linéaire des expressions macroscopiques des pôles purs indépendants, plus une fonction de déviation dépendante de $W_{ames-daph}$, $W_{ames-clin}$ et $W_{clin-daph}$:

$$\begin{aligned} RT \ln(\gamma_{fames}) &= -RT \ln(\gamma_{ames}) - \frac{4}{5} RT \ln(\gamma_{daph}) + \frac{4}{5} RT \ln(\gamma_{clin}) \\ &\quad - \frac{4}{5} W_{ames-daph} + \frac{4}{5} W_{ames-clin} + \frac{16}{25} W_{clin-daph} \end{aligned} \quad (A.45)$$

Cette relation est la condition pour que le $\Delta RT \ln(\gamma_{reaction})$ s'annule.

(3) Le potentiel chimique standard de la réaction interne peut quant à lui s'écrire :

$$\begin{aligned} \Delta \mu_{reaction}^0 &= \sum_{i=1}^n v_i (\mu_i^0) \\ &= 4 \mu_{clin}^0 + 5 \mu_{fames}^0 - 4 \mu_{daph}^0 - 5 \mu_{ames}^0 \end{aligned} \quad (A.46)$$

On peut maintenant calculer le $\Delta \mu_{reaction}$ à partir de l'équation A.29 en la combinant avec les équations du $\Delta \mu_{reaction}^0$ (Eq. A.46), du $\Delta RT \ln(a_{ideale_{reaction}})$ (Eq. A.35) et du $\Delta RT \ln(\gamma_{reaction})$ (Eq. A.44), soit :

$$\begin{aligned} \Delta \mu_{reaction} &= RT \ln \left[\frac{(X_{Fe,M1})^4 (X_{Mg,M2M3})^4}{(X_{Fe,M2M3})^4 (X_{Mg,M1})^4} \right] \\ &\quad + 4 \mu_{clin}^0 + 5 \mu_{fames}^0 - 4 \mu_{daph}^0 - 5 \mu_{ames}^0 \\ &\quad + 4 W_{ames-daph} - 4 W_{ames-clin} - \frac{16}{5} W_{clin-daph} \end{aligned} \quad (A.47)$$

soit pour $\Delta\mu_{reaction} = 0$,

$$\begin{aligned}\mu_{fames}^0 = & \mu_{ames}^0 + \frac{4}{5} \mu_{daph}^0 - \frac{4}{5} \mu_{clin}^0 \\ & + \frac{4}{5} W_{ames-daph} - \frac{4}{5} W_{ames-clin} - \frac{16}{25} W_{clin-daph}\end{aligned}\tag{A.48}$$

qui est la relation interne pour estimer μ_{fames}^0 sans utiliser des propriétés standards de *fames*. En effet, μ_{fames}^0 peut être calculé à partir des μ_i^0 de *ames*, *daph* et *clin* avec un terme non-idéal. Comme nous venons de le démontrer, cette "relation interne" peut être obtenue en calculant le $\Delta\mu_{reaction}$ de la réaction interne.

L'une des conséquences majeures de l'utilisation de cette relation interne est, que pour n'importe quelle composition de chlorite et conditions de pression et de température, le $\Delta\mu_{reaction}$ de la réaction interne sera toujours égal à zéro.

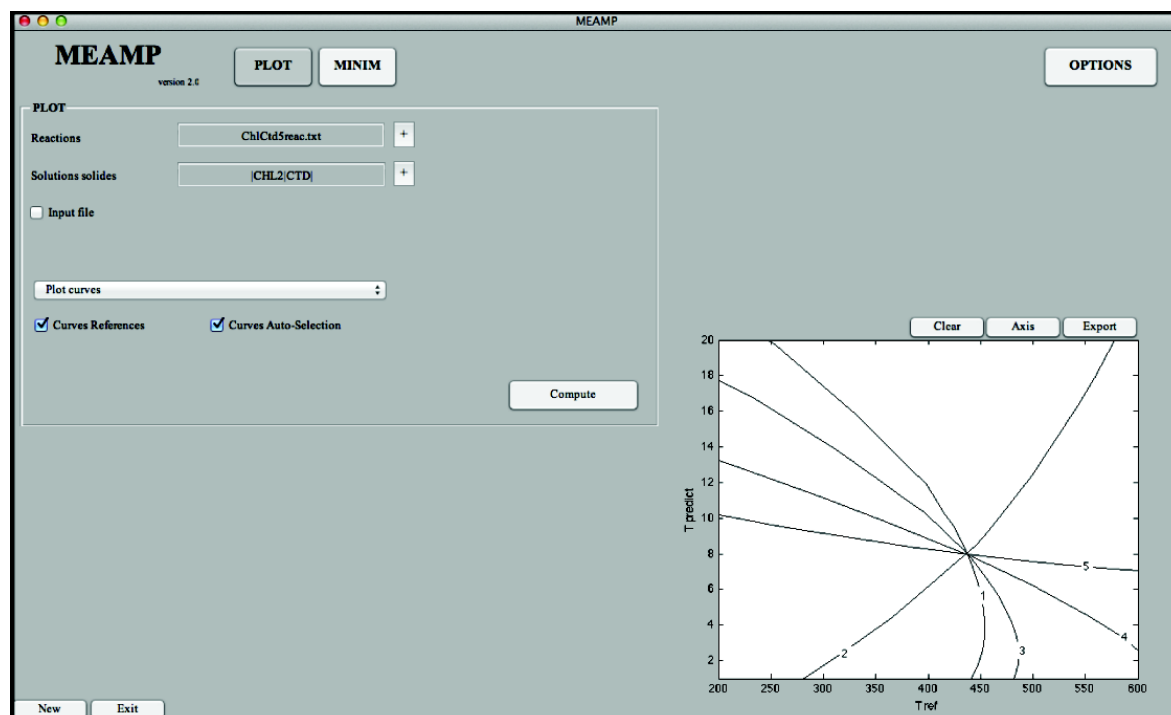


FIGURE A.1 – Logiciel MEAMP en mode « Plot »

A.2 LOGICIEL MEAMP

Le logiciel MEAMP (Multi-Equilibrium And Minimization Program) fonctionne avec la base de données et le formalisme de [Holland et Powell \(1998\)](#). C'est ce logiciel qui a été utilisé lors de la calibration du modèle Chl(LWV) présenté dans le manuscrit (Part. 2.3.3). Nous l'avons développé pour pouvoir tracer des réactions dans un champ pression température (mode « Plot ») et ajuster par minimisation des paramètres thermodynamiques en fonction de données expérimentales ou naturelles (mode « Minim »).

A.2.1 Mode « Plot »

Le mode Plot de MEAMP (Fig. A.1) permet de tracer dans un diagramme P-T des réactions (dépendantes et indépendantes), des surfaces correspondant à des $\Sigma \Delta G_{reaction}$, ou encore des lignes d'équilibres pour une paragenèse donnée, avec une variable de composition comme, par exemple, l'hydratation pour le modèle $phg + qtz + H_2O$. Les différentes réactions intervenant pour un assemblage donné peuvent être calculées en utilisant la fonction « new assemblage ». Ces réactions

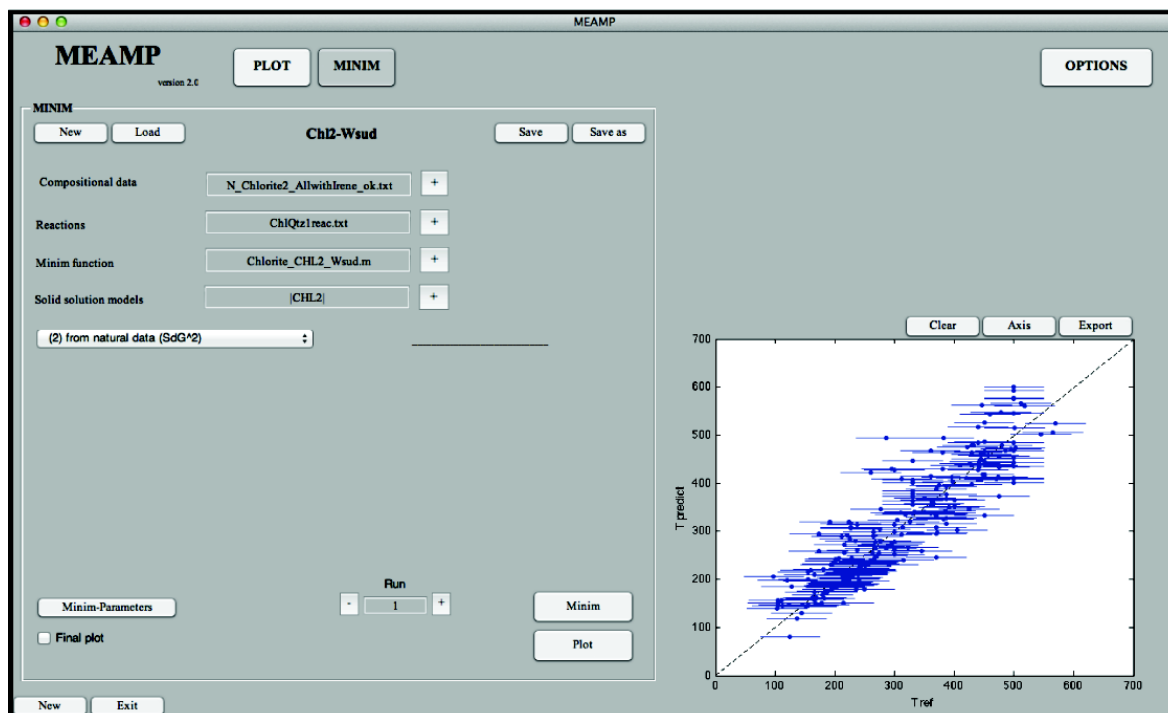


FIGURE A.2 – Logiciel MEAMP en mode "Minim"

sont stockées dans des fichiers texte (*.txt). Pour les minéraux avec une solution solide, il faut sélectionner le modèle d'activité et donner les variables de compositions (par exemple x , y , z pour les chlorites).

A.2.2 Mode « Minim »

Le mode Minim de MEAMP (Fig. A.2) permet d'ajuster automatiquement des paramètres thermodynamiques en utilisant des contraintes à partir de données expérimentales ou naturelles. Cet ajustement est réalisé en utilisant une fonction de minimisation qui s'adapte aux différents cas rencontrés (une ou plusieurs réactions, une ligne P-T, etc...). Cette fonction requiert pour chaque ajustement à réaliser : (1) des valeurs expérimentales, (2) une fonction «Vari» pour définir les paramètres à ajuster et les gammes de variations autorisées, (3) un fichier avec les différentes réactions et (4) des modèles de solutions solides. Nous allons illustrer les différents fichiers nécessaires en utilisant l'exemple de l'ajustement des paramètres standards de la sudoite.

```
> Vidal et al., (1992) (a = papier) Sud-Carph-Qtz
7.6 355 1 SUD1 :(0.74) CARPH1 :(0.6) 1
6.9 350 1 SUD1 :(0.74) CARPH1 :(0.6) 1
6.5 400 1 SUD1 :(0.74) CARPH1 :(0.6) 1
7.6 400 1 SUD1 :(0.74) CARPH1 :(0.6) 1
6.6 450 1 SUD1 :(0.74) CARPH1 :(0.6) 1
7.2 456 1 SUD1 :(0.74) CARPH1 :(0.6) 1
6.9 475 1 SUD1 :(0.74) CARPH1 :(0.6) 1
6.3 495 1 SUD1 :(0.74) CARPH1 :(0.6) 1
END
```

» Données "Data_SudCarphQtz.txt" (ici expérimentales)

```
function [Vari,scalParm,MoveParm,Thdata,solidsolval] =
..... Sudoite(Vari,scalParm,MoveParm,Thdata,solidsolval,LesSSbase,ListMineralsDB)
% Fonction d'input pour la minimisation
%
% P. Lanari (27/07/11) updated 21/12/11

if isempty(Vari) && isempty(scalParm) && isempty(MoveParm)

% ----- Edit BELOW Only -----
% (1) Ou
leQuel = find(ismember(ListMineralsDB,'Sudoite-Mg'));
% (2) Les Vari
Vari(1) = Thdata(leQuel).ST(2); % Ho
Vari(2) = Thdata(leQuel).ST(3); % So
Vari(3) = Thdata(leQuel).ST(4); % Vo
Vari(3) = Thdata(leQuel).C3(1); % CP1
Vari(4) = Thdata(leQuel).C3(2); % CP2
Vari(5) = Thdata(leQuel).C3(3); % CP3
Vari(6) = Thdata(leQuel).C3(4); % CP4

% (3) Tester les Vari
Vari = VerifVari(Vari); % do not change

% (4) les Parametres
scalParm = Vari;
MoveParm = [30000,10,0.5,100000,100000,10000];
% ----- Edit ABOVE Only -----

Vari = Vari./scalParm;

else

Vari = Vari.*scalParm;

% ----- Edit BELOW Only -----
% (1) Ou
leQuel = find(ismember(ListMineralsDB,'Sudoite-Mg'));
% (2) Les Vari
Thdata(leQuel).ST(2) = Vari(1); % Ho
Thdata(leQuel).ST(3) = Vari(2); % So
Thdata(leQuel).ST(4) = Vari(3); % Vo
Thdata(leQuel).C3(1) = Vari(3); % CP1
Thdata(leQuel).C3(2) = Vari(4); % CP2
Thdata(leQuel).C3(3) = Vari(5); % CP3
Thdata(leQuel).C3(4) = Vari(6); % CP4
% ----- Edit ABOVE Only -----

end

function [Vari] = VerifVari(Vari)
for i=1:length(Vari), if Vari(i) == 0, Vari(i) = 1e-10; end, end
return
```

» Fonction "Vari_SudCarphQtz.m" pour définir les paramètres à ajuster

(1) *Les données* (expérimentales ou naturelles) sont listées dans un fichier (voir le fichier d'exemple :DataSudCarphQtz.txt). Pour chaque jeu de données, on commence toujours la première ligne par un ">" suivi d'un espace et du nom que l'on peut attribuer à ce jeu de données. Les lignes suivantes indiquent les données expérimentales en utilisant le code suivant : "*Pression Température SS ± COMP₁ : (V₁ V₂ ... V_n) COMP₂ (V₁ V₂ ... V_n) ... COMP_n : (V₁ V₂ ... V_n) Reac*". Si *SS* = 1 alors il y a une ou plusieurs solutions solides et on doit donc préciser les compositions correspondantes. Pour définir les solutions solides, on utilise le code : "*NOM : (V₁ V₂ ... V_n)*" avec *NOM* le nom de code de la solution solide (dans l'exemple *SUD1* pour la sudoite et *CARPH1* pour la carpholite), et *V₁ V₂ ... V_n* les valeurs des différentes variables de compositions séparées par des espaces. Enfin, *Reac* indique le numéro de la réaction définie dans le fichier *réactions* (dans l'exemple la réaction *n°1*).

(2) *Une fonction Vari.m* est programmée pour chaque ajustement. C'est cette fonction qui indique les paramètres à ajuster et les limites de variations autorisées par l'utilisateur. Elle est divisée en deux parties grâce à l'utilisation d'une condition "*if*". La première partie (si *Vari* n'est pas définie) permet de définir une variable contenant les paramètres à ajuster (*Vari*) déterminés à partir de la base de données, une variable de mise à l'échelle (*scalParm* qui est généralement égal à *Vari*) et une variable avec les amplitudes de variations maximales autorisées (*MoveParm*). Ces trois variables sont envoyées dans la fonction de minimisation. Comme cette fonction va faire varier automatiquement la variable *Vari*, il est nécessaire lors de chaque calcul de mettre à jour la base de données. La deuxième partie est exécutée si *Vari* est définie et va donc mettre à jour la base de données thermodynamiques avec les nouveaux paramètres. En utilisant cette méthode très simple, plusieurs fonctions avec plusieurs jeux de paramètres peuvent être définies par l'utilisateur pour chaque type d'ajustement. Dans cet exemple, l'enthalpie standard, l'entropie standard et le volume, ainsi que les quatre coefficients de *C_p*, ont été ajustés.

```
Reaction(s) exported :
```

```
> 1
Sudoite-Mg - 2 Carpholite-Mg + Quartz
Sudoite-Mg Carpholite-Mg Quartz
1 -2 1

END
```

» Fichier réactions "Reactions_SudCarphQtz.txt"

(3) *Le fichier réactions* contient les équilibres chimiques utiles pour chaque ajustement. Ce fichier est automatiquement généré en utilisant l'option « new assemblage ». Pour chaque réaction, la première ligne commence toujours par un ">" suivi du numéro de la réaction. À la ligne suivante, la réaction est écrite littéralement (signe négatif pour les produits, ici $Sudoite-Mg + Quartz \rightleftharpoons 2 Carpholite - Mg$). Puis, la ligne suivante contient les noms des minéraux impliqués dans la réaction (correspondant à ceux de la base de données), et enfin la dernière ligne les coefficients stœchiométriques. Le mot clef "END" est indispensable à la fin du fichier réactions. Il permet de stocker des informations en dessous, qui ne seront pas lues par le programme.

(4) *Les modèles d'activités* qui apparaissent dans le fichier "données" (c.f. (1)) doivent être indiqués ici (c.f. "Solid solution models" Fig. A.2).

Dans la fenêtre principale de MEAMP (mode «Minim») le bouton "Minim" permet de lancer un calcul d'ajustement des paramètres et le bouton "Plot" permet de tracer les résultats (Fig. A.2). Lors du calcul, un certain nombre d'informations sont affichées dans le "Command Window" de MATLAB®. Pour les ajustements en utilisant des données naturelles pour lesquelles on connaît les conditions P-T, on affiche un diagramme avec les températures de référence (T_{ref}) vs les températures calculées (T_{calc}) pour chaque analyse (voir Fig. A.2, qui correspond au diagramme de la Fig. 2.26). Pour les ajustements, en utilisant des données expérimentales sur la position d'un équilibre, on affiche un diagramme avec les données expérimentales (carrés rouges sur la Fig. A.3) et l'équilibre calculé pour chaque composition (étoiles bleues sur la Fig. A.3).

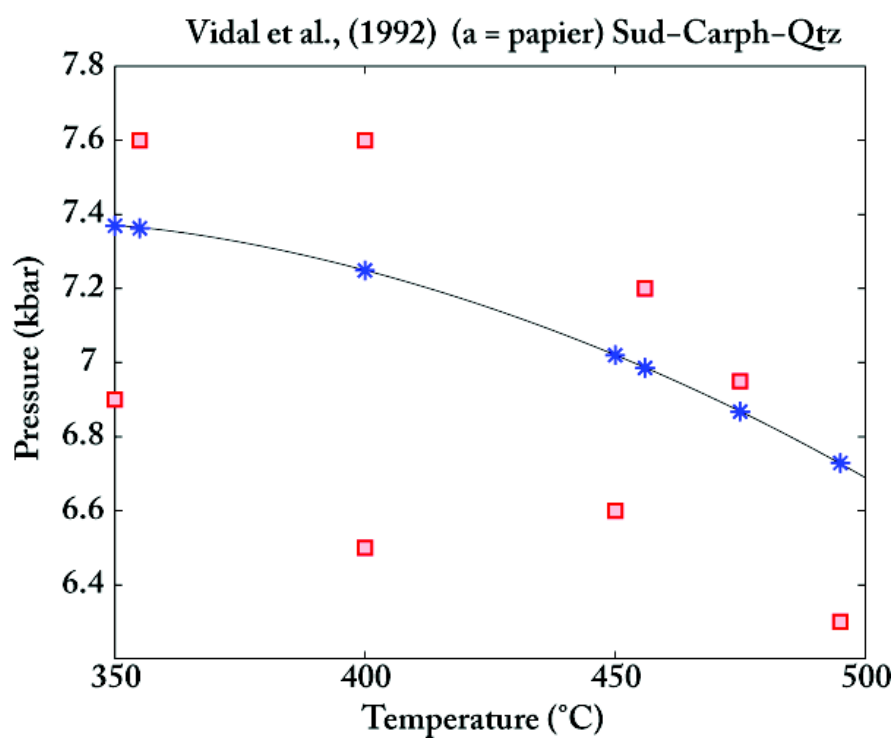


FIGURE A.3 – Résultat de l'ajustement des paramètres thermodynamiques de la sudoite. Les carrés rouges correspondent aux données expérimentales de Vidal et al. (1992). Les étoiles bleues correspondent à la position de l'équilibre Sudoite-Mg + Quartz \rightleftharpoons 2 Carpholite - Mg calculé en utilisant les propriétés standards pour la sudoite listées Tab. 2.7 (cette étude) et les données de Holland et Powell (1998) pour la carpholite et le quartz.

A.3 MODÈLE CLAY

Clay-1

8 linearly independent end-members: cel, fcel, mu, pa, ma, phl, prl, prl1h

1 dependent end-member: fphl

Site allocation table

	A1	M2A	M2B	M1	T2	T1	A2	A3	A4
fcel	K	Fe	Al	Va	Si ₂	Si ₂	Va	Va ₂	Va ₃
cel	K	Mg	Al	Va	Si ₂	Si ₂	Va	Va ₂	Va ₃
mu	K	Al	Al	Va	AlSi	Si ₂	Va	Va ₂	Va ₃
pa	Na	Al	Al	Va	AlSi	Si ₂	Va	Va ₂	Va ₃
ma	Ca	Al	Al	Va	Al ₂	Si ₂	Va	Va ₂	Va ₃
fphl	K	Fe	Fe	Fe	AlSi	Si ₂	Va	Va ₂	Va ₃
phl	K	Mg	Mg	Mg	AlSi	Si ₂	Va	Va ₂	Va ₃
prl	Va	Al	Al	Va	Si ₂	Si ₂	Va	Va ₂	Va ₃
prl1h	H ₂ O	Al	Al	Va	Si ₂	Si ₂	Va	Va ₂	Va ₃

Reciprocal relationships

$$G_{\text{fphl}} = G_{\text{phl}} + 3G_{\text{fcel}} - 3G_{\text{cel}} + \frac{6V_{\text{phl}}V_{\text{fcel}}}{V_{\text{fphl}}(V_{\text{phl}} + V_{\text{fcel}})}W_{\text{fcel-phl}} - \frac{6V_{\text{phl}}V_{\text{cel}}}{V_{\text{fphl}}(V_{\text{phl}} + V_{\text{cel}})}W_{\text{cel-phl}} \\ - \frac{18V_{\text{fcel}}V_{\text{cel}}}{V_{\text{fphl}}(V_{\text{fcel}} + V_{\text{cel}})}W_{\text{fcel-cel}}$$

Van Laar sizes

$$V_{\text{fcel}} = 0.63$$

$$V_{\text{cel}} = 0.63$$

$$V_{\text{mu}} = 0.63$$

$$V_{\text{pa}} = 0.37$$

$$V_{\text{ma}} = 0.37$$

$$V_{\text{fphl}} = 0.63$$

$$V_{\text{phl}} = 0.63$$

$$V_{\text{prl}} = 0.50$$

$$V_{\text{prl1h}} = 0.50$$

Excess properties macroscopic (J, K, bar)

$$W_{\text{fcel-cel}} = 0$$

$$W_{\text{fcel-mu}} = 0.2 \cdot P$$

$$W_{\text{fcel-pa}} = 52000$$

$$W_{\text{fcel-ma}} = 30000$$

$$W_{\text{fcel-phl}} =$$

$$W_{\text{fcel-prl}} = 25000 + 0.2 \cdot P$$

$$W_{\text{fcel-prl1h}} =$$

$$W_{\text{cel-mu}} = 0.2 \cdot P$$

$$W_{\text{cel-pa}} = 52000$$

$$W_{\text{cel-ma}} = 30000$$

$$W_{\text{cel-phl}} =$$

$$W_{\text{cel-prl}} = 25000 + 0.2 \cdot P$$

$$W_{\text{cel-prl1h}} =$$

$$W_{\text{mu-pa}} = 10120 + 3.4 \cdot T + 0.353 \cdot P$$

$$W_{\text{mu-ma}} = 30000$$

$$W_{\text{mu-phl}} =$$

$$W_{\text{mu-prl}} = 20000 + 0.2 \cdot P$$

$$\begin{aligned}
W_{\text{mu-pr11h}} &= \\
W_{\text{pa-ma}} &= 14500 \\
W_{\text{pa-phl}} &= \\
W_{\text{pa-prl}} &= 20000 + 0.2 \cdot P \\
W_{\text{pa-pr11h}} &= \\
W_{\text{ma-phl}} &= \\
W_{\text{ma-prl}} &= 30000 + 0.2 \cdot P \\
W_{\text{ma-pr11h}} &= \\
W_{\text{phl-prl}} &= \\
W_{\text{phl-pr11h}} &= \\
W_{\text{prl-pr11h}} &=
\end{aligned}$$

Composition variables

$$\begin{aligned}
x &= \text{Fe} / (\text{Fe} + \text{Mg}) \\
y &= 2 - 1/2 \cdot \text{Si} = x_{\text{Al,T2}} \\
z &= x_{\text{Va,A1}} \\
n &= x_{\text{Na,A1}} \\
c &= x_{\text{Ca,A1}} \\
p &= (\text{Si} + \text{Al} + \text{Fe} + \text{Mg}) - 6.0 \\
h &= x_{\text{H2O,A1}} \\
x &= (x_{\text{fcel}} + 3x_{\text{fphl}}) / (x_{\text{fcel}} + 3x_{\text{fphl}} + x_{\text{cel}} + 3x_{\text{phl}}) \\
y &= x_{\text{ma}} + 1/2 \cdot (x_{\text{mu}} + x_{\text{pa}} + x_{\text{phl}} + x_{\text{fphl}}) \\
z &= x_{\text{prl}} \\
n &= x_{\text{pa}} \\
c &= x_{\text{ma}} \\
p &= x_{\text{phl}} + x_{\text{fphl}} \\
h &= x_{\text{pr11h}}
\end{aligned}$$

Site fractions

$$\begin{aligned}
x_{\text{K,A1}} &= 1 - z - n - c - h \\
x_{\text{Na,A1}} &= n \\
x_{\text{Ca,A1}} &= c \\
x_{\text{Va,A1}} &= z \\
x_{\text{H2O,A1}} &= h \\
x_{\text{Fe,M2A}} &= x \cdot (1 - 2y - z + c - h + p) \\
x_{\text{Mg,M2A}} &= (1-x) \cdot (1 - 2y - z + c - h + p) \\
x_{\text{Al,M2A}} &= 2y + z - c + h - p \\
x_{\text{Fe,M2B}} &= x \cdot p \\
x_{\text{Mg,M2B}} &= (1-x) \cdot p \\
x_{\text{Al,M2B}} &= 1 - p \\
x_{\text{Fe,M1}} &= x \cdot p \\
x_{\text{Mg,M1}} &= (1-x) \cdot p \\
x_{\text{Va,M1}} &= 1 - p \\
x_{\text{Al,T2}} &= y \\
x_{\text{Si,T2}} &= 1 - y
\end{aligned}$$

Proportions of independent end-members

$$\begin{aligned}
p_{\text{fcel}} &= x \cdot (1 - 2y - z + c - h + 3p) \\
p_{\text{cel}} &= (1-x) \cdot (1 - 2y - z + c - h + 3p) - 3p \\
p_{\text{mu}} &= 2y - n - 2c - p \\
p_{\text{pa}} &= n \\
p_{\text{ma}} &= c
\end{aligned}$$

$$\begin{aligned} p_{\text{phl}} &= p \\ p_{\text{prl}} &= z \\ p_{\text{prl1h}} &= h \end{aligned}$$

Ideal mixing activities

$$\begin{aligned} a_{\text{fcel}} &= x_{\text{K,A1}} \cdot x_{\text{Fe,M2A}} \cdot x_{\text{Al,M2B}} \cdot x_{\text{Va,M1}} \cdot (x_{\text{Si,T2}})^2 \\ a_{\text{cel}} &= x_{\text{K,A1}} \cdot x_{\text{Mg,M2A}} \cdot x_{\text{Al,M2B}} \cdot x_{\text{Va,M1}} \cdot (x_{\text{Si,T2}})^2 \\ a_{\text{mu}} &= 4 \cdot x_{\text{K,A1}} \cdot x_{\text{Al,M2A}} \cdot x_{\text{Al,M2B}} \cdot x_{\text{Va,M1}} \cdot x_{\text{Al,T2}} \cdot x_{\text{Si,T2}} \\ a_{\text{pa}} &= 4 \cdot x_{\text{Na,A1}} \cdot x_{\text{Al,M2A}} \cdot x_{\text{Al,M2B}} \cdot x_{\text{Va,M1}} \cdot x_{\text{Al,T2}} \cdot x_{\text{Si,T2}} \\ a_{\text{ma}} &= x_{\text{Ca,A1}} \cdot x_{\text{Al,M2A}} \cdot x_{\text{Al,M2B}} \cdot x_{\text{Va,M1}} \cdot (x_{\text{Al,T2}})^2 \\ a_{\text{fphl}} &= 4 \cdot x_{\text{K,A1}} \cdot x_{\text{Fe,M2A}} \cdot x_{\text{Fe,M2B}} \cdot x_{\text{Fe,M1}} \cdot x_{\text{Al,T2}} \cdot x_{\text{Si,T2}} \\ a_{\text{phl}} &= 4 \cdot x_{\text{K,A1}} \cdot x_{\text{Mg,M2A}} \cdot x_{\text{Mg,M2B}} \cdot x_{\text{Mg,M1}} \cdot x_{\text{Al,T2}} \cdot x_{\text{Si,T2}} \\ a_{\text{prl}} &= x_{\text{Va,A1}} \cdot x_{\text{Al,M2A}} \cdot x_{\text{Al,M2B}} \cdot x_{\text{Va,M1}} \cdot (x_{\text{Si,T2}})^2 \\ a_{\text{prl1h}} &= x_{\text{H2O,A1}} \cdot x_{\text{Al,M2A}} \cdot x_{\text{Al,M2B}} \cdot x_{\text{Va,M1}} \cdot (x_{\text{Si,T2}})^2 \end{aligned}$$

Phi terms

$$\begin{aligned} \phi_{\text{fcel}} &= \frac{p_{\text{fcel}} V_{\text{fcel}}}{p_{\text{fcel}} V_{\text{fcel}} + p_{\text{cel}} V_{\text{cel}} + p_{\text{mu}} V_{\text{mu}} + p_{\text{pa}} V_{\text{pa}} + p_{\text{ma}} V_{\text{ma}} + p_{\text{phl}} V_{\text{phl}} + p_{\text{prl}} V_{\text{prl}} + p_{\text{prl1h}} V_{\text{prl1h}}} \\ \phi_{\text{cel}} &= \frac{p_{\text{cel}} V_{\text{cel}}}{p_{\text{fcel}} V_{\text{fcel}} + p_{\text{cel}} V_{\text{cel}} + p_{\text{mu}} V_{\text{mu}} + p_{\text{pa}} V_{\text{pa}} + p_{\text{ma}} V_{\text{ma}} + p_{\text{phl}} V_{\text{phl}} + p_{\text{prl}} V_{\text{prl}} + p_{\text{prl1h}} V_{\text{prl1h}}} \\ \phi_{\text{mu}} &= \frac{p_{\text{mu}} V_{\text{mu}}}{p_{\text{fcel}} V_{\text{fcel}} + p_{\text{cel}} V_{\text{cel}} + p_{\text{mu}} V_{\text{mu}} + p_{\text{pa}} V_{\text{pa}} + p_{\text{ma}} V_{\text{ma}} + p_{\text{phl}} V_{\text{phl}} + p_{\text{prl}} V_{\text{prl}} + p_{\text{prl1h}} V_{\text{prl1h}}} \\ \phi_{\text{pa}} &= \frac{p_{\text{pa}} V_{\text{pa}}}{p_{\text{fcel}} V_{\text{fcel}} + p_{\text{cel}} V_{\text{cel}} + p_{\text{mu}} V_{\text{mu}} + p_{\text{pa}} V_{\text{pa}} + p_{\text{ma}} V_{\text{ma}} + p_{\text{phl}} V_{\text{phl}} + p_{\text{prl}} V_{\text{prl}} + p_{\text{prl1h}} V_{\text{prl1h}}} \\ \phi_{\text{ma}} &= \frac{p_{\text{ma}} V_{\text{ma}}}{p_{\text{fcel}} V_{\text{fcel}} + p_{\text{cel}} V_{\text{cel}} + p_{\text{mu}} V_{\text{mu}} + p_{\text{pa}} V_{\text{pa}} + p_{\text{ma}} V_{\text{ma}} + p_{\text{phl}} V_{\text{phl}} + p_{\text{prl}} V_{\text{prl}} + p_{\text{prl1h}} V_{\text{prl1h}}} \\ \phi_{\text{phl}} &= \frac{p_{\text{phl}} V_{\text{phl}}}{p_{\text{fcel}} V_{\text{fcel}} + p_{\text{cel}} V_{\text{cel}} + p_{\text{mu}} V_{\text{mu}} + p_{\text{pa}} V_{\text{pa}} + p_{\text{ma}} V_{\text{ma}} + p_{\text{phl}} V_{\text{phl}} + p_{\text{prl}} V_{\text{prl}} + p_{\text{prl1h}} V_{\text{prl1h}}} \\ \phi_{\text{prl}} &= \frac{p_{\text{prl}} V_{\text{prl}}}{p_{\text{fcel}} V_{\text{fcel}} + p_{\text{cel}} V_{\text{cel}} + p_{\text{mu}} V_{\text{mu}} + p_{\text{pa}} V_{\text{pa}} + p_{\text{ma}} V_{\text{ma}} + p_{\text{phl}} V_{\text{phl}} + p_{\text{prl}} V_{\text{prl}} + p_{\text{prl1h}} V_{\text{prl1h}}} \\ \phi_{\text{prl1h}} &= \frac{p_{\text{prl1h}} V_{\text{prl1h}}}{p_{\text{fcel}} V_{\text{fcel}} + p_{\text{cel}} V_{\text{cel}} + p_{\text{mu}} V_{\text{mu}} + p_{\text{pa}} V_{\text{pa}} + p_{\text{ma}} V_{\text{ma}} + p_{\text{phl}} V_{\text{phl}} + p_{\text{prl}} V_{\text{prl}} + p_{\text{prl1h}} V_{\text{prl1h}}} \end{aligned}$$

Activity coefficients

$$\begin{aligned} \text{RT ln } \gamma_{\text{fcel}} &= \phi_{\text{cel}} \cdot (1 - \phi_{\text{fcel}}) \cdot 2V_{\text{fcel}} / (V_{\text{cel}} + V_{\text{fcel}}) \cdot W_{\text{fcel-cel}} + \phi_{\text{mu}} \cdot (1 - \phi_{\text{fcel}}) \cdot 2V_{\text{fcel}} / (V_{\text{mu}} + V_{\text{fcel}}) \cdot W_{\text{fcel-mu}} \\ &+ \phi_{\text{pa}} \cdot (1 - \phi_{\text{fcel}}) \cdot 2V_{\text{fcel}} / (V_{\text{pa}} + V_{\text{fcel}}) \cdot W_{\text{fcel-pa}} + \phi_{\text{ma}} \cdot (1 - \phi_{\text{fcel}}) \cdot 2V_{\text{fcel}} / (V_{\text{ma}} + V_{\text{fcel}}) \cdot W_{\text{fcel-ma}} \\ &+ \phi_{\text{phl}} \cdot (1 - \phi_{\text{fcel}}) \cdot 2V_{\text{fcel}} / (V_{\text{phl}} + V_{\text{fcel}}) \cdot W_{\text{fcel-phl}} + \phi_{\text{prl}} \cdot (1 - \phi_{\text{fcel}}) \cdot 2V_{\text{fcel}} / (V_{\text{prl}} + V_{\text{fcel}}) \cdot W_{\text{fcel-prl}} \\ &+ \phi_{\text{prl1h}} \cdot (1 - \phi_{\text{fcel}}) \cdot 2V_{\text{fcel}} / (V_{\text{prl1h}} + V_{\text{fcel}}) \cdot W_{\text{fcel-prl1h}} - \phi_{\text{cel}} \cdot \phi_{\text{mu}} \cdot 2V_{\text{fcel}} / (V_{\text{cel}} + V_{\text{mu}}) \cdot W_{\text{cel-mu}} \\ &- \phi_{\text{cel}} \cdot \phi_{\text{pa}} \cdot 2V_{\text{fcel}} / (V_{\text{cel}} + V_{\text{pa}}) \cdot W_{\text{cel-pa}} - \phi_{\text{cel}} \cdot \phi_{\text{ma}} \cdot 2V_{\text{fcel}} / (V_{\text{cel}} + V_{\text{ma}}) \cdot W_{\text{cel-ma}} \\ &- \phi_{\text{cel}} \cdot \phi_{\text{phl}} \cdot 2V_{\text{fcel}} / (V_{\text{cel}} + V_{\text{phl}}) \cdot W_{\text{cel-phl}} - \phi_{\text{cel}} \cdot \phi_{\text{prl}} \cdot 2V_{\text{fcel}} / (V_{\text{cel}} + V_{\text{prl}}) \cdot W_{\text{cel-prl}} \\ &- \phi_{\text{cel}} \cdot \phi_{\text{prl1h}} \cdot 2V_{\text{fcel}} / (V_{\text{cel}} + V_{\text{prl1h}}) \cdot W_{\text{cel-prl1h}} - \phi_{\text{mu}} \cdot \phi_{\text{pa}} \cdot 2V_{\text{fcel}} / (V_{\text{mu}} + V_{\text{pa}}) \cdot W_{\text{mu-pa}} \\ &- \phi_{\text{mu}} \cdot \phi_{\text{ma}} \cdot 2V_{\text{fcel}} / (V_{\text{mu}} + V_{\text{ma}}) \cdot W_{\text{mu-ma}} - \phi_{\text{mu}} \cdot \phi_{\text{phl}} \cdot 2V_{\text{fcel}} / (V_{\text{mu}} + V_{\text{phl}}) \cdot W_{\text{mu-phl}} \\ &- \phi_{\text{mu}} \cdot \phi_{\text{prl}} \cdot 2V_{\text{fcel}} / (V_{\text{mu}} + V_{\text{prl}}) \cdot W_{\text{mu-prl}} - \phi_{\text{mu}} \cdot \phi_{\text{prl1h}} \cdot 2V_{\text{fcel}} / (V_{\text{mu}} + V_{\text{prl1h}}) \cdot W_{\text{mu-prl1h}} \\ &- \phi_{\text{pa}} \cdot \phi_{\text{ma}} \cdot 2V_{\text{fcel}} / (V_{\text{pa}} + V_{\text{ma}}) \cdot W_{\text{pa-ma}} - \phi_{\text{pa}} \cdot \phi_{\text{phl}} \cdot 2V_{\text{fcel}} / (V_{\text{pa}} + V_{\text{phl}}) \cdot W_{\text{pa-phl}} \\ &- \phi_{\text{pa}} \cdot \phi_{\text{prl}} \cdot 2V_{\text{fcel}} / (V_{\text{pa}} + V_{\text{prl}}) \cdot W_{\text{pa-prl}} - \phi_{\text{pa}} \cdot \phi_{\text{prl1h}} \cdot 2V_{\text{fcel}} / (V_{\text{pa}} + V_{\text{prl1h}}) \cdot W_{\text{pa-prl1h}} \\ &- \phi_{\text{ma}} \cdot \phi_{\text{phl}} \cdot 2V_{\text{fcel}} / (V_{\text{ma}} + V_{\text{phl}}) \cdot W_{\text{ma-phl}} - \phi_{\text{ma}} \cdot \phi_{\text{prl}} \cdot 2V_{\text{fcel}} / (V_{\text{ma}} + V_{\text{prl}}) \cdot W_{\text{ma-prl}} \end{aligned}$$

$$\begin{aligned}
& -\phi_{ma} \cdot \phi_{pr11h} \cdot 2V_{fcel}/(V_{ma}+V_{pr11h}) \cdot W_{ma-pr11h} - \phi_{phl} \cdot \phi_{prl} \cdot 2V_{fcel}/(V_{phl}+V_{prl}) \cdot W_{phl-prl} \\
& -\phi_{phl} \cdot \phi_{pr11h} \cdot 2V_{fcel}/(V_{phl}+V_{pr11h}) \cdot W_{phl-pr11h} - \phi_{prl} \cdot \phi_{pr11h} \cdot 2V_{fcel}/(V_{prl}+V_{pr11h}) \cdot W_{prl-pr11h}
\end{aligned}$$

$$\begin{aligned}
RT \ln \gamma_{cel} = & \phi_{fcel} \cdot (1-\phi_{cel}) \cdot 2V_{cel}/(V_{fcel}+V_{cel}) \cdot W_{fcel-cel} + \phi_{mu} \cdot (1-\phi_{cel}) \cdot 2V_{cel}/(V_{mu}+V_{cel}) \cdot W_{cel-mu} \\
& + \phi_{pa} \cdot (1-\phi_{cel}) \cdot 2V_{cel}/(V_{pa}+V_{cel}) \cdot W_{cel-pa} + \phi_{ma} \cdot (1-\phi_{cel}) \cdot 2V_{cel}/(V_{ma}+V_{cel}) \cdot W_{cel-ma} \\
& + \phi_{phl} \cdot (1-\phi_{cel}) \cdot 2V_{cel}/(V_{phl}+V_{cel}) \cdot W_{cel-phl} + \phi_{prl} \cdot (1-\phi_{cel}) \cdot 2V_{cel}/(V_{prl}+V_{cel}) \cdot W_{cel-prl} \\
& + \phi_{pr11h} \cdot (1-\phi_{cel}) \cdot 2V_{cel}/(V_{pr11h}+V_{cel}) \cdot W_{cel-pr11h} - \phi_{fcel} \cdot \phi_{mu} \cdot 2V_{cel}/(V_{fcel}+V_{mu}) \cdot W_{fcel-mu} \\
& - \phi_{fcel} \cdot \phi_{pa} \cdot 2V_{cel}/(V_{fcel}+V_{pa}) \cdot W_{fcel-pa} - \phi_{fcel} \cdot \phi_{ma} \cdot 2V_{cel}/(V_{fcel}+V_{ma}) \cdot W_{fcel-ma} \\
& - \phi_{fcel} \cdot \phi_{phl} \cdot 2V_{cel}/(V_{fcel}+V_{phl}) \cdot W_{fcel-phl} - \phi_{fcel} \cdot \phi_{prl} \cdot 2V_{cel}/(V_{fcel}+V_{prl}) \cdot W_{fcel-prl} \\
& - \phi_{fcel} \cdot \phi_{pr11h} \cdot 2V_{cel}/(V_{fcel}+V_{pr11h}) \cdot W_{fcel-pr11h} - \phi_{mu} \cdot \phi_{pa} \cdot 2V_{cel}/(V_{mu}+V_{pa}) \cdot W_{mu-pa} \\
& - \phi_{mu} \cdot \phi_{ma} \cdot 2V_{cel}/(V_{mu}+V_{ma}) \cdot W_{mu-ma} - \phi_{mu} \cdot \phi_{phl} \cdot 2V_{cel}/(V_{mu}+V_{phl}) \cdot W_{mu-phl} \\
& - \phi_{mu} \cdot \phi_{prl} \cdot 2V_{cel}/(V_{mu}+V_{prl}) \cdot W_{mu-prl} - \phi_{mu} \cdot \phi_{pr11h} \cdot 2V_{cel}/(V_{mu}+V_{pr11h}) \cdot W_{mu-pr11h} \\
& - \phi_{pa} \cdot \phi_{ma} \cdot 2V_{cel}/(V_{pa}+V_{ma}) \cdot W_{pa-ma} - \phi_{pa} \cdot \phi_{phl} \cdot 2V_{cel}/(V_{pa}+V_{phl}) \cdot W_{pa-phl} \\
& - \phi_{pa} \cdot \phi_{prl} \cdot 2V_{cel}/(V_{pa}+V_{prl}) \cdot W_{pa-prl} - \phi_{pa} \cdot \phi_{pr11h} \cdot 2V_{cel}/(V_{pa}+V_{pr11h}) \cdot W_{pa-pr11h} \\
& - \phi_{ma} \cdot \phi_{phl} \cdot 2V_{cel}/(V_{ma}+V_{phl}) \cdot W_{ma-phl} - \phi_{ma} \cdot \phi_{prl} \cdot 2V_{cel}/(V_{ma}+V_{prl}) \cdot W_{ma-prl} \\
& - \phi_{ma} \cdot \phi_{pr11h} \cdot 2V_{cel}/(V_{ma}+V_{pr11h}) \cdot W_{ma-pr11h} - \phi_{phl} \cdot \phi_{prl} \cdot 2V_{cel}/(V_{phl}+V_{prl}) \cdot W_{phl-prl} \\
& - \phi_{phl} \cdot \phi_{pr11h} \cdot 2V_{cel}/(V_{phl}+V_{pr11h}) \cdot W_{phl-pr11h} - \phi_{prl} \cdot \phi_{pr11h} \cdot 2V_{cel}/(V_{prl}+V_{pr11h}) \cdot W_{prl-pr11h}
\end{aligned}$$

$$\begin{aligned}
RT \ln \gamma_{mu} = & \phi_{fcel} \cdot (1-\phi_{mu}) \cdot 2V_{mu}/(V_{fcel}+V_{mu}) \cdot W_{fcel-mu} + \phi_{cel} \cdot (1-\phi_{mu}) \cdot 2V_{mu}/(V_{cel}+V_{mu}) \cdot W_{cel-mu} \\
& + \phi_{pa} \cdot (1-\phi_{mu}) \cdot 2V_{mu}/(V_{pa}+V_{mu}) \cdot W_{mu-pa} + \phi_{ma} \cdot (1-\phi_{mu}) \cdot 2V_{mu}/(V_{ma}+V_{mu}) \cdot W_{mu-ma} \\
& + \phi_{phl} \cdot (1-\phi_{mu}) \cdot 2V_{mu}/(V_{phl}+V_{mu}) \cdot W_{mu-phl} + \phi_{prl} \cdot (1-\phi_{mu}) \cdot 2V_{mu}/(V_{prl}+V_{mu}) \cdot W_{mu-prl} \\
& + \phi_{pr11h} \cdot (1-\phi_{mu}) \cdot 2V_{mu}/(V_{pr11h}+V_{mu}) \cdot W_{mu-pr11h} - \phi_{fcel} \cdot \phi_{cel} \cdot 2V_{mu}/(V_{fcel}+V_{cel}) \cdot W_{fcel-cel} \\
& - \phi_{fcel} \cdot \phi_{pa} \cdot 2V_{mu}/(V_{fcel}+V_{pa}) \cdot W_{fcel-pa} - \phi_{fcel} \cdot \phi_{ma} \cdot 2V_{mu}/(V_{fcel}+V_{ma}) \cdot W_{fcel-ma} \\
& - \phi_{fcel} \cdot \phi_{phl} \cdot 2V_{mu}/(V_{fcel}+V_{phl}) \cdot W_{fcel-phl} - \phi_{fcel} \cdot \phi_{prl} \cdot 2V_{mu}/(V_{fcel}+V_{prl}) \cdot W_{fcel-prl} \\
& - \phi_{fcel} \cdot \phi_{pr11h} \cdot 2V_{mu}/(V_{fcel}+V_{pr11h}) \cdot W_{fcel-pr11h} - \phi_{cel} \cdot \phi_{pa} \cdot 2V_{mu}/(V_{cel}+V_{pa}) \cdot W_{cel-pa} \\
& - \phi_{cel} \cdot \phi_{ma} \cdot 2V_{mu}/(V_{cel}+V_{ma}) \cdot W_{cel-ma} - \phi_{cel} \cdot \phi_{phl} \cdot 2V_{mu}/(V_{cel}+V_{phl}) \cdot W_{cel-phl} \\
& - \phi_{cel} \cdot \phi_{prl} \cdot 2V_{mu}/(V_{cel}+V_{prl}) \cdot W_{cel-prl} - \phi_{cel} \cdot \phi_{pr11h} \cdot 2V_{mu}/(V_{cel}+V_{pr11h}) \cdot W_{cel-pr11h} \\
& - \phi_{pa} \cdot \phi_{ma} \cdot 2V_{mu}/(V_{pa}+V_{ma}) \cdot W_{pa-ma} - \phi_{pa} \cdot \phi_{phl} \cdot 2V_{mu}/(V_{pa}+V_{phl}) \cdot W_{pa-phl} \\
& - \phi_{pa} \cdot \phi_{prl} \cdot 2V_{mu}/(V_{pa}+V_{prl}) \cdot W_{pa-prl} - \phi_{pa} \cdot \phi_{pr11h} \cdot 2V_{mu}/(V_{pa}+V_{pr11h}) \cdot W_{pa-pr11h} \\
& - \phi_{ma} \cdot \phi_{phl} \cdot 2V_{mu}/(V_{ma}+V_{phl}) \cdot W_{ma-phl} - \phi_{ma} \cdot \phi_{prl} \cdot 2V_{mu}/(V_{ma}+V_{prl}) \cdot W_{ma-prl} \\
& - \phi_{ma} \cdot \phi_{pr11h} \cdot 2V_{mu}/(V_{ma}+V_{pr11h}) \cdot W_{ma-pr11h} - \phi_{phl} \cdot \phi_{prl} \cdot 2V_{mu}/(V_{phl}+V_{prl}) \cdot W_{phl-prl} \\
& - \phi_{phl} \cdot \phi_{pr11h} \cdot 2V_{mu}/(V_{phl}+V_{pr11h}) \cdot W_{phl-pr11h} - \phi_{prl} \cdot \phi_{pr11h} \cdot 2V_{mu}/(V_{prl}+V_{pr11h}) \cdot W_{prl-pr11h}
\end{aligned}$$

$$\begin{aligned}
RT \ln \gamma_{pa} = & \phi_{fcel} \cdot (1-\phi_{pa}) \cdot 2V_{pa}/(V_{fcel}+V_{pa}) \cdot W_{fcel-pa} + \phi_{cel} \cdot (1-\phi_{pa}) \cdot 2V_{pa}/(V_{cel}+V_{pa}) \cdot W_{cel-pa} \\
& + \phi_{mu} \cdot (1-\phi_{pa}) \cdot 2V_{pa}/(V_{mu}+V_{pa}) \cdot W_{mu-pa} + \phi_{ma} \cdot (1-\phi_{pa}) \cdot 2V_{pa}/(V_{ma}+V_{pa}) \cdot W_{pa-ma} \\
& + \phi_{phl} \cdot (1-\phi_{pa}) \cdot 2V_{pa}/(V_{phl}+V_{pa}) \cdot W_{pa-phl} + \phi_{prl} \cdot (1-\phi_{pa}) \cdot 2V_{pa}/(V_{prl}+V_{pa}) \cdot W_{pa-prl} \\
& + \phi_{pr11h} \cdot (1-\phi_{pa}) \cdot 2V_{pa}/(V_{pr11h}+V_{pa}) \cdot W_{pa-pr11h} - \phi_{fcel} \cdot \phi_{cel} \cdot 2V_{pa}/(V_{fcel}+V_{cel}) \cdot W_{fcel-cel} \\
& - \phi_{fcel} \cdot \phi_{mu} \cdot 2V_{pa}/(V_{fcel}+V_{mu}) \cdot W_{fcel-mu} - \phi_{fcel} \cdot \phi_{ma} \cdot 2V_{pa}/(V_{fcel}+V_{ma}) \cdot W_{fcel-ma} \\
& - \phi_{fcel} \cdot \phi_{phl} \cdot 2V_{pa}/(V_{fcel}+V_{phl}) \cdot W_{fcel-phl} - \phi_{fcel} \cdot \phi_{prl} \cdot 2V_{pa}/(V_{fcel}+V_{prl}) \cdot W_{fcel-prl} \\
& - \phi_{fcel} \cdot \phi_{pr11h} \cdot 2V_{pa}/(V_{fcel}+V_{pr11h}) \cdot W_{fcel-pr11h} - \phi_{cel} \cdot \phi_{mu} \cdot 2V_{pa}/(V_{cel}+V_{mu}) \cdot W_{cel-mu} \\
& - \phi_{cel} \cdot \phi_{ma} \cdot 2V_{pa}/(V_{cel}+V_{ma}) \cdot W_{cel-ma} - \phi_{cel} \cdot \phi_{phl} \cdot 2V_{pa}/(V_{cel}+V_{phl}) \cdot W_{cel-phl} \\
& - \phi_{cel} \cdot \phi_{prl} \cdot 2V_{pa}/(V_{cel}+V_{prl}) \cdot W_{cel-prl} - \phi_{cel} \cdot \phi_{pr11h} \cdot 2V_{pa}/(V_{cel}+V_{pr11h}) \cdot W_{cel-pr11h} \\
& - \phi_{mu} \cdot \phi_{ma} \cdot 2V_{pa}/(V_{mu}+V_{ma}) \cdot W_{mu-ma} - \phi_{mu} \cdot \phi_{phl} \cdot 2V_{pa}/(V_{mu}+V_{phl}) \cdot W_{mu-phl} \\
& - \phi_{mu} \cdot \phi_{prl} \cdot 2V_{pa}/(V_{mu}+V_{prl}) \cdot W_{mu-prl} - \phi_{mu} \cdot \phi_{pr11h} \cdot 2V_{pa}/(V_{mu}+V_{pr11h}) \cdot W_{mu-pr11h} \\
& - \phi_{ma} \cdot \phi_{phl} \cdot 2V_{pa}/(V_{ma}+V_{phl}) \cdot W_{ma-phl} - \phi_{ma} \cdot \phi_{prl} \cdot 2V_{pa}/(V_{ma}+V_{prl}) \cdot W_{ma-prl} \\
& - \phi_{ma} \cdot \phi_{pr11h} \cdot 2V_{pa}/(V_{ma}+V_{pr11h}) \cdot W_{ma-pr11h} - \phi_{phl} \cdot \phi_{prl} \cdot 2V_{pa}/(V_{phl}+V_{prl}) \cdot W_{phl-prl} \\
& - \phi_{phl} \cdot \phi_{pr11h} \cdot 2V_{pa}/(V_{phl}+V_{pr11h}) \cdot W_{phl-pr11h} - \phi_{prl} \cdot \phi_{pr11h} \cdot 2V_{pa}/(V_{prl}+V_{pr11h}) \cdot W_{prl-pr11h}
\end{aligned}$$

$$\begin{aligned}
RT \ln \gamma_{ma} = & \phi_{fcel} \cdot (1-\phi_{ma}) \cdot 2V_{ma}/(V_{fcel}+V_{ma}) \cdot W_{fcel-ma} + \phi_{cel} \cdot (1-\phi_{ma}) \cdot 2V_{ma}/(V_{cel}+V_{ma}) \cdot W_{cel-ma} \\
& + \phi_{mu} \cdot (1-\phi_{ma}) \cdot 2V_{ma}/(V_{mu}+V_{ma}) \cdot W_{mu-ma} + \phi_{pa} \cdot (1-\phi_{ma}) \cdot 2V_{ma}/(V_{pa}+V_{ma}) \cdot W_{pa-ma}
\end{aligned}$$

$$\begin{aligned} \text{RT ln } \gamma_{\text{prl1h}} = & \phi_{\text{fcel}} \cdot (1 - \phi_{\text{prl1h}}) \cdot 2V_{\text{prl1h}} / (V_{\text{fcel}} + V_{\text{prl1h}}) \cdot W_{\text{fcel-prl1h}} + \phi_{\text{cel}} \cdot (1 - \phi_{\text{prl1h}}) \cdot 2V_{\text{prl1h}} / (V_{\text{cel}} + V_{\text{prl1h}}) \cdot W_{\text{cel-prl1h}} \\ & + \phi_{\text{mu}} \cdot (1 - \phi_{\text{prl1h}}) \cdot 2V_{\text{prl1h}} / (V_{\text{mu}} + V_{\text{prl1h}}) \cdot W_{\text{mu-prl1h}} + \phi_{\text{pa}} \cdot (1 - \phi_{\text{prl1h}}) \cdot 2V_{\text{prl1h}} / (V_{\text{pa}} + V_{\text{prl1h}}) \cdot W_{\text{pa-prl1h}} \\ & + \phi_{\text{ma}} \cdot (1 - \phi_{\text{prl1h}}) \cdot 2V_{\text{prl1h}} / (V_{\text{ma}} + V_{\text{prl1h}}) \cdot W_{\text{ma-prl1h}} + \phi_{\text{phl}} \cdot (1 - \phi_{\text{prl1h}}) \cdot 2V_{\text{prl1h}} / (V_{\text{phl}} + V_{\text{prl1h}}) \cdot W_{\text{phl-prl1h}} \\ & + \phi_{\text{prl}} \cdot (1 - \phi_{\text{prl1h}}) \cdot 2V_{\text{prl1h}} / (V_{\text{prl}} + V_{\text{prl1h}}) \cdot W_{\text{prl-prl1h}} - \phi_{\text{fcel}} \cdot \phi_{\text{cel}} \cdot 2V_{\text{prl1h}} / (V_{\text{fcel}} + V_{\text{cel}}) \cdot W_{\text{fcel-cel}} \\ & - \phi_{\text{fcel}} \cdot \phi_{\text{mu}} \cdot 2V_{\text{prl1h}} / (V_{\text{fcel}} + V_{\text{mu}}) \cdot W_{\text{fcel-mu}} - \phi_{\text{fcel}} \cdot \phi_{\text{pa}} \cdot 2V_{\text{prl1h}} / (V_{\text{fcel}} + V_{\text{pa}}) \cdot W_{\text{fcel-pa}} \\ & - \phi_{\text{fcel}} \cdot \phi_{\text{ma}} \cdot 2V_{\text{prl1h}} / (V_{\text{fcel}} + V_{\text{ma}}) \cdot W_{\text{fcel-ma}} - \phi_{\text{fcel}} \cdot \phi_{\text{phl}} \cdot 2V_{\text{prl1h}} / (V_{\text{fcel}} + V_{\text{phl}}) \cdot W_{\text{fcel-phl}} \\ & - \phi_{\text{fcel}} \cdot \phi_{\text{prl}} \cdot 2V_{\text{prl1h}} / (V_{\text{fcel}} + V_{\text{prl}}) \cdot W_{\text{fcel-prl}} - \phi_{\text{cel}} \cdot \phi_{\text{mu}} \cdot 2V_{\text{prl1h}} / (V_{\text{cel}} + V_{\text{mu}}) \cdot W_{\text{cel-mu}} \\ & - \phi_{\text{cel}} \cdot \phi_{\text{pa}} \cdot 2V_{\text{prl1h}} / (V_{\text{cel}} + V_{\text{pa}}) \cdot W_{\text{cel-pa}} - \phi_{\text{cel}} \cdot \phi_{\text{ma}} \cdot 2V_{\text{prl1h}} / (V_{\text{cel}} + V_{\text{ma}}) \cdot W_{\text{cel-ma}} \\ & - \phi_{\text{cel}} \cdot \phi_{\text{phl}} \cdot 2V_{\text{prl1h}} / (V_{\text{cel}} + V_{\text{phl}}) \cdot W_{\text{cel-phl}} - \phi_{\text{cel}} \cdot \phi_{\text{prl}} \cdot 2V_{\text{prl1h}} / (V_{\text{cel}} + V_{\text{prl}}) \cdot W_{\text{cel-prl}} \\ & - \phi_{\text{mu}} \cdot \phi_{\text{pa}} \cdot 2V_{\text{prl1h}} / (V_{\text{mu}} + V_{\text{pa}}) \cdot W_{\text{mu-pa}} - \phi_{\text{mu}} \cdot \phi_{\text{ma}} \cdot 2V_{\text{prl1h}} / (V_{\text{mu}} + V_{\text{ma}}) \cdot W_{\text{mu-ma}} \\ & - \phi_{\text{mu}} \cdot \phi_{\text{phl}} \cdot 2V_{\text{prl1h}} / (V_{\text{mu}} + V_{\text{phl}}) \cdot W_{\text{mu-phl}} - \phi_{\text{mu}} \cdot \phi_{\text{prl}} \cdot 2V_{\text{prl1h}} / (V_{\text{mu}} + V_{\text{prl}}) \cdot W_{\text{mu-prl}} \\ & - \phi_{\text{pa}} \cdot \phi_{\text{ma}} \cdot 2V_{\text{prl1h}} / (V_{\text{pa}} + V_{\text{ma}}) \cdot W_{\text{pa-ma}} - \phi_{\text{pa}} \cdot \phi_{\text{phl}} \cdot 2V_{\text{prl1h}} / (V_{\text{pa}} + V_{\text{phl}}) \cdot W_{\text{pa-phl}} \\ & - \phi_{\text{pa}} \cdot \phi_{\text{prl}} \cdot 2V_{\text{prl1h}} / (V_{\text{pa}} + V_{\text{prl}}) \cdot W_{\text{pa-prl}} - \phi_{\text{ma}} \cdot \phi_{\text{phl}} \cdot 2V_{\text{prl1h}} / (V_{\text{ma}} + V_{\text{phl}}) \cdot W_{\text{ma-phl}} \\ & - \phi_{\text{ma}} \cdot \phi_{\text{prl}} \cdot 2V_{\text{prl1h}} / (V_{\text{ma}} + V_{\text{prl}}) \cdot W_{\text{ma-prl}} - \phi_{\text{phl}} \cdot \phi_{\text{prl}} \cdot 2V_{\text{prl1h}} / (V_{\text{phl}} + V_{\text{prl}}) \cdot W_{\text{phl-prl}} \end{aligned}$$

8 linearly independent end-members: cel, fcel, mu, pa, ma, phl, prl1h, prl2h
1 dependent end-member: fppl

	A1	M2A	M2B	M1	T2	T1	A2	A3	A4
cel	K	Mg	Al	Va	Si ₂	Si ₂	Va	Va ₂	Va ₃
fcel	K	Fe	Al	Va	Si ₂	Si ₂	Va	Va ₂	Va ₃
mu	K	Al	Al	Va	AlSi	Si ₂	Va	Va ₂	Va ₃
pa	Na	Al	Al	Va	AlSi	Si ₂	Va	Va ₂	Va ₃
ma	Ca	Al	Al	Va	Al ₂	Si ₂	Va	Va ₂	Va ₃

phl	K	Mg	Mg	Mg	AlSi	Si ₂	Va	Va ₂	Va ₃
fphl	K	Fe	Fe	Fe	AlSi	Si ₂	Va	Va ₂	Va ₃
prl1h	H ₂ O	Al	Al	Va	Si ₂	Si ₂	Va	Va ₂	Va ₃
prl2h	H ₂ O	Al	Al	Va	Si ₂	Si ₂	H ₂ O	Va ₂	Va ₃

Reciprocal relationships

$$G_{\text{fphl}} = G_{\text{phl}} + 3G_{\text{fccl}} - 3G_{\text{cel}} + \frac{6V_{\text{phl}}V_{\text{fccl}}}{V_{\text{fphl}}(V_{\text{phl}} + V_{\text{fccl}})}W_{\text{fccl-phl}} - \frac{6V_{\text{phl}}V_{\text{cel}}}{V_{\text{fphl}}(V_{\text{phl}} + V_{\text{cel}})}W_{\text{cel-phl}} \\ - \frac{18V_{\text{fccl}}V_{\text{cel}}}{V_{\text{fphl}}(V_{\text{fccl}} + V_{\text{cel}})}W_{\text{fccl-cel}}$$

Composition variables

$$x = \text{Fe} / (\text{Fe} + \text{Mg})$$

$$y = 2 - 1/2 \cdot \text{Si} = x_{\text{Al,T2}}$$

$$n = x_{\text{Na,A1}}$$

$$c = x_{\text{Ca,A1}}$$

$$p = (\text{Si} + \text{Al} + \text{Fe} + \text{Mg}) - 6.0$$

$$h = x_{\text{H2O,A1}}$$

$$Q1 = (x_{\text{H2O,A1}} - x_{\text{H2O,A2}})$$

$$x = (x_{\text{fccl}} + 3x_{\text{fphl}}) / (x_{\text{fccl}} + 3x_{\text{fphl}} + x_{\text{cel}} + 3x_{\text{phl}})$$

$$y = x_{\text{ma}} + 1/2 \cdot (x_{\text{mu}} + x_{\text{pa}} + x_{\text{phl}} + x_{\text{fphl}})$$

$$n = x_{\text{pa}}$$

$$c = x_{\text{ma}}$$

$$p = x_{\text{phl}} + x_{\text{fphl}}$$

$$h = (x_{\text{prl1h}} + x_{\text{prl2h}})$$

$$Q1 = (x_{\text{prl1h}} + x_{\text{prl2h}}) - x_{\text{prl2h}}$$

Site fractions

$$x_{\text{K,A1}} = 1 - n - c - h$$

$$x_{\text{Na,A1}} = n$$

$$x_{\text{Ca,A1}} = c$$

$$x_{\text{H2O,A1}} = h$$

$$x_{\text{Fe,M2A}} = x \cdot (1 - 2y + c - h + p)$$

$$x_{\text{Mg,M2A}} = (1-x) \cdot (1 - 2y + c - h + p)$$

$$x_{\text{Al,M2A}} = 2y - c + h - p$$

$$x_{\text{Fe,M2B}} = x \cdot p$$

$$x_{\text{Mg,M2B}} = (1-x) \cdot p$$

$$x_{\text{Al,M2B}} = 1 - p$$

$$x_{\text{Fe,M1}} = x \cdot p$$

$$x_{\text{Mg,M1}} = (1-x) \cdot p$$

$$x_{\text{Va,M1}} = 1 - p$$

$$x_{\text{Al,T2}} = y$$

$$x_{\text{Si,T2}} = 1 - y$$

$$x_{\text{H2O,A2}} = h - Q1$$

$$x_{\text{Va,A2}} = 1 - (h - Q1)$$

Proportions of independent end-members

$$p_{\text{fccl}} = x \cdot (1 - 2y + c - h + 3p)$$

$$p_{\text{cel}} = (1-x) \cdot (1 - 2y + c - h + 3p) - 3p$$

$$p_{\text{mu}} = 2y - n - 2c - p$$

$$p_{\text{pa}} = n$$

$$\begin{aligned}
p_{ma} &= c \\
p_{phl} &= p \\
p_{pr1h} &= Q1 \\
p_{pr2h} &= h - Q1
\end{aligned}$$

Ideal mixing activities

$$\begin{aligned}
a_{fcel} &= x_{K,A1} \cdot x_{Fe,M2A} \cdot x_{Al,M2B} \cdot x_{Va,M1} \cdot (x_{Si,T2})^2 \cdot x_{Va,A2} \\
a_{cel} &= x_{K,A1} \cdot x_{Mg,M2A} \cdot x_{Al,M2B} \cdot x_{Va,M1} \cdot (x_{Si,T2})^2 \cdot x_{Va,A2} \\
a_{mu} &= 4 \cdot x_{K,A1} \cdot x_{Al,M2A} \cdot x_{Al,M2B} \cdot x_{Va,M1} \cdot x_{Al,T2} \cdot x_{Si,T2} \cdot x_{Va,A2} \\
a_{pa} &= 4 \cdot x_{Na,A1} \cdot x_{Al,M2A} \cdot x_{Al,M2B} \cdot x_{Va,M1} \cdot x_{Al,T2} \cdot x_{Si,T2} \cdot x_{Va,A2} \\
a_{ma} &= x_{Ca,A1} \cdot x_{Al,M2A} \cdot x_{Al,M2B} \cdot x_{Va,M1} \cdot (x_{Al,T2})^2 \cdot x_{Va,A2} \\
a_{fphl} &= 4 \cdot x_{K,A1} \cdot x_{Fe,M2A} \cdot x_{Fe,M2B} \cdot x_{Fe,M1} \cdot x_{Al,T2} \cdot x_{Si,T2} \cdot x_{Va,A2} \\
a_{phl} &= 4 \cdot x_{K,A1} \cdot x_{Mg,M2A} \cdot x_{Mg,M2B} \cdot x_{Mg,M1} \cdot x_{Al,T2} \cdot x_{Si,T2} \cdot x_{Va,A2} \\
a_{pr1h} &= x_{H2O,A1} \cdot x_{Al,M2A} \cdot x_{Al,M2B} \cdot x_{Va,M1} \cdot (x_{Si,T2})^2 \cdot x_{Va,A2} \\
a_{pr2h} &= x_{H2O,A1} \cdot x_{Al,M2A} \cdot x_{Al,M2B} \cdot x_{Va,M1} \cdot (x_{Si,T2})^2 \cdot x_{H2O,A2}
\end{aligned}$$

Phi terms

$$\begin{aligned}
\phi_{fcel} &= \frac{p_{fcel} V_{fcel}}{p_{fcel} V_{fcel} + p_{cel} V_{cel} + p_{mu} V_{mu} + p_{pa} V_{pa} + p_{ma} V_{ma} + p_{phl} V_{phl} + p_{pr1h} V_{pr1h} + p_{pr2h} V_{pr2h}} \\
\phi_{cel} &= \frac{p_{cel} V_{cel}}{p_{fcel} V_{fcel} + p_{cel} V_{cel} + p_{mu} V_{mu} + p_{pa} V_{pa} + p_{ma} V_{ma} + p_{phl} V_{phl} + p_{pr1h} V_{pr1h} + p_{pr2h} V_{pr2h}} \\
\phi_{mu} &= \frac{p_{mu} V_{mu}}{p_{fcel} V_{fcel} + p_{cel} V_{cel} + p_{mu} V_{mu} + p_{pa} V_{pa} + p_{ma} V_{ma} + p_{phl} V_{phl} + p_{pr1h} V_{pr1h} + p_{pr2h} V_{pr2h}} \\
\phi_{pa} &= \frac{p_{pa} V_{pa}}{p_{fcel} V_{fcel} + p_{cel} V_{cel} + p_{mu} V_{mu} + p_{pa} V_{pa} + p_{ma} V_{ma} + p_{phl} V_{phl} + p_{pr1h} V_{pr1h} + p_{pr2h} V_{pr2h}} \\
\phi_{ma} &= \frac{p_{ma} V_{ma}}{p_{fcel} V_{fcel} + p_{cel} V_{cel} + p_{mu} V_{mu} + p_{pa} V_{pa} + p_{ma} V_{ma} + p_{phl} V_{phl} + p_{pr1h} V_{pr1h} + p_{pr2h} V_{pr2h}} \\
\phi_{phl} &= \frac{p_{phl} V_{phl}}{p_{fcel} V_{fcel} + p_{cel} V_{cel} + p_{mu} V_{mu} + p_{pa} V_{pa} + p_{ma} V_{ma} + p_{phl} V_{phl} + p_{pr1h} V_{pr1h} + p_{pr2h} V_{pr2h}} \\
\phi_{pr1h} &= \frac{p_{pr1h} V_{pr1h}}{p_{fcel} V_{fcel} + p_{cel} V_{cel} + p_{mu} V_{mu} + p_{pa} V_{pa} + p_{ma} V_{ma} + p_{phl} V_{phl} + p_{pr1h} V_{pr1h} + p_{pr2h} V_{pr2h}} \\
\phi_{pr2h} &= \frac{p_{pr2h} V_{pr2h}}{p_{fcel} V_{fcel} + p_{cel} V_{cel} + p_{mu} V_{mu} + p_{pa} V_{pa} + p_{ma} V_{ma} + p_{phl} V_{phl} + p_{pr1h} V_{pr1h} + p_{pr2h} V_{pr2h}}
\end{aligned}$$

Activity coefficients

$$\begin{aligned}
RT \ln \gamma_{fcel} &= \phi_{cel} \cdot (1 - \phi_{fcel}) \cdot 2V_{fcel} / (V_{cel} + V_{fcel}) \cdot W_{fcel-cel} + \phi_{mu} \cdot (1 - \phi_{fcel}) \cdot 2V_{fcel} / (V_{mu} + V_{fcel}) \cdot W_{fcel-mu} \\
&+ \phi_{pa} \cdot (1 - \phi_{fcel}) \cdot 2V_{fcel} / (V_{pa} + V_{fcel}) \cdot W_{fcel-pa} + \phi_{ma} \cdot (1 - \phi_{fcel}) \cdot 2V_{fcel} / (V_{ma} + V_{fcel}) \cdot W_{fcel-ma} \\
&+ \phi_{phl} \cdot (1 - \phi_{fcel}) \cdot 2V_{fcel} / (V_{phl} + V_{fcel}) \cdot W_{fcel-phl} + \phi_{pr1h} \cdot (1 - \phi_{fcel}) \cdot 2V_{fcel} / (V_{pr1h} + V_{fcel}) \cdot W_{fcel-pr1h} \\
&+ \phi_{pr2h} \cdot (1 - \phi_{fcel}) \cdot 2V_{fcel} / (V_{pr2h} + V_{fcel}) \cdot W_{fcel-pr2h} - \phi_{cel} \cdot \phi_{mu} \cdot 2V_{fcel} / (V_{cel} + V_{mu}) \cdot W_{cel-mu} \\
&- \phi_{cel} \cdot \phi_{pa} \cdot 2V_{fcel} / (V_{cel} + V_{pa}) \cdot W_{cel-pa} - \phi_{cel} \cdot \phi_{ma} \cdot 2V_{fcel} / (V_{cel} + V_{ma}) \cdot W_{cel-ma} \\
&- \phi_{cel} \cdot \phi_{phl} \cdot 2V_{fcel} / (V_{cel} + V_{phl}) \cdot W_{cel-phl} - \phi_{cel} \cdot \phi_{pr1h} \cdot 2V_{fcel} / (V_{cel} + V_{pr1h}) \cdot W_{cel-pr1h} \\
&- \phi_{cel} \cdot \phi_{pr2h} \cdot 2V_{fcel} / (V_{cel} + V_{pr2h}) \cdot W_{cel-pr2h} - \phi_{mu} \cdot \phi_{pa} \cdot 2V_{fcel} / (V_{mu} + V_{pa}) \cdot W_{mu-pa} \\
&- \phi_{mu} \cdot \phi_{ma} \cdot 2V_{fcel} / (V_{mu} + V_{ma}) \cdot W_{mu-ma} - \phi_{mu} \cdot \phi_{phl} \cdot 2V_{fcel} / (V_{mu} + V_{phl}) \cdot W_{mu-phl} \\
&- \phi_{mu} \cdot \phi_{pr1h} \cdot 2V_{fcel} / (V_{mu} + V_{pr1h}) \cdot W_{mu-pr1h} - \phi_{mu} \cdot \phi_{pr2h} \cdot 2V_{fcel} / (V_{mu} + V_{pr2h}) \cdot W_{mu-pr2h} \\
&- \phi_{pa} \cdot \phi_{ma} \cdot 2V_{fcel} / (V_{pa} + V_{ma}) \cdot W_{pa-ma} - \phi_{pa} \cdot \phi_{phl} \cdot 2V_{fcel} / (V_{pa} + V_{phl}) \cdot W_{pa-phl} \\
&- \phi_{pa} \cdot \phi_{pr1h} \cdot 2V_{fcel} / (V_{pa} + V_{pr1h}) \cdot W_{pa-pr1h} - \phi_{pa} \cdot \phi_{pr2h} \cdot 2V_{fcel} / (V_{pa} + V_{pr2h}) \cdot W_{pa-pr2h}
\end{aligned}$$

$$\begin{aligned} \text{RT} \ln \gamma_{\text{mu}} = & \phi_{\text{fcel}} \cdot (1 - \phi_{\text{mu}}) \cdot 2V_{\text{mu}} / (V_{\text{fcel}} + V_{\text{mu}}) \cdot W_{\text{fcel-mu}} + \phi_{\text{cel}} \cdot (1 - \phi_{\text{mu}}) \cdot 2V_{\text{mu}} / (V_{\text{cel}} + V_{\text{mu}}) \cdot W_{\text{cel-mu}} \\ & + \phi_{\text{pa}} \cdot (1 - \phi_{\text{mu}}) \cdot 2V_{\text{mu}} / (V_{\text{pa}} + V_{\text{mu}}) \cdot W_{\text{mu-pa}} + \phi_{\text{ma}} \cdot (1 - \phi_{\text{mu}}) \cdot 2V_{\text{mu}} / (V_{\text{ma}} + V_{\text{mu}}) \cdot W_{\text{mu-ma}} \\ & + \phi_{\text{phl}} \cdot (1 - \phi_{\text{mu}}) \cdot 2V_{\text{mu}} / (V_{\text{phl}} + V_{\text{mu}}) \cdot W_{\text{mu-phl}} + \phi_{\text{prl1h}} \cdot (1 - \phi_{\text{mu}}) \cdot 2V_{\text{mu}} / (V_{\text{prl1h}} + V_{\text{mu}}) \cdot W_{\text{mu-prl1h}} \\ & + \phi_{\text{prl2h}} \cdot (1 - \phi_{\text{mu}}) \cdot 2V_{\text{mu}} / (V_{\text{prl2h}} + V_{\text{mu}}) \cdot W_{\text{mu-prl2h}} - \phi_{\text{fcel}} \cdot \phi_{\text{cel}} \cdot 2V_{\text{mu}} / (V_{\text{fcel}} + V_{\text{cel}}) \cdot W_{\text{fcel-cel}} \\ & - \phi_{\text{fcel}} \cdot \phi_{\text{pa}} \cdot 2V_{\text{mu}} / (V_{\text{fcel}} + V_{\text{pa}}) \cdot W_{\text{fcel-pa}} - \phi_{\text{fcel}} \cdot \phi_{\text{ma}} \cdot 2V_{\text{mu}} / (V_{\text{fcel}} + V_{\text{ma}}) \cdot W_{\text{fcel-ma}} \\ & - \phi_{\text{fcel}} \cdot \phi_{\text{phl}} \cdot 2V_{\text{mu}} / (V_{\text{fcel}} + V_{\text{phl}}) \cdot W_{\text{fcel-phl}} - \phi_{\text{fcel}} \cdot \phi_{\text{prl1h}} \cdot 2V_{\text{mu}} / (V_{\text{fcel}} + V_{\text{prl1h}}) \cdot W_{\text{fcel-prl1h}} \\ & - \phi_{\text{fcel}} \cdot \phi_{\text{prl2h}} \cdot 2V_{\text{mu}} / (V_{\text{fcel}} + V_{\text{prl2h}}) \cdot W_{\text{fcel-prl2h}} - \phi_{\text{cel}} \cdot \phi_{\text{pa}} \cdot 2V_{\text{mu}} / (V_{\text{cel}} + V_{\text{pa}}) \cdot W_{\text{cel-pa}} \\ & - \phi_{\text{cel}} \cdot \phi_{\text{ma}} \cdot 2V_{\text{mu}} / (V_{\text{cel}} + V_{\text{ma}}) \cdot W_{\text{cel-ma}} - \phi_{\text{cel}} \cdot \phi_{\text{phl}} \cdot 2V_{\text{mu}} / (V_{\text{cel}} + V_{\text{phl}}) \cdot W_{\text{cel-phl}} \\ & - \phi_{\text{cel}} \cdot \phi_{\text{prl1h}} \cdot 2V_{\text{mu}} / (V_{\text{cel}} + V_{\text{prl1h}}) \cdot W_{\text{cel-prl1h}} - \phi_{\text{cel}} \cdot \phi_{\text{prl2h}} \cdot 2V_{\text{mu}} / (V_{\text{cel}} + V_{\text{prl2h}}) \cdot W_{\text{cel-prl2h}} \\ & - \phi_{\text{pa}} \cdot \phi_{\text{ma}} \cdot 2V_{\text{mu}} / (V_{\text{pa}} + V_{\text{ma}}) \cdot W_{\text{pa-ma}} - \phi_{\text{pa}} \cdot \phi_{\text{phl}} \cdot 2V_{\text{mu}} / (V_{\text{pa}} + V_{\text{phl}}) \cdot W_{\text{pa-phl}} \\ & - \phi_{\text{pa}} \cdot \phi_{\text{prl1h}} \cdot 2V_{\text{mu}} / (V_{\text{pa}} + V_{\text{prl1h}}) \cdot W_{\text{pa-prl1h}} - \phi_{\text{pa}} \cdot \phi_{\text{prl2h}} \cdot 2V_{\text{mu}} / (V_{\text{pa}} + V_{\text{prl2h}}) \cdot W_{\text{pa-prl2h}} \\ & - \phi_{\text{ma}} \cdot \phi_{\text{phl}} \cdot 2V_{\text{mu}} / (V_{\text{ma}} + V_{\text{phl}}) \cdot W_{\text{ma-phl}} - \phi_{\text{ma}} \cdot \phi_{\text{prl1h}} \cdot 2V_{\text{mu}} / (V_{\text{ma}} + V_{\text{prl1h}}) \cdot W_{\text{ma-prl1h}} \\ & - \phi_{\text{ma}} \cdot \phi_{\text{prl2h}} \cdot 2V_{\text{mu}} / (V_{\text{ma}} + V_{\text{prl2h}}) \cdot W_{\text{ma-prl2h}} - \phi_{\text{phl}} \cdot \phi_{\text{prl1h}} \cdot 2V_{\text{mu}} / (V_{\text{phl}} + V_{\text{prl1h}}) \cdot W_{\text{phl-prl1h}} \\ & - \phi_{\text{phl}} \cdot \phi_{\text{prl2h}} \cdot 2V_{\text{mu}} / (V_{\text{phl}} + V_{\text{prl2h}}) \cdot W_{\text{phl-prl2h}} - \phi_{\text{prl1h}} \cdot \phi_{\text{prl2h}} \cdot 2V_{\text{mu}} / (V_{\text{prl1h}} + V_{\text{prl2h}}) \cdot W_{\text{prl1h-prl2h}} \end{aligned}$$

$$RT \ln \gamma_{ma} = \phi_{fcel} \cdot (1 - \phi_{ma}) \cdot 2V_{ma} / (V_{fcel} + V_{ma}) \cdot W_{fcel-ma} + \phi_{cel} \cdot (1 - \phi_{ma}) \cdot 2V_{ma} / (V_{cel} + V_{ma}) \cdot W_{cel-ma}$$

$$\begin{aligned} \text{RT ln } \gamma_{\text{prl2h}} = & \phi_{\text{cel}} \cdot (1 - \phi_{\text{prl2h}}) \cdot 2V_{\text{prl2h}} / (V_{\text{cel}} + V_{\text{prl2h}}) \cdot W_{\text{fel-prl2h}} + \phi_{\text{cel}} \cdot (1 - \phi_{\text{prl2h}}) \cdot 2V_{\text{prl2h}} / (V_{\text{cel}} + V_{\text{prl2h}}) \cdot W_{\text{cel-prl2h}} \\ & + \phi_{\text{mu}} \cdot (1 - \phi_{\text{prl2h}}) \cdot 2V_{\text{prl2h}} / (V_{\text{mu}} + V_{\text{prl2h}}) \cdot W_{\text{mu-prl2h}} + \phi_{\text{pa}} \cdot (1 - \phi_{\text{prl2h}}) \cdot 2V_{\text{prl2h}} / (V_{\text{pa}} + V_{\text{prl2h}}) \cdot W_{\text{pa-prl2h}} \\ & + \phi_{\text{ma}} \cdot (1 - \phi_{\text{prl2h}}) \cdot 2V_{\text{prl2h}} / (V_{\text{ma}} + V_{\text{prl2h}}) \cdot W_{\text{ma-prl2h}} + \phi_{\text{phl}} \cdot (1 - \phi_{\text{prl2h}}) \cdot 2V_{\text{prl2h}} / (V_{\text{phl}} + V_{\text{prl2h}}) \cdot W_{\text{phl-prl2h}} \\ & + \phi_{\text{prl1h}} \cdot (1 - \phi_{\text{prl2h}}) \cdot 2V_{\text{prl2h}} / (V_{\text{prl1h}} + V_{\text{prl2h}}) \cdot W_{\text{prl1h-prl2h}} - \phi_{\text{fel}} \cdot \phi_{\text{cel}} \cdot 2V_{\text{prl2h}} / (V_{\text{fel}} + V_{\text{cel}}) \cdot W_{\text{fel-cel}} \\ & - \phi_{\text{fel}} \cdot \phi_{\text{mu}} \cdot 2V_{\text{prl2h}} / (V_{\text{fel}} + V_{\text{mu}}) \cdot W_{\text{fel-mu}} - \phi_{\text{fel}} \cdot \phi_{\text{pa}} \cdot 2V_{\text{prl2h}} / (V_{\text{fel}} + V_{\text{pa}}) \cdot W_{\text{fel-pa}} \\ & - \phi_{\text{fel}} \cdot \phi_{\text{ma}} \cdot 2V_{\text{prl2h}} / (V_{\text{fel}} + V_{\text{ma}}) \cdot W_{\text{fel-ma}} - \phi_{\text{fel}} \cdot \phi_{\text{phl}} \cdot 2V_{\text{prl2h}} / (V_{\text{fel}} + V_{\text{phl}}) \cdot W_{\text{fel-phl}} \\ & - \phi_{\text{fel}} \cdot \phi_{\text{prl1h}} \cdot 2V_{\text{prl2h}} / (V_{\text{fel}} + V_{\text{prl1h}}) \cdot W_{\text{fel-prl1h}} - \phi_{\text{cel}} \cdot \phi_{\text{mu}} \cdot 2V_{\text{prl2h}} / (V_{\text{cel}} + V_{\text{mu}}) \cdot W_{\text{cel-mu}} \\ & - \phi_{\text{cel}} \cdot \phi_{\text{pa}} \cdot 2V_{\text{prl2h}} / (V_{\text{cel}} + V_{\text{pa}}) \cdot W_{\text{cel-pa}} - \phi_{\text{cel}} \cdot \phi_{\text{ma}} \cdot 2V_{\text{prl2h}} / (V_{\text{cel}} + V_{\text{ma}}) \cdot W_{\text{cel-ma}} \\ & - \phi_{\text{cel}} \cdot \phi_{\text{phl}} \cdot 2V_{\text{prl2h}} / (V_{\text{cel}} + V_{\text{phl}}) \cdot W_{\text{cel-phl}} - \phi_{\text{cel}} \cdot \phi_{\text{prl1h}} \cdot 2V_{\text{prl2h}} / (V_{\text{cel}} + V_{\text{prl1h}}) \cdot W_{\text{cel-prl1h}} \\ & - \phi_{\text{mu}} \cdot \phi_{\text{pa}} \cdot 2V_{\text{prl2h}} / (V_{\text{mu}} + V_{\text{pa}}) \cdot W_{\text{mu-pa}} - \phi_{\text{mu}} \cdot \phi_{\text{ma}} \cdot 2V_{\text{prl2h}} / (V_{\text{mu}} + V_{\text{ma}}) \cdot W_{\text{mu-ma}} \\ & - \phi_{\text{mu}} \cdot \phi_{\text{phl}} \cdot 2V_{\text{prl2h}} / (V_{\text{mu}} + V_{\text{phl}}) \cdot W_{\text{mu-phl}} - \phi_{\text{mu}} \cdot \phi_{\text{prl1h}} \cdot 2V_{\text{prl2h}} / (V_{\text{mu}} + V_{\text{prl1h}}) \cdot W_{\text{mu-prl1h}} \\ & - \phi_{\text{pa}} \cdot \phi_{\text{ma}} \cdot 2V_{\text{prl2h}} / (V_{\text{pa}} + V_{\text{ma}}) \cdot W_{\text{pa-ma}} - \phi_{\text{pa}} \cdot \phi_{\text{phl}} \cdot 2V_{\text{prl2h}} / (V_{\text{pa}} + V_{\text{phl}}) \cdot W_{\text{pa-phl}} \\ & - \phi_{\text{pa}} \cdot \phi_{\text{prl1h}} \cdot 2V_{\text{prl2h}} / (V_{\text{pa}} + V_{\text{prl1h}}) \cdot W_{\text{pa-prl1h}} - \phi_{\text{ma}} \cdot \phi_{\text{phl}} \cdot 2V_{\text{prl2h}} / (V_{\text{ma}} + V_{\text{phl}}) \cdot W_{\text{ma-phl}} \\ & - \phi_{\text{ma}} \cdot \phi_{\text{prl1h}} \cdot 2V_{\text{prl2h}} / (V_{\text{ma}} + V_{\text{prl1h}}) \cdot W_{\text{ma-prl1h}} - \phi_{\text{phl}} \cdot \phi_{\text{prl1h}} \cdot 2V_{\text{prl2h}} / (V_{\text{phl}} + V_{\text{prl1h}}) \cdot W_{\text{phl-prl1h}} \end{aligned}$$

8 linearly independent end-members: cel, fcel, mu, pa, ma, phl, prl2h, prl4h
1 dependent end-member: fphl

	A1	M2A	M2B	M1	T2	T1	A2	A3	A4
cel	K	Mg	Al	Va	Si ₂	Si ₂	Va	Va ₂	Va ₃
fcel	K	Fe	Al	Va	Si ₂	Si ₂	Va	Va ₂	Va ₃
mu	K	Al	Al	Va	AlSi	Si ₂	Va	Va ₂	Va ₃
pa	Na	Al	Al	Va	AlSi	Si ₂	Va	Va ₂	Va ₃

ma	Ca	Al	Al	Va	Al ₂	Si ₂	Va	Va ₂	Va ₃
phl	K	Mg	Mg	Mg	AlSi	Si ₂	Va	Va ₂	Va ₃
fphl	K	Fe	Fe	Fe	AlSi	Si ₂	Va	Va ₂	Va ₃
prl2h	H ₂ O	Al	Al	Va	Si ₂	Si ₂	H ₂ O	Va ₂	Va ₃
prl4h	H ₂ O	Al	Al	Va	Si ₂	Si ₂	H ₂ O	(H ₂ O) ₂	Va ₃

Reciprocal relationships

$$G_{\text{fphl}} = G_{\text{phl}} + 3G_{\text{fccl}} - 3G_{\text{cel}} + \frac{6V_{\text{phl}}V_{\text{fccl}}}{V_{\text{fphl}}(V_{\text{phl}} + V_{\text{fccl}})}W_{\text{fccl-phl}} - \frac{6V_{\text{phl}}V_{\text{cel}}}{V_{\text{fphl}}(V_{\text{phl}} + V_{\text{cel}})}W_{\text{cel-phl}} \\ - \frac{18V_{\text{fccl}}V_{\text{cel}}}{V_{\text{fphl}}(V_{\text{fccl}} + V_{\text{cel}})}W_{\text{fccl-cel}}$$

Composition variables

$$x = \text{Fe} / (\text{Fe} + \text{Mg})$$

$$y = 2 - 1/2 \cdot \text{Si} = x_{\text{Al,T2}}$$

$$n = x_{\text{Na,A1}}$$

$$c = x_{\text{Ca,A1}}$$

$$p = (\text{Si} + \text{Al} + \text{Fe} + \text{Mg}) - 6.0$$

$$h = x_{\text{H2O,A1}}$$

$$Q2 = (x_{\text{H2O,A2}} - x_{\text{H2O,A3}})$$

$$x = (x_{\text{fccl}} + 3x_{\text{fphl}}) / (x_{\text{fccl}} + 3x_{\text{fphl}} + x_{\text{cel}} + 3x_{\text{phl}})$$

$$y = x_{\text{ma}} + 1/2 \cdot (x_{\text{mu}} + x_{\text{pa}} + x_{\text{phl}} + x_{\text{fphl}})$$

$$n = x_{\text{pa}}$$

$$c = x_{\text{ma}}$$

$$p = x_{\text{phl}} + x_{\text{fphl}}$$

$$h = (x_{\text{prl2h}} + x_{\text{prl4h}})$$

$$Q2 = (x_{\text{prl2h}} + x_{\text{prl4h}}) - x_{\text{prl4h}}$$

Site fractions

$$x_{\text{K,A1}} = 1 - n - c - h$$

$$x_{\text{Na,A1}} = n$$

$$x_{\text{Ca,A1}} = c$$

$$x_{\text{H2O,A1}} = h$$

$$x_{\text{Fe,M2A}} = x \cdot (1 - 2y + c - h + p)$$

$$x_{\text{Mg,M2A}} = (1-x) \cdot (1 - 2y + c - h + p)$$

$$x_{\text{Al,M2A}} = 2y - c + h - p$$

$$x_{\text{Fe,M2B}} = x \cdot p$$

$$x_{\text{Mg,M2B}} = (1-x) \cdot p$$

$$x_{\text{Al,M2B}} = 1 - p$$

$$x_{\text{Fe,M1}} = x \cdot p$$

$$x_{\text{Mg,M1}} = (1-x) \cdot p$$

$$x_{\text{Va,M1}} = 1 - p$$

$$x_{\text{Al,T2}} = y$$

$$x_{\text{Si,T2}} = 1 - y$$

$$x_{\text{H2O,A2}} = h$$

$$x_{\text{Va,A2}} = 1 - h$$

$$x_{\text{H2O,A3}} = (h - Q2)$$

$$x_{\text{Va,A3}} = 1 - (h - Q2)$$

Proportions of independent end-members

$$p_{\text{fccl}} = x \cdot (1 - 2y + c - h + 3p)$$

$$\begin{aligned}
p_{\text{cel}} &= (1-x) \cdot (1-2y + c - h + 3p) - 3p \\
p_{\text{mu}} &= 2y - n - 2c - p \\
p_{\text{pa}} &= n \\
p_{\text{ma}} &= c \\
p_{\text{phl}} &= p \\
p_{\text{prl2h}} &= Q2 \\
p_{\text{prl4h}} &= h - Q2
\end{aligned}$$

Ideal mixing activities

$$\begin{aligned}
a_{\text{fcel}} &= X_{K,A1} \cdot X_{Fe,M2A} \cdot X_{Al,M2B} \cdot X_{Va,M1} \cdot (X_{Si,T2})^2 \cdot X_{Va,A2} \cdot (X_{Va,A3})^2 \\
a_{\text{cel}} &= X_{K,A1} \cdot X_{Mg,M2A} \cdot X_{Al,M2B} \cdot X_{Va,M1} \cdot (X_{Si,T2})^2 \cdot X_{Va,A2} \cdot (X_{Va,A3})^2 \\
a_{\text{mu}} &= 4 \cdot X_{K,A1} \cdot X_{Al,M2A} \cdot X_{Al,M2B} \cdot X_{Va,M1} \cdot X_{Al,T2} \cdot X_{Si,T2} \cdot X_{Va,A2} \cdot (X_{Va,A3})^2 \\
a_{\text{pa}} &= 4 \cdot X_{Na,A1} \cdot X_{Al,M2A} \cdot X_{Al,M2B} \cdot X_{Va,M1} \cdot X_{Al,T2} \cdot X_{Si,T2} \cdot X_{Va,A2} \cdot (X_{Va,A3})^2 \\
a_{\text{ma}} &= X_{Ca,A1} \cdot X_{Al,M2A} \cdot X_{Al,M2B} \cdot X_{Va,M1} \cdot (X_{Al,T2})^2 \cdot X_{Va,A2} \cdot (X_{Va,A3})^2 \\
a_{\text{fphl}} &= 4 \cdot X_{K,A1} \cdot X_{Fe,M2A} \cdot X_{Fe,M2B} \cdot X_{Fe,M1} \cdot X_{Al,T2} \cdot X_{Si,T2} \cdot X_{Va,A2} \cdot (X_{Va,A3})^2 \\
a_{\text{phl}} &= 4 \cdot X_{K,A1} \cdot X_{Mg,M2A} \cdot X_{Mg,M2B} \cdot X_{Mg,M1} \cdot X_{Al,T2} \cdot X_{Si,T2} \cdot X_{Va,A2} \cdot (X_{Va,A3})^2 \\
a_{\text{prl2h}} &= X_{H2O,A1} \cdot X_{Al,M2A} \cdot X_{Al,M2B} \cdot X_{Va,M1} \cdot (X_{Si,T2})^2 \cdot X_{H2O,A2} \cdot (X_{Va,A3})^2 \\
a_{\text{prl4h}} &= X_{H2O,A1} \cdot X_{Al,M2A} \cdot X_{Al,M2B} \cdot X_{Va,M1} \cdot (X_{Si,T2})^2 \cdot X_{H2O,A2} \cdot (X_{H2O,A3})^2
\end{aligned}$$

Phi terms

$$\begin{aligned}
\phi_{\text{fcel}} &= \frac{p_{\text{fcel}} V_{\text{fcel}}}{p_{\text{fcel}} V_{\text{fcel}} + p_{\text{cel}} V_{\text{cel}} + p_{\text{mu}} V_{\text{mu}} + p_{\text{pa}} V_{\text{pa}} + p_{\text{ma}} V_{\text{ma}} + p_{\text{phl}} V_{\text{phl}} + p_{\text{prl2h}} V_{\text{prl2h}} + p_{\text{prl4h}} V_{\text{prl4h}}} \\
\phi_{\text{cel}} &= \frac{p_{\text{cel}} V_{\text{cel}}}{p_{\text{fcel}} V_{\text{fcel}} + p_{\text{cel}} V_{\text{cel}} + p_{\text{mu}} V_{\text{mu}} + p_{\text{pa}} V_{\text{pa}} + p_{\text{ma}} V_{\text{ma}} + p_{\text{phl}} V_{\text{phl}} + p_{\text{prl2h}} V_{\text{prl2h}} + p_{\text{prl4h}} V_{\text{prl4h}}} \\
\phi_{\text{mu}} &= \frac{p_{\text{mu}} V_{\text{mu}}}{p_{\text{fcel}} V_{\text{fcel}} + p_{\text{cel}} V_{\text{cel}} + p_{\text{mu}} V_{\text{mu}} + p_{\text{pa}} V_{\text{pa}} + p_{\text{ma}} V_{\text{ma}} + p_{\text{phl}} V_{\text{phl}} + p_{\text{prl2h}} V_{\text{prl2h}} + p_{\text{prl4h}} V_{\text{prl4h}}} \\
\phi_{\text{pa}} &= \frac{p_{\text{pa}} V_{\text{pa}}}{p_{\text{fcel}} V_{\text{fcel}} + p_{\text{cel}} V_{\text{cel}} + p_{\text{mu}} V_{\text{mu}} + p_{\text{pa}} V_{\text{pa}} + p_{\text{ma}} V_{\text{ma}} + p_{\text{phl}} V_{\text{phl}} + p_{\text{prl2h}} V_{\text{prl2h}} + p_{\text{prl4h}} V_{\text{prl4h}}} \\
\phi_{\text{ma}} &= \frac{p_{\text{ma}} V_{\text{ma}}}{p_{\text{fcel}} V_{\text{fcel}} + p_{\text{cel}} V_{\text{cel}} + p_{\text{mu}} V_{\text{mu}} + p_{\text{pa}} V_{\text{pa}} + p_{\text{ma}} V_{\text{ma}} + p_{\text{phl}} V_{\text{phl}} + p_{\text{prl2h}} V_{\text{prl2h}} + p_{\text{prl4h}} V_{\text{prl4h}}} \\
\phi_{\text{phl}} &= \frac{p_{\text{phl}} V_{\text{phl}}}{p_{\text{fcel}} V_{\text{fcel}} + p_{\text{cel}} V_{\text{cel}} + p_{\text{mu}} V_{\text{mu}} + p_{\text{pa}} V_{\text{pa}} + p_{\text{ma}} V_{\text{ma}} + p_{\text{phl}} V_{\text{phl}} + p_{\text{prl2h}} V_{\text{prl2h}} + p_{\text{prl4h}} V_{\text{prl4h}}} \\
\phi_{\text{prl2h}} &= \frac{p_{\text{prl2h}} V_{\text{prl2h}}}{p_{\text{fcel}} V_{\text{fcel}} + p_{\text{cel}} V_{\text{cel}} + p_{\text{mu}} V_{\text{mu}} + p_{\text{pa}} V_{\text{pa}} + p_{\text{ma}} V_{\text{ma}} + p_{\text{phl}} V_{\text{phl}} + p_{\text{prl2h}} V_{\text{prl2h}} + p_{\text{prl4h}} V_{\text{prl4h}}} \\
\phi_{\text{prl4h}} &= \frac{p_{\text{prl4h}} V_{\text{prl4h}}}{p_{\text{fcel}} V_{\text{fcel}} + p_{\text{cel}} V_{\text{cel}} + p_{\text{mu}} V_{\text{mu}} + p_{\text{pa}} V_{\text{pa}} + p_{\text{ma}} V_{\text{ma}} + p_{\text{phl}} V_{\text{phl}} + p_{\text{prl2h}} V_{\text{prl2h}} + p_{\text{prl4h}} V_{\text{prl4h}}}
\end{aligned}$$

Activity coefficients

$$\begin{aligned}
RT \ln \gamma_{\text{fcel}} &= \phi_{\text{cel}} \cdot (1 - \phi_{\text{fcel}}) \cdot 2V_{\text{fcel}} / (V_{\text{cel}} + V_{\text{fcel}}) \cdot W_{\text{fcel-cel}} + \phi_{\text{mu}} \cdot (1 - \phi_{\text{fcel}}) \cdot 2V_{\text{fcel}} / (V_{\text{mu}} + V_{\text{fcel}}) \cdot W_{\text{fcel-mu}} \\
&\quad + \phi_{\text{pa}} \cdot (1 - \phi_{\text{fcel}}) \cdot 2V_{\text{fcel}} / (V_{\text{pa}} + V_{\text{fcel}}) \cdot W_{\text{fcel-pa}} + \phi_{\text{ma}} \cdot (1 - \phi_{\text{fcel}}) \cdot 2V_{\text{fcel}} / (V_{\text{ma}} + V_{\text{fcel}}) \cdot W_{\text{fcel-ma}} \\
&\quad + \phi_{\text{phl}} \cdot (1 - \phi_{\text{fcel}}) \cdot 2V_{\text{fcel}} / (V_{\text{phl}} + V_{\text{fcel}}) \cdot W_{\text{fcel-phl}} + \phi_{\text{prl2h}} \cdot (1 - \phi_{\text{fcel}}) \cdot 2V_{\text{fcel}} / (V_{\text{prl2h}} + V_{\text{fcel}}) \cdot W_{\text{fcel-prl2h}} \\
&\quad + \phi_{\text{prl4h}} \cdot (1 - \phi_{\text{fcel}}) \cdot 2V_{\text{fcel}} / (V_{\text{prl4h}} + V_{\text{fcel}}) \cdot W_{\text{fcel-prl4h}} - \phi_{\text{cel}} \cdot \phi_{\text{mu}} \cdot 2V_{\text{fcel}} / (V_{\text{cel}} + V_{\text{mu}}) \cdot W_{\text{cel-mu}} \\
&\quad - \phi_{\text{cel}} \cdot \phi_{\text{pa}} \cdot 2V_{\text{fcel}} / (V_{\text{cel}} + V_{\text{pa}}) \cdot W_{\text{cel-pa}} - \phi_{\text{cel}} \cdot \phi_{\text{ma}} \cdot 2V_{\text{fcel}} / (V_{\text{cel}} + V_{\text{ma}}) \cdot W_{\text{cel-ma}} \\
&\quad - \phi_{\text{cel}} \cdot \phi_{\text{phl}} \cdot 2V_{\text{fcel}} / (V_{\text{cel}} + V_{\text{phl}}) \cdot W_{\text{cel-phl}} - \phi_{\text{cel}} \cdot \phi_{\text{prl2h}} \cdot 2V_{\text{fcel}} / (V_{\text{cel}} + V_{\text{prl2h}}) \cdot W_{\text{cel-prl2h}} \\
&\quad - \phi_{\text{cel}} \cdot \phi_{\text{prl4h}} \cdot 2V_{\text{fcel}} / (V_{\text{cel}} + V_{\text{prl4h}}) \cdot W_{\text{cel-prl4h}} - \phi_{\text{mu}} \cdot \phi_{\text{pa}} \cdot 2V_{\text{fcel}} / (V_{\text{mu}} + V_{\text{pa}}) \cdot W_{\text{mu-pa}} \\
&\quad - \phi_{\text{mu}} \cdot \phi_{\text{ma}} \cdot 2V_{\text{fcel}} / (V_{\text{mu}} + V_{\text{ma}}) \cdot W_{\text{mu-ma}} - \phi_{\text{mu}} \cdot \phi_{\text{phl}} \cdot 2V_{\text{fcel}} / (V_{\text{mu}} + V_{\text{phl}}) \cdot W_{\text{mu-phl}}
\end{aligned}$$

[illegible]

Clay-4

8 linearly independent end-members: cel, fcel, mu, pa, ma, phl, prl4h, prl7h

1 dependent end-member: fphl

Site allocation table

	A1	M2A	M2B	M1	T2	T1	A2	A3	A4
cel	K	Mg	Al	Va	Si ₂	Si ₂	Va	Va ₂	Va ₃
fccl	K	Fe	Al	Va	Si ₂	Si ₂	Va	Va ₂	Va ₃

mu	K	Al	Al	Va	AlSi	Si ₂	Va	Va ₂	Va ₃
pa	Na	Al	Al	Va	AlSi	Si ₂	Va	Va ₂	Va ₃
ma	Ca	Al	Al	Va	Al ₂	Si ₂	Va	Va ₂	Va ₃
phl	K	Mg	Mg	Mg	AlSi	Si ₂	Va	Va ₂	Va ₃
fphl	K	Fe	Fe	Fe	AlSi	Si ₂	Va	Va ₂	Va ₃
prl4h	H ₂ O	Al	Al	Va	Si ₂	Si ₂	H ₂ O	(H ₂ O) ₂	Va ₃
prl7h	H ₂ O	Al	Al	Va	Si ₂	Si ₂	H ₂ O	(H ₂ O) ₂	(H ₂ O) ₃

Reciprocal relationships

$$G_{\text{fphl}} = G_{\text{phl}} + 3G_{\text{fccl}} - 3G_{\text{cel}} + \frac{6V_{\text{phl}}V_{\text{fccl}}}{V_{\text{fphl}}(V_{\text{phl}} + V_{\text{fccl}})}W_{\text{fccl-phl}} - \frac{6V_{\text{phl}}V_{\text{cel}}}{V_{\text{fphl}}(V_{\text{phl}} + V_{\text{cel}})}W_{\text{cel-phl}} \\ - \frac{18V_{\text{fccl}}V_{\text{cel}}}{V_{\text{fphl}}(V_{\text{fccl}} + V_{\text{cel}})}W_{\text{fccl-cel}}$$

Composition variables

$$x = \text{Fe} / (\text{Fe} + \text{Mg})$$

$$y = 2 - 1/2 \cdot \text{Si} = x_{\text{Al,T2}}$$

$$n = x_{\text{Na,A1}}$$

$$c = x_{\text{Ca,A1}}$$

$$p = (\text{Si} + \text{Al} + \text{Fe} + \text{Mg}) - 6.0$$

$$h = x_{\text{H2O,A1}}$$

$$Q3 = (x_{\text{H2O,A3}} - x_{\text{H2O,A4}})$$

$$x = (x_{\text{fccl}} + 3x_{\text{fphl}}) / (x_{\text{fccl}} + 3x_{\text{fphl}} + x_{\text{cel}} + 3x_{\text{phl}})$$

$$y = x_{\text{ma}} + 1/2 \cdot (x_{\text{mu}} + x_{\text{pa}} + x_{\text{phl}} + x_{\text{fphl}})$$

$$n = x_{\text{pa}}$$

$$c = x_{\text{ma}}$$

$$p = x_{\text{phl}} + x_{\text{fphl}}$$

$$h = (x_{\text{prl4h}} + x_{\text{prl7h}})$$

$$Q3 = (x_{\text{prl4h}} + x_{\text{prl7h}}) - x_{\text{prl7h}}$$

Site fractions

$$x_{\text{K,A1}} = 1 - n - c - h$$

$$x_{\text{Na,A1}} = n$$

$$x_{\text{Ca,A1}} = c$$

$$x_{\text{H2O,A1}} = h$$

$$x_{\text{Fe,M2A}} = x \cdot (1 - 2y + c - h + p)$$

$$x_{\text{Mg,M2A}} = (1-x) \cdot (1 - 2y + c - h + p)$$

$$x_{\text{Al,M2A}} = 2y - c + h - p$$

$$x_{\text{Fe,M2B}} = x \cdot p$$

$$x_{\text{Mg,M2B}} = (1-x) \cdot p$$

$$x_{\text{Al,M2B}} = 1 - p$$

$$x_{\text{Fe,M1}} = x \cdot p$$

$$x_{\text{Mg,M1}} = (1-x) \cdot p$$

$$x_{\text{Va,M1}} = 1 - p$$

$$x_{\text{Al,T2}} = y$$

$$x_{\text{Si,T2}} = 1 - y$$

$$x_{\text{H2O,A2}} = h$$

$$x_{\text{Va,A2}} = 1 - h$$

$$x_{\text{H2O,A3}} = h$$

$$x_{\text{Va,A3}} = 1 - h$$

$$x_{\text{H2O,A4}} = (h - Q3)$$

$$x_{V_a,A4} = 1 - (h - Q3)$$

Proportions of independent end-members

$$p_{fcel} = x \cdot (1 - 2y + c - h + 3p)$$

$$p_{cel} = (1-x) \cdot (1 - 2y + c - h + 3p) - 3p$$

$$p_{mu} = 2y - n - 2c - p$$

$$p_{pa} = n$$

$$p_{ma} = c$$

$$p_{phl} = p$$

$$p_{prl4h} = Q3$$

$$p_{prl7h} = h - Q3$$

Ideal mixing activities

$$a_{fcel} = x_{K,A1} \cdot x_{Fe,M2A} \cdot x_{Al,M2B} \cdot x_{Va,M1} \cdot (x_{Si,T2})^2 \cdot x_{Va,A2} \cdot (x_{Va,A3})^2 \cdot (x_{Va,A4})^3$$

$$a_{cel} = x_{K,A1} \cdot x_{Mg,M2A} \cdot x_{Al,M2B} \cdot x_{Va,M1} \cdot (x_{Si,T2})^2 \cdot x_{Va,A2} \cdot (x_{Va,A3})^2 \cdot (x_{Va,A4})^3$$

$$a_{mu} = 4 \cdot x_{K,A1} \cdot x_{Al,M2A} \cdot x_{Al,M2B} \cdot x_{Va,M1} \cdot x_{Al,T2} \cdot x_{Si,T2} \cdot x_{Va,A2} \cdot (x_{Va,A3})^2 \cdot (x_{Va,A4})^3$$

$$a_{pa} = 4 \cdot x_{Na,A1} \cdot x_{Al,M2A} \cdot x_{Al,M2B} \cdot x_{Va,M1} \cdot x_{Al,T2} \cdot x_{Si,T2} \cdot x_{Va,A2} \cdot (x_{Va,A3})^2 \cdot (x_{Va,A4})^3$$

$$a_{ma} = x_{Ca,A1} \cdot x_{Al,M2A} \cdot x_{Al,M2B} \cdot x_{Va,M1} \cdot (x_{Al,T2})^2 \cdot x_{Va,A2} \cdot (x_{Va,A3})^2 \cdot (x_{Va,A4})^3$$

$$a_{fphl} = 4 \cdot x_{K,A1} \cdot x_{Fe,M2A} \cdot x_{Fe,M2B} \cdot x_{Fe,M1} \cdot x_{Al,T2} \cdot x_{Si,T2} \cdot x_{Va,A2} \cdot (x_{Va,A3})^2 \cdot (x_{Va,A4})^3$$

$$a_{phl} = 4 \cdot x_{K,A1} \cdot x_{Mg,M2A} \cdot x_{Mg,M2B} \cdot x_{Mg,M1} \cdot x_{Al,T2} \cdot x_{Si,T2} \cdot x_{Va,A2} \cdot (x_{Va,A3})^2 \cdot (x_{Va,A4})^3$$

$$a_{prl4h} = x_{H2O,A1} \cdot x_{Al,M2A} \cdot x_{Al,M2B} \cdot x_{Va,M1} \cdot (x_{Si,T2})^2 \cdot x_{H2O,A2} \cdot (x_{H2O,A3})^2 \cdot (x_{Va,A4})^3$$

$$a_{prl7h} = x_{H2O,A1} \cdot x_{Al,M2A} \cdot x_{Al,M2B} \cdot x_{Va,M1} \cdot (x_{Si,T2})^2 \cdot x_{H2O,A2} \cdot (x_{H2O,A3})^2 \cdot (x_{H2O,A4})^3$$

Phi terms

$$\phi_{fcel} = \frac{p_{fcel} V_{fcel}}{p_{fcel} V_{fcel} + p_{cel} V_{cel} + p_{mu} V_{mu} + p_{pa} V_{pa} + p_{ma} V_{ma} + p_{phl} V_{phl} + p_{prl4h} V_{prl4h} + p_{prl7h} V_{prl7h}}$$

$$\phi_{cel} = \frac{p_{cel} V_{cel}}{p_{fcel} V_{fcel} + p_{cel} V_{cel} + p_{mu} V_{mu} + p_{pa} V_{pa} + p_{ma} V_{ma} + p_{phl} V_{phl} + p_{prl4h} V_{prl4h} + p_{prl7h} V_{prl7h}}$$

$$\phi_{mu} = \frac{p_{mu} V_{mu}}{p_{fcel} V_{fcel} + p_{cel} V_{cel} + p_{mu} V_{mu} + p_{pa} V_{pa} + p_{ma} V_{ma} + p_{phl} V_{phl} + p_{prl4h} V_{prl4h} + p_{prl7h} V_{prl7h}}$$

$$\phi_{pa} = \frac{p_{pa} V_{pa}}{p_{fcel} V_{fcel} + p_{cel} V_{cel} + p_{mu} V_{mu} + p_{pa} V_{pa} + p_{ma} V_{ma} + p_{phl} V_{phl} + p_{prl4h} V_{prl4h} + p_{prl7h} V_{prl7h}}$$

$$\phi_{ma} = \frac{p_{ma} V_{ma}}{p_{fcel} V_{fcel} + p_{cel} V_{cel} + p_{mu} V_{mu} + p_{pa} V_{pa} + p_{ma} V_{ma} + p_{phl} V_{phl} + p_{prl4h} V_{prl4h} + p_{prl7h} V_{prl7h}}$$

$$\phi_{phl} = \frac{p_{phl} V_{phl}}{p_{fcel} V_{fcel} + p_{cel} V_{cel} + p_{mu} V_{mu} + p_{pa} V_{pa} + p_{ma} V_{ma} + p_{phl} V_{phl} + p_{prl4h} V_{prl4h} + p_{prl7h} V_{prl7h}}$$

$$\phi_{prl4h} = \frac{p_{prl4h} V_{prl4h}}{p_{fcel} V_{fcel} + p_{cel} V_{cel} + p_{mu} V_{mu} + p_{pa} V_{pa} + p_{ma} V_{ma} + p_{phl} V_{phl} + p_{prl4h} V_{prl4h} + p_{prl7h} V_{prl7h}}$$

$$\phi_{prl7h} = \frac{p_{prl7h} V_{prl7h}}{p_{fcel} V_{fcel} + p_{cel} V_{cel} + p_{mu} V_{mu} + p_{pa} V_{pa} + p_{ma} V_{ma} + p_{phl} V_{phl} + p_{prl4h} V_{prl4h} + p_{prl7h} V_{prl7h}}$$

Activity coefficients

$$\begin{aligned} RT \ln \gamma_{fcel} = & \phi_{cel} \cdot (1 - \phi_{fcel}) \cdot 2V_{fcel} / (V_{cel} + V_{fcel}) \cdot W_{fcel-cel} + \phi_{mu} \cdot (1 - \phi_{fcel}) \cdot 2V_{fcel} / (V_{mu} + V_{fcel}) \cdot W_{fcel-mu} \\ & + \phi_{pa} \cdot (1 - \phi_{fcel}) \cdot 2V_{fcel} / (V_{pa} + V_{fcel}) \cdot W_{fcel-pa} + \phi_{ma} \cdot (1 - \phi_{fcel}) \cdot 2V_{fcel} / (V_{ma} + V_{fcel}) \cdot W_{fcel-ma} \\ & + \phi_{phl} \cdot (1 - \phi_{fcel}) \cdot 2V_{fcel} / (V_{phl} + V_{fcel}) \cdot W_{fcel-phl} + \phi_{prl4h} \cdot (1 - \phi_{fcel}) \cdot 2V_{fcel} / (V_{prl4h} + V_{fcel}) \cdot W_{fcel-prl4h} \\ & + \phi_{prl7h} \cdot (1 - \phi_{fcel}) \cdot 2V_{fcel} / (V_{prl7h} + V_{fcel}) \cdot W_{fcel-prl7h} - \phi_{cel} \cdot \phi_{mu} \cdot 2V_{fcel} / (V_{cel} + V_{mu}) \cdot W_{cel-mu} \end{aligned}$$

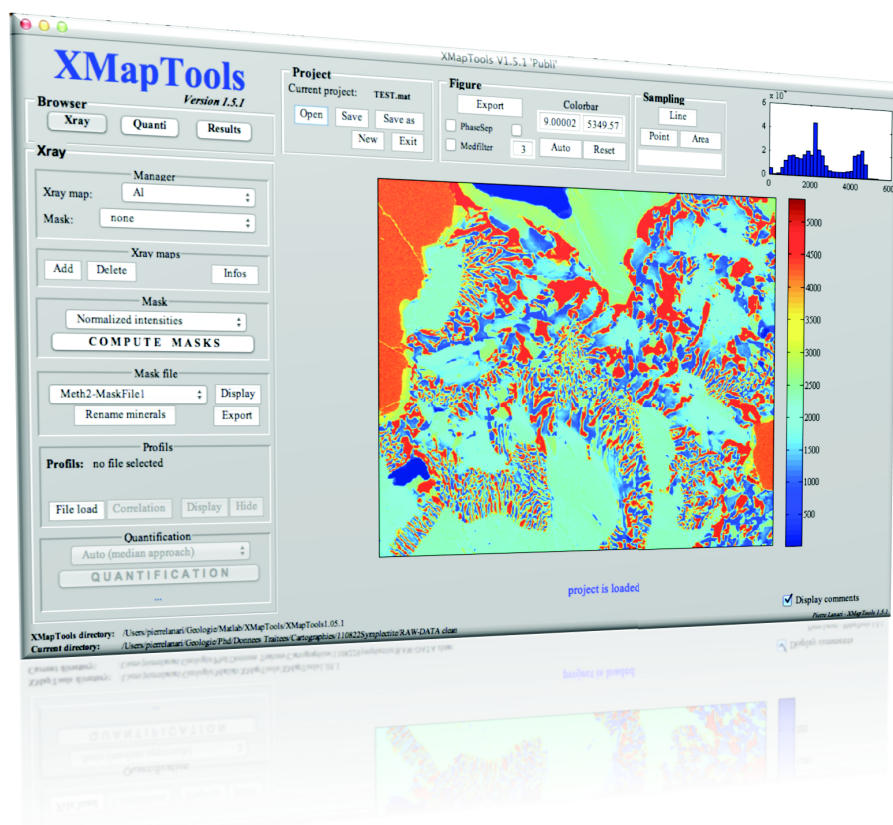
A.4 XMAPTOOLS - USER NOTICE

XMapTools

V1.5.3 (Publication)

USER NOTICE

Lanari, P., Vidal, O. and Grosch E.*



Last Update: 2012-08-29

This notice is provided with all the XMapTools V 1.5.X versions. Download the last available version online at: <http://www.xmaptools.com>.

* ISTerre, Joseph Fourier Grenoble 1 University; email: pierre.lanari@ujf-grenoble.fr

1. Citation guidelines.....	4
2. Introduction.....	5
3. Analytical procedure	6
4. How to get started.....	7
4.1. Requirements	7
4.2. Download the latest version	7
4.3. Setup	7
4.4. Update & Uninstall XMapTools	8
4.5. Diary file	8
4.6. Required data	10
4.7. Report a bug	10
5. Software description	11
5.1. Browser	11
5.2. Specific button-groups.....	12
5.2.1. Xray.....	13
5.2.1.1. Manager.....	13
5.2.1.2. Xray Maps	13
5.2.1.3. Mask.....	15
5.2.1.4. Mask file	19
5.2.1.5. Profiles.....	20
5.2.1.6. Standardization.....	23
5.2.2. Quanti.....	24
5.2.2.1. Manager.....	24
5.2.2.2. Infos	24
5.2.2.3. Options.....	25
5.2.2.4. Structural Formula & Thermometry	28
5.2.2.5. Bulk composition	29
5.2.3. Results	32
5.2.3.1. Manager.....	32
5.2.3.2. Options.....	32
5.2.3.3. Filtering.....	34
5.2.3.4. Chemical Modules.....	34
5.3. Project window	34
5.4. Figure commands	35
5.5. Chem2D.....	37
5.6. Triplot3D	39
6. Supplementary	42
6.1. Export mask-image with changing colors.....	42
6.2. How can I check the results of a function?.....	44
6.3. What is the reference number?.....	45
6.4. How to convert this reference number into the pixel coordinates?.....	47

Authors warmly thank

A.-M. Boullier, N. Riel, B. Gardonio, F. Bernier E., Lewin, S. Guillot M. Munoz, K. Malamoud,

(ISTerre Grenoble)

C. Loury, Y. Rolland (GeoAzur Nice)

C. Martin (Vrije Universiteit Brussel)

A. Robert (CSIC Barcelona)

P. Agard, M. Jentzer (ISTEP Paris)

B. Dubacq (Cambridge)

V. De Andrade (NSLS II Brookhaven)

A. Pourteau (University of Potsdam)

F. Guillot (Université de Lille)

***For help, comments and/or collaborations in order to develop and test the different
versions of XMapTools.***

1. Citation guidelines

Please use the **correct citations** in your publications when you refer to XMapTools. The XMapTools version must be specified just after the name (for example XMapTools V 1.5.X).

Software:

Lanari, P., Vidal, O., Lewin, E., Dubacq, B., De Andrade, V., Schwartz, S., (submitted) XMapTools a Matlab®-based graphic user interface for microprobe quantified image processing. Computers and Geosciences.

Mapping technique:

De Andrade, V., Vidal, O., Lewin, E., O'Brien, P., Agard, P., (2006). Quantification of electron microprobe compositional maps of rock thin sections: an optimized method and examples. Journal of Metamorphic Geology 24, 655–668.

Application examples:

Lanari, P., Riel, N., Guillot, S., Vidal, O., Schwartz, S., Pêcher, A., Hattori, K. (in press). Deciphering High-Pressure metamorphism in collisional context using microprobe-mapping methods: application to the Stak eclogitic massif (NW Himalaya). Geology.

Lanari, P., Guillot, S., Schwartz, S., Vidal, O., Tricart, P., Riel, N., Beyssac, O., (2012). Diachronous evolution of the alpine continental subduction wedge: evidence from P- T estimates in the Briançonnais Zone houillère (France - Western Alps). Journal of Geodynamics. Vol. 56-57, pp. 39-54.

Martin, C., Debaille, V., Lanari, P., Godderis, S., Vanhaecke, F., Vidal, O., Claeys, P., (submitted). REE and Hf distribution among mineral phases in the CV-CK clan: a way to explain the ϵ_{Hf} heterogeneities in CHUR. Earth and Planetary Science Letters.

2. Introduction

XMapTools is a Matlab-based graphic user interface (GUI) software for quantified microprobe X-ray image processing. Pierre Lanari developed this software at the University of Grenoble at ISTerre (Institut des Sciences de la Terre, France) with the collaboration of Olivier Vidal and Eric Lewin. XMapTools aims to make the treatment of petrological electron probe data easy with a large set of functions that import and standardize the X-ray raw data, calculate structural formulae as well as metamorphic pressure and temperature estimates. Many additional processing tools have been developed and will be frequently updated. A website (<http://www.xmaptools.com>) is available, that provides the latest version of XMapTools software that includes online updates with additional tools and notices.

XMapTools software (Lanari et al., submitted) uses a Castaing approach (method of De Andrade et al., 2006) to standardize qualitative X-ray map data from electron microprobe analyses into maps of mineral oxide composition. This goal is achieved using high precision point analysis as a standard. Different chemical groups corresponding to the different minerals are separated using a K-means statistical approach. From maps of element oxide composition, it is possible to estimate the bulk composition of the mapped area or of a selected local microdomain. One of the main advantages of the software is that it can calculate composition, structural formulae and phase equilibrium conditions, such as pressure and temperature, at each pixel on a thin section scale. This allows for integrated textural interpretation of recorded physico-chemical conditions on a micro-scale. This goal is achieved using various geothermometers or geobarometers (~50 functions available). In addition, binary and ternary chemical diagrams can be plotted using the modules Chem2D and TriPlot3D. These modules are available to identify the main chemical variations and to identify the groups of composition within the map.

A set of examples of the XMapTools use can be found in the §1.

Note: In this user's notice, in order to introduce the XMapTools functionalities, a set of maps of an eclogite sample from the Stak massif in NW Himalaya is used as an example (sample description in Lanari et al., submitted).

3. Analytical procedure

In order to acquire high-quality X-ray maps for quantitative analysis, it is recommended to follow the procedure provided in De Andrade et al. (2006). There are two parts required in this microprobe data acquisition procedure that involves (1) qualitative elemental mapping and (2) *in-situ* spot analyses of mineral compositions used in standardization of maps. The section below briefly outlines some important aspects of this analytical procedure along with recommended electron microprobe operating conditions:

Microprobe elemental mapping (calibration)

- Wavelength dispersive mode
- 15 KeV accelerating voltage
- 100 nA specimen current
- 300ms counting time per pixel.
- 1-10 μm resolution (size of pixel)

The acquisition is typically realized in two passes that includes 8-10 elements depending on the number of spectrometers available and the elements Na and K must be acquired during the first pass.

Be careful of the image resolution and always remember that the pixels at the boundaries between two mineral phases represents mixed composition pixels. The smallest analyzed object/mineral grain must have the size of 5-10 pixels. Use a beam size of $< 5 \mu\text{m}$ and that is always $<$ pixel size!

Microprobe point analyses (calibration)

- Wavelength dispersive mode
- 15 KeV accelerating voltage
- 10 nA specimen current
- 20-40s counting time including background measurement.

Several analytical transects consisting of about 40 point analyses each are required and these transects should cross-cut the main mineral grain boundaries (e.g. transects across symplectites, etc.) A total of 20 point analyses per mineral phase is recommended for a good standardization. The step size between two point analyses in transects must be greater than the pixel resolution.

As the thin-section can move between the mapping and the point analyses, be careful to locate the profiles in a BSE image with the best possible precision, i.e. select a starting point and an end point for each profile/transect across different areas of the mineral assemblage (Example: see Fig. 16 in §5.2.1.5).

4. How to get started

4.1. Requirements

Matlab is a requirement for XMapTools software and it can be run with a MATLAB® version 7.5 release R2007b or later version with the statistics toolbox (k-means function).

It uses a graphical interface named XMapTools.fig built using the Matlab® Graphical User Interface Development Environment (GUIDE) tool.

Each GUI component dragged with the GUIDE is associated to a callback function in the program file XMapTools.p, corresponding to a content-obscured version.

4.2. Download the latest version

Before starting, are you sure that you have the last available version of XMapTools?

You can find the last version on our website: <http://www.xmaptools.com>. This step is important, because identified bugs are fixed in new updates. The website allows to you to stay informed of the software development and evolution. Registration in the website is required before the download of XMapTools.

4.3. Setup

XMapTools requires a setup.

(1) Unzip the package XMapTools1-4-X.zip in a suitable repertory (Setup repertory). You can use for example C:/xmaptools/folder (WINDOWS computers) or a folder in your personal folder (MAC & LINUX computers).

(2) Run Matlab.

(3) Select the folder where XMapTools will be unzipped (step 1) in the 'path directory window'.

(4) Run the file Setup.m using the command `>> Setup;`

(5) Write "1" and hit return to continue.

(6) The first part is achieved and the 'config.txt' file has been updated with your current directory.

In case of error in this first part (step 6), you can run the command «cd» in the command window, which prints out the current directory as a string. Copy this directory. Edit the file «config.txt», and paste the directory. It is crucial to edit this file with the new path if you change this folder. Save and close the file.

(7) The setup program asks if you want to add XMapTools to your favourite paths. Write 1 and return to continue. If Matlab errors occur, follow the step 8b. If not, follow the step 8a.

(8a) The setup is finished (no error during step 7) and XMapTools is added to your favourite paths. You can go into the file directory and launch XMapTools (command >>XMapTools).

(8b) The step 7 has failed and you must do it manually. In the main Matlab window, select the menu 'File' and 'Set Path...' Use the button 'Add folder' to add your XMapTools folder in your favourite paths. Use the button 'Save' to save the favourite path file that will be loaded when Matlab is running.

If the step (8) is correct, you can close Matlab and Run a new session. If you run the command «XMapTools» (using Maj and Min), XMapTools must open. If not, you have not correctly saved the Set Path. Try again.

If your setup is completed, you can run and use XMapTools from any folder, without the risk of modifying the main installation. The XMapTools directory and the current directory are indicated at the bottom of the XMapTools window.

Warning: *Microprobe data must be in a separate directory, not in the XMapTools setup directory!*

4.4. Update & Uninstall XMapTools

If you want to update (i.e. install a new version of) XMapTools, you first need to uninstall the old version on your computer.

- (1) Delete the setup repertory in which XMapTools setup files are installed. This operation removes the main program and all the functions.
- (2) Open the set path window in Matlab (file > set path). Select the XMapTools shortcut and remove it. Save and close this window.

XMapTools was correctly removed from your computer, but your data directory is always available (if different, see warning in §4.3).

4.5. Diary file

When you start a new session of XMapTools, the software displays lines of text in the Matlab comment window.

Diary-2012 6 24 14 41.txt

```
#####
#
#           X M a p T o o l s           #
#           v X.X.X                     #
#           (created by: P. Lanari)      #
#           - version XXX - XXXX 2012 -  #
#                                           #
#####
```

24/6/2012 14h41'46"

Loading ... (Setting parameters) ... OK
 Loading ... (Comments database) ... OK
 Loading ... (list of thermometers) ... OK

A new file (in this example called 'Diary-2012 6 24 14 41.txt') was created in the folder XMapTools-Diary/ in which all the text displayed in the command window during the session is stored.

 24/6/2012 14h49'30"

-- END OF EXECUTION (Exit) --

The diary file is closed at the end of the session when END OF EXECUTION is written in the command window.

Warning

If you frequently use XMapTools, you can store a lot of diary files. We recommend to frequently clean up the XMapTools-dairy/ folder content.

4.6. Required data

We recommend to use the following files (Table 1).

Files	Type	Required
<i>Si.txt - Al.txt - Fe.txt - Mg.txt - Na.txt - Ca.txt - Mn.txt - K.txt</i>	X-ray raw data files	Yes
<i>RawProfiles.txt</i>	Point mode analysis file	No
<i>ProfilesOK.txt</i>	Formatted file including point mode analysis and map coordinates	Yes
<i>Informations.txt</i>	File that contains information about this map (coordinates, resolution...)	No

Table 1: List of files provided in order to test XMapTools.

The X-ray raw files (that are a matrix of intensities) must have a *.txt extension and no head line.

The “profilesOK.txt” file format is described in detail in §5.2.1.5.

4.7. Report a bug

You can report a bug using the html-form available on the website. You must be connected to report a bug (the link is visible in the right menu only by connected users).

Before posting please check that your bug was not previously reported in the available list.

All reported bugs are added to this list, and commented on when the bug is fixed.

5. Software description

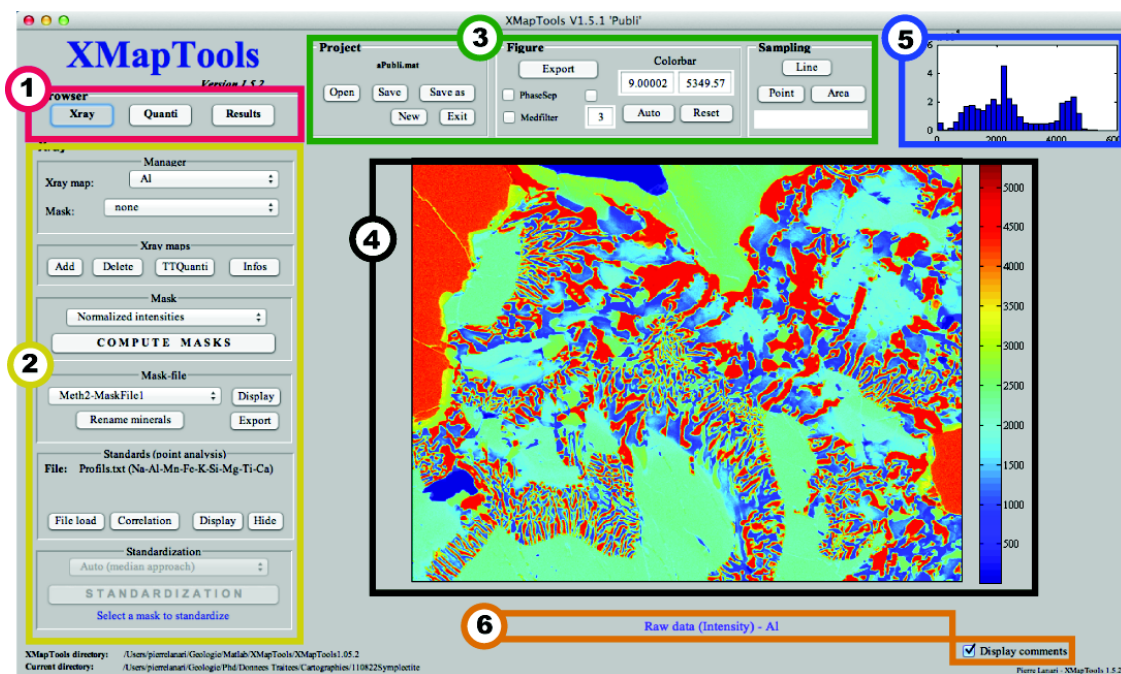


Figure 1: The XMapTools window (1) Browser (Xray; Quanti; Results); (2) Specific button-group; (3) General button-groups (project, figure and sampling); (4) Main map display; (5) histogram of displayed data; (6) Comment (user help) display and options.

The XMapTools interface is presented in Figure 1. It contains annotated parts that are listed and described below:

5.1. Browser

XMapTools software is divided into three parts (Xray, Quanti, Results, see Fig. 2) that are activated using the browser buttons. This menu allows navigating between the different tabs:

- '**Xray**': Automatically selected during the software opening. This part allows adding maps, to compute the masks and identify minerals, to load a profile file and to transform X-ray maps into maps of oxide composition (Standardization). For a list of available functions, see the first column in Fig. 2 and §5.2.1.
- '**Quanti**': This second part is devoted to treatment of the oxide composition maps. It is possible to export data, to calculate structural formulae, and/or to apply empirical to semi-empirical geothermometers and geobarometers from the literature. A module is available to estimate local bulk compositions from the oxide maps.

- **'Results'**: This last part allows the calculated results (mineral structural formulae, P-T maps) to be exported, treated and displayed graphically using two external modules: 'Chem2D' and 'Triplot3D'.

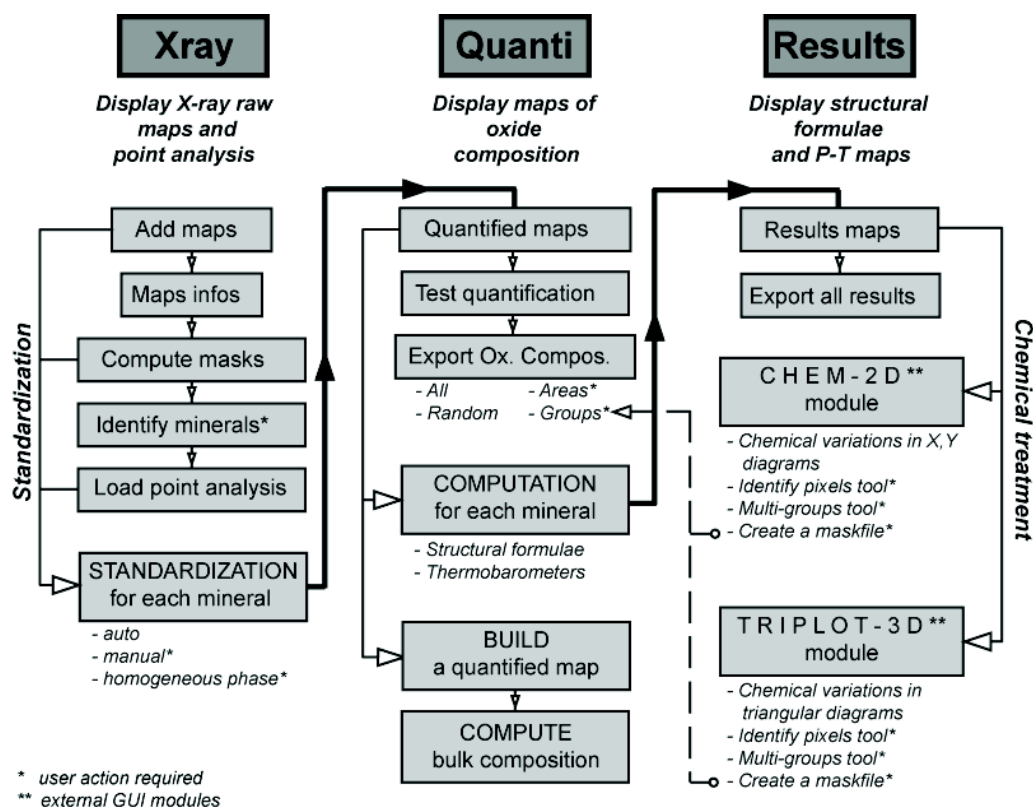


Figure 2: Scheme of XMapTools (Lanari et al., 2012, submitted) with the list of available functions in each tab.

5.2. Specific button-groups

Specific button-group (part 2 in fig. 1) changes automatically during the different steps of the processing. There are three button-groups for each part of the software and three tabs associated that can be activated using the browser (§5.1).

Each button-group is divided into several parts such as a manager for display maps and other groups of buttons for processing purposes.

5.2.1. Xray

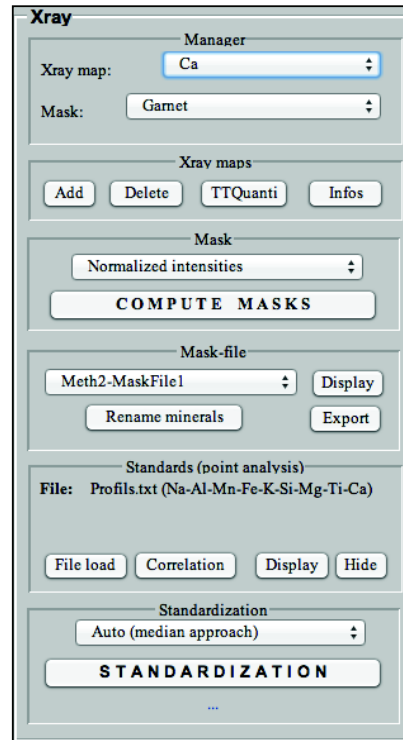


Figure 3: Xray menu.

5.2.1.1. Manager

The 'Manager' menu allows displaying of X-ray raw data for each element ('X-ray map' menu) for all mineral maps of the assemblage or for a selected mineral specified in the 'Mask' menu. To avoid the mask display mode, select 'none' in the mask menu (first choice). Note that the mask menu is available only when the masks have been computed, i.e. when pixels of the image have been allocated to different phases (see below).

5.2.1.2. Xray Maps

The button 'Add' (Fig. 3) allows adding new X-ray maps using the adding tool (fig. 4). Files with *.txt extensions could be preferentially used because it is a common format accepted by the generic Matlab function 'load' (ASCII option). Before opening, check that the files have no head lines (see details in §4.4).

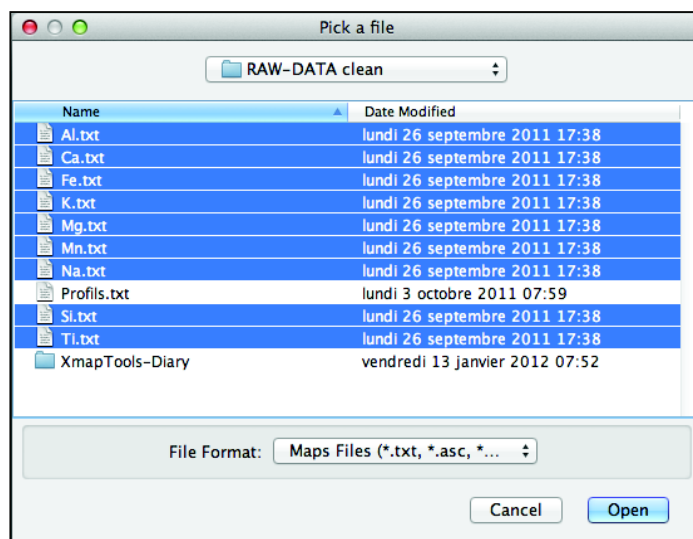


Figure 4: Dialog box to pick the files (X-ray maps).

In the dialog box, pick all the files and click open (Fig. 4). The XMapTools loading function checks all the files one by one and tries to detect the corresponding element (detection in auto mode only if the file name is the element name). XMapTools opens a dialog box for each file in which the user can select an element oxide of interest (fig. 5).

Note: The list of the supported elements is: Na Mg Al Si P S Cl K Ca Ti V Cr Mn Fe Co Ni Cu Zn Zr Ag Cd Sn Ce.

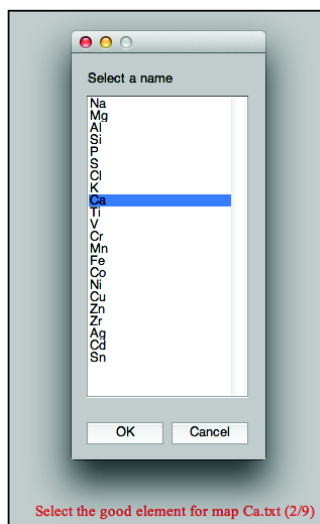


Figure 5: Auto-selection of the good element.
The name of the file is displayed in red.

When all the files are loaded, the X-ray image corresponding to the last file loaded is plotted (part 4 in Fig. 1). Thus, the user can use the manager to plot the different X-ray maps.

The button 'Delete' (fig. 3) allows deletion of a selected X-ray map. This function is available only if two or more X-ray maps have been added.

The button 'TTQuanti' (fig. 3) i.e. Transfert To Quanti, allows the transfer raw X-ray maps into the Quanti tab without standardization. Thus, it is possible to transfer the X-ray data from the Quanti tab to the Result tab using the function 'Gnrle-Intensity2Result' in the group 'General'. The TTQuanti function is very useful to plot the X-ray maps into chemical diagrams. Note that the different elements should be identified (Mask file) before the use of TTQuanti. We can transfer to Quanti tab all the X-ray data (select 'none' in the Mask menu, see fig. 3) or the data for one mineral (select the mineral in the Mask menu, see fig. 3).

The button 'Infos' allows displaying some information about the selected Xray map (Fig. 6).

- The name of the selected element (with the absolute reference).
- The map size in number of pixels (lines / columns)
- The mean intensity of the displayed pixels (if a mineral is selected only these pixels will be used).
- The precision (2σ) in '%' estimated from the mean intensity.
- The standard deviation (intensity).
- The minimum value (intensity).
- The maximum value (intensity).

```

*** RAW DATA INFORMATIONS ***
-----
* element: Mg (ref= 2)
-----
* map size: 520 lines & 670 columns
-----
* mean intensity = 1383.3231
* precision 2sigma (%) = 2.6887
* standard deviation = 758.1872
* min value = 1
* max value = 3122.9231

```

Figure 6: Info about the Xray-map displayed (in this example Mg for the 'eclogite' map).

5.2.1.3. *Mask*

The 'Compute Mask' function aims to attribute each pixel of the image to a distinct chemical phase. This function uses a clustering approach (k-means function) from the compositions of initial pixels selected by the user.

Two different methods are proposed and can be selected in the menu: 'classic' or 'normalized'. The difference between both methods is detailed in Lanari et al. (2012,

submitted). The method 'normalized' is automatically selected by XMapTools because this method is better in most cases.

The user must select the method and click on the 'compute masks' button. A dialog box opens and proposes to select the X-ray maps that will be used to compute the masks (fig. 7). The number of selected elements must be higher than 2. All the maps are automatically selected.

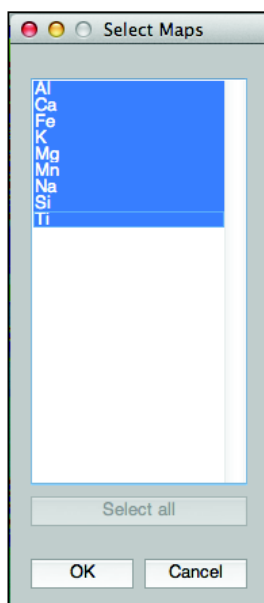


Figure 7: Element selection for the masks processing.

The user must define the initial pixels (magenta circles in Fig. 8) that will be used as input composition values in the mask function. These pixels can be clicked directly into the main image. This selection allows constraining the number of phases. When all the minerals (phases) have been selected, a right click allows finishing the selection step.

Note: If the selected area shows 4 distinct minerals (phases) and the user selects only 3 initial pixels, all the pixels will be allocated to only 3 groups.

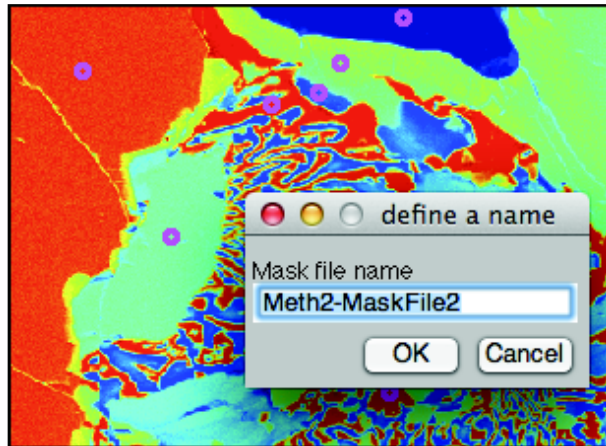


Figure 8: Initial pixel selection (magenta circles) and name of the mask file.

The user must select the name of the mask file. A name is automatically proposed which is composed of the method (1 for classic and 2 for normalized) and the number of this maskfile (for example the second in Fig. 8).

Run the computation using the button OK. The computation starts and the software displays a wait bar with an approximation of the computational time based on a 2009 MacBook.

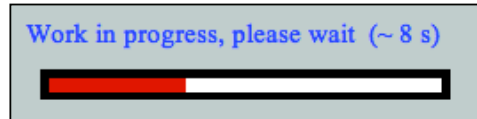


Figure 9: Wait bar and estimated computational time from the mask-function.

Note 1: The wait bar does not scroll during the mask function running because the software uses the *k-means* function in the Matlab statistical toolbox. When the computation stops, the wait bar is automatically hidden and the mask file is displayed in the main figure. Any error encountered is displayed as a red text message in the Matlab command window.

Note 2: If two initial pixels have very close composition, the *k-means* function must bug and an error occurs. Try to select another set of pixels.

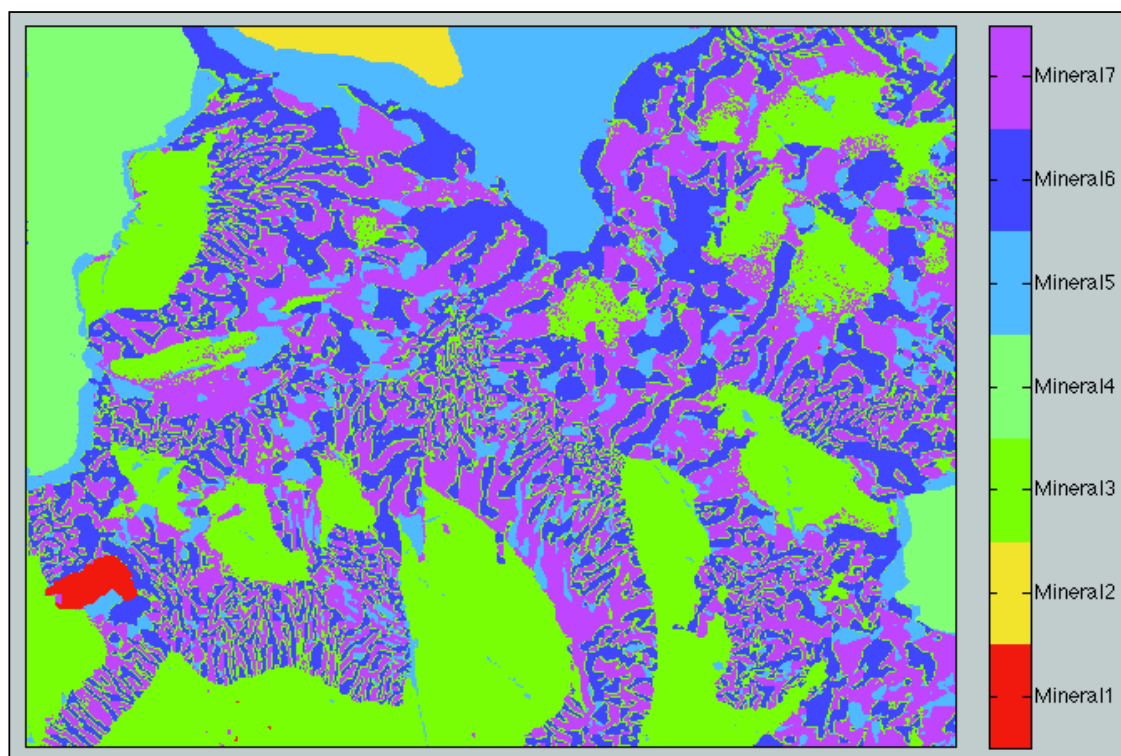


Figure 10: Mask image displayed after the mask function running.

When the computation is achieved, the software displays a 'mask image' in, which each color corresponds to an identified mineral. Default names are MineralX with X a number from 1 to the total number of minerals.

In our example, 7 groups of pixels were identified (Fig. 10).

In the Diary (§4.3) you will find information about the quantification:

**** Diary ****

In the command window, some information are displayed and saved in the diary file during the run of the computing mask function:

```
--
Mask creating ... (Meth2-MaskFile2) ...
Mask creating ... (Nb Masks: 7)
Mask creating ... (Method: Normalized intensities)
Mask creating ... (1 name: Mineral1 < 0.43255% >)
Mask creating ... (2 name: Mineral2 < 1.0962% >)
Mask creating ... (3 name: Mineral3 < 30.9693% >)
Mask creating ... (4 name: Mineral4 < 7.0003% >)
Mask creating ... (5 name: Mineral5 < 13.2035% >)
Mask creating ... (6 name: Mineral6 < 21.2577% >)
Mask creating ... (7 name: Mineral7 < 26.0405% >)
Mask creating ... (Meth2-MaskFile2) ... OK
--
```

The proportions proposed are the occurrence of each mineral in term of image surface.

If your purpose is to calculate the surface proportion (modal abundance) of each phase, you can use these values and test different mask computations with different methods/elements.

When the user computes a new mask, a new mask file is created by XMapTools. All the mask files are available in the mask file menu (& 5.2.1.4).

Note: In this version (1.5.X) the first mask file saved is automatically selected when you load a project.

5.2.1.4. *Mask file*

The 'Mask file' menu (Fig. 3) automatically displays the mask file previously built. All the mask files available can be selected using this menu.

The button 'Display' allows plotting the mask image of the selected mask file in the main display (4 on Figure 1).

The button 'Export' allows opening the same mask image into a new window. This figure can now be saved using the figure menu (files / save as...). The main export function (button export in the figure button group) does not work correctly with a mask image.

To change the colors of the mask-image see §6.2.

The button 'Rename minerals' allows the user to change the assigned mineral names. A new dialog box opens (Fig. 11) and the user can edit the names. When the button OK is clicked, a new mask image will be plotted with the new names (Fig. 12).

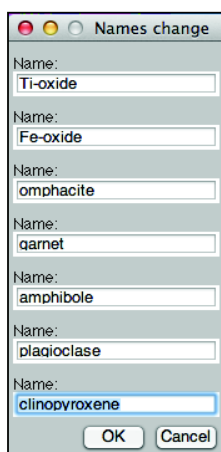


Figure 11: Mineral name editing tool.

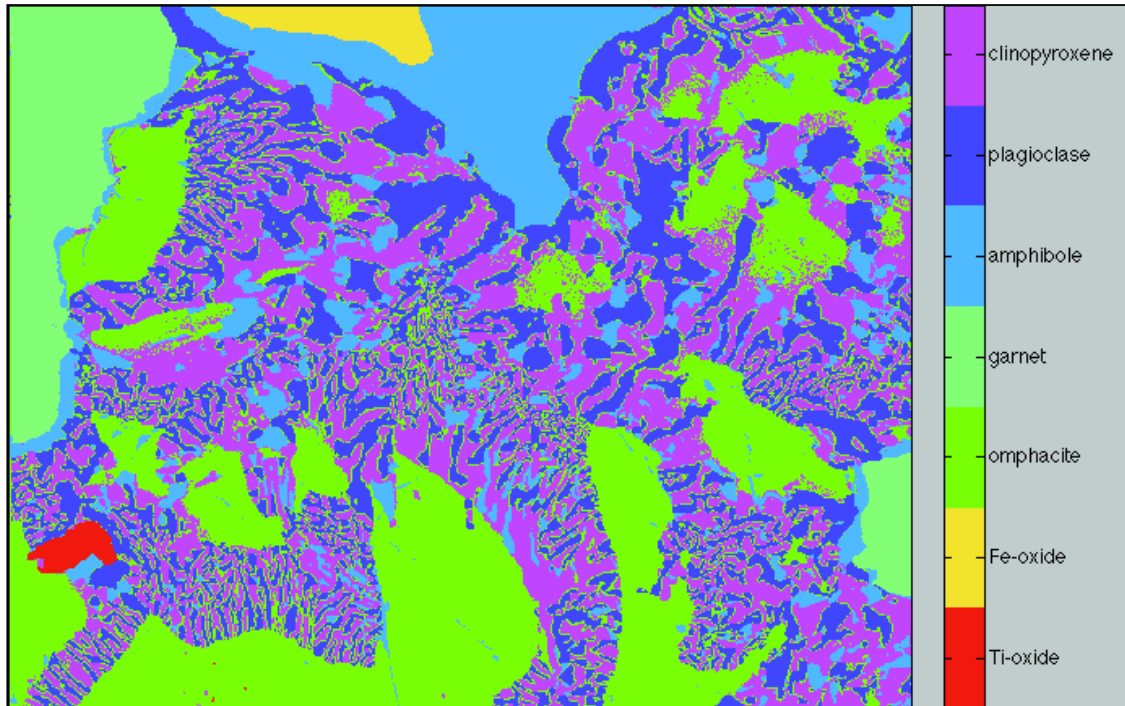


Figure 12: Mask image with personalized mineral names.

Note: In this case, we show that the mask defined for omphacite is composed of large crystals and grain boundaries between clinopyroxene and plagioclase within the symplectite. To avoid this artefact, the user can try to define a new mask for these borders. All these pixels can be filtered in the next steps. Remember that a pixel from a phase A close to a phase B may appear as compositional mixing between the two phases and may be displayed as an apparent false mineralogical composition in the mask.

**** Diary ****

--

```
Mask editing ... (Meth2-MaskFile2) ...
Mask editing ... (1 rename: Mineral1 --> Ti-oxide)
Mask editing ... (2 rename: Mineral2 --> Fe-oxide)
Mask editing ... (3 rename: Mineral3 --> omphacite)
Mask editing ... (4 rename: Mineral4 --> garnet)
Mask editing ... (5 rename: Mineral5 --> amphibole)
Mask editing ... (6 rename: Mineral6 --> plagioclase)
Mask editing ... (7 rename: Mineral7 --> clinopyroxene)
Mask editing ... (Meth2-MaskFile2) ... OK
```

--

The new names are saved in the diary with the corresponding old names.

5.2.1.5. Profiles

High-precision point analyses are required for the standardization step and this can be managed using the corresponding button group (Fig. 13).

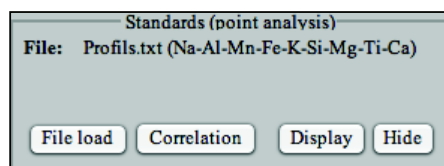


Figure 13: Button group for Standards (point analysis).

Standards (point analysis) are imported into XMapTools in a profile file. This file includes:

- The map coordinates. These values are listed below the keywords: ***** Map coordinates *****. This line is required by the reading function (do not change this line). The list of the map coordinates is X_left, X_right, Y_bottom and Y_top (coordinates of the borders of the images). The unit depends on the microprobe. In this example (profile.txt, see below) the unit used for the map coordinates (must be the same for analyses) is mm (Jeol® microprobe).
- The order of elements used in the list of point mode analyses must be defined below the keywords: ***** Elements order *****. Note that the order can be personalized for the oxides but not for the coordinates. X and Y coordinate must be at the end and with this order.
- The analyses must be listed below the keywords: ***** Analysis ***** with the order previously defined (use dots and not commas).

An example of profile file can be found below:

```

* * * * Profile file (profile.txt) * * * *

! xleft ! xright ! ybott ! ytop
*** Map coordinates ***
76.024
76.694
10.398
9.878

*** Elements order ***
Na2O Al2O3 MnO FeO K2O SiO2 MgO TiO2 CaO X Y

*** Analysis ***
5.540 11.925 0.022 4.039 0.028 55.608 9.034 0.202 14.141 76.357 10.314
5.731 11.844 0.000 4.015 0.015 55.432 8.735 0.240 14.143 76.363 10.314
5.665 11.852 0.048 4.000 0.000 55.646 8.925 0.215 14.097 76.368 10.312
5.782 11.878 0.050 4.134 0.012 55.650 8.992 0.249 14.084 76.372 10.311
5.635 11.619 0.051 4.106 0.008 55.346 8.994 0.198 14.175 76.377 10.311
5.669 11.689 0.004 4.194 0.011 55.625 8.882 0.236 14.404 76.382 10.309
5.423 11.682 0.010 4.138 0.014 55.565 8.986 0.246 14.489 76.387 10.308
5.402 11.611 0.000 4.162 0.012 55.278 9.174 0.195 14.634 76.392 10.307
5.266 11.705 0.034 4.220 0.027 54.699 9.357 0.231 14.837 76.397 10.306
5.267 11.560 0.058 4.295 0.006 54.827 9.269 0.253 15.071 76.402 10.305
4.171 9.277 0.066 4.962 0.009 54.138 10.360 0.140 17.022 76.407 10.304
3.820 8.397 0.021 5.230 0.015 54.462 10.813 0.063 17.682 76.411 10.303
3.275 7.628 0.024 4.908 0.016 54.397 11.628 0.122 18.750 76.416 10.302
2.824 7.123 0.009 4.759 0.020 53.947 12.223 0.171 19.447 76.422 10.301
2.333 5.867 0.030 5.214 0.143 53.466 12.651 0.196 19.594 76.426 10.300
2.417 9.748 0.046 7.176 0.295 49.557 13.734 0.554 15.481 76.432 10.299

```

The profile file can be created using the Matlab editor (paste the data from Excel spreadsheet) and save in the main directory with data and backups.

The button 'File load' allows loading a profile file. A dialog box opens and the user can select the profile file (Fig. 14).

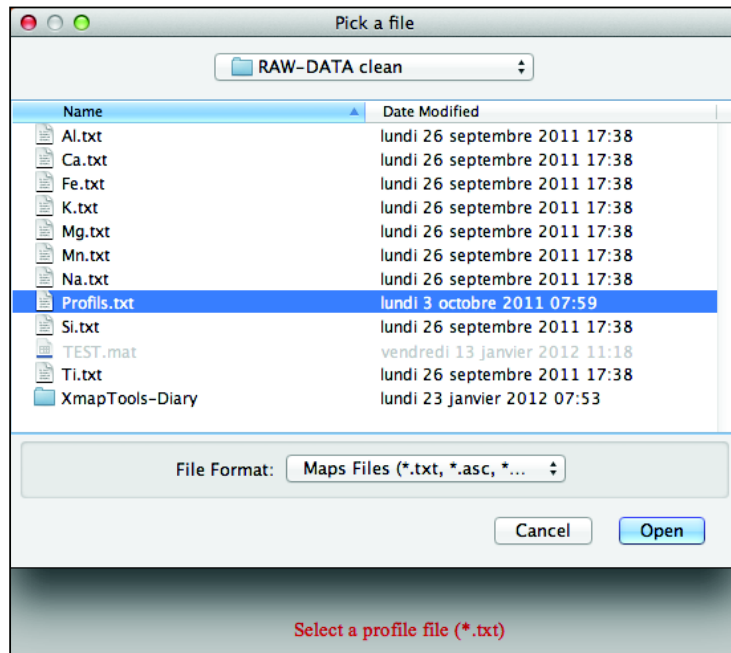


Figure 14: Loading function (the user must select a profile file).

If an error occurs during the reading, the software will indicate the section in, which the error has been found (example Fig. 15).

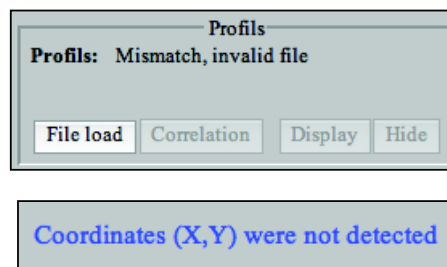


Figure 15: Example of error occurring during the profile file loading.

When the profile file is successfully loaded, the list of elements (in the same order) will be displayed in the Profile button group and the point locations are displayed into the map (black crosses in Fig. 16).

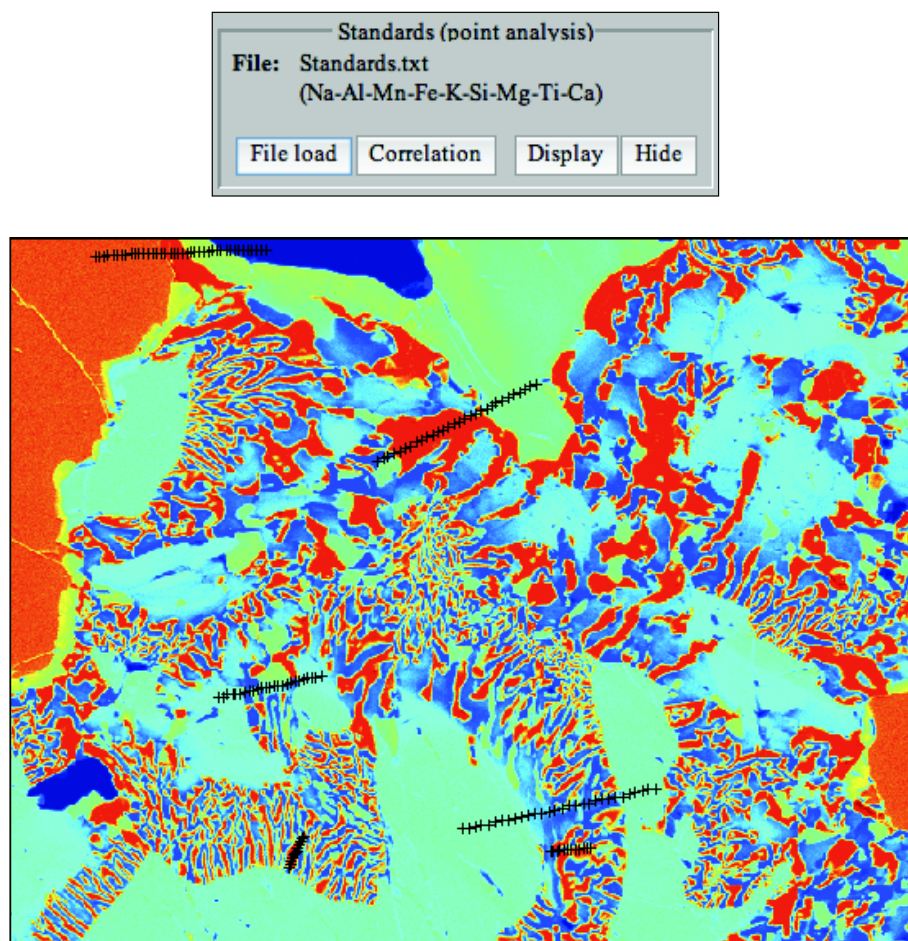


Figure 16: List of elements loaded from the profile file (top) and corresponding points (black crosses, bottom) plotted into a composition map (here raw data of Al).

5.2.1.6. *Standardization*

When all required steps are accomplished, and one mineral is selected, it is possible to transform X-ray maps into maps of oxide concentration.

Three methods are available for the standardization process and can be selected in the standardization menu (see Fig. 3):

- Auto (median approach)
- Manual (user's selection)
- Manual (homogeneous phases).

The method 'Auto (median approach)' is an automatic method of standardization in which the calibration curves were defined automatically using a median approach.

The method 'Manual (user's selection)' allows the user to define the calibration curves for each element.

The method **'Manual (homogeneous phases)'** allows for the standardization of homogeneous phases such as quartz.

These methods are described in detail in the forthcoming paper (Lanari et al., submitted).

***Note:** When the standardization process is achieved, the software moves automatically to the second tab 'Quanti' and changes the associated specific button group. The displayed map is also updated and the new oxide map is drawn.*

5.2.2. Quanti

5.2.2.1. Manager

The **'Manager'** allows displaying the map of oxide composition selected in the menu 'Oxide (Wt%)' of the standardized mineral selected with the menu 'Qmineral'.

For coding reasons, the first quantified mineral in the list is always 'none'. If none is selected, nothing happens in the plotting areas and the oxide weight menu is inactive.

5.2.2.2. Infos

Some information about the standardization is provided here. The number of standards used (i.e. point analyses used) is displayed (for example for garnet in Fig. 17).

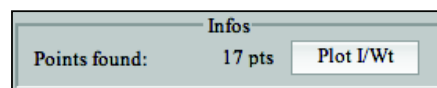


Figure 17: Infos in the Quanti part.

The button **Plot I/Wt** is used to display the standard compositions and the calibration curves into intensity VS oxide wt% diagram (Fig. 18).

The example presented in Fig. 18 is for garnet. Each element is plotted with a different color. The corresponding element can be found using the oxide and intensity values of the maps. For example in garnet, the first green group showing Wt% composition of 40% is SiO₂. The blue group is Al₂O₃, the red group FeO ...

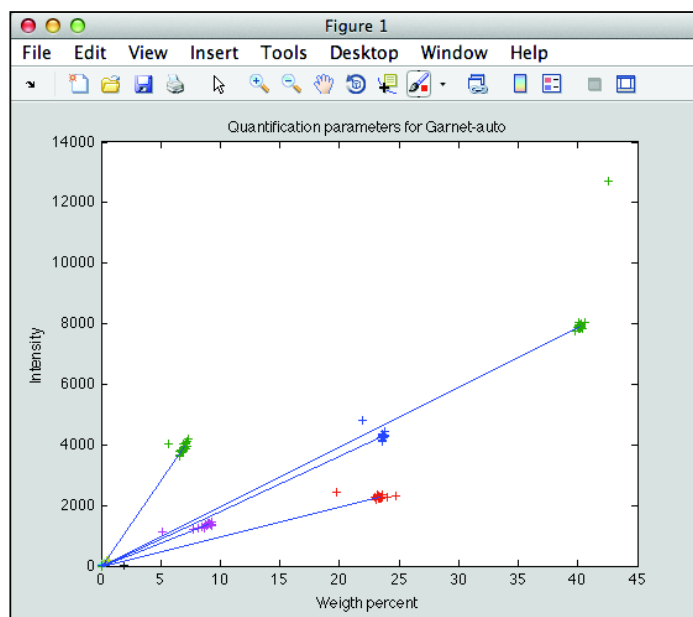


Figure 18: Standardization of garnet: intensity VS oxide wt% diagram.

A detailed description of this kind of diagram can be found in the forthcoming paper (Lanari et al., submitted).

5.2.2.3. Options

In this group, 5 buttons are available: Rename, Delete, Wt%sum, Export and Filter. Note that the Delete function is available only when two or more minerals have been standardized.

The button 'Rename' allows editing the name of the selected Qmineral. This name was automatically defined during the standardization.

The button 'Delete' allows deleting the selected map (available only if the number of map is higher than 2).

The button 'Filter' allows creating a new Qmineral from the selected Qmineral, but only with the composition values between the minimum and maximum values of the colorbar. For example the FeO map of garnet show homogeneous composition at 23% except for a thin rim (Fig. 19). We can define a new Qmineral called garnet_core using the filter button. We select the range of FeO composition between 22% and 24.5% in the Figure part and we use the PhaseSep option (min and max) to plot in black the unselected compositions (Fig. 20 & Fig. 21). Now, the button filter will create a new Qmineral automatically called Garnet_filtered with only the pixels in color in the Fig. 21.

This function is very useful to create different groups of composition for a zoned mineral. Example: Lanari et al., submitted (Geology).

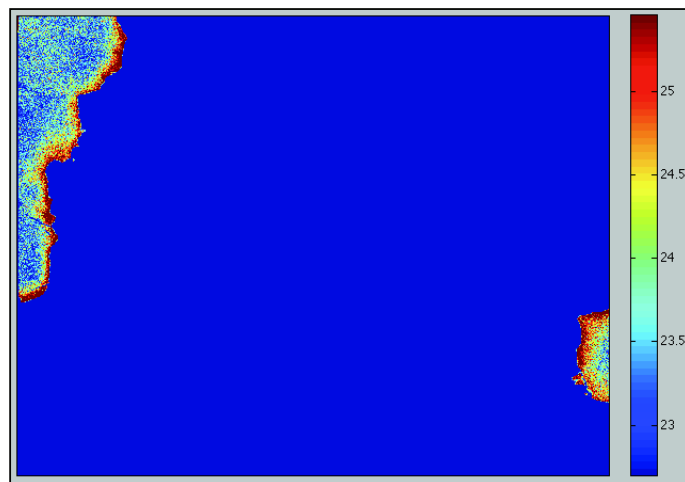


Figure 19: FeO map of garnet (Wt%).

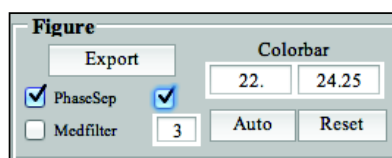


Figure 20: Selection of the garnet_core (figure tool).



Figure 21: Selection of the garnet_core (FeO map of garnet).

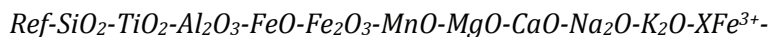
The button 'Export' allows exporting the maps of oxide composition into oxide analyses (see the exported oxide composition 'Example.txt' below).

The different methods available are listed in Table 2.

Method	Description
All	Export all the pixel compositions of the selected mineral as oxide weight analyses. If the map size is large, the created file will be very heavy. Some software can have problems to read this file (insufficient memory warning message).
Area	Export all the pixel compositions included in an area defined by the user. Select an area and right-click to finish, this last click will automatically close the area.
Random	Export a specified number of pixel compositions randomly selected into the map.
Groups	This method allows exporting average compositions for groups of pixels. Groups, also called masks can be created from the oxide data, or using an existing mask-file created during the chemical study (see §).

Table 2: Methods available in the function 'Export'.

In all methods, the format of the exported file can be edited. The default order proposed is:



You can change this order using the oxide names separated by '-'. Note that the reference number must be called 'Ref' and must be the first value. This value is detailed in §6.3 (what is the reference number?).

If the software does not recognize the oxide name, a value of zero is allocated. In the default order, zero values are allocated to Fe₂O₃ and XFe³⁺.

User can change the format of the separator ('space' or 'tabulation'). In the following example, we used 'space'.

In the exported file, each analysis (row) has a reference number, which is related to the pixel location in the map (see below).

* * * * Exported oxide compositions (Example.txt) * * * *

Oxide mineral compositions from XMapTools
02-May-2012
Analysis: 326
Quantified mineral: Garnet

```

18756.00 40.59 0.03 23.30 23.83 0.00 0.44 9.12 6.86 0.01 0.01 0.00
19276.00 40.21 0.03 23.74 23.85 0.00 0.46 8.93 6.65 0.03 0.01 0.00
19277.00 40.51 0.02 23.42 23.80 0.00 0.46 9.20 6.71 0.07 0.01 0.00
19795.00 40.26 0.03 23.56 23.27 0.00 0.46 9.61 6.48 0.05 0.01 0.00
19796.00 40.02 0.02 24.05 23.75 0.00 0.49 9.21 6.62 0.03 0.01 0.00
19797.00 40.81 0.02 23.25 22.93 0.00 0.42 8.78 6.71 0.04 0.01 0.00
19798.00 40.11 0.04 23.60 24.33 0.00 0.39 8.43 6.74 0.03 0.01 0.00
20312.00 40.97 0.02 23.70 22.39 0.00 0.46 9.08 6.72 0.04 0.01 0.00
20313.00 40.71 0.03 23.80 23.88 0.00 0.41 8.97 6.51 0.04 0.01 0.00
20314.00 40.72 0.02 22.86 23.53 0.00 0.50 9.15 6.81 0.04 0.01 0.00
20315.00 40.83 0.02 23.80 23.41 0.00 0.46 9.04 6.88 0.03 0.01 0.00
...

```

5.2.2.4. *Structural Formula & Thermometry*

XMapTools includes a large set of computational methods (list in Lanari et al., (Submitted)). This list will be updated in the future releases.

Advertisement: *Before the first use of a function, the user must perform tests in order to check the results of the function (see §6.2 'How can I check the results of one function?').*

For each computation, the user must follow these steps:

- (1) Select the Qmineral in the manager window.
- (2) Select the mineral type in the **menu 'Minerals'** in the structural formulae and thermobarometry window.
- (3) Select the method in the **menu 'Method'** in the structural formulae and thermobarometry window.

There are different types of methods available:

- One name of mineral (see list below) in which the computation will be applied on all the pixels of the selected Qmineral.
- Two names of minerals (see list below) in which the computation will be applied on a couple of pixels selected by the user.
- The general function (see below).

One Name: amphibole; biotite; chlorite; clinopyroxene; garnet; chloritoid; feldspars; phengite; rutile; serpentine.

Two names: amphibole+plagioclase; chlorite+chloritoid; garnet+biotite; garnet+mica; garnet+chlorite; garnet+amphibole; garnet+clinopyroxene.

General functions: (see the list below).

The button 'Compute' allows applying the selected methods (in the menu methods) to the selected mineral compositions (in the menu Qmineral).

General functions

Gnrle-StructForm: This function calculates the structural formula of all the selected pixels using the number of oxygens defined by the user.

Gnrle-Oxide2Results: This function allows sending the selected oxide composition into the result tab in order to use the chemical modules with the oxide compositions.

Gnrle-Intensity2Results: This function allows sending the selected intensity compositions into the result tab in order to use the chemical modules with the intensity compositions.

5.2.2.5. Bulk composition

The function **'Merge Qminerals'** aims to create a merged map of oxide composition for all the pixels (Fig. 22). The user must select the Qminerals in a list, and one element as reference. This element is used to estimate the composition of the missing pixels between two different phases. This interpolation occurs only if the boundaries have been separated in a new phase that has not been selected here (standardization impossible). Two additionally parameters (X-n->X+n and OnGarde) control this interpolation. X-n->X+n is the number of pixels used to interpolate and OnGarde is an interpolation parameter. Note that the proposed values (respectively 2 and 0.5) run correctly in most cases.

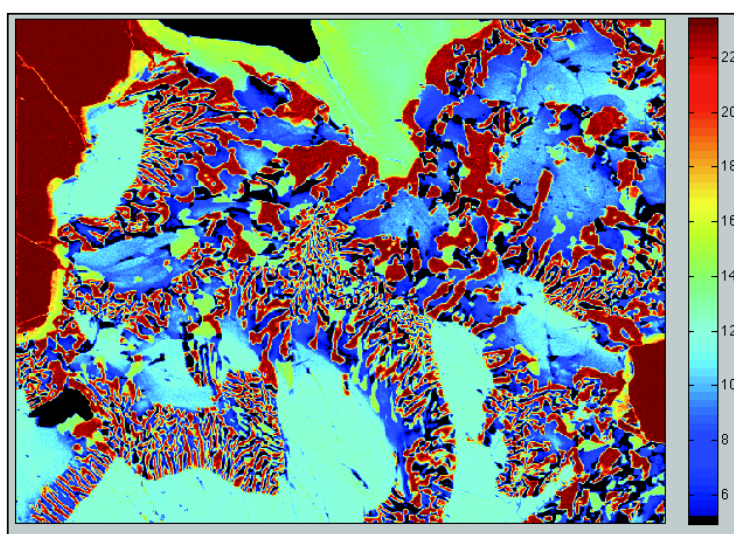


Figure 22 Map of oxide composition of Al₂O₃ (Wt%)

Once the merged map has been built, the compositions can be exported using the two following buttons:

The button **'Bulk map'** allows exporting the average oxide composition of the merged map. The user must specify the name of the file that will be exported in the folder Exported-bulk (see the bulk_map.txt file).

*** Exported bulk map compositions (bulk_map.txt) ***

Bulk composition (Map) from XMapTools

Al ₂ O ₃	13.3752
CaO	12.2151
FeO	5.6648
K ₂ O	0.12745
MgO	8.3694
MnO	0.058369
Na ₂ O	4.6869
TiO ₂	0.26575
SiO ₂	54.0232
SUM	98.7861

The button '**Bulk area**' allows exporting the average oxide composition of a selected area (Fig. 23). User must specify the name of the file that will be exported in the folder Exported-bulk (see the bulk_local.txt file).

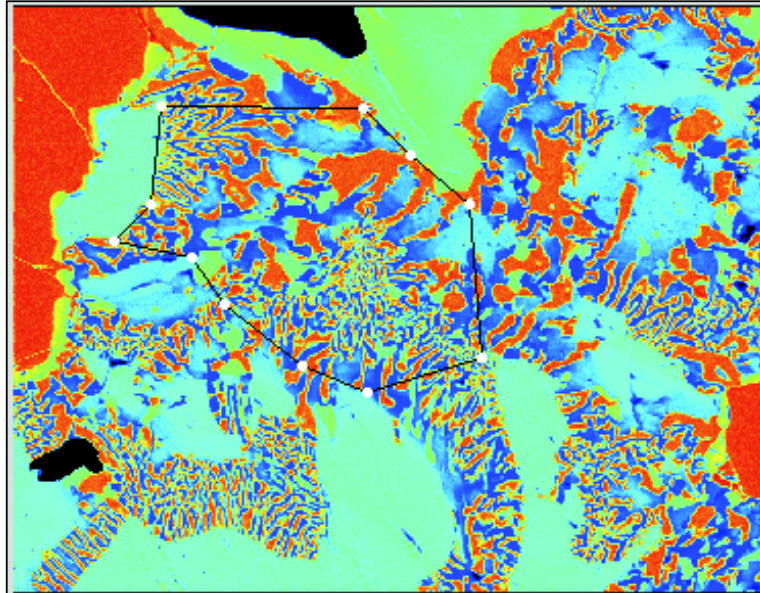


Figure 23: Selected area (white points and black lines) for which the bulk composition bulk_local.txt was exported. Map: bulk map Al₂O₃ (fig. 22 with a different color bar)

*** Exported bulk map compositions (bulk_local.txt) ***

Bulk composition (Area) from XMapTools

Al ₂ O ₃	12.8597
CaO	12.2953
FeO	3.6076
K ₂ O	0.10817
MgO	7.5572
MnO	0.023612
Na ₂ O	5.2575
TiO ₂	0.18673
SiO ₂	57.0682
SUM	98.964

The button '**Bulk prop**' allows exporting a bulk composition using mineral compositions and mineral proportions set by the user. For example, it is possible to estimate the bulk composition of an assemblage with 80% amphibole and 20% plagioclase using this tool:

- Define the number of minerals, here 2.
- Set the name of minerals, here 'Amphibole' and 'Plagioclase'.
- Set the proportion, here '80' and '20'.
- Select the input composition into the map (Fig. 24).

- Define the name of the file, here bulk_prop.txt

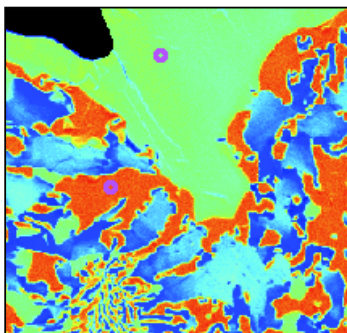


Figure 24: Selected composition for the 'bulk prop' computation. Map: bulk map Al₂O₃ (fig. 22 & 23)

*** Exported bulk map compositions (bulk_prop.txt) ***

Bulk composition (Proportions) from XMapTools

(1) Mineral proportions:

Amphibole	80
Plagioclase	20

(2) Minerals compositions:

	Amphibole	Plagioclase
Al ₂ O ₃	13.7275	22.732
CaO	9.6434	2.6064
FeO	10.4619	0.099749
K ₂ O	1.0399	0.08189
MgO	13.6934	0.042667
MnO	0.046126	0.010667
Na ₂ O	2.8573	10.5733
TiO ₂	1.532	0.01045
SiO ₂	44.2282	64.8127

(3) Bulk Composition:

Al ₂ O ₃	15.5284
CaO	8.236
FeO	8.3894
K ₂ O	0.84833
MgO	10.9632
MnO	0.039034
Na ₂ O	4.4005
TiO ₂	1.2277
SiO ₂	48.3451

Note: The bulk composition buttons allow estimating the bulk composition using an average of oxide composition approach. This approach using only oxide composition does not account for the volume of the different minerals and the structural formula compositions.

5.2.3. Results

5.2.3.1. Manager

The 'Manager' allows displaying the map - selected into the menu 'Display' - of the result selected into the menu 'Result'. Results can be maps of structural formulae, or maps of equilibrium conditions such as pressure maps and temperature maps.

Note: For coding reasons, the first result in the list is always 'none'. If none is selected, nothing appends in plotting areas and the 'Display' menu is inactive.

5.2.3.2. Options

In this group, three buttons are available, Rename, Delete and Export. Note that the Delete function is available only when two or more results have been computed.

The button 'Rename' allows editing the name of the selected result.

The button 'Delete' allows deleting the selected result.

The button 'Export' allows exporting the maps of the different results. As an example, the structural formulae of Garnet (Fig. 25) is selected. The results are XAlm (almandine), XSpe (Spessartine), XPyr (Pyrope), XGro (Grossular) and Si, Al, Mg, Fe, Mn, Ca in atoms per formula unit (a.p.f.u.)

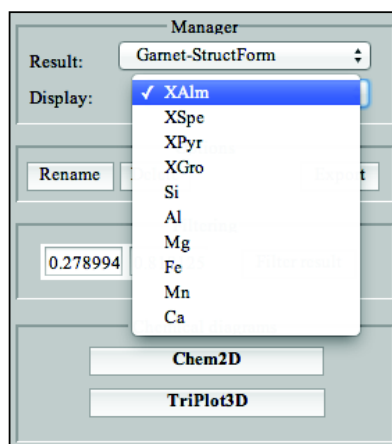


Figure 25: Structural formulae of garnet. Results to be exported.

In this example, the 4 maps of end-member proportions will be exported. In a new window, the user must select the results that will be exported (Fig. 26).

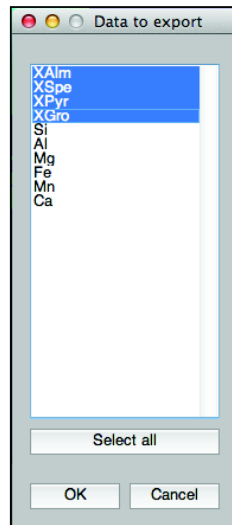


Figure 26: Results selection to be exported.

The user must define a filename (Fig. 27).

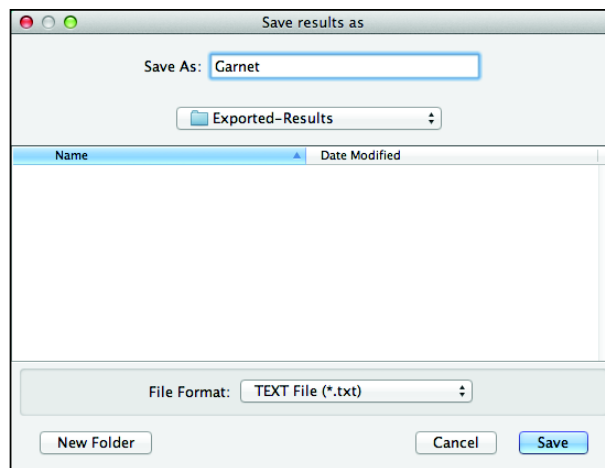


Figure 27: Select the filename for the exported results.

In this example, 4 files have been exported (Fig. 28).

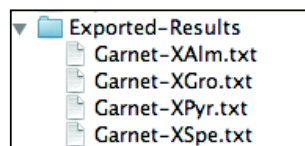


Figure 28: Exported files in the folder Exported-Results.

Each exported file is a matrix of data without header lines. This matrix can be easily loaded and displayed in Matlab using the commands:

```
>> XAlm = Load ('Exported-Results/Garnet-XAlm.txt');
>> imagesc(XAlm), axis image, colorbar;
```

Array arithmetic in Matlab:

A+B -> addition

A-B -> subtraction

A.*B -> multiplication

A./B -> division

Details in <http://www.mathworks.fr/help/techdoc/ref/arithmeticoperators.html>

5.2.3.3. *Filtering*

The button '**Filtering**' allows creating a new Result (filter results) from the selected Result, but only with the composition values between the minimum and maximum values in the filtering window (Fig. 29).

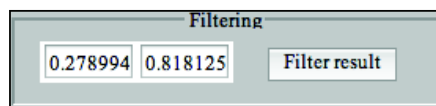


Figure 29: Filtering window.

This function works exactly as the filter function in the Quanti part (see §5.2.2.3). Select the range of composition and click "Filter result" to create the new result.

This function is very useful for create different groups of composition for a zoned mineral. Example: Lanari et al., submitted (Geology).

5.2.3.4. *Chemical Modules*

A result can be treated in binary diagrams (if the number of elements is > 2) or in triangular diagrams (if the number of elements is > 3). A complete description of both modules (Chem2D and TriPlot3D) is available in §5.5 and §5.6.

5.3. *Project window*

The '**Project window**' allows managing the current project (Fig. 30). The project can be saved in the same directory as the maps (working directory) using the buttons '**Save**' or '**Save as**'.

When a project is saved (or loaded), the name is displayed into the Project window (aaa.mat in Fig. 30).

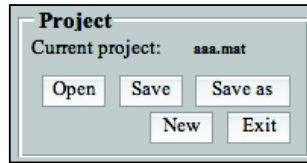


Figure 30: Project window with buttons available for project managing.

The buttons **'New'** and **'Exit'** drive the GUI software. When you try to close XMapTools, an option **'Save'** is always proposed.

Note that the button **'New'** allows re-loading of all XMapTools options (list of methods for example) and updates the last user's changes.

5.4. Figure commands

The **'Figure' window** shows all the buttons available for the main figure managing (fig. 31).

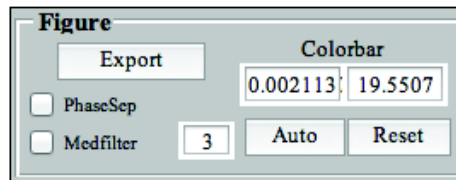


Figure 31: Figure window with buttons available for figure (image) managing.

The button **'Export'** allows exporting all the figures plotted in the main interface. This button opens exactly the same figure (including images and user's selections, points, lines...) in a new Matlab figure window. In the menu, select 'file > save as' and select the image format: ai, eps, png, jpeg.

The button **'Medfilter'** allows applying a median filter on the plotted data. The user can select the size of the filter in pixels (see example in Fig. 33).

'PhaseSep' is a phase separator option that adds a black colour in the first color bar value (minimum value). All the pixels lower than this value are painted in black.

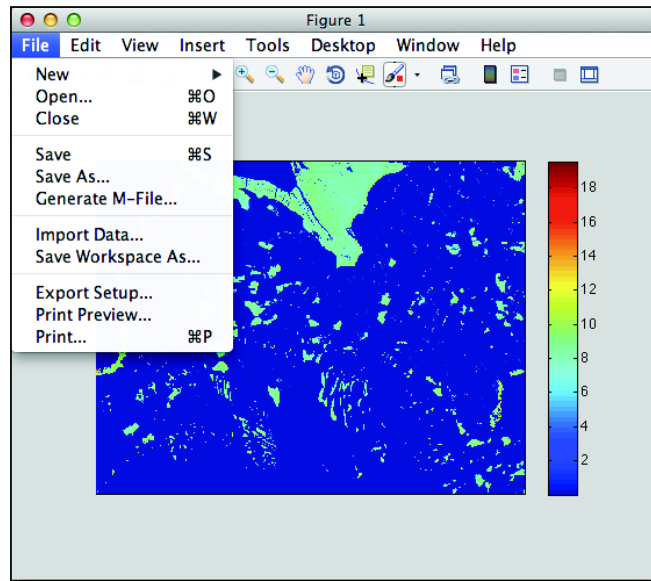


Figure 32: Image opened in a new figure using the button 'Export'. This image can be export edited and exported using the Matlab menu.

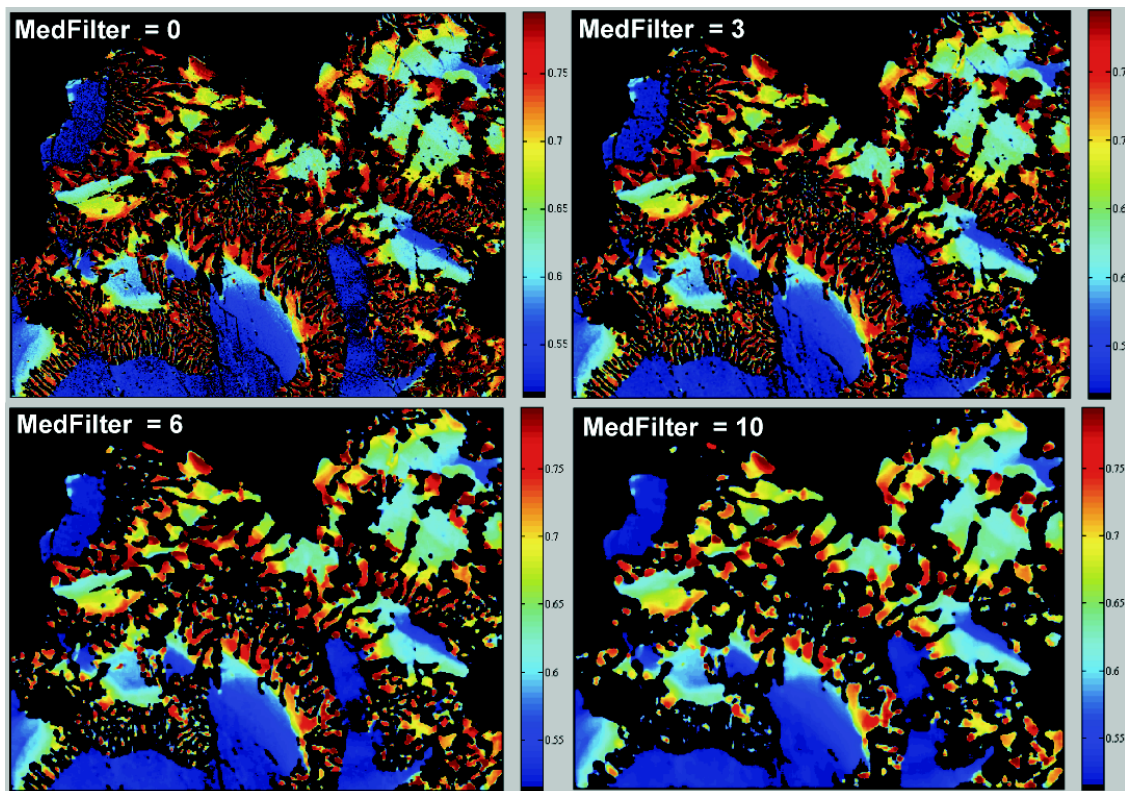


Figure 33: MedFilter of 0, 3, 6 and 10 on the Ca map (pfu) of clinopyroxenes.

5.5. Chem2D

Chem2D is an external graphic user interface (Fig. 34) called by XMapTools in the Results tab. This module will be illustrated using the calculated structural formulae for clinopyroxenes with the binary plot Xjd (jadeite) vs Xhed (hedenbergite).

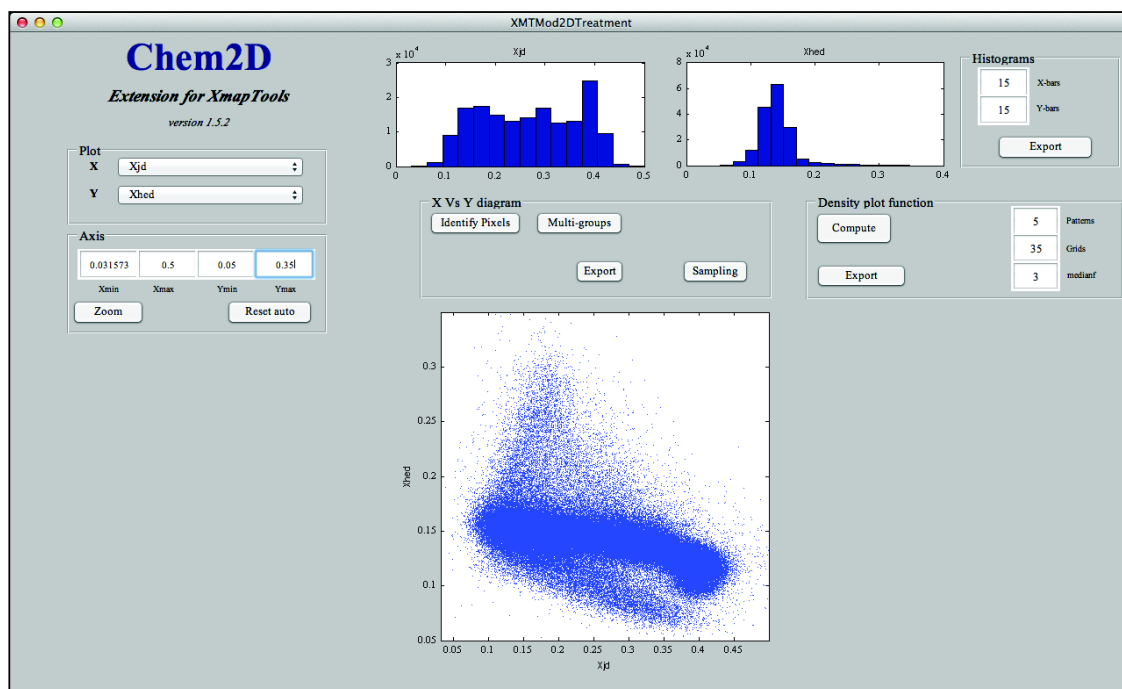


Figure 34: Chem2D module. Binary diagram Xjd VS Xhed (see text).

The 'Plot' window allows selecting the X and Y variables to plot the binary diagram X vs Y.

The 'Axis' window allows defining the X and Y ranges (Xmin, Xmax, Ymin, Ymax). The zoom function can be used to define these values in the figure (by clicking two points that define a rectangle). The button '**Reset auto**' resets the range to the minimum and maximum values (initial plot).

The 'Density plot function' is available to plot a point density diagram (Fig. 35). The user must set the number of density curves (patterns), the grid size and the median filter to be used and click the button '**Compute**'.

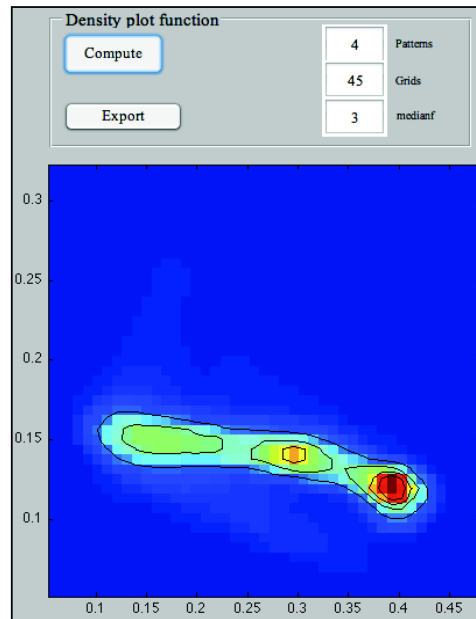


Figure 35: Density plot Xjd VS Xhed.

Two selection functions are available, the '**Identify pixels**' and '**Multi-groups**' function (Fig. 34). In both cases, the user can select a group of pixel compositions in the binary plot and display the corresponding pixels in a map. Statistics are displayed in a small window (right).

Warning: only rectangles can be defined by clicking two points.

For example, Jd-rich pixels were selected using the 'Identify pixels' function in the figure 36 and 4 groups using the 'Multi-groups' function in Figure 37.

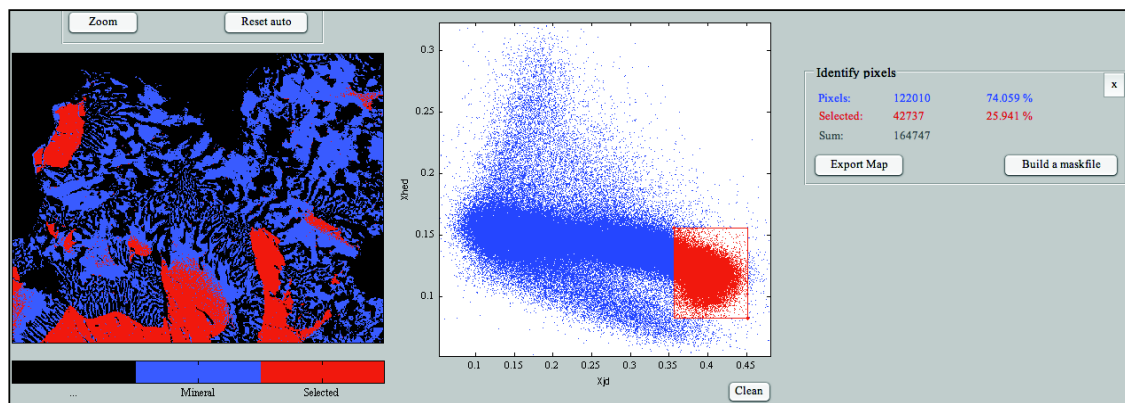


Figure 36: 'Identify pixels' function. The red compositions were selected into the binary diagram (right) and the corresponding pixels plotted into a map (left).

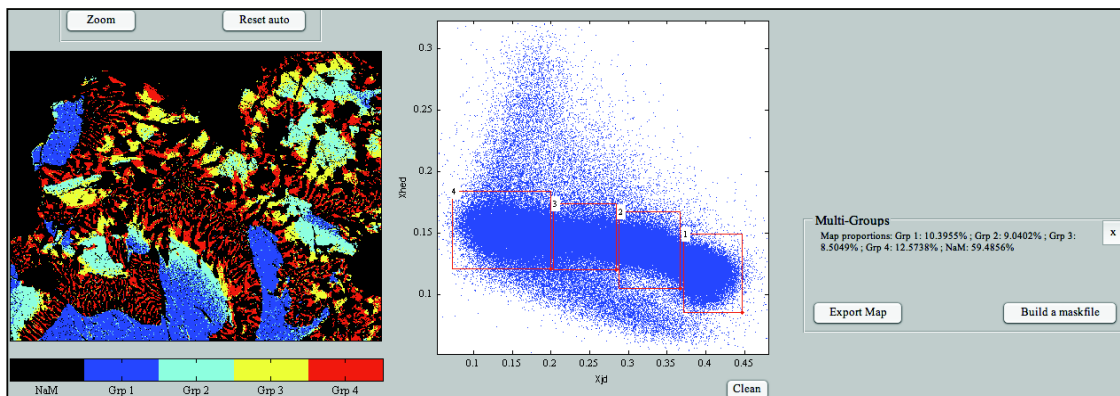


Figure 37: 'Multi-groups' function. The numbers in the binary diagram (left) correspond to the group numbers into the map(right).

A maskfile can be built from a selection using the button '**Build a maskfile**'. This maskfile will be stored into the folder MaskFile/ and can be used to export the average composition of each group of pixels (button 'Export' in the Quanti part).

5.6. Triplot3D

The Triplot3D module (Fig. 38) works as the Chem2d module with similar functions. Three variables can be selected (D1: bottom left, D2: top center, and D3: bottom right) and data are plotted into a ternary diagram (i.e. triangular diagram).

This module will be illustrated using the calculated structural formulae for clinopyroxenes with the ternary plot Xjd (jadeite); Xdi (diopside); Xhed (hedenbergite).

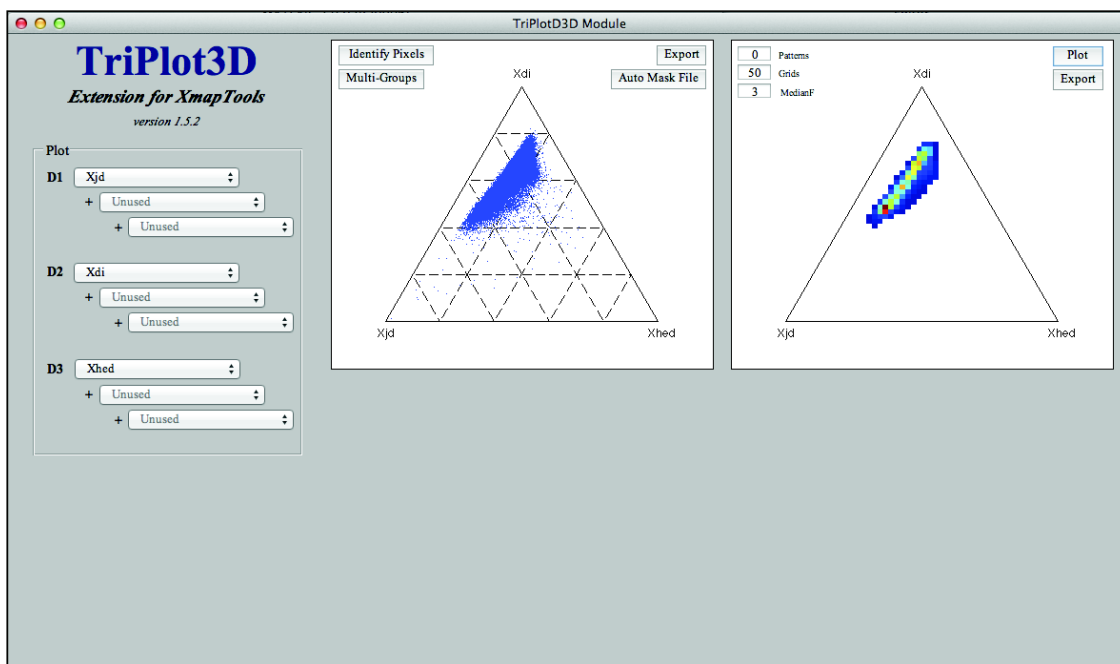


Figure 38: TriPlot3D module. Ternary plot Xjd, Xdi, Xhed (left) and point density plot (right).

Two selection functions are also available, the '**Identify Pixels**' (see example in Fig. 39) and '**Multi-groups**' functions (see example in Fig. 40).

Warning: Only rectangles can be defined by clicking two points.

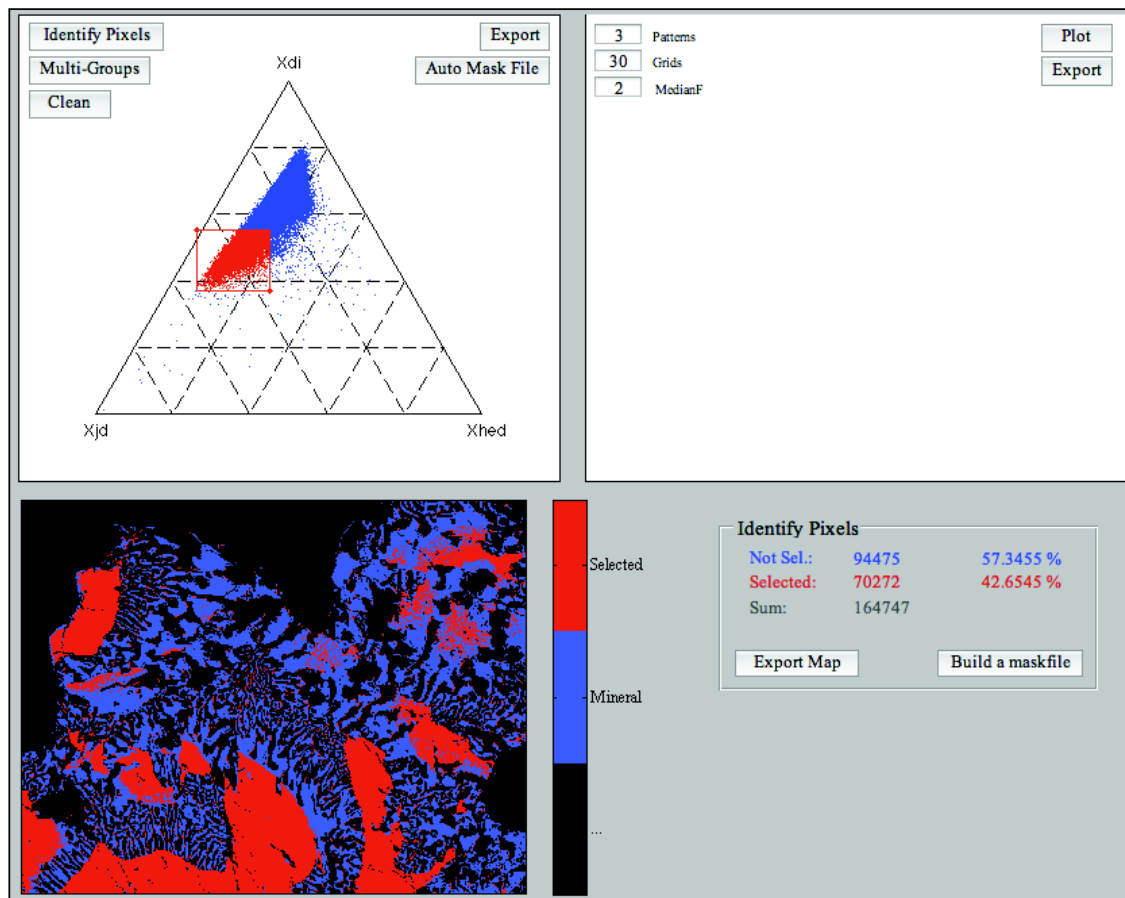


Figure 39: 'Identify Pixels' function.

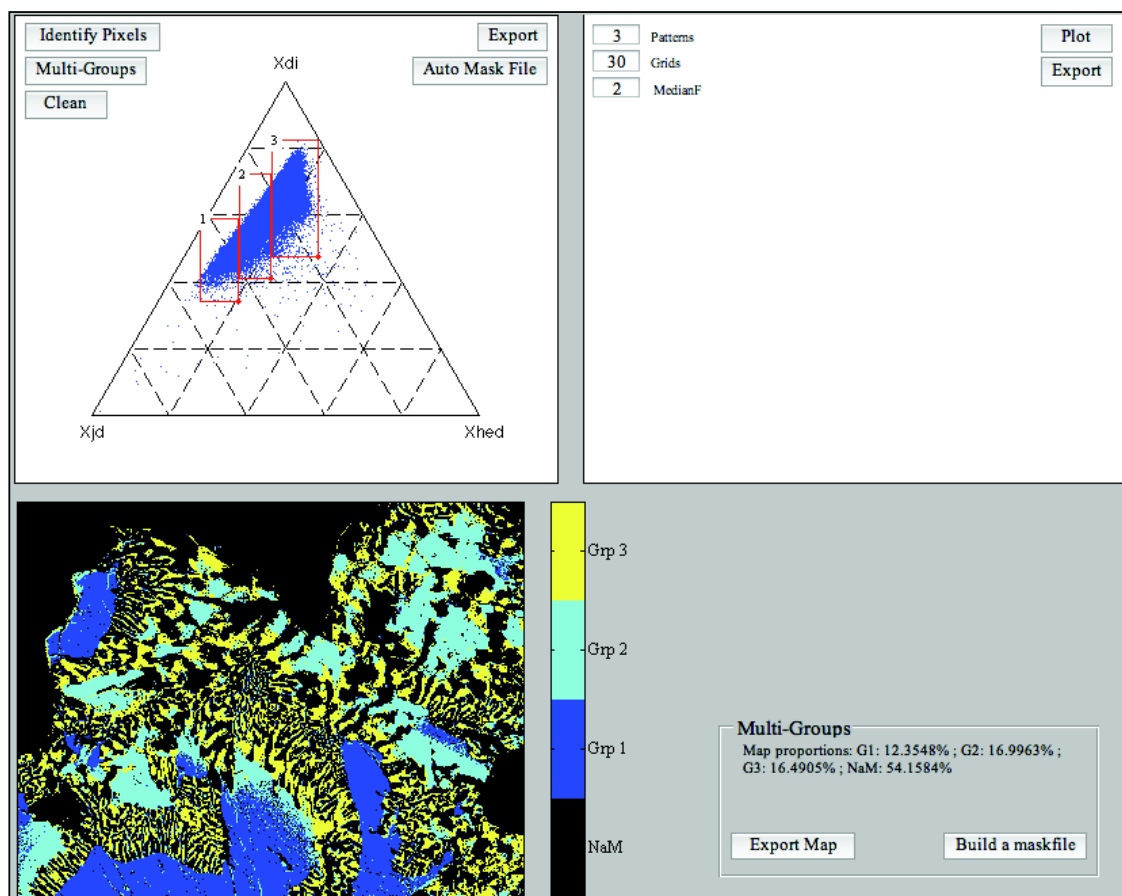


Figure 40: 'Multi-groups' function.

A maskfile can be built from a selection using the button '**Build a maskfile**'. This maskfile will be stored into the folder MaskFile/ and can be used to export the average composition of each group of pixels (button 'Export' in the Quanti part).

The function '**Auto Mask File**' is available only in TriPlot3D module. This function allows building a maskfile from the D1, D2, D3 data using a clustering approach. The user must select input compositions used in the k-mean function.

Note: If two initial pixels have very close compositions, the k-means function must bug and an error occurs. Try to select another set of pixels.

6. Supplementary

6.1. Export mask-image with changing colors

It is possible to use the plot tools of Matlab to change the colors of the mask-image. Export a mask-image (Fig. 41) using the button **'Export'** in the mask-file group of buttons (Xray tab).

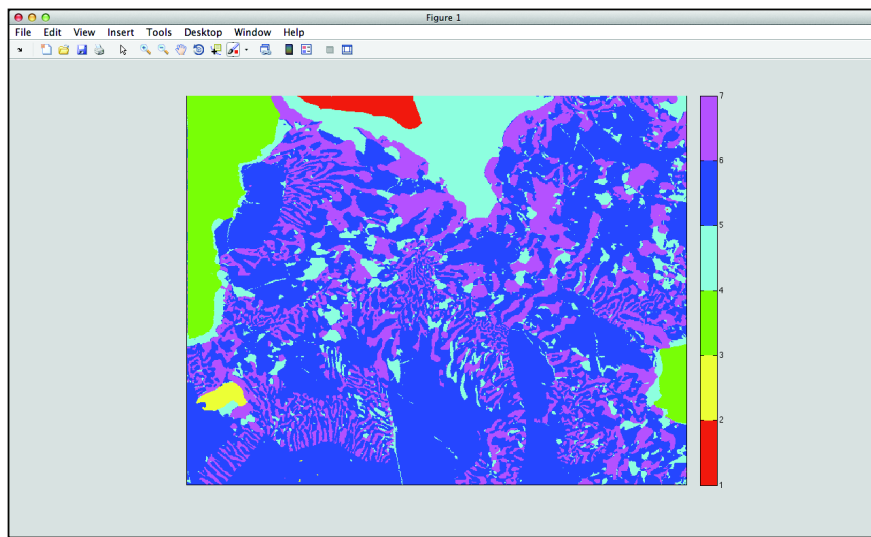


Figure 41: Mask-image exported using the function 'Export' (see text).

A list of icons is available below the menu. Activate the last one ('Show plot tools and Dock figure'). Matlab opens different tools for the figure editing (Fig. 42).

Use pop-up menu color map and select **'Custom'**. A new window 'Colormap editor' opens (fig. 43) and you can select the colors for each mineral by clicking on the color arrows (Fig. 44).

When the new colors are defined, it is possible to export the figure using the menu (see §5.4).

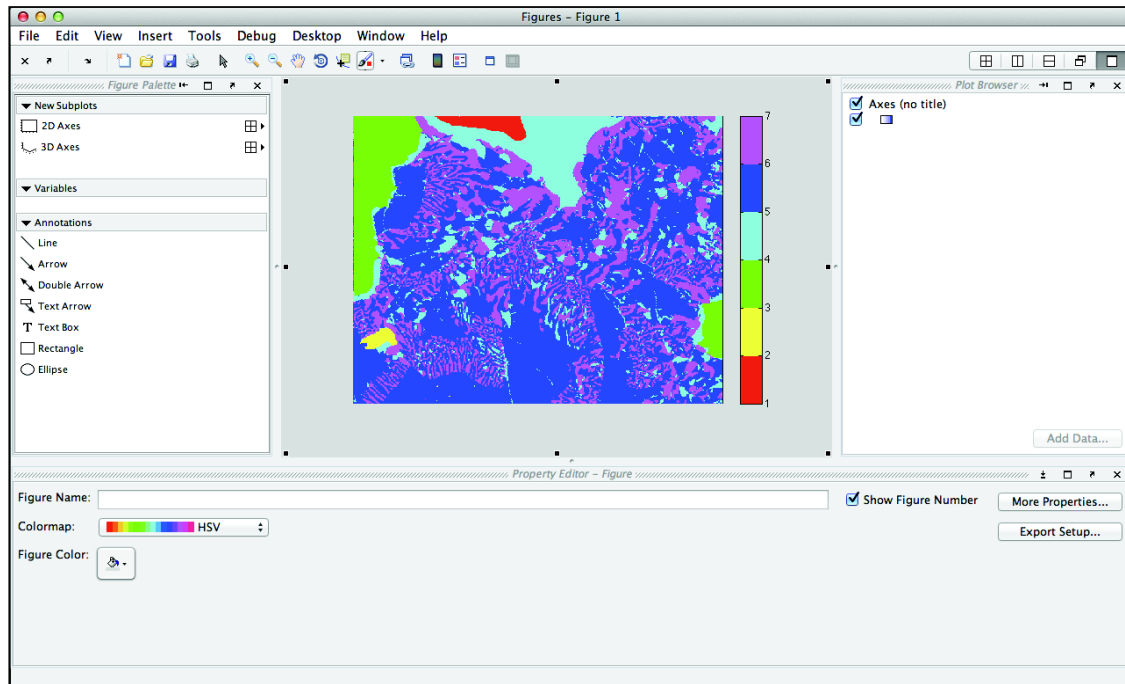


Figure 42: Mask-image with the Figure editor.

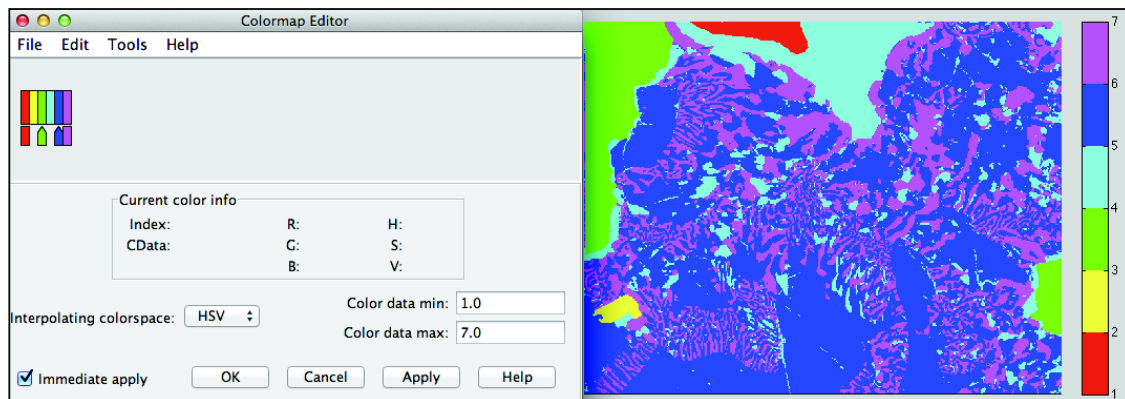


Figure 43: Colormap Editor with original colors

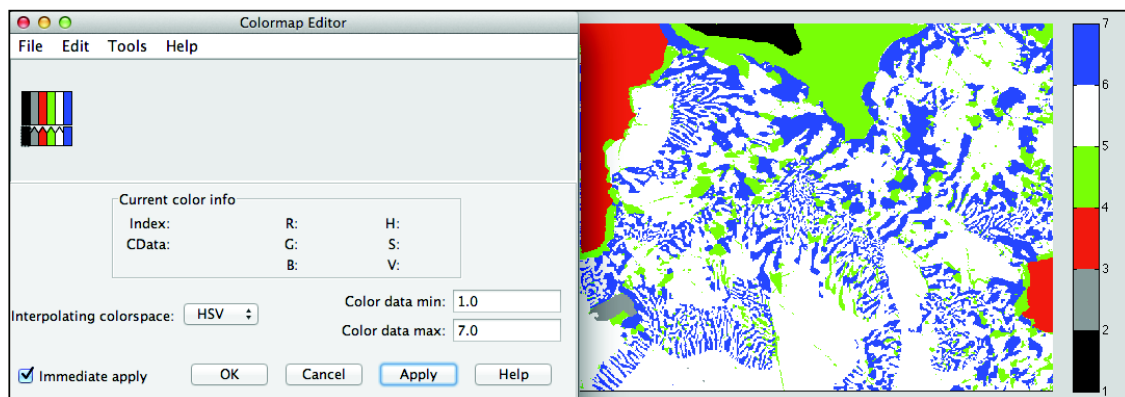


Figure 44: Colormap Editor with the new colors

6.2. *How can I check the results of a function?*

Close XMapTools, and open the setup directory of XMapTools and the file 'ListThermometers.txt'.

This file lists all the functions available and provides XMapTools with the input and output parameters for each function. Here for example, we can test the chlorite-chloritoid thermometer of Vidal et al., 1999.

Corresponding setup:

```
2>Chlorite+Chloritoid>T- Vidal etal 1999>NThermoCCVidal1999>T ln_Kd>SiO2 TiO2
Al2O3 FeO MnO MgO CaO Na2O K2O>
```

- The type is 2, corresponds to a two names function (selected compositions).
- This thermometer is in the 'Chlorite+Chloritoid' group of functions in the menu 'Minerals'.
- The name displayed in the menu 'Method' is 'T- Vidal etal 1999'.
- The real name of this function is 'NThermoCCVidal1999' (without the extension .m).
- The output parameters are: T and ln_Kd.
- The input parameters are: SiO2 TiO2 Al2O3 FeO MnO MgO CaO Na2O and K2O.

In this case the input data are a matrix in which the first line is the composition of the chlorite and the second line the composition of the chloritoid (same order of the name: Chlorite+Chloritoid).

Here the analyses PSB9210b are used (Table 2 in Vidal et al., 1999):

Chlorite: 25.63 0.03 23.37 22.82 0.22 15.13 0.06 0.02 0.02

Chloritoid: 24.15 0 40.80 22.81 0.16 3.02 0.04 0.01 0.02

Open the folder 'Functions' and use the following code to test the function:

% --- Start of code

```
Compos(1,:) = [25.63 0.03 23.37 22.82 0.22 15.13 0.06 0.02 0.02]; %Chl
```

```
Compos(2,:) = [24.15 0 40.80 22.81 0.16 3.02 0.04 0.01 0.02]; %Ctd
```

```
[T ln_Kd] = NThermoCCVidal1999(Compos)
```

% --- end of code

The temperature is 492°C and the ln_Kd is 1.61 in good agreement with the results of Vidal et al., (1999).

Note: The same test can be conducted with the 'One Name' function. In this case, you must use only one composition.

6.3. *What is the reference number?*

Consider the following map where each number is a pixel location. The image size is [10,10], 10 rows and 10 columns. These numbers are the reference numbers.

1	11	21	31	41	51	61	71	81	91
2	12	22	32	42	52	62	72	82	92
3	13	23	33	43	53	63	73	83	93
4	14	24	34	44	54	64	74	84	94
5	15	25	35	45	55	65	75	85	95
6	16	26	36	46	56	66	76	86	96
7	17	27	37	47	57	67	77	87	97
8	18	28	38	48	58	68	78	88	98
9	19	29	39	49	59	69	79	89	99
10	20	30	40	50	60	70	80	90	100

Now, we have analyses (SiO₂) for the numbers 45, 46, 55 and 56 and we would like to plot results only for these analyses.

```
> TheMap = NaN.*zeros(10,10); % NaN image created
> ListCoor = [45,46,55,56];
> SiO2 = [45,44,46,42];
> TheMap(ListCoor) = SiO2(:);
```

NaN	NaN	NaN	NaN	NaN	NaN	NaN	NaN	NaN	NaN
NaN	NaN	NaN	NaN	NaN	NaN	NaN	NaN	NaN	NaN
NaN	NaN	NaN	NaN	NaN	NaN	NaN	NaN	NaN	NaN
NaN	NaN	NaN	NaN	NaN	NaN	NaN	NaN	NaN	NaN
NaN	NaN	NaN	NaN	45	46	NaN	NaN	NaN	NaN
NaN	NaN	NaN	NaN	44	42	NaN	NaN	NaN	NaN
NaN	NaN	NaN	NaN	NaN	NaN	NaN	NaN	NaN	NaN
NaN	NaN	NaN	NaN	NaN	NaN	NaN	NaN	NaN	NaN
NaN	NaN	NaN	NaN	NaN	NaN	NaN	NaN	NaN	NaN
NaN	NaN	NaN	NaN	NaN	NaN	NaN	NaN	NaN	NaN

For display:

```
> imagesc(TheMap), axis image, colorbar horizontal
> caxis([Min Max]);
> colormap([0,0,0;jet(64)]) % option: phase separator
```

Where Min and Max are the minimum and maximum limits for the colorbar.

For example: `caxis([40,50])` % see fig 22.

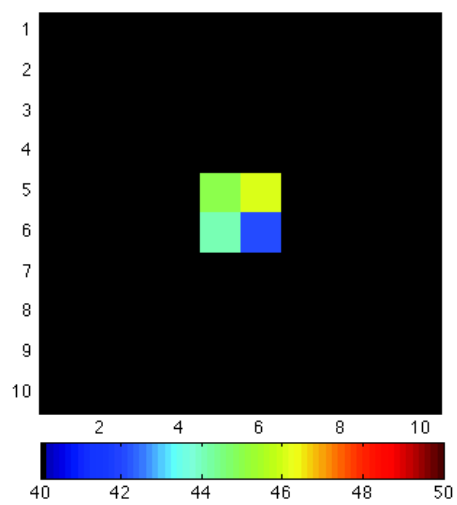


Figure 45: Image plotted in the example “what is the reference number”.

6.4. *How to convert this reference number into the pixel coordinates?*

Considering a smaller map with reference number provided below.

1	7	13	19	25
2	8	14	20	26
3	9	15	21	27
4	10	16	22	28
5	11	17	23	29
6	12	18	24	30

It is possible to find coordinates from the reference number. Two methods (small Matlab scripts) are provided in this notice. In order to run these scripts, you need the size of your map provided in the 'Info' button in the tab 'Xray'. NbLin is the number of rows (first value in 'Info') and NbCol is the number of columns.

```
% - - - Start of code
NbLin = 6;
NbCol = 5;
% for example to find the coordinates of Ref 20
Position = 20;
for i = 1:NbCol
    for j = 1:NbLin
        OuOnEst = (i-1)*NbLin + j;
        if OuOnEst == Position
            lesCoord = [j,i];
            break % we stopped because we found the solution
        end
    end
end
disp(lesCoord) % display coordinates
% - - - end of code
```

In this case, the result is [2,4]. The reference number is in the row 2 and the column 4.

An other method is available. The user can build a new vector 'position' with a size of NbLin*NbCol. This vector can be transformed into a matrix using the Matlab function 'reshape'. It is possible to find the exact position (row/column) of the reference number.

```
% - - - Start of code
NbLin = 6;
NbCol = 5;
% for example to find the coordinates of Ref 20
Position = 20;
lesPositions = 1:1:(NbLin*NbCol); % New vector
lesPositions = reshape(lesPositions,NbLin,NbCol); % this vector is transformed into matrix with the
same size of our original map.
[lesCoord(1),lesCoord(2)] = find(lesPositions == Position) ; % Coordinates
disp(lesCoord) % display coordinates
% - - - end of code
```

A.5 ARTICLES SUPPLÉMENTAIRES

Cette annexe contient les articles auxquels j'ai collaboré et qui n'ont pas été directement introduits dans le manuscrit principal.

- ▷ Article 8 : Guillot, F., Bertrand, J. M., Bussy, F., Lanari, P., Cosma, L. and Pin, C. (in press) Early Variscan I-type pluton in the pre-Alpine basement of the Western Alps : The ca. 360 Ma Cogné diorite (NW - Italy). *Lithos*.
- ▷ Article 9 : Pourteau, A., Sudo, M., Candan, O., Lanari, P., Vidal, O. and Oberhänsli, R. (in revision). Neotethys closure history of Anatolia : insight from $^{40}\text{Ar}/^{39}\text{Ar}$ geochronology and P-T estimation in high-pressure metasediments. *Journal of Metamorphic Geology*.
- ▷ Article 10 : Riel, N., Guillot, S., Jaillard, E., Martelat, J. E., Paquette, J. L., Schwartz, S., Goncalves, P., Duclaux, G., Thebaud, N., Lanari, P., Janots, E. and Yuquilema, J. (in press). Implications for high-temperature metamorphism in a forearc zone : a metamorphic and geochronological study of the Triassic El Oro metamorphic complex in Ecuador. *Lithos*

Cette dernière annexe est disponible uniquement dans la version numérique du manuscrit téléchargeable à l'adresse suivante : <http://www.pierre-lanari.com/TheseLanari2012.pdf>.

A.5.1 Article 8 : Guillot et al., (in press), Lithos



Contents lists available at SciVerse ScienceDirect

Lithos

journal homepage: www.elsevier.com/locate/lithos

Early Variscan I-type pluton in the pre-Alpine basement of the Western Alps: The ca. 360 Ma Cogne diorite (NW-Italy)

François Guillot ^{a,*}, Jean-Michel Bertrand ^{b,1}, François Bussy ^c, Pierre Lanari ^d, Ludovic Cosma ^{c,2}, Christian Pin ^e

^a Université Lille Nord de France, CNRS – FRE 3298 Géosystèmes, UFR Sciences de la Terre, F-59655 villeneuve d'Ascq CEDEX, France

^b 15 chemin d'Avat, F-38240 Meylan, France

^c Institut de Minéralogie et de Géochimie, Université de Lausanne, Anthropole, CH-1015 Lausanne, Switzerland

^d ISTerre, Université de Grenoble I, UMR CNRS/UJF 5275, 1381 rue de la Piscine, F-38041 Grenoble, France

^e Département de Géologie, CNRS Université Blaise Pascal, 5 rue Kessler, F-63038 Clermont-Ferrand CEDEX, France

ARTICLE INFO

Article history:

Received 31 October 2011

Accepted 5 April 2012

Available online xxxx

Keywords:

Early Variscan

Hornblende

Sm–Nd isotopic ratios

Magmatic thermobarometry

Magmatic sources

Alpine nappe model

ABSTRACT

Located at the internal border of the Grand-Saint-Bernard Zone, the diorite and its aureole lie on top of intensively studied Alpine eclogitic units but this pluton, poorly studied yet, has kept locally almost undeformed. The pluton intruded, at ~360 Ma, country-rocks mostly composed of dark shales with Na₂O > K₂O and minor mafic intercalations of tholeiitic basalt affinity. This association is characteristic of the Vanoise (France) basement series, where available age determinations suggest an Early Paleozoic age. Parts of the pluton, and of its hornfels aureole that is evidenced here for the first time, in the Punta Bioula section of Valsavaranche valley (NW-Italy), have been well-preserved from the Alpine deformation. Syn-emplacement hardening, dehydration-induced, probably prevented strain-enhanced Alpine recrystallization. Magmatic rock-types range continuously from subordinate mafic types at SiO₂ ~ 48%, of hornblende with cumulative or appinite affinities, to the main body of quartz diorite to quartz monzonite (SiO₂ up to 62%). P–T estimates for the pluton emplacement, based on the abundance of garnet in the hornfels, using also zircon and apatite saturation thermometry and Al-in-hornblende barometry, suggest T ~ 800–950 °C and minimum P in the 0.2–0.5 GPa range, with records of higher pressure conditions (up to 1–2 GPa?) in hornblende phlogopite-cored amphibole. The high-K, Na > K, calc-alkaline geochemistry is in line with a destructive plate-margin setting. Based on major element data and radiogenic isotope signature ($\epsilon_{\text{Nd}_{360 \text{ Ma}}}$ from -1.2 to $+0.9$, $^{87}\text{Sr}/^{86}\text{Sr}_{360 \text{ Ma}}$ from 0.7054 to 0.7063), the parental magmas are interpreted in terms of deep-seated metabasaltic partial melts with limited contamination from shallower sources, the low radiogenic Nd-content excluding a major contribution from Vanoise tholeiites. There is no other preserved evidence for Variscan magmatism of similar age and composition in the Western Alps, but probable analogs are known in the western and northern parts of French Massif Central. Regarding the Alpine tectonics, not only the age of the pluton and its host-rocks (instead of the Permo-Carboniferous age previously believed), but also its upper mylonitic contact, suggest revisions of the Alpine nappe model. The Cogne diorite allegedly constituted the axial part of the E-verging “pli en retour [backfold] du Valsavaranche”, a cornerstone of popular Alpine structural models: in fact, the alleged fold limbs, as attested here by field and geochemical data, do not belong to the same unit, and the backfold hypothesis is unfounded.

© 2012 Elsevier B.V. All rights reserved.

1. Introduction

Assessing the tectonic setting and P–T conditions of emplacement of granitoid bodies relies on a wide choice of methods. For fresh rocks, the study of mineral assemblages, mineral zoning and mineral chemistry may be privileged upon the consideration of “blind” whole-rock geochemical indicators. In case of secondarily metamorphosed plutons,

this approach is not applicable any more, and it is necessary to use more indirect methods, based on immobile element contents at the whole rock scale, and refractory minerals. Here we attempt to characterize the Cogne diorite, a plutonic body that belongs to the polycyclic, pre-Triassic basement of the Western Alps, with special effort to separate the pre-Alpine heritage from the Alpine overprinting.

The Cogne diorite pluton crops out in the basement of the Middle Penninic Zone. Its igneous emplacement occurred near the Devonian–Carboniferous boundary, as documented by U–Pb zircon dating (Bertrand et al., 2000b) at ~360 Ma, so that this pluton is a rare, if not the only, piece of evidence of the early stage of the Variscan events in the Western Alps. Here we present new geochemical and petrological

* Corresponding author. Tel.: +33 320436731; fax: +33 320434910.

E-mail address: francois.guillot@univ-lille1.fr (F. Guillot).

¹ Deceased, March 18th, 2011.

² Present address: 8bis route d'Avignon, F-13410 Lambesc, France.

data for the Cogne diorite as an opportunity to assess the Early Carboniferous, or older, tectonic setting of yet poorly known pre-Alpine domains. In a context of Alpine high pressure and subduction-related nappes, tracing the origin of the units requires to take into account their protolith ages. A number of protolith age determinations have been obtained during the last decades on such pre-Alpine basement units, often with unexpected results, leading to various paleogeographic inferences (Bertrand et al., 2005; Michard and Goffé, 2005; Ring et al., 2005). It seems timely to unravel the pre-Alpine geological history of some of those recently dated units.

2. Geological context

Many unresolved questions arise from the location of the Cogne pluton in the internal zone of the Alpine orogen (Figs. 1–3, Table 1), inserted in a complex nappe stack. Regarding the Alpine events, P–T estimates of 1.5–3 GPa, 575 °C at 45–30 Ma have been published for the Gran Paradiso basement massif (Gabudianu Radulescu et al., 2009) and its Alpine cover (Angiboust et al., 2009; Beltrando et al., 2009). The determination of these eclogitic conditions is critical, because these units, corresponding to the most deeply subducted

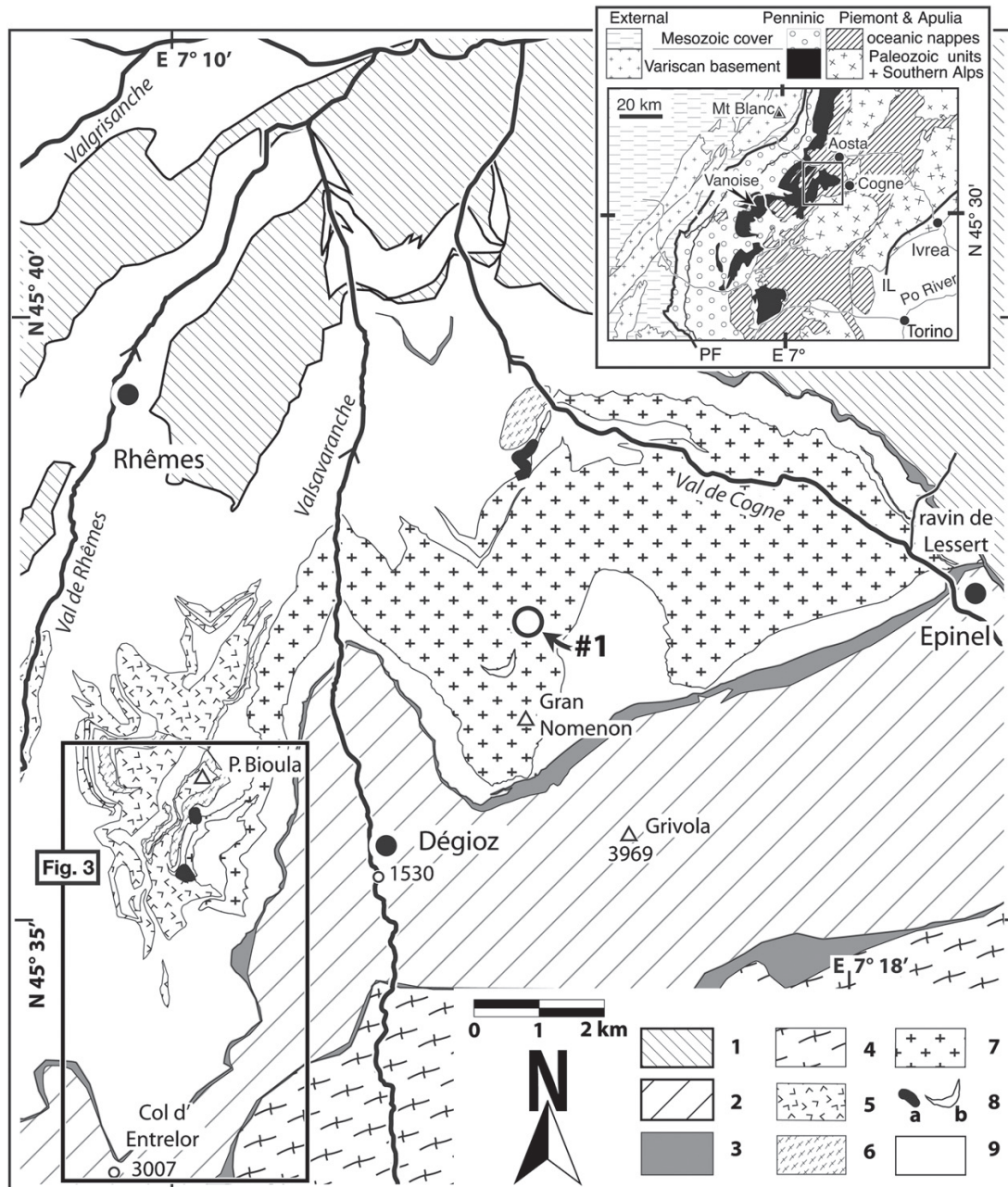


Fig. 1. Geological map of the Cogne diorite. Key to symbols and abbreviations. *Inset* — PF, Penninic Front — IL, Insubric Line. *Main frame* — #1, location of sample 1 — *Key to formations*. — 1, Combin calcschists with minor ophiolite — 2, eclogitic Zermatt-Saas Fee calcschists and major eclogitized metaophiolite — 3, evaporite-rich and often brecciated, carbonated rocks of presumed Triassic age — 4, eclogitized Gran Paradiso Permian orthogneiss — 5, Punta Bioula summit gneiss minuti — 6, Punta Bioula summit augengneiss — 7, Cogne diorite — 8a, appinite pods — 8b, leucogranite — 9, carbonaceous host rocks — P. Bioula, Punta Bioula.

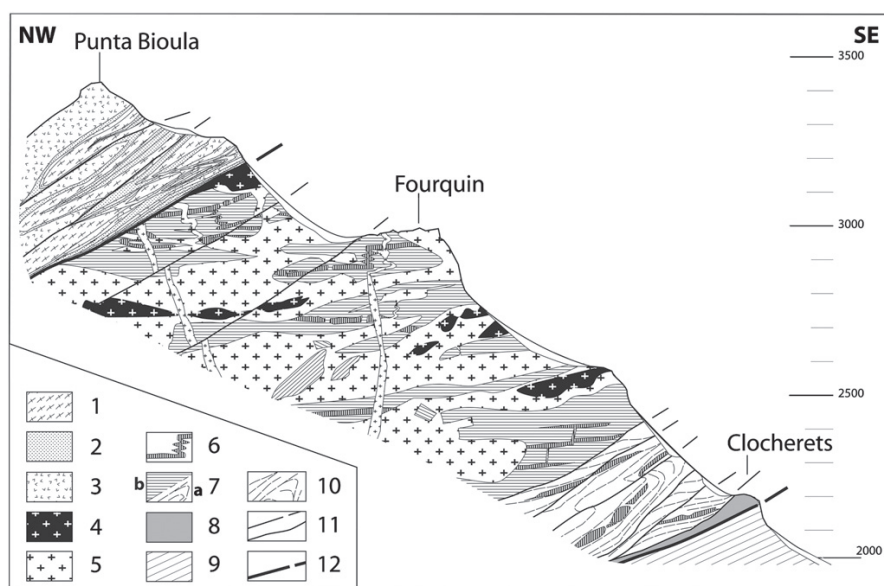


Fig. 2. Interpretative sketch of the Punta Bioula section. 1–3, TPBU formations (resp. augengneiss, quartz-mylonite, gneiss minuti) – 4–10, Cogne diorite unit formations; 4, horn-blendite – 5, diorite – 6, host rock mafic sills and dykes – 7a, host rock metapelites, 7b, hornfelses and migmatites – 8, carbonated breccia, presumably from a Triassic dolomite protolith – 9, calcschists with eclogitized ophiolite (Jurassic) – 10–12, Alpine foliation and faults (Tertiary).

Alpine units, lie right under the diorite-hosting basement unit. Based on the presence of garnet- and glaucophane-white mica assemblages in some diorite samples and of jadeite pseudomorphs in augengneiss (Cigolini, 1995) of the Top Punta Bioula Unit (TPBU, as defined in Section 2.2.2), Bucher and Bousquet (2007) have concluded that the Cogne pluton suffered a high-P event. Discussing either the Alpine vs. pre-Alpine age of mineral assemblages, or the peak Alpine conditions, is out of the scope of this paper. A provisional pseudosection, based on analysis #9 and garnet–actinolite–phengite–clinozoisite–quartz mineral chemistry of the same rock, yields 1.7 ± 0.2 GPa with 540 ± 50 °C (work in progress). This strongly recrystallized mafic diorite was sampled a couple of meters under the top of the diorite-hosting unit. There, our field data (Section 2.2.2) provide evidence for a first order tectonic contact separating the diorite-hosting unit, almost free of Alpine deformation, from the heavily deformed overlying TPBU, and we further document (Section 3) geochemical differences between those units.

2.1. Milestone works on the Cogne diorite

Novarese (1894, 1909) defined the pluton as a quartz diorite, inferring its intrusive nature from apophyses and nodular schists. Based on their graphite content and black color, the host rocks were interpreted as Carboniferous meta-sediments and a Permo-Carboniferous age was proposed for the intrusion (Novarese, 1909: p. 511). Followed by many other authors, Argand (1910, 1911) admitted those ages, a stratigraphic tenet which partly founded his seminal tectonic interpretation of the Alps as a nappe pile. The Cogne diorite was supposed to be at the heart of a key Alpine anticline of nappes, the “Valsavaranche backfold”. The Cogne region was also the place where Amstutz, while again defending a Permo-Carboniferous age, coined the notion of subduction (in 1949, after White et al., 1970) in order to explain the outward dip of the nappe stack, to the NW, as an alternative to Argand’s backthrust model. A petrographical study of the Cogne diorite and of its aureole was performed by Grasso (1974), by means of optical microscopy only. He described relict pre-Alpine feldspars, largely replaced by burgeoning albite. He also proposed criteria for separating ancient minerals (biotite, garnet, amphibole) from Alpine re-crystallized ones,

reporting a biotite ghost inside an amphibole phenocryst, and one inferred andalusite crystal replaced by sericite.

2.2. Field data

2.2.1. Main units

The pluton and its aureole, the latter being tentatively contoured for the first time in the present paper, have not yet been subjected to a systematic mapping of their various rock types, except by Amstutz (1962) to the E of the Valsavaranche valley. Here we focus on the W side of the Valsavaranche where most of our rocks were sampled, in the Punta Bioula massif (Fig. 1). As a summary of our field work, a tentative section has been drawn along the trail that leads from Valsavaranche up to the top of the Punta Bioula (Fig. 2), together with a provisional, local map of the high crest joining Punta Bioula to Col d’Entrelor (Fig. 3).

At its footwall, the diorite-hosting unit rests upon a thin veneer of Triassic-looking limestone lenses, also named Entrelor Shear Zone. Both tectonically overlie oceanic Piemont units with their calcschist cover (Jurassic to Tertiary in age) imbricated with ophiolite basement slivers (dated elsewhere in the Western Alps around 155–165 Ma). The Entrelor Shear Zone is interpreted as a major low-angle fault, although its reverse (backthrust) or normal (exhumation) kinematics remains controversial. This debate is related to the model of “Valsavaranche backfold”, subject of a well-documented discussion by Bousquet (2008, his Fig. 3, and references therein). From the field data exposed hereafter, another major low-angle fault is probably also present at the hanging wall of the diorite-hosting unit.

2.2.2. TPBU unit

At its top, the diorite-hosting unit is capped directly by a rock unit, that we call TPBU, devoid of diorite. Here, along the Punta Bioula-Col d’Entrelor crest line, Cigolini (1992, 1995) has mapped in detail various formations (reddish quartzite and white quartzite bands, augengneiss, albitic gneiss, prasinitic gneiss) constituting the Punta Bioula above 3100 m (Figs. 1–3). Cigolini further proposed an Upper Permian age for this unit, interpreted to represent an unconformable cover for the diorite. Following Cabry (1968) and Hermann (1925), he also mentioned the prominent, km-sized recumbent folds outlined by the TPBU

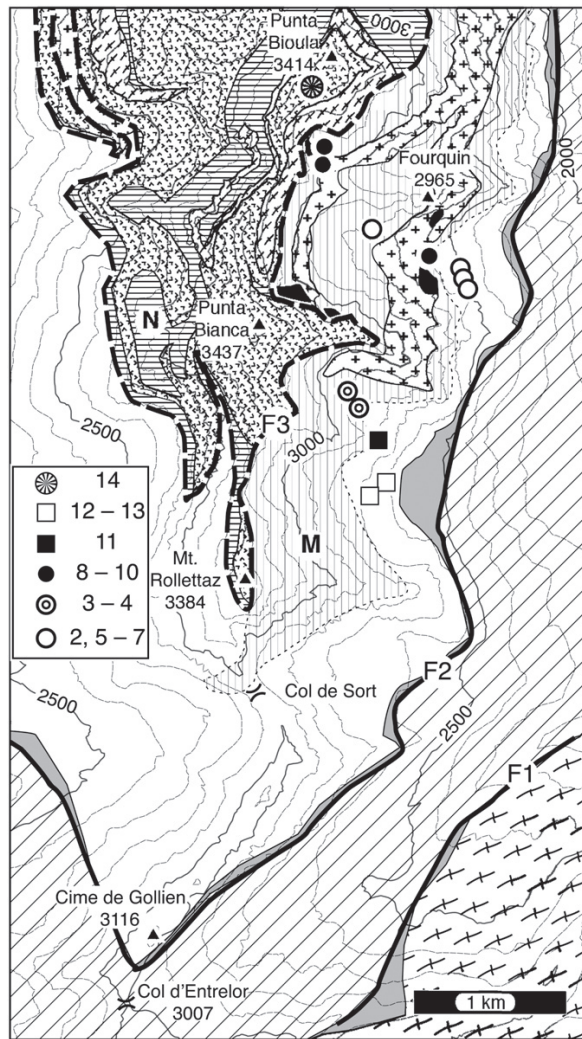


Fig. 3. Geological map of the Punta Bioula area (after Cigolini, 1992, and new field work). Key to formations as in Fig. 1, except: M (vertical cross-hatching), quartz-veined hornfels and migmatized country-rock related to the diorite pluton intrusion; N, undetermined rocks from the TPBU (analog of 7a in Fig. 2, after Cigolini, 1992). Main tectonic contacts: F1, low-angle fault separating oceanic, Jurassic calcshists and ophiolite of the Col d'Entrelor from Gran Paradiso orthogneiss – F2, low-angle fault between oceanic unit and Middle Penninic basement – F3, presumed tectonic contact of the TPBU over the Cogné diorite-hosting unit.

Table 1
Main rock types, classified by their presumed age, in the Punta Bioula section (Fig. 2).
Explanations in text.

Age/rock type	Mafic formations	Felsic formations	Sediments, volcanics
356–360 Ma calc-alkaline pluton	Hornblende (appinite?) anal. 8 to 10	Quartz diorite to granodiorite anal. 1 to 7	Unknown
Unknown age, TPBU	Prasinite	Augengneiss, quartzite	Gneiss minuti, anal. 14
510–480 Ma A-type, bimodal rocks, and associated dark metapelite	Tholeiite levels anal. 11 + anal. in litt.	Granophyre felsic metavolcanites anal. in litt.	Metapelite and metagreywacke series anal. 12–13 + in litt.

reddish quartzite levels. We concur with Cigolini that the TPBU does not contain any diorite body and appears to be in sharp contact with the diorite and its aureole. However a dilemma arises from his age assumptions, not only because no dating has yet been performed of the supposedly Upper Permian formations, but also because the intense deformation rather suggests a tectonic emplacement over the diorite-hosting unit, a hypothesis supported by our field observations near the contact.

The lowermost outcrop at the footwall of the TPBU is an ~10 m thick quartzite layer (Fig. 4) outcropping at 3180 m a.s.l. between Fourquin and Punta Bioula (Fig. 2). The rock is made of sub parallel, mm- to cm-thick quartz-ribbons separated by feldspar- and phengite-rich, scaly-looking bands (Fig. 4a) that resemble the overlying augengneiss. Actually, transitional terms are observable: e.g., following this formation to the NE, the quartzite layer gets thicker (~30 m) around 3220 m a.s.l., with a flat-lying, crude layering affected by isoclinal, mm- to m-scale, W-verging folds (Fig. 4b), comprising folded augengneiss lenses. The intimate association with augengneiss and their isoclinal folding are suggestive of a mylonitic zone, with a top-

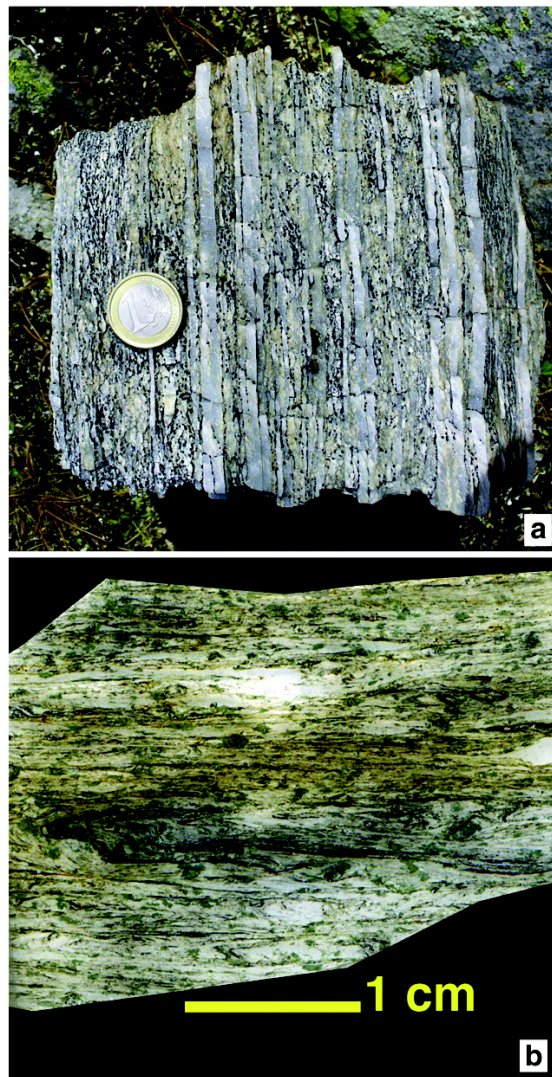


Fig. 4. Mylonites at the footwall of the TPBU. a, Mylonite of alternating bluish quartzite lens and micaschist-augengneiss layers – b, tight folds in mylonitic micaschist (scanned thin section, sample G03101). Location, 3170 m a.s.l., Punta Bioula trail.

to-the-W sense of shear, rather than of a metasedimentary sequence. Taking also into account the tight recumbent folds that affect the TPBU formations, the diorite and its aureole (M in Fig. 3) are interpreted as in tectonic contact with the TPBU, along an Alpine thrust plane (F3 in Fig. 3) gently dipping W to NW (parallel, top-to-the-W, minor shear zones have also been observed across the diorite-hosting unit near the Fourquin, that were suggestively sketched in Fig. 2). This provisional interpretation departs from the traditional view of a two-limbed anticline, with the Cogné diorite in its hinge (the “Valsavaranche backfold”), and

needs to be checked by further works. Hereafter it is shown that the geochemical characters of the diorite and its host-rocks present distinct differences with the TPBU.

2.2.3. Diorite and aureole outcrops

The diorite-hosting unit has a basal part near the Clocherets (Fig. 2, 2200 to 2450 m a.s.l.) of metapelites with dismembered greenstone levels, heavily deformed (Fig. 5a), as it is usual in Vanoise. In those banded, black, gray or greenish metapelites, no obvious

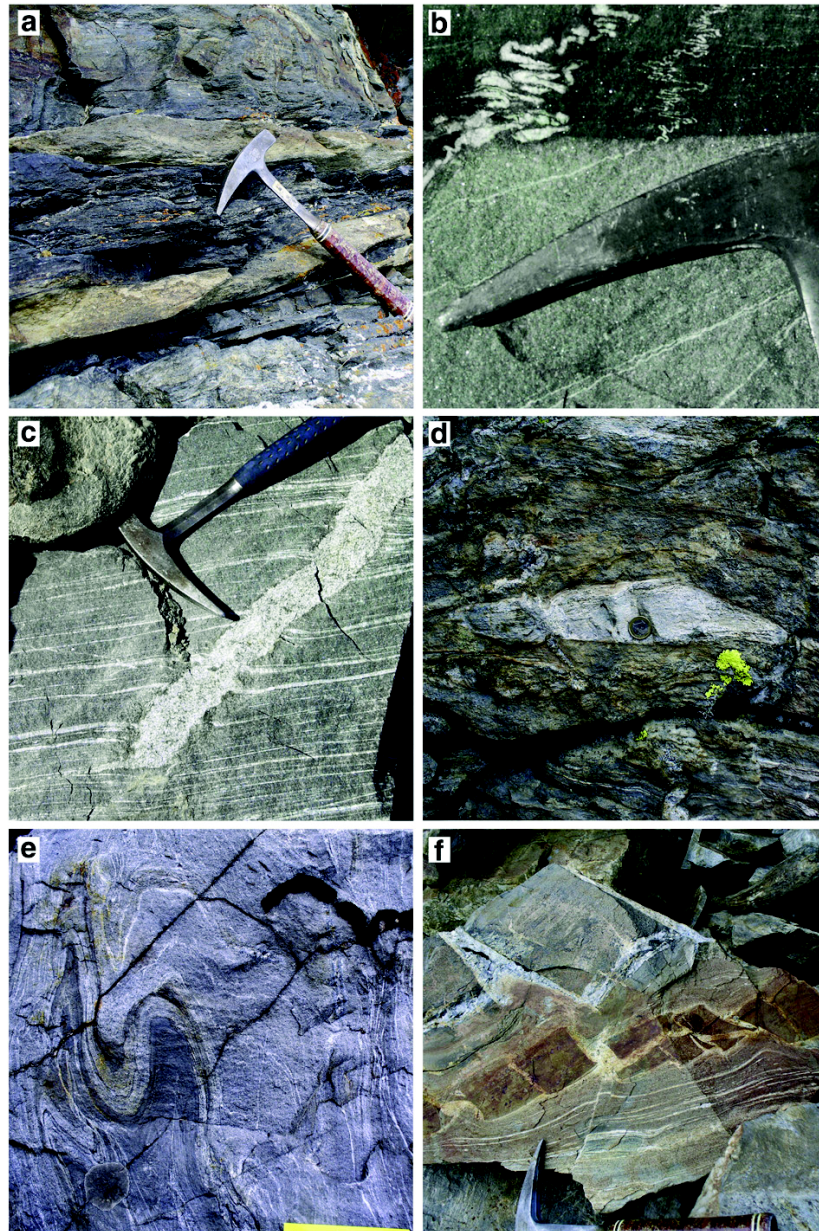


Fig. 5. Host-rocks. a, Distal relative to the diorite, Vanoise-type banded metapelite, with sub-horizontal Alpine cleavage – b, ptygmatically folded quartz veins across a lithological boundary between light, quartzitic level and a dark, carbonaceous level, revealing a much stronger deformation of the latter – c, melt-fed vein cross-cutting a sub-parallel net of early quartz veins – d, proximal [to a diorite body] melt-fed, lozenge-shaped wedge – e, proximal, contorted folds, – f, proximal, fragile boudinage of a reddish, mafic refractory level enclosed in veined metapelites, with leucocratic inter-boudin melt, and [bluish] late quartz-pegmatite veins at the top. Scales: hammer in a, b, c, f; 1-euro coin in d; 12-cm yellow paper sticker in e. No Alpine deformation is observable, except in a. Locations (names as in Fig. 3) – a, 2500 m, base of Punta Bianca eastern cliff – b, 2700 m, 1 km NE from Mt. Rollettaz – c, moraine at 2500–2800 m along the Punta Bioula trail – d and f, Fourquin, 2950 m – e, 2825 m, NE slope of Punta Bianca. (For interpretation of the references to color in this figure legend, the reader is referred to the web version of this article.)

bedding polarity was ever ascertained (except a rather loose mention of cross-bedding by [Debelmas et al., 1991](#) without localization). By contrast over 2450 m a.s.l., hornfelses, migmatites and magmatic rocks prevail, that suffered much less intense Alpine deformation. Whether the greenstone levels of the country-rock represent lava flows, or later intrusions as sills, could not be ascertained elsewhere in Vanoise because of the stronger Alpine overprint. Here, branched networks of dark green bands observed in the proximal aureole near the Fourquin, a possible sill-and-dike system ([Fig. 2](#)), suggest an intrusive emplacement.

Near the Fourquin summit ([Fig. 2](#)), a number of well-preserved granitic rock types occur between 2450 and 3170 m a.s.l., complexly interleaved with strongly migmatized host-rocks ([Figs. 5c–e, 6](#)) characterized by a rusty weathering ([Fig. 5d,f](#)) and a dense veining. These rocks are all suggestive of a relatively high degree of partial melting: garnet-rich leucocratic lenses ([Fig. 5d](#)); zoned granitic veins ([Figs. 5c, 6c](#)); diorite pods with sub-orbicular texture, pegmatite veins and pockets ([Fig. 5f](#)); various transitions between felsic and mafic varieties ([Fig. 6a](#)); syn-magmatic deformation of the migmatized host-rock ([Fig. 5e,f](#)). Details about the hornblendites, that we only observed as drift, are given along with their geochemical description (see [Fig. 6 a–b](#), and [Section 3.4.1](#)).

To the south of those proximal facies, more distal hornfelses have been observed, especially on the eastern slopes of Mt. Rollettaz and Punta Bianca (M in [Fig. 3](#)). The rocks are massive, fine-grained, very hard, and do not show any Alpine foliation, a major difference with

the common Vanoise metapelites ([Fig. 5a](#)). A preserved layering made of alternating, cm to m-thick, black and gray bands, is crossed at all angles by a network of white quartz veins with intricate pygmatic folding ([Fig. 5b](#)). A primitively high kerogen-content of the black layers is suggested by a study of the pygmatic veining ([Guillot, 2011](#)) and differential flattening between gray and black layers ([Fig. 5b](#)). Hence, the emplacement of the diorite might have happened under C-rich, fluid-saturated conditions.

2.3. Age of the pluton and of its host-rocks

The Penninic basement units, though dominant in volume relative to the cover units of Meso-Cainozoic age, were poorly known until the late nineties. Traditional views favored a Permo-Carboniferous age emplacement for the Cogne diorite, merely based on the black color of its host-rocks believed to reflect a Late Carboniferous age. However, [Bertrand et al. \(2000b\)](#) measured a 363 ± 24 Ma (2σ) U–Pb zircon upper intercept age by ID-TIMS on a light-colored granodiorite, and a more precise 357 ± 6 Ma (2σ) age by SHRIMP on a darker sample, richer in amphibole, both samples taken near Epinel (loc. [Fig. 1](#)).

This result implies a pre-Carboniferous age for the host rocks. Due to the lack of fossils and to the scarcity of detrital zircon, the age of this dark metapelite series, and of its m-thick intercalations of tholeiitic greenstone, has not yet been better constrained but is certainly older than the ~360 Ma intrusion of the Cogne diorite. The mafic rocks

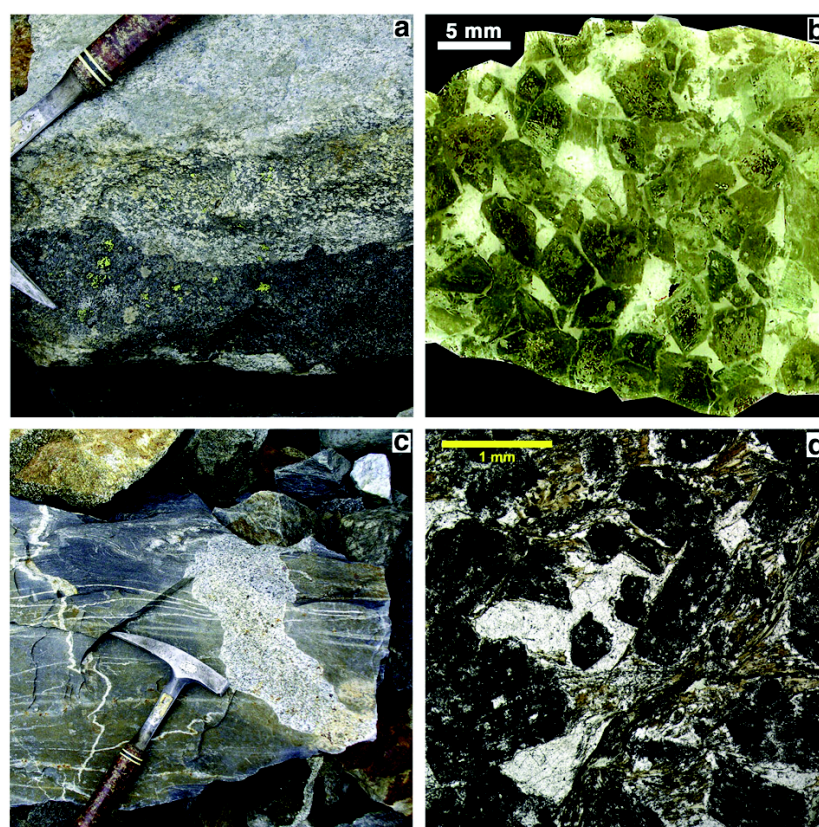


Fig. 6. Cogne diorite rock types. a, Hornblende horizon (bottom, under the hammer pick) with lobate contact with (at middle height) porphyritic diorite (anal. 2, 6, 7 in [Table 2](#)), succeeded (top) by a leucocratic rock type – b, hornblende (anal. 8 in [Table 2](#)) thin section (scanned image, enhanced colors), with white xenomorphic feldspar and quartz, green euhedral hornblende crystals often containing a biotite core and/or brown hornblende (dark red dyes); – c, dm-thick plagiodiorite vein, in host-rock metapelite crossed by a net of pygmatic quartz veins – d, plagiodiorite (anal. 5 in [Table 2](#)) thin section with euhedral, cloudy plagioclase (dark), xenomorphic, clear quartz (white), biotite (brown) (see also SM2, image 5). Note the absence (in b) or weakness (in d) of post-magmatic deformation. – Location: moraine at 2500–2800 m along the Punta Bioula trail. (For interpretation of the references to color in this figure legend, the reader is referred to the web version of this article.)

Table 2

Analyzed samples. ROCK-TYPES (thin section images given as electronic supplementary data SM2, mineral assemblages as Table SM3): 1, granodiorite – 2, porphyritic diorite – 3–4, deformed granodiorite – 5, plagioclite – 6, 7, porphyritic diorite – 8–10, hornblende – 11, mafic layer in the host-rock series – 12, black host-rock metapelite – 13, pale gray host-rock metapelite – 14, TPBU albitic gneiss. – present. CHEMICAL DATA: <L.D., lower than detection level. T.sat.Ap, Apatite saturation temperature (Harrison and Watson, 1984). T.sat.Zr, zircon saturation temperature (Watson and Harrison, 1983).

Analysis	1	2	3	4	5	6	7	8	9	10	11	12	13	14
Field sample	BK048	G03069	G03051	G03054	BK031	BK006	G03070	BK009	G03099	G03103	G03058	BK034	BK033	BK018
<i>Major elements (wt.%)</i>														
SiO ₂	62.25	58.56	61.59	61.36	55.26	53.44	52.96	50.96	50.51	48.12	50.90	59.14	64.13	72.16
Al ₂ O ₃	16.00	17.44	18.60	18.55	21.00	15.83	14.39	8.70	12.82	10.58	15.71	17.68	16.60	13.98
Fe ₂ O ₃	4.50	5.79	3.80	4.24	5.63	7.90	8.93	7.94	10.74	9.05	9.34	8.01	5.52	2.64
MnO	0.09	0.10	0.06	0.07	0.08	0.13	0.14	0.15	0.20	0.14	0.13	0.16	0.08	0.05
MgO	2.79	2.78	1.68	1.68	2.06	6.55	5.83	14.15	8.40	10.42	8.06	3.67	2.34	0.23
CaO	4.08	5.37	4.51	4.16	5.16	7.15	7.29	11.06	8.47	10.53	8.09	1.85	2.98	1.18
Na ₂ O	3.76	4.05	4.37	4.73	4.99	3.23	4.25	1.73	2.71	2.07	3.68	3.60	4.67	4.55
K ₂ O	3.22	2.33	2.55	2.67	2.48	2.26	1.72	1.16	1.67	2.69	1.14	2.41	1.21	3.52
TiO ₂	0.61	0.84	0.78	0.69	0.81	1.40	1.21	0.69	1.78	2.00	0.87	0.90	0.73	0.23
P ₂ O ₅	0.25	0.30	0.32	0.32	0.44	0.53	0.92	0.46	1.02	2.78	0.08	0.18	0.16	0.06
LOI	1.24	1.55	1.64	1.51	1.50	1.88	1.30	2.23	2.25	1.88	2.12	2.30	1.51	1.22
Total	98.77	99.10	99.89	99.98	99.40	100.29	98.93	99.23	100.54	100.25	100.12	99.90	99.94	99.80
A/CNK	0.94	0.92	1.02	1.02	1.04	0.76	0.65	0.36	0.59	0.42	0.71	1.49	1.15	1.04
mg#	55	49	47	44	42	62	56	78	61	70	63	48	46	14
<i>Trace-elements (ppm)</i>														
Ba	1168	1194	1044	1703	1701	1087	834.3	833.9	616.5	1906	201.3	638.6	437.7	638.2
Sr	580.6	771.8	862.2	875.5	1052	527.2	457.1	231.8	319.3	274.8	228.4	175.7	388.4	44.95
V	75.63	112.6	59.6	54.97	68.07	212.3	214.4	158.3	373.9	208.7	123.2	111.3	91.87	3.174
Zn	64.22	77.74	49.36	85.45	91.27	98.04	101.8	75.36	129.6	129.1	106	116.8	65.52	60.97
Zr	156.8	193.8	421.3	379.8	381.6	232.7	225.9	144.5	117.1	119	59.79	154.4	210.5	306.8
Rb	107.7	77.49	81.39	89.47	85.67	75.54	57.6	21.73	54.85	90.62	38.61	71.05	39.66	93.08
Y	15.48	19.91	9.245	17.05	14.61	33.63	38.38	15.98	47.33	43.61	16.61	25.87	19.99	68.54
Cr	76.73	13.43	14.6	15.7	16.91	192.6	91.38	1196	65.29	39.2	201.9	80.71	73.53	<L.D.
Cu	6.871	4.707	3.487	11.9	8.579	18.01	39.57	24.28	20.65	35.71	6.685	<L.D.	6.665	8.298
Co	10.68	12.49	5.764	6.719	5.729	27.13	27.48	40.59	35.76	29.3	38.12	21.11	13.2	1.346
Nb	7.037	11.58	6.858	10.05	10.03	10.07	12.77	9.316	14.05	21.96	1.48	11.3	9.842	10.07
Ga	19.51	21.71	21.73	22.82	24.39	22.13	21.57	11.7	21.41	19.36	15.84	22.9	19.3	22.75
Pb	32.75	27.95	34.25	37.04	35.31	25.19	23.74	7.52	13.90	19.10	7.73	6.01	7.22	3.46
Th	27.41	13.55	8.301	23.53	26.39	6.249	10.72	5.227	9.759	16.45	0.616	7.978	7.153	11.67
U	7.474	6.457	5.838	8.028	7.14	5.335	6.694	2.616	7.442	8.597	0.278	2.002	1.486	3.468
Ni	23.68	6.328	5.802	7.163	6.041	73.6	29.12	128.1	13.81	6.894	69.39	48	33.43	<L.D.
Hf	4.503	5.251	10.11	9.566	9.942	6.235	7.279	4.156	4.346	4.501	1.581	4.499	5.643	8.705
Sn	2.561	2.818	0.685	1.518	1.876	2.698	6.206	3.093	7.636	3.983	1.528	2.061	1.216	4.167
Cs	4.968	3.233	3.136	4.202	3.706	3.286	3.78	0.745	1.528	3.817	1.415	2.049	1.72	1.28
As	3.145	5.824	3.431	2.678	1.735	2.098	6.164	2.59	7.849	3.371	<L.D.	3.945	1.425	<L.D.
Be	3.146	3.519	3.198	3.788	3.521	3.195	3.972	2.143	3.932	3.118	0.88	1.693	1.8	2.911
Ge	1.425	1.306	0.997	1.106	1.064	1.489	1.551	1.718	1.942	1.957	1.535	1.478	1.244	1.534
Ta	0.614	0.755	0.244	0.697	0.52	0.456	0.939	0.634	0.824	1.869	0.129	0.92	0.8	0.933
Mo	<L.D.	<L.D.	1.861	<L.D.	<L.D.	<L.D.	<L.D.	<L.D.	0.525	0.814	<L.D.	<L.D.	<L.D.	<L.D.
W	0.74	0.36	1.497	0.257	0.243	0.222	0.263	0.512	1.084	0.785	0.907	1.182	0.686	1.45
Sb	0.784	0.782	0.749	0.286	0.345	0.393	0.323	0.458	0.593	0.451	0.41	0.235	0.262	0.105
Bi	<L.D.	<L.D.	<L.D.	<L.D.	<L.D.	<L.D.	<L.D.	<L.D.	<L.D.	0.217	0.35	<L.D.	<L.D.	<L.D.
In	<L.D.	0.075	<L.D.	<L.D.	<L.D.	0.104	0.113	0.062	0.142	0.06	0.067	0.096	<L.D.	0.095
Cd	<L.D.	<L.D.	<L.D.	<L.D.	<L.D.	<L.D.	<L.D.	<L.D.	<L.D.	<L.D.	<L.D.	<L.D.	<L.D.	<L.D.
T.sat.Ap (°C)	921	899	943	940	905	905	987	846	966	1142	643			870
T.sat.Zr (°C)	755	762	853	841	829	732	701	533	630	544	619			845
<i>REE (ppm)</i>														
La	47.84	31.56	17.15	54.47	62.92	27.33	34.21	24.06	47.79	88.44	3.568	26.62	29.76	40.32
Ce	92.57	62.12	29.94	98.05	116.3	66.11	92.27	55.58	125.8	204.1	8.84	55.61	58.64	86.37
Pr	9.862	7.369	3.292	10.5	12.43	8.863	13.46	7.098	16.8	26.47	1.322	6.727	6.868	10.72
Nd	33.57	28.31	12.18	35.98	43.27	38.94	59	28.67	67.81	110.6	6.572	26.18	26.11	42.85
Sm	5.267	5.505	2.223	5.797	6.648	8.927	12.59	5.769	13.34	21.24	2.057	5.644	4.991	10.03
Eu	1.186	1.517	1.253	1.559	1.757	1.987	2.832	1.424	2.791	4.651	0.868	1.327	1.278	1.372
Gd	3.715	4.391	1.896	4.116	4.38	7.967	9.795	4.371	10.66	14.91	2.565	5.12	4.279	10.2
Tb	0.519	0.629	0.259	0.562	0.564	1.132	1.356	0.599	1.522	1.853	0.439	0.788	0.64	1.762
Dy	2.841	3.595	1.494	3.048	2.812	6.337	7.445	3.173	8.533	9.117	2.831	4.812	3.754	11.12
Ho	0.529	0.685	0.308	0.576	0.507	1.162	1.354	0.552	1.567	1.511	0.595	0.936	0.726	2.304
Er	1.476	1.93	0.936	1.654	1.485	3.133	3.638	1.491	4.325	3.911	1.709	2.713	2.083	6.826
Tm	0.22	0.293	0.155	0.26	0.228	0.449	0.518	0.213	0.607	0.525	0.253	0.412	0.317	1.068
Yb	1.525	2.033	1.168	1.856	1.673	2.913	3.356	1.399	4.054	3.343	1.701	2.829	2.147	7.272
Lu	0.236	0.318	0.212	0.312	0.284	0.438	0.516	0.209	0.616	0.495	0.271	0.434	0.33	1.088
Σ REE	201	150	72	219	255	176	242	135	306	491	34	140	142	233
La _N /Lu _N	21.7	10.6	8.7	18.7	23.7	6.7	7.1	12.3	8.3	19.1	1.4	6.6	9.7	4.0
(Eu/Eu*) _N	0.82	0.94	1.87	0.98	1.00	0.72	0.78	0.87	0.72	0.80	1.16	0.75	0.85	0.41

might possibly have an age in the 510–480 Ma range, as measured for the A-type felsic rocks associated to a similar series in Vanoise (loc. Fig. 1, inset) and Val de Rhêmes (Bertrand and Leterrier, 1997; Bertrand et al., 2000a; Guillot et al., 1991) and further North in Valais (Bussy et al., 1996), and their intrusive character would imply a Cambrian or older age for the metasedimentary country-rocks.

2.4. Previous data on rock and mineral chemistry

Four major element analyses of the Cogne diorite were found in the literature (I to IV, Table SM1). One analysis by Novarese (1894) was performed on a “schistose rock”, interpreted as the result of the “dynamic metamorphism” of a previously granitic diorite. When compared to the geochemical data available at that time, his analysis allowed him to name the protolith as a quartz diorite, with a primitive plagioclase $An < 50$. Fenoglio and Rigault (1962) gave three analyses, one from a felsic rock comparable to the Novarese analysis (both plotting in the tonalite field of the R1–R2 diagram: Sandrone et al., 2004), and two from more mafic rocks from the Punta Bioula section.

The Cogne diorite host-rocks belong to the Vanoise basement series. Previous analyses of rocks from Vanoise have been used (Beucler et al., 2000; Bussy et al., 1996; Cosma, 1999; Guillot, 1987; Guillot et al., 1993; Saliot, 1978; Leterrier, unpubl. data). They comprise 47 whole-rock data for metashales or metagreywackes, 96 for intercalated mafic rocks and 37 for associated, A-type felsic rocks such as rhyolite and granophyre that, together with the mafic rocks, compose a bimodal magmatic series.

3. Petrology and geochemistry

3.1. Materials and methods

About 150 polished thin sections were prepared from the samples collected along the Punta Bioula section, and about 50 of them were subjected to micro-chemical investigations using a scanning electron microscope equipped with an energy dispersive system for micro-analysis and elemental mapping (SEM-EDS, Univ. Lille). Dubious mineral phases were also investigated by Raman spectroscopy (green laser 532 nm, model LabRam HR800, Univ. Lille). Fourteen whole-rock analyses (Table 2) were complemented by five Sr–Nd isotope measurements (Table 4). Analyses of major, trace and rare-earth elements were performed at the “Service d'Analyse des Roches et des Minéraux du CRPG-CNRS” at Nancy (in 2004; analytical procedure and precisions: Carignan et al., 2001). $^{143}\text{Nd}/^{144}\text{Nd}$ and $^{87}\text{Sr}/^{86}\text{Sr}$ isotope ratios have been determined by Thermal Ionization Mass Spectrometry in five representative samples of the Cogne igneous rocks, following analytical techniques broadly similar to those described by Pin and Santos Zalduegui (1997). The measured ratios are listed in Table 4, along with “initial” values corrected for *in situ* decay of ^{147}Sm and ^{87}Rb since 360 Ma, by using $^{147}\text{Sm}/^{144}\text{Nd}$ and $^{87}\text{Rb}/^{86}\text{Sr}$ ratios calculated from trace element data obtained by ICP-MS.

Views of the fourteen thin sections of the analyzed samples are given as electronic supplementary material (SM2), where their mineral assemblage is also listed (SM3). The sample locations are given in Figs. 1 and 3. Ten samples (1 to 10, Table 2) are representative types from the diorite itself as seen from the field. In order to compare the host rocks to analogous Vanoise rocks (see Section 2.4) and to document potential contamination of the diorite, three host-rocks (11 to 13, Table 2) were analyzed, one black metashale (12) and one metagreywacke (13), which account for a major part of the country-rocks of the Cogne pluton, plus one intercalated mafic rock (11). The last analysis (14) comes from the TPBU (see Section 2.2.2): this massive, fine-grained, albite-rich gneiss with green biotite constitutes the top of the Punta Bioula.

The range of granitoid rock-types includes all the intermediates between the following end-members (with analysis numbers as in Table 2):

Table 3

Selected CIPW-norm data for magmatic rock-types. Analysis numbers refer to the first line of Table 2. CIPW-norms computed using Zhou and Li (2006) Geoplot program. Indicated ranges, in weight %, denote the attribution of Fe, either fully to Fe^{3+} (first value) or fully to Fe^{2+} (second value) – fm, ferro-magnesian minerals – qf, felsic minerals – ox, accessories, including titanite plus rutile (Ttn + Rut) – mg#, $100 \times \text{MgO}/(\text{MgO} + \text{FeO}_{\text{tot}})$ – Ap, apatite.

Analysis	1	2	5	6	7	8	9	10	11
SiO_2	62	59	55	53	53	51	51	48	51
wt. %									
fm	7–15	7–18	5–10	19–27	20–29	53–59	26–37	33–40	26–36
qf	86–83	84–80	87–85	68–65	66–63	36–35	56–52	46–46	62–62
ox	6–2	9–2	8–5	13–7	14–8	11–6	18–11	21–14	12–2
mg#	55	49	42	62	56	78	61	70	63
Ttn + Rut	1.1–0	1.6–0	0.7–0	3.1–0	2.7–0	1.3–0	3.9–0	4.6–0	1.8–0
Ap	0.6	0.7	1.0	1.3	2.2	1.1	2.4	6.5	0.2

- (1) dominant, granodiorite to quartz diorite varieties with feldspar, quartz, amphibole and biotite (1 to 4),
- (2) leucocratic, feldspar-rich rock types with biotite, quartz and amphibole (5 to 7),
- (3) melanocratic mafic rocks with up to 80% of modal amphibole (8 to 10),
- (4) one occurrence of two-mica leucogranite (near Gran Nomenon, Fig. 1; not sampled).

It must be stressed again that the rock classification is tentative. In such a geological context, with added effects of primary complexity, including auto-metamorphic effects, plus the Alpine deformation and HP-metamorphism, any attempt at classifying those metagranitic rocks from modal data inevitably yields poorly assessed names. This adds to the necessity of a geochemical approach.

3.2. Rock classification based on geochemical data

3.2.1. Major element and normative data

A selection of CIPW normative data is given in Table 3 for rocks of clearly igneous origin. Their SiO_2 contents range from 48 to 62 wt.%. Accordingly, CIPW norms show 1% to 17% of quartz, 35% to 85% of quartz plus feldspar (qf in Table 3), 40% to 7% of ferro-magnesian silicates (fm) and 21% to 4% of oxides and accessories (ox), respectively. From normative data of samples 1 to 7 and following Le Maitre (1976), or from the R1–R2 diagram, the rocks plot as monzonite to granodiorite. Only by allocating a major part of K to biotite, based on its primitive modal content estimated from thin sections (imaged in SM2), these rocks plot into the fields of tonalite, quartz diorite and quartz monzodiorite.

The texturally preserved quartz diorite to granodiorite (anal. 1), which represents the bulk of the pluton to the east of Valsavaranche (Fig. 1), contains approximately equal modal contents of amphibole and pale biotite, totaling around 15 vol.%, their mg# being around 40 from EDS microanalyses. Amphibole and biotite appear to have been significantly modified by the Alpine metamorphism, e.g. partially transformed into chlorite, and Al-in-hornblende barometry proved to be no longer usable. The primitive (Mg-rich?) biotite has been partly transformed into Mg-rich phengite or chlorite, partly into an Al-rich Alpine biotite.

Major element oxide vs. SiO_2 plots (Harker's diagrams, not shown) display increasing Al-, Na-, K-contents, and decreasing contents in Ca, Mg, Fe, Mn, Ti, and P. This may be related to an increasing modal content of alkali feldspar together with a decreasing anorthite component. Major element based classification diagrams do not allow us to give clear-cut rock names, as a probable reflection of either secondary alteration of Alpine age (e.g. samples 3 and 4, more schistose), or primary mineral accumulation processes, especially plagioclase [anal. 5], amphibole [anal. 8 to 10] or both [anal. 6 and 7], and/or apatite

[anal. 10] as suggested by petrographic observations. Here, only an AFM plot is shown (Fig. 7a) in order to highlight the contrast between the bimodal pattern, and tholeiitic signature of meta-igneous rocks sampled in the diorite country-rocks, on the one hand, and the continuous array of the diorite data points, in the calc-alkaline field, on the other. The host-rock metapelites plot in the calc-alkaline domain, in correlation with their high albite modal content, in the same field (marked p on diagrams) as the Vanoise metapelite series that was interpreted to derive from probable volcano-sedimentary protoliths (Guillot, 1987; Guillot et al., 1993).

3.2.2. Trace elements

In geotectonic classification diagrams based on immobile trace elements, the more felsic diorites (1 to 7) plot in the calc-alkaline field or volcanic arc granitoids (VAG in Fig. 7b; Pearce et al., 1984). More mafic diorites (8 to 10) accordingly plot into the field named “destructive plate margin magmatism” by Wood (1980: Th-Ta-Hf/3 triangle, not shown), where the host-rock tholeiite (11) also plots, though very close to “primitive arc tholeiites”. Host-rock metasediments (#12 and 13,

with resp. SiO_2 contents at 59% and 64%), a family of rocks for which a remote andesite derivation has been suggested based on high $\text{Na}_2\text{O}/\text{K}_2\text{O}$ (Guillot et al., 1993), also plot in the VAG field (Fig. 7b). By contrast, in the same diagram the TPBU sample (#14, SiO_2 at 72%) plots in the within-plate granitoid field (WPG), as do the felsic rocks from Vanoise.

Chondrite-normalized REE data (Fig. 8a) show steep patterns for both the more felsic diorite types (La_N/Lu_N at 6.7–23.7) and the most mafic varieties (La_N/Lu_N at 8.3–19.1), while porphyritic diorites (Fig. 8a) and host-rock metapelites (Fig. 8b) have a La_N/Lu_N ratio near 7. By contrast, analysis #11, a mafic sample taken from the diorite country-rocks, yields a flat REE-pattern, with a normalized ratio La_N/Lu_N at 1.4 (Fig. 8b) coupled with much lower contents ($\sum \text{REE}$ of 34 instead of 72 to 491 ppm for the diorite); its REE pattern resembles those observed for mafic rocks from the Vanoise basement (m, after Guillot et al., 1993). A comparison (Fig. 8) of diorite REE patterns with profiles averaged from Vanoise rocks also points to markedly different geochemical styles. Specifically, while the mafic rocks from Vanoise (m or 11, in Fig. 8b) are less REE-rich than their associated felsics (f'), the contrary holds for the Cogné diorite suite. In other words, *mafic diorites are often REE-richer than more felsic diorites* ($\sum \text{REE}$ at 135–491 ppm, vs. 72–255 ppm, respectively). This reflects the remarkable abundance of titanite, apatite, allanite and zircon in mafic diorites, suggesting a prevailing role of accessory mineral crystallization during the emplacement of the diorite. Invoking hornblende accumulation at the origin of more mafic diorites might also account for their moderate enrichment in HREE relative to felsic types, though our sampling of fresh rock-types (only #8 for mafic rocks) is too limited to allow any definite conclusion.

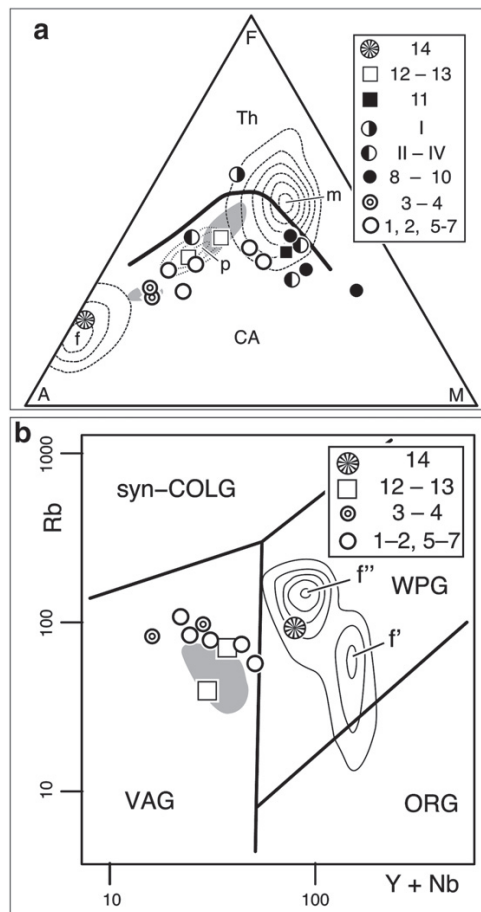


Fig. 7. Geotectonic classification diagrams. Numbers I to IV refer to Table SM1, 1 to 14 refer to Table 2; contouring refers to Vanoise basement rocks; gray pattern is for the Limousin tonalites (Shaw et al., 1993). a, AFM triangle (Irvine and Baragar, 1971). Th, domain for tholeiitic series – CA, domain for calc-alkaline series – frequency contourings for Vanoise basement analyses refer to (f) 37 Vanoise felsic rocks, (p) 47 Vanoise metapelites, (m) 96 Vanoise mafic rocks – b, Rb vs. Y + Nb diagram (Pearce et al., 1984) – VAG, volcanic arc granites – syn-COLG, syn-collision granites – ORG, oceanic ridge granites – WPG, within-plate granites with contouring for 16 Vanoise felsic rocks: f', 6 Thyon granite analyses (Bussy et al., 1996) – f'', 10 Mt. Pourri and Val de Rhêmes granophyre analyses (Bertrand et al., 2000a; Beucler et al., 2000; Guillot et al., 1993).

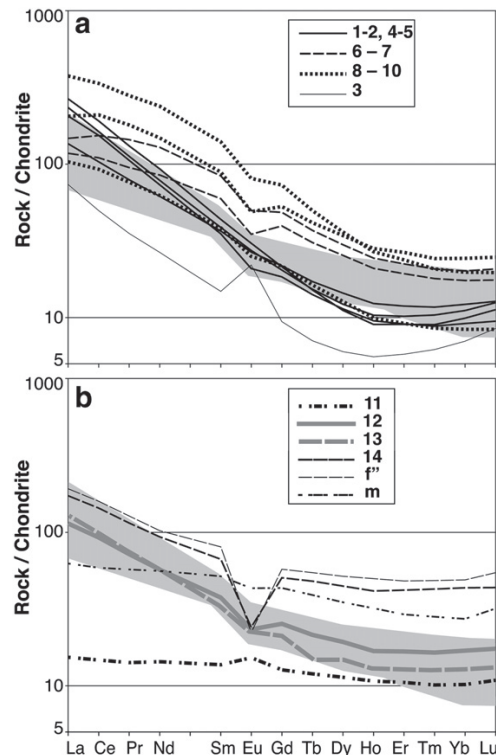


Fig. 8. Selected REE-data normalized to chondrite (Sun and McDonough, 1989). a, Cogné diorite rock-types – b, comparison between diorite rock-types (gray zone), country-rocks (11 to 13), TPBU (14), and Vanoise rocks (f' , m). Key to symbols: 1 to 14 refer to analyses listed in Table 2 – f' , m, average of analyses from Vanoise (in litt, cf. Fig. 7) for 5 A-type granophyres, and 2 associated mafic tholeiites, respectively. The gray pattern refers to REE-profiles of Limousin tonalites (Shaw et al., 1993).

3.3. Information from accessory minerals

A distinctive feature of the various Cogné diorite rock-types is the presence of euhedral, often arrow-shaped titanite crystals up to 1 cm in length. Euhedral titanite was not observed, either in the country-rocks or in the TPBU (anal. 11 to 14), but was preserved even in deformed diorite samples (3–4). In thin section, the rocks also show abundant smaller (0.1 to 0.3 mm), euhedral, zoned allanite crystals, occasionally surrounded by a spongy association of clear epidote and quartz. Zircon is commonly observed as euhedral, concentrically zoned crystals, even in the mafic rock-types. Apatite is also widespread in these rocks, often as euhedral inclusions in the hornblende crystals.

Titanite contains poikilitic, euhedral apatite inclusions, and is often itself included in amphibole. Based on such textural arguments, the proposed order of crystallization is: apatite, Mg-biotite, allanite, titanite, amphibole, plagioclase, Fe-biotite, [garnet-]quartz, K-feldspar. This is somewhat at variance with the canonical Bowen's sequence, and can be attributed to a stepwise crystallization at decreasing depths. Regarding this presumed order of crystallization other arguments have been found considering liquidus and saturation temperatures, as exposed hereafter.

Zircon saturation temperatures of 850 °C were proposed (Guillot et al., 1993) for the Vanoise granophyres (using the approach of Watson and Harrison, 1983) and it is also the temperature obtained here for the TPBU sample (see Section 3.4.3). Results for the diorite rock-types are generally lower, in the range 700–850 °C for the more felsic diorites (1 to 7), and still lower for the most mafic rocks (530–630 °C). Apatite saturation temperatures (Harrison and Watson, 1984) and liquidus temperature (using Sisson and Grove, 1993, or Grove and Juster, 1989, depending on the rock-type, namely mafic types 8 to 10, or more felsic types 1 to 7) were also computed. Modifying a diagram after Harrison and Watson (1984), we propose to use a logarithmic scale for the P_2O_5 axis, in order to convert the curves of apatite saturation temperatures into straight lines (Fig. 9; temperatures listed in Table 2). The felsic

diorite types (analyses 1 to 7) form an almost linear array, roughly along or slightly above the 900 °C isotherm.

The metaluminous compositions of our samples allow the use of the apatite saturation thermometer, with $A/CNK < 1$ in most analyses (Table 2: except #3 and 4 at 1.02, #5 at 1.04, beside higher values for metasediments #12–13). However, the measured P_2O_5 contents might point to some kind of apatite accumulation. This explanation is most straightforward for mafic samples such as analysis #10 with a grossly abnormal 2.78 wt. % of P_2O_5 , while the representative points of analyses 8 to 10 (Fig. 9) form an almost vertical array [excluding analyses III and IV, as visible outliers: either Fenoglio and Rigault (1962) sampled other rock-types – a tholeiite host-rock, alike analysis 11 that plots nearby? – or phosphorus was not measured accurately in 1962]. Apart from such outliers, it might be considered that the saturation temperature estimates is valid, implying that apatite crystallization, occurred at 900–950 °C. Liquidus temperatures being always higher (in the range 1100 °C–1200 °C) than the latter results suggests they were probably never attained. Taking into account the above-proposed order of crystallization, this interpretation would be in line with progressive crystallization of a deep-originated magma at decreasing depth and temperature, most of this process taking place between 900–950 °C (apatite saturation) and 700–850 °C (zircon saturation).

3.4. Peculiar rock-types

3.4.1. Hornblende

Amphibole-rich rock-types have been reported in the Punta Bioula section (Fenoglio and Rigault, 1959, 1962; Grasso, 1974; Novarese, 1894) and one similar occurrence was mapped (Amstutz, 1962) in the Val de Cogné (Fig. 1). Massive, practically undeformed hornblendites (Fig. 6a,b) occur in apparent continuity with the main pluton SW-wards, on the eastern slope of the Punta Bioula-Punta Bianca ridge (Fig. 3). The relationship of this rock-type with the rest of the pluton

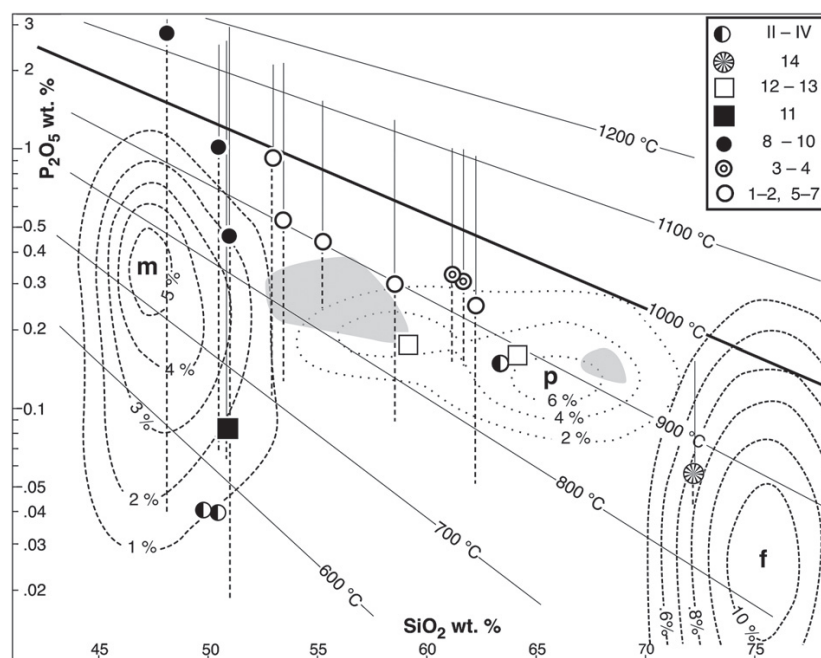


Fig. 9. P_2O_5 vs. SiO_2 with apatite saturation isotherms (after Harrison and Watson, 1984). Key to symbols as in Fig. 7a, sample numbers as in Table SM1 and Table 2. Vertical bars issued upward from each representative points join to the liquidus temperatures around 1100–1150 °C computed from each analysis (Sisson and Grove, 1993); downward dotted bars join to the zircon saturation temperature (Watson and Harrison, 1983).

has not yet been fully elucidated, since only a handful of small outcrops were tentatively mapped (Fig. 3), though lobate contacts observed between three variously colored diorites (Fig. 6a) suggest that the rocks were concomitantly in a partly molten state. All the previous authors have attributed these amphibole-rich rock-types to local accumulations of mafic minerals. The rocks have a prominent mafic mineral content, with more than 60 vol.%, up to 2 cm in size, dark-green, euhedral amphibole crystals. Whatever the dark color of the rock, quartz is present as interstitial crystals that have kept a magmatic habit and have probably crystallized later than subhedral alkali feldspars. The euhedral amphibole crystals are generally poikilitic (image 8 in suppl. data SM2), with a magnesiohornblende composition in sample #8 (Fig. 6b), while the smaller grains of samples #9 and #10 are actinolite. Apatite, zircon and titanite are idiomorphic and frequently partly included in the magnesiohornblende crystals. The amphiboles of sample #8 also enclose areas of associated Mg-rich phengite and Mg-rich chlorite, from possible phlogopite-rich precursors. The early-formed apatite (see Section 3.3), too, might suggest a deep-seated source to those magmatic rocks, a primitive character being also supported by whole-rock mg# in the range 61–78 (Table 3).

Similar “hollow” amphiboles have been described in appinites (Roach, 1964; Wells and Bishop, 1955), their core enclosing an assemblage of felsic composition, related to a late magmatic episode. The classical appinite occurrences of Great Britain form minor pods distributed marginally relative to the main body of Caledonian granitic plutons, often associated to hypabyssal breccias of the host-rocks. The authors interpreted these rocks as transformed gabbroic relicts in late-magmatic conditions under high water pressure. Accounts from the Canadian Cordillera Westcoast Crystalline Complex (DeBari et al., 1999; Larocque and Canil, 2010) report a continuous range of rock-types from mid-crustal ultramafic cumulates to shallower hornblende gabbro and granodiorite. In a recent reappraisal on the appinite problem (based on outcrops resembling those of Fig. 6a: Pe-Piper et al., 2010), the chemistry of the appinites was shown not to characterize a definite tectonic setting, but rather and only a peculiar magmatic process leading to hydrated mafic rocks. Field evidence of transitional facies between deep-seated mafic cumulates and calc-alkaline, shallower plutons resembling the Cogne diorite, were described in the Western Canadian coastal ranges (DeBari et al., 1999), with a continuous array between hornblende gabbro, hornblendite and hornblende granodiorite.

The Al-in-hornblende barometry [based on a compilation by Tindle and Webb (1994) of the various versions of the Al-in-hornblende barometer], applied to all the EDS-analyzed amphibole crystals, gave consistent results only for cm-sized amphiboles from hornblendite of sample #8, where K-feldspar, biotite and quartz are present as required, yielding 0.35 ± 0.15 GPa. Inherited features of higher pressure might be found (1) in the possible phlogopite inclusions of those hornblende poikilocrysts, (2) in the presence of apparently early formed epidote streaks inside preserved plagioclase, and (3) in epidote/quartz symplectite around allanite.

3.4.2. Mafic country rocks

In Vanoise, the mafic rocks display a tholeiitic composition. Their tectonic setting was debated, some authors favoring a MORB-character (Guillot, 1987) and others a within-plate, extensional setting (Cosma, 1999). Here one analysis (11 in Table 2) is given for a greenstone septum in metapelites, already mentioned above for its flat REE pattern (Fig. 8b). In thin section, the rock also displays important differences with the diorite mafic rock types, specifically the presence of blue-green Na, Ca-amphibole as a major component, and different accessory minerals: neither allanite, nor idiomorphic apatite nor titanite was observed, and only relictual, tiny shells of zircon could be detected after a careful SEM-examination. Instead, the thin sections are spotted with grains of Fe, Ti-oxide surrounded by leucoxene haloes, suggesting degraded magmatic titanomagnetite, which is characteristic of Vanoise mafic rocks.

3.4.3. TPBU analysis

Based on geochemical data only, marked differences exist between the diorite-hosting unit and the TPBU. The analyzed TPBU rock plots consistently (Figs. 7a, b, 8b, 9) near the field of A-type granophyres from Vanoise. From their geochemistry and field aspect, these “gneiss minuti” [fine-grained] might derive from a rhyolite or ignimbrite protolith. This is in line with other similarities, e.g. the presence of green biotite as the main ferro-magnesian mineral, which was also observed in Vanoise granophyres, themselves of hypabyssal character (Beucler et al., 2000), together with very low mg# and Ca, Mg-contents.

4. Igneous sources

4.1. Bulk composition melts

Not excluding *a priori* a mantle origin, identifying the type of a possible crustal source for the diorite can be attempted through a major element diagram (Fig. 10a) devised from a compilation of experimental melt analyses (Altherr et al., 2000). Among the nearby rocks, only the TPBU metavolcanite (anal. 14) plots alike melts from metagreywackes. The host-rock metapelites (anal. 12–13) plot inside the domain of Vanoise metapelites (denoted by “p” contouring in Fig. 10a), and the mafic level from country-rocks (anal. 11) into the domain of Vanoise mafics (“m” contouring), both out of crustal melt fields. The Vanoise granophyres and granites (“f”) plot clearly apart from the diorite, in the field of melts from metapelites. While the hornblendite samples (8–10) have an ambiguous position, out of all the experimental fields for crustal melts, the dominant felsic rock-types of the Cogne diorite (anal. 1–7) plot into the field of partial melts issued from metabasaltic to metatonalitic sources.

4.2. Sr–Nd radiogenic isotopes

Five diorite, two more felsic rock-types (1, 4), one intermediate rock (5) and two hornblendites (8, 9) have been measured (Table 4). The age-corrected Nd isotope data, expressed with the usual epsilon-notation, display a limited range of values, from -1.2 to $+0.9$, as do $^{87}\text{Sr}/^{86}\text{Sr}_{360}$, from 0.7054 (a mafic rock) to 0.7063 (the most SiO_2 -rich rock).

In spite of a relatively large spread of $^{147}\text{Sm}/^{144}\text{Nd}$ (from 0.0928 to 0.1215), no clear correlation can be observed with ϵNd_{360} values, in contrast with what would occur if combined assimilation and fractional crystallization (AFC) had played an important role during the late-stage evolution of the magmas which formed the Cogne intrusive body. Likewise, there is no inverse relationship between ϵNd_{360} values and $^{87}\text{Sr}/^{86}\text{Sr}_{360}$ ratios, at variance with what is commonly found in igneous systems. Admittedly, age-corrected $^{87}\text{Sr}/^{86}\text{Sr}$ isotopes do not provide very robust information due to the possibly very significant mobility of both Rb and Sr during deformation and metamorphism, although the relatively small spread of initial ratios may suggest that gross disturbances did not play a major role in this case. If not disturbed at a post-igneous stage, the more radiogenic Sr isotope signature observed in the most silica-rich rock might be interpreted to reflect the assimilation of hydrous fluids relatively rich in ^{87}Sr , but unable to induce any shift of Nd isotope composition due to their typically REE-poor characteristics.

Albeit of little (if any) geological significance due to the most likely multi-stage evolution of the source reservoir(s) of the ca. 360 Ma magmas, T_{DM} model ages (DePaolo, 1981) are rather tightly grouped, and much older (0.78–0.98 Ga) than the igneous emplacement age established by U–Pb zircon dating. This suggests that, if an ultimate depleted mantle source reservoir was tapped, ancient recycled materials were also involved.

Taken at face value, the ϵNd_{360} data close to the chondritic (or Bulk Silicate Earth) value indicate that the overall, average source

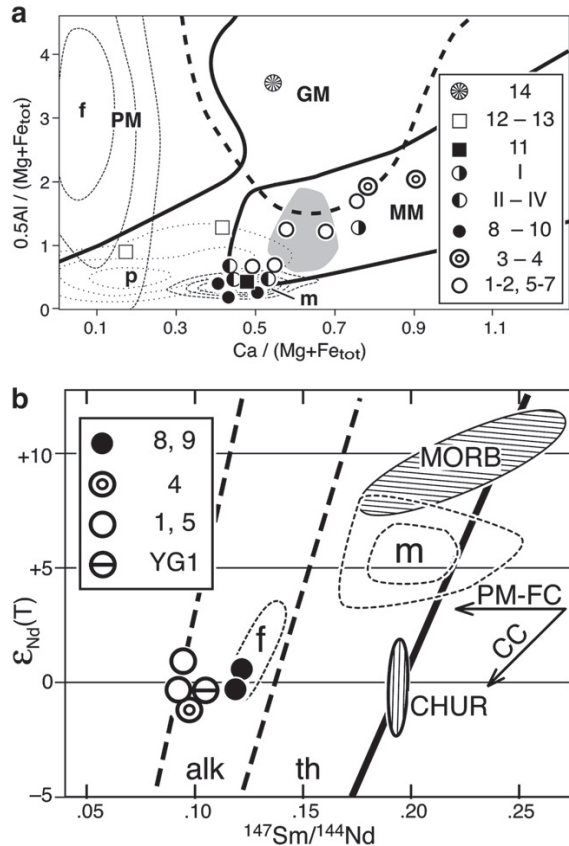


Fig. 10. Magmatic source diagrams. Key to sample numbers as in Table SM1 and Table 2, plus: YG1, unspecified Cogné diorite sample from Cosma (1999). a, Diagram A/MF vs. C/MF (from a compilation by Altherr et al., 2000) with Vanoise basement contourings (m, p, f) as in Fig. 9. – MM, partial melts from metabasaltic to metatonsalitic sources – GM, partial melts from metagreywackes – PM, partial melts from metapelitic sources. b, $\epsilon_{Nd}(T)$ vs. $^{147}Sm / ^{144}Nd$ after DePaolo (1988) – PM-FC, partial melt-fractional crystallization vector – CC, crustal contamination vector – m, f: contouring of the Vanoise magmatic rocks, after Cosma (1999) using, respectively, 8 mafic rocks and 3 felsic rocks.

materials of the Cogné diorite magma were, on a time-integrated basis, neither enriched, nor depleted in Sm relative to Nd. Whatever its possible geological interpretation, this feature is shared by many continental flood basalts worldwide. In practical terms, this might

Table 4
Isotope data. Sample numbers refer to the first line of Table 2.

Sample	1	4	5	8	9
Sm	5.27	5.80	6.65	5.77	13.3
Nd	33.6	36.0	43.3	28.7	67.8
$^{147}Sm / ^{144}Nd$	0.0948	0.0974	0.0928	0.1215	0.1186
$^{143}Nd / ^{144}Nd$	0.512444	0.512345	0.512381	0.512490	0.512439
± 2 S.E.	0.000004	0.000004	0.000008	0.000005	0.000019
$\epsilon_{Nd360Ma}$	0.9	–1.2	–0.3	0.5	–0.3
T_{DM} (Ga)	0.78	0.92	0.84	0.97	0.98
Rb	108	89.5	85.7	21.7	54.9
Sr	581	876	1052	232	319
$^{87}Rb / ^{86}Sr$	0.538	0.296	0.236	0.271	0.498
$^{87}Sr / ^{86}Sr$	0.709082	0.707539	0.707083	0.706768	0.708130
± 2 S.E.	0.000006	0.000004	0.000005	0.000004	0.000004
$^{87}Sr / ^{86}Sr_{360Ma}$	0.7063	0.7060	0.7059	0.7054	0.7056

reflect a direct derivation from a source reservoir with $\epsilon_{Nd360} \sim 0$, which might have been extracted, for example, from a typical, long-term depleted mantle (with radiogenic – i.e., positive ϵ_{Nd} – isotope signature) in the Late Proterozoic, as inferred from T_{DM} model ages. Another possible scenario would envision a long-term depleted mantle source which suffered contamination by old crustal materials (enriched in LREE and with negative ϵ_{Nd}) recycled into the upper mantle via subduction, at some undefined time prior to 360 Ma.

Alternatively, the Nd isotope signature of the Cogné magmas might reflect primary mafic melts extracted from a depleted (with $\epsilon_{Nd360} > 0$) mantle source, that were contaminated by assimilation of materials with negative ϵ_{Nd360} during their ascent through, and possible ponding in, the continental crust. In this interpretation, the major assimilation would have been accompanied, or followed, by a process of homogenization of the blended magmas before final ascent to their emplacement level, thereby accounting for their broadly homogeneous Nd and Sr whole-rock isotopic features.

Our isotopic data set is too limited, by itself, to allow us to favor any of these possible interpretations.

For the sake of completeness, the Cogné diorite characters have to be confronted to data from the Vanoise basement, to which belonged the present country-rocks. Cosma (1999) performed one Sm–Nd isotopic analysis of the Cogné diorite (his sample YG1) in agreement with our results (0.1039, 0.512422 and -0.7 for $^{147}Sm / ^{144}Nd$, $^{143}Nd / ^{144}Nd$ and $\epsilon_{Nd300Ma}$, resp.), hence allowing comparisons. Most of his analyses concern Vanoise mafic and felsic rocks. Adding his data to a plot of ϵ_{Nd} vs. $^{147}Sm / ^{144}Nd$ (Fig. 10b), the vectors MORB-to-diorite and Vanoise-mafics-to-diorite almost parallel the crustal contamination vector (CC, after DePaolo, 1988). However, an ancient MORB as source would yield magmas with highly radiogenic Nd, which was not observed in the present case.

5. Discussion and conclusions

5.1. I-type characters for the Cogné diorite

Based on a wealth of criteria, an I-type may be proposed for the Cogné diorite: a magmatic assemblage with amphibole, pale biotite, titanite, allanite \pm epidote; no monazite and no muscovite; $0.7054 < ^{87}Sr / ^{86}Sr_{360} < 0.7063$, $-1.2 < \epsilon_{Nd360} < +0.9$ (Barbarin, 1999; Clemens et al., 2011; McCulloch and Chappell, 1982). For comparison purposes, the I-type quartz-diorites of Limousin (Shaw et al., 1993) were plotted in the various diagrams (Figs. 7 to 10). With SiO_2 -contents at 53–58% for seven plutons, plus one at 68%, an age range at 350–380 Ma, and their isotopic values $0.7047 < ^{87}Sr / ^{86}Sr_1 < 0.7059$, $-0.7 < \epsilon_{Nd360} < +1.8$, the Limousin quartz diorites are directly comparable to the Cogné diorite. They have been considered as related to a N-directed subduction by some authors (Refs. in Shaw et al., 1993). Further investigations, based on a larger number of Late Devonian–Early Carboniferous plutons in the northern part of French Massif central, favored a pre-collisional, Sward subduction of the Rheic oceanic crust (Pin and Paquette, 2002) as the cause of this magmatism.

A number of uncertainties prevent any definite correlation between Internal Penninic basement units and possible counterparts of the stable (during Alpine times) European plate. The pre-Alpine location of the Cogné diorite-bearing unit may have been somewhere to the South of Marseille during the Early Mesozoic times after Stampfli and Kozur (2006), and earlier motions, e.g. along major strike-slip faults of Carboniferous age, may have brought our unit from unpredictable distances and directions. Following the same authors, at 360 Ma the Vanoise, as part of the Briançonnais terrane, belonged to a narrow continental (?) ribbon between two opposed subducting oceanic crusts, the S-directed subduction of Rheno-Hercynian oceanic crust, to the North, and the N-directed subduction of Paleotethys oceanic crust, to the South (Stampfli and Kozur, 2006; their Fig. 1C); this continental ribbon would have been previously separated at ~ 400 Ma

from the N margin of Gondwana by the Paleotethyan rifting (ibid., Fig. 1A–B). Hence, a possible similarity exists with the above cited scenario of Pin and Paquette (2002). Nevertheless, the “destructive plate margin” characters of the Cogne diorite documented in the present paper may at least contribute to a better knowledge of this important igneous marker of paleogeodynamic settings.

5.2. Emplacement conditions

Our geochemical data, which are probably quite comparable for most I-type rocks, yield: liquidus temperatures tending toward 1200 °C for hornblendites (from major element contents; Grove and Juster, 1989), and near 1100 °C for more felsic diorites; apatite saturation temperatures at 950–900 °C (based only on felsic rocks); zircon saturation temperatures at 700–850 °C for the ordinary felsic diorites and at 630–530 °C for the hornblendites. Pressures from Al-in-hornblende barometry on the latter rocks can be estimated at 0.35 ± 0.15 GPa (i.e. 6 to 15 km in depth) for final emplacement, while phlogopite-related inclusions of the same hornblende crystals suggest a protracted history of crystallization at decreasing depths and temperatures. Other P–T criteria, out of the scope of this paper, are being searched in the mineralogy of the proximal hornfels, which are rich in pre-Alpine, pea-sized garnets (work in progress).

5.3. Alpine context

A major shear zone exists at the top of the diorite, possibly some hundreds of meters thick when taking into account the recumbent folds of the TPBU. It dips to the W, and might be equivalent to the Ophelmaz shear zone, a W-dipping imbricate of basement, cover and ophiolitic rocks, that Malusà et al. (2005) have described nearby, along the western flank of Val de Rhêmes (loc. Fig. 1). This shear zone comprises a Vanoise-type granophyre dated at 511 ± 9 Ma (Bertrand et al., 2000a). This is in line with many similarities documented above between our A-type TPBU sample and the Vanoise felsic rocks, and would suggest an Early Paleozoic age for the TPBU protoliths. Following Malusà et al. (2005), the TPBU might represent an Alpine mélange. From this respect it would be interesting to investigate the nature and age of the associated augengneiss. Whatever the answers and waiting for further field work, instead of the classical tectonic model of a two-limbed “pli en retour du Valsavaranche”, we have evidenced here a highly dissymmetric structure in the Punta Bioula massif, with the diorite almost undeformed at the foot-wall of the highly deformed TPBU sheet.

5.4. Established facts and future research

The analyses of host-rocks in the present study confirm that they belong to the Vanoise series. The host-rocks have the same characters as typical Vanoise rocks, a fact that adds a nail in the coffin of the traditional attribution to Permo-Carboniferous of all the Penninic basement protoliths. Field occurrences of flattened sill-and-dyke systems suggest that the tholeiitic mafic levels of this basement were intrusive in the metapelite–metagreywacke series, which might be of Cambrian or even older age.

Neither the country-rock metapelites, nor other Lower Paleozoic basement units like the Rutor massif (Guillot et al., 2002), the latter as possible candidate for an ~360 Ma lower crust, have yet been investigated isotopically. Obviously, further data are needed before reconstituting the local lithosphere at 360 Ma.

Supplementary data to this article can be found online at <http://dx.doi.org/10.1016/j.lithos.2012.04.010>.

Acknowledgments

Jean-Luc Potdevin, Marie Lefranc and Monique Gentric (UMR 8110 PBDS-CNRS) helped in funding the analyses. The staff and director of the Parco Nazionale del Gran Paradiso have allowed sampling inside the Park and sheltered us in mountain refuges of Orville and Gran Nomenon. Renaud Caby (Montpellier) and Enzo Callegari (Torino) provided unpublished documentation, and Marco Malusà (Milano) proposed new ideas on the Alpine shear zones. Abdoulaye Baldé, Thomas Maurin, Bénédicte Knafel, Riccardo Polino, Floriane van Leendert and Frédérique Liotard-Schneider took part to the field and lab work. We also thank Y. Rolland and an anonymous reviewer for their constructive comments. We miss Jean-Michel Bertrand, still on the Punta Bioula in September, 2009, who passed away on March 18th, 2011.

References

- Altherr, R., Holl, A., Hegner, E., Langer, C., Kreuzer, H., 2000. High-potassium, calc-alkaline I-type plutonism in the European Variscides: northern Vosges (France) and northern Schwarzwald (Germany). *Lithos* 50, 51–73.
- Amstutz, A., 1962. Notice pour une carte géologique de la vallée de Cogne et de quelques autres espaces au sud d'Aoste. Archives des Sciences, Société de Physique et d'Histoire Naturelle de Genève (eds) 15, 1–104.
- Angiboust, S., Agard, P., Jolivet, L., Beyssac, O., 2009. The Zermatt-Saas ophiolite: the largest (60-km wide) and deepest (c. 70–80 km) continuous slice of oceanic lithosphere detached from a subduction zone? *Terra Nova* 21, 171–180.
- Argand, E., 1910. Les nappes de recouvrement des Alpes Pennines et leurs prolongements structuraux, une carte tectonique et deux stéréogrammes avec texte explicatif. Beiträge zur Geologischen Karte der Schweiz, n.F. XXXI 25 pp.
- Argand, E., 1911. Sur les plissements en retour et la structure en éventail dans les Alpes occidentales (17 mai 1911). Bulletin de la Société Vaudoise des Sciences Naturelles XLVII, XXXIII–XXXVI.
- Barbarin, B., 1999. A review of the relationships between granitoid types, their origins and their geodynamic environments. *Lithos* 46, 605–626.
- Beltrando, M., Lister, G.S., Forster, M., Dunlap, W.J., Fraser, G., Hermann, J., 2009. Dating microstructures by the $40\text{Ar}/39\text{Ar}$ step-heating technique: deformation–pressure–temperature–time history of the Penninic Units of the Western Alps. *Lithos* 113, 801–819.
- Bertrand, J.-M., Leterrier, J., 1997. Granitoïdes d'âge Paléozoïque inférieur dans le socle de Vanoise méridionale: géochronologie U–Pb du métagranite de l'Arpont (Alpes de Savoie, France). Comptes Rendus de l'Académie des Sciences – Série IIa 325, 839–844.
- Bertrand, J.-M., Guillot, F., Leterrier, J., 2000a. Early Paleozoic U–Pb age of zircons from metagranophyres of the Grand-Saint-Bernard Nappe (zona interna, Aosta Valley, Italy) [abridged English version]. Comptes Rendus de l'Académie des Sciences – Série IIa 330, 473–478.
- Bertrand, J.-M., Pidgeon, R.T., Leterrier, J., Guillot, F., Gasquet, D., Gattiglio, M., 2000b. SHRIMP and IDTIMS U–Pb zircon ages of the pre-Alpine basement in the Internal Western Alps (Savoy and Piemont). Schweizerische Mineralogische und Petrographische Mitteilungen 80, 225–248.
- Bertrand, J.-M., Paquette, J.-L., Guillot, F., 2005. Permian zircon U–Pb ages in the Gran Paradiso massif: revisiting post-Variscan events in the Western Alps. Schweizerische Mineralogische und Petrographische Mitteilungen 85, 15–29.
- Beucler, M., Guillot, F., Hernandez, J., 2000. Granophyric rocks of the Mont Pourri area (northern Vanoise, Savoie, France): lithostratigraphy and petrology. Bulletin de la Société Vaudoise de Sciences Naturelles 87, 29–60.
- Bousquet, R., 2008. Metamorphic heterogeneities within a single HP unit: overprint effect or metamorphic mix? *Lithos* 103, 46–69.
- Bucher, S., Bousquet, R., 2007. Metamorphic evolution of the Briançonnais units along the ECORS-CROP profile (Western Alps): new data on metasedimentary rocks. *Swiss Journal of Geosciences* 100, 227–242.
- Bussy, F., Derron, M.-H., Jacquot, J., Sartori, M., Thélín, P., 1996. The 500 Ma-old Thyon metagranite: a new A-type granite occurrence in the western Penninic Alps (Wallis, Switzerland). *European Journal of Mineralogy* 8, 565–575.
- Caby, R., 1968. Contribution à l'étude structurale des Alpes Occidentales: subdivisions stratigraphiques et structure de la zone du Grand-Saint-Bernard dans la partie sud du Val d'Aoste (Italie). Travaux du Laboratoire de Géologie de la Faculté des Sciences de Grenoble 44, 95–111.
- Carignan, J., Hild, P., Mevelle, G., Morel, J., Yeghicheyan, D., 2001. Routine analyses of trace elements in geological samples using flow injection and low pressure on-line liquid chromatography coupled to ICP-MS: a study of geochemical reference materials BR, DR-N, UB-N, AN-G and GH. *Geostandards Newsletter: The Journal of Geostandards and Geoanalysis* 25, 187–198.
- Cigolini, C., 1992. Note illustrative alla carta geologica del ricoprimento del Gran San Bernardo tra la Valsavarenche e la Val di Rhêmes (Valle d'Aosta) scala 1:20.000. Documento tecnico, Regione Autonoma della Valle d'Aosta - Assessorato Agricoltura, Forestazione e Risorse Naturali (eds.), 25 p.
- Cigolini, C., 1995. Geology of the Internal Zone of the Grand Saint Bernard Nappe: a metamorphic Late Paleozoic volcano-sedimentary sequence in South-Western Aosta Valley (Western Alps). In: Lombardo, B. (Ed.), *Studies on Metamorphic*

- Rocks and Minerals of the Western Alps. A Volume in Memory of Ugo Pognante, 13. Bollettino del Museo Regionale di Scienze Naturali, Torino, pp. 293–328.
- Clemens, J.D., Stevens, G., Farina, F., 2011. The enigmatic sources of I-type granites: the peritectic connexion. *Lithos* 126, 174–181.
- Cosma, L., 1999. Géologie et magmatisme paléozoïque en Vanoise septentrionale (La Sauvire, Plan Richard). Implications géodynamiques. Unpubl. mem., Dipl. Géol. Min. Univ. Lausanne, 117 p.
- DeBari, S.M., Anderson, R.G., Mortensen, J.K., 1999. Correlation among lower to upper crustal components in an island arc: the Jurassic Bonanza arc, Vancouver Island, Canada. *Canadian Journal of Earth Sciences* 36, 1371–1413.
- Debelmas, J., Caby, R., Desmons, J., Dabrovsky, H., Fabre, J., Mercier, D., Pachoud, A., 1991. Notice explicative de la Feuille Sainte-Foy-Tarentaise. Carte géol. Fr. (1/50 000), Bureau de Recherches Géologiques et Minières eds, Orléans 728, 43 p.
- DePaolo, D.J., 1981. Neodymium isotopes in the Colorado Front Range and crust–mantle evolution in the Proterozoic. *Nature* 291, 193–196.
- DePaolo, D.J., 1988. Neodymium isotope geochemistry: an introduction. *Minerals and rocks Series*, Springer eds. Berlin-New York 20, XI–187 p.
- Fenoglio, M., Rigault, G., 1959. Studi geologico-petrografici sulla formazione dioritica di Cogne – Valsavaranche (Valle d'Aosta). *Rendiconti della Accademia nazionale dei Lincei VIII (XXVI)*, 335–344.
- Fenoglio, M., Rigault, G., 1962. Studi geologico-petrografici sulla formazione dioritica di Cogne – Valsavaranche: gabbrodiorite della zona Punta Bioula – Punta Bianca (Valle d'Aosta). *Atti della Accademia delle Scienze di Torino* 96, 506–516.
- Gabudianu Radulescu, I., Rubatto, D., Gregory, C., Compagnoni, R., 2009. The age of HP metamorphism in the Gran Paradiso Massif, Western Alps: a petrological and geochronological study of “silvery micaschists”. *Lithos* 110, 95–108.
- Grasso, E., 1974. Studi geologico-petrografici sul massiccio intrusivo di Cogne-Valsavaranche, con particolare riguardo ai suoi contatti. Unpubl. Thesis Mem. Ist. Petr. Univ. Torino, 219 p.
- Grove, T.L., Juster, T.C., 1989. Experimental investigations of low-Ca pyroxene stability and olivine–pyroxene–liquid equilibria at 1-atm in natural basaltic and andesitic liquids. *Contributions to Mineralogy and Petrology* 103, 287–305.
- Guillot, F., 1987. Géologie de l'Antépermien de Vanoise septentrionale (zone Briançonnaise interne, Alpes occidentales, Savoie, France). Unpubl. mem., Thèse Doct. Univ. Lille, 280 p.
- Guillot, F., 2011. Syn-emplacement softening of host-rock around the Cogne diorite pluton (W-Alps, Valle d'Aosta). VII Hutton Symposium, Avilà 4–9 July 2011, pp. 63–64. Abstract volume.
- Guillot, F., Liégeois, J.-P., Fabre, J., 1991. Late Cambrian Mt Pourri granophyres, first dating by U–Pb on zircon of a basement in the internal French Alps (Penninic Alps, Briançonnaise Zone, Vanoise) [abridged English version]. *Comptes Rendus de l'Académie des Sciences – Série II* 313, 239–244.
- Guillot, F., Desmons, J., Ploquin, A., 1993. Lithostratigraphy and geochemical composition of the Mt. Pourri volcanic basement, Middle Penninic W-Alpine zone, France. *Schweizerische Mineralogische und Petrographische Mitteilungen* 73, 319–334.
- Guillot, F., Schaltegger, U., Bertrand, J.M., Deloule, É., Baudin, T., 2002. Zircon U–Pb geochronology of Ordovician magmatism in the polycyclic Ruitor Massif (Internal W-Alps). *International Journal of Earth Sciences* 91, 964–978.
- Harrison, T.M., Watson, E.B., 1984. The behavior of apatite during crustal anatexis: equilibrium and kinetic considerations. *Geochimica et Cosmochimica Acta* 48, 1467–1477.
- Hermann, F., 1925. Sur le faisceau de plis en retour de Valsavarenche et les prolongements de l'éventail de Bagnes dans les Alpes franco-italiennes. *Comptes Rendus de l'Académie des Sciences* 180, 1515–1517.
- Irvine, T.N., Baragar, W.R.A., 1971. A guide to the chemical classification of the common volcanic rocks. *Canadian Journal of Earth Sciences* 8, 523–548.
- Larocque, J., Canil, D., 2010. The role of amphibole in the evolution of arc magmas and crust: the case from the Jurassic Bonanza arc section, Vancouver Island, Canada. *Contributions to Mineralogy and Petrology* 159, 475–492.
- Le Maitre, R.W., 1976. Some problems of the projection of chemical data into mineralogical classifications. *Contributions to Mineralogy and Petrology* 56, 181–189.
- Malusà, M.G., Polino, R., Martin, S., 2005. The Gran San Bernardo nappe in the Aosta valley (western Alps): a composite stack of distinct continental crust units. *Bulletin de la Société Géologique de France* 176, 417–431.
- McCulloch, M.T., Chappell, B.W., 1982. Nd isotopic characteristics of S- and I-type granites. *Earth and Planetary Science Letters* 58, 51–64.
- Michard, A., Goffé, B., 2005. Recent advances in Alpine studies: tracking the Caledonian–Variscan belt in the internal western Alps. *Comptes Rendus Geoscience* 337, 715–718.
- Novarese, V., 1894. Dioriti granitoidi e gneissiche della Valsavaranche (Alpi Graie). *Bollettino del Reale Comitato Geologico d'Italia* 3, 275–301.
- Novarese, V., 1909. Il profilo della Grivola (Alpi Graie). *Bollettino del Reale Comitato Geologico d'Italia* 40, 497–525.
- Pearce, J.A., Harris, N.B.W., Tindle, A.G., 1984. Trace element discrimination diagrams for the tectonic interpretation of granitic rocks. *Journal of Petrology* 25, 956–983.
- Pe-Piper, G., Piper, D.J.W., Tsikouras, B., 2010. The late Neoproterozoic Frog Lake hornblende gabbro pluton, Avalon Terrane of Nova Scotia: evidence for the origins of appinites. *Canadian Journal of Earth Sciences* 47, 103–120.
- Pin, C., Paquette, J.-L., 2002. Sr–Nd isotope and trace element evidence for a Late Devonian active margin in northern Massif-Central (France). *Geodinamica Acta* 15, 63–77.
- Pin, C., Santos Zalduegui, J.F., 1997. Sequential separation of light rare-earth elements, thorium and uranium by miniaturized extraction chromatography: application to isotopic analyses of silicate rocks. *Analytica Chimica Acta* 339, 79–89.
- Ring, U., Collins, A.S., Kassem, O.K., 2005. U–Pb SHRIMP data on the crystallization age of the Gran Paradiso augengneiss, Italian Western Alps: further evidence for Permian magmatic activity in the Alps during break-up of Pangea. *Eclogae Geologicae Helvetiae* 98, 363–370.
- Roach, R.A., 1964. Mineral banding and appinites in the Bon Repos meladiorite, Guernsey, Channel Islands. *Proceedings of the Geologists' Association* 75, 185–198.
- Salot, P., 1978. Le métamorphisme dans les Alpes françaises. Unpubl. mem., Thèse Univ. Paris-Orsay, 190 p.
- Sandrone, R., Colombo, A., Fiora, L., Fornaro, M., Lovera, E., Tunesi, A., Cavallo, A., 2004. Contemporary natural stones from the Italian western Alps (Piedmont and Aosta Valley Regions). *Periodico di Mineralogia* 73, 211–226.
- Shaw, A., Downes, H., Thirlwall, M.F., 1993. The quartz-diorites of Limousin: elemental and isotopic evidence for Devonian–Carboniferous subduction in the Hercynian belt of the French Massif Central. *Chemical Geology* 107, 1–18.
- Sisson, T.W., Grove, T.L., 1993. Temperatures and H₂O contents of low-MgO high-alumina basalts. *Contributions to Mineralogy and Petrology* 113, 167–184.
- Stampfli, G.M., Kozur, H.W., 2006. Europe from the Variscan to the Alpine cycles. *Geological Society, London, Memoirs* 32, 57–82.
- Sun, S.-s., McDonough, W.F., 1989. Chemical and isotopic systematics of oceanic basalts: implications for mantle composition and processes. *Geological Society of London, Special Publications* 42, 313–345.
- Tindle, A.G., Webb, P.C., 1994. Probe-AMPH—A spreadsheet program to classify microprobe-derived amphibole analyses. *Computers & Geosciences* 20, 1201–1228.
- Watson, E.B., Harrison, T.M., 1983. Zircon saturation revisited: temperature and composition effects in a variety of crustal magma types. *Earth and Planetary Science Letters* 64, 295–304.
- Wells, A.K., Bishop, A.C., 1955. An appinitic facies associated with certain granites in Jersey, Channel Islands. *Quarterly Journal of the Geological Society* 111, 143–166.
- White, D.A., Roeder, D.H., Nelson, T.H., Crowell, J.C., 1970. Subduction. *Geological Society of America Bulletin* 81, 3431–3432.
- Wood, D.A., 1980. The application of a Th–Hf–Ta diagram to problems of tectonomagmatic classification and to establishing the nature of crustal contamination of basaltic lavas of the British Tertiary Volcanic Province. *Earth and Planetary Science Letters* 50, 11–30.
- Zhou, J., Li, X., 2006. GeoPlot: an Excel VBA program for geochemical data plotting. *Computers & Geosciences* 32, 554–560.

A.5.2 Article 9 : Pourteau et al. (in revision), Journal of Metamorphic Geology

Neotethys closure history of Anatolia: insight from ^{40}Ar - ^{39}Ar geochronology and P - T estimation in high-pressure metasedimentsPourteau A.^{1*}, Sudo M.¹, Candan O.², Lanari, P.³, Vidal O.³, Oberhänsli R.¹¹Institut für Erd- und Umweltwissenschaften, Universität Potsdam, Karl-Liebknecht-Straße 24-25, 14476 Potsdam-Golm, Germany²Dokuz Eylül Üniversitesi, Mühendislik Fakültesi, Jeoloji Mühendisliği Bölümü, Tınaztepe Kampusu, 35160 Buca-Izmir, Turkey³Isterre, Université Joseph Fourier Grenoble, CNRS, 1381 rue de la Piscine, 38041 Grenoble cedex 09, France

*Corresponding author:

E-mail: pourteau@geo.uni-potsdam.de

Tel.: +49 331 977 5846

Fax: +49 331 977 5700

ABSTRACT

High-pressure (HP), low-temperature (LT) metamorphic rocks represent essential tracers of the evolution of ancient convergent plate boundaries. Their occurrence at the Earth's surface, as well as their spatiotemporal distribution are useful for unravelling the geodynamic evolution and the palaeogeography of complex tectonic mosaics, such as the Eastern Mediterranean region. There, HP-LT rocks document the accretion of Gondwana-derived continental terranes to Southern Eurasia between late Cretaceous and Neogene times. In Western and Central Anatolia, subduction- and collision-related metamorphism along the northern edge of the Anatolide-Tauride Block occurred in an uncommonly long interval of 50-40 Ma. Recent reports of the HP-LT index mineral Fe-Mg-carpholite in three metasedimentary units of this microcontinent (namely the Afyon Zone, the Ören Unit and the southern Menderes Massif) suggest a more complicated scenario than the single-continental accretion model generally put forward in previous studies. We present the first radiometric ages (phengite ^{40}Ar - ^{39}Ar geochronology) combined with P - T estimates (multi-equilibrium thermobarometry) on carpholite-bearing rocks from these three HP-LT metasedimentary units. We show that, in the Afyon Zone, carpholite-bearing assemblages experienced retrogression through greenschist-facies conditions (0.9 GPa/400°C to 0.6 GPa/350°C) around 66-61 Ma. The early retrograde stages in the Ören Unit occurred around 62-59 Ma. In the Kurudere-Nebiler Unit (HP Mesozoic cover of the southern Menderes Massif) carpholite retrogression is dated to ca. 45 Ma, and post-collisional cooling to ca. 26 Ma. Based on these new results, we discuss the tectonic relations between these HP-LT units. We argue that the Ören Unit represents the westernmost continuation of the Afyon Zone, while the Kurudere-Nebiler Unit correlates with the Cycladic Blueschists of the Aegean Domain. In Western Anatolia, three successive HP-LT metamorphic belts thus formed: the northernmost Tavşanlı Zone (around 88-80 Ma), the Ören-Afyon Zone (between 70 and 60 Ma), and the Kurudere-Nebiler Unit (around 53-45 Ma). Radiometric HP metamorphic ages hence display younging of the HP-LT metamorphism towards deeper and more external (southwards) structural units. We restore the easternmost part of the Aegean Pindos Ocean into Western Anatolia between the Ören-Afyon Zone and the Kurudere-Nebiler Unit. Therefore, we explain the accretion of the Anatolian-Tauride Block by the successive closures of two Neotethyan oceanic basins during continuous northward subduction.

Keywords: High-pressure metasediments • Anatolia • ^{40}Ar - ^{39}Ar geochronology • Multi-equilibrium thermobarometry

INTRODUCTION

High-pressure (HP), low-temperature (LT) metamorphic rocks exposed at the Earth's surface represent premier tracers of the evolution of past and modern convergent plate boundaries, and hence are useful to investigate subduction-related processes. Although the mechanisms of HP-LT rock exhumation remains intensely discussed, their spatiotemporal distribution are essential to unravel the geodynamic evolution of complex tectonic mosaics, such as the Alpine-Himalayan convergence belt. Palaeotectonic and palaeogeographic reconstructions of the Mediterranean region (e.g. Şengör & Yılmaz, 1981; Robertson *et al.*, 1991; Stampfli *et al.*, 1991; Dercourt *et al.*, 1993; Barrier & Vrielinck, 2008) showed that, during most of the Mesozoic, the western Tethyan realm consisted of a collection of narrow oceanic basins separating microcontinents, likely similar to the modern Caribbean and South-eastern Asian regions. Continuous convergence between Africa-Arabia and Eurasia since the middle Cretaceous (e.g. Dewey *et al.*, 1989; Torsvik *et al.*, 2008) was accommodated by the subduction of these oceanic basins, which led to drag (part of) these microcontinents into depth. Our study provides new insights into the geodynamic evolution of this region by investigating of the metamorphic history of ancient continental terranes.

In Western and Central Anatolia, subduction- and collision-related metamorphic events associated to the accretion of the Gondwana-derived Anatolide-Tauride Block to the southern composite margin of Eurasia occurred in an interval greater than 40 m.y. – 88-78 Ma for the HP-LT metamorphism vs. 40-30 Ma for the Barrovian metamorphism; see details below). For comparison, a period of only 15-20 m.y. is generally observed in other collisional zones, like the Central Alps (e.g. Wiederkehr *et al.*, 2009). Although this is known for more than a decade (Sherlock *et al.*, 1999), no tectonic reconstruction for Anatolia accounts for this peculiar feature yet.

In the last past years, Fe-Mg-carpholite-bearing assemblages, as evidence for HP-LT metamorphism, were documented in several tectonic units of Western and Central Anatolia (Oberhänsli *et al.*, 2001; Rimmelé *et al.*, 2003a; Rimmelé *et al.*, 2003b; Candan *et al.*, 2005; Rimmelé *et al.*, 2006; Pourteau *et al.*, 2010) that were until then supposedly characterized by greenschist-facies metamorphism (e.g. Okay *et al.*, 1996). These discoveries, although shattering previous geodynamic reconstructions, have opened perspectives towards a better understanding of the regional tectonic evolution. The timing of subduction-related metamorphism in these units still needs to be determined to place their burial and exhumation into an accurate timeframe. In this study, we combined ^{40}Ar - ^{39}Ar geochronology and multi-equilibrium thermobarometry in white mica-, carpholite-bearing rocks and were able to establish the exact significance of the age results. Based on these new data, we propose a new evolutionary model for the evolution of Western Anatolia from 85 to 15 Ma.

GEOLOGICAL SETTINGS

Tectonic domains of western Anatolia

Western to Central Anatolia is composed of three tectonic regions that experienced contrasting tectonic histories between Late Cretaceous to Palaeogene times (Ketin, 1966). Northern Anatolia exposes a polystage fold-thrust belt known as the Pontides, which are characterized by pre-Jurassic metamorphic rocks with unconformable non-metamorphosed Jurassic to Cretaceous sediments and volcanic rocks (Altiner *et al.*, 1991; Yılmaz *et al.*, 1995; Okay & Sahinturk, 1997). Central Anatolia is composed of the Central Anatolian Crystalline Complex made of late Cretaceous intrusions and Barrovian metamorphic rocks (e.g. Seymen, 1981; Göncüoğlu *et al.*, 1997; Aydın *et al.*, 1998; Whitney *et al.*, 2001) with inferred early Palaeozoic to Mesozoic protolithic ages (Kocak & Leake, 1994; Göncüoğlu, *et al.*, 1997). In the Late Cretaceous and early Cenozoic, arc magmatism above the north-dipping Neotethys subduction zone took place in the Pontides (Şengör & Yılmaz, 1981; Okay & Satır, 2006) and the Central Anatolian Crystalline Complex (Kadioğlu *et al.*, 2003; Ilbeyli *et al.*, 2004).

Western and Southern Anatolia consists of metamorphosed and non-metamorphosed Precambrian to Eocene rocks, known as the Anatolide-Tauride Block (Okay & Tüysüz, 1999). This domain is characterized by a Precambrian crystalline basement of Gondwana affinity (Pan-African orogeny, late Ordovician glaciation; Monod *et al.*, 2003), and late Cretaceous to early Cenozoic HP-LT metamorphism that affected its northern passive margin (e.g. Şengör & Yılmaz, 1981; Pourteau, et al., 2010).

Anatolide-Tauride units

Following the definitions of Ketin (1966) and Şengör & Yılmaz (1981), the term ‘Anatolides’ is used to designate the rocks affected by Alpine regional metamorphism, and the term ‘Taurides’ designates the non-metamorphosed thrust and folded external platform (Fig. 1).

The Taurides, which consist of Precambrian to Eocene sediments and Neotethyan ophiolites, were affected by multistage deformation between latest Cretaceous and late Miocene times, leading to the formation of regional-scale nappe systems (e.g. Lycian Nappes; Gutnic *et al.*, 1979; Collins & Robertson, 1998). The NW edge of the Menderes Nappes is thrust below the Bornova Zone, representing a non-metamorphosed, tectonized Maastrichtian-Danian “megaolistostrom”, which likely formed along a sinistral transform zone at the edge of the Anatolide-Tauride Block (Okay, et al., 1996).

We summarize the main characteristics and nomenclature of the western Anatolides, where it was best described, and expand this tectono-stratigraphy eastwards. For further details, the reader is referred to Jolivet *et al.* (2012). The Western Anatolides are composed of a metamorphosed Mesozoic sedimentary sequence, and its substratum represented by Precambrian high-grade metamorphic and intrusive rocks and Palaeozoic sedimentary and volcanic formations (e.g. Şengör & Yılmaz, 1981; Okay, et al., 1996). The general Mesozoic lithostratigraphy consists of a continuous succession of Triassic clastic sediments (with volcanic intercalations) followed by upper Triassic to upper Cretaceous neritic carbonates followed by pelagic limestones, cherts, flysches and olistostroms (e.g. Bozkurt & Oberhänsli, 2001). This sequence is interpreted as the continuous record of the development of a continental passive margin from rifting in the early Triassic (e.g. Akal *et al.*, 2011) to oceanization in the middle Triassic, and later carbonate platform drowning in the late Cretaceous, as it entered the trench of the north-dipping Neotethyan subduction zone (Okay *et al.*, 2001). Between the Late Cretaceous and the early Cenozoic, parts of the continental margin were metamorphosed in a subduction zone, as evidenced by the occurrence of widespread HP-LT minerals in lower Triassic sediments and volcanic rocks (Okay, et al., 1996; Pourteau, et al., 2010). Owing to contrasting lithostratigraphies and metamorphic grades, the Anatolides are subdivided into several tectonic units (Fig. 1).

The Tavşanlı Zone is a late Cretaceous HP-LT metamorphic belt (Okay, 1984), derived from the most distal parts of the north-facing Anatolide-Tauride platform (Candan, *et al.*, 2005). In its western part, the Tavşanlı Zone is characterized by well-preserved lawsonite-glaucophane-bearing assemblages in metasediments and metavolcanic rocks, for which peak *P-T* conditions were estimated as 2.0 to 2.6 GPa and 430 to 550°C (Okay & Kelley, 1994; Okay, 2002; Davis & Whitney, 2006; Çetinkaplan *et al.*, 2008; Davis & Whitney, 2008). Sporadic occurrence of blueschist blocks in mélange localities near Konya, in the Bolkar Mountains and near Kayseri (van der Kaaden, 1966; Droop *et al.*, 2005) outline the eastward continuation of the Tavşanlı Zone into Central Anatolia (Okay, 1984; Pourteau, et al., 2010). Lawsonite blueschists from near Konya experienced 0.9-1.1 GPa and 375-450°C (Droop *et al.*, 2005). The good preservation of lawsonite throughout the unit indicates cooling during decompression. Radiometric ages obtained on blueschists from the western Tavşanlı Zone range between 88 and 78 Ma (^{40}Ar - ^{39}Ar and ^{87}Rb - ^{86}Sr on phengite; Table 1 and references therein). Near Orhanlı and Sivrihisar, the Tavşanlı Zone is overlain by an ophiolitic complex, composed of peridotites and an ophiolitic mélange. The tectonic contact between the HP-

LT rocks and the ophiolites is sealed by early Eocene calc-alkaline intrusions derived from mantle wedge melts (Harris *et al.*, 1994; Delaloye & Bingol, 2000).

The Afyon Zone, which occurs south of and structurally below the Tavşanlı Zone, is a low-grade HP metamorphic belt (Pourteau, *et al.*, 2010), representing the complete segment of a Mesozoic continental passive margin, including a polymetamorphic Precambrian substratum (Candan, *et al.*, 2005). Fe-Mg-carpholite, glaucophane and calcite pseudomorphs after aragonite documented throughout the Afyon Zone are evidence for blueschist-facies metamorphism (Candan, *et al.*, 2005; Pourteau, *et al.*, 2010). Based on carpholite-chloritoid assemblages in metasediments, metamorphic conditions experienced by the Afyon Zone were estimated as 0.8-1.1 GPa and 250 to 350°C (Candan, *et al.*, 2005; Pourteau, 2011). No radiometric age information is available yet for the metamorphic evolution of the Afyon Zone, but stratigraphic relations leave a possible interval between the end of the Campanian and the Late Palaeocene (Dirik *et al.*, 1999; Candan, *et al.*, 2005; Özer & Tansel Öngen, 2012).

The Menderes Massif, which occurs as a regional tectonic window below the other metamorphic units (Fig. 1), exhibits a complicated internal structure (e.g. Şengör *et al.*, 1984; Gessner *et al.*, 2001b; Okay, 2001; Ring *et al.*, 2001). Yet, a general lithostratigraphy can be restored. It consists of a polymetamorphic (Pan-African and Alpine metamorphisms; Candan *et al.*, 2011) gneiss core overlain by monometamorphic Palaeozoic schist and Mesozoic marble covers, and a Palaeogene olistostrom (Schuiling, 1962; Dürr, 1975; Özer *et al.*, 2001). The Menderes Massif is generally characterized by Barrovian-type metamorphism (Bozkurt & Oberhänsli, 2001; Gessner *et al.*, 2001a; van Hinsbergen, 2010) for which *P-T* estimates are 0.4-0.5 GPa and 330-530°C (monometamorphic Palaeozoic schists from the southern Menderes Massif; Whitney & Bozkurt, 2002; Régnier *et al.*, 2003). In the same region, Fe-Mg-carpholite relics were described at the base of the Mesozoic carbonate sequence, as evidence for HP-LT metamorphism in this part of the massif (Rimmelé, *et al.*, 2003b; Whitney *et al.*, 2008). The preservation of carpholite (i.e. the occurrence of relics vs. pseudomorphs) correlates with that of diaspore in metabauxite horizon in platform-type marbles (see Rimmelé, *et al.*, 2003b), as also mentioned in the Cycladic Blueschists (Candan *et al.*, 1997). *P-T* estimates are 1.2-1.4 GPa/470-550°C in Kurudere, 0.6-0.8 GPa/400-450°C in Bahçekaya, and 0.9-1.1 GPa/380-480°C in Nebiler (Rimmelé, *et al.*, 2003b; Rimmelé *et al.*, 2005; Whitney, *et al.*, 2008). This HP-LT metamorphic event likely affected the entire Mesozoic marble sequence, described as stratigraphically continuous (Dürr, 1975; Özer, *et al.*, 2001), but not the Palaeozoic schist cover, which, even in parts only affected by low-grade conditions (chlorite zone; Schuiling, 1962), lacks HP minerals. We therefore consider that, in this region, only the marble cover (including basal conglomerates containing carpholite relics) experienced HP-LT metamorphism. Hence, we subdivide the Menderes Massif *sensu lato* into the low- to middle-*P* Menderes Nappes (Gessner, *et al.*, 2001a), and the new-termed HP-LT Kurudere-Nebiler Unit (Fig. 1). This HP-LT metamorphism was not dated radiometrically yet, but it is predated by the middle Palaeocene depositional age of the olistostrom topping the Cretaceous marble (Özer *et al.*, 2001), and post-dated by the Barrovian metamorphism, which likely occurred around 35 ± 5 Ma (Satır & Friedrichsen, 1986; Bozkurt & Satır, 2000; Lips *et al.*, 2001). Therefore, the HP-LT metamorphic history of the Kurudere-Nebiler Unit likely occurred some time between the late Palaeocene and the Eocene. It is noteworthy that Ring *et al.* (1999) have regarded most of the Mesozoic cover of the entire Menderes Massif *sensu lato* as the continuation of the Cycladic Blueschists, even parts free of HP relics.

The Ören Unit (Pourteau, *et al.*, 2010), formerly referred to as the metamorphosed part of the Lycian Nappes (Oberhänsli *et al.*, 2001; Rimmelé *et al.*, 2003a), lies structurally over the Kurudere-Nebiler Unit, the Menderes Massif, and the Cycladic Blueschists (Fig. 1). Kinematic indicators (Rimmelé *et al.*, 2003a; Rimmelé *et al.*, 2006) indicate that, during the late stage of its exhumation, the Ören Unit was transported over these units towards the ESE (after restoration from the Neogene extensional deformation; see Pourteau *et al.*, 2010; van Hinsbergen, 2010). Fe-Mg-

carpholite in the lower metasediments and calcite pseudomorphs after aragonite in marbles are widespread evidence for blueschist-facies metamorphism (Oberhänsli *et al.*, 2001; Rimmelé *et al.*, 2003a, 2006). Peak P - T conditions were estimated to be about 1.2 GPa and 400°C (Rimmelé *et al.*, 2005). Rocks near the base of the Ören Unit (including the klippen) experienced isothermal decompression at ca. 400-450°C, while at higher tectonostratigraphic positions rocks experienced cooling during decompression. This shows that the thermal evolution of HP-LT rocks during their exhumation can significantly vary within a single tectonic unit. Poorly constrained ^{40}Ar - ^{39}Ar ages between 90 and 70 Ma were obtained on high-Si phengite from metasediments as the only radiometric metamorphic age estimate for the Ören Unit (Ring & Layer, 2003). Stratigraphic relations constrain the HP-LT metamorphic event into a latest Cretaceous to Eocene interval (Rimmelé *et al.*, 2003a). Owing to its structural position, metamorphic evolution and lithostratigraphy, the Ören Unit might be envisaged to represent the western continuation of the Afyon Zone.

In Western Anatolia, the Cycladic Blueschists, which are also widely exposed in the Aegean Domain, consist of two HP metamorphic units (a lower platform sequence and an upper metamorphic mélange) that lie tectonically over the western Menderes Nappes (Candan *et al.*, 1997; Oberhänsli *et al.*, 1998; Ring *et al.*, 1999; Okay, 2001). Peak P - T estimates are 1.1-1.5 GPa and 440-550°C (Çetinkaplan, 2002; Ring *et al.*, 2007). These HP rocks were exhumed to upper-crust depths around 38-32 Ma, following an isothermal decompression path through the greenschist facies (Ring *et al.*, 2007). An ^{40}Ar - ^{39}Ar age of 40.1 ± 0.4 Ma was obtained on retrograde phengite from epidote blueschists (Oberhänsli *et al.*, 1998), consistently with the metamorphic evolution of the Cycladic Blueschists in the Aegean Domain (see Jolivet & Brun, 2008; Ring *et al.*, 2010).

Several tectonic units of the Anatolide-Tauride Block are topped by widespread ophiolites (Fig. 1), which were generated above a subduction zone (e.g. Önen & Hall, 1993; Parlak *et al.*, 1996). Greenschist- to amphibolite-facies sub-ophiolitic metamorphic soles formed during subduction initiation were dated to 95-90 Ma (see Robertson, 2002; Çelik *et al.*, 2006).

P - T ESTIMATION AND ^{40}Ar - ^{39}Ar GEOCHRONOLOGY

Fe-Mg-carpholite-bearing metasediments are the main, or locally the only evidence of Alpine HP-LT metamorphism in the Afyon Zone, the Ören Unit and the Kurudere-Nebiler Unit. K-rich white mica (below referred to as phengite), often accompanied by chlorite, commonly occurs in carpholite-bearing rocks, offering the chance to determine the age of metamorphism by using ^{40}Ar - ^{39}Ar geochronology. Several studies previously showed that this approach yields reliable metamorphic ages (Jolivet *et al.*, 1996; Agard *et al.*, 2002; Wiederkehr *et al.*, 2009; Oberhänsli *et al.*, 2010, 2012). In these rocks, phengite may have formed before, during and after carpholite growth, so several generations can coexist in a single sample and thus provide various radiometric ages (Agard *et al.*, 2002; Wiederkehr *et al.*, 2008, 2009). In order to evaluate the possibility of such situations, P - T conditions prevailing during the growth of the dated phengite can be estimated by chlorite-phengite thermobarometry (multi-equilibrium approach; see Vidal & Parra, 2000). Therefore, when possible, we combined ^{40}Ar - ^{39}Ar age determination with P - T estimation in individual samples to decipher the actual significance of radiometric dating results.

Sample selection

Selection criteria

For ^{40}Ar - ^{39}Ar geochronology, we selected samples, in which white mica: a) is rich in potassium and poor in sodium, b) white mica is obviously of metamorphic origin, c) occurs as medium-sized to coarse crystals ($> 125 \mu\text{m}$), d) is not intergrown with chlorite or pyrophyllite, and e) was not affected by late fluid circulation (i.e. no fractures, no late calcite crystallization). Bearing in mind that carpholite-bearing quartz vein originates from the crystallization of a fluid phase under HP-LT

conditions, phengite in such rock type is exclusively of metamorphic origin. In order to avoid the risk of the age inheritance of detrital mica recrystallized during metamorphism, we therefore preferentially selected quartz vein samples. Both fine grain size and common intergrowth of phengite with chlorite critically restricted sample selection.

Selected samples

The Afyon Zone encompasses a wide variety of carpholite-bearing rocks (Pourteau, 2011). In the region of Kütahya (Fig. 1), carpholite, in quartz veins, is mainly accompanied by chloritoid + pyrophyllite ± chlorite, and more rarely by phengite + chlorite. Samples Afy0206 (39°24'18"N 29°47'26"E), Afy0212 (39°24'35"N 29°53'51"E) and Küt0815 (39°24'27.5"N 29°48'02.2"E) were collected from the area of Kütahya. In the sample Afy0206, phengite and chlorite occur as elongated pseudomorphs after carpholite (Fig. 2a). Intergrowth is frequent, but in some areas pseudomorphs are only composed of phengite, making it possible to use in-situ laser ablation for ^{40}Ar - ^{39}Ar geochronology. The sample Afy0212 was described by Pourteau (2011) for remarkable carpholite-chloritoid textures. Pyrophyllite, which occurs as large crystals wrapping carpholite and chloritoid, contains discrete layers of low-Si (i.e. muscovite-rich) phengite. In the sample Küt0815, carpholite is rather well preserved but displays evidence for local breakdown into chlorite and pyrophyllite that here again contains thin low-Si phengite interlayers. In the region of Afyon, carpholite-bearing metapelites and metaconglomerates contain abundant, fine-grained phengite, intergrown with pyrophyllite, quartz and iron oxides, but notably no chlorite (Candan *et al.*, 2005; Pourteau, 2011). We retained the sample Bay0851 (39°02'51"N 30°49'05"E) from a carpholite-bearing silvery phyllite (Fig. 2b). The notable absence of chlorite in this sample, on the one hand, prevents its use for accurate *P-T* estimation, but, on the other hand, indicates that peak mineral assemblage (carpholite and chloritoid) was well preserved. Phengite in Bay0851 commonly contains up to 15% of the celadonite end-member (Table 2), which represents among the highest Si-content (Tschermack substitution) found in the Afyon Zone. This suggests that ^{40}Ar - ^{39}Ar radiometric dating of mica in this sample might provide near-peak metamorphic ages. In the Konya region (Fig. 1), some carpholite-quartz veins also contain white mica, but this contains a significant paragonite component, preventing any accurate *P-T* estimation and, a priori, hampering ^{40}Ar - ^{39}Ar geochronologic investigations. We tentatively performed Ar isotope analyses on a sample (38°09'55"N 32°32'50"E) from the region of Konya, but laser ablation experiments did not release any significant gas amount for Ar isotope analysis. In the easternmost regions of Yahyalı and Kayseri (Fig. 1), carpholite was substantially pseudomorphed into phengite and chlorite, locally accompanied by chloritoid. We selected the sample Yah04 (38°06'04"N 35°16'31"E), in which phengite and chlorite are mostly intergrown, but also occur as isolated crystals, allowing easy mineral separation.

In the Ören Unit, carpholite documented in quartz veins is commonly accompanied by phengite and chlorite (Oberhänsli *et al.*, 2001; Rimmelé *et al.*, 2003a). We selected the sample Ören001 (37°05'52"N 27°58'05"E; Fig. 1) from a quartz vein encompassing well-preserved carpholite needles accompanied by phengite and chlorite (Rimmelé *et al.*, 2003a). Carpholite-chlorite-phengite equilibrium in this sample accounts for *P-T* conditions of 0.8-1.1 GPa and 320-380°C (Rimmelé *et al.*, 2005).

From the Kurudere-Nebiler Unit, we retained the samples Kuru0110 (37°23'55"N 27°37'14"E; located at the diaspore-corundum isograde) and Nebil0101 (37°28'59"N 28°35'49"E; within the corundum zone), for which *P-T* estimates are available in literature (Rimmelé *et al.*, 2005). The sample Kuru0110 is a quartz vein containing the main assemblage carpholite + kyanite + chlorite + phengite + pyrophyllite. Kyanite, chlorite and phengite obviously grew coevally as the breakdown product of carpholite, which is only preserved as small fibres in quartz (Fig 2c). The easterly sample Nebil0101 is a metamorphosed quartz microconglomerate bearing kyanite + chloritoid + phengite as main assemblage. Chlorite was reported to be abundant in this sample (Rimmelé *et al.*, 2003b),

but was not seen in the sample fragment that we selected. Furthermore, no carpholite relic was observed in this sample, whereas kyanite-chlorite pseudomorphs after carpholite were described from the same locality. In the selected sample, phengite obviously formed after kyanite (Fig. 2d).

P-T estimation

P-T conditions were estimated using the chlorite-phengite-quartz-water multi-equilibrium approach proposed by Vidal & Parra (2000) and previously applied in different geological contexts (e.g. Trotet *et al.*, 2001; Parra *et al.*, 2002; Le Hebel *et al.*, 2002; Ganne *et al.*, 2003; Arkai *et al.*, 2003; Trotet *et al.*, 2006; Vidal *et al.*, 2006; Schwartz *et al.*, 2009; Verlaquet *et al.*, 2011; Grosch *et al.*, 2012; Ganne *et al.*, 2012; Lanari *et al.*, 2012a, 2012b). When possible, *P-T* conditions were also estimated from chlorite-chloritoid-quartz-water assemblages.

Method

Element mapping combined with spot analysis were performed using an electron microprobe JEOL JXA8200 (Potsdam University), following the procedure described by De Andrade *et al.* (2006). Areas selected for mapping contain the coarsest grains possible and display sharp grain boundaries (i.e. limited intergrowths). Maps dimensions are about 2,270*1,030 and 1,200*350 μm in Afy0206 and Yah04, respectively. Operating conditions for maps were 15-keV accelerating voltage, 5- μm beam size, 100-nA beam current, for counting times of 300 ms on peak. Spot analyses were acquired with 15-keV accelerating voltage, 5- μm beam size, 10-nA beam current, for counting times of 20 s on peak and 10 s on background. Standards of pyrope for Si, rutile for Ti, pyrope for Al, hypersthene for Fe, fayalite for Mn (in order to analyse accurately very low amount of Mn), diopside for Mg, diopside for Ca, anorthite for Na and microcline for K were used.

Profiles of individual spot quantitative analyses were traced across phengite-chlorite aggregates. Using these profiles as standards, each pixel of the qualitative element maps was quantified into a quantitative analysis (in oxide weight percent). This was done using XMapTools software (Lanari *et al.*, 2012a, 2012b; <http://www.xmaptools.com>). In each investigated area, a large number of spot analyses were acquired for each phase in order to ensure the precision of this quantification. Structural formulae and atom site repartition of chlorites and phengites were calculated following the solid solution models of Vidal & Parra (2000), Vidal *et al.* (2006) and Dubacq *et al.* (2010). The K-means clustering method (Saporta, 1990) was used to distribute chlorite and phengite compositions into various groups. Each group was first considered individually to calculate temperatures using the chlorite-quartz-water equilibrium (at a given pressure) following the method of Vidal *et al.* (2005, 2006). For phengite, the method of Dubacq *et al.* (2010) was used to plot a *P-T* line corresponding to the phengite-quartz-water equilibrium, with variable hydration states (% of water in interlayer vacancies). It was then possible to estimate the equilibrium pressure and phengite hydration state at the temperatures of the chlorite-quartz-water equilibria (Lanari *et al.*, 2012a). In complement, the combinations of chlorite and mica groups were tested in order to calculate *P-T* conditions with the multi-equilibrium approach including chlorite and phengite end-members (Vidal *et al.*, 2006). The presence of tiny chloritoid in Yah04, albeit not allowing element mapping, provided the possibility to calculate *P-T* conditions prevailing for local chlorite-chloritoid-quartz-water equilibrium, using the Mg- and Fe-chloritoid thermodynamic properties of Vidal *et al.* (2001) and Vidal *et al.* (1999), respectively.

Mineral analyses

In each sample, chlorite compositions were distributed into three groups: C1 to C3 (upper case) in Afy0206, and c1 to c3 (lower case) in Yah04. On the other hand, mica compositions were distributed into three groups: M1, M2, M+P in Afy0206, and m1, m2, m+p in Yah04, where M+P and m+p stand for muscovite-paragonite mixtures. Average compositions for each of these groups, except the muscovite-paragonite mixtures, are shown in the Table 2. In both samples, chlorite compositional

groups display an increase of the sudoite-content from C1 to C3 and from c1 to c3, while the proportion of the other end-members does not significantly change (Fig. 3a-a'). At fixed bulk rock composition, the abundance of the sudoite end-member (vacancy on the octahedral site [M1]) mainly depends on temperature (Cathelineau & Nieva, 1986; Hillier & Velde, 1991; Vidal *et al.*, 2001). Therefore the decrease of sudoite-content from the inner to the outer crystals (Fig. 3b-b') is interpreted as a growth of chlorite under decreasing temperature. The abundance of celadonite and pyrophyllite end-members and thus the Si-content of phengite increase with pressure. Therefore, phengites M1 and m1, which exhibit higher Si-contents than phengites M2 and m2 (Fig. 3a-a'), formed at higher pressure. Analysis of chloritoid in Yah04 reveals that X_{Mg} ($= Mg/(Fe^{2+} + Mn + Mg)$) covers a range between 0.12 and 0.15.

Thermobarometry

In Afy0206, C1, C2 and C3 chlorite average compositions give temperatures of about 351, 258 and $197 \pm 50^\circ\text{C}$ and $X_{Fe^{3+}}$ of 6, 19 and 28 % respectively. Mica groups M1 and M2 yield pressures of 6 and < 0.3 GPa at 350°C , respectively. Multi-equilibrium calculations reveal that C1 chlorite and M1 mica equilibrated at P - T conditions of ca. 0.6 GPa and ca. 350°C (Fig. 3c), which are consistent with those determined individually using chlorite-quartz-water and phengite-quartz-water equilibria.

In Yah04, the chlorite groups c1, c2 and c3 correspond to temperatures of 384, 320 and $248 \pm 50^\circ\text{C}$ at 1.0 GPa and $X_{Fe^{3+}}$ of 6, 19 and 28 % respectively. For a temperature set to 380°C , m1 and m2 micas equilibrated at 0.7 and < 0.4 GPa, respectively. Unfortunately, no equilibrium was found between the c1 chlorite and the m1 mica, but we identified an equilibrium between the c1 chlorite and average chloritoid composition ($X_{Mg} = 0.14$) at P - T conditions of ca. 0.6 GPa and ca. 350°C (Fig. 3c). In addition, P - T conditions prevailing for chlorite-chloritoid equilibrium were estimated for individual pairs of spot analyses. Conditions between 0.82 and 1.13 GPa and between 383 and 425°C were calculated (Table 3). These P - T estimates out of the stability field of carpholite (Fig. 3d-d') are consistent with the fact that chlorite and phengite in these samples occur as pseudomorphs after carpholite. No relic of HP phengite (high celadonite content) was found. ^{40}Ar - ^{39}Ar geochronology will thus consistently provide retrograde ages.

^{40}Ar - ^{39}Ar geochronology

Sample preparation

Phengite was extracted from the samples Afy0212, Küt0815, Yah04 and ÖREN001 in order to perform Ar extraction by stepwise heating of mineral separates with a CO_2 laser. Pure phengite grain bunches were obtained by scratching gently the freshly cut surface of the quartz vein samples followed by enrichment and purification using conventional techniques for mineral separation, including washing, sieving, adherence to paper and handpicking under binoculars. In order to perform Ar extraction dating by in-situ UV laser ablation, 1-mm-thick, polished rock chips were prepared from the samples Afy0206, Bay0851, Kuru0110 and Nebil0101.

Analytical procedure

Procedure for ^{40}Ar - ^{39}Ar analysis in the University of Potsdam was described in detail in the recent literature (e.g. Wiederkehr *et al.*, 2009; Willner *et al.*, 2009; Vásquez *et al.*, 2010; Wilke *et al.*, 2010). Neutron activation of polished sections and mineral separates was performed at Geesthacht Neutron Facility (GeNF), GKSS research centre in Geesthacht, Germany. The ^{40}Ar - ^{39}Ar ages were obtained as the relative age against the age of a neutron flux (or J value) monitoring mineral standard, Fish Canyon tuff sanidine, which was irradiated together with the samples of unknown ages. The Fish Canyon Tuff sanidine used was prepared by the Geological Survey of Japan and the age of 27.5 Ma was obtained and adopted (Uto *et al.*, 1997; Ishizuka, 1998; Ishizuka *et al.*, 2002). Crystals of K_2SO_4 and CaF_2 were also irradiated together in order to correct the interference of Ar isotopes produced by the nuclear reactions of K and Ca in the samples with neutron fluxes. After the

irradiation and subsequent cooling down for a month, the samples were brought back to ^{40}Ar - ^{39}Ar laboratory in the University of Potsdam for Ar isotope analysis. Analyzed samples were then loaded on a copper disc in the sample chamber and baked at 100°C during pumping for two days for reduction of atmospheric argon contamination.

The Ar isotopic analytical system in the University of Potsdam consists of: (1) a New Wave Gantry Dual Wave laser ablation system with a 50W CO₂ laser (wavelength 10.6 µm) and 6 mJ UV pulse laser (wavelength 266 nm, frequency-quadrupled) for heating and extracting gas from the samples, (2) an ultra-high vacuum purification line with SAES getters and cold trap with temperature of frozen ethanol, and (3) a Micromass 5400 noble gas mass spectrometer with a high sensitivity and a ultra-low background. The mass spectrometer has adopted a pulse counting system with an electron multiplier, which effectively works for the very small amounts of gas.

Age spectra obtained by stepwise heating of bulk grain samples were produced from bunches of 3 to 7 grains of size ranging between 125 and 500 µm, which were heated by scanning laser beam with a diameter of 1600 microns for 45 to 90 seconds with 70 µm/sec scan speed. In-situ UV laser ablation was carried out with a beam with a diameter of 50 µm and a 5 µm/sec scan speed. When phengite grains were small, the in-situ ablation was performed following long paths (up to 1500 µm) to release sufficient gas amount. Ar isotope analysis may thus yield average ages for several coexisting generations of white mica. This is evaluated below. Data have been corrected for blank, mass discrimination, decay of radiogenic ^{37}Ar and ^{39}Ar , and interference of Ar isotopes derived from K and Ca.

Raw age results

Results of Ar isotope analyses are shown in the Table 4. Representative age diagrams are presented in the Fig. 4. A significant plateau age is defined by a series of adjacent steps, which represent individually more than 5 % and in all more than 50 % of the total ^{39}Ar release and contiguously agree within 2-SD error limits as McDougall & Harrison (1999) mentioned. The age spectra obtained fully satisfy these conditions. On the other hand, in-situ age results are displayed in 'pseudo-plateau' diagrams (Fig. 4b) in order to show the representability of each spot analysis in terms of released gas amount.

Afyon Zone. In-situ laser ablation in Afy0206 provided age results scattered between 47.1 ± 3.8 and 66.4 ± 6.1 Ma, without apparent correlation between age, atmospheric Ar content and released-gas amount. Five of the ten steps, representing about 52% of the total ^{39}Ar release, give an average age of 62.8 ± 1.5 Ma (Fig. 5a). In-situ laser ablation in Bay0851 provided scattered age results that, except one analyse, are distributed into two groups (Fig. 5a): one around 83.4 ± 0.7 Ma (4 analyses) and another one 74.6 ± 1.1 Ma (3 analyses). Mineral separates from the sample Yah04 yielded well-defined plateaus (Fig. 5b), indicating consistent ages of 65.3 ± 0.5 Ma, 65.7 ± 0.2 Ma and 64.8 ± 0.4 Ma. For each separate, isochron and inverted isochron ages, as well as total gas ages, are similar to these plateau ages within the 2-SD analytical uncertainty.

Ören Unit. Mineral separates from the sample Ören001 furnished well-defined plateaus (Fig. 5b), indicating ages of 60.3 ± 0.3 Ma, 62.6 ± 0.4 Ma and 59.4 ± 0.7 Ma. For each separate, isochron and inverted isochron ages, as well as total gas ages, are similar to these plateau ages within the 2-SD analytical uncertainty.

Kurudere-Nebiler Unit. In-situ laser ablation in Kuru0110 provided age results scattered between 35.0 ± 2.5 and 49.2 ± 3.3 Ma. Five of the eight steps, representing about 71% of the total ^{39}Ar release, give an average age of 45.2 ± 2.0 Ma (Fig. 5a). In-situ laser ablation in Nebil0101 provided age results scattered between 24.2 ± 1.8 and 30.2 ± 2.5 Ma. Five of the seven steps, representing about 56% of the total ^{39}Ar release, give an average age of 26.5 ± 0.8 Ma (Fig. 5a).

AGE SIGNIFICANCE

Significance of the ages individually

Argon retention

After decades of debates, it has become widely accepted that Ar starts to diffuse out of white mica from temperatures above 450-500°C, or even higher (e.g. Hammerschmidt & Franz, 1991; Di Vincenzo *et al.*, 2001; Balogh & Dunkl, 2005; Allaz, 2008). Since little is known about the effect of the Tschermak substitution on argon diffusivity in white mica, phengite closure temperature is generally assumed to be similar to that of muscovite (Wijbrans & McDougall, 1986; Hames & Bowring, 1994; Reddy *et al.*, 1996). This assumption is here probably reasonable because phengite dated in this study shows little Tschermak substitution. Bearing in mind that temperature in the Afyon Zone and Ören Unit did not exceed 400-450°C, white mica ^{40}Ar - ^{39}Ar ages from these regions represent crystallization ages. By contrast, in the Kurudere-Nebiler Unit, the extensive Barrovian metamorphism, which erased most of the HP minerals, reached up to 520°C (Whitney & Bozkurt, 2002; Régnier *et al.*, 2003), and might therefore have reset, even partially, the ^{40}Ar - ^{39}Ar isotopic system.

Radiometric ages and petrology

Afyon Zone. In-situ laser ablation in the carpholite-bearing phyllite sample Bay0851 yielded two age trends: around 75 and 83 Ma (Fig. 4b). Fine grain size of analyzed phengite required laser ablation on relatively large area in order to extract sufficient gas amount, so any textural distinction between these two age groups is not possible yet. Owing to this lack of textural control, these results cannot be interpreted unequivocally.

In the samples Afy0206, Afy0212 and Yah04, phengite obviously formed after carpholite. Accordingly, thermobarometric results from these samples show that ^{40}Ar - ^{39}Ar phengite ages concern the retrograde path of the HP-LT loop. Although the two samples investigated for *P-T* estimations (Afy0206 and Yah04) yielded homogeneous phengite composition and temperatures lower than Ar closure in phengite, scattered ^{40}Ar - ^{39}Ar ages were obtained (from one spot analysis to the other in Afy0206; from one mineral separate bunch to the other for Yah04; Fig. 4). Phengite that equilibrated under middle-pressure conditions (0.6-0.7 GPa) provided ^{40}Ar - ^{39}Ar ages of about 63 and 65 Ma for the retrograde path of the western and eastern parts of the Afyon Zone, respectively.

Ören Unit. According to the *P-T* estimates of Rimmelé *et al.* (2005), phengite and chlorite from the sample Ören001 formed between 1.1 GPa/400°C (interpreted as near-peak conditions) and 0.8 GPa/300°C, depicting a syn-decompression cooling path. The ^{40}Ar - ^{39}Ar ages between 60 and 62 Ma obtained for the sample Ören001 therefore prevail for earliest HP-LT retrograde stages in the Ören Unit.

Kurudere-Nebiler Unit. For this unit, we obtained contrasting ages from the two dated localities. Since petrographic textures in Kuru0110 indicate that white mica formed along with chlorite and kyanite from the breakdown of carpholite, the mean ^{40}Ar - ^{39}Ar age of 45.2 ± 2.0 Ma obtained from this sample, represents post-HP retrograde stages. As suggested by the partial preservation of diaspore in metabauxites from this area, we infer that the Barrovian metamorphism did not affect significantly this part of the unit, so that mica formed during post-HP decompression preserved its initial Ar ratio signature.

In the sample Nebil0101, the mean ^{40}Ar - ^{39}Ar age 26.5 ± 0.8 Ma, which we obtained on phengite aligned to a post-kyanite and -chloritoid foliation, represents a late metamorphic stage. The lack, in this area, of relics of carpholite (entirely replaced by chlorite and kyanite) and diaspore (entirely replaced by corundum), is regarded as the result of more intense thermal overprint at low to middle

pressure with respect to that in the area of Kurudere. This ^{40}Ar - ^{39}Ar age might hence represent post-Barrovian cooling.

DISCUSSION

Tectonic implications

The new data presented above indicate that the Ören Unit and the Afyon Zone were metamorphosed in the same period, i.e. in Maastrichtian-Danian times (retrograde ages between 65 and 60 Ma). These units therefore represent parts of the same HP-LT metamorphic belt, for which no lateral equivalent towards Eastern Anatolia and in the Aegean Domain is known yet. The new-termed Ören-Afyon Zone was continuous from the Aegean Coast to Central Anatolia before extensional tectonics started in the Menderes region. The fact that the Ören-Afyon Zone was metamorphosed ca. 15-20 m.y. later than the Tavşanlı Zone is consistent with the interpretation that it represents more proximal facies of the ancient continental margin (see Candan *et al.*, 2005).

In turn, the Kurudere-Nebiler Unit experienced HP-LT metamorphism coevally with the Cycladic Blueschists, i.e. in the early Eocene (see Jolivet & Brun, 2008; Ring *et al.*, 2010). Owing to differences in rock type and *P-T* conditions, the Kurudere-Nebiler Unit and the Cycladic Blueschists cannot be considered a single tectonic unit, so we rather propose that they form a continuous, internally imbricated, Eocene HP-LT metamorphic belt. To explain the 20-m.y. gap between the HP-LT metamorphism in the Ören-Afyon Zone and the Kurudere-Nebiler Unit, we assume that the units were once separated by a narrow basin correlating the Pindos Ocean (see Jolivet *et al.*, 2004; Papanikolaou, 2009), also referred to as the Selçuk Ocean (Gessner *et al.*, 2001c). Whether this basin was floored by oceanic or thinned continental crust remains an unresolved issue out the scope of this study. Nevertheless, the oceanic-floor view is supported by the occurrence of oceanic relics in the metamorphosed mélange unit (blocks of eclogitic late Cretaceous metabasalts and metagabbros, as well as meta-serpentinite) (e.g. Bröcker & Enders, 2001; Çetinkaplan, 2002; Bulle *et al.*, 2012), and tectonic lenses of serpentinite (Rimmelé *et al.*, 2003a) intercalated between the Ören Unit and the Cycladic Blueschists or Kurudere-Nebiler Unit. The northward subduction of negatively buoyant oceanic crust underneath the Tavşanlı and Ören-Afyon Zones constitutes the most likely explanation for: a) mantle melting beneath the Tavşanlı Zone (early Eocene plutons; Harris *et al.*, 1994) synchronous with HP metamorphism in the Kurudere-Nebiler Unit, and b) the period of 20 m.y. between the HP metamorphic events in the Ören-Afyon Zone and the Kurudere-Nebiler Unit. The absence of any Eocene HP-LT metamorphic rocks and calc-alkaline plutons towards Central Anatolia indicates that the Pindos Ocean did not reach so far east, as already envisaged by Gessner *et al.* (2001c).

In consequence, Western Anatolia encloses three HP-LT metamorphic units that are successively younger from top to bottom, and from the internals towards the externals of the collision zone. Such a situation, also described in other convergence zones like the Aegean Domain, may be interpreted to reflect the successive accretion of distinct continental fragment in a continuous subduction context (see van Hinsbergen *et al.*, 2005; Jolivet & Brun, 2008). Following this model, northward subduction was likely continuous between 90 and 60 Ma in Central Anatolia, and between 90 and 30 Ma in Western Anatolia.

Geodynamic evolution of Central Anatolia

In the western and southern parts of the Central Anatolian Crystalline Complex, the exhumation of Barrovian-type metamorphic rocks in core-complexes took place between 85 and 70 Ma (e.g. Whitney *et al.*, 2007; Gautier *et al.*, 2008; Lefebvre *et al.*, 2011), i.e. coevally with the exhumation of

the Tavşanlı Zone (Sherlock *et al.*, 1999). Although, in this period, these terranes were separated by a strand of supra-subduction-zone oceanic crust (corresponding to the Neotethyan ophiolites; see Pourteau *et al.*, 2010), HP-rock exhumation during continuous subduction (HP-LT metamorphism in the Afyon Zone around 70 Ma; this study) and substantial extension in the upper plate might be related tectonic processes.

The continent accretion history of Central Anatolia is reconstructed as follows:

1. onset of intra-oceanic subduction around 95-90 Ma (e.g. Dilek *et al.*, 1999; Parlak & Delaloye, 1999),
2. burial of the most distal part of the Anatolide-Tauride passive continental margin (Tavşanlı Zone) until metamorphic peak around 88-78 Ma (assuming similar ages to the western part of the unit) (e.g. Sherlock *et al.*, 1999; Seaton *et al.*, 2009),
3. exhumation of the Tavşanlı Zone up to Moho depths, coevally with the burial of more proximal parts of the margin (Afyon Zone) before 65 Ma (this study),
4. exhumation of both HP-LT units up to the surface around the Maastrichtian-Danian boundary (ca. 65 Ma), coevally with ophiolite emplacement on external platform units (Central and Eastern Taurides; Fig. 1) (e.g. Dilek *et al.*, 1999),
5. Palaeocene to upper Eocene sedimentation sealing the suture zone (Görür *et al.*, 1998; Clark & Robertson, 2002)

After the cease of subduction in the earliest Cenozoic, continuous north-south convergence was likely accommodated along the Cyprus trench.

Geodynamic evolution of Western Anatolia

Western Anatolia encompasses three HP-LT metamorphic units: the Tavşanlı Zone buried to 50-80 km around 88-78 Ma, the Ören-Afyon Zone buried to 30-45 km around 70-60 Ma, and the Kurudere-Nebiler Unit, connected westwards to the Cycladic Blueschists, buried to 30-50 km around 53-45 Ma. Hereafter we propose the first geodynamic scenario for Western Anatolia that accounts for the formation of these three successive HP belts (Fig. 6).

From 95 to 75 Ma

North-dipping intra-oceanic subduction started between the Anatolide-Tauride Block and the Pontides around 95-90 Ma (see Robertson, 2002; Çelik *et al.*, 2006). Around 85 Ma, that is, shortly after subduction initiation, the rocks of the Tavşanlı Zone, representing the most distal parts of a continental passive margin, attained the deepest burial levels (ca. 70-80 km; e.g. Okay *et al.*, 1998; Sherlock *et al.*, 1999; Çetinkaplan *et al.*, 2008). In this period, sedimentation persisted in the more external units, i.e. the Afyon Zone, the Kurudere-Nebiler Unit and the Taurides (Fig. 6a) (see Candan *et al.*, 2005).

Then, blueschists and eclogites of the Tavşanlı Zone were exhumed along a very-low apparent geothermal gradient, accounting for the good preservation of lawsonite along the retrograde path (Davis & Whitney, 2006). Such syn-decompression cooling is evidence for mid-speed to slow exhumation during continuous subduction (e.g. Ernst, 1988; Liou *et al.*, 1994), i.e. during the underplating of the Afyon Zone.

From 75 to 55 Ma

The Ören-Afyon Zone, including a carbonate platform and its Precambrian-Palaeozoic substratum, was metamorphosed under low-grade HP conditions around 70 Ma, while the carbonate platform of the Kurudere-Nebiler Unit recorded subsidence from neritic to pelagic environments (see Candan *et al.*, 2005). The Ören-Afyon and the Tavşanlı Zones were then exhumed synchronously up to shallow crustal levels from Maastrichtian to Palaeocene times. Coevally, the ophiolites from the İzmir-Ankara and Inner-Tauride oceanic branches were emplaced southwards on top of Mesozoic

platform sediments (Okay *et al.*, 2001), initiating the formation of the Tauride nappe complexes (e.g. Collins & Robertson, 1998; Elitok & Drüppel, 2008).

In Western Anatolia, the active trench was transferred southwards within the Pindos Ocean sometime around the early Palaeocene due to continuous regional convergence. We envisage that the southward migration of the subduction zone was accommodated by a décollement along either a weak surface separating the upper-middle from the lower crust (see Jolivet *et al.*, 2003), or the crust-mantle interface (“tectonic Moho”). For readability, the latter scenario is depicted in our geodynamic sketch (Fig. 6).

From 55 to 35 Ma

The northward subduction in the Pindos Ocean was accompanied by melting in the overlying mantle wedge, resulting in the intrusion of calc-alkaline magmas in the overriding Tavşanlı Zone and Western Pontides (Harris *et al.*, 1994; Delaloye & Bingöl, 2000). In this period, while some parts of the Tavşanlı Zone still laid at a depth of ca. 10 km (Harris *et al.*, 1994), others, as well as the Afyon Zone, were already exposed at the Earth’s surface and unconformably covered by shallow-marine sediments (Özcan *et al.*, 1988).

Coevally, the Kurudere-Nebiler Unit, representing the northern edge of the Menderes-Tauride platform, was dragged down to HP-LT conditions and subsequently exhumed from the middle Eocene on. This correlates a second imbrication stage in the Tauride nappe complexes (incorporation of Eocene and older platform sequences; e.g. Collins & Robertson, 1998).

From 35 Ma onwards

Around the Eocene-Oligocene boundary, the collision of Menderes-Tauride platform and the overlying terranes, as recorded by Barrovian metamorphism in the Menderes Massif *sensu lato* (see Bozkurt & Oberhänsli, 2001; Gessner *et al.*, 2001a; Régnier *et al.*, 2003), attained an orogenic stage characterized by a regional sedimentary hiatus and local molasse-type sedimentation in the Taurides (see Şengör *et al.*, 1984; Yılmaz, 2000; MTA, 2002).

Subduction below western Anatolia ceased subsequently to the continental collision, while it continued in the Aegean Domain through repeated southward trench migration accommodated by crust-mantle decoupling (see Jolivet *et al.*, 2003; van Hinsbergen *et al.*, 2005). We propose that the impossibility for post-collision decoupling along the crust-mantle interface below western Anatolia led to lock the subduction in Western Anatolia, while it has persisted in the Aegean Domain. In the same way, subduction in Central Anatolia ceased after the accretion of the Afyon Zone and Taurides around 65 Ma.

Continuation (like in Aegea) *versus* cease (like in Anatolia) of subduction is likely controlled by the possibility of tectonic decoupling between the accreted, buoyant continental crust and the dense lithospheric mantle, and might thus depend on palaeogeography.

Continental collision was thus followed by slab roll-back and then slab break-off (van Hinsbergen *et al.*, 2010), as depicted by seismic tomography (Biryol *et al.*, 2011; Salaün *et al.* 2012). This led to the unroofing of the Menderes Nappes along detachment faults in the Miocene (see e.g. Hetzel *et al.*, 1995; Gessner *et al.*, 2001b). Shortening, however, persisted in the Taurides, leading to the final emplacement of the Lycian Nappes onto lower-middle Miocene foredeep sediments and the autochthonous platform (Gutnic *et al.*, 1979; Collins & Robertson, 1998).

CONCLUSIONS

In this study, we present first results of phengite ^{40}Ar - ^{39}Ar geochronology and chlorite-phengite multi-equilibrium thermobarometry on Fe-Mg-carpholite-bearing rocks from three tectonic units of Western and Central Anatolia and discuss the tectonic relations between them. The exhumation of the Afyon Zone through greenschist-facies conditions (ca. 0.6 GPa/300-350°C) was dated to 66-61

Ma, and earliest retrograde stages in the Ören Unit (0.8-1.1 GPa/320-400°C; Rimmelé *et al.*, 2005) to 62-59 Ma. Consequently, the Ören Unit is considered the western continuation of the Afyon Zone until extensional tectonics led to its transport away from the suture zone. The Kurudere-Nebiler Unit (Mesozoic cover of the southern Menderes Massif) was retrogressed under greenschist-facies conditions around 46 Ma, subsequently affected by a Barrovian overprint (likely around 35 Ma) and cooled down below ca. 500°C around 26 Ma. The Kurudere-Nebiler Unit therefore is correlated with the Cycladic Blueschists, which experienced a similar, synchronous metamorphic evolution. These units represent parts of an Eocene HP-LT belt resulting from the entrance of the Apulia microcontinent in the Pindos subduction zone.

Our study shows that combining radiometric geochronology and thermobarometric calculations in individual samples allows ascribing specific *P-T* conditions to age results, and thus deciphering with more accuracy the evolution of metamorphic rocks at regional scale. Based on the lateral continuation or break of the Anatolian HP-LT metamorphic belts, we argue that subduction was blocked earlier in Central Anatolia (early Palaeocene) than in Western Anatolia (Oligocene) while it still is active in the Aegean Domain.

ACKNOWLEDGEMENTS

Financial support by the Deutsche Forschungsgemeinschaft (OB80/34) is kindly acknowledged. We thank Stefan Schmid, Gwenaëlle Salaün, Mark Handy and Romain Bousquet for fruitful discussions on early versions of this manuscript, as well as Donna Whitney (editor) and two anonymous reviewers for their constructive comments.

REFERENCES

- Agard, P., Monié, P., Jolivet, L. & Goffé, B., 2002. Exhumation of the Schistes Lustrés complex: in situ laser probe $^{40}\text{Ar}/^{39}\text{Ar}$ constraints and implications for the Western Alps. *Journal of Metamorphic Geology*, **20**(6), 599-618.
- Akal, C., Candan, O., Koralay, E., Oberhänsli, R., Chen, F. & Prelevic, D., 2011. Early Triassic potassic volcanism in the Afyon Zone of the Anatolides/Turkey: implications for the rifting of the Neo-Tethys. *International Journal of Earth Sciences*.
- Allaz, J., 2008. *Metamorphic evolution of the Central Alps: Linking ^{39}Ar - ^{40}Ar dating with thermobarometry*, PhD thesis, Universität Bern.
- Altiner, D., Koçyiğit, A., Farinacci, A., Nicosia, U. & Conti, M.A., 1991. Jurassic-Lower Cretaceous stratigraphy and paleogeographic evolution of the southern part of north-western Anatolia. *Geologica Romana*, **27**, 13-80.
- Arkaï, P., Faryad, S.W., Vidal, O. & Balogh, K., 2003. Very low-grade metamorphism of sedimentary rocks of the Meliata unit, Western Carpathians, Slovakia: implications of phyllosilicate characteristics. *International Journal of Earth Sciences*, **92**(1), 68-85.
- Aydın, N.S., Göncüoğlu, M.C. & Erler, A., 1998. Latest Cretaceous Magmatism in the Central Anatolian Crystalline Complex: Review of Field, Petrographic and Geochemical Features. *Turkish Journal of Earth Sciences*, **7**, 259-268.
- Balogh, K. & Dunkl, I., 2005. Argon and fission track dating of Alpine metamorphism and basement exhumation in the Sopron Mts. (Eastern Alps, Hungary): thermochronology or mineral growth? *Mineralogy and Petrology*, **83**(3-4), 191-218.
- Barrier, E. & Vrielinck, B., 2008. Palaeotectonic maps of the Middle East, Commission for the Geological Map of the World, Paris.
- Biryol, C.B., Beck, S.L., Zandt, G. & Ozacar, A.A., 2011. Segmented African lithosphere beneath the Anatolian region inferred from teleseismic P-wave tomography. *Geophysical Journal International*, **184**(3), 1037-1057.
- Bozkurt, E. & Oberhänsli, R., 2001. Menderes Massif (Western Turkey): structural, metamorphic and magmatic evolution - a synthesis. *International Journal of Earth Sciences*, **89**(4), 679-708.
- Bozkurt, E. & Satir, M., 2000. The southern Menderes Massif (western Turkey): geochronology and exhumation history. *Geological Journal*, **35**(3-4), 285-296.
- Bröcker, M. & Enders, M., 2001. Unusual bulk-rock compositions in eclogite-facies rocks from Syros and Tinos (Cyclades, Greece): implications for U-Pb zircon geochronology. *Chemical Geology*, **175**(3-4), 581-603.
- Bulle, F., Bröcker, M., Gaertner, C. & Keasling, A., 2010. Geochemistry and geochronology of HP melanges from Tinos and Andros, cycladic blueschist belt, Greece. *Lithos*, **117**(1-4), 61-81.
- Candan, O., Çetinkaplan, M., Oberhänsli, R., Rimmelé, G. & Akal, C., 2005. Alpine high-P/low-T metamorphism of the Afyon Zone and implications for the metamorphic evolution of Western Anatolia, Turkey. *Lithos*, **84**(1-2), 102-124.

- Candan, O., Dora, O.Ö., Oberhänsli, R., Oelsner, F. & Dürr, S., 1997. Blueschist relics in the Mesozoic cover series of the Menderes Massif and correlations with Samos Island, Cyclades. *Schweizerische Mineralogische und Petrographische Mitteilungen*, **77**, 95-99.
- Candan, O., Oberhänsli, R., Dora, O.Ö., Çetinkaplan, M., Koralay, E., Rimmelé, G., Chen, F. & Akal, C., 2011. Polymetamorphic evolution of the Pan-African basement and Palaeozoic-Early Tertiary cover series of the Menderes Massif. *Bulletin of the Mineral Research and Exploration Institute of Turkey*, **142**, 121-163.
- Cathelineau, M. & Nieva, D., 1985. A chlorite solid-solution geothermometer - The Los-Azufres (Mexico) geothermal system. *Contributions to Mineralogy and Petrology*, **91**(3), 235-244.
- Çelik, Ö.F., Delaloye, M. & Feraud, G., 2006. Precise Ar-40-Ar-39 ages from the metamorphic sole rocks of the Tauride Belt Ophiolites, southern Turkey: implications for the rapid cooling history. *Geological Magazine*, **143**(2), 213-227.
- Çetinkaplan, M., 2002. *Tertiary High-Pressure / Low-Temperature Metamorphism in the Mesozoic Cover Series of the Menderes Massif and Correlation with the Cycladic Crystalline Complex*. Unpub. PhD Thesis, Universitesi Izmir.
- Çetinkaplan, M., Candan, O., Oberhänsli, R. & Bousquet, R., 2008. Pressure-temperature evolution of lawsonite eclogite in Sivrihisar; Tavasli Zone-Turkey. *Lithos*, **104**(1-4), 12-32.
- Clark, M. & Robertson, A.H.F., 2002. The role of the Early Tertiary Ulukışla Basin, southern Turkey, in suturing of the Mesozoic Tethys ocean. *Journal of the Geological Society, London*, **159**, 673-690.
- Collins, A.S. & Robertson, A.H.F., 1998. Processes of Late Cretaceous to Late Miocene episodic thrust-sheet translation in the Lycian Taurides, SW Turkey. *Journal of the Geological Society, London*, **155**, 759-772.
- Davis, P.B. & Whitney, D.L., 2006. Petrogenesis of lawsonite and epidote eclogite and blueschist, Sivrihisar Massif, Turkey. *Journal of Metamorphic Geology*, **24**(9), 823-849.
- Davis, P.B. & Whitney, D.L., 2008. Petrogenesis and structural petrology of high-pressure metabasalt pods, Sivrihisar, Turkey. *Contributions to Mineralogy and Petrology*, **156**(2), 217-241.
- De Andrade, V., Vidal, O., Lewin, E., O'Brien, P. & Agard, P., 2006. Quantification of electron microprobe compositional maps of rock thin sections: an optimized method and examples. *Journal of Metamorphic Geology*, **24**(7), 655-668.
- Delaloye, M. & Bingöl, E., 2000. Granitoids from Western and Northwestern Anatolia: Geochemistry and modeling of geodynamic evolution. *International Geology Review*, **42**(3), 241-268.
- Dercourt, J., Ricou, L.E. & Vrielinck, B., 1993. *Atlas Tethys, paleoenvironmental maps*. Gauthier-Villars, Paris.
- Dewey, J.F., Helman, M.L., Knott, S.D., Turco, E. & Hutton, D.H.W., 1989. Kinematics of the western Mediterranean. In: *Alpine Tectonics* (eds Coward, M.P., Dietrich, D., Park, R.G.) *Geological Society, London, Special Publications*, **45**, 265-283.
- Di Vincenzo, G. & Palmeri, R., 2001. An ⁴⁰Ar-³⁹Ar investigation of high-pressure metamorphism and the retrogressive history of mafic eclogites from the Lanterman Range (Antarctica): evidence against a simple temperature control on argon transport in amphibole. *Contributions To Mineralogy And Petrology*, **141**(1), 15-35.
- Dilek, Y., Thy, P., Hacker, B. & Grundvig, S., 1999. Structure and petrology of Tauride ophiolites and mafic dike intrusions (Turkey): implications for the Neotethyan ocean. *Bulletin of the Geological Society of America*, **111**(8), 1192-1216.
- Dirik, K., Göncüoğlu, M.C. & Kozlu, H., 1999. Stratigraphy and pre-Miocene tectonic evolution of the southwestern part of the Sivas Basin, Central Anatolia, Turkey. *Geological Journal*, **34**(3), 303-319.
- Droop, G.T.R., Karakaya, M.Q., Eren, Y. & Karakaya, N., 2005. Metamorphic evolution of blueschists of the Altinekin Complex, Konya area, south central Turkey. *Geological Journal*, **40**(2), 127-153.
- Dubacq, B., Vidal, O. & De Andrade, V., 2010. Dehydration of dioctahedral aluminous phyllosilicates: thermodynamic modelling and implications for thermobarometric estimates. *Contributions To Mineralogy And Petrology*, **159**(2), 159-174.
- Dürr, S., 1975. *Über Alter und geotektonische Stellung des Menderes-Kristallins/SW-Anatolien und seine Äquivalente in der mittleren Aegaeis*. Unpub. Habilitation Thesis, Uni Marburg/Lahn.
- Elitok, O. & Drüppel, K., 2008. Geochemistry and tectonic significance of metamorphic sole rocks beneath the Beyşehir-Hoyran ophiolite (SW-Turkey). *Lithos*, **100**(1-4), 322-353.
- Ernst, W.G., 1988. Tectonic history of subduction zones inferred from retrograde blueschist p-t paths. *Geology*, **16**(12), 1081-1084.
- Ganne, J., Bussy, F. & Vidal, O., 2003. Multi-stage garnet in the internal Briançonnais basement (Ambin massif, Savoy): New petrological constraints on the blueschist- facies metamorphism in the Western Alps and tectonic implications. *Journal of Petrology*, **44**(7), 1281-1308.
- Ganne, J., De Andrade, V., Weinberg, R.F., Vidal, O., Dubacq, B., Kagambega, N., Naba, S., Baratoux, L., Jessell, M. & Allibon, J., 2012. Modern-style plate subduction preserved in the Palaeoproterozoic West African craton. *Nature Geoscience*, **5**(1), 60-65.
- Gautier, P., Bozkurt, E., Bosse, V., Hallot, E. & Dirik, K., 2008. Coeval extensional shearing and lateral underflow during Late Cretaceous core complex development in the Nigde Massif, Central Anatolia, Turkey. *Tectonics*, **27**(TC1003).
- Gessner, K., Piazzolo, S., Güngör, T., Ring, U., Kröner, A. & Passchier, C.W., 2001a. Tectonic significance of deformation patterns in granitoid rocks of the Menderes nappes, Anatolide belt, southwest Turkey. *International Journal of Earth Sciences*, **89**(4), 766-780.
- Gessner, K., Ring, U., Johnson, C., Hetzel, R., Passchier, C.W. & Güngör, T., 2001b. An active bivergent rolling-hinge detachment system: Central Menderes metamorphic core complex in western Turkey. *Geology*, **29**(7), 611-614.

- Gessner, K., Ring, U., Passchier, C.W. & GÜNGÖR, T., 2001c. How to resist subduction: evidence for large-scale out-of-sequence thrusting during Eocene collision in western Turkey. *Journal of the Geological Society, London*, **158**, 769-784.
- Göncüoğlu, M.C., Dirik, K. & Kozlu, H., 1997. General Characteristics of pre-Alpine and Alpine Terranes in Turkey: Explanatory notes to the terrane map of Turkey. *Annales Géologiques des Pays Helleniques*, **37**, 515-536.
- Görür, N., Tüysüz, O. & Şengör, A.M.C., 1998. Tectonic Evolution of the Central Anatolian Basins. *International Geology Review*, **40**, 831-850.
- Grosch, E.G., Vidal, O., Abu-Alam, T. & McLoughlin, N., 2012. P-T Constraints on the Metamorphic Evolution of the Paleoproterozoic Kromberg Type-Section, Barberton Greenstone Belt, South Africa. *Journal of Petrology*, **53**(3), 513-545.
- Güngör, T. & Erdoğan, B., 2002. Tectonic significance of mafic volcanic rocks in a Mesozoic sequence of the Menderes Massif, West Turkey. *International Journal of Earth Sciences*, **91**, 386-397.
- Gutnic, M., Monod, O., Poisson, A. & Dumont, J.-F., 1979. *Géologie des Taurides occidentales (Turquie)*. Société Géologiques de France, Paris.
- Hames, W.E. & Bowring, S.A., 1994. An empirical-evaluation of the argon diffusion geometry in muscovite. *Earth and Planetary Science Letters*, **124**(1-4), 161-167.
- Hammerschmidt, K. & Frank, E., 1991. Relics of high-pressure metamorphism in the Lepontine Alps (Switzerland) - 40Ar/39Ar and microprobe analyses on white K-micas. *Schweizerische Mineralogische und Petrographische Mitteilungen*, **71**, 261-274.
- Harris, N.B.W., Kelley, S. & Okay, A.I., 1994. Postcollision Magmatism and Tectonics in Northwest Anatolia. *Contributions to Mineralogy and Petrology*, **117**(3), 241-252.
- Hetzl, R., Passchier, C.W., Ring, U. & Dora, O.Ö., 1995. Bivergent Extension in Orogenic Belts - the Menderes Massif (Southwestern Turkey). *Geology*, **23**(5), 455-458.
- Hillier, S. & Velde, B., 1991. Octahedral occupancy and the chemical-composition of diagenetic (low-temperature) chlorites. *Clay Minerals*, **26**(2), 149-168.
- İlbeyli, N., Pearce, J.A., Thirlwall, M.F. & Mitchell, J.G., 2004. Petrogenesis of collision-related plutonics in Central Anatolia, Turkey. *Lithos*, **72**(3-4), 163-182.
- Ishizuka, O., 1998. Vertical and horizontal variation of the fast neutron flux in a single irradiation capsule and their significance in the laser-heating 40Ar/39Ar analysis: Case study for the hydraulic rabbit facility of the JMTR reactor, Japan. *Geochemical Journal*, **32**(4), 243-252.
- Ishizuka, O., Yuasa, M. & Uto, K., 2002. Evidence of porphyry copper-type hydrothermal activity from a submerged remnant back-arc volcano of the Izu-Bonin arc - Implications for the volcanotectonic history of back-arc seamounts. *Earth and Planetary Science Letters*, **198**(3-4), 381-399.
- Jolivet, L. & Brun, J.-P., 2008. Cenozoic geodynamic evolution of the Aegean. *International Journal of Earth Sciences*, **99**(1), 109-138.
- Jolivet, L., Faccenna, C., Goffé, B., Burov, E.B. & Agard, P., 2003. Subduction tectonics and exhumation of high-pressure metamorphic rocks in the Mediterranean orogens. *American Journal of Science*, **303**(5), 353-409.
- Jolivet, L., Faccenna, C., Huet, B., Labrousse, L., Le Pichet, L., Lacombe, O., Lecomte, E., Burov, E., Denèle, Y., Brun, J.-P., Philippon, M., Paul, A., Salaün, G., Karabulut, H., Piromallo, C., Monié, P., Gueydan, F., Okay, A., Oberhänsli, R., Pourteau, A., Augier, R., Gadenne, L. & Driussi, O., 2012. Aegean tectonics: Strain localisation, slab tearing and trench retreat. *Tectonophysics*, **in press**.
- Jolivet, L., Goffé, B., Monié, P., Truffert-Luxey, C., Patriat, M. & Bonneau, M., 1996. Miocene detachment in Crete and exhumation P-T-t paths of high-pressure metamorphic rocks. *Tectonics*, **15**(6), 1129-1153.
- Jolivet, L., Rimmelé, G., Oberhänsli, R., Goffé, B. & Candan, O., 2004. Correlation of syn-orogenic tectonic and metamorphic events in the Cyclades, the Lycian nappes and the Menderes massif. Geodynamic implications. *Bulletin De La Société Géologique De France*, **175**(3), 217-238.
- Kadioğlu, Y.K., Dilek, Y., Güleç, N. & Foland, K.A., 2003. Tectonomagmatic evolution of bimodal plutons in the central Anatolian crystalline complex, Turkey. *Journal of Geology*, **111**(6), 671-690.
- Ketin, I., 1966. Tectonic units of Anatolia. *Maden Tetkik ve Arama Bulletin*, **66**, 23-34.
- Kocak, K. & Leake, B.E., 1994. The petrology of the Ortaköy district and its ophiolite at the western edge of the Middle Anatolian Massif, Turkey. *Journal of African Earth Sciences*, **18**(2), 163-174.
- Lanari, P., Guillot, S., Schwartz, S., Vidal, O., Tricart, P., Riel, N. & Beyssac, O., 2012a. Diachronous evolution of the alpine continental subduction wedge: Evidence from P-T estimates in the Briançonnais Zone houillère (France - Western Alps). *Journal of Geodynamics*, **56-57**, 39-54.
- Lanari, P., Riel, N., Guillot, S., Vidal, O., Schwartz, S., Pêcher, A. & Hattori, K., 2012b. Deciphering High-Pressure metamorphism in collisional context using microprobe-mapping methods : application to the Stak eclogitic massif (NW Himalaya). *Geology*, **in press**.
- Le Hebel, F., Vidal, O., Kienast, J.R. & Gapais, D., 2002. Evidence for HP-LT Hercynian metamorphism within the 'Porphyroides' of South Brittany (France). *Comptes Rendus Geoscience*, **334**(3), 205-211.

- Lefebvre, C., Barnhoorn, A., van Hinsbergen, D.J.J., Kaymakci, N. & Vissers, R.L.M., 2011. Late Cretaceous extensional denudation along a marble detachment fault zone in the Kırşehir massif near Kaman, central Turkey. *Journal of Structural Geology*, **33**, 1220-1236.
- Liou, J.G., Zhang, R. & Ernst, W.G., 1994. An introduction to ultrahigh-pressure metamorphism. *The Island Arc*, **3**, 1-24.
- Lips, A.L.W., Cassard, D., Sözbilir, H., Yılmaz, H. & Wijbrans, J.R., 2001. Multistage exhumation of the Menderes Massif, western Anatolia (Turkey). *International Journal of Earth Sciences*, **89**(4), 781-792.
- McDougall, I. & Harrison, T.M., 1999. *Geochronology and thermochronology by the ⁴⁰Ar/³⁹Ar method*. Oxford University Press, New York Oxford.
- Monod, O., Kozlu, H., Ghienne, J.F., Dean, W.T., Gunay, Y., Herisse, A.L., Paris, F. & Robardet, M., 2003. Late Ordovician glaciation in southern Turkey. *Terra Nova*, **15**(4), 249-257.
- MTA, 2002. Geological Map of Turkey, 1:500,000, MTA, Ankara.
- Oberhänsli, R., Bousquet, R., Candan, O. & Okay, A., 2012. Dating subduction events in East Anatolia, Turkey. *Turkish Journal of Earth Sciences*, **21**, 1-17.
- Oberhänsli, R., Candan, O., Bousquet, R., Rimmelé, G., Okay, A.I. & Goff, J., 2010. Alpine HP evolution of the eastern Bitlis complex, SE Turkey. In: *Sedimentary Basin Tectonics from the Black Sea and Caucasus to the Arabian Platform* (eds Sossou, M., Kaymakci, N., Stephenson, R., Bergerat, F. & Starostenko, V.), *Geological Society, London, Special Publications*, **340**, 461-483.
- Oberhänsli, R., Monié, P., Candan, O., Warkus, F.C., Partzsch, J.H. & Dora, O.Ö., 1998. The age of blueschist metamorphism in the Mesozoic cover series of the Menderes Massif. *Schweizerische Mineralogische Und Petrographische Mitteilungen*, **78**(2), 309-316.
- Oberhänsli, R., Partzsch, J., Candan, O. & Cetinkaplan, M., 2001. First occurrence of Fe-Mg-carpholite documenting a high-pressure metamorphism in metasediments of the Lycian Nappes, SW Turkey. *International Journal of Earth Sciences*, **89**(4), 867-873.
- Okay, A.I., 1984. Distribution and characteristics of the north-west Turkish blueschists. In: *The Geological Evolution of the Eastern Mediterranean* (eds Dixon, J.E. & Robertson, A.H.F.), *Geological Society, London, Special Publications*, **17**, 455-466.
- Okay, A.I., 2001. Stratigraphic and metamorphic inversions in the central Menderes Massif: a new structural model. *International Journal of Earth Sciences*, **89**(4), 709-727.
- Okay, A.I., 2002. Jadeite-chloritoid-glaucophane-lawsonite blueschists in northwest Turkey: unusually high P/T ratios in continental crust. *Journal of Metamorphic Geology*, **20**(8), 757-768.
- Okay, A.I., Harris, N.B.W. & Kelley, S.P., 1998. Exhumation of blueschists along a Tethyan suture in northwest Turkey. *Tectonophysics*, **285**, 275-299.
- Okay, A.I. & Kelley, S.P., 1994. Tectonic Setting, Petrology and Geochronology of Jadeite Plus Glaucophane and Chloritoid Plus Glaucophane Schists from North-West Turkey. *Journal of Metamorphic Geology*, **12**(4), 455-466.
- Okay, A.I. & Sahinturk, O., 1997. Geology of the Eastern Pontides. In: *Regional and Petroleum Geology of the Black Sea and Surrounding Region* (ed Robinson, A.G.), pp. 291-311, AAPG Memoir.
- Okay, A.I. & Satir, M., 2006. Geochronology of Eocene plutonism and metamorphism in northwest Turkey: evidence for a possible magmatic arc. *Geodinamica Acta*, **19**(5), 251-266.
- Okay, A.I., Satir, M., Maluski, H., Siyako, M., Monié, P., Metzger, R. & Akyüz, S., 1996. Paleo- and Neo-Tethyan events in northwestern Turkey: Geologic and geochronologic constraints. In: *The Tectonic Evolution of Asia* (eds Yin, A. & Harrison, T.M.), pp. 420-441, University Press, Cambridge.
- Okay, A.I., Tansel, I. & Tüysüz, O., 2001. Obduction, subduction and collision as reflected in the Upper Cretaceous-Lower Eocene sedimentary record of western Turkey. *Geological Magazine*, **138**(2), 117-142.
- Okay, A.I. & Tüysüz, O., 1999. Tethyan sutures of northern Turkey. In: *The Mediterranean Basins: Tertiary Extension within the Alpine Orogen* (eds Durand, B., Jolivet, L., Horváth, F. & Séranne, M.), *Geological Society, London, Special Publications*, **156**, 475-515.
- Önen, A.P. & Hall, R., 1993. Ophiolites and related metamorphic rocks from the Kütahya region, North-West Turkey. *Geological Journal*, **28**(3-4), 399-412.
- Özcan, A., Göncüoğlu, M., Turan, N., Uysal, Ş., Senturk, K. & Işık, V., 1988. Late Paleozoic Evolution of the Kütahya-Bolkardağ Belt. *METU Journal of Pure and Applied Sciences*, **21**(1-3), 211-220.
- Özer, S., Sözbilir, H., Özkur, I., Tokur, V. & Sari, B., 2001. Stratigraphy of Upper Cretaceous-Palaeogene sequences in the southern and eastern Menderes Massif (western Turkey). *International Journal of Earth Sciences*, **89**(4), 852-866.
- Özer, S. & Tansel Öngen, I., 2012. Correlation of the Upper Cretaceous sequences between Afyon Zone and Menderes Massif based on the new palaeontologic data (rudist and planktic foraminifera). In: *65th Geological Congress of Turkey*, Ankara, Turkey.
- Papanikolaou, D., 2009. Timing of tectonic emplacement of the ophiolites and terrane paleogeography in the Hellenides. *Lithos*, **108**(1-4), 262-280.
- Parlak, O. & Delaloye, M., 1999. Precise ⁴⁰Ar-³⁹Ar ages from the metamorphic sole of the Mersin ophiolite (southern Turkey). *Tectonophysics*, **301**, 145-158.
- Parlak, O., Delaloye, M. & Bingöl, E., 1996. Mineral chemistry of ultramafic and mafic cumulates an indicator of the arc-related origin of Mersin ophiolite (southern Turkey). *Geologische Rundschau*, **85**(4), 647-661.

- Parra, T., Vidal, O. & Agard, P., 2002. A thermodynamic model for Fe-Mg dioctahedral K white micas using data from phase-equilibrium experiments and natural pelitic assemblages. *Contributions To Mineralogy And Petrology*, **143**, 706-732.
- Pourteau, A., 2011. *Closure of the Neotethys Ocean in Anatolia: structural, petrologic & geochronologic insights from low-grade high-pressure metasediments, Afyon Zone*, PhD thesis, Universität Potsdam.
- Pourteau, A., Candan, O. & Oberhänsli, R., 2010. High-Pressure metasediments in central Turkey: constraints on the Neotethyan closure history. *Tectonics*, **29**(TC5004).
- Reddy, S.M., Kelley, S.P. & Wheeler, J., 1996. A ⁴⁰Ar/³⁹Ar laser probe study of micas from the Sesia Zone, Italian Alps: Implications for metamorphic and deformation histories. *Journal of Metamorphic Geology*, **14**(4), 493-508.
- Régnier, J.L., Ring, U., Passchier, C.W., Gessner, K. & Güngör, T., 2003. Contrasting metamorphic evolution of metasedimentary rocks from the Cine and Selimiye nappes in the Anatolide belt, western Turkey. *Journal of Metamorphic Geology*, **21**(7), 699-721.
- Rimmelé, G., Jolivet, L., Oberhänsli, R. & Goffé, B., 2003a. Deformation history of the high-pressure Lycian Nappes and implications for tectonic evolution of SW Turkey. *Tectonics*, **22**(TC1007).
- Rimmelé, G., Oberhänsli, R., Candan, O., Goffé, B. & Jolivet, L., 2006. The wide distribution of HP-LT rocks in the Lycian Belt (Western Turkey): implications for accretionary wedge geometry In: *Tectonic Development of the Eastern Mediterranean Region* (eds Robertson, A.H.F. & Mountrakis, D.), *Geological Society, London, Special Publications*, **260**, pp. 447-466.
- Rimmelé, G., Oberhänsli, R., Goffé, B., Jolivet, L., Candan, O. & Çetinkaplan, M., 2003b. First evidence of high-pressure metamorphism in the "Cover Series" of the southern Menderes Massif. Tectonic and metamorphic implications for the evolution of SW Turkey. *Lithos*, **71**(1), 19-46.
- Rimmelé, G., Parra, T., Goffé, B., Oberhänsli, R., Jolivet, L. & Candan, O., 2005. Exhumation paths of high-pressure-low-temperature metamorphic rocks from the Lycian Nappes and the Menderes Massif (SW Turkey): a multi-equilibrium approach. *Journal of Petrology*, **46**(3), 641-669.
- Ring, U., Gessner, K., Güngör, T. & Passchier, C.W., 1999. The Menderes Massif of western Turkey and the Cycladic Massif in the Aegean - do they really correlate? *Journal of the Geological Society, London*, **156**, 3-6.
- Ring, U., Glodny, J., Will, T. & Thomson, S., 2010. The Hellenic Subduction System: High-Pressure Metamorphism, Exhumation, Normal Faulting, and Large-Scale Extension. *Annual Review of Earth and Planetary Sciences*, **38**, 45-76.
- Ring, U. & Layer, P.W., 2003. High-pressure metamorphism in the Aegean, eastern Mediterranean: Underplating and exhumation from the Late Cretaceous until the Miocene to Recent above the retreating Hellenic subduction zone. *Tectonics*, **22**(TC1022).
- Ring, U., Will, T., Glodny, J., Kumerics, C., Gessner, K., Thomson, S., Guengoer, T., Monie, P., Okrusch, M. & Drueppel, K., 2007. Early exhumation of high-pressure rocks in extrusion wedges: Cycladic blueschist unit in the eastern Aegean, Greece, and Turkey. *Tectonics*, **26**(2).
- Ring, U., Willner, A.P. & Lackmann, W., 2001. Stacking of nappes with different pressure-temperature paths: An example from the Menderes nappes of western Turkey. *American Journal of Science*, **301**(10), 912-944.
- Robertson, A.H.F., 2002. Overview of the genesis and emplacement of Mesozoic ophiolites in the Eastern Mediterranean Tethyan region. *Lithos*, **65**(1-2), 1-67.
- Robertson, A.H.F., Clift, P.D., Degnan, P.J. & Jones, G., 1991. Paleogeographic and paleotectonic evolution of the Eastern Mediterranean Neotethys. *Palaeogeography Palaeoclimatology Palaeoecology*, **87**(1-4), 289-343.
- Salaün, G., Pedersen, H.A., Paul, A., Farra, V., Karabulut, H., Hatzfeld, D., Papazachos, C., Childs, D.M. & Pequegnat, C., 2012. High-resolution surface wave tomography beneath the Aegean-Anatolia region: constraints on upper-mantle structure. *Geophysical Journal International*, **190**(1), 406-420.
- Saporta, G., 1990. *Probabilités, analyse des données et statistique*.
- Satir, M. & Friedrichsen, H., 1986. The origin and evolution of the Menderes Massif, W-Turkey: A rubidium/strontium and oxygen isotope study. *Geologische Rundschau*, **75**(3), 703-714.
- Schüling, R.D., 1962. On petrology, age and structure of the Menderes migmatite complex (SW-Turkey). *Bulletin of the Mineral Research and Exploration Institute of Turkey*, **58**, 71-84.
- Schwartz, S., Tricart, P., Lardeaux, J.M., Guillot, S. & Vidal, O., 2009. Late tectonic and metamorphic evolution of the Piedmont accretionary wedge (Queyras Schistes lustrés, western Alps): Evidences for tilting during Alpine collision. *Geological Society of America Bulletin*, **121**(3-4), 502.
- Seaton, N.C.A., Whitney, D.L., Teyssier, C., Toraman, E. & Heizler, M.T., 2009. Recrystallization of high-pressure marble (Sivrihisar, Turkey). *Tectonophysics*, **479**(3-4), 241-253.
- Şengör, A.M.C., Satir, M. & Akkoç, R., 1984. Timing of tectonic events in the Menderes Massif, Western Turkey - Implications for tectonic evolution and evidence for Pan-African basement in Turkey. *Tectonics*, **3**(7), 693-707.
- Şengör, A.M.C. & Yılmaz, Y., 1981. Tethyan Evolution of Turkey - a Plate Tectonic Approach. *Tectonophysics*, **75**(3-4), 181-241.
- Seymen, I., 1981. Stratigraphy and metamorphism of the Kırşehir Massif around Kaman (Kırşehir - Turkey). *Bulletin of the Geological Society of Turkey*, **24**, 7-14.

- Sherlock, S., Kelley, S., Inger, S., Harris, N.B.W. & Okay, A.I., 1999. Ar-40-Ar-39 and Rb-Sr geochronology of high-pressure metamorphism and exhumation history of the Tavsanli Zone, NW Turkey. *Contributions to Mineralogy and Petrology*, **137**(1-2), 46-58.
- Stampfli, G., Marcoux, J. & Baud, A., 1991. Tethyan margins in space and time. *Palaeogeography Palaeoclimatology Palaeoecology*, **87**(1-4), 373-409.
- Torsvik, T.H., Müller, R.D., Van der Voo, R., Steinberger, B. & Gaina, C., 2008. Global plate motion frames: Toward a unified model. *Review of Geophysics*, **46**.
- Trotet, F., Goffé, B., Vidal, O. & Jolivet, L., 2006. Evidence of retrograde Mg-carpholite in the Phyllite-Quartzite nappe of Peloponnese from thermobarometric modelisation - geodynamic implications. *Geodynamica Acta*, **19**(5), 323-343.
- Trotet, F., Jolivet, L. & Vidal, O., 2001. Tectono-metamorphic evolution of Syros and Sifnos islands (Cyclades, Greece). *Tectonophysics*, **338**, 179-206.
- Uto, K., Ishizuka, O., Matsumoto, A., Kamioka, H. & Togashi, S., 1997. Laser-heating ⁴⁰Ar/³⁹Ar dating system of the Geological Survey of Japan: System outline and preliminary results. *Bulletin of the Geological Society of Japan*, **48**, 23-46.
- van der Kaa-den, G., 1966. The significance and distribution of glaucophane rocks in Turkey. *Bulletin of the Mineral Research and Exploration Institute of Turkey*, **67**, 37-67.
- van Hinsbergen, D.J.J., 2010. A key extensional metamorphic complex reviewed and restored: The Menderes Massif of western Turkey. *Earth-Science Reviews*, **102**(1-2), 60-76.
- van Hinsbergen, D.J.J., Hafkenscheid, E., Spakman, W., Meulenkamp, J.E. & Wortel, R., 2005. Nappe stacking resulting from subduction of oceanic and continental lithosphere below Greece. *Geology*, **33**(4), 325-328.
- van Hinsbergen, D.J.J., Kaymakci, N., Spakman, W. & Torsvik, T.H., 2010. Reconciling the geological history of western Turkey with plate circuits and mantle tomography. *Earth and Planetary Science Letters*, **297**(3-4), 674-686.
- Vasquez, M., Altenberger, U., Romer, R.L., Sudo, M. & Manuel Moreno-Murillo, J., 2010. Magmatic evolution of the Andean Eastern Cordillera of Colombia during the Cretaceous: Influence of previous tectonic processes. *Journal of South American Earth Sciences*, **29**(2), 171-186.
- Verlaguet, A., Goffé, B., Brunet, F., Poinssot, C., Vidal, O., Findling, N. & Menut, D., 2011. Metamorphic veining and mass transfer in a chemically closed system: a case study in Alpine metabauxites (western Vanoise). *Journal of Metamorphic Geology*, **29**(3), 275-300.
- Vidal, O., De Andrade, V., Lewin, E., Munoz, M., Parra, T. & Pascarelli, S., 2006. P-T-deformation-Fe³⁺/Fe²⁺ mapping at the thin section scale and comparison with XANES mapping: application to a garnet-bearing metapelite from the Sambagawa metamorphic belt (Japan). *Journal of Metamorphic Geology*, **24**(7), 669-683.
- Vidal, O., Goffé, B., Bousquet, R. & Parra, T., 1999. Calibration and testing of an empirical chloritoid-chlorite exchange thermometer and thermodynamic data for daphnite. *Journal of Metamorphic Geology*, **17**(1), 25-39.
- Vidal, O. & Parra, T., 2000. Exhumation paths of high pressure metapelites obtained from local equilibria for chlorite-phengite assemblages. *Geological Journal*, **35**(3-4), 139-161.
- Vidal, O., Parra, T. & Trotet, F., 2001. A thermodynamic model for Fe-Mg aluminous chlorite using data from phase equilibrium experiments and natural pelitic assemblages in the 100-600°C, 1-25 kbar range. *American Journal of Science*, **301**, 557-592.
- Vidal, O., Parra, T. & Vieillard, P., 2005. Thermodynamic properties of the Tschermak solid solution in Fe-chlorite: Application to natural examples and possible role of oxidation. *American Mineralogist*, **90**(2-3), 347-358.
- Whitney, D.L. & Bozkurt, E., 2002. Metamorphic history of the southern Menderes massif, western Turkey. *Geological Society of America Bulletin*, **114**(7), 829-838.
- Whitney, D.L., Teyssier, C., Dilek, Y. & Fayon, A.K., 2001. Metamorphism of the Central Anatolian Crystalline Complex, Turkey: influence of orogen-normal collision vs. wrench-dominated tectonics on P-T-t paths. *Journal of Metamorphic Geology*, **19**(4), 411-432.
- Whitney, D.L., Teyssier, C. & Heizler, M.T., 2007. Gneiss domes, metamorphic core complexes, and wrench zones: Thermal and structural evolution of the Nigde Massif, central Anatolia. *Tectonics*, **26**(5).
- Whitney, D.L., Teyssier, C., Kruckenberg, S.C., Morgan, V.L. & Iredale, L.J., 2008. High-pressure-low-temperature metamorphism of metasedimentary rocks, southern Menderes Massif, western Turkey. *Lithos*, **101**(3-4), 218-232.
- Wiederkehr, M., Bousquet, R., Schmid, S.M. & Berger, A., 2008. From subduction to collision: Thermal overprint of HP/LT meta-sediments in the north-eastern Lepontine Dome (Swiss Alps) and consequences regarding the tectono-metamorphic evolution of the Alpine orogenic wedge. *Swiss Journal of Geosciences*, **101**, 127-155.
- Wiederkehr, M., Sudo, M., Bousquet, R., Berger, A. & Schmid, S.M., 2009. Alpine orogenic evolution from subduction to collisional thermal overprint: The (⁴⁰Ar)/(³⁹Ar) age constraints from the Valaisan Ocean, central Alps. *Tectonics*, **28**(TC6009).
- Wijbrans, J.R. & McDougall, I., 1986. ⁴⁰Ar/³⁹Ar Dating of White Micas from an Alpine High-Pressure Metamorphic Belt on Naxos (Greece) - the Resetting of the Argon Isotopic System. *Contributions To Mineralogy And Petrology*, **93**(2), 187-194.

- Wilke, F.D.H., O'Brien, P.J., Gerdes, A., Timmerman, M.J., Sudo, M. & Khan, M.A., 2010. The multistage exhumation history of the Kaghan Valley UHP series, NW Himalaya, Pakistan from U-Pb and Ar-40/Ar-39 ages. *European Journal of Mineralogy*, **22**(5), 703-719.
- Willner, A.P., Sepulveda, F.A., Herve, F., Massonne, H.-J. & Sudo, M., 2009. Conditions and Timing of Pumpellyite-Actinolite-facies Metamorphism in the Early Mesozoic Frontal Accretionary Prism of the Madre de Dios Archipelago (Latitude 50 degrees 20'S; Southern Chile). *Journal of Petrology*, **50**(11), 2127-2155.
- Yilmaz, Y., Genç, S.C., Güler, F., Bozcu, M., Yilmaz, K., Karacık, K., Altunkaynak, S. & Elmas, A., 2000. When did the western Anatolian grabens begin to develop? In: *Tectonics and Magmatism in Turkey and the Surrounding Area* (eds Bozkurt, E., Winchester, J.A. & Piper, J.D.A.), *Geological Society, London, Special Publications*, **173**, 353-384.
- Yilmaz, Y., Genç, S.C., Yiğitbaş, E., Bozcu, M. & Yilmaz, K., 1995. Geological Evolution of the Late Mesozoic Continental-Margin of Northwestern Anatolia. *Tectonophysics*, **243**(1-2), 155-171.

Captions

1. Figures captions

Figure 1: Tectonic units of Western and Central Anatolia (note the Ören Unit klippen atop the Cycladic Blueschists and northern Menderes Nappes) and distribution of the carpholite-bearing samples used for 40Ar-39Ar geochronology in the present study. Other carpholite localities discussed in text are Bahçeyaka in the southern Menderes Massif (Rimmelé et al., 2003b), and Konya in the central Afyon Zone (Pourteau et al., 2010). Unit abbreviations are: AlNa, Aladağ Nappes; BoZn, Bornova Zone; CyBs, Cycladic Blueschists; HBHNa, Hoyran-Beyşehir-Hadim Nappes; LyNa, Lycian Nappes; ÖrUn, Ören Unit. Toponymic abbreviations are: Af, Afyonkarahisar; An, Ankara; De, Denizli; Iz, Izmir; Ka, Kayseri; Ko, Konya; Kü, Kütahya; Me, Mersin; Or, Orhaneli; Si, Sivrihisar; Ya, Yahyalı.

Figure 2: Optical microphotographs (cross polars) of the samples investigated by in-situ UV laser ablation. Mineral abbreviations: Car, carpholite; Chl, chlorite, Ctd, chloritoid; Ky, kyanite; Phg, phengite; Qz, quartz.

Figure 3: Results of multi-equilibrium thermobarometry for the samples Afy0206 and Yah04. a-a') Ternary diagrams for white mica and chlorite compositions. Abbreviations: Am, amesite; Cel, celadonite; Cln, clinochlore; Dph, daphnite; Prl, pyrophyllite; Sud, sudoite. b-b') Map view of mineral distribution, and mica and chlorite chemical groups in the investigated areas. "XF" stands for Fe³⁺/Fetotal in chlorite. c-c') chlorite-mica-quartz-water (Afy0206) and chlorite-chloritoid-quartz-water (Yah04) multi-equilibrium calculations using average group compositions. d-d') Result summary. Grey fields represent the stability fields of carpholite with Mg/(Mg+Fe) = 0.30 (d) and 0.35 (d'), calculated with TheriakDomino (De Capitani & Petrakakis, 2010) following Pourteau (2011). See text for details.

Figure 4: Ar-Ar age spectra. a) Representative plateau age diagrams obtained by stepwise heating of mineral separates using a CO₂ laser. b) "Pseudo-plateau" age diagrams for in-situ ablation of rock sections using a UV laser. Box numbers refer to step numbers in the Table 4.

Figure 5: Synthetic P-T-t paths for the three Anatolide HP metamorphic belts. Superscript label refer to references: 1, Okay et al. (1998), Okay (2002); 2, Davis & Whitney (2006, 2008); 3, Çetinkaplan et al. (2008); 4, Droop et al., (2005); 5, Rimmelé et al. (2005); 6, Rimmelé et al., (2003b); 7, Candan et al. (1997); 8, Oberhänsli et al. (1998); 9, Pourteau (2011); *, this study. Age ranges for the Tavşanlı Zone are after Sherlock et al. (1999) as compiled by Davis (2011).

Figure 6: Schematic reconstruction of the geodynamic evolution of western Anatolia from the Late Cretaceous to the Neogene.

2. Table captions

Table 1: Summary of the published isotopic ages for high-pressure metamorphism in the Anatolides.

Table 2: Calculated average compositions of chlorite, mica and chloritoid in Afy0206 and Yah04 samples.

Table 3: Chlorite and chloritoid mineral compositions and Chl-Ctd-Qz-w multiequilibrium thermobarometric estimates obtained from pairs in Yah04.

Table 4: Summary of the results of ⁴⁰Ar-³⁹Ar geochronology.

Figures

Fig 1

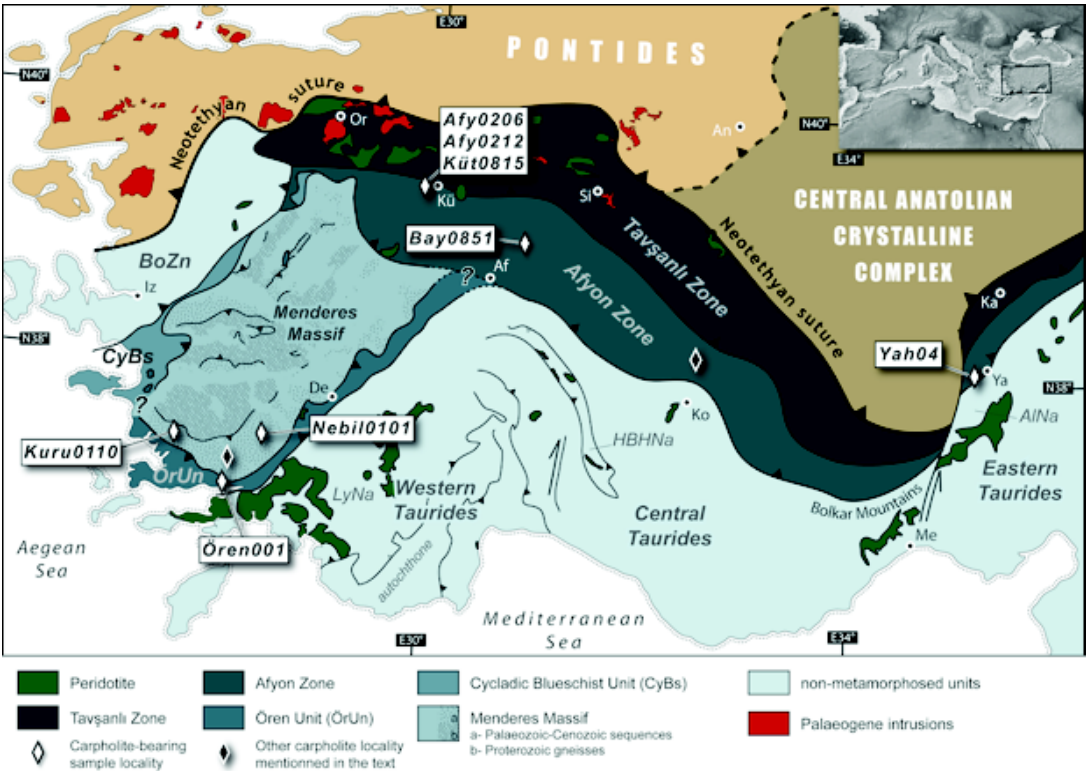


Fig. 2

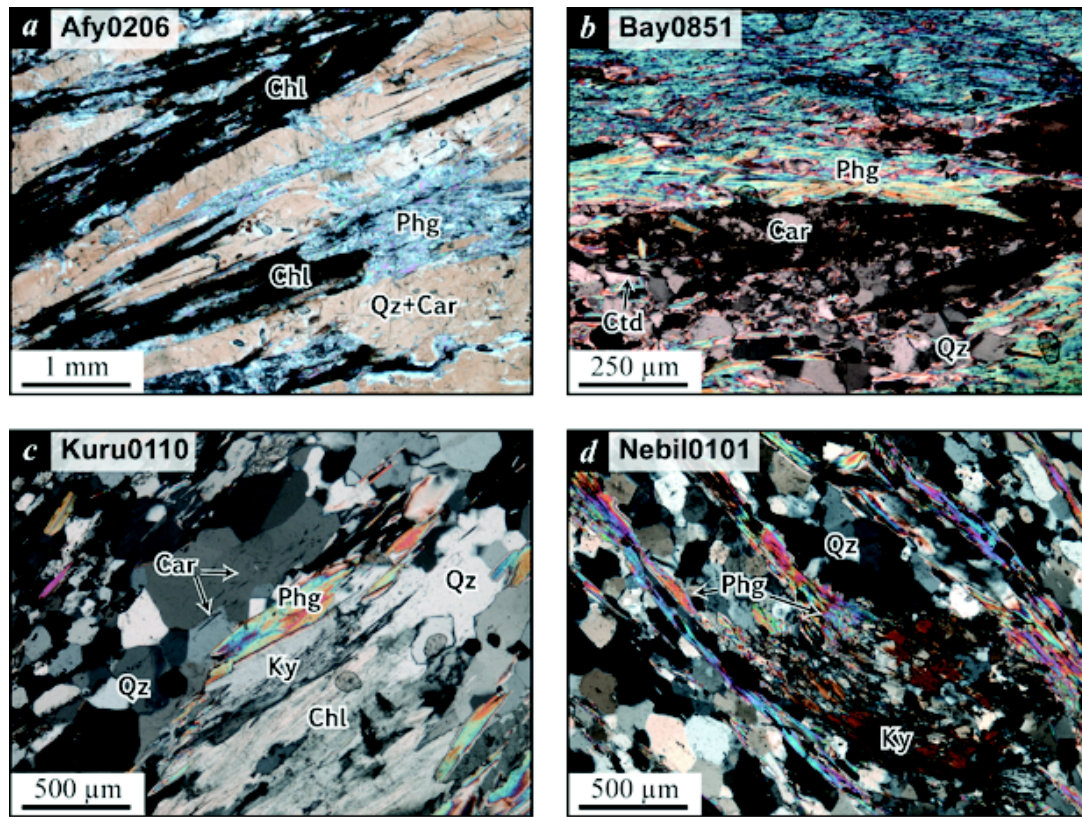


Fig. 3

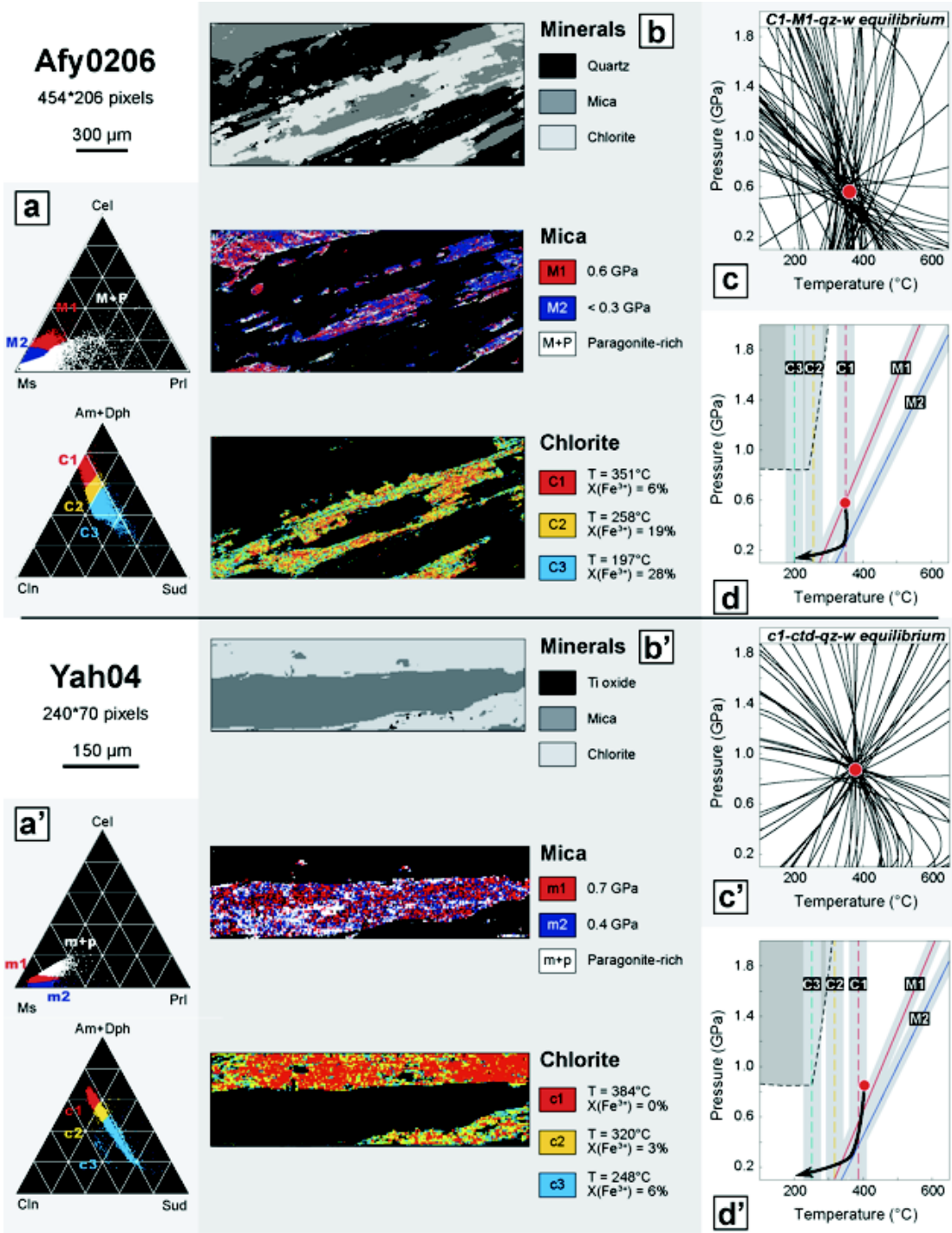


Fig. 4a

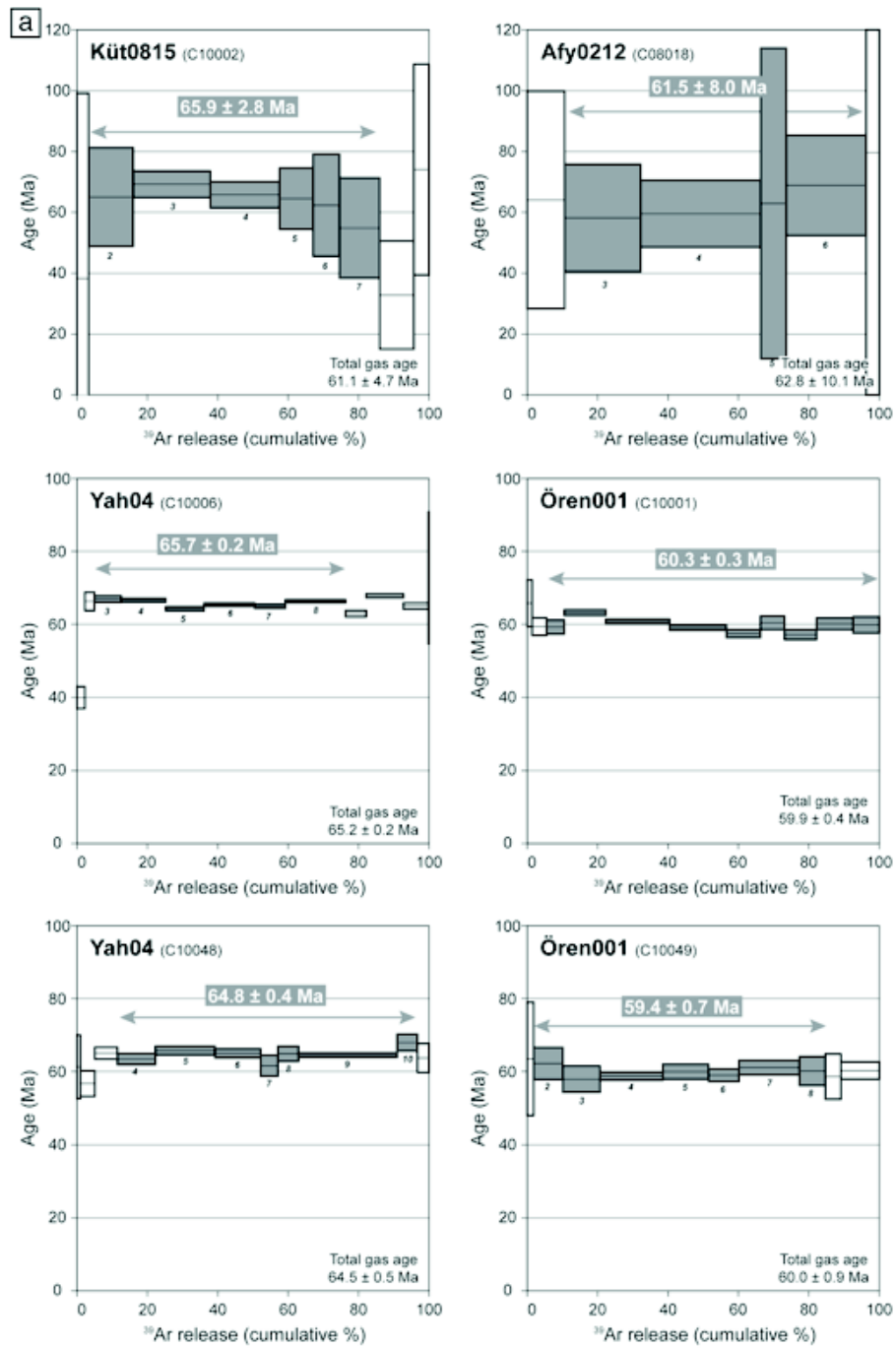


Fig. 4b

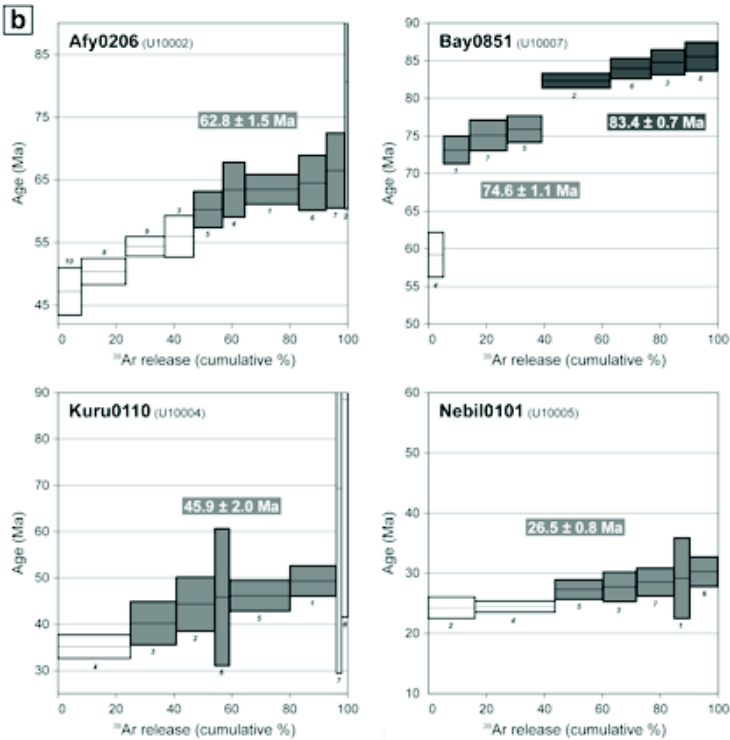


Fig. 5

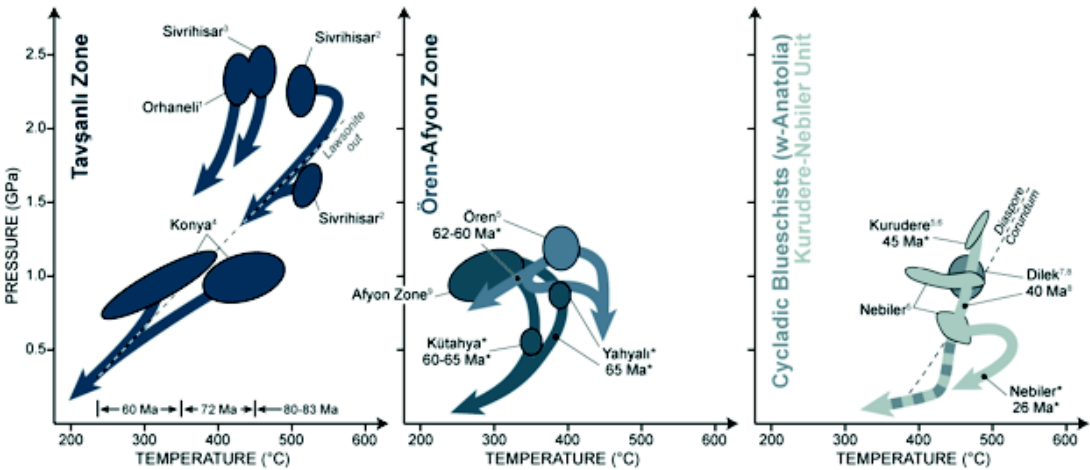


Fig. 6

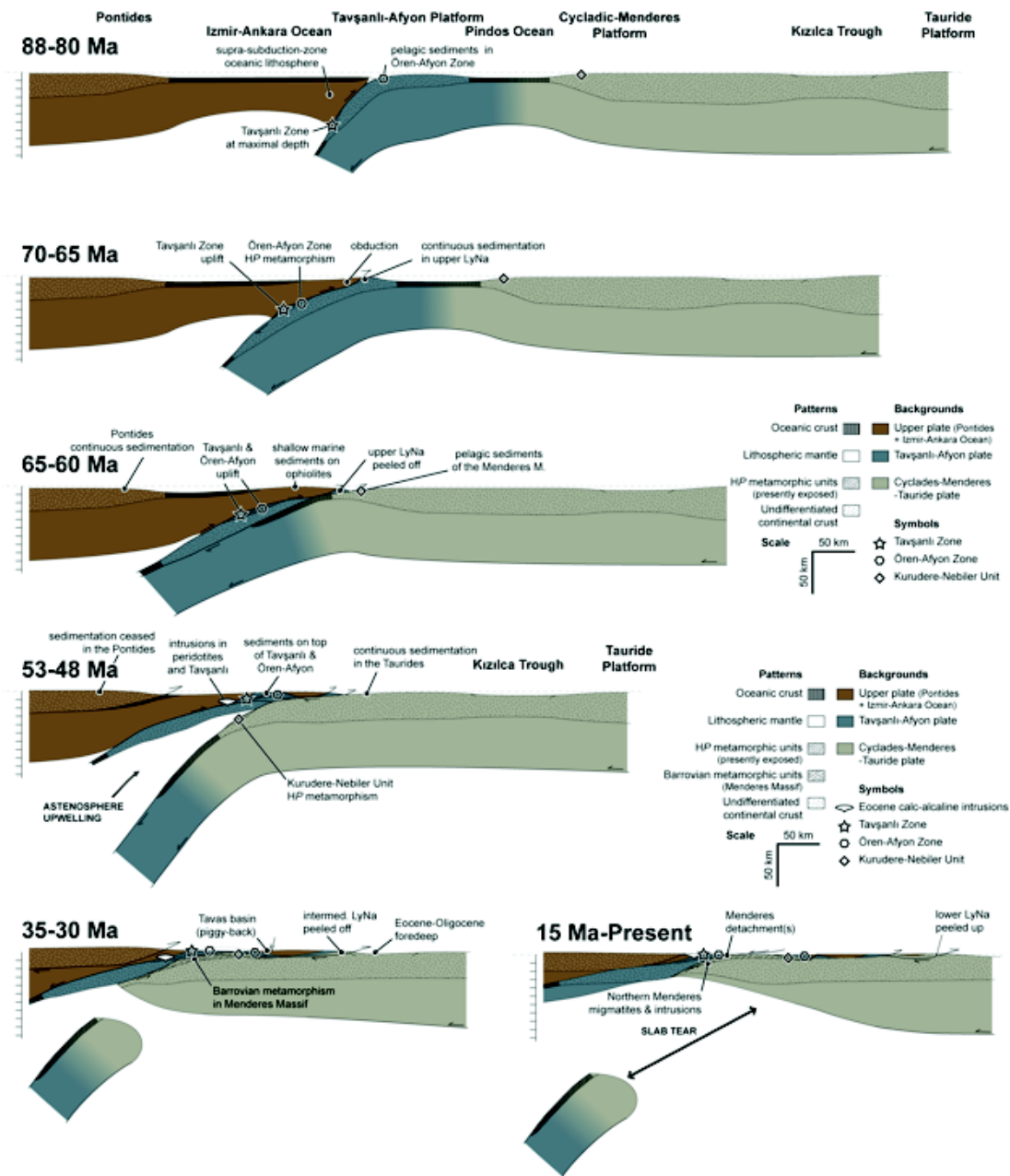


Table 1

Neotethys closure history of Anatolia

Pourteau *et al.*

Unit	Locality	Rock type	Geochronometer	Age type	Age	Error	Reference
Tavşanlı Zone	Orhaneli	Jadeite schist	Ar-Ar phengite	In-situ ablation (3 spots)	88.4	0.5	Okay & Kelley, 1994
	Orhaneli	Metabasite	Rb/Sr phengite	Isochron	78.5	1.6	Sherlock <i>et al.</i> , 1999
	Sivrihisar	Metabasite	Rb/Sr phengite	Isochron	79.7	1.6	Sherlock <i>et al.</i> , 1999
	Sivrihisar	Impure marble	Ar-Ar phengite	Stepwise heating (plateau)	87.9	0.6	Seaton <i>et al.</i> , 2009
Afyon Zone	Kütahya	Carpholite-quartz vein	Ar-Ar phengite	In-situ ablation (5 spots)	62.8	1.5	this study
	Kütahya	Carpholite-quartz vein	Ar-Ar phengite	Stepwise heating (plateau)	66.0	2.8	this study
	Kütahya	Carpholite-quartz vein	Ar-Ar phengite	Stepwise heating (plateau)	61.5	8.0	this study
	Afyon	Carpholite-bearing phyllite	Ar-Ar phengite	In-situ ablation (3 spots)	74.6	1.1	this study
	Afyon	Carpholite-bearing phyllite	Ar-Ar phengite	In-situ ablation (4 spots)	83.4	0.7	this study
	Yahyalı	Carpholite-quartz vein	Ar-Ar phengite	Stepwise heating (plateau)	65.7	0.2	this study
	Yahyalı	Carpholite-quartz vein	Ar-Ar phengite	Stepwise heating (plateau)	64.8	0.4	this study
	Yahyalı	Carpholite-quartz vein	Ar-Ar phengite	Stepwise heating (plateau)	66.7	0.4	this study
Ören Unit	Milas	Red-green phyllite	Ar-Ar phengite	Stepwise heating	70-90		Ring & Layer, 2003
	Ören	Carpholite-quartz vein	Ar-Ar phengite	Stepwise heating (plateau)	62.6	0.4	this study
	Ören	Carpholite-quartz vein	Ar-Ar phengite	Stepwise heating (plateau)	59.4	0.7	this study
	Ören	Carpholite-quartz vein	Ar-Ar phengite	Stepwise heating (plateau)	60.3	0.3	this study
Kurudere-Nebiler Unit	Kurudere	Carpholite-kyanite-quartz vein	Ar-Ar phengite	In-situ ablation (5 spots)	45.9	2.0	this study
	Nebiler	Chloritoid-kyanite microconglomerate	Ar-Ar phengite	In-situ ablation (5 spots)	26.5	0.8	this study
Cycladic Blueschists (Anatolian part)	Dilek	Epidote-blueschist	Ar-Ar phengite	Stepwise heating (plateau)	40.1	0.4	Oberhänsli <i>et al.</i> , 1998

Table 2

Final Amalgamation of Anatolia

Pourteau et al.

	Afy0206			Yah04		
Chlorite	C1	C2	C3	C1	C2	C3
SiO2	25,25	26,39	27,51	25,75	26,57	27,93
Al2O3	21,88	22,83	22,71	25,68	26,24	27,14
FeO	27,59	26,33	25,06	22,45	21,52	20,06
MnO	0,06	0,06	0,06	0,05	0,05	0,05
MgO	11,55	11,60	11,22	14,59	14,07	13,23
CaO	0,09	0,09	0,09	0,02	0,02	0,02
NaO	0,04	0,04	0,04	0,06	0,13	0,25
K2O	0,35	0,48	0,69	0,04	0,07	0,14

Atom site distribution (14 anhydrous oxygen basis including Fe3+)

Si(T1+T2)	2,67	2,74	2,82	2,62	2,68	2,77
Al(T2)	1,33	1,26	1,18	1,38	1,32	1,23
Al(M1)	0,33	0,26	0,18	0,38	0,32	0,23
Mg(M1)	0,23	0,21	0,20	0,25	0,24	0,22
Fe2+(M1)	0,30	0,22	0,18	0,22	0,20	0,18
V(M1)	0,14	0,31	0,44	0,15	0,24	0,37
Mg(M2+M3)	1,59	1,58	1,52	1,96	1,87	1,73
Fe2+(M2+M3)	2,00	1,63	1,37	1,69	1,58	1,39
Al(M2+M3)	0,34	0,69	0,99	0,32	0,51	0,81
Al(M4)	0,85	0,57	0,40	1,00	0,96	0,90
Fe3+(M4)	0,15	0,43	0,60	0,00	0,04	0,10
XFe3+ (%)	6	19	28	0	3	6
Temperature (°C)*	351	258	197	384	320	248

*Vidal et al. (2006), initial pressure = 5 kbar

	Afy0206		Yah04	
Mica	M1	M2	M1	M2
SiO2	48,13	47,19	47,78	47,55
Al2O3	32,55	33,60	35,85	36,11
FeO	2,25	2,07	0,40	0,40
MnO	0,01	0,01	0,01	0,01
MgO	0,96	0,84	0,45	0,42
CaO	0,04	0,04	0,03	0,03
NaO	1,05	1,36	1,10	1,31
K2O	9,21	8,86	8,86	8,39

Atom site distribution (11 anhydrous oxygen basis including Fe3+)

Si(T1+T2)	3,23	3,17	3,15	3,14
Al(T2)	0,77	0,83	0,85	0,86
V(M1)	0,98	0,97	1,00	0,99
Mg(M1)	0,01	0,01	0,00	0,01
Fe(M1)	0,01	0,02	0,00	0,00
Al(M2+M3)	1,80	1,83	1,94	1,95
Mg(M2+M3)	0,09	0,07	0,04	0,03
Fe(M2+M3)	0,11	0,10	0,02	0,02
K(A)	0,79	0,76	0,75	0,71
Na(A)	0,13	0,17	0,14	0,17
V(A)	0,08	0,07	0,11	0,12
Prp	0,07	0,06	0,11	0,12
Tri	0,02	0,03	0,01	0,01
Prg	0,14	0,18	0,14	0,17
Ms	0,61	0,62	0,70	0,68
Cel	0,16	0,11	0,04	0,02

Table 3

Final amalgamation of Anatolia

Pourteau et al.

	pair 1		pair 2		pair 3		pair 4		pair 5		pair 6		pair 7	
	Ctd	Chl	Ctd	Chl	Ctd	Chl	Ctd	Chl	Ctd	Chl	Ctd	Chl	Ctd	Chl
SiO2	24,645	25,462	24,432	29,956	24,579	25,114	24,577	25,162	24,800	25,611	25,843	25,927	24,263	25,942
Al2O3	42,154	25,893	41,991	26,045	41,849	25,875	41,640	25,749	41,628	25,290	39,713	25,542	41,845	25,127
FeO	25,389	23,254	25,191	22,044	25,400	22,520	25,779	22,776	25,322	23,212	24,784	22,225	24,690	22,147
MnO	0,291	0,078	0,233	0,071	0,209	0,000	0,212	0,000	0,328	0,042	0,181	0,021	0,283	0,088
MgO	2,309	14,029	2,563	14,471	2,561	14,924	2,427	14,757	2,337	14,846	3,631	15,465	2,451	15,598
CaO	0,010	0,049	0,001	0,017	0,000	0,018	0,000	0,024	0,000	0,023	0,013	0,024	0,004	0,027
Na2O	0,000	0,058	0,023	0,039	0,000	0,011	0,000	0,020	0,026	0,015	0,000	0,000	0,012	0,000
K2O	0,029	0,048	0,004	0,030	0,014	0,039	0,002	0,034	0,009	0,030	0,020	0,026	0,020	0,020
Total														
Si(T1+T2)	1,99	2,59	1,98	2,63	1,99	2,55	1,99	2,56	2,01	2,59	2,09	2,58	1,98	2,62
Al(T2)	4,01	1,40	4,01	1,37	3,99	1,45	3,98	1,44	3,97	1,41	3,79	1,42	4,02	1,38
Al(M1)		0,40		0,37		0,45		0,44		0,41		0,42		0,38
Mg(M1)	0,28	0,23	0,31	0,23	0,31	0,21	0,29	0,22	0,28	0,23	0,44	0,18	0,30	0,26
Fe2+(M1)	1,71	0,22	1,71	0,20	1,72	0,17	1,75	0,17	1,72	0,19	1,68	0,11	1,68	0,19
V(M1)		0,15		0,20		0,17		0,17		0,17		0,29		0,17
Mg(M2+M3)		1,90		1,95		2,04		2,05		2,01		2,11		2,09
Fe2+(M2+M3)		1,76		1,62		1,60		1,62		1,63		1,30		1,56
Al(M2+M3)		0,31		0,41		0,35		0,35		0,35		0,58		0,34
Al(M4)		1,00		0,95		0,85		0,85		0,85		0,56		0,88
Fe3+(M4)		0,00		0,05		0,15		0,14		0,15		0,44		0,12
Cln		0,23		0,23		0,21		0,22		0,23		0,18		0,26
Daph		0,22		0,20		0,17		0,17		0,19		0,11		0,19
Am		0,40		0,37		0,45		0,44		0,41		0,42		0,38
Sud		0,15		0,20		0,17		0,17		0,17		0,29		0,17
XMg(Ctd)	0,14		0,15		0,15		0,15		0,14		0,22		0,15	
P (Gpa)	0,82		0,89		0,95		0,96		0,95		1,13		0,96	
T (°C)	411		400		425		418		400		383		389	

A.5.3 Article 10 : Riel et al., (in press), Lithos

Implications for high-temperature metamorphism in a forearc zone: a metamorphic and geochronological study of the Triassic El Oro metamorphic complex in Ecuador

N. RIEL^a, S. GUILLLOT^a, E. JAILLARD^a, J.-E. MARTELAT^b, J.-L. PAQUETTE^c, S. SCHWARTZ^a, P. GONCALVES^d, G. DUCLAUX^e, N. THEBAUD^f, P. LANARI^a, E. JANOTS^a, J. YUQUILEMA^g

^a ISTERre, CNRS UMR5275, University of Grenoble I, 1381 rue de la Piscine, BP53, 38041 Grenoble, France

^b Laboratoire de Géologie de Lyon (LGLTPE), CNRS UMR5276, University de Lyon I, ENSL, 69622 Villeurbanne Cedex, France

^c LMV, CNRS UMR6524, University of Clermont-Ferrand I, 5 rue Kessler, 63038 Clermont-Ferrand, France

^d LCE, CNRS UMR6249, University of Franche-Comté, 16 rue de Gray, 25030 Besançon Cedex, France

^e CSIRO Earth Science and Resource Engineering, 26 Dick Perry Avenue, Kensington, WA 6151, Australia

^f Centre for Exploration Targeting, University of Western Australia, 35 Stirling Highway, Crawley WA 6009, Australia

^g Facultad de Geología y Petróleos, Escuela Politécnica Nacional, E-11 253, Quito, Ecuador

*Corresponding author. Université of Grenoble I; CNRS UMR5275; Institut des Sciences de la Terre, 1381 rue de la Piscine, BP53, 38041 Grenoble, France. Tel.: +33 476514057; fax: +33 476514058. E-mail address: a.nicolas.riel@gmail.com (N. Riel).

Abstract

In the forearc of the Andean active margin in southwest Ecuador, the metamorphic El Oro Complex exhibits a unique tilted forearc section partially migmatized. We used Raman spectroscopy on carbonaceous matter (RSCM) thermometry and pseudosections coupled with mineralogical and textural studies to constrain the pressure-temperature (P - T) evolution of the El Oro Complex during Triassic times. Our results show that anatexis of the continental crust occurred by white-mica and biotite dehydration melting along a 10 km thick cross section (from 4.5 to 8 kbar) with increasing temperature from 650 to 700 °C. In the biotite dehydration melting zone, temperature was buffered at 750–820 °C in a 5 km thick layer. The estimated average metamorphic gradient of 30 °C/km within the migmatitic section can be subdivided into two apparent gradients, of 40–45 °C/km in the upper part (from the surface to 17 km depth), and 10 °C/km (a quasi-adiabatic geotherm) in the lower part, corresponding to an isothermal melting zone. U-Th-Pb geochronology on migmatites yielded zircon ages 229.3 ± 2.1 Ma and monazite ages 224.5 ± 2.3 Ma. The thermal event generated S-type magmatism (Marcabelli granitoid) and was immediately followed by underplating of the high-pressure low-temperature (HP-LT) Arenillas-Panupalí unit at 225.8 ± 1.8 Ma. The association of high-temperature low-pressure (HT-LP) migmatites with HP-LT unit constitutes a new example of a paired metamorphic belt along the South American margin. We propose that in addition to crustal thinning, underplating of the Piedras gabbroic unit before 230 Ma provided the heat source necessary for crustal anatexis. Furthermore, its MORB signature shows that the asthenosphere was involved as the source of the heat anomaly. The fact that Late Triassic S-type felsic magmatism is widespread suggests that a large-scale thermal anomaly affected a large part of the South American margin at that time. We propose that crustal anatexis is related to an anomaly that arose during subduction of the Panthalassa ocean under the South American margin. Slab verticalization or slab break-off can be invoked.

1. Introduction

While the generation of HP-LT rocks, especially blueschist facies assemblage, is characteristic of a subduction setting (e.g., Ernst, 1988; Guillot et al., 2009), HT-LP rocks can be produced in a wide range of geological settings. In modern belts, HT-LP rocks and associated crustal anatexis (S-type magmatism) are typically generated in collisional orogens (Hodges, 2000). In such a setting, HT conditions are reached either by crustal thickening or by post-orogenic collapse (Gardien et al., 1997). Magmatic generation occurs on a timescale of 10 to 30 Ma and can produce large volumes of granites (Thompson and Connolly, 1995). In a subduction context, granitoids are usually of I-type and are not associated with HT-LP metamorphism, especially in a forearc setting (Huppert and Sparks, 1988; Brown, 2007).

In the present forearc region of the Andean active margin of southwest Ecuador, the El Oro metamorphic complex (Fig. 1) exhibits a continental sequence composed of metasediments (El Tigre and La Victoria units) partially molten metasediments (La Bocana unit) and intruded by S-type

granitoids (Marcabeli and El Prado plutonic rocks), juxtaposed with amphibolitic metagabbros (Piedras unit) and blueschist facies metabasalts (Arenillas–Panupalí unit) (Fig. 2). Because of the subvertical structures, this complex has been interpreted either as a shear zone active during the Triassic (Aspden et al., 1995), or as a remnant of a forearc zone tilted during a major tectonic event in the Late Triassic (Gabriele, 2002). However, little is known about the geological structures of the continental sequence and its relationships with the Piedras metagabbroic unit and the Arenillas–Panupalí blueschist unit.

Here, we focus our study on the HT–LP Triassic of the El Oro metamorphic complex (Fig. 2). Our aims are to: (1) characterize the deformation underwent by those units; (2) estimate the metamorphic P–T conditions; (3) date the migmatization; and (4) propose a model accounting for the HT–LP gradient and the crustal anatexis associated with underplating of HP–LT rocks. This was achieved by combining field work, textural observations, mineralogical identification, geothermobarometry and geochronological studies. The analytical methods are presented in the **Appendix A**.

2. Geological setting and previous studies

In southwest Ecuador various metamorphic terranes of both continental and oceanic affinity form the El Oro metamorphic complex (Feininger, 1978; Aspden et al., 1995). The latter is bounded to the south by the Cretaceous volcano–sedimentary sequence of the Celica–Lancones basin (Jaillard et al., 1996; 1999), to the NE by Tertiary volcanic deposits and to the NW by Cenozoic, recent sedimentary deposits (Fig. 2). This complex is characterized by its forearc position and by discordant E–W striking structures, within the NNE striking Andean orogenic belt (Fig. 1). The Late Paleozoic subduction related magmatic arc is known to occur within the Cordillera Central of Colombia (Vinasco et al., 2006), in NW Peru (Mišković, et al., 2009), and a Jurassic magmatic arc is known in Colombia and Ecuador, lying in the Subandean Zone (Jaillard et al., 2000). Consequently, since at least Carboniferous times, the El Oro metamorphic complex has been located in a forearc position relative to Pacific subduction zone (Fig. 1).

Three tectono–metamorphic groups are distinguished for the El Oro metamorphic complex:

(1) The Biron Complex, North of the La Palma–Guayabo Shear Zone (Fig. 2), consists of metasediments, migmatitic paragneisses, granitoids, metadiorites and amphibolites with a N–MORB–type geochemical affinity (Gabriele, 2002). Ar–Ar radiometric dating on biotite in migmatites and in metadiorites yielded ages of 75.5 ± 2.3 Ma and 78.4 ± 0.5 Ma, respectively. Pb–Pb dating on monazites yielded ages of 78 ± 1 Ma and 82 ± 1 Ma, and three U–Pb zircon analyses plot on a reverse discordia with a lower intercept at 200 ± 30 Ma (Noble et al., 1997). Noble *et al.* (1997) interpreted the lower intercept at 200 ± 30 Ma as the age of crystallization of the granitoid, and attributed the younger monazite ages to a later episode of deformation and metamorphism.

(2) South of the La Palma–Guayabo shear zone (Fig. 2), the Raspas complex (Feininger, 1980) consists of an ophiolitic massif, the El Toro metaperidotitic unit, and the Raspas eclogitic unit (Gabriele et al., 2003; John et al., 2010). The Lu–Hf ages of John et al. (2010) from the Raspas complex indicate that the ophiolite underwent prograde HP metamorphism at around 130 Ma. Radiometric dating yielded an age of 127 to 123 Ma (Ar/Ar on phengite), which was interpreted as the age of underplating of the Raspas eclogitic complex beneath the Ecuadorian margin (Feininger and Silberman, 1982; Gabriele, 2002; John et al., 2010).

(3) The El Oro paired metamorphic belt is located between the Raspas complex and the Cretaceous Celica–Lancones Basin (Figs 1 & 2) and consists of late Paleozoic sediments (Martinez, 1970) metamorphosed during the Triassic (Aspden et al., 1995), juxtaposed with the Piedras gabbroic unit (Aspden et al., 1992b) and with the Arenillas–Panupalí blueschist unit metamorphosed in the Triassic (Gabriele, 2002). From south to north (Fig. 2), the continental sequence is composed of the El Tigre and La Victoria low–to–high–grade metapelitic units, intruded by the Marcabeli S–type granitoid at 227 ± 0.5 Ma (U–Pb on zircon, Noble et al., 1997) and of the La Bocana migmatitic unit dated at 219 ± 22 Ma (Sm/Nd whole–rock/garnet isochron, Aspden et al., 1995). In the Piedras metagabbroic unit, U–Pb ages on zircon are 221 ± 17 Ma (Noble et al., 1997) and Ar–Ar ages on amphibole yielded an age of 226 ± 1.8 Ma (Gabriele, 2002). Geochemical studies indicate a MORB–type affinity for the Piedras gabbroic unit (Aspden et al., 1995; Gabriele, 2002; Bosch et al., 2002). Both the Piedras and the Arenillas–Panupalí units were retrogressed under greenschist–facies conditions (Gabriele, 2002).

The El Tigre unit strikes approximately E–W and dips to the north (50–60°), and is composed of turbidites with slump structures (Aspden *et al.*, 1992a). On its southern boundary the El Tigre unit is unconformably overlain by the Cretaceous sediments of the Celica–Lancones basin. In the north, the appearance of chlorite and biotite (Fig. 2) marks a gradational transition zone between the low metamorphic grade El Tigre unit and the moderate- to high-grade La Victoria unit. The La Victoria unit comprises a sequence of metapelites and metapsammites similar to that of the El Tigre unit. To the north, the La Victoria unit is typically composed of biotite ± muscovite ± fibrolite, albite and quartz with andalusite porphyroblasts. The Marcabelli S-type granitoid intrudes the La Victoria unit as an elongated E–W trending laccolithic body. This pluton principally consists of medium-grained biotite ± muscovite granodiorites, with hornblende-rich xenoliths (Aspden *et al.*, 1995). The contact between the La Victoria unit and the La Bocana unit has been interpreted as a syn- to late-magmatic dextral shear zone (Aspden *et al.*, 1995), which is coeval with sillimanite crystallization (Feininger, 1978). These shear zones show a sub-vertical foliation. A few kilometers north of Marcabelli, Feininger (1978) mapped a folded contact between the La Victoria and the La Bocana unit (Fig. 2), with a lens of the La Bocana unit cropping out within the metasediments of the La Victoria unit. Moreover, the metamorphic isograds follow the structure, implying that folding was post-metamorphic. The La Bocana unit (Fig. 2) has been described by Aspden *et al.* (1995) at its type locality as predominantly composed of garnet-bearing granitoid and lesser amounts of metatexites. North of the La Bocana unit, the contact with the Piedras unit (Fig. 2) is recognized as tectonic (Gabriele, 2002). However amphibolite xenoliths at the base of the La Bocana unit and granitic bodies within the Piedras unit suggest that the contact was originally intrusive (Aspden *et al.*, 1995). The Piedras unit strikes E–W, strongly dips to the south (70–90°), and is 3 to 5 km thick. This unit is mainly composed of amphibolites retrogressed under greenschist-facies conditions, and shows variable textures, massive to gneissic, fine to coarse grained (Gabriele, 2002). It can be traced from the Peruvian border for about 60 km to the east (Aspden & Litherland, 1992). The contact zone between the Piedras unit and the Arenillas–Panupalí unit is defined by the Naranjo shear zone (Gabriele, 2002). The Arenillas–Panupalí unit roughly strikes E–W and presents a sub-vertical foliation. It forms a 40 km long, 0.5 to 5 km wide belt. This unit is composed of metabasalts and metasediments retrogressed under greenschist-facies, relict blueschist-facies assemblage. The peak *P–T* conditions of this unit are estimated by Gabriele (2002) at ~9 kbar and 300 °C with garnet + glaucophane + titanite.

The El Oro metamorphic complex was first interpreted as a continental terrane accreted to the Andean margin during Late Jurassic to Early Cretaceous times (Mourier *et al.*, 1988). Aspden *et al.* (1995) interpreted the El Oro complex as a tectonic mélange formed in a Jurassic accretionary prism, preserving in the southern part a HT metamorphosed and migmatized unit of Late Triassic age. On the basis of the presence of garnet and glaucophane, they considered the Arenillas–Panupalí blueschist unit as part of the Late Jurassic–Early Cretaceous Raspas ophiolitic complex (Aspden & Litherland, 1992; Aspden *et al.* 1992a). Additionally, Aspden *et al.* (1995) suggested that the emplacement of the gabbroic Piedras unit into the active shear zone provided the heat source for crustal anatexis and formation of the S-type Marcabelli granitoid in HT–LP conditions. More recently, based on the MORB geochemical affinity and radiometric ages on amphibole at 225.3 ± 1.7 Ma, Gabriele (2002) described the Arenillas–Panupalí unit as a new tectono-metamorphic blueschist unit located between the Raspas complex to the north, and the Piedras unit to the south.

Based on the geochemical MORB-type affinity and on the radiometric age of 226 ± 1.8 Ma of the Piedras unit, Gabriele (2002) interpreted this unit as having originated during a pre-Jurassic subduction period, subsequently accreted to the continental margin. However, according to Noble *et al.* (1994), the zircons of the Piedras unit are of magmatic origin, and hence the age of 221 ± 17 Ma is considered to be the crystallization age. Although the Piedras unit shows a MORB-type signature, it is predominantly composed of amphibolites, with relicts of gabbroic textures, and no pillow basalts or sediments have been observed, thus favoring a plutonic origin. The continental sequence exhibits a northward increase in metamorphic temperature conditions (Feininger, 1978). Gabriele (2002) suggested this increase in thermal conditions from low-grade metasediments (El Tigre and La Victoria units) to high-grade migmatites (La Bocana unit) was related to the thermal gradient of a crustal sequence, and the present-day geometry with sub-vertical foliation resulted from the tilting of the entire sequence during a major tectonic event in the Late Triassic (~220 Ma).

3. Field relationships and migmatite morphology

From south to north, we focused our study on two subparallel cross-sections starting from the Cretaceous contact of the Celica–Lancones basin to the eclogitic unit of Ráspas. The studied samples are shown in Figure 2. We observed the same metamorphic evolution from south to north in the La Victoria unit as Feininger (1978) and Aspdén *et al.* (1995). Kinematic indicators (Fig. 3a, b) largely exhibit dextral transtensive apparent movement. The transition from the La Victoria to the La Bocana units is marked by the appearance of *in situ* melting and numerous metatexites. The southernmost evidence of partial melting in the La Victoria is represented by leucocratic veins emplaced within the unmolten metasediments (Fig. 4e).

Along the eastern cross-section, the migmatitic succession of the La Bocana unit crops out 3 km south of La Bocana village (Fig. 2). This succession can be followed along the Río Piedras with almost no interruption from low-melt fraction metatexites to the south, to the high-melt fraction mesocratic diatexites to the north (Figs. 2 & 4). Foliation is subvertical or strongly dipping to the south. The migmatitic succession starts with the appearance of small pockets of *in situ* melts that are only generated in fertile layers (Fig. 4, zone 2). As the fraction of melt increases in metatextitic migmatites, the sparse pockets of melts become connected (Fig. 4, zone 3). A psammite–pelite original layering similar to the La Victoria is still present and shows complex geometries due to contrasted rheological behavior controlled by the different amounts of melt or melt network. Leucocratic and melanocratic parts within pelitic layers are often folded together and crosscut by leucocratic veins. Psammitic layers are less fertile (lower white mica content) and more competent, and show dilatant structures (Figs 3c & 4c), which allow leaching and facilitate circulation of melt throughout the crustal pile. Close to the garnet zone, melting affects the whole metasedimentary pile (Fig. 4, zone 4) forming diatexites with large amounts of rafts of resistant lithologies (quartz-rich unmolten bodies which behave as resistant lithologies). Further north, garnet crystallizes and the volume of residual (biotite-rich) lithologies decreases drastically. At the top of this 7 km thick zone, melt is pervasive and homogeneously spreads out and early structures are erased. Resulting textures are mesocratic to melanocratic diatexites with a variable proportion of biotite and garnet (Fig. 4a). Within the garnet-bearing migmatitic layer, quartzite and other resistant bodies are dissolved in the melt toward the north, and are almost absent near the contact with the Piedras unit. Apparent kinematic indicators largely exhibit dextral transtension and roughly N–S dilatant structures. N–S structures of escaping melt are observed in competent layers (Fig. 4, zone 2 and 3) and show a southward direction of melt percolation (initially upward, taking into account subsequent tilting, Gabriele, 2002). Close to Piedras, the contact between the La Bocana and the Piedras units is tectonic and exhibits normal low-grade ductile faulting with top-to-the-south movement. In the western part, this contact zone exhibits mafic xenoliths (Fig. 2) and variably mixed dioritic magmas a short distance (up to 100 m) into the La Bocana unit. Resulting textures are produced by mingling and/or mixing of acidic and mafic melts (Fig. 3d). The Piedras unit as described by Aspdén *et al.* (1995) is made of saussuritized metagabbros (now amphibolites, Fig. 3e). In addition, we found ultramafic lenses with relicts of olivine along the eastern cross-section, south of the Piedras locality. Farther north, the contact between the Piedras and Arenillas–Panupali units (Naranjo Shear Zone) is diffuse and highly deformed with dextral transpressive shear sense under low-grade metamorphic conditions (Fig. 3f). In addition, we observed a limited amount of serpentinite (up to 10%) within the Arenillas–Panupali unit.

4. Petrography and mineral assemblages

Mineral assemblages of the continental sequence are described from the low-grade metasediments of the La Victoria unit to the south, to the high-grade molten metasediments of the La Bocana unit to the north. The location of studied samples is shown in Fig. 2 and characteristic mineral assemblages are presented in Table 1.

4.1. La Victoria metapelites

Near the boundary between the El Tigre and La Victoria units, the metapelite is composed of chlorite + biotite + quartz + plagioclase, thus defining a chlorite–biotite zone. Farther north, in the biotite zone (Fig. 2), the characteristic mineral assemblage is biotite + white mica + quartz + K-feldspar + plagioclase. In the psammitic layers, the mineral assemblage is dominated by quartz and subordinate biotite and white mica. In the andalusite zone (Fig. 2) (AV-08–19b, Table 1), the characteristic

mineral assemblage is biotite + white mica + andalusite + quartz + K-feldspar + plagioclase. Farther north, andalusite is progressively replaced by fibrolite (Feininger, 1978). Although cordierite is widely cited in this unit by Aspden *et al.* (1995), this mineral was not observed in examined samples. In the narrow andalusite-fibrolite zone, the characteristic assemblage is andalusite + sillimanite + biotite + white-mica + quartz + K-feldspar + plagioclase. Weakly strained chiasolitic andalusite occurs as large porphyroblasts up to 5 cm. In rare sample andalusite is statically replaced by kyanite on its outer edge (AV-08-15). On the rim of these andalusite/kyanite porphyroblasts, kyanite is replaced by biotite and fibers of sillimanite (fibrolite) (Fig. 5a & b). The fibrolite defines the main foliation (Fig. 5b), and deflects the older fabric with dextral transtensive apparent movements.

The andalusite fibrolite assemblage is transitional to the anatexis zone. Textural relationships observed in AV-08-15 sample show that the crystallization sequence was: andalusite, kyanite, and sillimanite. This suggests clock-wise *P-T* path that looped around the Al_2SiO_5 triple point (Whitney, 2002).

4.2. La Bocana migmatites

On the basis of the mineralogical assemblage, we distinguished two sub-units in the La Bocana unit. Near the contact with the unmolten metasediments of the La Victoria unit, the upper migmatitic zone is characterized by metatexites without garnet (Fig. 4, zones 1 to 4). The lower migmatitic zone is characterized by garnet-bearing diatexites (Fig. 4, zones 5). On the eastern cross-section, this zone begins near the locality of La Bocana and extends northward to the Piedras unit.

In the upper migmatitic zone (Fig. 4, zone 4), the melanosome characteristic mineral assemblage is biotite + sillimanite + quartz + K-feldspar + plagioclase \pm retrograde white-mica. Sillimanite occurs as prismatic aggregate of minerals associated with lath-like biotite and K-feldspar. Scarce spinel is present as small inclusions of hercynite within large prismatic sillimanite (Fig. 5d). Cesare (1994) showed that inclusion of hercynite in prismatic sillimanite formed after breakdown of staurolite at 585-655 °C. Therefore, hercynite in the upper La Bocana migmatites likely represents relicts of prograde metamorphism at subsolidus conditions. Fibrolite occurs on the outer rim of the prismatic sillimanite often surrounded by late white-mica. Leucocratic layers exhibit larger grain size, and are dominated by quartz, plagioclase and K-feldspar. Biotite occurs as well crystallized, or interstitial, grains. Late white-mica occurs as late interstitial crystals at grain boundaries of plagioclase and K-feldspar. Vermicular intergrowth of feldspar and quartz at K-feldspar grain boundary are widely observed (Fig. 6a). Symplectic intergrowth of muscovite and quartz are also common feature in this zone (Fig. 6a). These two last migmatitic microstructures are compatible with crystallization from melt (Sawyer, 2008). In this upper migmatite zone, garnet, orthopyroxene and cordierite are absent from the samples examined in this study. Biotite is present in every sample and its composition does not exhibit significant variation compared to the biotite of the La Victoria unit (Fig. 7d). Thus, natural observations are consistent with melting of the metasedimentary rocks in this zone within the stability field of the biotite at a temperature close to the solidus between 640 to 700 °C (Vielzeuf and Holloway, 1988; Patiño Douce and Harris, 1998). Melting reactions principally involved white mica breakdown. Two major melting reactions are thought to occur in this zone, either by fluid-present, or fluid-absent white-mica dehydration melting (Thompson and Tracy, 1979; Patiño Douce and Harris, 1998):

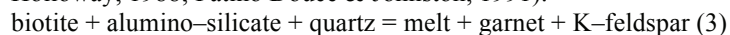


and

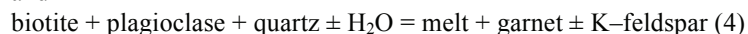


In the lower migmatitic zone, the most significant microstructure associated with partial melting is the segregation of felsic material surrounding peritectic products, erasing pre-melting structures and leading to the formation of relatively homogeneous mesocratic to melanocratic migmatites (Fig. 4a). Neither preferred orientation, nor migmatitic foliation can be recognized, at least at the macroscopic scale. The characteristic mineral assemblage is biotite + garnet + sillimanite + quartz + K-feldspar + plagioclase. Garnet contains inclusions of biotite, prismatic sillimanite and plagioclase, ilmenite and/or rutile. In the north of the lower migmatitic zone, modal percent of garnet increases, garnet becomes skeletal and elongated, and the sillimanite content decreases. Biotite occurs, either as elongated lath-like aggregate together with sillimanite, or as interstitial grains within quartz + plagioclase + K-feldspar rich layers (Fig. 5g). While garnet is well preserved in many samples, with only limited

breakdown into biotite at rims, K-feldspar belonging to residual aggregates (schlieren) appears to be largely recrystallized and/or breakdown. Fig. 6e & f show penetrative breakdown of K-feldspar in symplectic intergrowth of biotite + sillimanite + quartz + plagioclase indicating that these phases were crystallizing from the melt during cooling (Spear et al., 1999). In the lower migmatitic zone white-mica is almost absent. However in a few samples as AV-08-35, white mica overgrows plagioclase and K-feldspar, forming a common low-temperature alteration product (Fig. 6b). The appearance of garnet, absence of white mica and decreasing sillimanite and biotite content toward higher metamorphic grade implies incongruent melting produced by biotite dehydration (Vielzeuf and Holloway, 1988; Patiño Douce & Johnston, 1991):



and



Whether reactions 3 and 4 produce K-feldspar as peritectic phase is dependent on the activity of H₂O (Carrington and Watt, 1995). However graphite is omnipresent in examined samples of the La Victoria and of the La Bocana units. Connolly & Cesare (1993) showed that C-O-H fluid produced by the equilibration of H₂O and excess graphite must maintain the atomic H/O ratio of water, 2:1. This precludes water saturated conditions during partial melting and thus favors reaction (2) and (3) of dehydration melting in the Upper and the Lower La Bocana units, respectively.

Along the western cross-section, at the transition zone between the upper and lower migmatitic zone, garnet is associated in highly residual layers. Relict of kyanite are replaced by pluricentimetric sillimanite (Fig. 5e & f). Ilmenite and rutile are the two chief Ti-bearing minerals as ilmenite and rutile are stable at low and high pressure, respectively. Ilmenite and/or rutile present in the studied samples exhibits a South to North modal variability (Table 1, Fig. 2). Whereas in the La Victoria unit only ilmenite has been observed, in the lower migmatitic zone, we observe layers containing both ilmenite and rutile in equilibrium (Fig. 5g). North of this area only rutile is observed (see Fig. 2). This mineral succession, from ilmenite in the La Victoria unit to rutile in the La Bocana unit, suggests an increase in pressure conditions toward the north. In sample AV-08-28d, ilmenite is present in the matrix with relict rutile cores, whereas rutile is not observed as inclusions in garnet. Crystallization of sillimanite from kyanite and of ilmenite from rutile shows that the continental sequence recorded heating and/or decompression, which is coherent with the clock-wise *P-T* path around the Al₂O₃ triple point observed in sample AV-08-15. Furthermore, the lack of rutile inclusions in garnet in sample AV-08-28d indicates that decompression started before garnet crystallization.

4.3. Piedras amphibolites

In the Piedras unit, the characteristic mineral assemblage is hornblende + plagioclase + titanite + epidote + actinolite \pm quartz \pm clinopyroxene. Clinopyroxene is rare and its rims are always replaced by hornblende (Aspden et al., 1995). Plagioclase is widely saussuritized, and epidote and actinolite represent retrogressed minerals under greenschist facies conditions. Near the locality of Piedras, we identified ultramafic lenses (Fig. 2) with characteristic mineral assemblage of olivine + serpentine + magnetite \pm clinopyroxene characteristic mineral assemblage. In the western cross-section, in the contact zone with the La Bocana migmatites, mixing of acid and basic magmas (Fig. 3d) produced a mineral assemblage composed of hornblende + clinopyroxene + biotite + quartz + plagioclase (Fig. 5h).

4.4 Arenillas-Panupali blueschists

The Arenillas-Panupali unit is mainly represented by metabasalts metamorphosed under blueschist facies conditions, which underwent an intense greenschist facies overprint. Pressure peak-metamorphic conditions are characterized by the garnet + glaucophane + titanite assemblage (Gabriele, 2002). The greenschist overprint is documented by crystallization of fine-grained albite, chlorite and epidote, and by glaucophane breaking down to barroisite and actinolite (Gabriele, 2002).

5. Mineral chemistry

Representative analyses of garnet are presented in Table 2. Almost all garnets are found in the lower migmatitic zone, and are interpreted as peritectic phases (no sub-solidus garnet). Garnet exhibits little or no chemical variations from core to rim (Fig. 7a-c). X_{Alm} content from sample-to-sample (Table 1)

ranges from 0.70 to 0.80, X_{Prp} content from 0.13 to 0.20, X_{Grs} from 0.02 to 0.06 and X_{Sprs} from 0.02 to 0.06. X_{Alm} and X_{Prp} variations between different samples reflect their differences in $\text{MgO}/(\text{MgO}+\text{FeO})$ bulk composition (Table 7). Representative analyses of biotite are presented in Table 3. In metasediments, the X_{Mg} in biotite ranges from 0.33 to 0.46 in metapelites, and from 0.48 to 0.62 in garnet-bearing migmatites (Fig. 7d). Titanium content per formulae unit (p.f.u.) varies from 0.10 to 0.44 for unmolten metapelites, to a range of 0.40 to 0.60 for migmatites (Fig. 7d). X_{Mnx10} varies from 0.30 to 0.60 for metapelites and low grade migmatites (without garnet), whereas in garnet-bearing migmatites, X_{Mnx10} varies from 0.05 to 0.10. This drop in X_{Mnx10} correlates with the apparition of garnet and with the ongoing biotite dehydration melting.

Ti content and X_{Mg} increase in biotite is compatible with biotite progressive incongruent melting (Patiño-Douce & Harris, 1998). White mica is present in metapelites as a prograde and peak T phase, whereas in garnet-bearing migmatite, white mica occurs as a retrograde phase that results from saussuritization of feldspar or late back reaction from melt (Fig. 6 c–f). In metapelites and migmatites, white mica shows no significant compositional differences and is muscovite-rich ($X_{\text{Mu}} > 0.80$) with X_{Cel} accounting for the rest (Table 4). Silica content (p.f.u.) ranges from 3.00 to 3.05. In metapelite, plagioclase has high X_{Ab} , between 0.75 to 0.85. In high grade metapelites close to the anatectic zone, plagioclase is zoned and exhibits a slight enrichment in X_{Ab} from core to rim (0.77 to 0.83). In migmatites, plagioclase composition is more variable and X_{Ab} ranges from 0.60 to 1.00. Plagioclase commonly exhibits symplectite textures of micron-scale white mica + plagioclase with lower X_{An} .

6. Thermobarometry

Thermobarometry has been performed combining three independent approaches: the Raman Spectroscopy on Carbonaceous Matter thermometry (RSCM see **Appendix A**), pseudosections and Fe–Mg exchange thermometry.

6.1 RSCM thermometry and garnet–biotite thermometry

As carbonaceous material is present in all metasediments of the continental sequence, we used RSCM thermometry, which is based on the degree of organization of carbonaceous material. This method gives estimates on the maximal temperature undergone by the rocks for thermal conditions between 330 °C and 640 °C \pm 50 °C (Beyssac et al., 2002; 2004). RSCM is also applied on middle to relatively high grade metamorphic rocks up to the complete graphitization at \sim 640 °C (Robert et al., 2010). Table 6 shows the RSCM thermometry results. T_{max} estimated with the RSCM method, range from 475 to 640 °C, with a general increase in temperature from south to north.

PU–08–03 is the only unmolten metasediment in which small grains of garnet are present. Garnet–biotite thermometry on this sample yields temperatures of 556 \pm 40 °C and 571 \pm 40 °C, with the calibrations of Ferry and Spear (1978) and Perchuk and Lavrent'eva (1983), respectively. T_{max} with RSCM thermometry on the same sample gives 567 \pm 50 °C (Table 6), which is in very good agreement with the garnet–biotite temperature. For high grade migmatitic samples, inclusions of graphite were rare and often located on the surface of the host minerals. Few analyses were carried out on these samples (3–5 spectra per sample), but the obtained spectra are of good quality ($1\sigma < 8$ °C). T_{max} obtained in migmatites reach the graphitization T and are indicative of minimum temperature. We observe no discrepancy between the peak T mineralogical assemblages and the RSCM thermometry.

6.2 Pseudosections

P – T and T – X pseudosections have been calculated (1) to precise metamorphic P – T conditions and more particularly conditions of partial melting, and (2) to determine the type of prograde melting reactions. Phase relations have been modeled in the Ti(Mn)NKFMAH system using Perple_X'07 software (Connolly, 2005) and using the internally consistent thermodynamic database of Holland and Powell (1998). Bulk rock composition, solution models and end-member phases considered in the modeling are listed in Tables 7 and 8, respectively. Although the TiO_2 component is a minor component, it has been included to the model in order to take into account the rutile/ilmenite transition observed along the cross-section (Fig. 2, Table 1). MnO is taken into account for garnet-bearing migmatite in order to better estimate the endmember composition of garnet. In unmolten metasediments, the only phases bearing MnO are biotite and ilmenite while garnet which usually bear MnO has not been observed. Therefore MnO is not taken into consideration for the calculation of

pseudosections of unmolten metasediments as Mn has little effect on the stability field of biotite. Water content in the P - T pseudosections is kept constant for the entire range of P - T conditions. This water content was estimated for each sample by calculating T - X_{H_2O} pseudosection and P - X_{H_2O} pseudosections. The chosen water conditions correspond to the minimum amount of water necessary to saturate the sub-solidus assemblage just below the solidus with no free water. In these conditions C-O-H fluids in the graphitic saturated system of the metasediments of the La Victoria and the La Bocana units have not been modeled.

6.2.1 Metasediments

We selected one metapsammite (AV-08-13) and one metapelite (AV-08-15) belonging to a different structural level of the La Victoria unit in order to constrain the evolution of the P - T conditions within the metasedimentary sequence. Sample AV-08-15 and sample AV-08-13 are located in the narrow andalousite - fibrolite zone (Fig. 2).

In the metasediments of the La Victoria unit, the association of biotite + sillimanite \pm white mica defines the foliation (Fig. 5b). In sample AV-08-15, the observed mineral assemblage, X_{Mg} of biotite (0.36), X_{Ab} (0.79) shows that the P - T_{max} conditions lie in the field of biotite+plagioclase+K-feldspar + muscovite + sillimanite + quartz (Fig. 8). This is consistent with RSCM thermometry of $609 \pm 50^\circ\text{C}$. Thus, associated extensional microstructures observed in sample AV-08-15 during crystallization of sillimanite and the metastability of andalusite (Fig. 3a&b) constrains the P - T_{max} at 4 ± 2 kbar and $620 \pm 50^\circ\text{C}$ (Fig. 8).

In sample AV-08-13, the observed mineral assemblage, X_{Mg} of biotite (0.36), X_{Ab} (0.83) and RSCM thermometry ($580 \pm 50^\circ\text{C}$) show that the P - T_{max} lies in the field of biotite+plagioclase+K-feldspar+muscovite+andalusite+quartz mineral assemblage (Appendix C., Fig. 1). Estimated P - T_{max} are of 3 ± 2 kbar and $580 \pm 50^\circ\text{C}$.

6.2.2 Garnet-bearing migmatites

Four garnet-bearing migmatites have been selected, three samples were collected from the eastern cross-section near the La Bocana locality and represent different structural levels: AV-08-28d (Fig. 9), AV-08-32a (Fig. 10) and AV-08-33 (Appendix C. Fig. 3) (see position in Fig. 4). The fourth sample, PU-08-10 (Appendix C. Fig. 4), which is located in the same upper structural level as sample AV-08-27, belongs to the western cross-section. The bulk compositions used in the calculations are presented in Table 7. All pseudosections were made with the assumption that the bulk composition of our samples during garnet crystallization did not significantly changed. However, melt loss or gain is a widely accepted feature of migmatites (e.g., Kriegsman 2001, Brown 2002, 2007; White and Powell 2002) that could strongly influence the bulk composition, and consequently, the mineral assemblage of the rocks. In order to investigate the effect of melt transfer, we considered T - X_{melt} pseudosections (Appendix C. Fig. 2). T - X_{melt} pseudosections show the characteristic migmatitic mineral assemblage field, the positions of X_{Alm} , X_{Grs} , X_{Mg} of biotite and X_{Ab} isopleths and thus peak P - T conditions estimates at temperature above 690°C , are adversely affected by either loss or gain of melt. The supra-solidus domain, between the stability field of kyanite and cordierite (Fig. 9&10), is characterized by the mineral assemblage observed in the lower La Bocana unit: biotite + garnet + plagioclase + K-feldspar + sillimanite + quartz. P - T conditions were refined by contouring the X_{Alm} and X_{Grs} of garnet, X_{Mg} of biotite and X_{Ab} of plagioclase on each P - T pseudosections.

In sample AV-08-28d, garnet is modeled in all the P - T range and muscovite is absent of sub-solidus-region. The absence of muscovite in subsolidus domain can be related to extraction of low density melt produced during associated muscovite dehydration melting. P - T_{max} equilibration of garnet (Fig. 9) is of 7 ± 1 kbar and $760 \pm 20^\circ\text{C}$ ($X_{Alm} = 0.73$, $X_{Grs} = 0.05$). Biotite equilibration (Fig. 9) seems to have occurred at higher temperature ranging from 800 to 840°C ($X_{Mg} = 0.49$ to 0.59), compatible with plagioclase composition ($X_{Ab} = 0.67$) in schlieren. This apparent discrepancy which is also observed in sample AV-08-32 and sample AV-08-33 (Fig. 10 and Appendix C. Fig. 3&4) can be explained either by reequilibration of garnet during crystallization of residual melt or by the difficulty to estimate active bulk composition during partial melting due to inherited metastable phases as Ti-bearing phases.

The stability of Ti-bearing oxide provides a good constraint for pressure. Rutile-bearing assemblages that have been observed in the lowest structural domains (e.g., sample AV-08-33) are restricted to pressure conditions above 7.0 kbar (Fig. 3 in Appendix B). Whereas Ti-bearing phases have been observed in all examined samples, in modeled pseudosections Ti-bearing phases, in suprasolidus conditions, are restricted to domains of high temperature (> 780 - 800°C). Pseudosection models

theoretical mineral assemblage at each P – T conditions without taking into account metastability or heterogeneous reactions during metamorphism. In order to model the metastable Ti-bearing phases in suprasolidus domain we artificially saturated each pseudosections in Ti and reported the results over the original pseudosections (Fig. 9&10).

Results of pseudosections show that P – T_{max} conditions in garnet-bearing migmatites rise from 750 ± 20 °C for PU-08-10 to 750 – 820 °C for AV-08-28d, AV-08-32a and AV-08-33 while pressure increase continuously from 6 to 8 kbar for AV-08-28d, AV-08-32a and AV-08-33 and is ~ 7 kbar for PU-08-10.

7. Geochronological result

U–Th–Pb data obtained by SHRIMP at the University of Western Australia and LA-ICPMS methods at the university of Clermont–Ferrand on zircon and monazite are presented in Table 9 and 10, and in Figure 11; **Appendix A**.

7.1 Monazites

Ten subhedral and eighteen anhedral monazite grains were dated *in situ* in thin sections by LA-ICPMS, for the PU-08-10 and VI-08-12 garnet-bearing migmatitic samples of the La Bocana unit, respectively (Fig. 11a & b). They are compositionally homogeneous as no zoning was observed on backscattered images. Monazite $^{208}\text{Pb}/^{232}\text{Th}$ ages for sample PU-08-10 range from 228.9 ± 4.7 to 219.9 ± 4.5 and give a mean age of 223.2 ± 2.2 Ma (Fig. 11a). No inherited monazite grains were dated. Monazite $^{208}\text{Pb}/^{232}\text{Th}$ ages for VI-08-12 range from 229 ± 7 to 219 ± 5 Ma and give a mean age of 226.0 ± 1.3 Ma (Fig. 11b). Analyzed grains 1 and 6 of VI-08-12 sample exhibit a Th/U ratio of 0.6, and $^{208}\text{Pb}/^{232}\text{Th}$ ages of 235.7 ± 14.5 Ma and 236 ± 19.5 Ma (Table 9). The Th/U ratio (0.6) is consistent with xenotime rather than monazite. $^{208}\text{Pb}/^{232}\text{Th}$ dating on another xenotime grain yielded an older age (362.5 ± 12.3 Ma) with higher error and was considered in the mean age calculation.

7.2 Zircon

Fourteen and ten zircon grains were imaged and dated *in situ* by SHRIMP for the AV-08-31 and AV-08-28d garnet-bearing migmatitic samples of the La Bocana unit, respectively (Fig. 11c & d). The grains are subhedral to rounded, and are usually composite with a core surrounded by multiple rims. Most of the crystal cores are detrital and characterized by a corroded outline. These cores exhibit a magmatic Th/U ratio (>0.1) and yield $^{206}\text{Pb}/^{238}\text{U}$ ages ranging from late Archean to Ordovician. Rims are characterized by metamorphic Th/U ratio (0.01 to 0.1) and are concordant. U contents are lower in the inherited core (90–120 ppm) than in the rim (230–280 ppm). $^{206}\text{Pb}/^{238}\text{U}$ ages on zircon rims from sample AV-08-31 range from 236 ± 3 to 224 ± 3 Ma, with a mean age of 229.3 ± 2.4 Ma (Fig. 11c). Rim $^{206}\text{Pb}/^{238}\text{U}$ ages of AV-08-28d range from 221 ± 4 Ma to 229 ± 3 Ma, with a mean age of 225.7 ± 6.5 Ma (Fig. 11d). No systematic ages were obtained on multiple overgrowths. However, ages obtained from the rims yielded undistinguishable Late Triassic ages within the analytical uncertainty.

8 Discussion

Petrological, thermobarometric and geochronological informations acquired in this study are combined to reconstruct the thermal structure and the possible evolution of the south–western Ecuadorian margin during Late Triassic times.

8.1 Geochronological implications

The U–Th–Pb *in situ* ages on garnet-bearing migmatites of the La Bocana unit are coherent with, but more precise than, the age of 219 ± 22 Ma obtained by a Sm/Nd whole-rock/garnet isochron on similar migmatites (Aspden et al., 1992). The Piedras unit has been dated at 221 ± 17 Ma by the U–Pb method on magmatic zircons (Noble et al., 1997), and at 226 ± 1.8 Ma by the Ar/Ar method on hornblende (Gabriele, 2002). These two ages constrain the age of emplacement and crystallization of the Piedras gabbroic unit before 226 ± 1.8 Ma. The migmatitic ages obtained in this study (235–220 Ma) are compatible with a single Triassic thermal event producing the Piedras gabbroic unit and the Marcabelli S-type granitoid unit (227.5 ± 0.8 Ma, Noble et al., 1997). The Ar/Ar age of 225.3 ± 1.7 Ma on amphibole (Gabriele, 2002) for the Arenillas–Panupalí blueschist unit records either the cooling of the rock below 550 ± 50 °C isotherm (Harrison and McDougall, 1981), or mineral crystallized

below 550 ± 50 °C. The peak P – T conditions of the Arenillas–Panupalí unit have been estimated at 9 kbar and 300 °C (Gabriele, 2002), therefore the age at 225.3 ± 178 Ma dates the timing of the blueschist facies metamorphism. This age is statistically identical to the thermal event. However, the Arenillas–Panupalí blueschist unit, which was retrogressed under greenschist facies conditions (Gabriele, 2002), did not undergo any high temperature overprint. Therefore, underplating of the Arenillas–Panupalí oceanic unit postdated the thermal event. This interpretation is supported by the lack of zoning in migmatite garnets, which precludes a long cooling period. The timing of underthrusting of the Arenillas–Panupalí blueschist unit has important implications for the interpretation of the tectonic setting. The only setting to create blueschists is a subduction context (Ernst, 1988), and their exhumation mainly occur in forearc region (Cloos and Schreve, 1996; Guillot et al., 2009). Consequently, the age similarity for the whole Late Triassic metamorphic belt of El Oro massif implies that subduction was the only possible geodynamical setting that could produce anatexis and subsequent blueschist underplating.

8.2 P – T conditions

Estimates of P – T conditions in a metamorphic complex are of primary interest and are highly dependent on the geodynamical setting. The continental sequence of the El Oro metamorphic complex has been interpreted either as a regional shear zone undergoing partial melting (Aspden et al., 1995), or as a tilted continental sequence (Gabriele, 2002). The increase in metamorphic grade to the north from nonmetamorphic sediments to high grade migmatites has been interpreted either as resulting from the closing from the shear zone (Aspden et al., 1995), or as due to normal deepening in the crustal sequence (Gabriele, 2002). Peak temperature and pressure data are compiled in Fig. 12. Our results show an excellent correlation between increasing temperature and pressure conditions toward the north. This is supported by the commonly observed southward escape path of melt within dilatant structures, which must have been originally upward. Consequently the present geometry of the El Oro metamorphic complex is not representative of its Late Triassic geometry. As proposed by Gabriele (2002) on the basis of the increasing temperature conditions, the continental sequence has been tilted to acquire its present subvertical foliation. Because the Early Cretaceous Raspas eclogitic complex also exhibits a subvertical foliation (Aspden et al., 1995; Gabriele, 2002), tilting must have occurred during or after exhumation of the Raspas complex, i.e., in the Early Cretaceous or later. On the other hand, the unconformity of the gently dipping Celica–Lancones sediments (Jaillard et al., 1999) on the verticalized La Victoria unit implies that tilting occurred before Albian times. The present-day geometry has to be rotated $\sim 90^\circ$ (south to the north) along an east–west horizontal axis in order to reconstruct the original geometry during the thermal event. Rotation of the present day transtensive dextral movement indicates a low angle top–to–the–east or top–to–the–west normal movement during migmatization. Extension during Late Triassic times is supported by our mineralogical study: relict rutile in ilmenite core marks decompression before garnet crystallization and observed kyanite recrystallizing into sillimanite during migmatization. Note that extension is assumed to have occurred in north–western South America at that time (e.g., Vinasco et al., 2006; Mišković et al., 2009).

P – T estimates (Fig. 12) are direct proxies of the maximum geotherm during the early Late Triassic thermal anomaly. The pre-anatectic mineral assemblage in the La Victoria unit is recorded in the sample AV–08–15 by andalusite statically re-equilibrated into kyanite. The thermal event is marked by a strong temperature increase and active deformation in all the studied samples marked by sillimanite metamorphic foliation. It defines a hot maximum geothermal gradient (Fig. 12). This Late Triassic maximum geotherm exhibits two segments. In the upper unit, the geotherm shape is convex with high dT/dP , whereas in the lower unit, the geotherm shape is linear, almost vertical, with very low dT/dP . The migmatitic layer is of about 10 km thick. In the upper part, in the 2.5 km thick white–mica dehydration melting zone, temperature rises from sub–solidus conditions to 750 °C, thus representing a thermal gradient of 45 °C/km (down to 6 kbar) (Fig. 12). In contrast, temperature estimates in the garnet–bearing migmatites of La Bocana (7 km thick) are rather constant, ranging from 750 to 820 °C, which exhibits a thermal gradient of 10 °C/km. However, in this part pressure increases northward from 6 to 8 kbar (Fig. 12). Taking into account both melt modal percent and melt geometry we suggest that in the lower zone, maximum temperature is buffered in part by latent heat of biotite melting (e.g., Thompson and Connolly, 1995; Depine et al., 2008). Although the isothermal gradient could be explained by melt buffering alone, the high amount of melt and the lack of oriented

structures and magmatic fabric within the garnet-bearing migmatites, suggest that convective motions occurred throughout the lower migmatitic zone.

8.3 Heat source

Migmatization of the semi-pelitic sequence of the La Bocana unit, i.e., switching from a relatively cool to a high geothermal gradient requires heat input into the system. Three main possible mechanisms can provide additional heat to the continental crust (Huppert and Spark, 1988; Bergantz, 1992): (1) crustal thinning and isotherm tightening, (2) crustal thickening and enhanced radiogenic production, (3) emplacement of a plutonic body close to, or within the system. The very strong convex geothermal gradient for the upper El Oro units cannot be explained by thermal conduction alone. We suggest that this strong apparent geothermal gradient results from the combined effect of crustal thinning, and heat input in the La Bocana garnet-bearing migmatites. The mixing zone between the gabbroic magma of the Piedras unit and the acid magma of the La Bocana unit implies that the Piedras gabbroic unit is an *in situ* magmatic body emplaced during Triassic times (Aspden et al., 1995; Noble et al., 1997), and is not a tectonically underplated oceanic terrane, as suggested by Gabriele (2002) and Bosch *et al.* (2002). Hence, we propose that crustal anatexis occurred, due to a combination of crustal thinning, heat transfer from the magmatic underplating of the Piedras unit, and latent heat of crystallization of the latter. Based on structural (Figs 3a & b) and mineralogical evidence (rutile to ilmenite), the El Oro metamorphic complex underwent crustal thinning before and during migmatization. Even though crustal thinning likely played a role in the isotherms tightening, it was probably not the only heat source that caused the anatexis event.

In contrast the magmatic emplacement of the high temperature ($> 1000\text{ }^{\circ}\text{C}$) gabbroic Piedras unit before $226 \pm 1.8\text{ Ma}$ at crustal root level (Noble et al., 1997) is likely to have provided the local heat source for migmatization (Aspden et al., 1995). This assumption is supported by the presence of a relatively thin magma mixing zone ($\sim 100\text{ m}$), where gabbroic melts from the Piedras gabbroic unit and granitic melt from the La Bocana unit can be observed. If we can locally attribute the main heat source to the emplacement of the Piedras unit, the formation of the Piedras gabbro itself remains an open question. Based on the MORB origin of the Piedras gabbro (Aspden et al., 1995; Bosch et al., 2002), we propose that upwelling and subsequent decompression of the asthenosphere beneath the forearc zone were able to produce this MORB-like magma.

8.4 Geodynamical framework

Based on the similar ages of Tres Lagunas granite and Marcabelli granitoid, Noble *et al.* (1997) proposed that the El Oro metamorphic complex and the Cordillera Real of Ecuador (Fig. 1) were contiguous during the emplacement of S-type granites. Inherited core of zircons of sample AV-08-28d (Table 10) show two main peak at 550–525 Ma and 450–440 Ma. Those ages demonstrate that the protolith of the La Bocana migmatites is probably metasediments equivalent to the Isimanchi and Chiguinda Unit of the Cordillera Real in Ecuador, which are believed to be autochthonous to the Gondwana margin (Chew et al., 2007). Therefore these inherited ages support the idea that the El Oro metamorphic complex belonged to the Cordillera Real of Ecuador before Cretaceous tilting of the El Oro metamorphic complex and exhumation of the ophiolitic Raspas complex.

While partial melting of a significant part of a forearc continental crustal section is a rare feature in the Andes, evidence of a late Triassic tectono-thermal anomaly associated with granitic production are widespread all along the western South-American margin. From north to south, evidences of late Triassic granitoid emplacement are: the Amaga Granitic Stock in Colombia at $227.6 \pm 3.2\text{ Ma}$ (U-Pb, Vinasco et al., 2006), Tres Lagunas peraluminous granite within the Cordillera real of Ecuador (see Fig. 1) at $227.3 \pm 2.2\text{ Ma}$ (U-Pb, Litherland et al., 1994; Noble et al., 1997), Sabanilla migmatite of northern Peru at $230.4 \pm 3.2\text{ Ma}$ (Chew et al., 2008), Zongo granitoid in Bolivia at $225.1 \pm 4\text{ Ma}$ (U-Pb, Farrar et al., 1990), and Constitución granite in Chile at $224 \pm 1\text{ Ma}$ (Pb-Pb, Willner et al., 2005a,b). These authors agree that crustal thinning occurred during crustal melting and granitic intrusion. Farther East in Ecuador, ages at 245.7 ± 5.6 , 239.2 ± 2.2 , 234.2 ± 1.1 and $234.66 \pm 0.95\text{ Ma}$, from magmatic rims of zircons from acidic intrusive rocks the Loja Terrane and the El Oro complex, show the presence of a belt of Triassic migmatites across the southern Ecuador. Comparable events involving migmatization of the crust and S-type magmatism, dated from 260 to ca. 226 Ma, are well known from Northern Colombia to Northern Peru (Restrepo et al., 2011; Cardona et al., 2010,

Mišković et al., 2009) indicating a long period of S-type magmatism during late Permian to late Triassic times.

In Colombia and Ecuador, intrusions of the Amaga and Tres Lagunas granites were interpreted as related to the Tethyan rifting between North and northern South America (Aspden and Litherland, 1992). However Cardona et al., (2010) showed that subduction related magmatism was active until late Permian, thus North and northern South America were separated during Permian-Triassic times precluding a continental rifting model. Moreover, in a rifting model intense extension would have occurred to upwell the asthenosphere at shallow depth. In the La Victoria and the La Bocana units such intense deformation have not been observed. In Chile however, Willner *et al.* (2005b) interpreted the intrusion of the Constitución granite as indicating retreat of the subducting slab. More recently, Bustamante et al. (2011) showed that in the Central Cordillera of Colombia, amphibolitic schists related to subduction were tectonically juxtaposed with Triassic migmatites and granulites during a late Triassic subduction event. The presence of an underplated oceanic slab (Arenillas–Panupalí unit) at 225 Ma in the El Oro metamorphic complex and oceanic related underplated material in Colombia (Bustamante et al., 2011) imply that subduction was active at that time. Therefore, we interpret the thermal event affecting the Ecuadorian margin during Triassic times as the result of an anomaly arising from subduction processes.

During Permo–Triassic times, at 270–250 Ma, South America underwent a major shift in drift direction from northward to eastward directed (Torsvik et al., 2008; Tomezzoli, 2009; Geunal et al., 2010). This change in plate motion resulted from the counter-clockwise rotation of Gondwana during that time and ended in Late Triassic times, when South America resumed its movement toward the north (Torsvik et al., 2008).

We propose that this major eastward migration of South America provoked altogether a rapid trench retreat, and a generalized extensional regime associated with a steep to vertical slab (Fig. 13a). Slab verticalization, due to slab anchorage at depth, could have triggered dehydration of the slab and upwelling of the asthenosphere (Zhu et al., 2011). In this model, partial melting of the asthenosphere likely generated MORB-type identical to the Piedras gabbroic unit. Underplating of magma and melting of the crust would have started in arc and backarc position (Zhu et al., 2011) during late Permian to Triassic times and finally extended to the forearc position in late Triassic. Subsequent underplating at ~230 Ma of the Piedras gabbroic unit at crustal root level (Fig. 13b) in turn triggered migmatization of the semi–pelitic sequence of the La Bocana unit and emplacement of the Marcabelli S-type granitoid (Noble et al., 1997). At the same time (≈ 227 Ma), eastward migration of South America ceased (Torsvik et al., 2008), and we propose that slab breakoff occurred.

Based on U–Pb geochronology and geochemical study, Mišković et al. (2009) proposed that the Permian-Triassic magmatism in northwestern Gondwana from 260 to 220 Ma is related to a change in plate vector kinematics, resulting in thermal weakening of the subduction slab and eventually slab breakoff. They interpreted the subsequent upwelling of the asthenosphere as the cause of basaltic magma emplacement at the base of the lower crust triggering a vast region of extensive crustal melting from 260 to 200 Ma along the western Gondwana. Our model is similar except that we propose that slab breakoff occurred when South America resumed its course northward after a period of ~30 Ma of progressive slab verticalization ultimately reaching the forearc regions. Slab breakoff likely provoked an isostatic rebound of the oceanic plate, thus accounting for the tectonic underplating of the Arenillas–Panupalí blueschist unit (Fig. 13c) at ~226 Ma and underplating of oceanic material in Colombia in late Triassic (Bustamante et al., 2011). The latter process would explain the rapid cooling of both the Piedras unit and the El Oro metamorphic complex (≈ 226 Ma).

9. Conclusion

According to the results of our detailed thermobarometric study of the El Oro metamorphic Complex, the evolution of the Late Triassic paired metamorphic belt of southwestern Ecuador can be summarized as follows. After a period of relatively limited thinning of the continental crustal, melting of the Paleozoic psammite–pelite sequence of the La Bocana unit started at ~229 Ma. Crustal thinning and emplacement of the Piedras gabbroic unit provided the heat source that enhanced crustal anatexis. Melting of the metasediments occurred through white–mica and biotite dehydration processes. In the biotite dehydration melting zone, garnet was produced as the main peritectic phase, while modal percentage of biotite and sillimanite decreased with increasing metamorphic conditions. *P–T*

conditions estimates showed that crustal anatexis started at about 650 °C and ~ 4.5 kbar, and reach maximum of 820 °C. On a 7 km thick layer the apparent geotherm was of about 40 °C/km in the upper crustal unit and 5 °C/km in the lower unit. In the lower unit we suggest that temperature was buffered by biotite dehydration melting and by convective motions of magmas. The occurrence of numerous granite intrusions during Triassic times along the South American margin indicates that western South American underwent a widespread thermal anomaly between 230 and 225 Ma, which produced large amounts of S-type granitoids. We attribute the tectono-thermal event to a slab break-off event due to eastward migration of South America during Permian-Triassic times. Slab breakoff and/or slab verticalisation provoked upwelling and decompression of the asthenosphere, which underwent partial melting and provoked the magmatic underplating of the MORB-type Piedras gabbroic unit. This tectono-thermal event was immediately followed by renewed subduction processes and the underplating of the Arenillas-Panupali blueschist unit, which strongly contributed to the rapid cooling down of the forearc region of southwestern Ecuador by \approx 226 Ma.

Acknowledgements: This research was funded by the SEDIT programme (INSU, 2008–2009). We thank the IRD-Quito for logistical support during the 2008 and 2010 field campaigns. We thank Francis Coeur, François Senebier, Jean-Luc Devidal and Gilles Montagnac, for their help in sample preparation, microprobe and raman analysis. We thank the Laboratoire de Géologie de Lyon (ENS-Lyon) to give us access to the national raman instrument supported by the Institut national des sciences de l'Univers, CNRS. We also thank Bernado Cesare, Diego Villagomez and David Chew for their constructive review which highly contributed to improve the manuscript.

References

- Aspden, J. A. & Litherland, M., 1992. The geology and Mesozoic collisional history of the Cordillera Real, Ecuador. *Tectonophysics*, 205, 187–204.
- Aspden, J. A., Fortey, N., Litherland, M., Viteri, F. & Harrison, S. M., 1992a. Regional S-type granites in the Ecuadorian Andes: Possible remnants of the breakup of western Gondwana. *Journal of South American Earth Sciences*, 6, 123–132.
- Aspden, J. A., Harrison, S. H. & Rundle, C. C., 1992b. New geochronological control for the tectonomagmatic evolution of the metamorphic basement, cordillera real and el-oro province of Ecuador. *Journal of South American Earth Sciences*, 6, 77–96.
- Aspden, J.A., Bonilla, W. & Duque, P., 1995. The El Oro metamorphic complex, Ecuador: geology and economic mineral deposits. *Overseas Geology and Mineral Resources* (British Geological Survey publication), 67. combien de pages ?
- Bény-Bassez, C. & Rouzaud, J. N., 1985. Characterization of carbonaceous materials by correlated electron and optical microscopy and Raman microspectroscopy. In: *Scanning Electron Microscopy*, p. 119–132, SEM Inc, Chicago.
- Bergantz, G. W., 1992. Conjugate solidification and melting in multicomponent open and closed systems. *International Journal of Heat and Mass Transfer*, 35, 533–543.
- Beyssac, O., 2003. On the characterization of disordered and heterogeneous carbonaceous materials by Raman spectroscopy. *Spectrochimica Acta Part A: Molecular and Biomolecular Spectroscopy*, 59, 2267–2276.
- Beyssac, O., Goffé, B., Chopin, C. & Rouzaud, J. N., 2002. Raman spectra of carbonaceous material in metasediments: a new geothermometer. *Journal of Metamorphic Geology*, 20, 859–871.
- Beyssac, O., Bollinger, L., Avouac, J.-P. & Goffé, B., 2004. Thermal metamorphism in the lesser Himalaya of Nepal determined from Raman spectroscopy of carbonaceous material. *Earth and Planetary Science Letters*, 225, 233–241.
- Bosch, D., Gabriele, P., Lapiere, H., Malfere, J.-L. & Jaillard, E., 2002. Geodynamic significance of the Raspas Metamorphic Complex (SW Ecuador): geochemical and isotopic constraints. *Tectonophysics*, 345, 83–102.
- Brown, M., 2002. Retrograde processes in migmatites and granulites revisited. *Journal of Metamorphic Geology*, 20, 25–40.
- Brown, M., 2007. Metamorphism, Plate Tectonics, and the Supercontinent Cycle. *Earth Science Frontiers*, 14, 1–18.
- Bustamante, A., Juliani, C., Hall, C.M. & Essene, E.J., 2011. 40Ar/39Ar ages from blueschists of the Jambaló region, Central Cordillera of Colombia: implications on the styles of accretion in the Northern Andes. *Geologica Acta*, 9, 351–362.
- Carrington, D. P. & Watt, G. R., 1995. A geochemical and experimental study of the role of K-feldspar during water-undersaturated melting of metapelites. *Chemical Geology*, 122, 59–76.
- Cesare, B. Hercynite as the product of staurolite decomposition in the contact aureole of Vedrette di Ries, eastern Alps, Italy. *Contribution of Mineralogy and Petrology*, 116, 239–246.
- Cesare, B., Marchesi, C., Hermann, J. & Gómez-Pugnaire, M.T., 2003. Primary melt inclusions in andalusite from anatectic graphitic metapelites: implications for the position of the Al₂SiO₅ triple point. *Geology*, 31, 573–576.
- Chew, D.M., Magna, T., Kirkland, C.L., Miskovic, A., Cardona, A., Spinkings, R. & Schaltegger, U., 2008. Detrital zircon fingerprint of the Proto-Andes: Evidence for a Neoproterozoic active margin? *Precambrian Research*, 167, 186–200.
- Chew, D.M., Schaltegger, U., Košler, J., Whitehouse, M.J., Gutjahr, M., Spinkings, R.A. & Miškovic, A., 2007. U-Pb geochronologic evidence for the evolution of the Gondwanan margin of the north-central Andes. *Geological Society of America Bulletin*, 119, 697–711.
- Cloos, M. & Shreve, R. L., 1996. Shear-zone thickness and the seismicity of Chilean- and Marianas-type subduction zones. *Geology*, 24, 107–110.
- Cochrane, R., Spinkings, R., Winkler, W., Ulianov, A. & Chiaradia, M., 2011. Triassic to Early Cretaceous tectonic evolution of Ecuador: insights from U-Pb LA-ICP-MS geochronology, geochemistry and provenance studies. *Geophysical Research Abstracts*, 13, EGU2011-2650-2.
- Compston, W., Williams, I.S., Kirschvink, J.L., Zichao Zh. & Guogan, M., 1992. Zircon ages for the Early Cambrian timescale, *Journal of Geological Society of London*, 149, 171–184.
- Connolly, J. A. D., 2005. Computation of phase equilibria by linear programming: A tool for geodynamic modeling and its application to subduction zone decarbonation. *Earth and Planetary Science Letters*, 236, 524–541.

- Connolly, J. A. D., 1993. C–O–H–S fluid composition and oxygen fugacity in graphitic metapelites. *Journal of Metamorphic Geology*, 11, 379–388.
- Cotten, J., Le Dez, A., Bau, M., Caroff, M., Maury, R. C., Dulski, P., Fourcade, S., Bohn, M. & Brousse, R., 1995. Origin of anomalous rare-earth element and yttrium enrichments in subaerially exposed basalts: Evidence from French Polynesia. *Chemical Geology*, 119, 115–138.
- Depine, G.V., Andronicos, C.L., Phipps–Morgan, J., 2008. Near–isothermal conditions in the middle and lower crust induced by melt migration. *Nature*, 452, 80–83.
- Ernst, W. G., 1988. Tectonic history of subduction zones inferred from retrograde blueschist P–T paths. *Geology*, 16, 1081–1084.
- Farrar, E., Clark, A. & Heinrich, S., 1990. The age of the Zongo pluton and the tectonothermal evolution of the Zongo San–Gaban zone into the Cordillera Real, Bolivia. *Internat. Symp. Andean Geodynamics*, Grenoble, Abstract book.
- Feininger, T., 1978. Geologic map of Western El Oro Province. Escuela Politecnica Nacional, Quito, Ecuador.
- Feininger, T., 1980. Eclogite and related High–Pressure regional metamorphic rocks from the Andes of Ecuador. *Journal of Petrology*, 21, 107–140.
- Feininger, T. & Silberman, M.L., 1982. K–Ar geochronology of basement rocks on the Northern Flank of the Huancabamba deflection, Ecuador. U.S. Geological survey (Open–file report), 82–206.
- Ferry, J.M. & Spear, F.S., 1978. Experimental calibration of the partitioning of Fe and Mg between biotite and garnet. *Contributions to Mineralogy and Petrology*, 66, 113–117.
- Gabriele, P., 2002. HP Terranes exhumation in an active margin setting: geology, petrology and geochemistry of the Raspas complex in SW Ecuador. Unpub. PhD Thesis, Lausanne University, Switzerland.
- Gabriele, P., Ballèvre, M., Jaillard, E. & Hernandez, J., 2003. Garnet–chloritoid–kyanite metapelites from the Raspas Complex (SW Ecuador): a key eclogite–facies assemblage. *European Journal of Mineralogy*, 15, 977–989.
- Gardien, V., Lardeaux, J.M., Ledru, P., Allemand, P. & Guillot, S., 1997. Metamorphism during late orogenic extension: insights from the French Variscan belt. *Bulletin de la Société Géologique de France*, 168, 271–286.
- Gasquet, D., Bertrand, J. M., Paquette, J. L., Lehmann, J., Ratzov, G., Guedes, R. D., Tiepolo, M., Boullier, A. M., Scaillet, S. & Nomade, S., 2010. Miocene to Messinian deformation and hydrothermal activity in a pre–Alpine basement massif of the French western Alps: new U–Th–Pb and argon ages from the Lauziere massif. *Bulletin de la Société Géologique de France*, 181, 227–241.
- Geunal, S.E., Escosteguy, D. & Limarino C.O., 2010. Paleomagnetism of the Carboniferous–Permian Patquia Formation, Paganzo basin, Argentina: implications for the apparent polar wander path for South America and Gondwana during the Late Palaeozoic. *Geologica Acta*, 8, 373–397.
- Guillot, S., Hattori, K., Agard, P., Schwartz, S. & Vidal, O., 2009. Exhumation processes in oceanic and continental subduction contexts: a review. In S. Lallemand and F. Funiciello (eds.) "Subduction Zone Dynamics", Springer–Verlag Berlin Heidelberg, 175–204.
- Holland, T. J. B. & Powell, R., 1998. An internally consistent thermodynamic dataset for phases of petrological interest. *Journal of Metamorphic Geology*, 16, 309–343.
- Harrison, T. M. & McDougall, I., 1981. Excess ^{40}Ar in metamorphic rocks from Brocken Hill, South Wales: implications for $^{40}\text{Ar}/^{39}\text{Ar}$ age spectra and the thermal history of the region. *Earth and Planetary Science Letters*, 55, 123–149.
- Hodges, K.V., 2000. Tectonics of the Himalaya and southern Tibet from two perspectives. *Geological Society of America Bulletin*, 112, 324–350.
- Holland, T.J.B. and Powell, R., 1998. An internally–consistent thermodynamic dataset for phases of petrological interest. *Journal of Metamorphic Geology* 16, 309–344.
- Huppert, H. E. & Sparks, R. S. J., 1988. The Generation of Granitic Magmas by Intrusion of Basalt into Continental Crust. *Journal of Petrology*, 29, 599–624.
- Jackson, S.E., Pearson, N.J., Griffin, W.L. & Belousova, E.A., 2004. The application of laser ablation–inductively coupled plasma–mass spectrometry to in situ U–Pb zircon geochronology. *Chemical Geology*, 211, 47–69.
- Jaillard, E., Ordoñez, M., Bengtson, P., Berrones, G., Bonhomme, M., Jiménez, N. & Zambrano, I., 1996. Sedimentary and tectonic evolution of the arc zone of southwestern Ecuador during Late Cretaceous and Early Tertiary times. *Journal of South American Earth Sciences*, 9, 131–140.
- Jaillard, E., Laubacher, G., Bengtson, P., Dhondt, A. & Bulot, L., 1999. Stratigraphy and evolution of the forearc "Celica–Lancones Basin" of Southwestern Ecuador. *Journal of South American Earth Sciences*, 12, 51–68.
- Jaillard, E., Héral, G., Monfret, T., Díaz Martínez, E., Baby, P., Lavenue A. & Dumont J.–F., 2000. Tectonic evolution of the Andes of Ecuador, Peru, Bolivia and northernmost Chile. in: U.G. Cordani et al. (Eds.), *Tectonic evolution of South America*, Publ. 31st International Geological Congress, Rio de Janeiro, 481–559.
- John, T., Scherer, E.E., Schenk, V., Herms, P., Halama, R. & Garbe–Schönberg, D., 2010. Subducted seamounts in an eclogite–facies ophiolite sequence: the Andean Raspas Complex, SW Ecuador. *Contributions to Mineralogy and Petrology*, 159, 265–284.
- Kretz, R., 1983. Symbols for rock–forming minerals. *American Mineralogist*, 68, 277–279.
- Kriegsman, L. M., 2001. Partial melting, partial melt extraction and partial back reaction in anatectic migmatites. *Lithos*, 56, 75–96.
- Litherland, M., Aspdén, J.A. & Jemielita, R.A., 1994. The metamorphic belts of Ecuador. *British Geological Survey, Overseas Memoir*, 11, 147 p.
- Ludwig, K. J., 2003. *Isoplot 3.00*. Berkeley Geochronology Center (special publication), 4, 1–70.
- Martínez, M., 1970. Geología del basamento Paleozoico en las Montañas de Amotape y posible origen del petróleo en las rocas Paleozoicas del noreste de Perú. Lima 1^{er} Congreso Latinoamericano de Geología, No. 2, 105–138.
- Mišković, A., Schaltegger, U., Spinkings, R. A., Chew, D.M. & Košler, J., 2009. Tectono–magmatic evolution of Western Amazonia: geochemical characterisation and zircon U–Pb geochronologic constraints from the Peruvian Eastern Cordilleran granitoids. *Geological Society of America Bulletin*, 121, 1289–1324.
- Mourier, T., Laj, C., Mégard, F., Roperch, P., Mitouard, P. & Farfan Medrano, A., 1988. An accreted continental terrane in northwestern Peru. *Earth and planetary Science Letters*, 88, 182–192.
- Müller, W., Shelley, M., Miller, P. & Broude, S., 2009. Initial performance metrics of a new custom–designed ArF excimer LA–ICPMS system coupled to a two–volume laser–ablation cell. *Journal of analytical atomic spectrometry*, 24, 209–214.
- Noble, S.R., Aspdén, J. A., Jemielita, R. & Litherland, M., 1994. U–Pb geochronology of the Cordillera Real and the El Oro Provinces, Ecuador. Abstracts of the Eighth International Conference on Geochronology, Cosmochronology and Isotope Geology, Berkeley California, 234.
- Noble, S.R., Aspdén, J. A. & Jemielita, R., 1997. Northern Andean crustal evolution: New U–Pb geochronological constraints from Ecuador. *Geological Society of America Bulletin*, 109, 789–798.
- Paquette, J. & Tiepolo, M., 2007. High resolution (5 μm) U–Th–Pb isotope dating of monazite with excimer laser ablation (ELA)–ICPMS. *Chemical Geology*, 240, 222–237.
- Patiño–Douce, A. E. & Johnston, A. D., 1991. Phase equilibria and melt productivity in the pelitic system: implications for the origin of peraluminous granitoids and aluminous granulites. *Contributions to Mineralogy and Petrology*, 107, 202–218.

- Patiño-Douce, A. E. & Harris, N. W. B., 1998. Experimental constraints on Himalayan anatexis. *Journal of Petrology*, 39, 689–710.
- Pattison, D.R.M., 1992. Stability of andalusite and sillimanite and the Al_2SiO_5 triple point: constraints from the Ballachulish aureole, Scotland. *Journal of Geology*, 100, 423–446.
- Perchuk, L.L. & Lavrent'eva, 1983. Experimental investigation of exchange equilibria in the system cordierite–garnet–biotite. *Advances in Physical Geochemistry*, 3, 199–239.
- Restrepo, J.J., Ordóñez-Carmona, O., Armstrong, R. & Pimentel, M.M., 2011. Triassic metamorphism in the northern part of the Tahamí Terrane of the central cordillera of Colombia. *Journal of South American Earth Sciences*, 32, 497–507.
- Robert, A., Pubellier, M., de Sigoyer, J., Vergne, J., Lahfid, A., Cattin, R., Findling, N., & Zhu, J., 2010. Structural and thermal characters of the Longmen Shan (Sichuan, China). *Tectonophysics*, 491, 165–173.
- Seydoux-Guillaume, A.M., Wirth R., Deutsch A. & Schärer U., 2004. Microstructure of 24 – 1928 Ma concordant monazites: implications for geochronology and nuclear waste deposits. *Geochimica et Cosmochimica Acta*, 68, 2517–2527.
- Smith, J.B., Barley, M.E., Groves, D.I., Krapez, B., McNaughton, N.J., Bickle, M.J. & Chapman, H.J., 1998. The Scholl shear zone, West Pilbara: evidence for a terrane boundary structure from integrated tectonic analyses, SHRIMP U–Pb dating and isotopic and geochemical data of granitoids. *Precambrian Research*, 88, 143–17.
- Stacey, J. S. & Kramers, J.D., 1975. Approximation of terrestrial lead isotope evolution by a two-stage model. *Earth and Planetary Science Letters*, 26, 207–221.
- Stüwe, K., 2007. *Geodynamics of the lithosphere: an introduction*. Springer, 493 p.
- Thompson, A. B. & Tracy, R. J., 1979. Model systems for anatexis of pelitic rocks. *Contributions to Mineralogy and Petrology*, 70, 429–438.
- Thompson, A. B. & Connolly, J. A. D., 1995. Melting of the continental crust: Some thermal and petrological constraints on anatexis in continental collision zones and other tectonic settings. *Journal of Geophysical Research – Solid Earth*, 100, 15565–15579.
- Tiepolo, M., 2003. In situ Pb geochronology of zircon with laser ablation–inductively coupled plasma–sector field mass spectrometry. *Chemical Geology*, 199, 159–177.
- Tomezzoli, R.N., 2009. The apparent polar wander path for South America during the Permian–Triassic. *Gondwana Research*, 15, 209–215.
- Torsvik, T.H., Müller, R.D., Van der Voo, R., Steinberger, B. & Gaina, C., 2008. Global Plate Motion Frames: Toward a unified model. *Reviews Geophysics*, 46, 1–44.
- Van Acherbergh, E., Ryan, C.G., Jackson, S.E. & Griffin, W., 2001. Data reduction software for LA–ICP–MS. In *Laser ablation–ICPMS in the earth science*. Mineralogical Association of Canada, 29, 239–243.
- Vielzeuf, D. & Holloway, J. R., 1988. Experimental determination of the fluid–absent melting relations in the pelitic system. *Contributions to Mineralogy and Petrology*, 98, 257–276.
- Vinasco, C., Cordani, U., Gonzalez, H., Weber, M. & Pelaez, C., 2006. Geochronological, isotopic, and geochemical data from Permo–Triassic granitic gneisses and granitoids of the Colombian Central Andes. *Journal of South American Earth Sciences*, 21, 355–371.
- White, R.W. & Powell, R., 2002. Melt loss and the preservation of granulite facies mineral assemblages. *Journal of Metamorphic Geology*, 20, 621–632.
- Whitney, D.L., 2002. Coexisting andalusite, kyanite, and sillimanite: Sequential formation of three Al_2SiO_5 polymorphs during progressive metamorphism near the triple point, Sivrihisar, Turkey. *American Mineralogist*, 87, 405–416.
- Wiedenbeck, M., 1995. An example of reverse discordance during ion microprobe zircon dating: An artifact of enhanced ion yields from a radiogenic labile Pb. *Chemical Geology*, 125(3–4), 197–218.
- Willner, A.P., 2005a. Pressure–temperature evolution of an Upper Paleozoic paired metamorphic belt in Central Chile (34°–35°30'S). *Journal of Petrology*, 46, 1805–1833.
- Willner, A. P., 2005b. Time Markers for the Evolution and Exhumation History of a Late Palaeozoic Paired Metamorphic Belt in North–Central Chile (34°–35°30'S). *Journal of Petrology*, 46, 1835–1858.
- Zhu, G., Gerya, T.V., Honda, S., Tackley, P.J., Yuen, D.A., 2011. Influences of the buoyancy of partially molten rock on 3–D plume patterns and melt productivity above retreating slabs. *Physics of Earth Planetary Interiors*, 185, 112–121.

Supporting informations

Appendix A. Analytical techniques of methods used in this study.

Appendix B. Microprobe composition of garnet profiles

Appendix C. Supplementary pseudosections

Fig. 1. Simplified geological map of Ecuador and northern Peru modified after Chew *et al.* (2007) showing the location of the El Oro metamorphic complex. EO, El Oro; NSZ, Naranjo Shear Zone. Continuous line: documented magmatic arc position, dashed line: inferred magmatic arc position.

Fig. 2. Geological map of the western part of the El-Oro metamorphic complex of Ecuador modified after Feininger (1978) and Aspdén *et al.* (1995). The map shows the different tectono-metamorphic units. The main contacts, metamorphic isograds, the location of the studied samples are also indicated, and our thermometric results are indicated in Celsius degree (regular = RSCM thermometry; Bold = pseudosection thermometry). In unmolten metasediments we find good correlation between metamorphic isograds and estimated temperature with the RSCM; in the migmatitic zone the calibration limit of the RSCM thermometer is reached (640 °C) and temperatures are underestimated in comparison with the wet solidus (~650°C) and calculated pseudosection temperatures in garnet-bearing migmatites (~750 to 820 °C).

Fig. 3. Photograph of rocks of the HT units of the El Oro metamorphic complex. (a) Photograph of AV-08-15 outcrop of the La Victoria unit, dextral transtensive apparent kinematics indicators are indicated by the black arrows. (b) photomicrograph of AV-08-15 under polarized light, K-feldspar is recrystallized at the rims by fibrolite ± white mica ± biotite, underlining the high temperature foliation with dextral transtensive apparent movement (black arrows); (c) metatexite of the upper migmatitic zone, melt has percolated within resistant melanocratic layers, also showing a apparent dextral transtensive movement; (d) photograph of mixing zone between the Piedras unit and the La Bocana unit, gabbroic melt and acid melt are mixed (see Fig.5h), numerous mafic xenoliths are present; (e) photograph of the metagabbros of the Piedras unit; (f) photograph of the highly strained contact zone between the Piedras unit and the Arenillas-Panupalí unit, unfolding of the plagioclase vein yields >200 % of shortening. Insert blue arrows represent the north direction lying in a horizontal plane, the highlighted face of the cube shows the observed plane surface of the outcrop compared with the horizontal, and finally the line on the highlighted face of the cube shows the azimuth of the foliation.

Fig. 4. Migmatitic "log" of the upper part of the La Bocana unit. (a-e), photographs of outcrops in relation to their structural level in the migmatitic log; (f) schematic log representing the upper migmatitic section for a 4 km thick; internal structures are purposely magnified and the different generations of leucosomes are not distinguished; zone 1: first appearance of melt with a very low fraction of in situ melting; zone 2: melting occurs through white-mica dehydration in the pelitic rich layers producing metatexites and melt fraction is inferior to 25%; between the zones 1 to 2, 2 to 3 and 3 to 4, psammitic layers poor in micas, are not, or are weakly affected by in situ melting; zone 3: melt fraction increases, but the metatextitic texture is still dominant and several generations of leucosomes can be observed; they are either folded with residual layers or crosscutting the former ones; as the melt fraction increases, metatexites becomes diatexites of zone 4 with large rafts of resistant bodies (quartz rich); zone 5: garnet appears and the volume of resistant lithologies decreases. The migmatites acquire homogeneous diatexitic magma like rheology and no syn-migmatitic preferred orientation can be seen, at least at the macroscopic scale.

Fig. 5. Photograph of metasediments, under macroscopic view (a, e), polarized light (c, d,g, h), and polarized and analyzed light (b, f) . (a) sample AV-08-15, andalusite is statically replaced by kyanite at rim and main foliation is underlined by finely crystallized fibrolite and biotite; (b) detailed microphotograph of (a), showing the microstructural relationships among the aluminosilicates; (c) biotite-sillimanite peritectic aggregates produced by dehydration melting of white-mica at the boundary of large grain of quartz; (d) spinel (hercynite) inclusions in sillimanite; (e) macroscopic view of a highly residual garnet-bearing migmatite with leucosome and associated peritectic garnet; note the associated breakdown of kyanite to sillimanite; (f) microphotograph of (e), showing the recrystallization of kyanite into sillimanite; (g) characteristic texture and mineral assemblage of garnet-bearing migmatites, rutile and ilmenite are in equilibrium; (h) typical paragenesis of the mixing zone between the Piedras gabbroic unit and the La Bocana migmatitic unit.

Fig. 6. Microphotograph of partially molten metasediments under polarized and analyzed light (a, b, d, f) and polarized light (c, e). (a) sample PU-08-06, interaction between residual melt and K-feldspar forming myrmekite and muscovite + quartz symplectite; (b) late crystallization of muscovite in AV-08-35o garnet-bearing sample; (c, d) AV-08-28d garnet-bearing sample, retrograde interaction between residual melt and K-feldspar forming myrmekite and likely contributed to the penetrative saussuritization of the K-feldspar in muscovite + quartz; (e, f) PU-08-10 garnet-bearing sample, retrograde interaction between residual melt and a large crystal of K-feldspar. The former K-feldspar grain is largely breakdown by the formation of myrmekite, crystallization of quartz + biotite symplectite and late crystallization of crosscutting prismatic sillimanite crystal.

Fig. 7. Garnet and biotite chemical composition of the El Oro complex. (a, b, c) microprobe analysis across garnet crystal of AV-08-28d (a), AV-08-32a (b) and PU-08-10 (c) samples. Most of the endmembers exhibit relatively flat pattern for all samples, excepted for (b) and (c) where X_{pyr} and X_{sps} are respectively, slightly depleted and enriched at rim; (d) $X_{(\text{Ti}, \text{Mg}^*, \text{Mn} \times 10)}$ of biotite of various listed samples across the El Oro metamorphic complex. (1) La Victoria metasediments, (2) upper the La Bocana metatexites, (3) lower the La Bocana garnet-bearing migmatites. $\text{Mg}^* = \text{Mg}/(\text{Fe} + \text{Mg})$. The Mg^* tendency exhibits an increase from 0.36 in the zone (1) and (2) to 0.55 in the zone (3) where partial melting occurred under biotite dehydration melting. X_{Mn} (Mn p.f.u. $\times 10$, see Table 3) drops from 0.45 in zones (1) and (2) down to <0.1 in zone (3). This coincides with the condition of partial melting of biotite. Storage of Mn in biotite in lower metamorphic grades (zone (1) and (2)) can account for the absence of garnet whereas pseudosections stabilize garnet when MnO is used. X_{Ti} (p.f.u., see Table 3) is of 0.3 to 0.4 in zone (1) and (2) and becomes >0.4 in zone (3).

Fig. 8. P - T pseudosection of AV-08-15 metapelite in the NCKFMASHT system. The white star corresponds to P - T_{max} metamorphic conditions underwent by the sample. These conditions have been estimated using the observed paragenesis and RCSM thermometry (vertical dotted line passing through the star center). Estimated conditions are supported by the compositions of biotite and plagioclase. The heavy black arrow represents the suggested P - T path before P - T_{max} conditions based on aluminosilicate sequence of Fig. 5a & b. Bulk compositions used for each pseudosection are reported in Table 7. No shading = field divariant, then light to dark shading = increasing the variance (trivariant, quadrivariant, etc.).

AV-08-15 sample represents the pelitic endmember lithology which in the lower the La Bocana unit underwent partial melting under biotite dehydration melting. In order to validate this hypothesis, X_{Alm} , X_{Grs} isopleths of garnet and X_{Phlo} , X_{Ab} of biotite and plagioclase are also indicated in the suprasolidus region. Reported isopleth of solid-solutions in suprasolidus region are compatible with measured compositions in samples AV-08-28d, AV-08-32a, AV-08-33 and PU-08-10 (X_{Alm} , 0.72 to 0.80; X_{Grs} , 0.025 to 0.045; X_{Phlo} , 0.5 to 0.6, X_{Ab} , 0.6 to 0.7) and also indicate that partial melting occurred under biotite dehydration melting at P - T conditions of 5 to 8 kbar and 740 to 820 °C. Same calculations were performed for AV-08-13 sample which represents the psammitic endmember lithology observed in the La Victoria unit. Results are presented in supplementary data and show similar results.

Fig. 9. P - T pseudosections of garnet-bearing migmatite AV-08-28d in the NCKFMASHT system. Isopleths of almandine (X_{Alm}), grossular (X_{Grs}), phlogopite (X_{Phlo}) and albite (X_{Ab}) are plotted in the field of the observed peak P - T mineralogical assemblage; the white boxes represent the P - T conditions of garnet, biotite and plagioclase equilibration i.e., when measured composition matches the theoretical composition constructed by isopleths. Bulk compositions used for each pseudosection are reported in Table 7. Same shading as Fig. 8.

Fig. 10. P - T pseudosections of garnet-bearing migmatite AV-08-32a in the NCKFMASHT system. Isopleths of almandine (X_{Alm}), grossular (X_{Grs}), phlogopite (X_{Phlo}) and albite (X_{Ab}) are plotted in the field of the observed peak P - T mineralogical assemblage; the white boxes represent the P - T conditions of garnet, biotite and plagioclase equilibration i.e., when measured composition matches the theoretical composition constructed by isopleths. Bulk compositions used for each pseudosection are reported in Table 7. Same shading as Fig. 8.

Fig. 11. Geochronological results of La Bocana migmatites. (a,b); $^{206}\text{Pb}/^{238}\text{U}$ versus $^{208}\text{Pb}/^{232}\text{U}$ diagram of monazites from AV-08-31 and VI-08-12 samples; the mean $^{208}\text{Pb}/^{232}\text{U}$ age is indicated; (c, d) Concordia diagram of zircons from AV-08-31 and AV-08-28d samples, the mean $^{206}\text{Pb}/^{238}\text{U}$ age is indicated.

Fig.12. P - T diagram for El Oro metamorphic complex. (a) reported peak P - T_{max} conditions of studied samples in the simplified pseudosection of AV-08-15 sample (Fig. 8). Fields in greyscale show the domain of stability of observed mineral paragenesis of the La Victoria, the Upper and Lower La Bocana units. (Notice that the sample AV-08-15 (Fig. 5c) indicates that the pre-anatectic thermal history is marked by the transition from andalusite to kyanite, suggesting burial of the La Victoria unit before the high-temperature event.(black arrow). The white and dashed arrow present the maximum P - T condition recorded in the rock. We suggest that these last P - T conditions could represent the geothermal gradient during Triassic times. (b) schematic structural log of the El Oro from the La Victoria unit to the South to the Piedras unit to the North.**Fig. 13. Schematic proposed** geodynamical model of the Ecuadorian margin at Triassic times.(a) middle Triassic period, south America is moving eastward and the margin is affected by S-type magmatism likely due to a steep to vertical slab; (b) early Late Triassic period, partial melting of the asthenosphere produces the emplacement of the MORB-type gabbro of the Piedras unit at crustal root level, and subsequent migmatization of the La Bocana unit; (c) Shortly after slab breakoff, subduction resumes and the Arenillas-Panupali blueschist unit is underplated.

Table 1. Characteristic mineral assemblages of studied samples with pseudosections. AV-08-15, AV-08-22b and PU-08-06 are also reported. GPS coordinates are in decimal degrees. I, inherited mineral; P, Peak thermal mineral; R, retrograde mineral. Mineral abbreviations used in figures and tables are from Kretz (1983).

Table 2. Representative electron microprobe analysis of garnet in the La Bocana garnet-bearing migmatitic samples. Structural formulae have been calculated on the basis of 12 atoms oxygen; calculated end members shown in the table are used to calculate the P - T conditions in pseudosections. La Vic., La Victoria, U. B., Upper La Bocana, L. B., Lower La Bocana.

Table 3. Representative electron microprobe analysis of biotite in metasediments and migmatites. Structural formulae have been calculated on the basis of 11 atoms oxygen; analyzed samples are located in Fig. 2. La Vic., La Victoria, U. B., Upper La Bocana, L. B., Lower La Bocana.

Table 4. Representative electron microprobe analysis of muscovite in metasediments and migmatites. Structural formulae have been calculated on the basis of 11 atoms oxygen; analyzed samples are located in Fig. 2. La Vic., La Victoria, U. B., Upper La Bocana, L. B., Lower La Bocana.**Table 5.** Representative electron microprobe analysis of plagioclase in metasediments and migmatites. Structural formulae have been calculated on the basis of 32 atoms oxygen; analyzed samples are located in Fig. 2. La Vic., La Victoria, U. B., Upper La Bocana, L. B., Lower La Bocana.

Table 6. RSCM thermometry results of studied samples. Analytical uncertainty on the estimation of temperature are indicated at 1σ while the calibration error for each sample on the determination of absolute temperature is of ± 50 °C.

Table 7. Bulk rock composition used in this study. < LD, below limit of detection.

Table 8. Solution and end-members used for the pseudosections (see Fig.7 & 8). See Perple_X documentation (<http://www.perplex.ethz.ch>) for more detailed informations.

Table 9. LA-ICPMS U-Pb analytical data for migmatitic rocks of La Bocana unit.

Table 10. SHRIMP U-Pb analytical data for migmatitic rocks of La Bocana unit.

Fig. 1

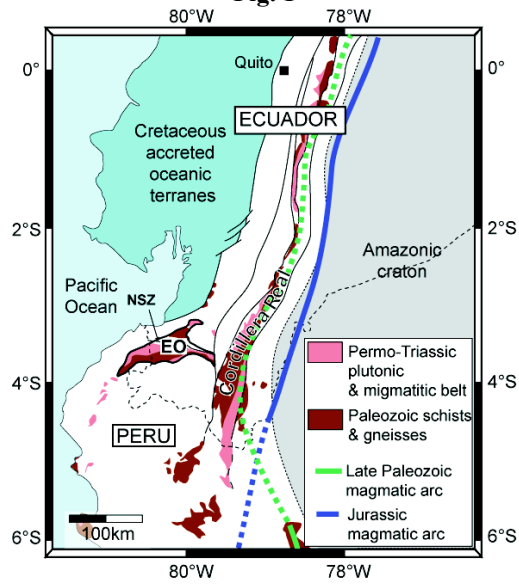


Fig. 2

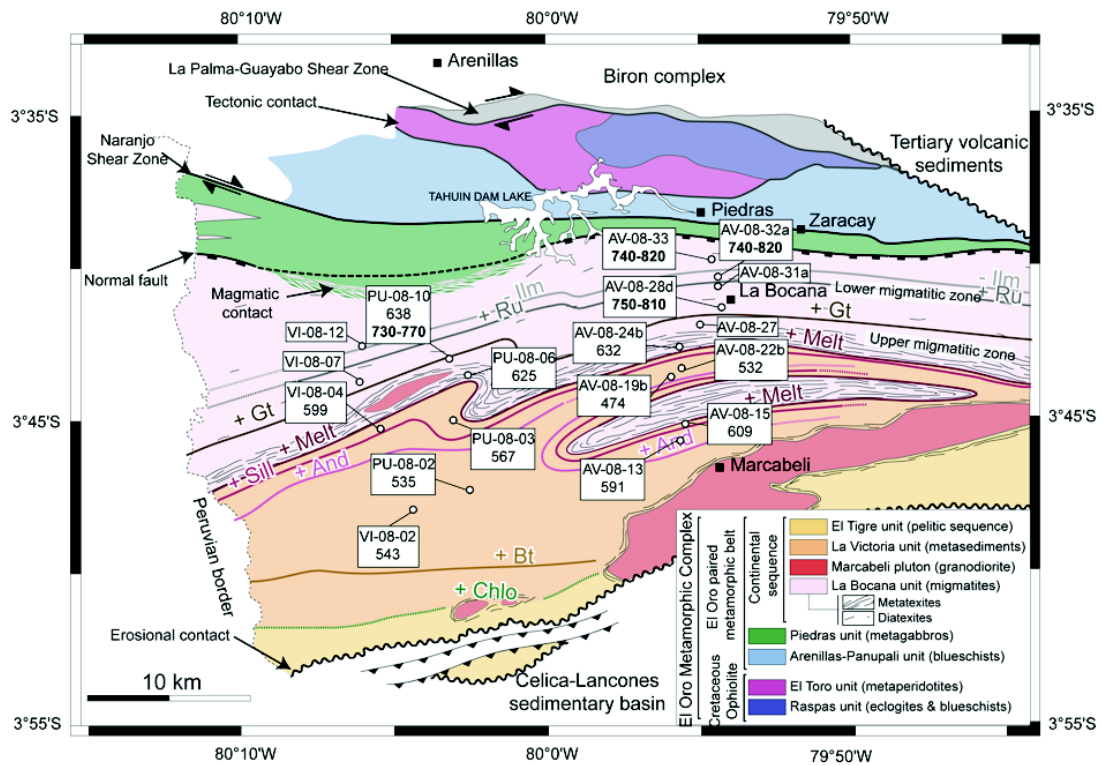


Fig. 3

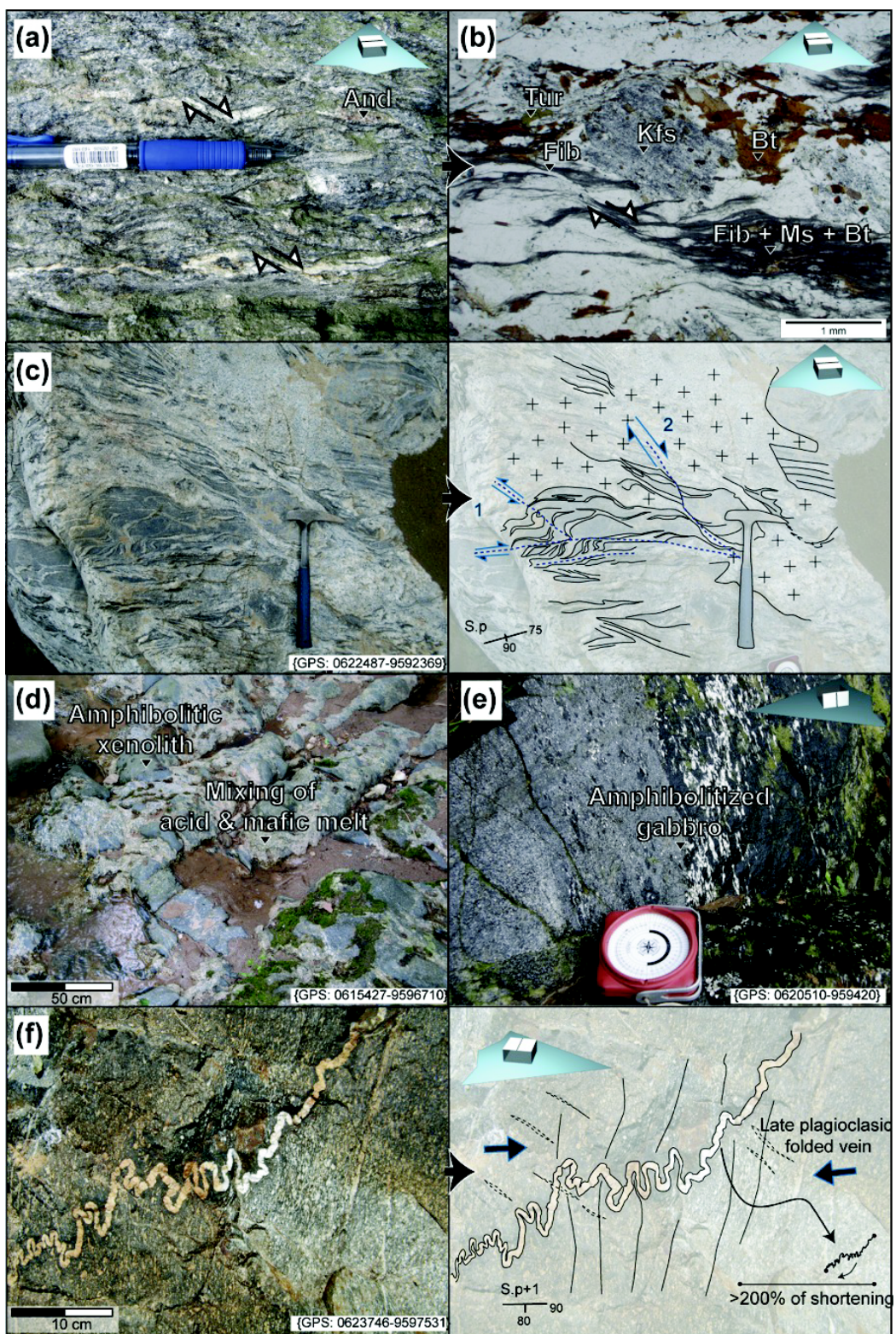


Fig. 4

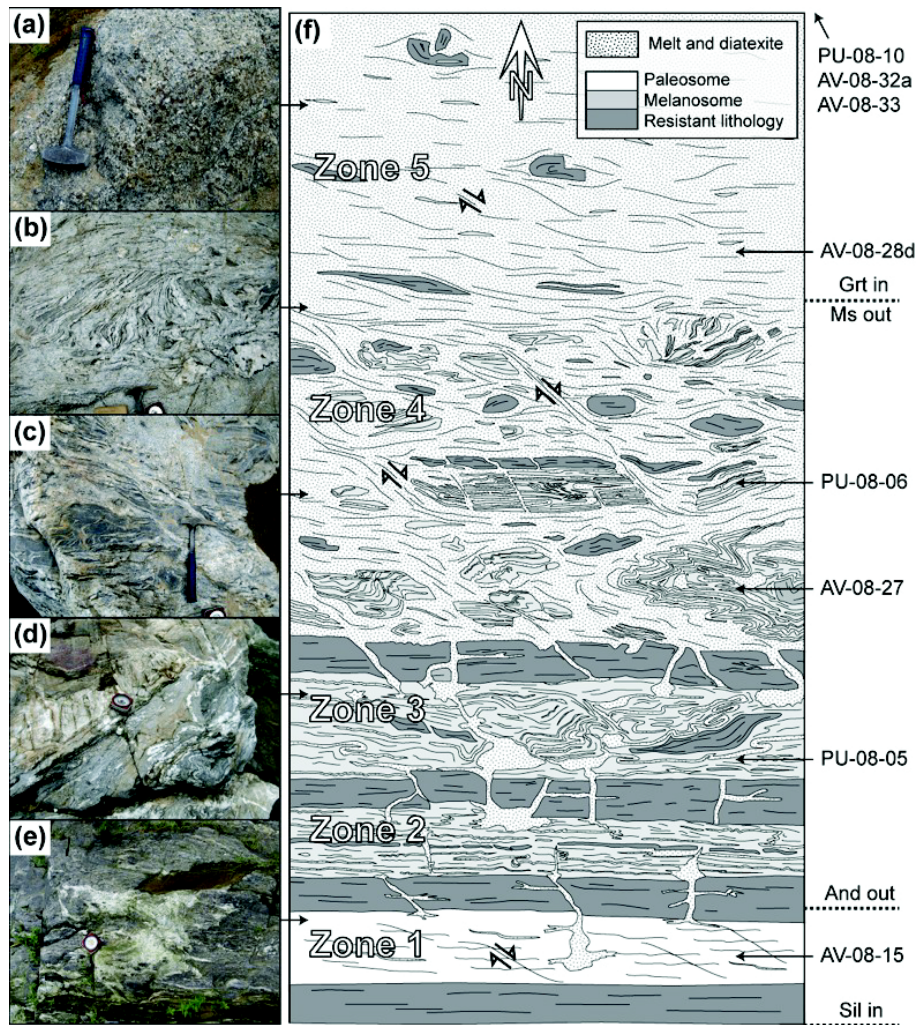


Fig. 5

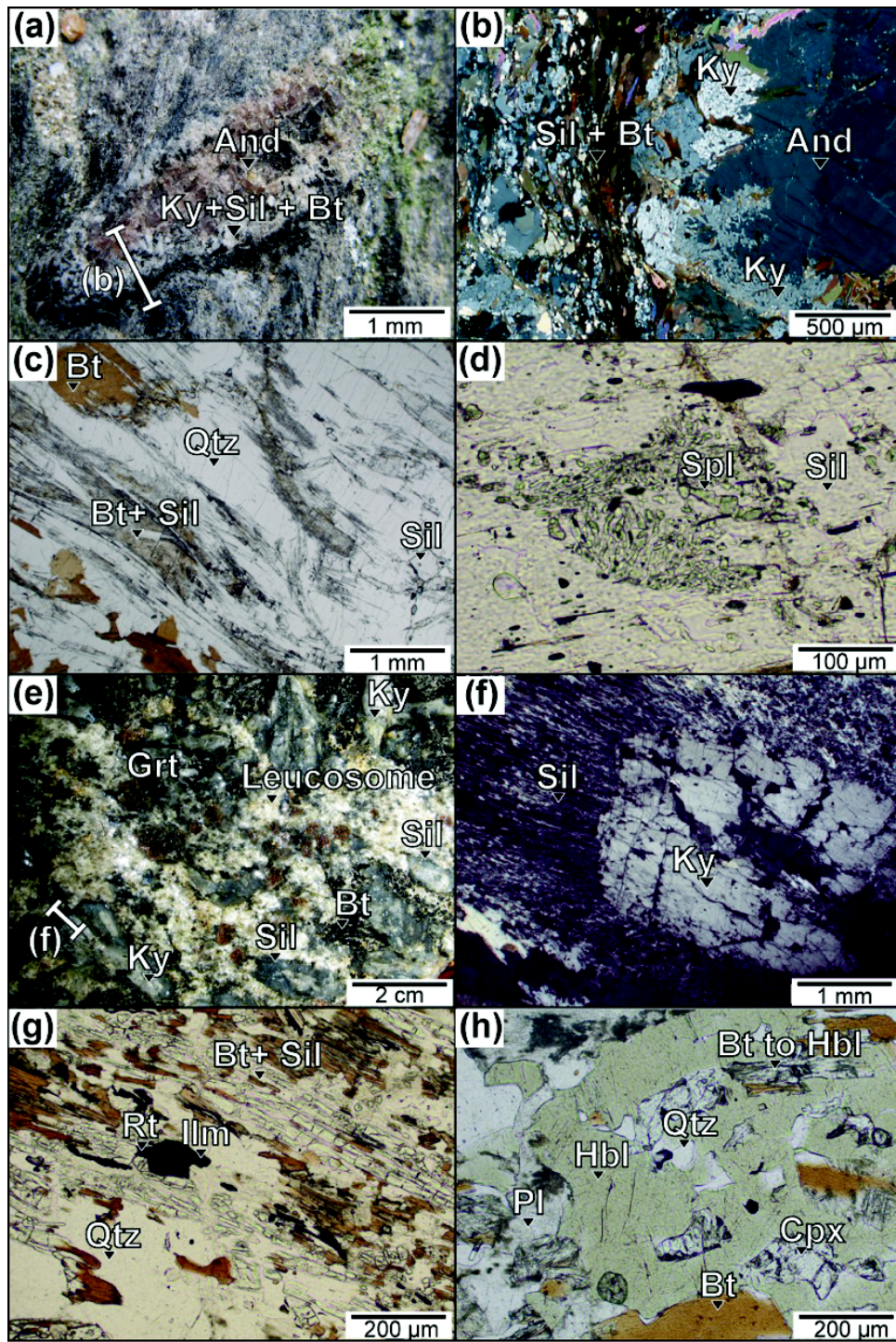


Fig. 6

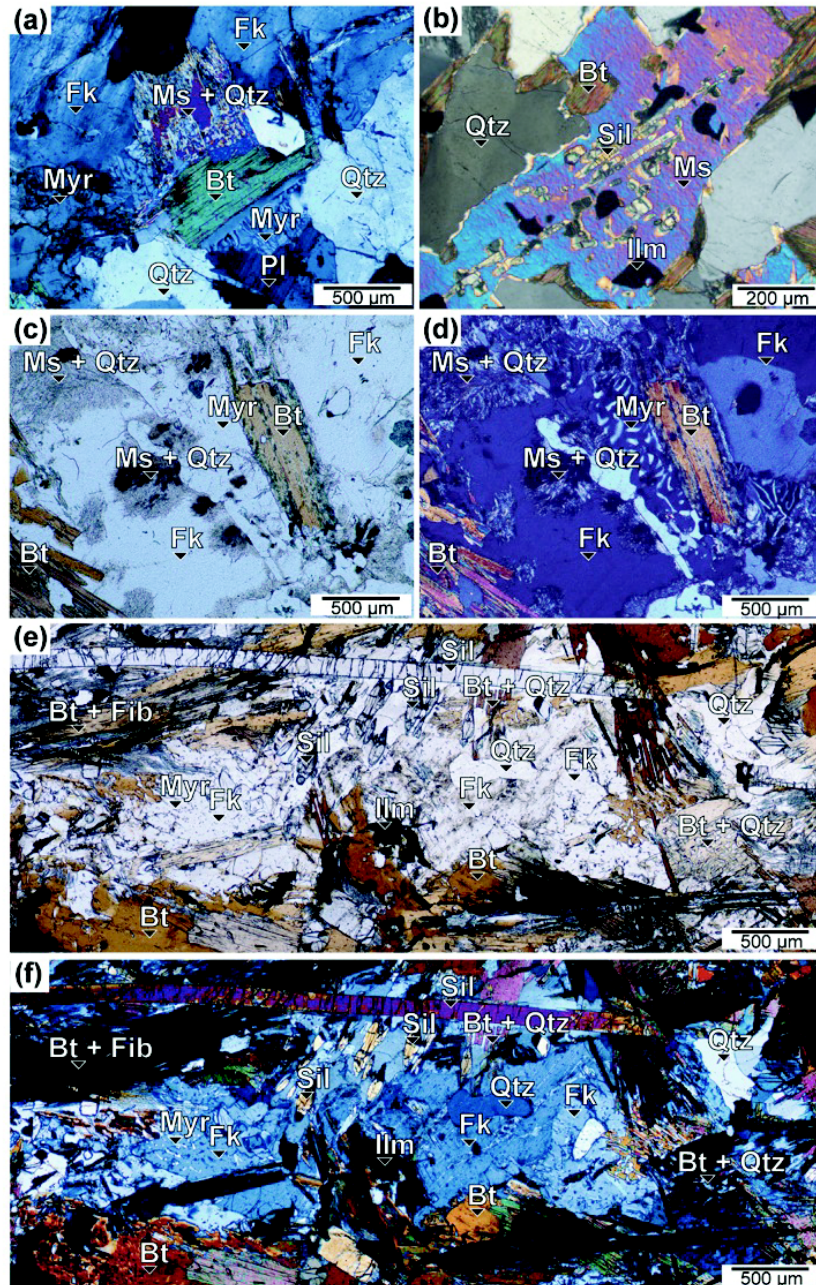


Fig. 7

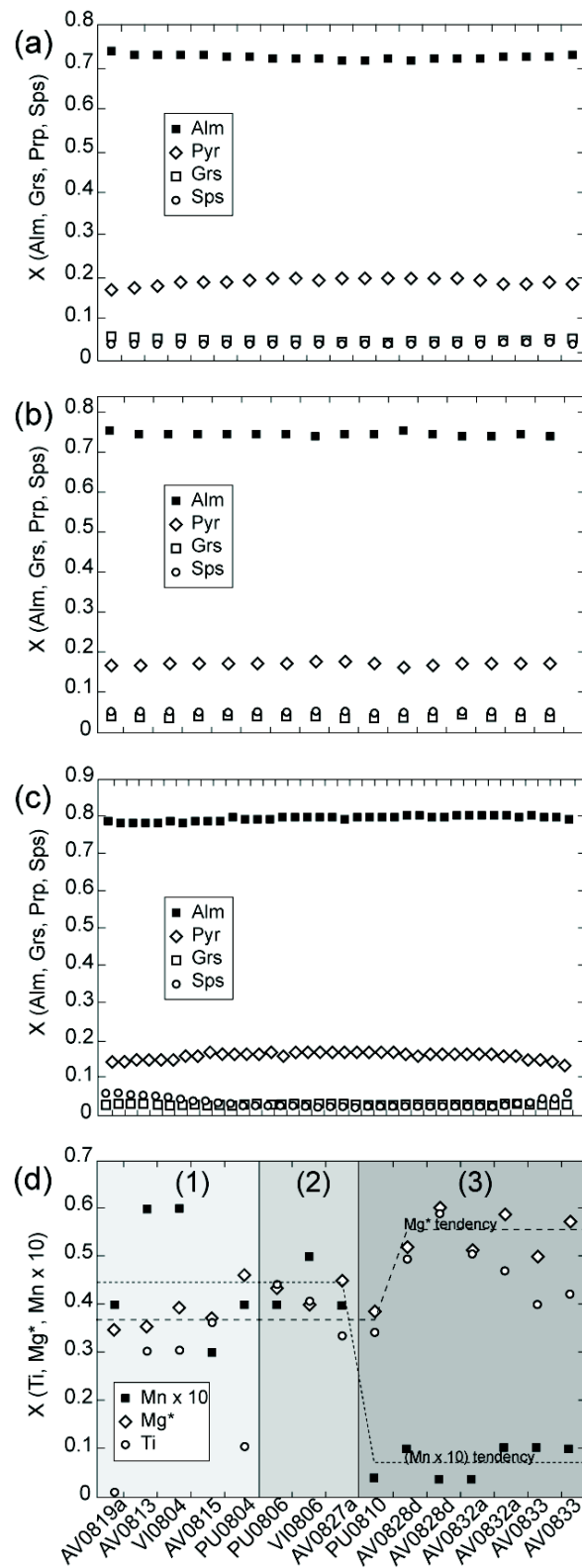


Fig. 8

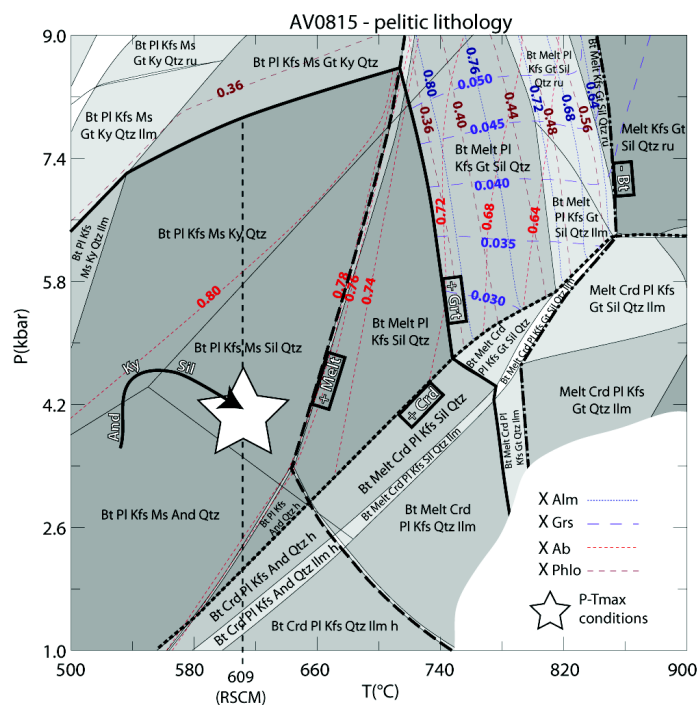


Fig. 9

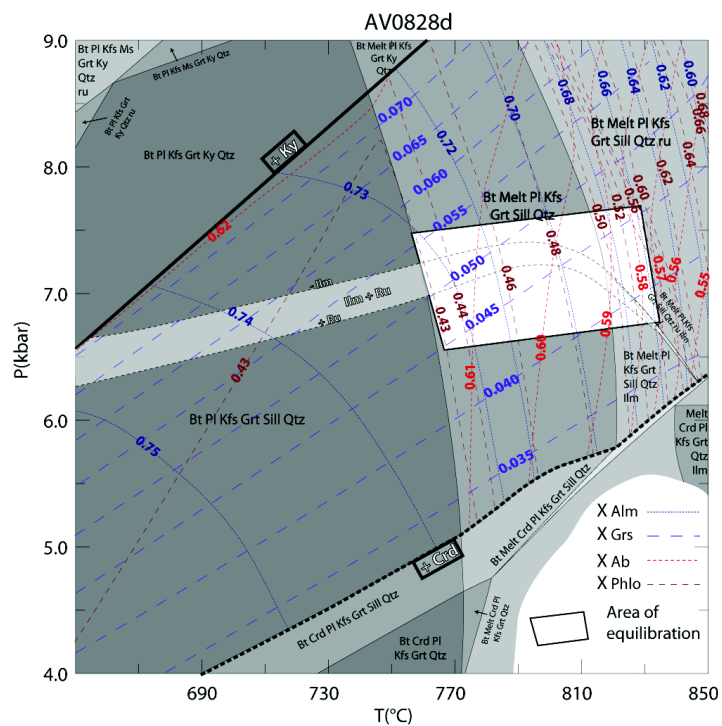


Fig. 10

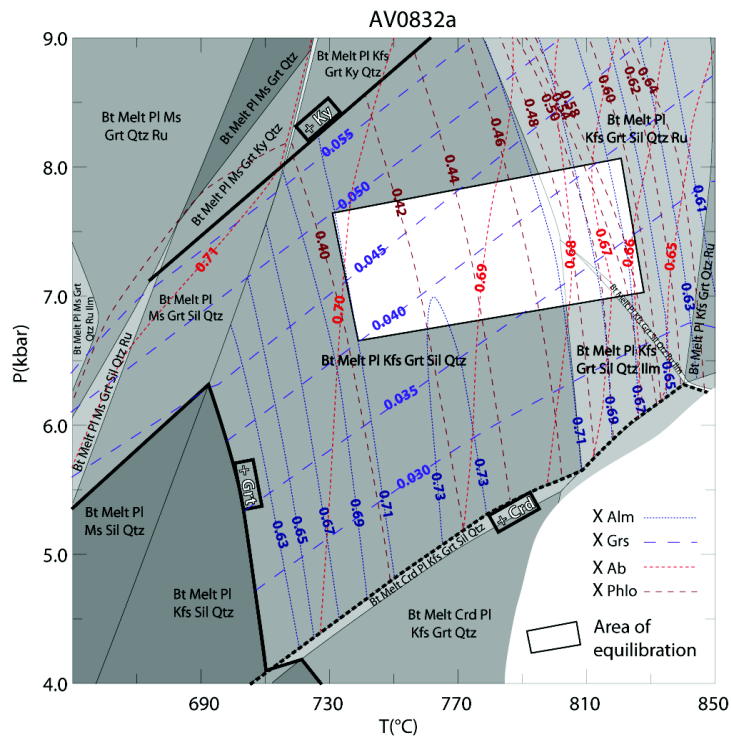


Fig. 11

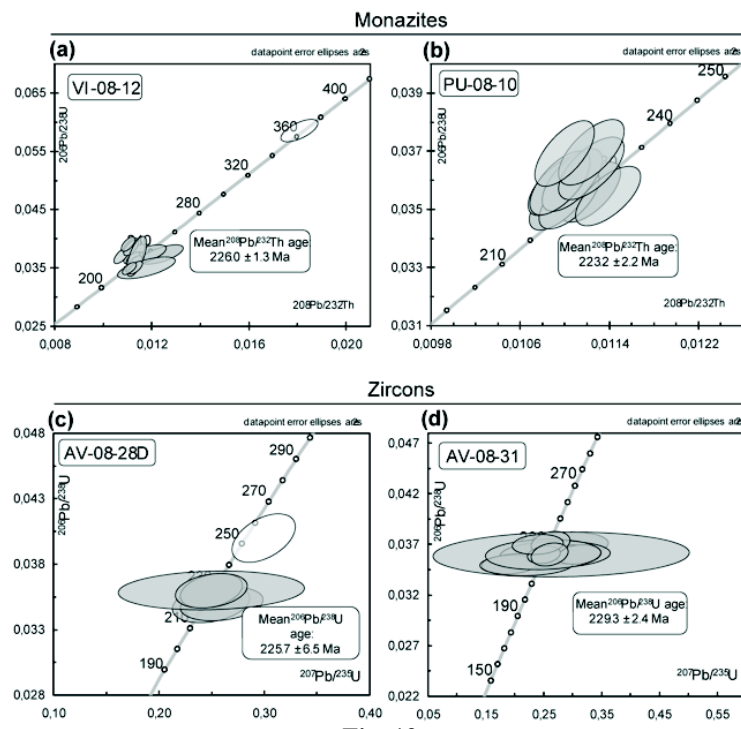


Fig. 12

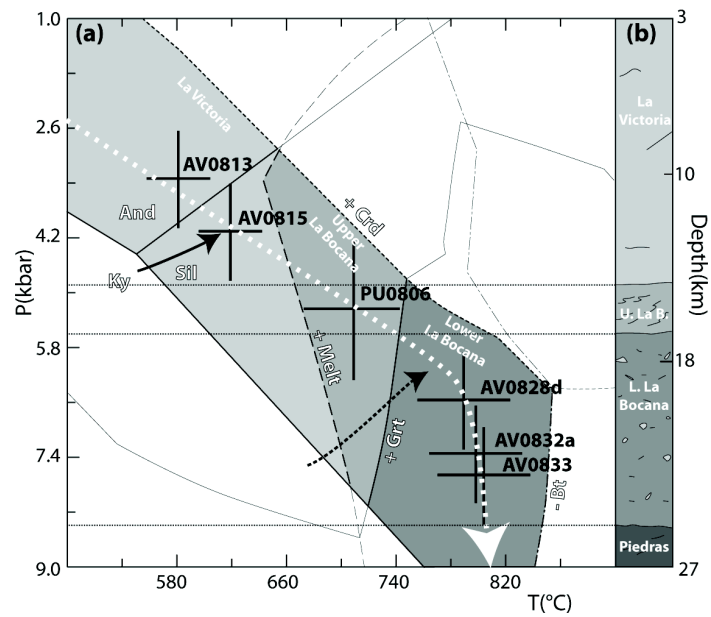
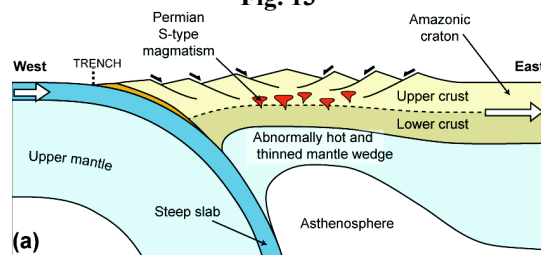
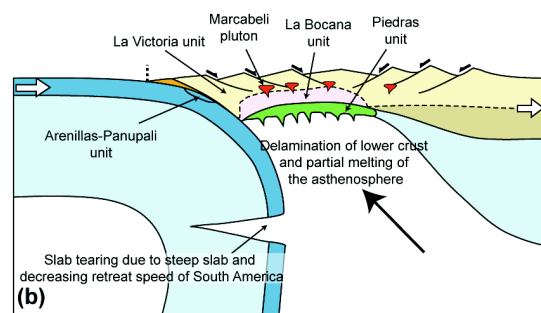


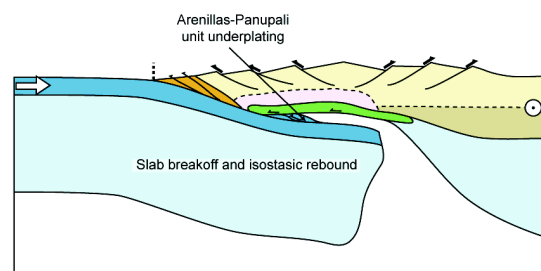
Fig. 13



EARLY TO MIDDLE TRIASSIC (250-235 Ma)



EARLY LATE TRIASSIC (235-225 Ma)



LATE TRIASSIC (225-220 Ma)

Table 5.

Sample	AV-08-13	AV-08-15	PU0806	AV0828d	AV0828d	PU0810	PU0810	AV0832a	AV0833
Unit	La Vic.	La Vic.	U. B.	L. B.	L. B.	L. B.	L. B.	L. B.	L. B.
Position	Core	Core	Core	Schlieren	Leucosome	Schlieren	Leucosome	Schlieren	Schlieren
Na ₂ O	9.47	9.34	9.52	6.98	7.90	9.08	10.20	8.23	7.92
MgO	0.00	0.00	0.00	0.00	0.00	0.00	0.00	0.00	0.00
Al ₂ O ₃	22.68	22.93	24.00	25.78	25.13	22.53	21.14	25.21	25.12
SiO ₂	63.36	63.62	62.71	59.39	60.27	63.90	65.72	60.42	59.87
K ₂ O	0.12	0.23	0.14	0.51	0.22	0.22	0.33	0.22	0.24
CaO	3.40	4.14	4.04	7.38	6.71	4.51	2.64	6.64	6.74
TiO ₂	0.00	0.02	0.02	0.02	0.00	0.04	0.02	0.02	0.05
MnO	0.00	0.04	0.03	0.04	0.01	0.00	0.00	0.03	0.01
FeO	0.00	0.04	0.21	0.24	0.04	0.05	0.00	0.03	0.03
Zr ₂ O ₃	0.00	0.02	0.00	0.00	0.00	0.00	0.00	0.00	0.00
Total	99.04	100.38	100.66	100.35	100.28	100.33	100.06	100.80	99.96
Numbers of ions on the basis of 32 O									
Si	11.38	11.42	11.26	10.66	10.82	11.47	11.80	10.85	10.75
Al	4.80	4.85	5.08	5.46	5.32	4.77	4.47	5.33	5.31
Fe(ii)	0.00	0.01	0.03	0.04	0.01	0.01	0.00	0.00	0.00
Ca	0.65	0.80	0.78	1.42	1.29	0.87	0.51	1.28	1.30
Na	3.30	3.25	3.31	2.43	2.75	3.16	3.55	2.86	2.76
K	0.03	0.05	0.03	0.12	0.05	0.05	0.08	0.05	0.05
Ba	0.00	0.00	0.00	0.00	0.00	0.00	0.00	0.00	0.00
TOTAL	20.15	20.38	20.49	20.12	20.23	20.33	20.41	20.38	20.17
Endmembers (mol.%)									
Anorthite	16.46	19.42	18.84	35.77	31.54	21.27	12.27	30.45	31.56
Albite	82.85	79.29	80.37	61.27	67.21	77.52	85.89	68.35	67.11
Orthose	0.69	1.29	0.79	2.97	1.26	1.22	1.84	1.21	1.33

Table 6.

Sample	n° analysis	R2	Std	T °C	1σ
				Beyssac (2002)	
AV0813	9	0.11	0.03	591	4.73
AV0815	7	0.07	0.01	609	2.47
AV0819b	10	0.38	0.05	474	6.93
AV0822b	8	0.24	0.04	532	5.79
AV0824b	4	0.02	0.01	632	1.09
PU0802	9	0.24	0.05	535	7.96
PU0803	8	0.17	0.04	567	6.06
PU0806	3	0.04	0.01	625	1.65
PU0811	3	0.01	0.01	638	2.03
VI0802	6	0.22	0.04	543	6.60
VI0804	5	0.09	0.03	599	5.77

Table 7.

Sample	AV-08-28d	AV-08-32a	AV-08-33	AV-08-13	AV-08-15	PU-08-10
SiO ₂	69.2	69.64	71.68	73.85	59.54	61.3
TiO ₂	0.78	0.8	0.66	0.52	0.90	0.94
Al ₂ O ₃	14.28	13.76	12.4	13.25	19.23	15.55
FeO	5.29	4.81	5.47	3.34	7.16	8.59
MnO	0.08	0.07	0.12	0.06	0.08	0.09
MgO	1.89	1.73	1.69	0.99	2.12	2.05
CaO	1.76	1.77	1.81	0.78	0.56	0.44
Na ₂ O	1.52	2.41	2	2.35	1.26	1.39
K ₂ O	2.25	2.61	2.21	3.36	4.53	3.74
P ₂ O ₅	0.2	<LD	<LD	<LD	1.75	0.39
LOI	2.15	1.63	1.22	1.58	2.17	3.11
Total	99.4	99.23	99.27	100.08	99.20	97.59

Table 8.

Phase	Solution model label in perpleX	End members	References
Chlorite	Chl(HP)	Clinochlore – daphnite – amesite – Al free chlorite	Holland & Powell. 1998
Plagioclase	Pl(h)	highalbite – anorthite	Newton et al 1981
Garnet	Gt(HP)	spessartine – grossular – pyrope – almandine	Holland & Powell. 1998
Cordierite	hCrd	Fe–cordierite – Mn–cordierite – cordierite	Holland & Powell. 1998
Melt	melt(HP)	H2O liquid – fayalite liquid – forsteriteliquid – albite liquid – anorthite liquid – K–feldsparliquid – Sillimanite liquid – Silicaliquid	Holland & Powell. 1998
Orthopyroxene	Opx(HP)	enstatite – ferrosilite	Holland & Powell. 1998
White–mica	Mica(CHA)	muscovite – celadonite – Fe–celadonite – paragonite – margarite	Holland & Powell. 1998
Staurolite	St(HP)	Fe–staurolite – Mg–staurolite – Mn–staurolite	Holland & Powell. 1998
Biotite	Bio(TCC)	Mn–biotite – Ti biotite – annite – phlogopite – eastonite – Fe3+–Biotite	Tajcmanova et al., 2009

Table 9.

Sample	Analysis_#	Pb (ppm)	Th (ppm)	U (ppm)	Th/U	$^{208}\text{Pb}/^{232}\text{Th}$	2 σ error $^{208}\text{Pb}/^{232}\text{Th}$	$^{206}\text{Pb}/^{238}\text{U}$	2 σ error $^{206}\text{Pb}/^{238}\text{U}$	Age (Ma) $^{208}\text{Pb}/^{232}\text{Th}$	2 σ error $^{208}\text{Pb}/^{232}\text{Th}$	Position
VI-08-12	1	20	344	553	0.6	0.01173	0.00072	0.03728	0.00138	235.7	14.5	core
	2	460	40053	1726	23.2	0.01077	0.00026	0.03713	0.00110	216.5	5.0	core
	3	492	40421	1951	20.7	0.01123	0.00026	0.03852	0.00106	225.7	5.1	core
	4	494	45777	782	58.5	0.01141	0.00026	0.03770	0.00114	229.2	5.2	core
	5	660	54308	3344	16.2	0.01114	0.00026	0.03878	0.00108	224.0	5.0	core
	6	32	507	917	0.6	0.01179	0.00098	0.03503	0.00152	236.9	19.5	core
	7	599	51791	1969	26.3	0.01135	0.00024	0.03612	0.00092	228.1	4.8	core
	8	645	53487	2881	18.6	0.01135	0.00024	0.03658	0.00092	228.1	4.8	core
	9	783	52372	8674	6.0	0.01118	0.00024	0.03546	0.00086	224.6	4.7	core
	10	660	47882	5640	8.5	0.01124	0.00024	0.03666	0.00090	225.9	4.7	core
	11	56	601	987	0.6	0.01810	0.00062	0.05861	0.00158	362.5	12.3	core
	12	545	45829	2298	19.9	0.01132	0.00024	0.03599	0.00092	227.6	4.8	core
	13	729	62434	2600	24.0	0.01115	0.00024	0.03844	0.00114	224.1	4.8	core
	14	69	5819	213	27.4	0.01139	0.00034	0.03698	0.00284	229.0	6.9	core
	15	516	42647	2440	17.5	0.01134	0.00024	0.03504	0.00088	228.0	4.8	core
	16	606	52860	2545	20.8	0.01109	0.00024	0.03491	0.00090	223.0	4.7	core
	17	552	44673	2876	15.5	0.01104	0.00024	0.03910	0.00100	221.8	4.6	core
PU-08-10	1	574	45262	3778	12.0	0.01123	0.00022	0.03560	0.00084	225.8	4.6	core
	2	651	45939	6723	6.8	0.01095	0.00022	0.03531	0.00084	220.2	4.5	core
	3	649	46894	6276	7.5	0.01094	0.00022	0.03581	0.00084	219.9	4.5	core
	4	633	48186	5208	9.3	0.01104	0.00022	0.03535	0.00084	221.8	4.5	core
	5	574	45428	3680	12.3	0.01107	0.00022	0.03602	0.00088	222.5	4.5	core
	6	465	38568	2501	15.4	0.01096	0.00022	0.03591	0.00090	220.4	4.5	core
	7	535	32502	6709	4.8	0.01139	0.00024	0.03546	0.00084	228.9	4.7	core
	8	497	30691	6063	5.1	0.01124	0.00024	0.03642	0.00088	226.0	4.6	core
	9	851	53582	1688	31.8	0.01124	0.00024	0.03697	0.00092	225.9	4.6	core
	10	868	48776	2888	16.9	0.01100	0.00022	0.03692	0.00092	221.2	4.5	core

Table 10.

Sample	Analysis_#	Th (ppm)	U (ppm)	Th/U	$^{207}\text{Pb}/^{206}\text{Pb}$	2σ error $^{208}\text{Pb}/^{232}\text{Th}$	$^{206}\text{Pb}/^{238}\text{Pb}$	2σ error $^{206}\text{Pb}/^{238}\text{Pb}$	$^{207}\text{Pb}/^{235}\text{Pb}$	2σ error $^{207}\text{Pb}/^{235}\text{Pb}$	$^{208}\text{Pb}/^{206}\text{Pb}$	2σ error $^{208}\text{Pb}/^{206}\text{Pb}$	Age (Ma)	2σ error $^{206}\text{Pb}/^{238}\text{U}$	Posi
AV-08-31	1	27	262	0.1	0.0507	5.9	0.037	1.4	0.29	10.2	0.053	6.9	233	3	rir
	2	19	297	0.1	0.1248	3.5	0.036	2.5	0.28	32.4	0.027	2.8	226	6	coi
	3	19	278	0.1	0.0501	6.2	0.036	1.5	0.27	14.4	0.035	8.6	230	3	rir
	4	189	119	1.6	0.0630	5.2	0.107	1.3	0.94	7.4	0.515	1.6	653	8	coi
	5	12	219	0.1	0.0479	6.6	0.036	1.1	0.29	5.5	0.047	10.3	231	2	rir
	6	4	249	0.0	0.0505	6.0	0.035	1.1	0.19	10.3	-0.022	17.0	223	2	coi
	7	16	236	0.1	0.0545	6.1	0.035	1.3	0.22	15.0	0.006	8.1	224	3	rir
	8	55	90	0.6	0.0650	4.7	0.129	1.3	1.16	4.9	0.200	2.8	782	9	coi
	9	23	224	0.1	0.0494	6.3	0.036	1.1	0.31	5.1	0.067	7.3	231	2	rir
	10	174	624	0.3	0.0584	2.4	0.078	1.0	0.62	2.6	0.098	1.9	482	5	rir
	11	24	507	0.0	0.0602	2.6	0.095	2.7	0.80	3.9	0.018	4.6	583	15	coi
	12	435	125	3.5	0.0622	4.4	0.095	1.3	0.91	8.0	1.114	1.2	584	7	coi
	13	296	146	2.0	0.0631	4.1	0.094	2.3	0.81	4.7	0.650	1.4	577	13	coi
	14	26	240	0.1	0.0505	6.1	0.036	1.7	0.25	16.3	0.038	7.0	229	4	coi
	15	116	180	0.6	0.1143	1.3	0.513	2.7	8.06	3.0	0.162	8.4	2671	59	coi
	16	137	582	0.2	0.1472	4.7	0.358	1.0	7.27	4.8	0.071	6.2	1974	17	coi
	17	27	283	0.1	0.0519	5.1	0.037	1.3	0.26	5.3	0.038	6.1	232	3	rir
	18	55	450	0.1	0.0496	4.5	0.036	1.0	0.25	4.6	0.038	5.2	228	2	rir
	19	89	172	0.5	0.0492	6.3	0.037	1.1	0.24	7.5	0.155	3.6	236	3	coi
	20	28	309	0.1	0.0513	5.0	0.036	1.3	0.26	5.1	0.033	6.2	231	3	rir

Table 10 (continued).

AV-08-28d															
	1	26	302	0.1	0.0572	3.9	0.052	5.3	0.41	6.6	0.032	5.2	329	17	rim
	2	391	377	1.0	0.0704	2.1	0.169	3.7	1.64	4.2	0.322	4.9	1009	34	core
	3	115	286	0.4	0.0653	2.9	0.087	1.5	0.78	3.3	0.132	4.9	538	8	rim
	4	50	1745	0.0	0.0561	1.7	0.072	2.0	0.56	2.6	0.008	7.3	447	9	core
	5	62	255	0.2	0.0645	5.1	0.085	3.7	0.76	6.3	0.074	3.7	525	19	core
	6	84	460	0.2	0.0545	3.7	0.040	1.9	0.30	4.1	0.056	3.7	252	5	core
	7	18	242	0.1	0.0516	5.7	0.035	1.7	0.25	6.0	0.021	9.2	221	4	rim
	8	77	186	0.4	0.0496	5.8	0.089	2.9	0.60	6.5	0.116	2.6	547	15	core
	9	11	203	0.1	0.0546	6.0	0.035	1.5	0.26	6.2	0.019	10.3	223	3	rim
	10	26	57	0.5	0.1926	4.5	0.538	1.8	14.28	4.9	0.140	2.1	2774	41	core
	11	22	591	0.0	0.0562	2.7	0.071	2.6	0.55	3.7	0.011	4.8	443	11	rim
	12	31	74	0.4	0.0777	4.0	0.164	1.7	1.75	4.4	0.140	3.1	977	15	core
	13	9	213	0.0	0.0499	14.4	0.036	1.7	0.25	14.5	0.012	10.9	226	4	rim
	14	45	78	0.6	0.0567	5.8	0.087	2.7	0.68	6.4	0.188	3.3	536	14	core
	15	40	383	0.1	0.0496	4.6	0.036	1.5	0.25	4.8	0.033	5.2	228	3	rim
	16	21	51	0.4	0.0744	20.4	0.143	3.6	1.47	20.7	0.114	3.7	863	29	core
	17	28	238	0.1	0.0621	3.8	0.072	2.3	0.62	4.5	0.073	3.6	451	10	rim
	18	16	243	0.1	0.0492	5.4	0.036	1.5	0.25	5.6	0.023	8.1	229	3	rim